Probing Star Formation with High Resolution Spectroscopy: Multiplicity, Disk Braking, and Accretion in Chamaeleon I and Taurus-Auriga

by

Duy Cuong Nguyen

A thesis submitted in conformity with the requirements
for the degree of Doctor of Philosophy
Graduate Department of Astronomy and Astrophysics
University of Toronto

Abstract

Probing Star Formation with High Resolution Spectroscopy: Multiplicity, Disk Braking, and Accretion in Chamaeleon I and Taurus-Auriga

Duy Cuong Nguyen
Doctor of Philosophy
Graduate Department of Astronomy and Astrophysics
University of Toronto
2010

In this thesis, we focus on obtaining and interpreting observational information on (i) the role of multiplicity on the properties of young stars; (ii) the early evolutionary influence of circumstellar disks; and (iii) the nature of accretion in young systems. To facilitate this research, we conducted an extensive multi-epoch high-resolution spectroscopic survey at optical wavelengths (3 200–10 000 Å) of ~ 200 T Tauri stars in the ~ 2 Myr old Chamaeleon I, and Taurus-Auriga star-forming regions with the Magellan Inamori Kyocera Echelle (MIKE) spectrograph on the Magellan Clay 6.5 m telescope.

From the spectroscopic data, we identify eight close binaries and four close triples, of which three and two, respectively, are new discoveries. We find that the multiplicity fraction for Cha I and Tau-Aur are similar to each other, and to the results of field star surveys. The frequency of systems with close companions in our sample is not seen to depend on primary mass or accretion.

We probed for evidence of disk braking. We did not see a statistically significant difference between the distribution of rotational velocities with the presence of an inner disk. Also, our findings show that F–K stars in our sample have larger rotational velocities and specific angular momentum than M stars.

We also analyzed accretion variability in our sample using the Hα 10% width and the Ca II-λ8662 line flux as accretion diagnostics. We find that the maximum extent of accretion variability in our sample was reached on timescale of a few days, indicating that rotation could significantly contribute to the variability.

Acknowledgements

By completing this thesis, I have fulfilled a lifelong dream of contributing significantly to the field of astrophysics. There are many people who have helped me to achieve this goal.

First, I would like to acknowledge the tireless support and guidance of my supervisors Ray Jayawardhana and Marten van Kerkwijk. This thesis could not have come to fruition without their outstanding efforts and endless dedication. Thank you so very much.

I would like to thank Alexis Brandeker for his remarkable acumen in our collaborations, for his charming quick wit that can wonderfully lighten any mood, and for teaching me how to drive standard transmission. My thanks to Aleks Scholz for always being a dependable source of knowledge, for hosting the most academically productive and intensive several weeks I have had yet, and for always keeping my feet on the ground even when my head is in the clouds. My sincere thanks to Brian Lee for always being supportive, and for going above and beyond the call of duty when I have needed assistance. To David Lafrenière and Vincent Geers for very useful discussions.

My thanks to Norm Murray for extraordinary insights that were invaluable for this work. To Christine Clement, Christopher Matzner, Dae-Sik Moon, John Percy, and Slavek Rucinski for some brilliant mentoring.

Many thanks to my peers Kaitlin Kratter, and Fernando Peña for always looking out for me, and for keeping me on target when I have strayed. Thank you to my fellow graduate students including but not limited to Ivana Damjanov, Daniela Gonçalves, Elizabeth Harper-Clark, Ilana MacDonald, Erin Mentuch, Arabindo Roy, Andrew Shannon, and Sherry Yeh who have made my time in graduate school an enjoyable and productive experience.

To the amazing support staff for making my life so much easier. Marc Goodman, Angie Ho, Lee Robbins, and Hugh Zhao, your assistance was very much appreciated.

Last but certainly not least, all my love and thanks to January Quynh-Nhu Nguyen whose enduring support and patience I will treasure forever.

This material is based upon work supported by the National Sciences and Engineering Research Council of Canada, the Government of Ontario, the Estate of Walter John Helm, and the University of Toronto.

Contents

List of Tables

List of Figures

Chapter 1

Introduction

Why do we need to study star formation? An answer to this question is suggested by Donald Lynden-Bell, "By comparing what we now know about star formation with what other parts of astronomy need from us, we shall see what is still needed and put in perspective what has been achieved." (Lynden-Bell, 1977) Star formation is the mechanism which influences the structure and evolution of galaxies, the accumulation of heavy elements in the universe with time, and which is responsible for the creation of the planetary environments in which life in the universe has become possible. Star formation is indeed an important field of study.

Scientific interest in star formation dates back several centuries. In 1734, the Swedish scientist Emanuel Swedenborg first proposed the nebular hypothesis to explain the formation of the solar system. This hypothesis maintains that the solar system was formed from the gravitational collapse of a great solar nebula. This idea was developed further by the philosopher Immanuel Kant in his work *Allgemeine Naturgeschichte und Theorie des Himmels* (Universal History of Nature and Theory of Heaven) in which he speculated that observed nebulae may be regions of star and planet formation (Kant, 1755). Over a century later, the English physicist James Jeans showed that a gas cloud would undergo runaway contraction if it exceeded a critical mass or density for which the internal gas pressure of the cloud is insufficient to balance the force of gravity (Jeans, 1902). The Jeans criterion lays the physical groundwork for currently accepted scenarios of star formation.

It is now generally accepted that stars form by the gravitational contraction of dense cores in molecular clouds; the association of pre-main sequence stars with molecular cloud cores was shown observationally using data from the *Infrared Astronomy Satellite (IRAS)*

by Beichman et al. (1986). The best known model that describes the star formation process is that by Shu et al. (1987). Their model predicts the free-fall collapse from the inside-out of an initially static core following the prescriptions of Shu (1977) and Terebey et al. (1984). Regardless of the specific process, typical clouds must contract by many orders of magnitude to form a star. Because of the significant and rapid reduction in size, angular momentum transfer during the contraction is fairly inefficient. Consequently, any initial rotation of the cloud results in collapse to a disk, a multiple star system, or both (Hartmann, 2009). The collapse is eventually mediated when the heating from gravitational binding energy, released during the infall, increases the pressure of the condensing material sufficiently to resist further contraction. The protostellar phase begins at this point, and ends when most of the surrounding cloud has either been dispersed or accreted. Next, the star enters the T Tauri phase.

1.1 T Tauri Stars

T Tauri stars will be the main focus of this thesis. The formal contraction ages of T Tauri stars range from ~ 0.2–$20\,\mathrm{Myr}$ (Shu et al., 1987). These objects are low-mass ($M \lesssim 2\,M_\odot$) pre-main sequence stars, having effective surface temperatures of $\sim 3\,000$–$7\,000\,\mathrm{K}$ which correspond to stellar spectral types of F–M (Joy, 1945; Herbig, 1962; Bertout, 1989). These attributes contrast those of Herbig Ae/Be stars (Herbig, 1960) which are higher-mass $\sim$2–$10\,M_\odot$ pre-main sequence stars with effective temperatures of $\sim 8\,000$–$30\,000\,\mathrm{K}$. These mass ranges are not exact because the classification depends on effective temperature or spectral type, which can vary substantially as the star evolves onto the main sequence.

1.1.1 Accretion Variability

T Tauri stars were first recognized by Joy (1945), and were initially classified as a new type of variable star. Indeed, the spectra of T Tauri stars are characterized by high variability and prominent emission lines (e.g. Rydgren et al., 1976), which can be traced to changes in continuum excess flux caused by varying accretion flow from a circumstellar disk (Hartigan et al., 1991). The hot spots formed by gas accretion are one of the most important sources of variability in young stars. This has been revealed by several photometric monitoring campaigns (e.g. Herbst et al., 1994; Bouvier et al., 1995; Fernandez

& Eiroa, 1996). However, it remains unclear to what extent the photometric and spectroscopic variability seen in T Tauri stars is related directly to accretion rate changes. This issue can be addressed by spectroscopic monitoring, but spectroscopic studies to date have been limited to small samples.

Furthermore, recent observations have shown a correlation between inferred mass accretion rate and central object mass of $\dot{M} \propto M^{\alpha}$, with $\alpha \sim 2$ (e.g. Muzerolle et al., 2003; Natta et al., 2004; Mohanty et al., 2005). However, all plots of $\dot{M}$ as a function of M show a large scatter. The basic question about this scatter in the $\dot{M}$ vs. M relation is whether it is due to object-to-object variations (i.e., the accretion rate for any individual object remains stable), or due to variable accretion rates over time in any given object (Scholz & Jayawardhana, 2006). Strong changes in accretion related lines have been reported for some objects, e.g., for the brown dwarf 2MASSW J1207334–393254 (Scholz et al., 2005; Stelzer et al., 2007), but it remains unclear if such variations are commonplace. Since most previous studies have been based on single-epoch measurement of accretion rates, it has been impossible thus far to address this issue.

1.1.2 Disk Braking

A large number of studies have explored the connection between the presence of disks and rotation in young stars to provide insight into the process known as disk braking. Disk braking is defined here as a process that provides rotational braking based on magnetic coupling between a star and its disk. The observational evidence for disk braking is somewhat inconsistent. Several photometric studies, e.g., Edwards et al. (1993) and Herbst et al. (2002), have found a correlation between rotational properties and near-infrared color excess, suggestive of disks, while other groups fail to detect such a correlation, e.g., Stassun et al. (1999).

Recent studies using *Spitzer Space Telescope* mid-infrared observations of the Orion Nebula Cluster (~ 1 Myr) and NGC 2264 (~ 2–3 Myr) indicate that stars with longer rotation periods are more likely than those with short periods to have infrared excesses (Rebull et al., 2006; Cieza & Baliber, 2007). However, both near-infrared and mid-infrared signatures suggest the presence of a dusty disk and not the coupling between star and disk as required by the disk braking scenario.

A more sensible diagnostic to correlate with stellar rotational velocities is on-going accretion which signifies a direct link between the inner disk and the central star. A

recent spectroscopic study of disk accretion in 41 low-mass young stars by Jayawardhana et al. (2006) found evidence of a possible accretion–rotation connection in the η Cha (~ 6 Myr) and TWA (~ 8 Myr) associations. However, they caution that those results should be checked with larger samples given the small number of accretors surveyed.

1.1.3 Multiplicity

Observations have long since revealed the prevalence of binary and multiple systems for low-mass field stars (e.g. Duquennoy & Mayor, 1991; Fischer & Marcy, 1992). In addition, early multiplicity surveys have shown that young stars are ubiquitously found in multiple systems and revealed an environment-dependent trend; for reviews see Mathieu et al. (2000) and (Duchêne et al., 2007). The multiplicity rates in stellar clusters are in agreement with that observed in main sequence field stars. In contrast, the sparsest T Tauri populations show about twice the multiplicity excess relative to low-mass field stars.

Simulations by Delgado-Donate et al. (2004) suggest that the companion frequency decreases during the first few Myr, since many of the initial multiple systems are unstable. Furthermore, models predict that the binary fraction is higher among higher mass stars (Goodwin et al., 2004). This trend of increased multiplicity with increasing primary mass has been established observationally by imaging surveys (Lafrenière et al., 2008).

Most surveys of young stars to date have been primarily done through high resolution imaging and are sensitive to companions in wide orbits, but not to those in close orbits. This has left open questions of whether the trends and statistics we observe in the population of young resolved binaries also apply their spectroscopic counterparts.

1.2 Outline of Thesis

In this thesis, we present the results of an extensive multi-epoch spectroscopic survey of several hundred T Tauri stars in nearby star-forming regions. The major source of data for this work is high-resolution optical spectra taken with the MIKE echelle spectrograph on the Magellan Clay 6.5 m telescope. This survey fulfills the previously established need for a large sample of spectroscopic data of T Tauri stars taken at multiple times in order to (i) monitor changes in accretion of young stars, (ii) provide more precise statistics to test the disk braking scenario, and (iii) improve the detection of close companions

at young ages. In addition, our general aim is to determine the relationships between the physical properties of T Tauri stars such as mass, accretion, disk presence, stellar rotation, and multiplicity. We present our findings essentially in order of progressively increasing complexity of the required data analysis.

In Chapter 2, we investigate the variability of accretion in a sample of 40 classical T Tauri stars in Chamaeleon I and Taurus-Auriga. As accretion indicators, we use the full-width of Hα at 10% of the peak, and the line flux of Ca II-λ8662, both known to correlate well with the accretion rate. In Chapter 3, we present a comprehensive study of accretion, rotation and disk signatures for 144 T Tauri stars in Cha I and Tau-Aur. For this investigation, we supplemented the Magellan/MIKE spectra with mid-infrared photometry from IRAC aboard the *Spitzer Space Telescope*. Applying the accretion and rotation analysis from the previous chapters, we report the results of an extensive multiplicity study of 212 T Tauri stars in Cha I and Tau-Aur in Chapter 4. We compare the binary fractions between various sub-populations in our sample determined by physical characteristics such as mass and accretion, as well as compare our overall results with those of field stars.

Chapter 2

How Variable is Accretion in Young Stars?

Published as:
"How Variable is Accretion in Young Stars?"
Nguyen, D. C., Scholz, A., van Kerkwijk, M. H., Jayawardhana, R., & Brandeker, A., 2009, ApJ, 694, L153

2.1 Abstract

We analyze the variability in accretion-related emission lines for 40 Classical T Tauri stars to probe the extent of accretion variations in young stellar objects. Our analysis is based on multi-epoch high-resolution spectra for young stars in Taurus-Auriga and Chamaeleon I. For all stars, we obtain typically four spectra, covering timescales from hours to months. As proxies for the accretion rate, we use the Hα 10% width and the Ca II-λ8662 line flux. We find that while the two quantities are correlated, their variability amplitude is not. Converted to accretion rates, the Ca II fluxes indicate typical accretion rate changes of 0.35 dex, with 32% exceeding 0.5 dex, while Hα 10% width suggests changes of 0.65 dex, with 66% exceeding 0.5 dex. We conclude that Ca II fluxes are a more robust quantitative indicator of accretion than Hα 10% width, and that intrinsic accretion rate changes typically do not exceed 0.5 dex on timescales of days to months. The maximum extent of the variability is reached after a few days, suggesting that rotation is the dominant cause of variability. We see a decline of the inferred accretion rates towards later spectral types, reflecting the $\dot{M}$ vs. M relationship. There is a gap between

accretors and non-accretors, pointing to a rapid shutdown of accretion. We conclude that the ~ 2 orders of magnitude scatter in the $\dot{M}$ vs. M relationship is dominated by object-to-object scatter instead of intrinsic source variability.

2.2 Introduction

Young low-mass stars that are still accreting while contracting towards the main-sequence are identified observationally with T Tauri stars (e.g. Bertout, 1989; Appenzeller & Mundt, 1989). One of their defining properties is variability (e.g. Knott, 1891; Joy, 1945; Rydgren et al., 1976), which can be traced to changes in continuum excess flux caused by varying accretion flow from a circumstellar disk (Hartigan et al., 1991); other possible sources of variability include cool spot rotation and extinction events. In addition to the continuum, this variability is seen in a number of emission lines, including the Hydrogen Balmer series, and has been attributed to rotation, variable accretion, and winds (e.g. Johns & Basri, 1995; Batalha et al., 2001; Alencar & Batalha, 2002; Alencar et al., 2005). Photometric monitoring campaigns for large numbers of objects have revealed that hot spots formed by gas accretion, co-rotating with the objects, are one of the most important sources of variability in young stars (e.g. Herbst et al., 1994; Bouvier et al., 1995; Fernandez & Eiroa, 1996). However, it remains unclear to what extent the photometric and spectroscopic variability seen in typical T Tauri stars is directly related to changes in the accretion rate. As we argue below, this issue can be addressed by spectroscopic monitoring, but so far spectroscopic studies have been limited to small samples.

Inferences about accretion are usually made in the framework of the magnetospheric accretion scenario (see the review by Bouvier et al., 2007). Recent observations have shown the presence of a correlation between inferred mass accretion rate and central object mass, extending over several orders of magnitude: $\dot{M} \propto M^{\alpha}$, with $\alpha \sim 2$ (e.g. Muzerolle et al., 2003; Natta et al., 2004; Mohanty et al., 2005). Apart from this correlation, all $\dot{M}$ vs. M plots feature a large scatter: at any given object mass, the accretion rates show a dispersion of about two orders of magnitude.

A number of ideas have been put forward to interpret these findings. The accretion rate vs. mass correlation has been attributed to a Bondi-Hoyle flow to the star-disk system (Padoan et al., 2005), to initial rotational velocities of collapsing cores (Dullemond et al., 2006), to a dispersion in disk parameters (Alexander & Armitage, 2006), to a complex magnetic field geometry (Gregory et al., 2006), and to a declining disk ionization

with stellar mass (Muzerolle et al., 2003; Mohanty et al., 2005). Alternatively, it has been argued that the correlation is not physical, but rather reflects selection effects; therefore, the dominant feature is the scatter itself (Clarke & Pringle, 2006). All these scenarios predict specific values for α (0–2) and specific properties of the scatter.

A basic question about the $\dot{M}$ vs. M relation is whether scatter around it is due to object-to-object variations (i.e. the accretion rate for any individual object remains mostly constant) or due to a variable accretion rate in any given object (Scholz & Jayawardhana, 2006). At least for some objects, strong changes in accretion related lines have been reported, e.g. for the brown dwarf 2MASSW J1207334-393254 (Scholz et al., 2005; Stelzer et al., 2007), but it is not clear if such variations are common or not. Since most previous studies were based on single-epoch measurements of accretion rates, it was impossible thus far to address this issue.

Previous work has established that a number of optical emission lines originate in the accretion flow and are affected by the accretion rate. In particular, the Hα 10% width and the Ca II-λ8662 line flux are found to correlate well with the accretion rate (Muzerolle et al., 1998; Natta et al., 2004; Mohanty et al., 2005). These empirical indicators facilitate studies of accretion, and for the first time, allow us to investigate accretion in multi-epoch spectra for large samples of objects. Here, we use both diagnostics to probe the intrinsic accretion variability in young stars in Taurus-Auriga and Chamaeleon I, to provide new observational limits for the aforementioned scenarios.

2.3 Observations and Data Analysis

We obtained multi-epoch high-resolution optical spectra of 40 members in the ~ 2 Myr old Chamaeleon I and Taurus-Auriga star forming regions. The targets span the spectral types from F2 to M5 based on published classifications, and consist of accretors without suspected close companions selected from the list of Nguyen et al. (2009b). The data were collected using the echelle spectrograph MIKE (Bernstein et al., 2003) on the Magellan Clay 6.5 meter telescope at the Las Campanas Observatory, Chile on 15 nights during four observing runs between 2006 February and 2006 December. Each target was observed typically at four epochs with baselines of hours, days, and months (only one target was observed just twice; 24, 12 and 3 targets were observed four, five and six times, respectively). For the data reduction, we used customized routines running in the ESO-MIDAS environment (described in detail in Brandeker et al., in preparation).

The Hα 10% widths were determined as follows. First, we estimated the continuum level by linearly interpolating flux values in the range of 500 km s^{-1} to 1000 km s^{-1} on either side of the line. Next, the maximum flux level of Hα emission was measured with respect to this continuum level. Finally, the crossing points of the Hα emission with the 10% flux level were identified, and the width was measured. Sometimes absorption components in the Hα emission line profile falls below the 10% flux level. In such cases, we ensured that we measured the width consistently for all epochs, i.e. we measured widths to the edges of any blue- or red-shifted absorption features. We did not correct for underlying photospheric absorption in Hα.

We derived the Ca II-λ8662 emission fluxes ($\mathcal{F}_{\rm Ca\,II}$) from the observed emission equivalent widths. To determine the widths, we integrated the emission above the continuum level. For emission profiles attenuated by a broad absorption feature, we used the median flux within 0.2 Å of the absorption minima as an approximate continuum level for integration, similar to what was done by Muzerolle et al. (1998). To infer the emission fluxes from the equivalent widths, we must know the underlying photospheric continuum flux. We used the continuum flux predicted by the PHOENIX synthetic spectra for a specified $T_{\rm eff}$ and surface gravity. We inferred $T_{\rm eff}$ from our spectral types, and assumed a surface gravity of $\log g = 4.0$ (cgs units). In our estimate, we ignore veiling, which could lead to an underestimate of the line flux. Indeed, for five targets shared by Mohanty et al. (2005), our results were lower by 0.05 to 0.41 dex. We tried to measure veiling from our spectra, but we found the relatively poor S/N prevented us from reaching sufficient accuracy (S/N of our spectra was typically ~ 20 at Hα, whereas literature studies for veiling, e.g. Hartigan et al. (1989), use spectra with S/N$\gtrsim$75). However, for our purposes of studying variability, the bias due to veiling is not important.

2.4 Accretion Indicators and Their Variability

Previous studies have shown that the Hα 10% width and the Ca II-λ8662 flux are correlated with accretion rates determined using the traditional method based on optical veiling (Natta et al., 2004; Mohanty et al., 2005), with Ca II showing significantly less scatter around the fit (Herczeg & Hillenbrand, 2008). In Fig. 2.1, we compare these two accretion indicators for our sample, with the points set to the average values from the multi-epoch spectra, and the 'error bars' indicating the range of values (the ranges are dominated by variability, not by measurement uncertainty). We find a clear linear

correlation between the Hα 10% width and log flux in Ca II-λ8662, with the deviations comparable to the scatter. This provides reassurance that both parameters are mainly determined by the same physical quantity, which we identify as the mass accretion rate based on published findings. For individual objects, the degree of correlation between the two accretion indicators varies, which may be explained by the varying extent to which accretion affects different emission lines. We do not see a significant correlation between the variability in the accretion indicators and stellar mass, Spitzer IR excess, or star forming region in our sample.

In Fig. 2.2, we compare the variability in the two accretion indicators. Here we use (max − min) for the Hα 10% width and (max/min) for the Ca II-λ8662 flux, because these quantities are directly proportional to accretion rate changes (Natta et al., 2004; Mohanty et al., 2005). One sees that the data are not correlated (correlation coefficient $r^2 \sim 0.02$), indicating that at least one of these parameters does not reflect changes in the accretion rate.

Using the correlations $\log \dot{M} = 1.06 \log \mathcal{F}_{\rm Ca\,II} - 15.40$ of Mohanty et al. (2005), and $\log \dot{M} = -12.89 + 0.0097$ Hα 10% [km s^{-1}] of Natta et al. (2004), we convert the variability seen in the spectroscopic indicators to accretion rate changes. Based on Ca II-λ8662 fluxes, the median accretion rate variability in our spectra is 0.35 dex, with 13/40 or 32% exceeding 0.5 dex and only 1/40 or 2.5% exceeding one order of magnitude. These numbers should be treated as upper limits, as the uncertainties in measuring Ca II fluxes likely contribute $\sim$ 0.1 dex to the scatter. In contrast, using the Hα 10% width gives a median variability of 0.65 dex, with the majority exceeding 0.5 dex (26/40 or 65%), and still a substantial fraction exceeding one order of magnitude (16/40 or 40%).

This result indicates clearly that the Ca II-λ8662 flux is a more robust quantitative diagnostic of accretion rate. Our empirical result is consistent with the models of Classical T Tauri stars of Azevedo et al. (2006), which find that Ca II broad components are formed predominantly in the accretion flow, and track accretion rate, while the hydrogen lines are much more affected by stellar winds.

The main reason to use Hα for accretion rate measurements is that it is much easier to measure, and is sensitive to lower levels of accretion. In comparison with line fluxes or equivalent widths, the 10% width also has the advantage of not being heavily affected by uncertainties in estimating the underlying continuum. This property is beneficial especially for faint objects: the typical variation in 10% width from continuum uncertainty is $\sim$ 15 km s^{-1}. Based on our findings, however, the 10% width should not be trusted

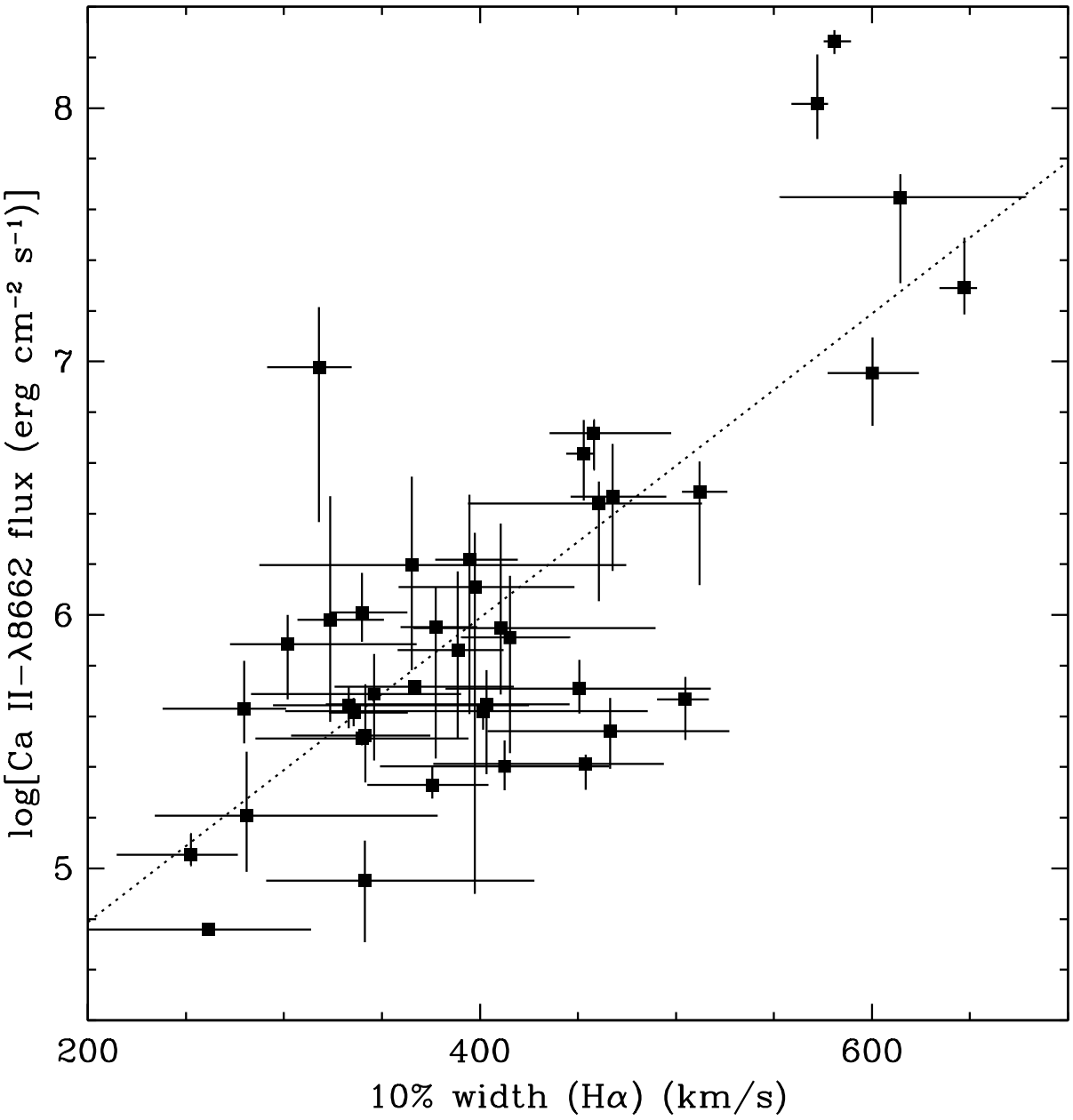

Figure 2.1 Ca II-λ8662 fluxes vs. Hα 10% widths in our sample: shown are the averages from our multi-epoch spectra with the error bars indicating the minimum-maximum range. From linear regression analysis, the probability that the data are not correlated is $< 10^{-6}$; the best linear fit is overdrawn. The outlier with strong Ca II-λ8662 flux and narrow Hα 10% width, DR Tau, has a strong P Cygni profile, which leads to a small 10% width measurement.

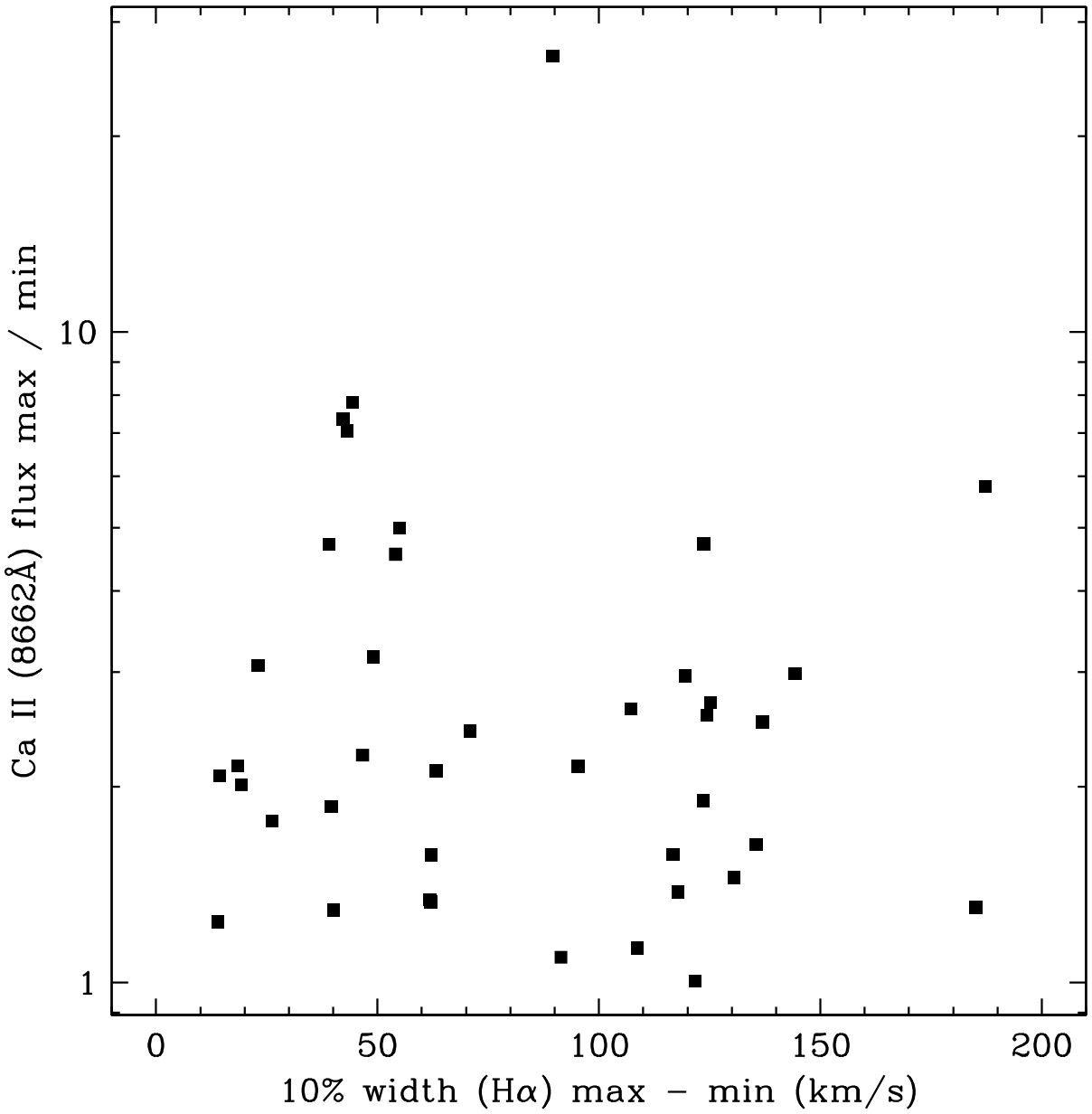

Figure 2.2 Variability in spectroscopic diagnostics of accretion measured in our multi-epoch spectra for individual objects: (max/min) in Ca II-λ8662 flux vs. (max − min) of the 10% width. Both quantities are supposed to be directly related to accretion rate changes. We do not find a significant correlation in this dataset (correlation coefficient $r^2 \sim 0.02$).

for quantitative measurements. Nevertheless, it is still useful as a qualitative indicator of accretion.

A major problem in the 10% width measurement is its strong dependence on the line profile. The majority of the accreting stars in our sample show absorption components in their Hα profile, caused by relatively cool gas, e.g. in stellar or disk winds, or parts of the accretion flow, seen in projection against the hot shock front. Since these absorption features are variable in intensity and in position relative to the emission, the maximum intensity and therefore the 10% level can vary considerably from epoch to epoch. This effect can cause large changes in 10% width not necessarily associated with accretion rate changes.

To probe the timescales of variability in the two line indicators, we used our time series baselines of hours to months: we examined indicator changes between all combinations of epochs for each object, e.g. if an object was observed at epochs A, B & C, then we reviewed changes between epochs A-B, A-C, and B-C. We show the changes graphically in Fig. 2.3. Both for the Hα 10% width and for the Ca II-λ8662 flux, we obtain consistent results: the extent of the variability increases on timescales ranging from hours to several days. On longer timescales, the amount of variability saturates. Thus, the dominant timescale for accretion-related variability is several days. This idea suggests the variability is determined near the star, where the timescales are sufficiently short. Probably, one major factor is rotation, since typical rotation periods in young stars are in the range of 1–10 d (Herbst et al., 2007). In addition, there may also be a connection to the characteristic infall timescale, typically hours, or magnetic field reconnection events, perhaps several days. Note that we cannot probe long-term variations on timescales of years with our dataset. However, the photometric results of Grankin et al. (2007), with observations secured over more than 20 years, find most Classical T Tauri stars to be fairly stable on long timescales.

2.5 The Origin of the Scatter in Accretion Rate vs. Mass

Our new constraints on accretion variability in a large sample allows us to constrain the origin of the distribution of data points in the accretion rate vs. mass diagram. In

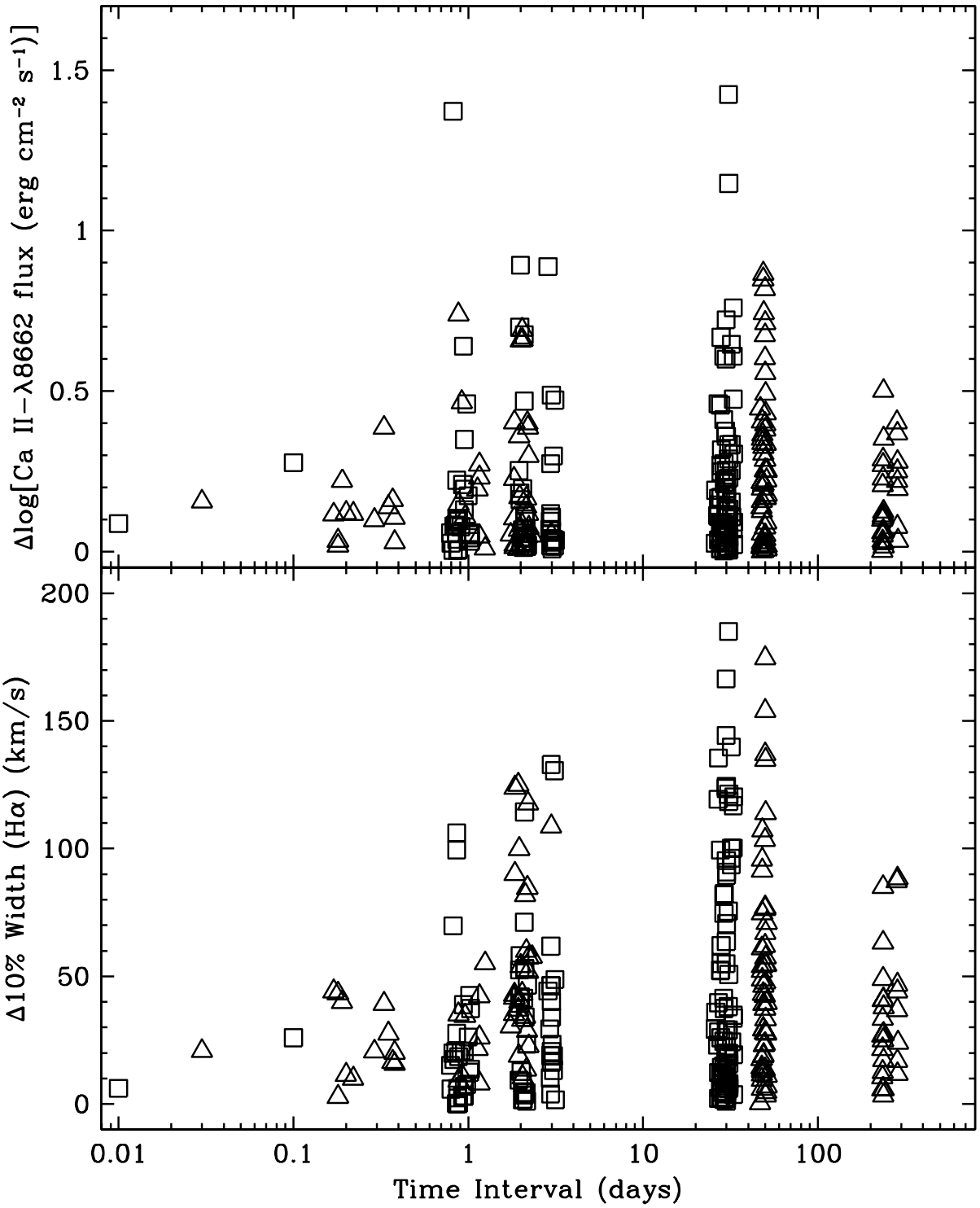

Figure 2.3 Change in Ca II-λ8662 flux (upper panel) and Hα 10% width (lower panel) vs. time. Data from Cha I are represented by triangles, and those from Tau-Aur are drawn as squares. The maximum extent of the variability is reached after a few days and does not further increase towards longer timescales.

Fig. 2.4, we show the two accretion indicators used in this study as a function of spectral type. For the Hα 10% width, we also include the non-accreting objects. In both cases, a clear trend is seen: the spectroscopic indicator drops towards later spectral types, which reflects the $\dot{M}$ vs. M correlation reported in previous studies (see §2.2). As can be seen in the Hα 10% widths, the opposite trend is seen for the non-accretors, which is likely due to increasing levels of magnetic activity towards later spectral types. This leads to a 'U-shaped' distribution of data points: accretors and non-accretors are separated by a large gap at F–K spectral types, but are harder to distinguish in M-type objects.

As can be seen in both panels, the total amount of scatter in the accretion indicator cannot be explained by intrinsic accretion rate variability, which is shown as error bars. This is particularly obvious from the Ca II-λ8662 fluxes, which we identified as the more robust accretion indicator in §2.4. Converted to accretion rates, the objects cover 1–2 orders of magnitude at any given spectral type, while the variability accounts only for a small fraction of this scatter (~ 0.35 dex, see §2.4). In other words, on timescales of days to months the objects do not move significantly in the diagram.

Although we cannot exclude the presence of significant variability on longer timescales, the scatter in the $\dot{M}$ vs. M plot is most likely dominated by object-to-object variations. This confirms previous claims by Natta et al. (2004) and is contrary to suggestions by Scholz & Jayawardhana (2006) based on a much smaller sample. Thus, stellar mass or parameters that strictly scale with stellar mass are clearly not the only factors that affect the accretion rate.

One possible explanation for the spread of accretion rates is the different evolutionary stages of the objects considered here. Accretion rates are expected to drop with age, either following a power law, if the timescale is determined by the slow viscous evolution of the disk (Clarke & Pringle, 2006), or in a more rapid process, consistent with the rapid inner disk clearing inferred from the scarcity of 'transition' objects with optically thin inner disks. The presence of the clear gap between the accreting and non-accreting populations in Fig. 2.4, particularly well-defined for the higher mass objects is thus highly interesting. The scarcity of objects in the transition from accretors to non-accretors argues for a rapid evolution between states, as suggested in disk evolution models including mass loss from the disk (e.g. Clarke et al., 2001; Armitage et al., 2003). This may be related to the similarly rapid timescale of transition between objects with IR excess and those without.

Apart from the evolutionary stage, a number of other factors have been suggested to influence the accretion rates. If disk ionization is a major factor, our findings imply

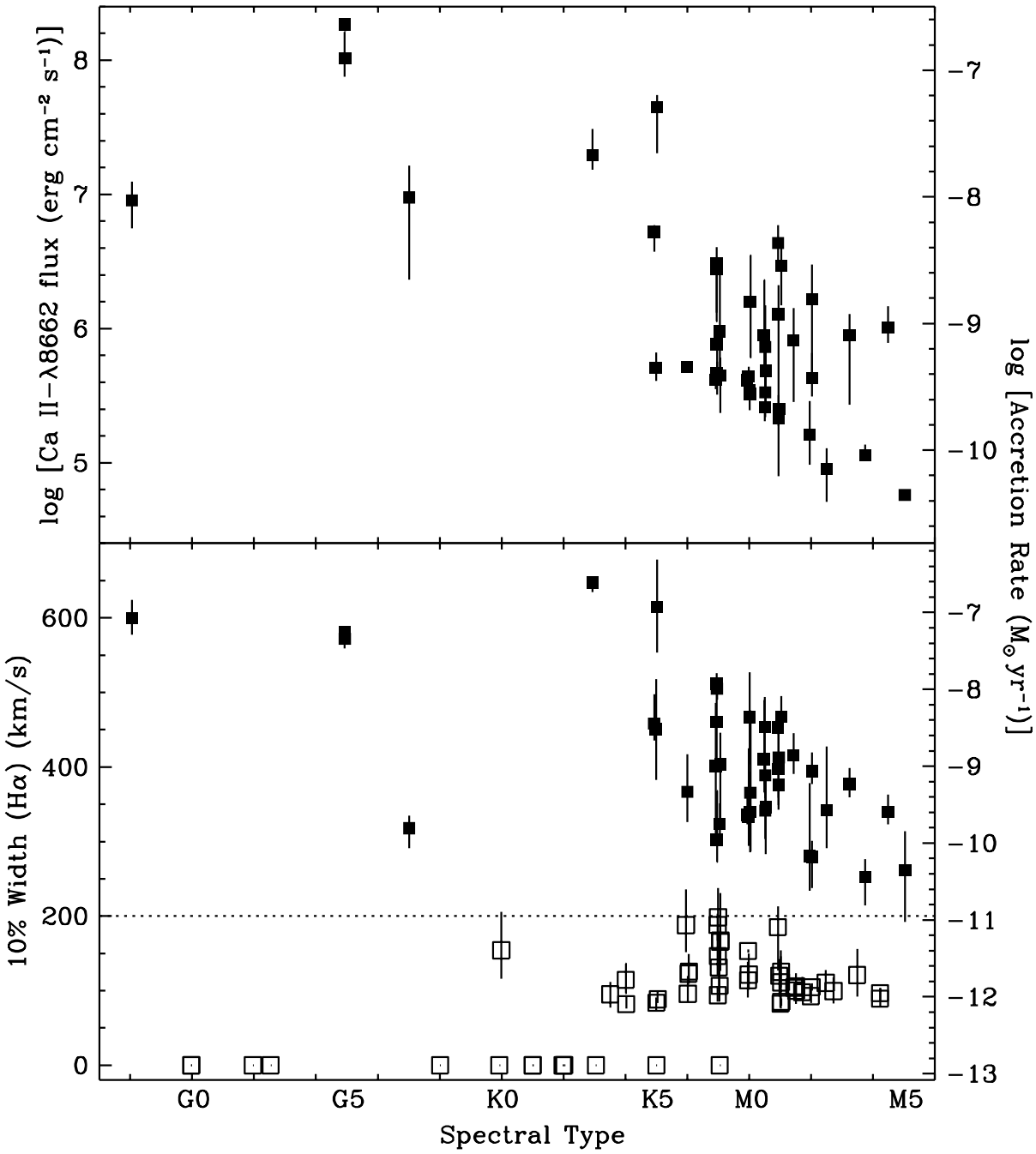

Figure 2.4 Ca II-λ8662 flux (upper panel) and Hα 10% width (lower panel) vs. spectral types. Error bars indicate the full range of the variations. In the lower panel, we also show the non-accretors (hollow symbols) with Hα 10% widths $< 200\,\mathrm{km\ s^{-1}}$ (after subtracting rotational broadening). Objects without Hα emission are shown with a 10% width of $0\,\mathrm{km\ s^{-1}}$. The right axis shows the accretion rates inferred from the relations from Mohanty et al. (2005) and Natta et al. (2004). For the M and K type stars, one sees a clear rise in Hα 10% width towards earlier spectral type, but at K0 and earlier, it appears to plateau, with no objects showing widths larger than $\sim 600\,\mathrm{km\ s^{-1}}$.

that the main source of ionization is probably external (e.g. cosmic rays), as the stellar ionising radiation is expected to scale with mass and thus would not allow for a wide range of accretion rates at constant mass. In general, our results favour scenarios where initial or environmental conditions are more important than stellar parameters. For instance, a model where the dispersion in initial disk parameters, e.g. mass and radius, determines the distribution of data points in the $\dot{M}$ vs. M plot, as recently described by Alexander & Armitage (2006), would be consistent with our results.

To constrain the influence of stellar and environmental parameters on the appearance of the $\dot{M}$ vs. M plot, it would be necessary to isolate them from evolutionary effects. It would be of particular interest to investigate accretion rates versus other parameters along lines of constant mass in the $\dot{M}$ vs. M diagram. Unfortunately, for these tasks the currently available samples may not be sufficiently large. In principle, however, such analyses have the potential to provide important information on the nature of the accretion process in young stars. Finally, the causal relationships between our accretion indicators and accretion rates are not fully understood, and we use them merely as empirical tools, based on published correlations. Nevertheless, the fact that indicators such as Ca II-λ8662 line flux correlate remarkably well with the current empirical framework of measuring accretion rates gives some confidence that these indicators relate to physical reality.

Acknowledgements

We thank the anonymous referee for a very helpful review and constructive critical comments that greatly improved the clarity of the letter. DCN acknowledges gratefully the hospitality of the astronomy group in St. Andrews during his visit. This work was supported in part by NSERC grants to RJ and MHvK and an Early Researcher Award from Ontario to RJ.

Chapter 3

Disk Braking in Young Stars

Published as:
"Disk Braking in Young Stars: Probing Rotation in Chamaeleon I and Taurus-Auriga"
Nguyen, D. C., Jayawardhana, R., van Kerkwijk, M. H., & Brandeker, A., 2009, ApJ, 695, 1648

3.1 Abstract

We present a comprehensive study of rotation, disk and accretion signatures for 144 T Tauri stars in the young (~ 2 Myr old) Chamaeleon I and Taurus-Auriga star forming regions based on multi-epoch high-resolution optical spectra from the Magellan Clay 6.5 m telescope supplemented by mid-infrared photometry from the *Spitzer Space Telescope*. In contrast to previous studies in the Orion Nebula Cluster and NGC 2264, we do not see a clear signature of disk braking in Tau-Aur and Cha I. We find that both accretors and non-accretors have similar distributions of $v \sin i$. This result could be due to different initial conditions, insufficient time for disk braking, or a significant age spread within the regions. The rotational velocities in both regions show a clear mass dependence, with F–K stars rotating on average about twice as fast as M stars, consistent with results reported for other clusters of similar age. Similarly, we find the upper envelope of the observed values of specific angular momentum j varies as $M^{0.5}$ for our sample which spans a mass range of $\sim 0.16\,M_\odot$ to $\sim 3\,M_\odot$. This power law complements previous studies in Orion which estimated $j \propto M^{0.25}$ for $\lesssim 2$ Myr stars in the same mass regime, and a sharp decline in j with decreasing mass for older stars (~ 10 Myr) with $M < 2\,M_\odot$. Furthermore,

the overall specific angular momentum of this $\sim 10\,\mathrm{Myr}$ population is five times lower than that of non-accretors in our sample, and implies a stellar braking mechanism other than disk braking could be at work. For a subsample of 67 objects with mid-infrared photometry, we examine the connection between accretion signatures and dusty disks: in the vast majority of cases (63/67), the two properties correlate well, which suggests that the timescale of gas accretion is similar to the lifetime of inner disks.

3.2 Introduction

One of the major outstanding issues in star formation theory is the regulation of angular momentum in young stars. The specific angular momentum of young single stars at $\sim 1\,\mathrm{Myr}$ is about four orders of magnitude lower than in molecular cloud cores, from which the stars formed, indicating efficient rotational braking in the early phases of stellar evolution (Bodenheimer, 1995). In this context, a large number of studies have explored the connection between the presence of disks and rotation (Herbst et al., 2007).

Disk braking is defined here as a process that provides rotational braking based on magnetic coupling between the star and the disk. One possible theoretical scenario for disk braking is 'disk-locking', originally proposed for T Tauri stars by Camenzind (1990), Koenigl (1991), and Shu et al. (1994). In that case, the magnetic connection between the star and the disk produces a torque onto the star, transfering angular momentum to the disk (presumably, from where it is eventually removed by, e.g., magnetically driven winds). An alternative scenario for disk braking is stellar winds powered by accretion, as recently modeled by Matt & Pudritz (2005). For a more detailed overview of the theoretical work on disk braking, see for example the review by Matt & Pudritz (2008).

If disk braking is at work, we expect to observe three kinds of stars: slow rotators with disks, slow rotators without disks, and fast rotators without disks. This distribution corresponds to the following evolutionary sequence: while stars are coupled to their disks, they will rotate slowly; once stars lose their disks, they will continue to rotate slowly for some time but gradually spin-up as they contract towards the main sequence, with some stars eventually becoming fast rotators. Thus, rapidly rotating stars with disks should not exist in an ideal disk braking scenario.

Observationally, the evidence for disk braking is confusing. Some photometric studies found a correlation between rotational properties and near-infrared color excess suggestive of disks (e.g. Edwards et al., 1993; Herbst et al., 2002), whereas others have not

(e.g. Stassun et al., 1999; Makidon et al., 2004). The photometric monitoring program of Lamm et al. (2005) observed disk braking in $\sim$2–3 Myr NGC 2264, but with the effect less pronounced for low mass stars. Recent studies using Spitzer mid-infrared observations of the $\sim$1 Myr Orion Nebula Cluster (ONC) and NGC 2264 support a disk-rotation connection: stars with longer rotation periods were found to be more likely than those with short periods to have IR excesses (Rebull et al., 2006; Cieza & Baliber, 2007). However, the mid-infrared study by Cieza & Baliber (2006) of IC 348 did not find the preferential distribution of rotation with disk presence.

While both near-infrared and mid-infrared signatures indicate the presence of a dusty disk, they do not prove the coupling between star and disk as required by the disk braking scenario. To demonstrate a direct link between the inner disk and the central star, a better diagnostic for disk braking may be ongoing accretion. For strongly active accretors, rotation periods are difficult to determine since period measurements rely on the presence of stable starspot regions; therefore, period samples may be biased towards weakly accreting stars. In some respects, it is advantageous to use projected rotational velocity ($v \sin i$) instead of rotation periods.

A recent spectroscopic study of disk accretion in low-mass young stars by Jayawardhana et al. (2006) found evidence of a possible accretion-rotation connection in the η Cha ($\sim$6 Myr) and TWA ($\sim$8 Myr) associations. All accretors in their sample of 41 stars were slow rotators, with $v \sin i \lesssim 20\,\mathrm{km\,s^{-1}}$, whereas the non-accretors showed a large span in rotational velocities, up to $50\,\mathrm{km\,s^{-1}}$. However, given the small number of accretors, they caution that those results should be checked with larger samples. A larger study of solar-like mass stars in NGC 2264 by Fallscheer & Herbst (2006) found disk braking signatures in using UV excess indicative of accretion. For a review of recent observational studies on rotation and angular momentum evolution of young stellar objects and brown dwarfs, see Herbst et al. (2007).

As part of a comprehensive, multi-epoch spectroscopic survey, we present here a study of rotation and disk-braking at ages of $\sim$2 Myr in the star forming regions Taurus-Auriga and Chamaeleon I. This study comprises 144 stars, which significantly enlarges the previously available sample of spectroscopic data in those two regions (see the summary by Rebull et al. (2004) for currently available rotational data). From the spectra, we extract $v \sin i$, and, as accretion indicators, the full width of Hα at 10% of the peak (hereafter, Hα 10% width) and Ca II fluxes. We investigate the distribution of $v \sin i$, estimate angular momentum values, and test for the signature of disk braking.

3.3 Target Selection and Observations

We used 572 high-resolution optical spectra of 144 members in the $\sim$2 Myr old Chamaeleon I and Taurus-Auriga star forming regions obtained with the echelle spectrograph MIKE (Bernstein et al., 2003) on the Magellan Clay 6.5 meter telescope at the Las Campanas Observatory, Chile. The data were collected on 15 nights during four observing runs between 2006 February and 2006 December. We complemented our optical spectra with infrared measurements from the InfraRed Array Camera (IRAC; Fazio et al., 2004) aboard the *Spitzer Space Telescope*. For Cha I, we used the results of Damjanov et al. (2007), and for Tau-Aur we analyzed publicly available images obtained between 2004 September and 2007 March, using the methods described in detail by Damjanov et al. (2007). Our results are listed in tables 3.1 & 3.2.

Our sample consists of a magnitude-limited subset ($R \leq 17.6$ for Cha I; $R \leq 13.4$ for Tau-Aur) of targets from Leinert et al. (1993), Ghez et al. (1993), Simon et al. (1995), Köhler & Leinert (1998), Briceño et al. (2002), and Luhman (2004a,b). To isolate the possible influence of binarity on disk braking in this study, we excluded from our sample unresolved wide binaries and double-lined spectroscopic binaries. Our targets span the spectral type range from F2 to M5 based on published classifications. In addition, we observed a sample of 25 slowly rotating velocity standard stars selected from the list of Nidever et al. (2002); these cover the same spectral range as our targets. We determined the spectral type for 13 targets without prior classification by fitting their spectra against those of the standard stars, and identifying the best fits.

MIKE is a slit-fed double echelle spectrograph with blue and red arms. For this study, we used only the red spectra, which cover the range of 4 900–9 300 Å in 34 spectral orders. The 0.35″ slit was used with no binning to obtain the highest possible spectral resolution, R $\sim$60 000. The pixel scale was 0.14″ pixel^{-1} in the spatial direction, and approximately 0.024 Å pixel^{-1} at 6 500 Å in the spectral direction. In MIKE, the spatial direction of the projected slit is wavelength dependent, and not aligned with the CCD columns. To extract these slanted spectra, we used customized routines running in the ESO-MIDAS environment (described in detail in Brandeker et al., in preparation). Integration times were chosen such that we obtained signal-to-noise ratios (S/N) $>$ 30 per spectral resolution element at 6 500 Å; they typically ranged from 60 to 1 200 seconds depending on seeing.

3.4 Analysis

3.4.1 Accretion Signatures

The Hα equivalent width (EW) has long been used to distinguish accreting or classical T Tauri stars (EW >10 Å) from non-accreting or weak-line T Tauri stars (EW <10 Å). In accretors, in the context of the magnetospheric accretion scenario, the Hα emission arises largely from the gas falling in from the inner disk edge onto the star. In non-accretors, chromospheric activity is the main source of Hα emission, and is thus generally weaker. The Hα profiles of accretors also tend to be much broader than those of non-accretors due to the high velocity of the infalling gas and Stark broadening. (The latter is expected to be important in Hα, since the line optical depths are high; see Muzerolle et al. (2001) for further discussion.) Asymmetry in the Hα profile of accretors is also commonly observed as a result of viewing geometry, absorption by a wind component, or both.

Since the Hα EW depends on the spectral type, White & Basri (2003) proposed to use as a more robust accretion diagnostic the Hα 10% width. By comparing this measurement with veiling in their stellar spectra, they found that a Hα 10% width larger than $270\,\mathrm{km\,s^{-1}}$ reliably indicates accretion. A less conservative accretion cutoff of $200\,\mathrm{km\,s^{-1}}$ was adopted by Jayawardhana et al. (2003) for their study of young very low mass objects, based on empirical results and physical reasoning; however, they cautioned that it should be used in combination with additional diagnostics whenever possible. In later studies, it was found that Hα 10% width not only appears to be a good qualitative indicator of accretion but also correlates with the mass accretion rates derived by other means: the $200\,\mathrm{km\,s^{-1}}$ threshold corresponds to a mass accretion rate of $\sim 10^{-11}\,M_\odot\,\mathrm{yr}^{-1}$ (Natta et al., 2004).

For this study, we use the Hα 10% width as one accretion diagnostic, which we computed as follows. First, we estimated the continuum level at Hα by linearly interpolating between flux measurements in the range of $500\,\mathrm{km\,s^{-1}}$ to $1000\,\mathrm{km\,s^{-1}}$ on either side of the line. Next, the maximum flux level of Hα emission was measured with respect to this continuum level. Finally, the crossing points of the Hα emission with the 10% flux level are identified, and the width was measured. The results for our targets are listed in tables 3.1 & 3.2; we note that for some objects, the measurements were uncertain, e.g. because of absorption components or double-peaked profiles with one peak close to 10% of the height of the main peak. Note, however, this is not critical: all these sources are clearly accretors.

To obtain mass accretion rates, we use the Ca II-λ8662 emission fluxes ($\mathcal{F}_{\mathrm{Ca\,II}}$) which have been shown to be a more robust quantitative indicator of accretion than Hα 10% width (Nguyen et al., 2009a). We derived the fluxes from the observed emission equivalent widths. To determine the widths, we integrated the emission above the continuum level. For emission profiles attenuated by a broad absorption feature, we used the median flux within 0.2 Å of the absorption minima as an approximate continuum level for integration, similar to what was done by Muzerolle et al. (1998). To infer the emission fluxes from the equivalent widths, we must know the underlying photospheric continuum flux. We used the continuum flux predicted by the PHOENIX synthetic spectra for a specified T_{eff} and surface gravity. We inferred T_{eff} from our spectral types, and assumed a surface gravity of $\log g = 4.0$ (cgs units). For five targets shared by Mohanty et al. (2005), our results were lower by 0.05 to 0.41 dex. We ignored veiling, which may lead to an underestimate of line fluxes.

3.4.2 Projected Rotational Velocity

The projected rotational velocity $v \sin i$ of each target was determined by fitting the target spectra against sets of artificially broadened template spectra derived from one of the observed slowly rotating standard stars. For each target, we initially selected the standard star closest in spectral type as a template. To broaden the templates, we convolved the original template spectra with the analytical rotational broadening function of Gray (2005) assuming a limb darkening factor of 0.65.

Our routine to estimate $v \sin i$ of a target consists of four steps. First, we fitted the target spectra with template spectra broadened from 0 to 200 km s^{-1} in steps of 10 km s^{-1}, and recorded the $v \sin i$ value of the best fit for each echelle order. Second, we refined our search to projected rotational velocities within 10 km s^{-1} of the first-pass results in steps of 1 km s^{-1}, and revised our estimates accordingly. Third, we computed weighted averages over the echelle orders, after removing outliers using a standard Tukey filter, i.e. values lying 1.5 times the interquartile range below the first quartile and above the third quartile were discarded (see Hoaglin et al. (2000); for a Gaussian distribution, this filter corresponds to removing data points beyond 2.7 σ). Fourth, we calculated the weighted average across epochs and used it as a provisional $v \sin i$ estimate of the target.

To finalize our $v \sin i$ estimates, we checked the provisional results using different templates and found that the variation in estimates was typically an order of magnitude

larger than the weighted standard error of individual estimates. Therefore, for each target, we calculated two additional $v \sin i$ estimates using the next two closest standard stars by spectral type, and adopted as $v \sin i$ the estimate from the best-fit template, and as uncertainty, the standard deviation of the estimates between different templates. The results are listed in Tables 3.1 & 3.2. We considered the potential influence of veiling on our $v \sin i$ estimates: strong mass accretors will have strong veiling which could affect the $v \sin i$ estimates. However, we found no correlation between accretion signatures and rotational velocities when comparing these values for individual stars over time.

Table 3.1. Summary of Disk-Braking Results for Cha I

Object	SpT	$v \sin i$[a] (km s^{-1})	10% width[b] (km s^{-1})	Hα EW (Å)	Ca II EW (Å)	S/N[c] at Hα	3.6μm (mJy)	4.5μm (mJy)	5.8μm (mJy)	8.0μm (mJy)
T4	M0.5	12.4 ± 0.4	341 ± 28	-15 ± 2	-0.34 ± 0.12	14.7 ± 1.2	···	···	···	···
T7	K8	11.3 ± 0.8	365 ± 76	-30 ± 9	-1.6 ± 1.1	13.0 ± 1.0	···	···	···	···
T8	K2	35 ± 2	347	-18	-0.1	40 ± 5	···	···	···	···
T10	M3.75	5.4 ± 0.8	252 ± 24	-90 ± 27	-0.2 ± 0.02	5.7 ± 0.8	···	···	···	···
T11	K6	14.3 ± 1.1	367 ± 38	-41 ± 4	-0.318 ± 0.012	32 ± 2	···	···	···	···
T12	M4.5	10.7 ± 0.2	262 ± 35	-38 ± 7	···	4.6 ± 1.0	···	···	···	···
ISO 52	M4	9.9 ± 0.6	126 ± 15	-5.4 ± 1.0	···	4.9 ± 1.0	29.0 ± 1.0	24.0 ± 1.0	17 ± 2	18.4 ± 0.9
CHXR 14N	K8	13.7 ± 0.6	114 ± 20	-2.0 ± 0.9	-0.29 ± 0.02	14.3 ± 1.1	···	···	···	···
CHXR 14S	M1.75	5.7 ± 0.3	98 ± 14	-3.24 ± 0.19	-0.39 ± 0.04	10.1 ± 1.0	···	···	···	···
T16	M3	11.3 ± 0.9	101	-9	-0.28 ± 0.04	3.5 ± 1.0	···	26.0 ± 1.0	···	21.0 ± 1.0
T20	M1.5	48.3 ± 1.4	192 ± 21	-3.8 ± 0.4	···	14.6 ± 1.3	···	···	···	···
Hn 5	M4.5	7.8 ± 0.4	340 ± 20	-56 ± 16	-2.3 ± 0.9	5.6 ± 1.0	63 ± 2	66 ± 2	71 ± 2	94 ± 2
T22	M3	60 ± 10	228	-3	···	5.9 ± 0.9	65 ± 2	42 ± 2	32 ± 2	16.3 ± 0.9
CHXR 20	K6	14.6 ± 0.9	Absorp.	0.6	-0.19 ± 0.02	12.7 ± 1.7	113 ± 2	86 ± 2	81 ± 3	109 ± 2
CHXR 74	M4.25	5.8 ± 1.0	97 ± 7	-5.5 ± 0.8	-0.23 ± 0.11	4.3 ± 0.9	30 ± 2	20.0 ± 1.0	12 ± 2	7.7 ± 0.7
CHXR 21	M3	48 ± 5	135 ± 61	-4.0 ± 1.9	···	4.6 ± 0.9	···	···	···	···
T24	M0.5	10.5 ± 0.4	454 ± 53	-18 ± 7	-0.26 ± 0.04	10.9 ± 1.2	98 ± 2	79 ± 2	70 ± 2	70 ± 2
T25	M2.5	12.6 ± 0.3	341 ± 62	-14 ± 3	-0.13 ± 0.06	8.0 ± 1.0	···	···	···	···
CHXR 76	M4.25	9.8 ± 0.6	89 ± 12	-5.8 ± 1.8	-0.13 ± 0.07	3.2 ± 1.0	16.7 ± 0.9	11.6 ± 0.8	4 ± 2	4.2 ± 0.5
T33A	K3.5	12.9 ± 0.5	95 ± 15	-0.6 ± 0.2	-0.22 ± 0.04	15.9 ± 1.4	···	···	···	···
T33B	G7	50 ± 4	318 ± 21	-61 ± 12	-2.3 ± 1.5	8.1 ± 1.1	···	···	···	···
T34	M3.75	5.8 ± 0.8	84 ± 8	-2.5 ± 1.1	···	5.6 ± 0.8	34 ± 2	23.0 ± 1.0	16 ± 2	8.3 ± 0.8
T35	K8	21.0 ± 1.8	466 ± 46	-91 ± 49	-0.35 ± 0.09	7.7 ± 0.9	···	100 ± 2	···	45 ± 2
CHXR 33	M0	16.5 ± 1.5	153 ± 3	-2.9 ± 0.2	-0.18 ± 0.03	15.0 ± 1.5	67 ± 2	45 ± 2	36 ± 2	17.9 ± 0.9
T38	M0.5	18.7 ± 1.5	389 ± 23	-107 ± 37	-0.7 ± 0.7	5.6 ± 1.0	···	···	···	···
T39A sw	K7	7.7 ± 1.6	131 ± 27	-5.2 ± 1.4	-0.41 ± 0.09	11.9 ± 1.0	···	···	···	···
T39A w	M1.5	4.1 ± 0.3	100 ± 16	-2.6 ± 0.6	-0.26 ± 0.06	9.8 ± 1.0	···	···	···	···
T39B e	M1.5	12.8 ± 0.4	106 ± 13	-5.3 ± 1.2	-0.25 ± 0.03	7.2 ± 0.8	···	···	···	···

Table 3.1 (cont'd)

Object	SpT	$v \sin i$[a] (km s^{-1})	10% width[b] (km s^{-1})	Hα EW (Å)	Ca II EW (Å)	S/N[c] at Hα	3.6μm (mJy)	4.5μm (mJy)	5.8μm (mJy)	8.0μm (mJy)
Hn 10E	M3.25	8.2 ± 0.5	377 ± 17	-62 ± 3	-1.6 ± 0.8	4.3 ± 1.0	···	···	···	···
T44	K5	87 ± 16	614 ± 53	-67 ± 13	-27 ± 10	15.9 ± 1.5	···	···	···	···
T45A	M0	12.4 ± 0.5	340 ± 77	-2.7 ± 0.8	-0.33 ± 0.03	16.3 ± 1.7	···	···	···	···
T47	M2	16.2 ± 0.9	395 ± 18	-42 ± 7	-2 ± 2	3.1 ± 1.0	···	···	···	···
CHXR 48	M2.5	13.8 ± 0.5	110 ± 12	-4.3 ± 1.9	-0.4 ± 0.3	9.2 ± 1.0	45 ± 2	29.0 ± 1.0	19 ± 2	11.1 ± 0.7
T49	M2	8.2 ± 0.8	280 ± 25	-87 ± 19	-0.6 ± 0.2	6.3 ± 0.8	···	120 ± 3	···	117 ± 2
CHX 18N	K6	26.5 ± 1.3	188 ± 39	-3.3 ± 0.7	-0.26 ± 0.06	30 ± 2	···	358 ± 4	···	196 ± 3
T50	M5	12.0 ± 0.4	262 ± 52	-22 ± 3	-0.1627 ± 0.0007	5.9 ± 0.9	52 ± 2	44 ± 2	35 ± 2	39 ± 2
T52	G9	28 ± 3	562	-48	-8	35 ± 4	···	···	···	···
T53	M1	22.2 ± 0.6	468 ± 22	-62 ± 20	-3.5 ± 1.5	7.4 ± 0.9	···	···	···	···
CHXR 54	M1	10.9 ± 0.2	120 ± 22	-1.3 ± 0.3	-0.21 ± 0.03	17.1 ± 1.3	···	···	···	···
Hn 17	M4	8.7 ± 0.5	72 ± 10	-2.6 ± 0.4	···	4.9 ± 0.9	···	···	···	···
CHXR 57	M2.75	11.8 ± 1.2	100 ± 15	-3.1 ± 1.1	-0.29 ± 0.09	9.2 ± 1.0	···	···	···	···
Hn 18	M3.5	7.6 ± 0.8	121 ± 24	-6.0 ± 1.7	-0.101 ± 0.018	5.4 ± 0.7	27.0 ± 1.0	24.0 ± 1.0	20 ± 2	19.1 ± 0.9
CHXR 60	M4.25	0.8 ± 0.7	95 ± 12	-5.8 ± 1.1	-0.1	4.5 ± 0.9	22.0 ± 1.0	17.1 ± 0.9	11 ± 2	5.4 ± 0.5
T56	M0.5	7.2 ± 0.5	346 ± 41	-49 ± 11	-0.49 ± 0.17	15.2 ± 1.1	···	···	···	···

[a]The Hα 10% width uncertainty does not correspond to the measurement uncertainty, but to the scatter in our multi-epoch data.

[b]The $v \sin i$ uncertainty represents the combined measurement scatter between results using different template spectra, and over different epochs.

[c]The S/N is based on the continuum on either side of Hα used for the 10% width calculations, and the uncertainty represents the standard error of the estimate.

Table 3.2. Summary of Disk-Braking Results for Tau-Aur

Object	SpT	$v \sin i$[a] (km s^{-1})	10% width[b] (km s^{-1})	Hα EW (Å)	Ca II EW (Å)	S/N[c] at Hα	3.6μm (mJy)	4.5μm (mJy)	5.8μm (mJy)	8.0μm (mJy)
NTTS 034903+2431	K5	36 ± 2	229 ± 31	-1.6 ± 0.2	···	24.9 ± 1.7	···	···	···	···
NTTS 035120+3154SW	G0	62 ± 3	Absorp.	2.1 ± 0.3	···	22.7 ± 1.5	···	···	···	···
HD 285281	K0	76 ± 3	Absorp.	0.15 ± 0.08	···	48 ± 3	···	···	···	···
NTTS 040047+2603E	M2	5.85 ± 0.11	93 ± 11	-3.7 ± 0.9	-0.18 ± 0.08	14.8 ± 0.9	22.3 ± 0.7	15.9 ± 0.7	11.9 ± 0.7	6.4 ± 0.5
RX J0405.1+2632	K2	17.5 ± 1.3	Absorp.	0.7 ± 0.2	-0.089 ± 0.004	29.7 ± 1.9	···	···	···	···
RX J0405.3+2009	K1	24.1 ± 1.4	Absorp.	0.64 ± 0.04	-0.084 ± 0.011	41 ± 3	81.1 ± 1.2	48.9 ± 1.0	133.1 ± 1.0	18.2 ± 0.7
HD 284135	G0	72 ± 4	Absorp.	2.03 ± 0.14	···	58 ± 3	···	···	···	···
HD 284149	F8	27.0 ± 1.9	Absorp.	2.45 ± 0.10	···	51 ± 3	···	···	···	···
RX J0407.8+1750	K4	28.7 ± 1.0	115 ± 17	-0.59 ± 0.15	-0.14 ± 0.02	24.7 ± 1.7	···	···	···	···
RX J0408.2+1956	K2	75 ± 4	Absorp.	-0.1	···	20.8 ± 1.4	···	···	···	···
RX J0409.1+2901	G8	24 ± 2	Absorp.	0.3 ± 0.07	-0.12 ± 0.02	37 ± 2	···	···	···	···
RX J0409.2+1716	M1	70.5 ± 1.1	223 ± 23	-3.9 ± 0.7	···	14.9 ± 1.0	36.1 ± 0.8	22.7 ± 0.7	15.5 ± 0.8	8.7 ± 0.5
RX J0409.8+2446	M1	5.9 ± 0.4	83 ± 8	-1.9 ± 0.7	-0.22 ± 0.05	19.6 ± 1.4	···	···	···	···
RX J0412.8+1937	K6	11.2 ± 0.8	96 ± 16	-0.34 ± 0.09	-0.19 ± 0.05	18.9 ± 1.2	35.5 ± 0.8	23.0 ± 0.7	14.9 ± 0.8	8.7 ± 0.5
HD 285579	G0	9.6 ± 1.1	Absorp.	1.9 ± 0.5	-0.066 ± 0.010	26.6 ± 1.5	···	···	···	···
LkCa 1	M4	30.9 ± 1.1	173	-4	···	24 ± 3	54.0 ± 1.0	31.5 ± 0.8	23.6 ± 0.8	14.6 ± 0.5
CW Tau	K3	33 ± 5	647 ± 7	-87 ± 45	-9 ± 3	21.0 ± 1.4	719 ± 5	694 ± 5	632 ± 5	572 ± 3
FP Tau	M4	32 ± 2	378 ± 12	-12 ± 3	···	14.1 ± 1.0	84.8 ± 1.4	63.8 ± 1.2	53.5 ± 1.2	37.1 ± 0.9
CX Tau	M2	19.8 ± 0.6	319	-13	-0.08	34 ± 5	56.6 ± 1.0	47.1 ± 1.0	48.2 ± 1.2	65.5 ± 1.2
RX J0415.3+2044	K0	35 ± 3	Absorp.	1.16 ± 0.08	···	37 ± 2	···	···	···	···
RX J0415.8+3100	G6	31.7 ± 1.9	Absorp.	1.6 ± 0.4	···	20.2 ± 1.5	···	···	···	···
LkCa 4	K7	30 ± 2	198 ± 30	-4.8 ± 0.9	-0.23 ± 0.08	17.4 ± 1.3	72.3 ± 1.2	47.4 ± 1.0	32.4 ± 1.2	18.2 ± 0.7
CY Tau	M1.5	10.6 ± 0.4	415 ± 28	-78 ± 13	-1.0 ± 0.7	29 ± 2	89.5 ± 1.4	77.7 ± 1.2	67.4 ± 1.4	63.6 ± 1.2
LkCa 5	M2	38.3 ± 1.1	163	-4	···	20 ± 3	38.0 ± 0.8	24.9 ± 0.7	16.5 ± 0.7	9.4 ± 0.5
NTTS 041529+1652	K5	5.1 ± 1.3	Absorp.	0.3 ± 0.2	-0.17 ± 0.04	14.8 ± 1.1	8.8 ± 0.5	5.8 ± 0.5	4.1 ± 0.7	2.1 ± 0.3
Hubble 4	K7	16.5 ± 1.4	188 ± 16	-3.2 ± 0.6	-0.216 ± 0.017	20.2 ± 1.4	201 ± 3	135.5 ± 1.7	89.7 ± 1.5	51.3 ± 1.0
NTTS 041559+1716	K7	74 ± 4	210 ± 29	-1.5 ± 0.6	···	20.8 ± 1.3	27.7 ± 0.8	18.0 ± 0.7	13.1 ± 0.7	6.2 ± 0.5
BP Tau	K5	13.1 ± 1.6	458 ± 28	-109 ± 9	-3.2 ± 0.6	24.6 ± 1.7	155.4 ± 1.7	135.5 ± 1.7	117.5 ± 1.5	164.7 ± 1.7

Table 3.2 (cont'd)

Object	SpT	$v \sin i$[a] (km s^{-1})	10% width[b] (km s^{-1})	Hα EW (Å)	Ca II EW (Å)	S/N[c] at Hα	3.6μm (mJy)	4.5μm (mJy)	5.8μm (mJy)	8.0μm (mJy)
V819 Tau	K7	9.1 ± 0.6	166 ± 41	-2.1 ± 1.5	-0.22 ± 0.09	18.4 ± 1.3	73.1 ± 1.2	47.8 ± 1.0	35.0 ± 1.0	19.2 ± 0.7
DE Tau	M1	9.7 ± 0.3	453 ± 6	-53 ± 9	-5.2 ± 1.8	17.9 ± 1.3	208 ± 3	179.7 ± 1.7	149.4 ± 1.7	156.0 ± 1.7
RY Tau	F8	48 ± 3	600 ± 24	-12 ± 4	-0.8 ± 1.1	58 ± 3	1562 ± 7	1675 ± 7	2311 ± 7	3479 ± 9
HD 283572	G2	79 ± 3	Absorp.	1.01 ± 0.14	···	75 ± 4	253 ± 3	160.9 ± 1.7	108.7 ± 1.7	60.5 ± 1.2
LkCa 21	M3	46 ± 3	277	-5	···	24 ± 3	68.4 ± 1.2	44.7 ± 1.0	31.8 ± 1.0	18.7 ± 0.7
HD 285751	G5	26.6 ± 1.4	125	-0.3 ± 0.18	-0.119 ± 0.015	27.8 ± 1.7	···	···	···	···
BD +26 718	K0	32.4 ± 1.8	Absorp.	0.4 ± 0.2	-0.06 ± 0.02	29 ± 2	···	···	···	···
IP Tau	M0	12.3 ± 0.8	333 ± 54	-15 ± 8	-0.45 ± 0.07	19.2 ± 1.3	105.2 ± 1.4	90.1 ± 1.4	73.2 ± 1.4	74.2 ± 1.2
BD +17 724B	G5	49 ± 3	Absorp.	2.16 ± 0.08	···	51 ± 3	···	···	···	···
NTTS 042417+1744	K1	17.6 ± 1.5	Absorp.	1.1 ± 0.3	-0.12 ± 0.03	36 ± 2	64.2 ± 1.2	40.6 ± 0.8	26.0 ± 0.8	15.4 ± 0.7
DH Tau	M1	10.9 ± 0.6	348	-59	-2	29 ± 4	···	···	···	···
IQ Tau	M0.5	14.4 ± 0.3	411 ± 48	-25 ± 10	-0.9 ± 0.8	19.0 ± 1.2	226 ± 3	213 ± 3	178 ± 3	177 ± 3
FX Tau a	M2[d]	9.61 ± 0.19	281 ± 67	-6 ± 2	-0.23 ± 0.13	12.5 ± 1.0	···	···	···	···
FX Tau b	M1[d]	7.9 ± 0.3	413 ± 53	-21 ± 12	-0.3 ± 0.06	16.3 ± 1.2	···	···	···	···
DK Tau A	K7	17.5 ± 1.2	461 ± 54	-36 ± 27	-2.2 ± 0.9	25.4 ± 1.8	···	···	···	···
DK Tau B	M1[d]	14.0 ± 0.8	397 ± 35	-46 ± 16	-1.6 ± 1.1	10.5 ± 0.9	···	···	···	···
RX J0430.8+2113	G8	41 ± 4	Absorp.	0.5 ± 0.4	···	45 ± 3	···	···	···	···
HD 284496	G0	20.0 ± 1.0	Absorp.	0.88 ± 0.11	-0.08 ± 0.02	35 ± 2	···	···	···	···
NTTS 042835+1700	K5	14.8 ± 1.3	84 ± 7	-0.36 ± 0.15	-0.17 ± 0.03	22.9 ± 1.6	22.0 ± 0.7	13.9 ± 0.5	10.4 ± 0.7	5.4 ± 0.3
V710 Tau A	M0.5	21.5 ± 0.4	192	-3	···	13.5 ± 1.9	···	···	···	···
V710 Tau B	M2	18.31 ± 0.19	371	-37	-0.4	16 ± 2	···	···	···	···
L1551-51	K7	32.1 ± 1.4	146 ± 26	-1.0 ± 0.4	-0.16 ± 0.02	21.6 ± 1.5	41.9 ± 0.8	26.8 ± 0.8	16.0 ± 0.7	10.6 ± 0.5
V827 Tau	K7	20.9 ± 1.3	168 ± 15	-4.4 ± 1.3	-0.26 ± 0.07	16.6 ± 1.2	74.8 ± 1.2	48.8 ± 1.0	33.3 ± 0.8	18.7 ± 0.7
GG Tau A a	K7	11.5 ± 0.7	512 ± 10	-51 ± 4	-2.5 ± 1.0	21.2 ± 1.6	···	···	···	···
RX J0432.7+1853	K1	25.2 ± 1.6	Absorp.	0.66 ± 0.16	-0.09 ± 0.03	34 ± 2	···	···	···	···
L1551-55	K7	7.7 ± 0.7	94 ± 9	-1.2 ± 0.4	-0.32 ± 0.10	18.4 ± 1.4	28.9 ± 0.8	18.0 ± 0.7	12.6 ± 0.7	7.1 ± 0.5
RX J0432.8+1735	M2	11.18 ± 0.11	105 ± 4	-1.8 ± 0.3	-0.28 ± 0.07	18.0 ± 1.2	37.8 ± 0.8	23.7 ± 0.7	16.6 ± 0.8	9.5 ± 0.5
V830 Tau	K7	32.0 ± 1.5	121	-2	-0.2	15 ± 2	59.1 ± 1.0	36.9 ± 0.8	24.8 ± 0.8	14.4 ± 0.5

Table 3.2 (cont'd)

Object	SpT	$v \sin i$[a] (km s^{-1})	10% width[b] (km s^{-1})	Hα EW (Å)	Ca II EW (Å)	S/N[c] at Hα	3.6μm (mJy)	4.5μm (mJy)	5.8μm (mJy)	8.0μm (mJy)
GI Tau	K7	12.7 ± 1.9	302 ± 45	-14 ± 5	-0.62 ± 0.19	15.5 ± 1.3	···	···	···	···
RX J0433.5+1916	G6	58 ± 3	Absorp.	1.5 ± 0.3	-0.04	17.8 ± 1.2	···	···	···	···
DL Tau	G	19 ± 4	581 ± 6	-96 ± 9	-41 ± 4	17.7 ± 1.3	233 ± 3	254 ± 3	246 ± 3	283 ± 3
DM Tau	M1	4.0 ± 0.7	376 ± 27	-126 ± 37	-0.26 ± 0.03	14.8 ± 1.2	24.1 ± 0.7	15.9 ± 0.7	11.2 ± 0.7	10.7 ± 0.5
CI Tau	G	13 ± 2	572 ± 9	-78 ± 7	-23 ± 9	23.1 ± 1.7	225 ± 3	217 ± 5	188 ± 3	231 ± 3
HBC 407	G8	8.8 ± 1.8	Absorp.	0.9	-0.09	12 ± 2	15.4 ± 0.7	10.2 ± 0.5	6.1 ± 0.7	4.5 ± 0.3
AA Tau	K7	12.8 ± 1.1	402 ± 89	-14 ± 8	-0.34 ± 0.04	21.1 ± 1.5	172 ± 3	166.0 ± 1.7	152.8 ± 1.7	168.1 ± 1.7
HBC 412 A+B e	M1.5[d]	4.1 ± 0.2	104 ± 6	-3.3 ± 1.2	-0.157 ± 0.008	15.0 ± 1.5	···	···	···	···
HBC 412 A+B w	M1.5[d]	4.9 ± 0.3	105 ± 4	-4.0 ± 1.3	-0.23 ± 0.03	14.4 ± 1.5	···	···	···	···
DN Tau	M0	12.3 ± 0.6	336 ± 16	-35 ± 6	-0.42 ± 0.05	20.4 ± 1.3	135.1 ± 1.7	118.5 ± 1.7	108.7 ± 1.7	119.6 ± 1.7
HQ Tau	K0[d]	48 ± 2	442 ± 93	-2.0 ± 0.6	-0.03 ± 0.05	26.7 ± 1.8	378 ± 3	364 ± 3	367 ± 3	506 ± 3
RX J0435.9+2352	M1	4.2 ± 0.5	125 ± 21	-2.7 ± 1.5	-0.21 ± 0.07	18.8 ± 1.4	52.7 ± 1.0	32.9 ± 0.8	21.9 ± 0.8	13.0 ± 0.5
LkCa 14	M0	22.7 ± 1.0	122 ± 20	-0.42 ± 0.15	-0.17 ± 0.03	27.0 ± 1.6	52.7 ± 1.0	32.9 ± 0.8	21.7 ± 0.8	12.8 ± 0.5
HD 283759	F2	57 ± 6	Absorp.	3.92 ± 0.10	···	46 ± 3	62.8 ± 1.2	43.0 ± 1.0	27.2 ± 1.0	16.1 ± 0.7
RX J0437.2+3108	K4	11.3 ± 0.8	82 ± 9	-0.32 ± 0.05	-0.21 ± 0.04	22.4 ± 1.6	···	···	···	···
RX J0438.2+2023	K2	16.1 ± 1.7	Absorp.	0.24 ± 0.06	-0.13 ± 0.05	24.0 ± 1.7	25.3 ± 0.7	16.6 ± 0.7	10.5 ± 0.8	6.1 ± 0.5
RX J0438.2+2302	M1	4.5 ± 0.4	111 ± 29	-2.2 ± 1.0	-0.3 ± 0.07	18.8 ± 1.4	18.2 ± 0.7	12.2 ± 0.7	7.6 ± 0.8	4.2 ± 0.5
HD 285957	K2	22.5 ± 1.2	Absorp.	-0.132 ± 0.014	-0.15 ± 0.03	33 ± 2	···	···	···	···
LkCa 15	K5	13.9 ± 1.2	451 ± 51	-15 ± 3	-0.31 ± 0.06	24.2 ± 1.5	122.8 ± 1.5	94.7 ± 1.4	66.7 ± 1.4	69.3 ± 1.2
CoKu Tau4	M1	25.8 ± 0.4	185 ± 33	-1.8 ± 0.5	-0.13 ± 0.04	23.8 ± 1.4	55.7 ± 1.0	37.1 ± 0.8	26.0 ± 0.8	16.5 ± 0.7
HD 283798	G2	25.2 ± 1.2	Absorp.	1.96 ± 0.09	-0.091 ± 0.018	62 ± 4	···	···	···	···
RX J0444.4+1952	M1	4.5 ± 0.4	Absorp.	0.09 ± 0.04	-0.06 ± 0.02	20.5 ± 1.4	···	···	···	···
HD 30171	G5	108 ± 4	Absorp.	1.4 ± 0.2	···	65 ± 4	···	···	···	···
RX J0446.8+2255	M1	8.0 ± 0.3	85 ± 4	-1.3 ± 0.4	-0.26 ± 0.04	20.9 ± 1.5	···	···	···	···
RX J0447.9+2755 e	G2[d]	27.9 ± 1.4	Absorp.	1.2 ± 0.5	···	19.8 ± 1.7	···	···	···	···
RX J0447.9+2755 w	G2.5[d]	30.5 ± 1.8	Absorp.	1.035 ± 0.019	-0.05 ± 0.02	20 ± 2	···	···	···	···
UY Aur A+B a	K7	23.8 ± 1.3	324 ± 19	-40 ± 11	-0.8 ± 0.9	23.5 ± 1.5	···	···	···	···
RX J0452.5+1730	K4	8.8 ± 0.6	89	-0.2	-0.22 ± 0.04	22.2 ± 1.6	27.9 ± 0.8	16.8 ± 0.7	11.2 ± 0.8	7.3 ± 0.5

3.5 Results

3.5.1 Accretion and Disk Presence

To examine the correlation between disk presence and accretion, we show in Fig. 3.1 the 8μm excess against Hα 10% widths for those targets for which both measurements are available. (The error bars on the Hα 10% width refer to the standard deviation of the estimates over epochs.) Out of the 67 objects in this subsample, 22 show evidence of both accretion and disk presence (cf. upper right regions in Fig. 3.1), implying that gas from the inner disk is still being channeled onto the star, and 41 objects have neither infrared excess nor signs of accretion. Thus, in nearly all cases (63/67), the accretion signature is well correlated with disk presence.

Of the four exceptions, the three non-accretors with infrared excess, all in Cha I, are CHXR 20, Hn 18, and ISO 52. For these objects, accretion rates may have dropped below measurable levels in Hα 10% width even though the disks persist. The Ca II-λ8662 flux of Hn 18 is detectable and indicates a negligible accretion rate of $4.4 \times 10^{-11}\,M_{\odot}\,\mathrm{yr}^{-1}$. Also, accretion may be variable on short timescales (Nguyen et al. 2008, submitted to ApJL). For CHXR 20, Ca II-λ8662 emission was undetected at one epoch, and is present at two other epochs with a suggested small accretion rate of $2.6 \times 10^{-10}\,M_{\odot}\,\mathrm{yr}^{-1}$. The only accretor without infrared excess, LkCa 21, was observed on a single epoch with a Hα 10% width of $277\,\mathrm{km\,s}^{-1}$; this value includes a contribution from rotational broadening of $46\,\mathrm{km\,s}^{-1}$. The net 10% width is below the threshold for accretors originally set out by (White & Basri, 2003). In addition, Ca II-λ8662 emission was not observed in LkCa 21 implying that it likely is not an accretor.

3.5.2 Stellar Mass and Rotational Velocity

Rotational velocity is known to vary as a function of stellar mass in young stars, likely because the efficiency of angular momentum removal depends on magnetic activity, which in turn depends on stellar mass (cf. Scholz et al., 2007). To probe the rotation-mass dependence, we show the projected rotational velocity as a function of spectral type in Fig. 3.2. Here late-K spectral type corresponds to $\sim 1\,M_{\odot}$ (Baraffe et al., 1998). The results are similar to what was found previously (e.g. Scholz et al., 2007; Rebull et al., 2002). Higher mass stars tend to have faster projected rotational velocity overall than their lower mass counterparts.

Table 3.2 (cont'd)

Object	SpT	$v \sin i$[a] (km s^{-1})	10% width[b] (km s^{-1})	Hα EW (Å)	Ca II EW (Å)	S/N[c] at Hα	3.6μm (mJy)	4.5μm (mJy)	5.8μm (mJy)	8.0μm (mJy)
RX J0452.8+1621	K6	24.9 ± 1.2	123 ± 12	-0.7 ± 0.05	-0.18 ± 0.04	26.3 ± 1.8	70.1 ± 1.2	44.4 ± 1.0	30.2 ± 1.0	17.2 ± 0.7
RX J0452.9+1920	K5	4.8 ± 1.3	89 ± 8	-0.43 ± 0.04	-0.23 ± 0.02	26.9 ± 1.8	···	···	···	···
HD 31281	G0	79 ± 4	Absorp.	1.88 ± 0.09	···	62 ± 4	···	···	···	···
GM Aur	K7	14.8 ± 0.9	505 ± 11	-88 ± 15	-0.37 ± 0.08	22.1 ± 1.6	80.4 ± 1.2	56.4 ± 1.0	44.3 ± 1.0	47.8 ± 1.0
LkCa 19	K0	20.1 ± 1.1	154 ± 40	-0.9 ± 0.3	-0.27 ± 0.03	37 ± 2	76.3 ± 1.2	47.9 ± 1.0	31.8 ± 0.8	18.4 ± 0.7
RX J0455.7+1742	K3	12 ± 2	Absorp.	0.1 ± 0.04	-0.131 ± 0.014	30 ± 2	···	···	···	···
SU Aur	G2	59 ± 2	561 ± 58	-5.0 ± 1.9	0.042 ± 0.012	78 ± 5	873 ± 5	816 ± 5	771 ± 5	976 ± 5
RX J0456.2+1554	K7	9.7 ± 0.6	106 ± 20	-0.7 ± 0.2	-0.26 ± 0.05	25.0 ± 1.8	···	···	···	···
HD 286179	G0	17.1 ± 1.2	Absorp.	2.12 ± 0.09	···	40 ± 2	···	···	···	···
RX J0457.0+3142	K2	25.5 ± 1.5	Absorp.	1.0 ± 0.5	···	55 ± 3	···	···	···	···
RX J0457.2+1524	K1	42 ± 2	Absorp.	0.3 ± 0.07	···	40 ± 2	110.8 ± 1.5	68.6 ± 1.2	47.5 ± 1.0	26.5 ± 0.9
RX J0457.5+2014	K3	33 ± 3	Absorp.	0.39 ± 0.18	···	30.8 ± 1.9	48.6 ± 1.0	30.0 ± 0.8	19.7 ± 0.8	11.6 ± 0.5
RX J0458.7+2046	K7	7.8 ± 0.5	Absorp.	0.066 ± 0.017	-0.167 ± 0.018	27.6 ± 1.7	42.0 ± 1.0	25.6 ± 0.8	17.3 ± 0.8	10.1 ± 0.5
RX J0459.7+1430	K4	14.5 ± 0.6	53	···	-0.193 ± 0.017	24.0 ± 1.7	37.1 ± 0.8	23.0 ± 0.7	16.1 ± 0.8	8.8 ± 0.5
V836 Tau	K7	13.4 ± 1.1	403 ± 58	-55 ± 17	-0.36 ± 0.13	20.4 ± 1.4	72.9 ± 1.2	61.8 ± 1.2	52.3 ± 1.2	57.9 ± 1.0
RX J05072+2437	K6	19.7 ± 1.0	126 ± 14	-1.4 ± 0.4	-0.3 ± 0.03	21.3 ± 1.4	26.0 ± 0.7	17.3 ± 0.7	12.7 ± 0.7	0.7 ± 0.5

[a]The Hα 10% width uncertainty does not correspond to the measurement uncertainty, but to the scatter in our multi-epoch data.

[b]The $v \sin i$ uncertainty represents the combined measurement scatter between results using different template spectra, and over different epochs.

[c]The S/N is based on the continuum on either side of Hα used for the 10% width calculations, and the uncertainty represents the standard error of the estimate.

[d]Spectral type determined by this work.

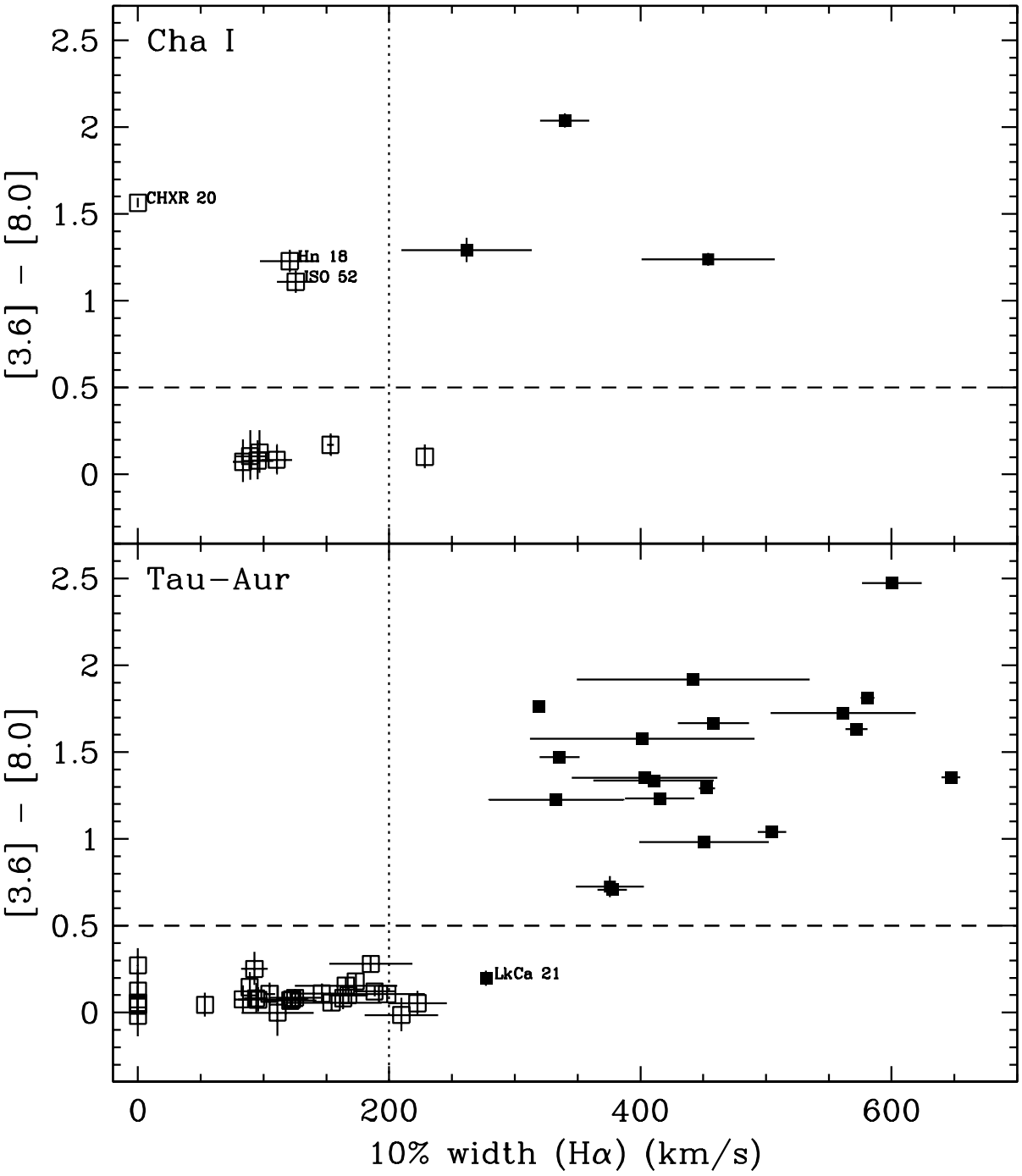

Figure 3.1 The 8μm excess vs. the full width of Hα at 10% of the peak (Hα 10% width) for 13 Cha I and 54 Tau-Aur members. Suspected accretors and non-accretors based on Hα emission are denoted by solid and hollow symbols, respectively. The Hα 10% width error bars do not correspond to the measurement uncertainty, but to the scatter in our multi-epoch data. There is a clear separation of disk candidates above (and the non-disk candidates below) $[3.6] - [8.0] = 0.5$ illustrated by the dashed line, and a delineation between accretors and non-accretors at the cutoff of $200\,\mathrm{km\,s^{-1}}$ adopted originally by Jayawardhana et al. (2003). Note that some non-accretors appear above the cutoff because of the additional broadening due to rapid rotation, see Fig. 3.3.

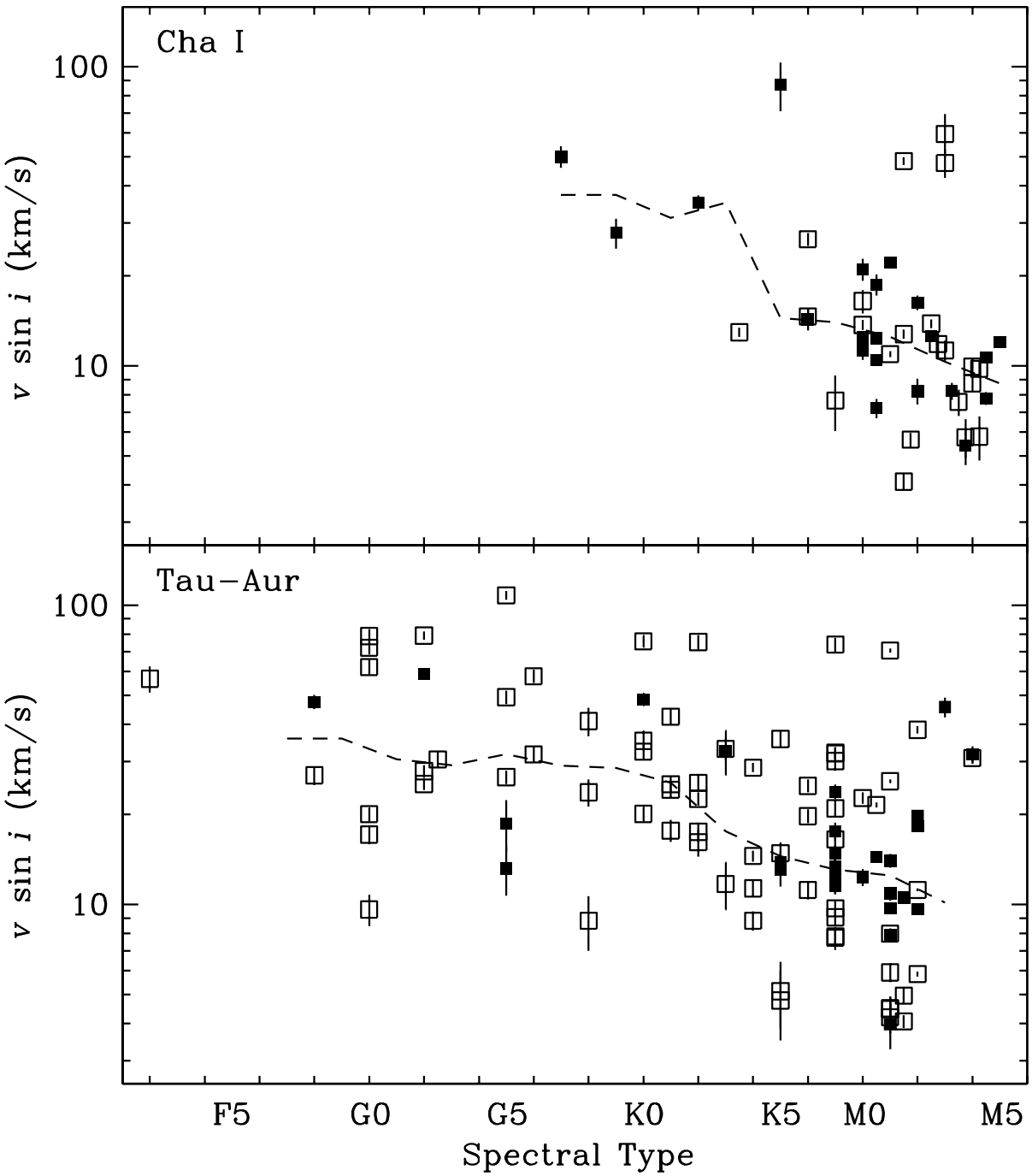

Figure 3.2 Projected rotational velocities v sin i as a function of spectral type. Suspected accretors and non-accretors based on Hα emission are denoted by solid and hollow symbols, respectively. The v sin i errors represent the combined uncertainty between results using different template spectra, and over different epochs. The dashed line represents the median v sin i for bins covering on either side two spectral subtypes. The overall appearance of this plot is comparable to v sin i distribution in other young clusters: projected rotational velocity tends to increase with stellar mass.

To examine this rotation-mass trend further, we divided our targets into two mass bins consisting of F–K type stars, and M type stars. In Fig. 3.3, we show boxplots of $v \sin i$ for the two mass bins: the horizontal lines inside the rectangles indicate the median values. Clearly, in both Cha I and Tau-Aur, the median $v \sin i$ for the higher mass bins, $26\,\mathrm{km\,s^{-1}}$ and $24\,\mathrm{km\,s^{-1}}$, are significantly faster than those of the lower mass bins, both at $11\,\mathrm{km\,s^{-1}}$.

To get a quantitative sense of the difference in rotational velocity between the high and low mass stars, we applied the Kolmogorov-Smirnov (K-S) test. This analysis shows there is a probability of only $\sim$0.5% for Cha I, and $\sim$0.1% for Tau-Aur that the $v \sin i$ for the two mass bins were drawn from the same distribution.

When interpreting this finding, one should take into account that the stars in our sample assuming an age of $\sim 2\,\mathrm{Myr}$ span roughly a range of 1–4 $R_\odot$ in stellar radii. To gauge the contribution of stellar radius on $v \sin i$, we evaluated the specific angular momentum in our sample as follows. First, we converted spectral type to effective temperature by looking up and interpolating values from Sherry et al. (2004). Second, we used the effective temperature to obtain estimates of mass M, radius R, and moment of inertia I from the models of D'Antona & Mazzitelli (1997). Third, we combined these values with our $v \sin i$ estimates to compute the projected specific angular momentum using the relation $j \sin i = (v \sin i)I/MR$. In Fig. 3.4, we show $j \sin i$ as a function of stellar mass. From the best linear fit to the upper envelope of the datapoints, we find by eye that $j \propto M^{0.5}$. Indeed, there is an increase in specific angular momentum with increasing stellar mass.

3.5.3 Accretion and Rotational Velocity

To check for a connection between accretion and rotation, in Fig. 3.5 & 3.6, we show $v \sin i$ as a function of Hα 10% width and of 8 μm excess for our targets. In addition, the figures show both the intrinsic contribution of rotation to the line widths, and the separation between accretors and non-accretors.

We compared the distribution of $v \sin i$ for accretors and non-accretors using a number of K-S tests. To account for the rotation-mass dependence (see §3.5.2), we carried out these tests for the two mass bins (F–K type and M type) separately. The probability that the $v \sin i$ of accretors and non-accretors were drawn from the same distribution in Cha I is 6% for the high-mass targets, and 50% for the low-mass ones. The probabilities

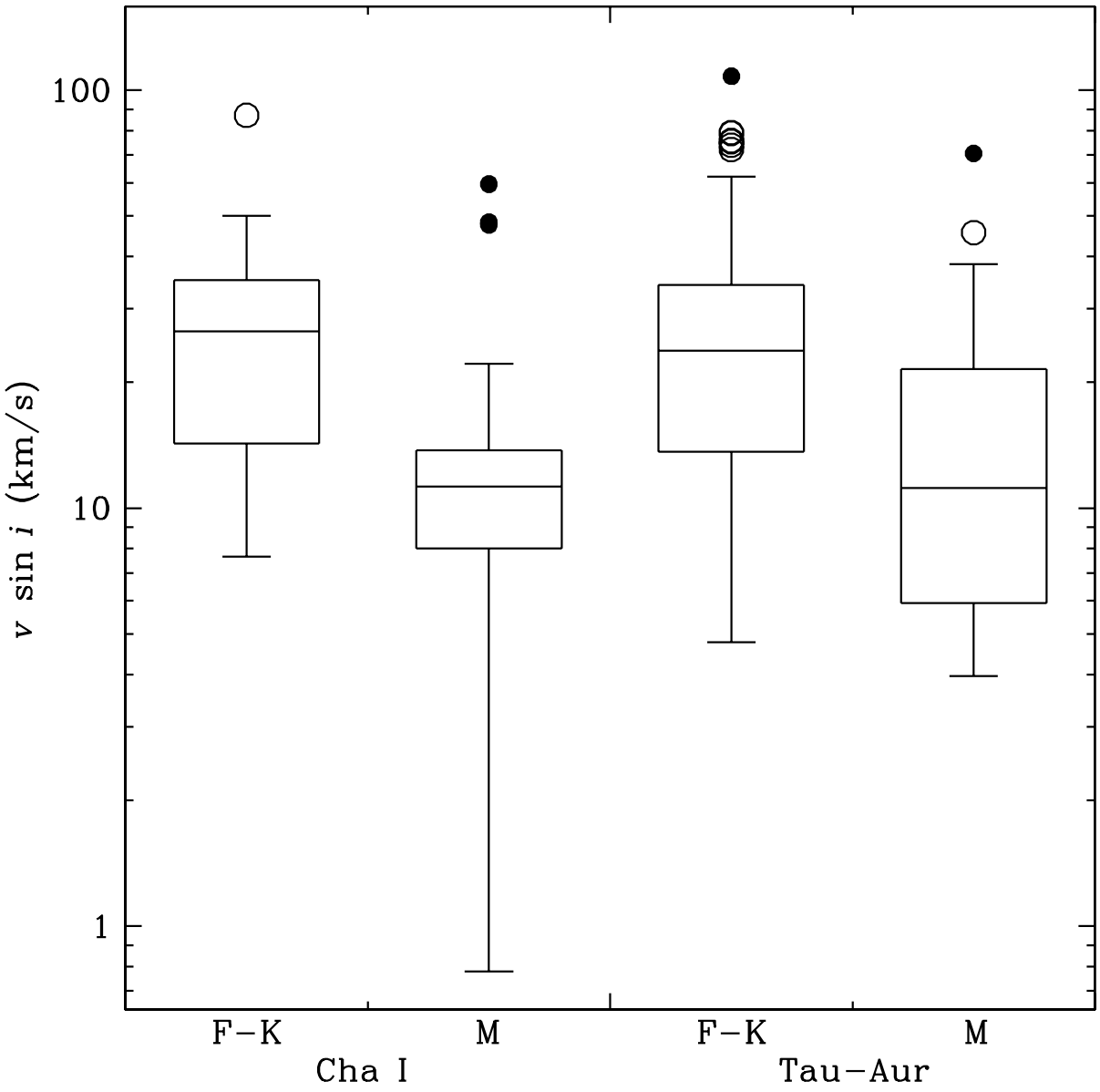

Figure 3.3 Boxplots of v sin i for Cha I and Tau-Aur grouped into two mass bins. Clearly, for both regions, the rotational velocities of high mass stars is faster than their lower mass counterparts by a factor of 2–2.5. The central rectangles span the first quartile to the third quartiles with the segment inside indicating the median values, and "whiskers" above and below the box show the locations of the minima and maxima after applying a Tukey filter; statistical outliers and suspected outliers are shown as filled dots and hollow dots, respectively.

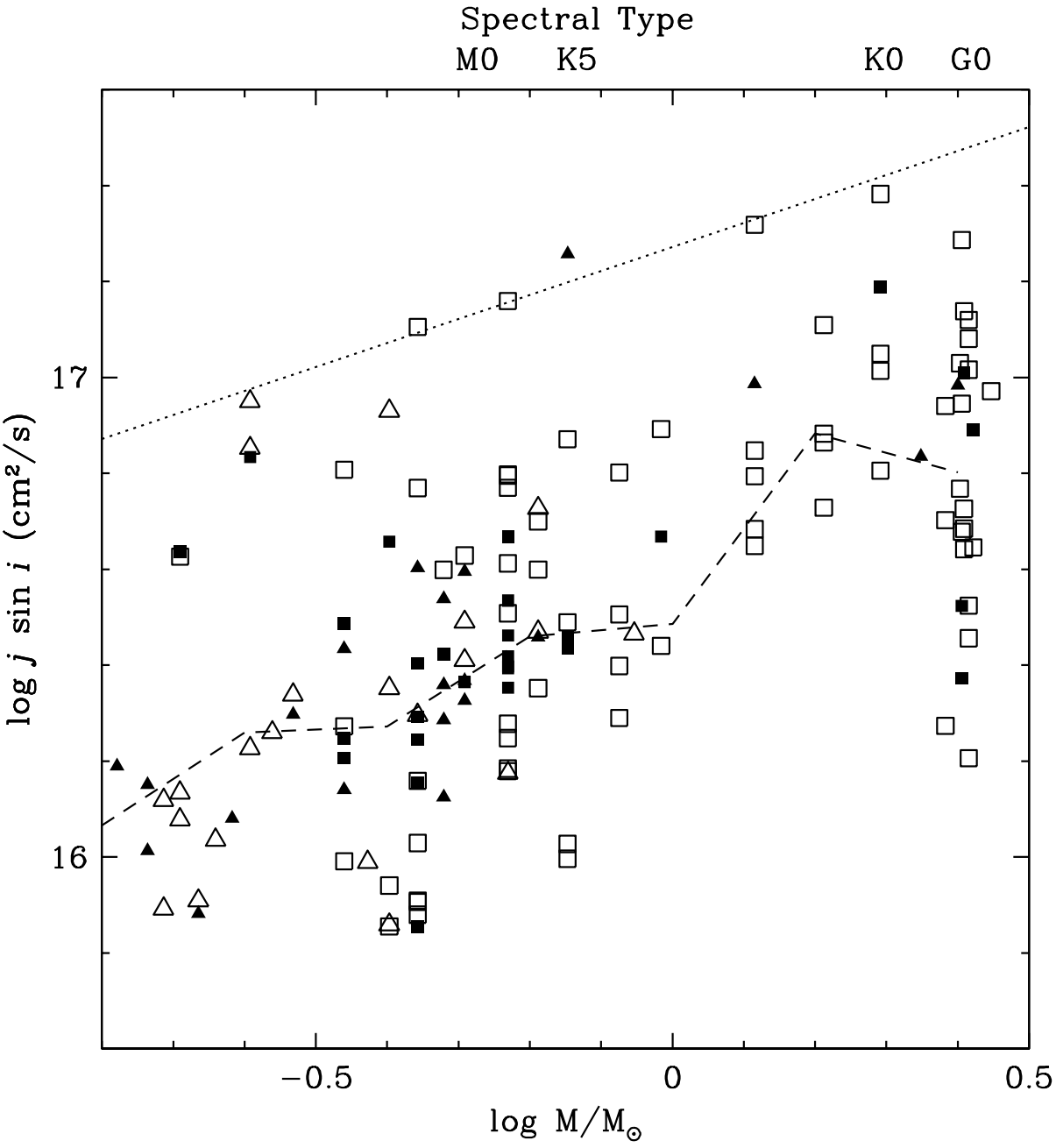

Figure 3.4 Specific angular momentum j as a function of stellar mass computed assuming an age of 2 Myr from the models of D'Antona & Mazzitelli (1997). Suspected accretors and non-accretors based on Hα emission are denoted by solid and hollow symbols, respectively. Targets from Cha I are represented by triangles, and those from Tau-Aur are drawn as squares. The dashed line represents the median $v \sin i$ for bins spanning $\log M/M_{\odot} \pm 0.1$. The dotted line is a linear fit by eye to the upper bound of the data and has a slope of 0.5.

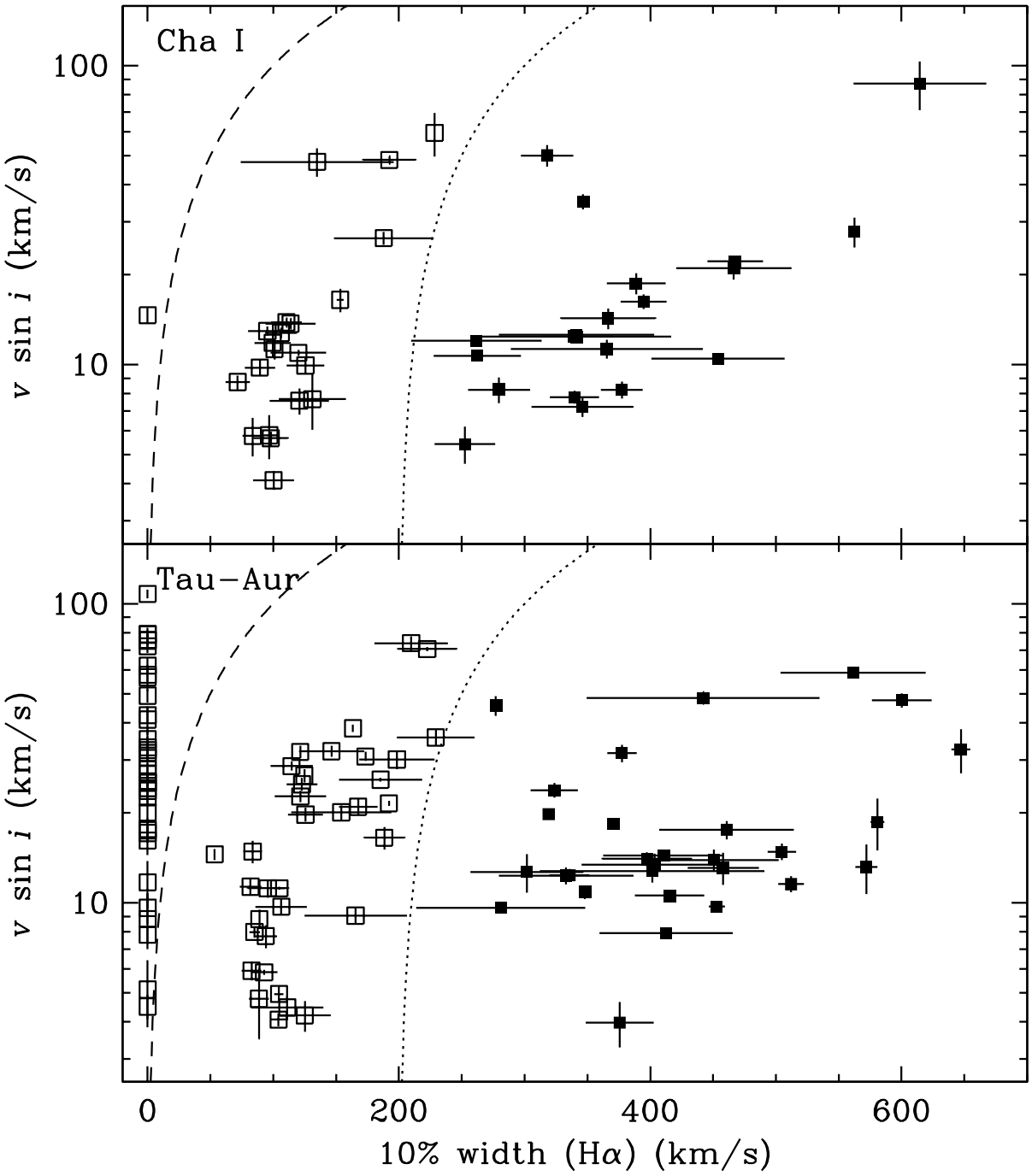

Figure 3.5 Projected rotational velocity v sin i vs. Hα 10% width for a sample of T Tauri stars in the Chamaeleon I and Taurus-Auriga star forming regions. Suspected accretors and non-accretors based on Hα emission are denoted by solid and hollow symbols, respectively. The Hα 10% width error bars do not correspond to the measurement uncertainty, but to the scatter in our multi-epoch data. The v sin i errors represent the combined uncertainty between results using different template spectra, and over different epochs. The intrinsic contribution of rotation to line width is shown by the dashed line. The adopted boundary between accretors and non-accretors is shown by the dotted line.

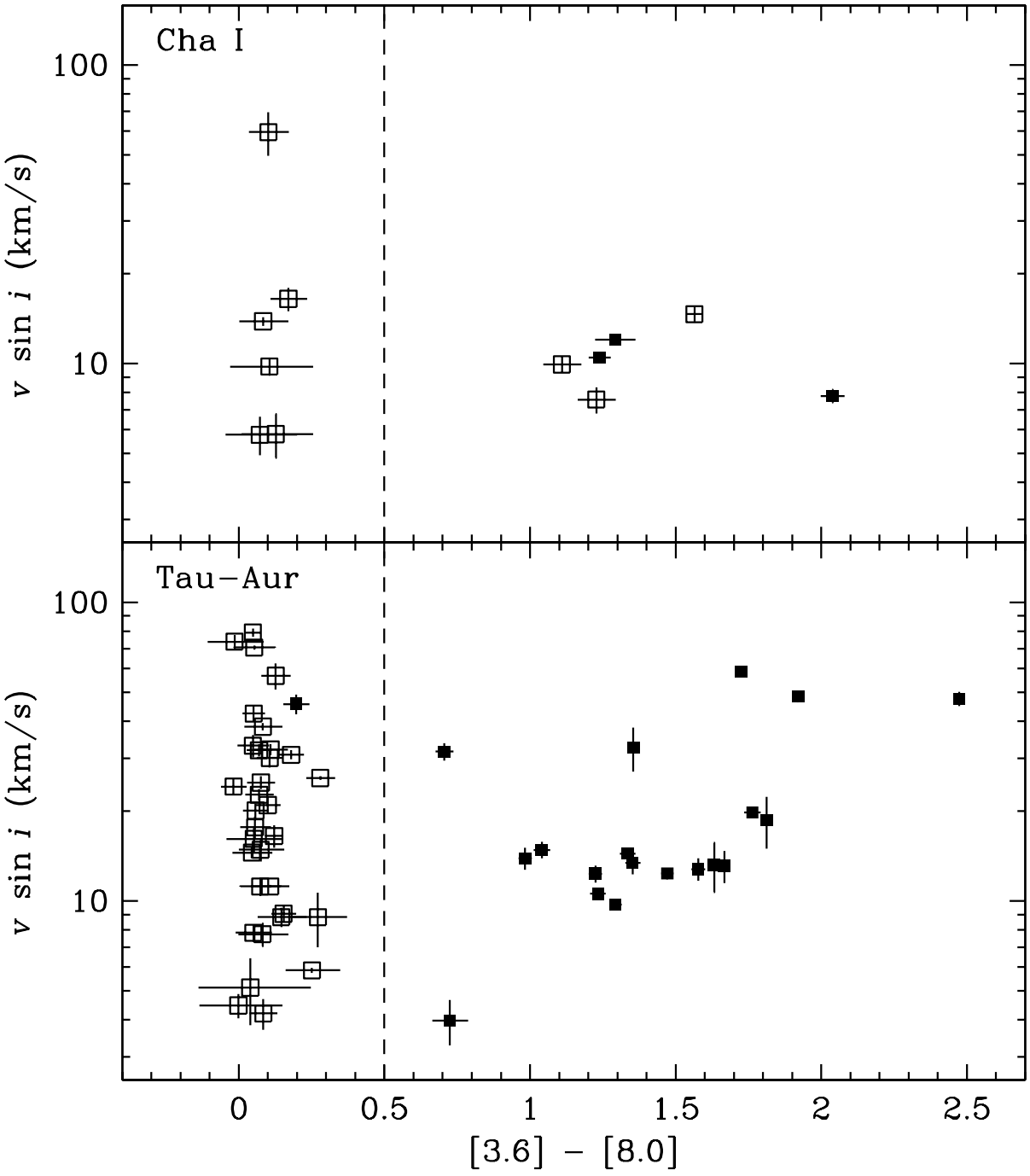

Figure 3.6 Projected rotational velocity v sin i as a function of 8μm excess. Suspected accretors and non-accretors based on Hα emission are denoted by solid and hollow symbols, respectively. The v sin i errors represent the combined uncertainty between results using different template spectra, and over different epochs. The separation of disk and non-disk candidates is illustrated by the dashed line. The v sin i distributions for stars with and without inner disks are not statistically distinct.

for high- and low-mass targets in Tau-Aur are 8% and 10%, respectively. For the entire sample, the corresponding probabilities for high- and low-mass targets is 30% and 7%, respectively. Thus, any connection between accretion and projected rotational velocity is at best marginally significant. The $v \sin i$ distributions are shown in Fig. 3.7.

Since the presence of dusty disks is strongly correlated with accretion in our targets, it is not surprising there is, for high and low mass stars in Tau-Aur respectively, a 9% and 13% probability that the $v \sin i$ for stars with and without disks were drawn from the same distribution. It would appear that the presence of ongoing accretion or a disk has no significant effect on the rotation in our sample. This is contrary to the standard disk braking scenario, as outlined in §3.2.

One particular reason for the negative test results is the presence of a significant number of rapidly rotating accretors, as seen in Fig. 3.5. Based on Spitzer data, Rebull et al. (2006) find that the fraction of stars with disks is very low for rotation periods $P < 1.8\,\mathrm{d}$ (see their Fig. 3). For a radius of $1\,R_\odot$ and an average $\sin i$, this period corresponds to a projected rotational velocity of $22\,\mathrm{km\,s^{-1}}$. This value scales linearly with stellar radius. In our sample, we see 5–10 objects rotating faster than this threshold, where the exact number depends on the inclinations and stellar radii. This type of objects is not expected in the evolutionary sequence for the standard disk braking scenario described in §3.2.

Previous studies drew conclusions about the disk-braking scenario based on rotation periods from photometric data, while we use projected rotational velocity. To check whether this makes a difference, we ran Monte Carlo simulations based on published data from previous photometric studies, e.g. Stassun et al. (1999), Herbst et al. (2002) surveys in the ONC. In the simulations, rotation periods were converted to $v \sin i$ by selecting random viewing angles and using uniformly distributed stellar radii of 1–4$R_\odot$. In the case of Herbst et al. (2002), where there was previous indication of disk-braking, we found probabilities of $<1\%$ that diskless stars have the same distribution of $v \sin i$ as disk harboring stars, hence we recovered their evidence for disk braking. Furthermore, for data from Stassun et al. (1999), where disk-braking was not observed, we found that the simulated $v \sin i$ distributions for diskless and disk-harboring stars were similar, with probabilities consistently $>10\%$. We conclude that our results are insensitive to our use of projected rotational velocity to probe disk-braking scenarios.

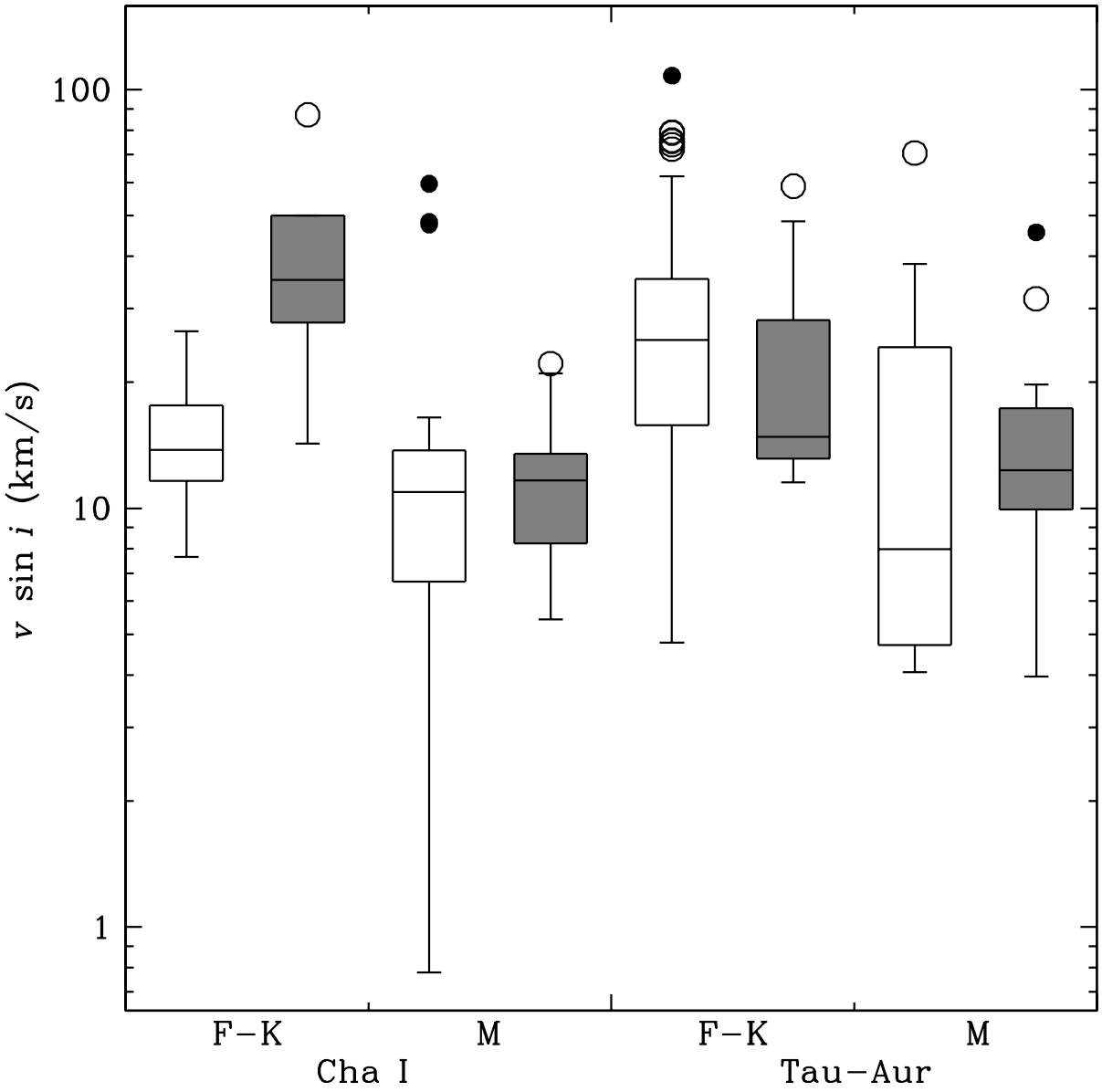

Figure 3.7 Boxplots of $v \sin i$ for accretors vs. non-accretors grouped by region and spectral type. The distributions in black and gray represent accretors and non-accretors, respectively. The central rectangles span the first quartile to the third quartiles with the segment inside indicating the median values, and "whiskers" above and below the box show the locations of the minima and maxima after applying a Tukey filter; statistical outliers and suspected outliers are shown as filled dots and hollow dots, respectively. The $v \sin i$ distributions between accretors and non-accretors are statistically similar. Note, the comparison for Cha I high-mass stars involves only nine objects, and may appear deceivingly distinct by-eye.

3.6 Summary and Discussion

We present a comprehensive study of projected rotational velocities and Hα 10% widths for young stars in Taurus-Auriga and Chamaeleon I. Our three main results are:

1. *Indicators for accretion and inner disks agree for* $> 94\%$ *of our total sample.* For nearly all objects, the dissipation of the dusty inner disk and the drop in accretion rate below measurable levels occur simultaneously. Consequently, the lifetimes of inner disks are similar to the timescales of gas accretion. Based on our large sample, systems with inner disk clearings and ongoing gas accretion are rare (1/67); the same holds for systems with non-accreting inner disks (3/67). This consistency shows that timescales for inner disk clearing and accretion decline are much shorter than typical disk lifetimes ($\sim 10^5$ years instead of several 10^6 years).

2. *F–K stars have on average 2–2.5 times larger rotational velocities than M stars.* Although rotational velocity is proportional to stellar radius, from the models of D'Antona & Mazzitelli (1997) at 2 Myr, the typical radius of our F–K stars is less than 1.5 times that of the M stars in our sample. Moreover, the specific angular momentum is proportional to $M^{0.5}$. This mass dependence complements findings in Orion of Wolff et al. (2004) where the upper envelope of the observed values of angular momentum per unit mass varies as $M^{0.25}$ for stars on convective tracks (~ 1 Myr) with a break in the power law with a sharp decline in j with decreasing mass for stars with $M < 2\,M_\odot$ for slightly older stars on radiative tracks (see their Fig. 3). They posit that these broad trends can be accounted for by simple models where stars lose angular momentum before they are deposited on the birth line, plausibly through star-disk interaction, and for stars with $M < 2\,M_\odot$, the amount of braking increases with time spent evolving down their convective tracks. Our analysis of ~ 2 Myr old T Tauri stars in Cha I and Tau-Aur showed an angular momentum mass trend in-between that of the two age groups studied in Orion for the same mass regime. This intermediate result could hint at only the beginning stages of disk braking, a significant age spread, or both.

3. *The presence of accretion or an inner disk does not significantly affect the distribution of rotational velocities in Taurus-Auriga and Chamaeleon I.* This finding adds to the ongoing debate on disk braking in young stars, as it is in stark contrast to recent studies in the ONC and NGC 2264 (e.g. Rebull et al., 2006; Cieza & Baliber, 2007), where a clear increase in disk fraction is found with increasing rotation period.

Part of the explanation may be that the stars have had insufficient time to brake.

Hartmann (2002) estimate a disk-magnetosphere braking timescale $\tau_{\rm DB} \gtrsim 4.5 \times 10^6\,{\rm yr}\,M_{0.5}\,\dot{M}_{-8}^{-1} f$, where $M_{0.5}$ is the stellar mass in units of $0.5\,M_\odot$, $\dot{M}_{-8}$ is the mass accretion rate in units of the typical value of $10^{-8}\,M_\odot\,{\rm yr}^{-1}\,(M/0.5M_\odot)$, and f is the stellar rotation as a fraction of breakup velocity, then $\tau_{\rm DB}$ for our sample (typically $\sim$5 Myr) is somewhat larger than the estimated age of the stars ($\sim$ 2 Myr). Adopting the accretion and rotation results of Rebull et al. (2000) and Clarke & Bouvier (2000), we find a shorter typical $\tau_{\rm DB}$ of $\sim$ 1 Myr for the ONC where disk braking is observed. Therefore, disk-locking in Cha I and Tau-Aur may be ineffective overall.

In addition, there is evidence for spin-down not involving accretion from the inner disk. The specific angular momentum values for $\sim$10 Myr solar-like mass stars in Orion, where strong braking is observed (Wolff et al., 2004), are typically lower than those found in our sample of similar mass non-accretors (where disk-locking should have expired) by a factor of $\sim$5. In contrast, the j values for $\sim$ 1 Myr solar-like mass stars in Orion are similar to those of our non-accretors. These measurements could imply another braking mechanism is at work after disks have dissipated. Of course, this indication for another braking mechanism relies on accurate age estimates.

Another possible explanation for the lack of strong disk braking in our sample is age spread, which might be larger in Taurus-Auriga and Chamaeleon I than in the cluster cores of ONC and NGC 2264. Covering objects in varying stages of their rotational history could dilute a disk braking signature. In addition, the contrast between our results and those of previous studies that find strong evidence of disk braking may stem from different initial conditions at evolutionary stages before the stars became optically observable, e.g. at the birth line. The initial rotational velocity distributions for dense star forming regions like ONC and NGC 2264 could be very different from Tau-Aur and Cha I where star formation has occurred in an environment with much lower stellar density. Future investigation of a similar kind should aim to take into account a more complete understanding of stellar properties when looking at correlations between rotation and disk/accretion signatures. In combination with previous results in other young clusters, our data will serve as an empirical basis for future studies on the timescales and efficiency of disk braking mechanisms.

Acknowledgements

We thank the anonymous referee for helpful comments that improved the clarity of the

paper. We would like to thank David Lafrenière, and Nairn Baliber for useful suggestions relating to the work presented in this paper. This paper includes data gathered with the 6.5 meter Magellan Telescopes located at Las Campanas Observatory, Chile. We would also like to thank the Magellan staff for their tireless effort and patience on accommodating our aggressive observing program. This work was supported in part by NSERC grants to RJ and MHvK, and an Early Researcher Award from the province of Ontario to RJ.

Chapter 4

Close Companions: Cha I and Tau-Aur

4.1 Abstract

We present the results of a multiplicity survey of 212 T Tauri stars in the Chamaeleon I and Taurus-Auriga star-forming regions, based on high-resolution spectra from the Magellan Clay 6.5 m telescope. For 174 of these stars, we obtained multi-epoch data with sufficient time baselines to identify binaries based on radial velocity variations. We identified eight close binaries and four close triples, of which three and two, respectively, are new discoveries. The overall spectroscopic multiplicity fraction we find for Cha I (7%) and Tau-Aur (6%) are similar to each other, and to the results of field star surveys in the same mass and period regime. The frequency of systems with close companions in our sample is not seen to depend on primary mass, and contrasts the findings from imaging surveys of wide binaries among young stars and field dwarfs. We also find no strong correlation between accretion and multiplicity. This implies that close companions are not likely the main source of accretion cutoff observed in weak-lined T Tauri stars.

4.2 Introduction

Most stars, both in the solar neighborhood and in young clusters are members of binary or multiple systems. Yet, the formation and early evolution of binary and multiple stars is not well understood theoretically and poorly constrained observationally. For instance, the binary fraction in dense star-forming regions such as the Orion Nebula Cluster and

IC 348 are comparable to that of field stars (Duchêne et al., 1999; Köhler et al., 2006) whereas the frequency of binaries is much higher among young stars in dispersed T associations like Taurus-Auriga (e.g. Simon et al., 1995; Ghez et al., 1997a; Brandeker et al., 2003); for reviews see Mathieu et al. (2000) and Duchêne et al. (2007). Furthermore, high-order multiples are more common in nearby star-forming regions than for solar-type main-sequence stars in the solar neighborhood (Correia et al., 2006). Multiplicity may well be an important ingredient for star formation.

Some recent simulations suggest that stars usually form in triples and higher-order multiple systems only to be dispersed later. The fraction of stars in multiple systems decreases from 80% down to 40% by about 10 Myrs (Delgado-Donate et al., 2004). Predictions are that the binary fraction is higher among higher mass stars, and that brown dwarfs are never close companions to stars (Goodwin et al., 2004).

While past multiplicity surveys, using speckle imaging and adaptive optics on 4-m class telescopes, have drawn attention to the ubiquity of binaries in star forming regions (e.g. Ghez et al., 1993; Leinert et al., 1993), their limited contrast and angular resolution have left many key questions unanswered or only partially answered. For instance, the frequency of higher-order multiples is uncertain, and so is the frequency of very low-mass stellar and sub-stellar companions. Multiple systems are probably not uncommon.

With adaptive optics on 8-m class telescopes, it has become straightforward to detect all stellar and even all brown dwarf companions down to the deuterium-burning limit with separations of tens of AU for nearby young stars (e.g. Lafrenière et al., 2008). Our radial velocity study is complementary and cover the close separations.

We present the results of a high-resolution spectroscopic survey of 212 stars spanning ~ 0.2–$3\,M_{\odot}$ in the nearby (~ 140 pc) ~ 2 Myr old star-forming regions Chamaeleon I (hereafter Cha I) and Taurus-Auriga (hereafter Tau-Aur). Previously, we presented a study of rotation, disk, and accretion signatures for a subsample of 144 stars having no unresolved companions and line profiles showing only a single source (Nguyen et al., 2009b), and use the derived projected rotational velocities ($v \sin i$) and accretion signatures (Hα 10% width) for this work. Furthermore, we also analyzed the variability in accretion-related emission lines for a subsample of 40 classical T Tauri stars (Nguyen et al., 2009a). Lafrenière et al. (2008) presented a census of wide binaries in Cha I that encompasses our sample while Damjanov et al. (2007) investigated circumstellar disks, including the effect of companions on disks, for a subsample of Cha I targets with available near-IR data.

Among the specific empirical issues we address in this work is the dependence of multiplicity on primary mass, i.e., whether higher mass stars are more likely to be in binaries and multiples than their lower mass counterparts. An increase in wide binaries with increasing mass has been observed for both young stars and field dwarfs. Furthermore, we look at how close-in multiplicity varies with between different star-forming regions and the field; the multiplicity of $\sim$0.1–2 $M_{\odot}$ field dwarfs in the solar neighborhood has been studied extensively (e.g. Duquennoy & Mayor, 1991; Fischer & Marcy, 1992). We also explore whether close companions contribute to the observed difference between classical T Tauri stars (CTTS), which are accreting, and weak-lined T Tauri star (WTTS), which are not accreting based on weak Hα emission. Although the source of dichotomy between CTTS and WTTS is currently unknown, the presence of non-accreting 2 Myr old stars is surprising. It has been suggested that the inner disks around weak-lined objects may have been truncated by close binary companions.

4.3 Observations

We used 813 high-resolution optical spectra of 212 members in the $\sim$2 Myr old Chamaeleon I and Taurus-Auriga star-forming regions obtained with the echelle spectrograph MIKE (Bernstein et al., 2003) on the Magellan Clay 6.5-m telescope at the Las Campanas Observatory, Chile. The data were collected on 15 nights during four observing runs between 2006 February and 2006 December. Our results are listed in tables 4.1 & 4.2.

Our sample consists of a magnitude-limited subset (R $\leq$ 17.6 for Cha I; R $\leq$ 13.4 for Tau-Aur) of targets from Luhman (2004a) for Cha I, and from Leinert et al. (1993), Ghez et al. (1993), Simon et al. (1995), Köhler & Leinert (1998), Briceño et al. (2002) and Luhman (2004b) for Tau-Aur. Our targets span the spectral type range from F2 to M5 based on published classifications. In addition, we observed a sample of 25 slowly rotating velocity standard stars selected from the list of Nidever et al. (2002); these cover the same spectral range as our targets. We determined the spectral type for 13 targets without prior classification by fitting their spectra against those of the standard stars, and identifying the best fits.

MIKE is a slit-fed double echelle spectrograph with blue and red arms. For this study, we used only the red region spanning 4 800–9 400 Å in 32 spectral orders. The 0.35″ slit was used with no binning to obtain the highest possible spectral resolution, R $\sim$ 60 000. The pixel scale was 0.14″ pixel^{-1} in the spatial direction, and approximately

$0.024\,\text{Å}\,\text{pixel}^{-1}$ at 6 500 Å in the spectral direction. The raw data were bias-subtracted and flat-fielded, and before extraction, the scattered background in the spectrograph was subtracted by fitting splines to inter-order pixels. Since the sky background is insignificant compared to the stellar spectrum in the majority of cases, our optimal extraction routine does not separate the sky background from the source spectrum. To keep a consistent reduction procedure, we used the same extraction routine also for the few cases where the sky was significant, resulting in some spectra being contaminated by the sky. The In MIKE, the spatial direction of the projected slit is wavelength dependent, and not aligned with the CCD columns. To extract these slanted spectra, we used customized routines running in the ESO-MIDAS environment (described in detail in Brandeker et al., in preparation). For wavelength calibration, we used exposures of a thorium-argon lamp as well as observed telluric absorption lines. Integration times were chosen such that we obtained signal-to-noise ratios (S/N) > 30 per spectral resolution element at 6 500 Å; they typically ranged from 60 to 1 200 seconds depending on seeing.

4.4 Analysis Techniques

To find close binaries and higher-order multiples in our sample, we used both line profile and radial velocity analysis. The former was used to identify double-lined spectroscopic binaries (hereafter SB2s) and triple-lined spectroscopic binaries (hereafter SB3s); these systems are characterized by two or more prominent peaks in the line profile. The latter was used to detect single-lined spectroscopic binaries (hereafter SB1s); acceleration would be suggested by significant radial velocity scatter in our data. Both analyses involve fitting the target spectra with comparison spectra to minimize χ^2,

$$\chi^2 \equiv \sum_i \left(\frac{Y(\lambda_i) - P(\lambda_i)}{\sigma(\lambda_i)} \right)^2 \tag{4.1}$$

where Y and σ are the fluxes and uncertainties of the target spectra, and P are the fluxes of the comparison spectra. The comparison spectra are produced using template spectra from the observed slowly rotating standard stars. To match a standard star with each target star, we examined the spectra from the three standard stars closest in spectral type to the target, and selected the standard star spectrum that best fits that of the target. For the fits, we masked telluric absorption lines, Li-λ6708 which is present in

young stars but absent in our standard stars, and activity-related emission lines Hα, Hβ, Pa6 through 9, Pa11, Pa14, He I (λ5876, λ6678, λ7065), O I (λ7774, λ8446, λ8456), [O I] (λ5577, λ6300, λ6364), Na I D doublet, Ca II IR triplet, and Fe II 42 multiplet from the spectra. We used χ^2 analysis instead of Fourier techniques for SB1s, or TODCOR techniques (Zucker & Mazeh, 1994) for SB2s and SB3s to take advantage of uncertainties at each individual wavelength. We processed data for each echelle order separately to avoid discontinuities resulting from poorly corrected blaze, and combined the output to get our results.

4.4.1 Line Profiles

The line profiles of each target were derived using the technique described in Rucinski (1999). This techniques computes the discrete broadening function $B(v_j)$ that minimizes χ^2 in Eq. 4.1 for,

$$P(\lambda_i) = \left[\sum_j B(v_j) \cdot S((1 + v_j/c)\lambda_i)\right] \cdot C(\lambda_i) \tag{4.2}$$

where B is the broadening function, S is the template spectrum from a slowly rotating standard star, and C is the best-fit polynomial to the continuum.

Our routine to derive the line profile of a target at a given epoch consists of two steps. First, for each echelle order, we fit the target spectra with comparison spectra to produce a broadening function spanning -120 to $+120\,\mathrm{km\,s^{-1}}$ with a sampling interval of $6\,\mathrm{km\,s^{-1}}$. This interval is close to the velocity resolution of the spectrograph, and reduces possible covariance between points from oversampling. Second, we compute the weighted mean of the broadening function across the echelle orders.

4.4.2 Radial Velocity

The radial velocity measurements of each target were computed by fitting the target spectra with series of velocity shifted comparison spectra. This technique computes the velocity shift $v_\star$ that minimizes χ^2 in Eq. 4.1 for,

$$P(\lambda_i, v_\star) = (G(v \sin i) * S)\,[(1 + v_\star/c)\lambda_i] \cdot C(\lambda_i) \tag{4.3}$$

where G is the analytic rotational broadening function from Gray (2005) assuming a limb darkening coefficient of 0.65, $v \sin i$ is the projected rotational velocity of the target star, S is the template spectrum from a slowly rotating standard star, and C is the best-fit polynomial to the continuum. The projected rotational velocity for each target star was computed by fitting the target spectra with a series of template spectra rotationally broadened from 0 to $200\,\mathrm{km\,s^{-1}}$, and calculating the best fit value (see Nguyen et al., 2009b).

Our routine to estimate the radial velocity of a target at a given epoch consists of four steps. First, for each echelle order, we fitted the target spectra with comparison spectra velocity shifted from -120 to $+120\,\mathrm{km\,s^{-1}}$ in steps of $10\,\mathrm{km\,s^{-1}}$, and recorded the velocity value of the best fit for each echelle order. Second, we refined our search to radial velocities within $10\,\mathrm{km\,s^{-1}}$ of the first-pass results in steps of $0.01\,\mathrm{km\,s^{-1}}$, and revised our estimates accordingly. Third, comparing the results for different orders, we removed outliers using a standard Tukey filter, i.e. values lying 1.5 times the interquartile range below the first quartile and above the third quartile were discarded (see Hoaglin et al., 2000). For a Gaussian distribution, this filter corresponds to removing data points beyond $2.7\,\sigma$. Fourth, we computed the weighted mean and standard error across the echelle orders, and used those values as the radial velocity and measurement uncertainty of the target at that epoch.

For some targets with heavily veiled spectra (e.g., DR Tau; see Fig. 4.201), this technique did not produce consistent radial velocity results. In these cases, we derived the radial velocities from fits to the line profiles corrected for veiling. This correction involved adding to Eq. 4.2 a linear component alongside the rotational broadening function to estimate and account for the contribution from veiling. Furthermore, we considered the overall potential influence of accretion and veiling on our radial velocity estimates by comparing both the estimated radial velocity measurement uncertainties and scatter within the observing runs against the accretion signature Hα 10% width (see §4.6.1). This comparison is illustrated in Fig. 4.1 & 4.2. There appears to be no significant difference in the radial velocity measurement uncertainties nor the radial velocity scatter within the observing runs between accretors and non-accretors in Cha I and Tau-Aur. The final radial velocity results are listed in tables 4.1 & 4.2.

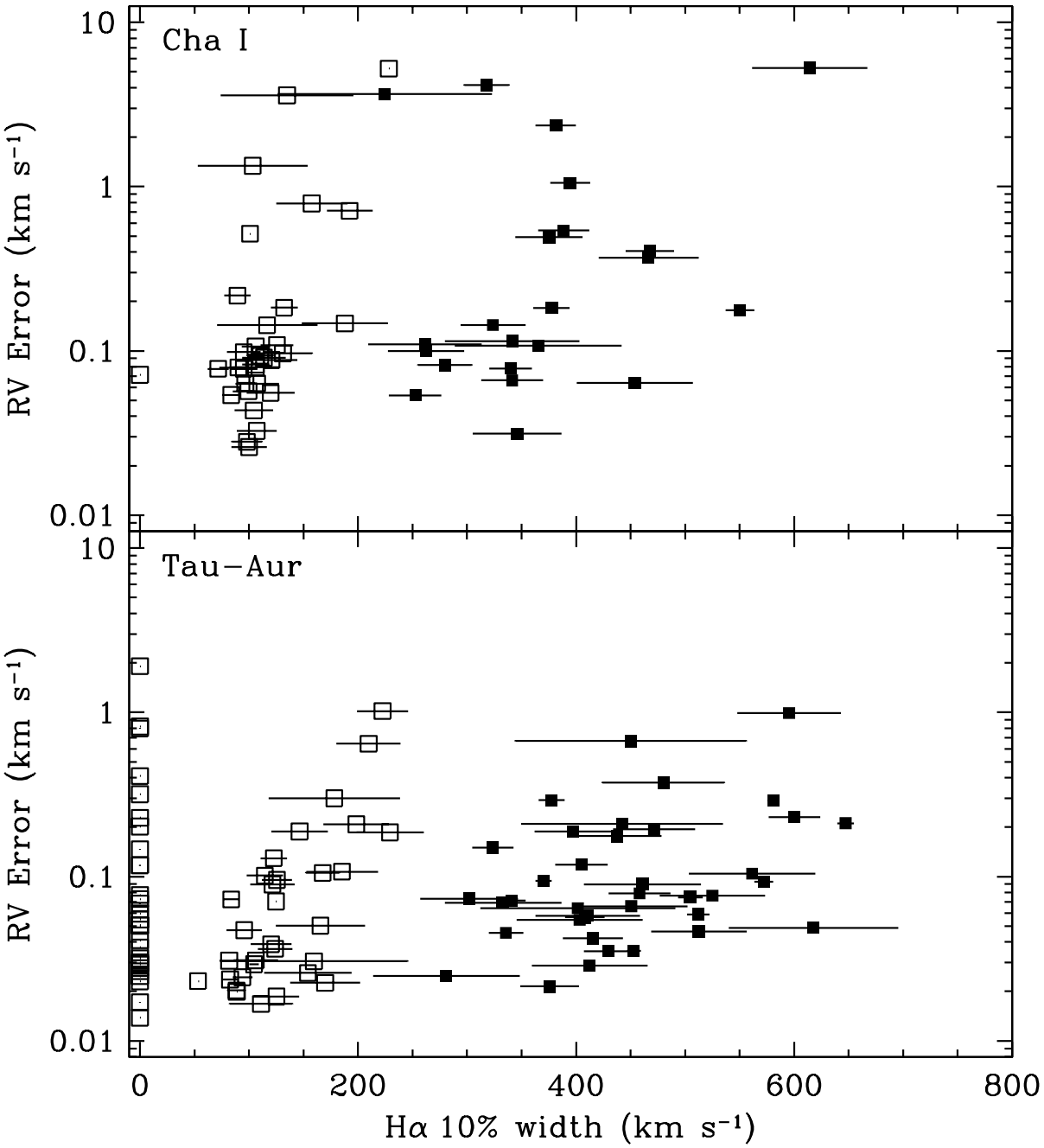

Figure 4.1 The weighted mean radial velocity measurement uncertainty for members of Cha I and Tau-Aur with single-line profiles as a function of the accretion signature Hα 10% width. Accretors and non-accretors are denoted by solid and hollow symbols, respectively. There appears to be no significant difference in the radial velocity measurement uncertainties between accretors and non-accretors.

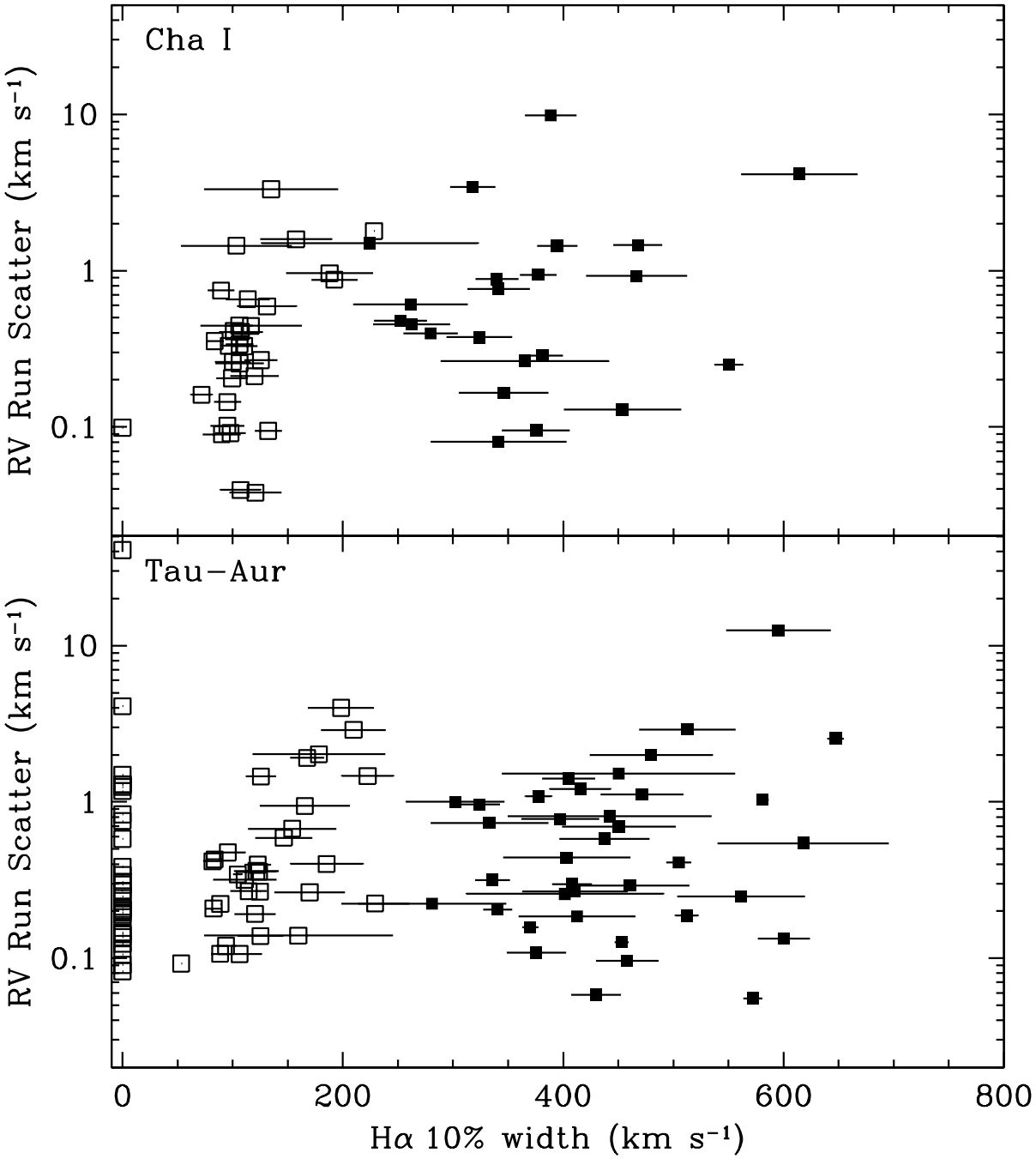

Figure 4.2 Radial velocity scatter within the observing runs for members of Cha I and Tau-Aur with single-line profiles as a function of the accretion signature Hα 10% width. Accretors and non-accretors are denoted by solid and hollow symbols, respectively. There appears to be no significant difference in the radial velocity scatter within the observing runs between accretors and non-accretors.

4.5 Identifying Close Companions

Our approach to identify close companions consists of two basic parts. First, we checked the line profiles of each star for multiple peaks suggestive of SB2s. Second, we examined the radial velocity measurements for variations consistent with SB1s.

4.5.1 Identifying SB2 Candidates

We identified SB2 candidates as targets that have line profiles with prominent multiple peaks that cannot be accounted for by non-companion sources. An extra peak at the observer's rest frame could be attributed to possible contamination from moonlight or twilight sky. This occurs relatively frequently in our data, since we did not correct for sky in our reduction (see §4.3). To assess this contamination, we checked the angular distance of the target to the moon and the altitude of the sun below the horizon at the time the data were taken, and we inspected the raw data frames.

Additional peaks in the line profile may be caused by light from nearby resolved companions. We collected information on known visual binaries by cross-referencing our target list with those of speckle and direct imaging surveys: for Cha I, we used Lafrenière et al. (2008), and for Tau-Aur we checked Leinert et al. (1993), Ghez et al. (1993), Simon et al. (1995), Ghez et al. (1997b), and Köhler & Leinert (1998). To gauge the significance of the visual binaries on the line profiles, we used the ΔK magnitudes and K-band flux ratios reported in the surveys to calculate corresponding R-band flux ratios. This calculation consists of the following eight steps: (i) use the spectral type of the targets to estimate effective temperatures $T_{\rm eff}$ (Sherry et al., 2004); (ii) with $T_{\rm eff}$, compute luminosities L from the models of D'Antona & Mazzitelli (1997); (iii) with L, compute bolometric magnitudes $M_{\rm bol} = 4.75 - 2.5\log(L/L_{\odot})$; (iv) use the spectral type of the targets and the color-temperature relation of Sherry et al. (2004) to compute the bolometric correction BC, and the V–R and V–K colors of the primary stars; (v) combine the above to calculate the absolute R and K magnitudes of the primary stars; (vi) apply the reported ΔK magnitudes and K-band flux ratios of the systems to derive the absolute K magnitudes of the companions; (vii) use these absolute K magnitudes to estimate the corresponding absolute R magnitudes by interpolating the color-temperature relation of Sherry et al. (2004); and (viii) combine the derived absolute R magnitudes of the primary stars and the companions to find the R-band flux ratios of the systems. Obviously, the above calculation relies on numerous assumptions, and the resulting estimated R-band

flux ratios are thus only approximate. However, they suffice for our purpose of gauging whether a significant contribution to the line profile from a resolved companion is likely.

Our ability to identify SB2 candidates from the line profiles is limited by several factors. First, the contribution of companions to the line profile must be sufficiently large to discriminate them from their primary stars. The SB2 candidates we could identify had a flux ratio lower bound of $\sim$0.1. Second, the radial velocity separation of component stars with similar $v \sin i$ must be large enough to distinguish each star in the line profile. The minimum measurable velocity separation is equal to the sampling interval of $6\,\mathrm{km\,s^{-1}}$; however, we empirically find the lower limit of the velocity separation for our identified SB2 candidates is $\sim 10\,\mathrm{km\,s^{-1}}$. Third, the $v \sin i$ of the component stars with similar radial velocities must be large enough to distinguish each star in the line profile. Among applicable SB2 candidates, the smallest difference between component star $v \sin i$ is $\sim 24\,\mathrm{km\,s^{-1}}$.

We identified five SB2s, two suspected SB2s and one SB3 in Cha I. In Tau-Aur, we identified nine SB2s, one suspected SB2, and three SB3s. For all these SB2 and SB3 candidates, we measured the flux ratios of the systems as well as the radial velocities and projected rotational velocities of each component star by fitting the line profiles with multiple rotational broadening functions. For SB2 systems showing no acceleration, we checked if wide companions are responsible for the secondary profiles by considering the separation of known resolved companions, and comparing the flux ratios estimated from the line profiles with those of the resolved companions. We found that resolved companions are likely the source of the secondary profiles in three out of the four and five out of the seven SB2 candidates showing no acceleration in Cha I and Tau-Aur, respectively.

4.5.2 Identifying SB1 Candidates

We identified SB1 candidates as targets that have radial velocity scatter that cannot be accounted for by noise. We consider not only measurement noise but also possible intrinsic noise from the star. Of particular relevance are radial velocity changes due to spots which effectively attenuate light from part of the star. Combined with rotation, this leads to apparent velocity changes on cycles connected to the rotation period of the star. To test the significance of the radial velocity changes of each target, we calculate several relevant statistics.

First, to evaluate the overall radial velocity scatter of each target, we compute the χ^2 statistic of the radial velocity measurements with the null hypothesis of no acceleration using the relation

$$\chi^2_{\rm RV} = \sum_i \left(\frac{v_i - \langle v \rangle}{\sigma_i} \right)^2 \tag{4.4}$$

where v_i and σ_i are the radial velocities and measurement uncertainties of the target at epochs t_i, and $\langle v \rangle$ is the weighted mean of the radial velocity of the target. We would like to achieve a confidence level of $> 95\%$ that no single star is mistakenly identified as an SB1 in our sample. Given that we have ~ 200 targets, this condition requires a confidence level of $> 99.97\%$ for correct identification of individual targets. For a typical target observed at four epochs, this implies that we require $\chi^2_{\rm RV} > 19.1$ to identify a target as an SB1.

Second, to estimate systematic noise for each target, we consider the measurements for each observing run separately. Since each observing run is only a few days long, velocity changes of a few $\mathrm{km\,s^{-1}}$ are much more likely to be due to rotation than to orbits. Specifically, for each target, we calculate the systematic noise during each observing run,

$$\sigma_{{\rm N},j} = \sqrt{\sigma^2_{{\rm S},j} - \sigma^2_{{\rm E},j}} \tag{4.5}$$

where $\sigma_{{\rm S},j}$ is the weighted standard deviation of the radial velocities for observing run j, and $\sigma_{{\rm E},j}$ is the weighted mean of the radial velocity errors for observing run j. The weighted standard deviation is given by

$$\sigma^2_{{\rm S},j} = \left(\frac{N'_j}{N'_j - 1} \right) \frac{\sum_k w_k (v_k - \langle v \rangle_j)^2}{\sum_k w_k} \tag{4.6}$$

where v_k are the velocities at epochs t_k from observing run j, $\langle v \rangle_j$ is the corresponding weighted mean of the velocities, $w_k \equiv 1/\sigma^2_k$ are the statistical weights based on measurement uncertainties at epochs t_k, and N'_j is the normalized number of frames defined as

$$N'_j \equiv N_j \frac{\langle w \rangle^2_j}{\langle w^2 \rangle_j} \tag{4.7}$$

where N_j is the number of frames taken of the given target during observing run j. Note,

in the case of all equal weights, Eq. 4.6 reduces to the equation for simple standard deviation. Finally, we adopt as the systematic noise for a given target $\sigma_{\rm N} \equiv \langle \sigma_{{\rm N},j} \rangle$ the weighted mean of the systematic noise for all the observing runs of the target.

Third, to re-evaluate the radial velocity scatter of each target with compensation for systematic noise, we add in quadrature the systematic noise $\sigma_{\rm N}$ of a given target to the radial velocity uncertainties σ_i of the target, and re-evaluate the χ^2 statistic (Eq. 4.4) using the radial velocities and uncertainties aggregated by observing run, i.e., using v_j and σ_j the weighted means and standard errors of the targets during observing runs j. Analogous to the assessment for overall radial velocity scatter, for a typical target observed during two observing runs, we require a run aggregated $\chi^2_{\rm RV} > 13.4$ to identify a target as an SB1.

Fourth, we estimate the extent of the radial velocity fluctuations induced by star spots. Since the influence of star spots on observed radial velocity is related to the rotational velocity of the star, we show in Fig. 4.3 the radial velocity scatter within the observing runs for single-line targets in our sample as a function of projected rotational velocity $v \sin i$. For both Cha I and Tau-Aur, the upper bound of the short-period velocity scatter is $\sim$15% of $v \sin i$. Single-line targets with radial velocity scatter larger than this value are likely SB1s.

We identified one SB1 and two suspected SB1s in Cha I. In Tau-Aur, we identified two SB1s and two suspected SB1s.

4.5.3 Detection Limits

The companion detection limits of the radial velocity measurements are a function of both companion mass M_2 and orbital period P. For each mass and period, the detailed orbital elements such as inclination angle i and orbital phase ϕ may inhibit detection. Although eccentricity might facilitate or hinder the detection of a companion in an individual case, the effect is canceled out statistically (Fischer & Marcy, 1992).

To derive the probability of detection of a given point in the (M_2, P) space, we simulate binaries with combinations of i incremented in a $\cos i$ distribution, and ϕ incremented uniformly over their full ranges. For each combination of orbital elements, we generate 1000 sinusoidal radial velocity curves, and add random errors drawn from a normal distribution centered on zero and with a chosen rms value $\sigma_{\rm noise} = 0.34\,{\rm km\,s^{-1}}$ which is equal to

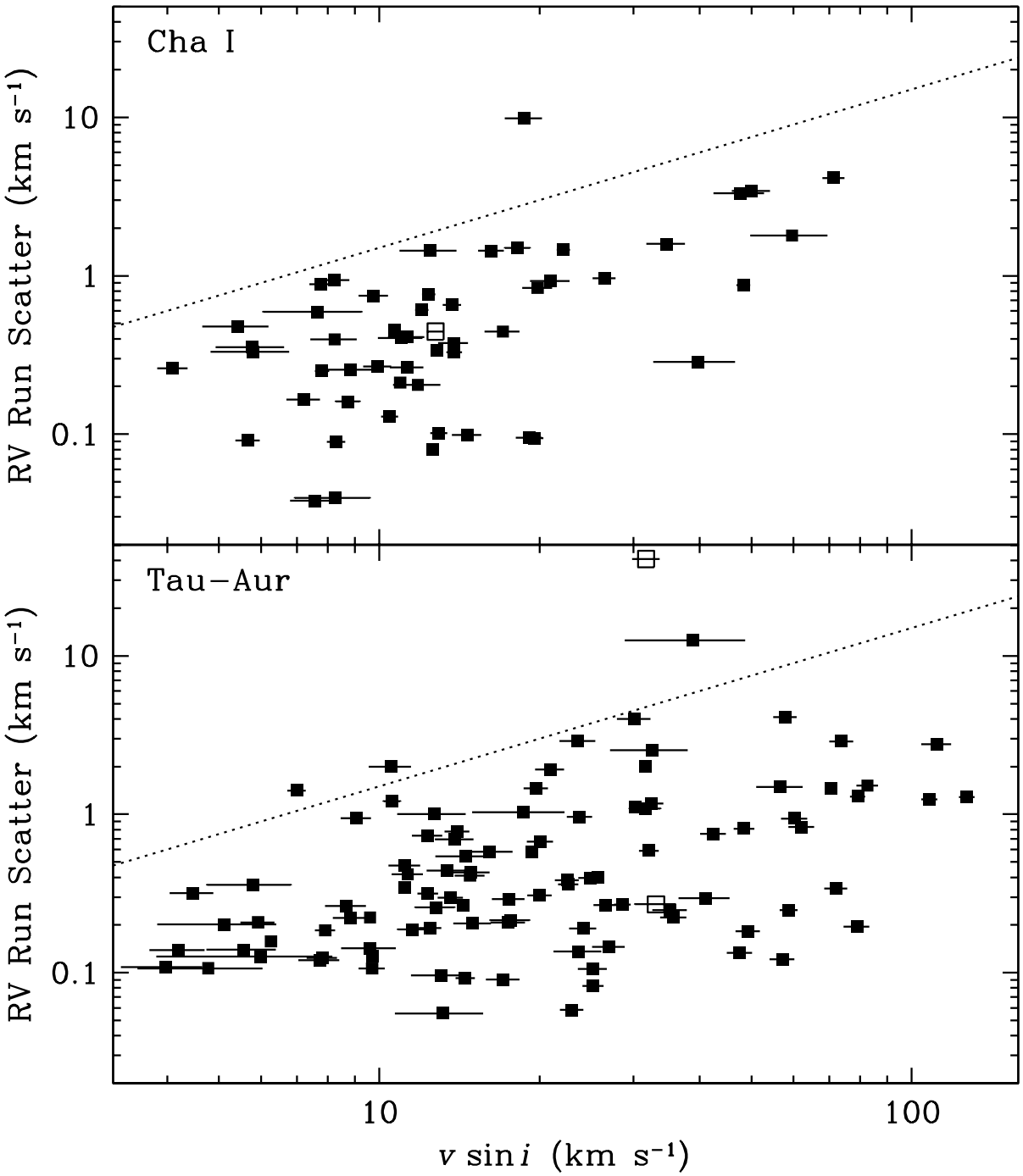

Figure 4.3 Radial velocity scatter within the observing runs for members of Cha I and Tau-Aur with single-line profiles as a function of projected rotational velocity $v \sin i$. Single stars and SB1 candidates are denoted by solid and hollow symbols, respectively. The dotted-line is drawn at 15% of $v \sin i$ and represents the approximate upper bound of the radial velocity scatter. The single stars above this limit have large measurement uncertainties due to poor spectra.

the typical intrinsic noise in our actual stars. Furthermore, like our typical observations of actual stars, we sample each simulated radial velocity curve four times (e.g., at epochs $t = 0, 0.2, 2$ and 30 days), and we adopt as measurement uncertainty the median value of $0.10\,\mathrm{km\,s^{-1}}$ from our actual data. The χ^2 and minimum velocity scatter conditions described in §4.5.2 are used as detection criteria for the simulations. For a given (M_2, P) pair, we define the detection probability as the fraction of successful detections over the number of trials for that point. The result of these simulations in the (M_2, P) plane for a typical T Tauri star in our sample ($0.6\,M_\odot$; $v \sin i = 15\,\mathrm{km\,s^{-1}}$) is shown in Fig. 4.4 as iso-probability curves of detection. We see for example that we have a 75% probability of detecting a companion of mass $0.1\,M_\odot$ with a period of 60 days if the typical $0.6\,M_\odot$ primary star has been observed four times with our 30 day baseline. From Fig. 4.4, we also deduce that detection biases vary significantly for orbital periods $\lesssim$50 days. This is due to aliasing from the sampling times.

The selection criteria for our study contain biases which affect a determination of the multiplicity rate. Specifically, a magnitude-limited sample favours the inclusion of double-lined spectroscopic binaries (Branch, 1976). This is especially the case for young stars where the dependence of luminosity on mass is comparatively gradual, i.e., $L \propto M^\alpha$, with $\alpha \sim 2$ for pre-main sequence stars rather than $\alpha \sim 4$ for stars on the main sequence.

4.6 Results and Discussion

In our entire sample of 212 members of Cha I and Tau-Aur, we have identified a total of 12 systems that show accelerations due to close companions and 7 systems for which we suspect this is the case. To reduce sampling bias in our close companion statistics, we trim our sample to include only targets that have observations spanning multiple observing runs (> 25 days). This ensures that all targets included for statistics have observations with time baselines sufficiently long to capture the radial velocity scatter from most SB1s. With this condition, there are 11 systems with close companions and 6 systems with suspected close companions from a final sample of 174 systems. Of the 11 targets with close companions, three are SB1s, five are SB2s, and three are SB3s.

Below, we will first look for differences between our two regions, with primary mass and accretion, and with stars in the field. Second, we will look at possible non-companion contributions to radial velocity variations. Third, we will discuss 13 somewhat puzzling

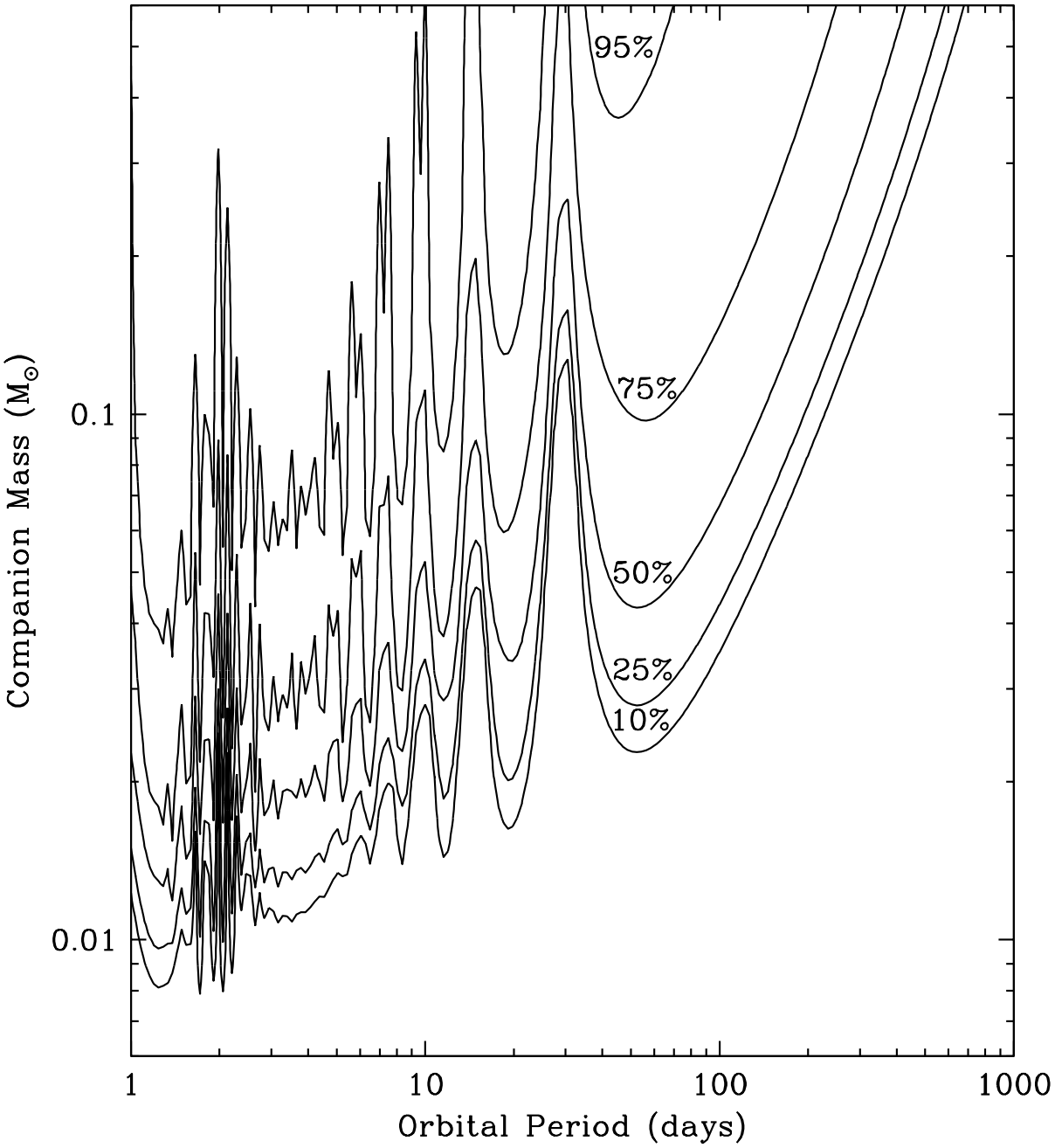

Figure 4.4 Detection probabilities for a given companion mass and orbital period for typical T Tauri stars in our sample ($0.6\,M_\odot$; $v \sin i = 15\,\mathrm{km\,s^{-1}}$) observed four times at epochs $t = 0$, 0.2, 2 and 30 days and assuming a measurement uncertainty of $0.1\,\mathrm{km\,s^{-1}}$. At each point in the (M_2, P) space, the inclination angle i and the orbital phase ϕ were incremented over their full range. For each combination of orbital elements, 1000 radial velocity curves were generated, and Gaussian noise with an rms value of $0.34\,\mathrm{km\,s^{-1}}$ was added to each curve in Monte Carlo fashion to represent the typical intrinsic noise in our actual sample. The detection criteria used are the χ^2 and minimum velocity scatter conditions described in §4.5.2.

stars that have mean velocities that deviate from the velocity of the cluster, yet appear to be members from all other indicators.

4.6.1 Comparison of Binary Populations

We first compare the multiplicity fraction (MF) in Cha I and in Tau-Aur with each other. The Chamaeleon I and Taurus-Auriga star-forming regions are both T associations of similar age. Previous surveys using speckle and direct imaging show a similar multiplicity fraction for both regions (Lafrenière et al., 2008). The multiplicity fractions MF = $(\mathrm{SB1}+\mathrm{SB2}+\cdots)/(\mathrm{Singles}+\mathrm{SB1}+\mathrm{SB2}+\cdots)$ we find using high-resolution spectroscopy in our sample are $0.07^{+0.05}_{-0.03}$ (4/61) for Cha I, and $0.06^{+0.03}_{-0.02}$ (7/113) for Tau-Aur.

We can compare the multiplicity fractions formally as follows. For random variables Q and R, the probability P that Q is greater than R is given by the formula

$$P[Q > R] = \int_{-\infty}^{+\infty} \left(f_Q(x) \int_{-\infty}^{x} f_R(y)\, dy \right) dx \tag{4.8}$$

where f_Q and f_R are the probability distribution functions of Q and R, respectively. In our case, the random variables are the underlying multiplicity fractions of stellar populations. By sampling a population, we will find k binaries out of n targets with the outcome governed by the binomial distribution $B(n, p)$ where p is the true multiplicity fraction of the population. Consequently, the probability distribution function of p given k observed binaries out of n targets is

$$f(p|k, n) = (n+1) \begin{pmatrix} n \\ k \end{pmatrix} p^k (1-p)^{n-k} \tag{4.9}$$

Applying this function to Eq. 4.8, we get the probability that the multiplicity fraction of population Q is greater than that of population R is

$$P[p_Q > p_R] = \int_0^1 \left(f(p_Q|k_Q, n_Q) \int_0^{p_Q} f(p_R|k_R, n_R)\, dp_R \right) dp_Q \tag{4.10}$$

By substituting the MF results from Cha I and Tau-Aur into this formula, we find the probability that the MF of Cha I is greater than that of Tau-Aur is only 58%. Therefore, the two regions have similar MF values. Subsequently, we will use the combined results

when making comparisons with those of other populations, and between various subpopulations in our sample determined by physical characteristics.

To investigate the change in close multiplicity as a function of primary mass, we divide our sample into two nearly equal mass bins and calculate the MF in each bin. We find multiplicity fractions of $0.06^{+0.03}_{-0.02}$ (6/98) for F–K spectral type targets, and $0.07^{+0.04}_{-0.03}$ (5/76) for M spectral type targets. There is no clear dependence in the spectroscopic regime of multiplicity fraction with primary mass: the probability that the multiplicity fraction of the F–K type stars is greater than that of M-type stars is only 44%. This is in stark contrast to the results of imaging surveys (e.g. Lafrenière et al., 2008) which show, for Chamaeleon I, Taurus, Upper Scorpius A and field stars, a marked increase in wide companions with increasing primary mass.

To address the question of whether close companions are responsible for the observed difference between classical and weak-lined T Tauri stars from §4.2, we measure the full width of Hα at 10% of the peak (hereafter, Hα 10% width) of our targets to differentiate accretors and non-accretors. As suggested by previous spectroscopic studies (e.g. Jayawardhana et al., 2003), we classify accretors or CTTSs as stars with Hα 10% widths larger than 200 km s^{-1} after subtracting rotational broadening. We measured Hα 10% widths previously for a subsample of our targets (Nguyen et al., 2009b), and apply the same technique here. Five targets in our statistical sample did not have reliable measurements for Hα 10% width. Of the remaining 169 targets, we find a close binary fraction of $0.08^{+0.04}_{-0.03}$ (8/104) and $0.05^{+0.04}_{-0.02}$ (3/65) for non-accretors and accretors, respectively. The populations of WTTS and CTTS have statistically similar close binary fractions: the probability from our data that the true multiplicity fraction of WTTSs is greater than that of CTTSs is 75% which is approximately 1σ. Therefore, we cannot say confidently that close companions are the main source of the attenuated accretion in weak-lined T Tauri stars.

Finally, we compare our multiplicity fractions with values for field stars from the G dwarf survey of Duquennoy & Mayor (1991), and the M dwarf surveys of Fischer & Marcy (1992). Comparison between our sample and those of the field population is not straightforward because the surveys have different time baselines and companion mass sensitivities. Specifically, we observed each of our stars typically at four epochs with baselines of up to several months whereas the aforementioned field dwarf surveys generally had more than a dozen observations per star spanning a four year interval. Furthermore, the field dwarf surveys are sensitive to companions having masses less than

the primary mass, extending to the hydrogen burning limit, $0.08\,M_\odot$ whereas our survey should detect $\sim$50% of substellar companions with masses of $0.05\,M_\odot$ for orbital periods $\lesssim$100 days.

A meaningful comparison of multiplicity fractions requires that we correct for the differences in the detection completeness of the surveys. To accomplish this, we restrict our statistical comparison to common orbital periods and companion mass ranges. Since our stars are typically observed four times, to determine the likely range of companion masses and orbital periods for our survey we make use of probability theory.

Let $\mathcal{M}(m,p)$ be the a priori distribution of multiplicity rates for our star population in the companion mass and orbital period (M_2, P) space. In the same space, let $\mathcal{D}(m,p)$ be the detection success rates of our observing scheme, i.e., the results of our simulations in §4.5.3. Using Bayes' theorem (Bayes et al., 1763), from the prior distribution $\mathcal{M}(m,p)$, and the likelihood function $\mathcal{D}(m,p)$, we calculate the probability $\mathcal{P}$ that a detected companion is in the given intervals $[M_{2,\min},\, M_{2,\max}]$ and $[P_{\min},\, P_{\max}]$,

$$\mathcal{P} = \frac{\sum_{m=M_{2,\min}}^{M_{2,\max}} \sum_{p=P_{\min}}^{P_{\max}} \mathcal{M}(m,p)\mathcal{D}(m,p)}{\sum_m \sum_p \mathcal{M}(m,p)\mathcal{D}(m,p)} \tag{4.11}$$

Since we have no prior knowledge about X, we use the most ignorant prior distribution $\mathcal{M}(m,p) = 1$, and assume companions can have masses up to that of the primary star. Furthermore, we do not expect orbital periods of our binary systems to be much less than a day (see Appendix 4.9). From our simulation results, we estimate that 95% of our detected companions have stellar masses with orbital periods up to ~ 200 days. In this range, the mean detection probability is 0.87. Therefore, we estimate a corrected MF of $(11/174) \times 0.95 \div 0.87 = 0.07^{+0.03}_{-0.02}$ in the companion mass and orbital period intervals $[0.08\,M_\odot,\, 0.6\,M_\odot]$ and $[1\,d,\, 200\,d]$, respectively. In the same range, counting the companion detections of Duquennoy & Mayor (1991) and Fischer & Marcy (1992), we find an MF of $0.09^{+0.03}_{-0.02}$ and $0.03^{+0.04}_{-0.02}$ for field G and M dwarfs, respectively. The results are illustrated graphically in Fig. 4.5.

4.6.2 Radial Velocity Scatter

One obvious source of stellar radial velocity fluctuations over time is a close companion. However, close companions are not the only plausible explanation for oscillatory radial

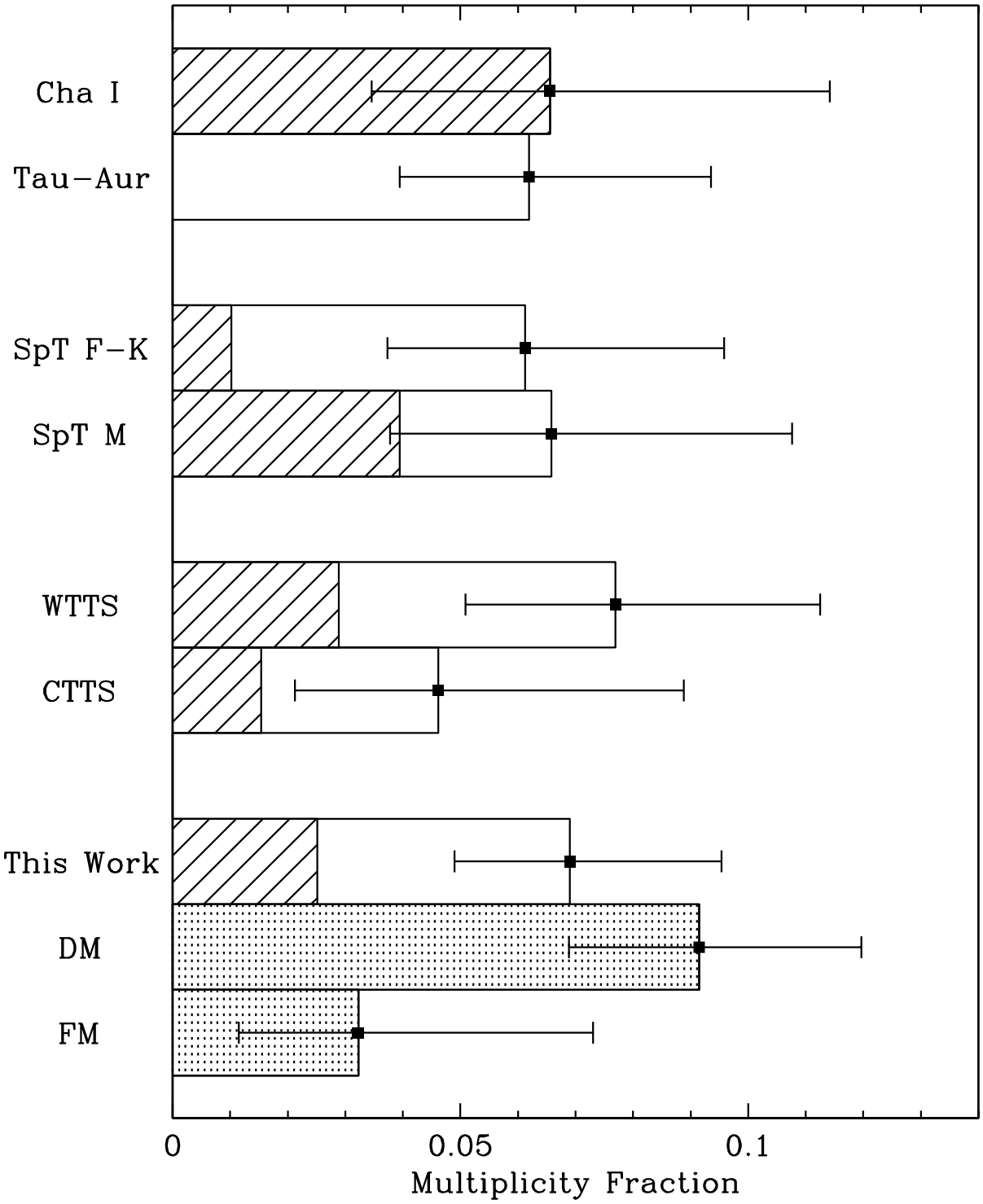

Figure 4.5 Comparisons of the multiplicity fractions of various sub-populations in Cha I and Tau-Aur, and between this work and those of Duquennoy & Mayor (1991) (DM) and Fischer & Marcy (1992) (FM). The contribution from the Cha I sample is denoted by striped areas. The unshaded areas represent the contribution from the Tau-Aur sample. The results from the field dwarf surveys of DM and FM are stippled, and count only companions with stellar masses and orbital periods between 1 and 200 days which is comparable to the detection coverage of this work. For the comparison with the field dwarf surveys, the multiplicity fraction for this work has been corrected for detection sensitivity.

velocity behaviour. Periodic variations in radial velocity, especially in young stars using measurements at optical wavelengths, can be caused by star spots (e.g., see Huerta et al., 2008; Huélamo et al., 2008). To gauge the maximum amplitude of this effect, let us consider a star spot on the equator of a star observed edge-on. For simplicity, we will model the star as a rigid unit sphere, and the star spot as a black spherical cap. Furthermore, we will ignore limb darkening, and assume the face of the star is a uniformly illuminated stellar disk. From this model, with the stellar rotation about the y-axis, and the line of sight to the observer along the z-axis, the observed net radial velocity shift caused by the star spot is

$$\Delta v = \frac{\iint_T v_0 x \, dy \, dx}{\iint_S dy \, dx - \iint_T dy \, dx} \tag{4.12}$$

where S is the region of the stellar disk (a unit circle), T is the region of the star spot projected onto the stellar disk, and v_0 is the linear rotational velocity of the star at the equator. Trivially, we see from symmetry that the net RV shift is zero when the star spot directly faces the observer. When the star spot is observed after a quarter-rotation or edge-on, Eq. 4.12 equals

$$\Delta v_{\pi/2} = \frac{8}{3}\left(\frac{(1-x_0)^{3/2}}{3\pi + 2(x_0\sqrt{1-x_0^2} + \sin^{-1}x_0)}\right) v_0 \tag{4.13}$$

where x_0 is the location of the spot edge projected on the stellar disk. For a spherical cap modelled spot, $x_0 = 1 - 2f$ where f is the size of the star spot as a fraction of the stellar surface. For a star spot covering 10% of the stellar surface, the net RV shift is $\sim 0.05\, v_0$ when the spot is edge-on.

Since only half of the star spot is visible when it is edge-on, the rotational phase that produces the largest RV shift actually lies between face-on and edge-on, and depends on the size of the spot. Evaluating Eq. 4.12 over all phases, we find that a star spot covering 10% of the stellar surface can produce a theoretical maximum RV oscillation semi-amplitude of $\sim 0.20\, v_0$. This amplitude is similar to the RV scatter upper bound of 15% $v \sin i$ observed in our sample. However, real star spots do not affect all spectral features equally nor do they have identical impact at all optical depths. A technique such as line bisector analysis, which probes radial velocity bias at different depths, is required to properly assess the contribution of star spots on variations in radial velocity.

The net affect of star spots on radial velocity measurements relies on the asymmetry that the spots produce on the stellar surface. In terms of contribution to radial velocity bias, multiple star spots can partially negate one another at different rotational phases. Therefore, since the total number of star spots, not their effective asymmetry, is connected to stellar activity, we do not necessarily expect a correlation between activity and radial velocity scatter. In Fig. 4.6, we show the radial velocity scatter over time for single non-accretors grouped by Hα equivalent width, an activity indicator, in our sample and as a function of $v \sin i$. As expected, the upper bound of RV scatter increases with $v \sin i$. More importantly, there is no clear separation of stars by Hα equivalent width. Thus, while spot-induced RV variability obviously requires some activity, it is perhaps not surprising that the level of activity does not correlate well with the amount of variability.

4.6.3 Radial Velocity Outliers

The targets in our original sample were identified as either members of Cha I by Luhman (2004a), or members of Tau-Aur by Leinert et al. (1993), Ghez et al. (1993), Simon et al. (1995), Köhler & Leinert (1998), Briceño et al. (2002) and Luhman (2004b) based on a combination of one or more indicators such as Li-λ6708 absorption, reddening, emission lines, and IR excess emission. However, we find among the 146 single stars in our sample that five stars in Cha I, and eight stars in Tau-Aur have overall radial velocities that deviate substantially from the velocities of their associated clusters, i.e., the weighted mean velocities of these targets are Tukey outliers with respect to the rest of the sample. We examine several possible sources for these abnormal mean radial velocities.

First, to see if localized phenomena in the star-forming regions are responsible for the radial velocity anomalies, we examine the positions of the radial velocity outliers on the sky. The projected spatial distributions of Cha I and Tau-Aur are shown in Fig. 4.7. From the plots, we see no pattern in the spatial distribution of the radial velocity outliers, i.e., the radial velocity deviations are not confined to a particular area within the star-forming regions. Hence, it is unlikely that the radial velocity outliers in Cha I and Tau-Aur are the result of peculiarities in specific parts of the clusters.

Next, we examine the possibility that the targets with unusual mean radial velocity are the result of ejection from past multiple systems. If this is the case, we would expect the radial velocity outliers to have masses generally lower than the rest of the sample. The weighted mean radial velocity as a function of stellar mass derived from the models

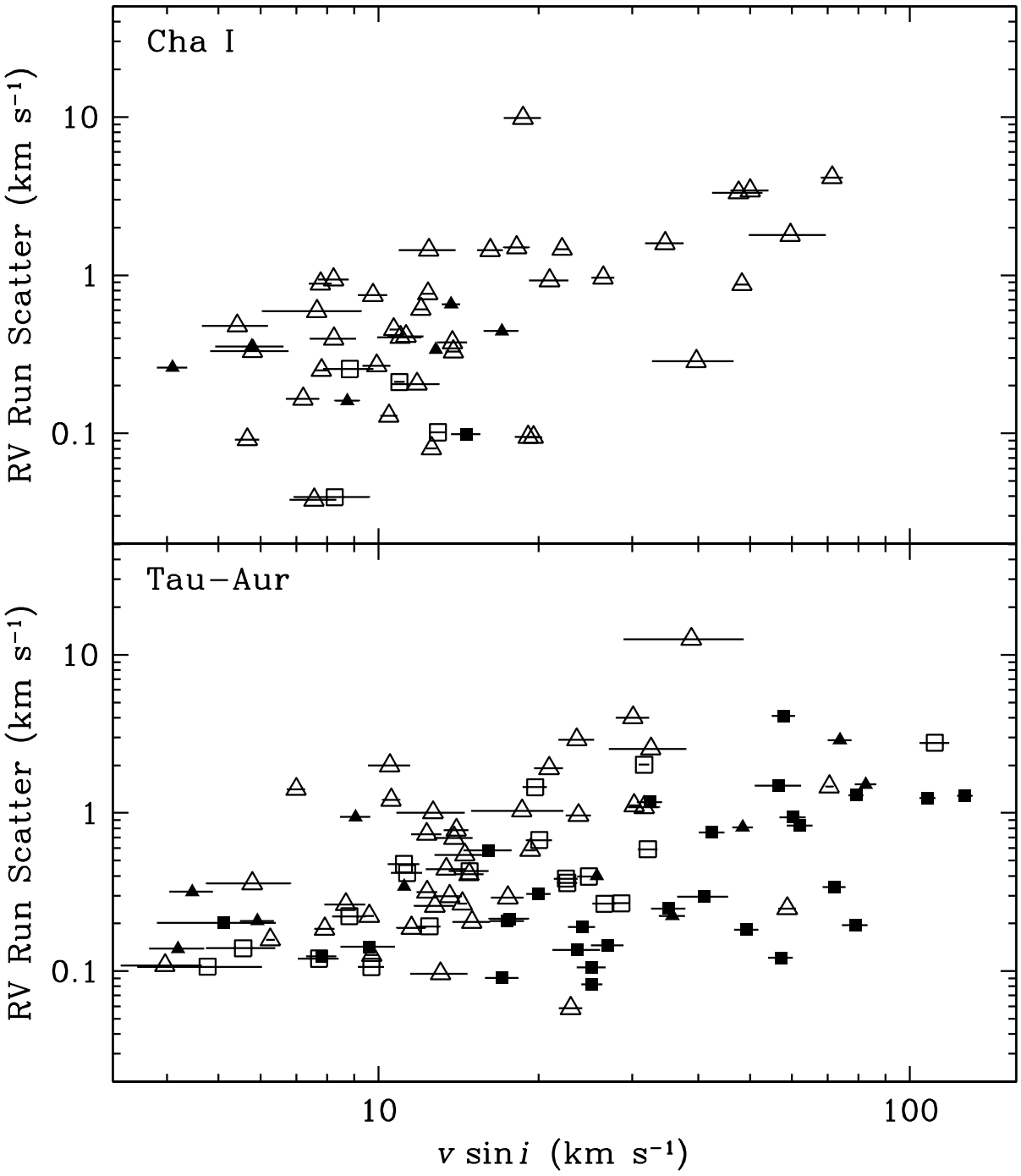

Figure 4.6 Radial velocity scatter within the observing runs for single non-accretors in Cha I and Tau-Aur as a function of projected rotational velocity $v \sin i$. The stars have been grouped by Hα equivalent width. Hollow triangles represent stars with Hα EW < -3. Solid triangles indicate stars with Hα EW in the range of $[-3, -1.5)$. Hollow squares represent stars with Hα EW in the range of $[-1.5, 0)$. Solid squares indicate stars with Hα EW ≥ 0. There is an increase in radial velocity scatter with $v \sin i$. However, the groups by Hα EW are not well separated from each other.

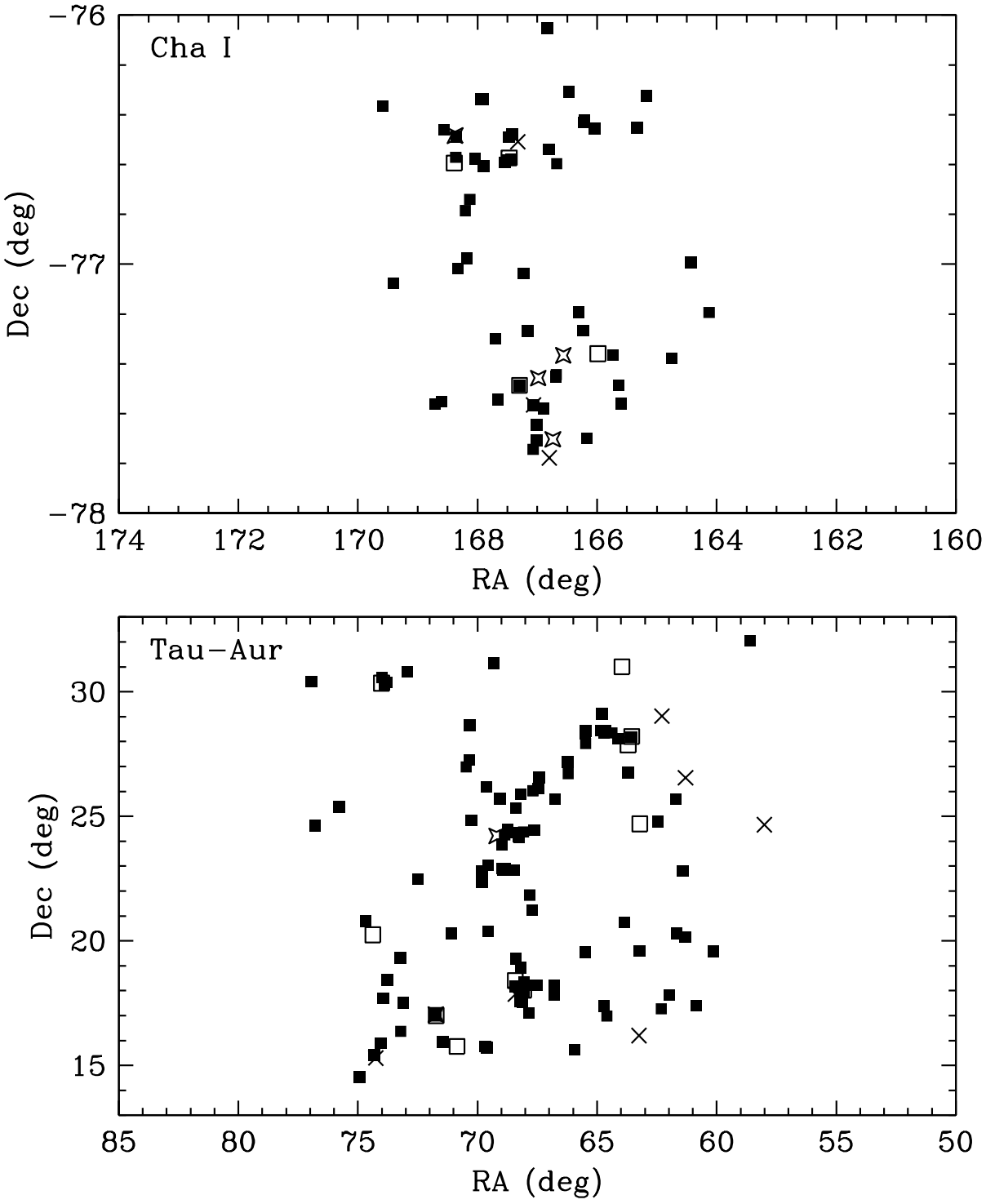

Figure 4.7 The spatial distribution of targets in our sample of Cha I and Tau-Aur. The solid symbols represent single stars that have mean radial velocities consistent with their respective clusters. Objects with mean radial velocities that are outliers with respect to their clusters are denoted by cross symbols for those moving faster away us, and starred symbols for those moving more toward us. Spectroscopic binaries are plotted as hollow symbols. The distribution of radial velocity outliers shows no particular pattern.

of D'Antona & Mazzitelli (1997) for our $\sim 2\,\mathrm{Myr}$ old sample is shown in Fig. 4.8. We see from the plots that the targets with outlying radial velocities have masses spanning the full range of the sample. In addition, ejected stars should show little or no accretion. However, we find that three out of the 13 radial velocity outliers are CTTSs. Therefore, from the accretion and mass distribution findings, we conclude that ejection is not likely the main source of radial velocity outliers in our sample.

Finally, we check if the anomalous radial velocities could be caused by unseen companions. The lower bound of flux ratio for our identified SB2 candidates was ~ 0.1. Using the models of D'Antona & Mazzitelli (1997) and assuming a stellar age of 2 Myr, if our lowest mass RV outlier ($0.19\,M_\odot$) had a companion of mass $\lesssim 0.08\,M_\odot$, we would not detect it as an SB2. Furthermore, our SB1 detection success rate for such a binary system from Monte Carlo simulations assuming a circular orbital period $> 1\,\mathrm{yr}$ is less than 2%. For a one-year period, the primary star would have an expected semi-amplitude of $\sim 5\,\mathrm{km\,s^{-1}}$ which is consistent with the radial velocity differences we observe of the low mass outliers in our sample. Similarly, if our highest mass RV outlier ($2.8\,M_\odot$) had a $2\,M_\odot$ companion in a circular orbit with a period of $> 1000\,\mathrm{days}$, we would not likely identify it as a binary. For a 1000-day period, the primary star would have a semi-amplitude of up to $\sim 15\,\mathrm{km\,s^{-1}}$ which is consistent with the radial velocity deviations we observe in the high mass outliers. The results for the rest of the radial velocity outliers is similar. Thus, some of the single stars with an overall radial velocity inconsistent with their cluster velocity may be SB1 candidates.

4.7 Notes on individual sources

Among our complete sample, we found three SB1s, five SB2s, and four SB3s. We will discuss the individual sources grouped in reverse order below.

4.7.1 SB3: Triple-lined Spectroscopic Binaries

T55 (Cha T 2-55) (Fig. 4.33) This is a previously unknown SB3 consisting of two rapidly accelerating sources and a stable brighter component. This system had not previously been studied spectroscopically, and no resolved companions were found by Lafrenière et al. (2008). From the four reliable sets of velocity measurements, for the close orbit, we infer a mass ratio of ~ 0.8 and a systemic velocity of $\sim 12\,\mathrm{km\,s^{-1}}$. The

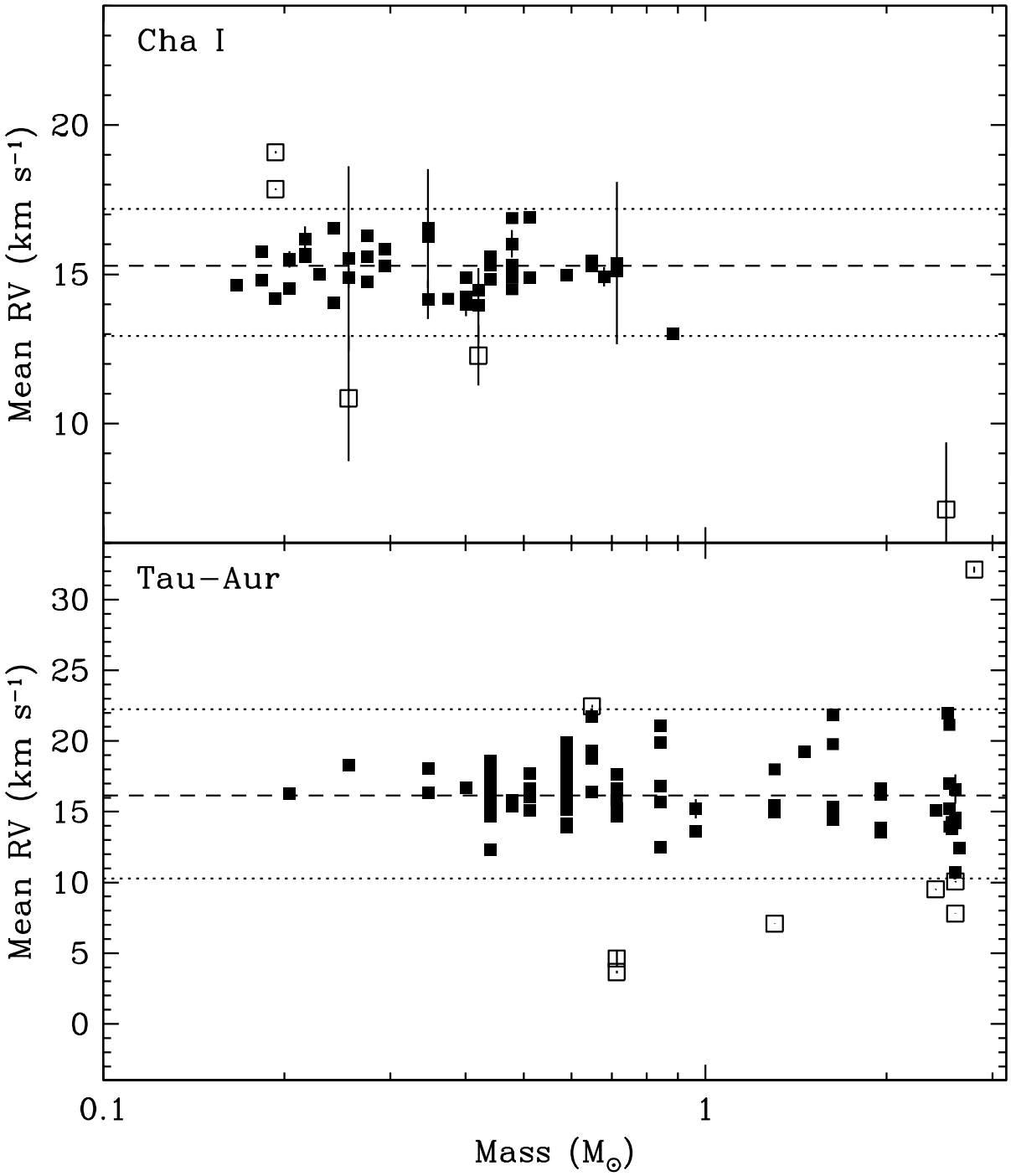

Figure 4.8 Mean radial velocity as a function of stellar mass derived from the models of D'Antona & Mazzitelli (1997) for our sample from Cha I and Tau-Aur ($\sim$2 Myr old). The solid symbols represent single stars that have mean radial velocities consistent with their respective clusters. Objects with mean radial velocities that are outliers with respect to their clusters are denoted by hollow symbols. The dashed-lines show the median radial velocity of the single stars. The Tukey outlier threshold is delineated by the dotted-lines. There appears to be no mass preference for radial velocity outliers.

maximum observed velocity separation is $\Delta v \simeq 150\,\mathrm{km\,s^{-1}}$, and the rapid change between the third and fourth epoch suggests a short period, of at most a few days. We do not have sufficient measurements to determine the period uniquely, but can derive some constraints. Assuming a total radial velocity amplitude $K \simeq \Delta v$, one can estimate the total mass and separation as $M \sin^3 i \simeq K^3 P/2\pi G \simeq 0.3(P/1\,\mathrm{d})\,M_\odot$ and $a \sin i = KP/2\pi = 3(P/1\,\mathrm{d})\,R_\odot$. We also have the following constraints. First, given the M4.5 spectral type, the expected mass of the brighter, stationary component, is $\sim 0.2\,M_\odot$. The other stars should be less massive, so the period cannot be much longer than one day. Second, the brighter star's radius should be around $1\,R_\odot$ and, given the flux ratios of 0.4 and 0.2, components B and C should have radii around 0.6 and $0.5\,R_\odot$. For these to fit in the orbit, the period can also not be much shorter than 1 day. Independent of the precise period, the orbit is sufficiently close that it should be circularized and the rotation of the stars synchronised. From the observed rotational broadenings of 34 and $31\,\mathrm{km\,s^{-1}}$, one infers rotation periods $P \sin i = 2\pi R \sin i / v \sin i \simeq 0.8\,\mathrm{d}$. From all evidence, we thus conclude that the orbital period is $\sim 0.8\,\mathrm{d}$. Given the mass ratio of ~ 0.8, the individual masses are $M_{B,C} \sin^3 i \simeq (0.14, 0.12)\,M_\odot$. For the outer orbit, from the fact that we do not see variations larger than a few $\mathrm{km\,s^{-1}}$ on our $\sim 300\,\mathrm{d}$ baseline, we can only limit the period to be longer than $\gtrsim 2\,\mathrm{yr}$. A long period is also suggested by the velocity separation of $\lesssim 5\,\mathrm{km\,s^{-1}}$ between the close binary centre of mass and component A.

LkCa 3 A (Fig. 4.36) This is an SB3 consisting of three sources, all of which show acceleration over our 1 month baseline. The source is listed as an SB1 in the review of Mathieu (1994), with $P = 12.941\,\mathrm{d}$, $e = 0.2$, $a \sin i = 0.032\,\mathrm{AU}$, and $\gamma = 14.9\,\mathrm{km\,s^{-1}}$, but it is not clear how reliable the numbers are given the additional components we see. It was found to have a resolved companion, Lk Ca 3 B, by Leinert et al. (1993) and Ghez et al. (1993). We see no direct evidence for this component in our line profile, even though it should contribute given the flux ratio, and in epoch 2 none of the other components overlap with its expected velocity (roughly the cluster velocity). Perhaps it is fainter in R than estimated, or rotates relatively rapidly. Nevertheless, we should caution that especially the velocity of the slowest and brightest component, Lk Ca 3 Aa, may be somewhat biased.

Considering all velocities, we infer that the close binary, Lk Ca 3 Ab1 and Ab2, has a mass ratio of about 0.5 (for its center of mass to orbit Aa), and that its total mass is similar to that of Aa. From the rapid change in velocity in the day between epochs 2

and 3, the orbital period should be at most a few days. Like for Cha T 2-55 above, we can estimate a total mass and orbital separation assuming the radial-velocity amplitude is similar to the maximum observed velocity separion, $K \simeq \Delta v = 115\,\mathrm{km\,s^{-1}}$; one finds $M_{\rm Ab} \sin^3 i \simeq 0.3(P/2\,\mathrm{d})\,M_\odot$ and $a \sin i \simeq 4.5(P/2\,\mathrm{d})\,R_\odot$. We can again constrain this using other information. First, the total mass should be similar to that of Aa, which is estimated at $\sim 0.4\,M_\odot$ based on its M1 spectral type. Thus, the period should be a few days. Second, component Aa has an estimated radius of $1.3\,R_\odot$; given the measured flux ratios of 0.75 and 0.21, one thus expects radii for Ab1 and Ab2 of 1.1 and $0.6\,R_\odot$, respectively. Thus, the orbit cannot be shorter than about one day. Finally, assuming the stars are synchronised with the orbit, the measured projected rotational velocities of 16 ± 2 and 12 ± 4 imply periods $P \sin i = 3.5$ and 2.6 d, respectively. We conclude that the inner period is likely about 3 d, and that the masses are $(M_{\rm Ab1,Ab2} \sin^3 i \simeq (0.30, 0.15)\,M_\odot$. From the above, the implied mass for component Aa is then $M_{\rm Aa} \sin^3 i \simeq 0.45\,M_\odot$.

RX J0412.8+2442 (V1198 Tau) (Fig. 4.34) This is a previously unknown SB3 consisting of two rapidly accelerating sources (with a maximum velocity difference of at least $115\,\mathrm{km\,s^{-1}}$), and a stable fainter component, which is likely a less massive star in a wide orbit. The B and C components have a flux ratio of 0.88 ± 0.12 and 0.36 ± 0.04 to the A component, respectively. Based on the spectral type of the primary and the flux ratios, we find that the secondary is likely of G9/K0 type, and the tertiary a K1. Given the high theoretical mass of the inner binary ($2.23\,\mathrm{M_\odot}$+$2.16\,\mathrm{M_\odot}$), its maximum separation is $a_{\rm max} = 1.2\,\mathrm{AU}$. The tertiary, on the other hand, shows a velocity difference to the A-B center of mass which is smaller than $3\,\mathrm{km\,s^{-1}}$ – tiny, implying a maximum possible separation of 600 AU between the C component and the A–B mass center. Köhler & Leinert (1998) observed this system with high spatial resolution using speckle interferometry, but found no spatially resolved companions with a limiting contrast ratio of 0.13 at $0\farcs13$ (corresponding to the projected distance of 18 AU at 140 pc). The flux ratio between A+B and C is estimated to be 0.19 in R-band and 0.23 in K, which thus should be easily detected outside $0\farcs13$ by Köhler & Leinert (1998) The possibilities remain that we are seeing the tertiary in a strongly inclined orbit and/or in a special position in its orbit.

V773 Tau (HD 283447, HIP 19762, HBC 367) (Fig. 4.35) This is an SB3 and previosuly known quadruple system (Duchêne et al., 2003; Woitas, 2003). The fourth component is an infrared companion, which explains its absence from our spectra. Of the

other three, two are in a tight 51-day (2.8 mas, 0.38 AU) orbit (Boden et al., 2007), and the third in a 46 yr orbit around A–B (Duchêne et al., 2003).

4.7.2 SB2: Double-lined Spectroscopic Binaries

CHXR 12 (Fig. 4.16) This is an SB2 with no spatially detected companions (Lafrenière et al., 2008). The measured spectral type is M3.5 for the primary, and the flux ratio 0.2 ± 0.08 implies M6 for the secondary (again assuming an age of 2 Myr), corresponding to a system mass of $0.2\,M_\odot + 0.14\,M_\odot = 0.34\,M_\odot$. With the maximum observed velocity separation being $40\,\mathrm{km\,s^{-1}}$, we find the widest possible spatial separation to be 0.8 AU, well within the 13 AU limit reported by Lafrenière et al. (2008).

T42 (HBC 579, Sz 32) (Fig. 4.17) This is an SB2 with no spatially detected companions (Lafrenière et al., 2008). The measured SpT is K5 for the primary, and the flux ratio to the secondary is 0.8 ± 0.3, corresponding to a system mass of $0.70\,M_\odot + 0.65\,M_\odot = 1.35\,M_\odot$. With the maximum observed velocity separation being $\sim$55 $\mathrm{km\,s^{-1}}$, we find the widest possible spatial separation to be 1.6 AU, undetectable by Lafrenière et al. (2008).

DQ Tau (HBC 72) (Fig. 4.19) This is a known SB2, first reported by Mathieu et al. (1997) to have a period of 15.8 days, and a circumbinary disk. No spatially resolved companions were found in a high-resolution search using speckle interferometry by Leinert et al. (1993), but Boden et al. (2009) resolved the spectroscopic binary to a 0.96 mas semi-major axis orbit, corresponding to 0.13 AU at the 140 pc distance of the system.

HBC 427 (V397 Aur, NTTS 045251+3016) (Fig. 4.20) This is an SB2 in our spectra with a flux ratio between the components of 0.157 ± 0.014. The star was first noted as an SB1 by Walter et al. (1988), and subsequently monitored to find an orbital solution. Steffen et al. (2001) combined 58 RV measurements distributed over 14 yr with 17 astrometric spatially resolved measurements during 3.3 yr (using the *Fine Guidance Sensor* at the *Hubble Space Telescope*), and found an astrometric-spectroscopic orbital solution. They determined the orbital period to 6.912 ± 0.033 yr and dynamical masses to $1.45 \pm 0.19\,M_\odot$ and $0.81 \pm 0.09\,M_\odot$, respectively. They find a V-band flux ratio of 0.11, which translates to an R-band flux ratio of 0.17 assuming colors of an K5 and M2 atmosphere for the primary and secondary, consistent with our finding. Given their orbital elements, our observing epochs range between orbital phase 0.951 and 0.963, close

to the maximum RV separation of the components at the heliocentric RV $4\,\mathrm{km\,s^{-1}}$ and $35\,\mathrm{km\,s^{-1}}$, respectively. This is close to our derived 4–6 $\mathrm{km\,s^{-1}}$ and 32–35 $\mathrm{km\,s^{-1}}$.

V826 Tau (HBC 400) (Fig. 4.18) This is an SB2, and the first spectroscopic binary PMS star to be confirmed (Mundt et al., 1983). Reipurth et al. (1990) refined the orbital elements and found a period of 3.9 days. By comparing dynamical $Msin^3i$ masses to masses from theoretical evolutionary tracks, they infer the inclination $i = 13° \pm 1°$. Because the cubic dependence on inclination, this estimate is not sensitive to the determined mass, and using more modern models by D'Antona & Mazzitelli (1997) only changes the best fit inclination to 14.°9. Assuming that the rotations of the stars are tidally locked together with their measured $v \sin i = 4.2\,\mathrm{km\,s^{-1}}$, they derive stellar radii of $1.44\,\mathrm{R_\odot}$. This is consistent with the $1.4\,\mathrm{R_\odot}$ expected from a 2 Myr old K7 star (D'Antona & Mazzitelli, 1997), but inconsistent with our measurement of $v \sin i \sim 8.9\,\mathrm{km\,s^{-1}}$, which would double the radii. Our result is thus that the stars are likely not in synchronous rotation with their orbit. Unfortunately the close to pole-on inclination of the system makes it potentially difficult to measure periods from photometric modulation by star spots. Using high-resolution speckle interferometry, Leinert et al. (1993) did not find any additional companions.

T31 (VW Cha, Sz 24) (Fig. 4.31) T31 A is a suspected SB2. The entire system T31 is a known hierarchical quadruple system with a wide companion (C) at 16.″8 (Correia et al., 2006) and a tight 0.″1 binary (Ba,Bb) located 0.″7 from the primary A (Brandeker et al., 2001). A previously reported companion at 2.″7 (Ghez et al., 1997a) has not been confirmed (Brandeker et al., 2001; Correia et al., 2006). Our spectra of the primary show evidence for two components (Aa,Ab) separated by $20\,\mathrm{km\,s^{-1}}$, with a tentative flux ratio of 0.7 ± 0.3. The near-equal brightness of the components and good seeing conditions at the time of observations precludes the observed spectral components to be due to contamination by the known spatially resolved companions. Melo (2003) reports the presence of three components in the cross-correlation function, one which they attribute to contamination by B. Guenther et al. (2007) speculate that their observed erratic variability of RV, and the asymmetric shape of the cross-correlation function, are due to B contributing a varying amount of light, depending on the precise placement of the 2.″0 wide optical fibre. They do not rule out A being SB2, however, and we think this a more likely explanation given the small flux contribution by B.

We derive the spectral type K3 for the primary A, which is slightly earlier than the K5/K7 found by Brandner & Zinnecker (1997), but later than K2 found by Appenzeller & Mundt (1989). For Ba+Bb, we find the spectral type K7, same as Brandner & Zinnecker (1997), while we did not observe component D. With a radial velocity difference of $20\,\mathrm{km\,s^{-1}}$, the widest possible separation would be 18 AU, corresponding to observing the $2\,M_\odot$ system edge-on. AO observations rule out any projected separation greater than 75 mas, corresponding to 12 AU at an assumed distance of 160 pc (Lafrenière et al., 2008).

4.7.3 SB1: Single-lined Spectroscopic Binaries

T39 (Sz 30) (Fig. 4.9) This is a known triple system (Reipurth & Zinnecker, 1993) with an inner 1.″2 binary (Aa,Ab) of types K7 and M1.5, and an outer 4.″5 companion (B) of type M1.5. While Aa and Ab show no evidence for additional companions, T39 B is an SB1, making the system quadruple. The observed change in radial velocity is $2.6\,\mathrm{km\,s^{-1}}$ over 0.8 yr.

RX J0415.8+3100 (Fig. 4.10) This is an SB1 with a substantial RV variability amplitude of at least $70\,\mathrm{km\,s^{-1}}$ during a period of on the order of two days. This implies a companion at ∼0.04 AU of at least $0.36\,M_\odot$ (SpT M2), assuming a mass of $2.5\,M_\odot$ for the primary (SpT G6 and 2 Myr). The fraction of R-band flux from an M2 would only be 0.008 of the primary, explaining why it is not visible in our optical spectra. Köhler & Leinert (1998) report on an additional companion at 0.″94, making this system triple.

RX J0457.5+2014 (Fig. 4.11) This is an SB1 which shows a modest but significant $6\,\mathrm{km\,s^{-1}}$ increase in RV over 31 days. (Köhler & Leinert, 1998) report a companion B at 6.″86, too distant to be responsible for the RV change of A.

4.8 Concluding Remarks

By undertaking this extensive spectroscopic survey of T Tauri stars, we have gained some insight that could be beneficial to future efforts. First and foremost, we now know the main limiting factor for a radial velocity study of young stars is the strong intrinsic noise present in some objects. This noise would need to be reduced in some way in order

both to detect lower mass companions effectively, and to extend the measurement to longer orbital periods. One way to reduce the intrinsic noise is to observe at infrared wavelengths (Martín et al., 2006; Huélamo et al., 2008). Another option is to average out the noise by observing over its characteristic period, i.e., the rotation period of the noisy star. To some extent, we have already done this by taking multiple spectra of the same targets during an observing run. Ideally, one would multiplex observations, e.g., by using multiple fibers as in VLT/FLAMES. This solution may not be suitable for star-forming regions like Taurus-Auriga, which span a large area of the sky, but it would probably be quite useful for compact regions like Chamaeleon.

We have also learned that our high resolution and S/N were extremely beneficial. It was probably a major reason we could find so many SB2 candidates; being able to resolve the stellar rotation helped us to determine the stability of the line profiles. Less clear is whether one would really need the large spectral range, or whether a few well-chosen echelle orders would suffice. This consideration is relevant since it would determine whether or not multiplexing is feasible.

4.9 Appendix: Estimating Shortest Possible Orbital Periods

We define a close binary system as two bodies in orbit about a common center of mass where there is no consistent exchange of material between them, i.e., each object does not extend beyond its Roche lobe. The effective radius r_L of a Roche lobe for an object with mass M_1 in a binary system from the approximation of Eggleton (1983) is

$$r_L = \frac{0.49\, q^{2/3}}{0.6\, q^{2/3} + \ln\left(1 + q^{1/3}\right)} \quad , \quad 0 < q < \infty \tag{4.14}$$

where q is the mass ratio M_1/M_2, and r_L is in units of the orbital separation. Furthermore, the orbital period P in days for an object that just fills its Roche lobe is

$$P(q, \rho) = 0.1375 \left(\frac{q}{1+q}\right)^{1/2} r_L^{-3/2} \rho^{-1/2} \tag{4.15}$$

where ρ is the mean density of the object in cgs units. Therefore, the theoretical shortest

orbital period $P_{\rm min}$ of a binary system is

$$P_{\rm min} = \min\{\max\left[P(q,\rho_2), P(1/q,\rho_1)\right] \text{ for } 0<q\leq 1\} \tag{4.16}$$

where ρ_1 and ρ_2 are the mean densities of the primary and secondary objects, respectively. Using the densities derived from the models of D'Antona & Mazzitelli (1997), we estimate the shortest possible orbital period for a typical $\sim$2 Myr old T Tauri star in our survey ($0.6\,M_\odot$; $1.4\,R_\odot$) with a stellar mass companion is approximately 0.8 days.

Acknowledgements

We would like to thank David Lafrenière and Brian Lee for enlightening discussions relating to the work presented in this paper. This work was supported in part by NSERC grants to R.J. and M.H.vK. and an Early Researcher Award from Ontario to R.J..

Table 4.1. Measurements of Stars without Close Companions in Cha I & Tau-Aur

Region	Object	R.A. (J2000.0)	Dec. (J2000.0)	SpT	TTS[a]	10% width[bc] (km s^{-1})	$v \sin i$[de] (km s^{-1})	$\overline{RV}$ (km s^{-1})	σ_{RV}[f] (km s^{-1})	$\sigma_{\rm N}$[g] (km s^{-1})	# of obs.
Cha	T4	10 56 30.45	−77 11 39.3	M0.5	c	341 ± 28	12.4 ± 0.4	15.30 ± 0.03	0.58	0.77	5
Cha	T5	10 57 42.20	−76 59 35.7	M3.25	c	324 ± 30	13.8 ± 0.9	16.55 ± 0.08	0.23	0.38	4
Cha	T6	10 58 16.77	−77 17 17.1	K0	c	284	34 ± 2	14.99 ± 0.08	···	···	1
Cha	T8	10 59 06.99	−77 01 40.4	K2	c	347	35 ± 2	14.99 ± 0.06	···	···	1
Cha	T10	11 00 40.22	−76 19 28.1	M3.75	c	252 ± 24	5.4 ± 0.8	15.69 ± 0.03	0.25	0.48	5
Cha	CHXR 9C A	11 01 18.75	−76 27 02.5	M0.5	w	106 ± 13	12.8 ± 0.2	14.50 ± 0.04	0.32	0.34	5
Cha	CHXR 9C Ba+Bb	11 01 18.75	−76 27 02.5	M1.5	w	132 ± 12	19.6 ± 0.8	14.89 ± 0.09	0.09	0.09	5
Cha	CHXR 71	11 02 32.65	−77 29 13.0	M3	w	117 ± 46	17.1 ± 1.3	15.54 ± 0.08	0.40	0.44	4
Cha	T12	11 02 55.05	−77 21 50.8	M4.5	c	262 ± 35	10.7 ± 0.2	14.82 ± 0.05	0.53	0.45	4
Cha	T14	11 04 09.09	−76 27 19.4	K5	c	550 ± 13	7.8 ± 0.2	15.13 ± 0.09	0.25	0.25	4
Cha	ISO 52	11 04 42.58	−77 41 57.1	M4	w	126 ± 15	9.9 ± 0.6	15.52 ± 0.06	0.18	0.27	4
Cha	CHXR 14N	11 04 51.00	−76 25 24.1	K8	w	114 ± 20	13.7 ± 0.6	14.90 ± 0.04	0.58	0.66	5
Cha	CHXR 14S	11 04 52.85	−76 25 51.5	M1.75	w	98 ± 14	5.7 ± 0.3	14.176 ± 0.015	0.089	0.091	4
Cha	T16	11 04 57.01	−77 15 56.9	M3	w	101	11.3 ± 0.9	14.9 ± 0.3	0.4	0.4	4
Cha	T20	11 05 52.61	−76 18 25.6	M1.5	w	192 ± 21	48.3 ± 1.4	14.0 ± 0.4	0.9	0.9	4
Cha	Hn 5	11 06 41.81	−76 35 49.0	M4.5	c	340 ± 20	7.8 ± 0.4	15.76 ± 0.07	0.51	0.88	4
Cha	T22	11 06 43.47	−77 26 34.4	M3	w	228	60 ± 10	16 ± 3	1	2	4
Cha	CHXR 20	11 06 45.10	−77 27 02.3	K6	w	Absorp.	14.6 ± 0.9	15.46 ± 0.06	1.18	0.10	3
Cha	CHXR 74	11 06 57.33	−77 42 10.7	M4.25	w	97 ± 7	5.8 ± 1.0	17.85 ± 0.03	0.25	0.33	4
Cha	CHXR 21	11 07 11.49	−77 46 39.4	M3	w	135 ± 61	48 ± 5	11 ± 2	3	3	4
Cha	T24	11 07 12.07	−76 32 23.2	M0.5	c	454 ± 53	10.5 ± 0.4	16.88 ± 0.03	0.09	0.13	4
Cha	T25	11 07 19.15	−76 03 04.8	M2.5	c	341 ± 62	12.6 ± 0.3	15.84 ± 0.06	0.11	0.08	4
Cha	T26	11 07 20.74	−77 38 07.3	G2	c	390	32.7 ± 1.6	12.04 ± 0.14	···	···	1
Cha	CHXR 76	11 07 35.19	−77 34 49.3	M4.25	w	89 ± 12	9.8 ± 0.6	14.19 ± 0.13	0.64	0.75	4
Cha	CHXR 28 Aa+Ab	11 07 55.89	−77 27 25.8	K3.5	?	···	8.7 ± 0.7	16.76 ± 0.05	0.02	0.02	2
Cha	ISO 126	11 08 02.98	−77 38 42.6	M1.25	c	381 ± 19	40 ± 7	14.0 ± 1.3	0.8	0.3	4
Cha	T33 A	11 08 15.10	−77 33 53.2	K3.5	w	95 ± 15	12.9 ± 0.5	13.00 ± 0.05	0.23	0.10	4
Cha	T33 B	11 08 15.10	−77 33 53.2	G7	c	318 ± 21	50 ± 4	7 ± 2	3	3	4
Cha	T34	11 08 16.49	−77 44 37.2	M3.75	w	84 ± 8	5.8 ± 0.8	15.58 ± 0.03	0.21	0.35	5
Cha	T35	11 08 39.05	−77 16 04.2	K8	c	466 ± 46	21.0 ± 1.8	16.90 ± 0.19	1.07	0.93	6
Cha	CHXR 33	11 08 40.69	−76 36 07.8	M0	w	153 ± 3	16.5 ± 1.5	18.71 ± 0.08	0.30	0.30	2
Cha	T38	11 08 54.64	−77 02 13.0	M0.5	c	389 ± 23	18.7 ± 1.5	16.0 ± 0.5	4.2	9.9	4
Cha	T39 Aa	11 09 11.72	−77 29 12.5	K7	w	131 ± 27	7.7 ± 1.6	14.97 ± 0.04	0.67	0.59	6
Cha	T39 Ab	11 09 11.72	−77 29 12.5	M1.5	w	100 ± 16	4.1 ± 0.3	14.258 ± 0.012	0.191	0.261	5
Cha	CHXR 37	11 09 17.70	−76 27 57.8	K7	w	178 ± 11	15.8 ± 0.6	14.82 ± 0.06	0.23	0.23	2
Cha	CHXR 79	11 09 18.13	−76 30 29.2	M1.25	w	103 ± 50	12.4 ± 1.5	12.3 ± 1.0	1.4	1.4	4
Cha	T40	11 09 23.79	−76 23 20.8	K6	c	498 ± 78	15.02 ± 0.14	11.0 ± 1.0	2.7	2.7	2
Cha	CHXR 40	11 09 40.07	−76 28 39.2	M1.25	w	104 ± 18	11.6 ± 0.5	14.46 ± 0.02	0.05	0.01	4

Table 4.1 (cont'd)

Region	Object	R.A. (J2000.0)	Dec. (J2000.0)	SpT	TTS[a]	10% width[bc] (km s^{-1})	$v \sin i$[de] (km s^{-1})	$\overline{RV}$ (km s^{-1})	σ_{RV}[f] (km s^{-1})	$\sigma_{\rm N}$[g] (km s^{-1})	# of obs.
Cha	Hn 10E	11 09 46.21	−76 34 46.4	M3.25	c	377 ± 17	8.2 ± 0.5	14.03 ± 0.10	0.68	0.94	4
Cha	T43	11 09 54.08	−76 29 25.3	M2	c	225 ± 98	18.2 ± 1.0	16.5 ± 2.0	1.4	1.5	4
Cha	T45	11 09 58.74	−77 37 08.9	K8	c	472 ± 6	6.6 ± 0.3	15.28 ± 0.06	0.97	0.97	2
Cha	T44	11 10 00.11	−76 34 57.9	K5	c	614 ± 53	71 ± 3	15 ± 3	6	4	4
Cha	T45A	11 10 04.69	−76 35 45.3	M0	c	340 ± 77	12.4 ± 0.5	16.94 ± 0.06	0.20	0.20	2
Cha	T46	11 10 07.04	−76 29 37.7	K8	c	437 ± 27	5.7 ± 0.9	14.79 ± 0.04	<0.01	<0.01	2
Cha	ISO 237	11 10 11.42	−76 35 29.3	K5.5	?	···	19.8 ± 1.3	14.9 ± 0.3	0.8	0.8	4
Cha	T47	11 10 49.60	−77 17 51.8	M2	c	395 ± 18	16.2 ± 0.9	14.2 ± 0.7	0.7	1.4	4
Cha	CHXR 48	11 11 34.75	−76 36 21.1	M2.5	w	110 ± 12	13.8 ± 0.5	15.29 ± 0.05	0.24	0.33	4
Cha	T49	11 11 39.66	−76 20 15.2	M2	c	280 ± 25	8.2 ± 0.8	16.26 ± 0.05	0.39	0.40	5
Cha	CHX 18N	11 11 46.32	−76 20 09.2	K6	w	188 ± 39	26.5 ± 1.3	15.29 ± 0.07	0.91	0.96	5
Cha	T50	11 12 09.85	−76 34 36.6	M5	c	262 ± 52	12.0 ± 0.4	14.62 ± 0.06	0.74	0.61	4
Cha	T51	11 12 24.41	−76 37 06.4	K3.5	c	381 ± 32	32.7 ± 1.1	13.32 ± 0.08	0.81	0.81	2
Cha	T52	11 12 27.72	−76 44 22.3	G9	c	562	28 ± 3	14.52 ± 0.08	···	···	1
Cha	T53	11 12 30.93	−76 44 24.1	M1	c	468 ± 22	22.2 ± 0.6	14.8 ± 0.2	1.5	1.5	5
Cha	CHXR 54	11 12 42.10	−76 58 40.0	M1	w	120 ± 22	10.9 ± 0.2	15.58 ± 0.03	0.20	0.21	5
Cha	T54	11 12 42.69	−77 22 23.1	G8	w	Absorp.	11.3 ± 2.0	13.27 ± 0.03	0.74	0.74	2
Cha	CHXR 55	11 12 43.00	−76 37 04.9	K4.5	?	···	14.8 ± 0.8	13.35 ± 0.08	0.91	0.91	2
Cha	Hn 17	11 12 48.61	−76 47 06.7	M4	w	72 ± 10	8.7 ± 0.5	14.53 ± 0.05	0.14	0.16	4
Cha	CHXR 57	11 13 20.13	−77 01 04.5	M2.75	w	100 ± 15	11.8 ± 1.2	16.30 ± 0.03	0.16	0.20	4
Cha	Hn 18	11 13 24.46	−76 29 22.7	M3.5	w	121 ± 24	7.6 ± 0.8	15.01 ± 0.04	0.39	0.04	5
Cha	CHXR 59	11 13 27.37	−76 34 16.6	M2.75	w	107 ± 20	11.0 ± 1.1	15.59 ± 0.03	0.41	0.41	4
Cha	CHXR 60	11 13 29.71	−76 29 01.2	M4.25	w	95 ± 12	0.8 ± 0.7	19.09 ± 0.04	0.12	0.14	4
Cha	CHXR 62	11 14 15.65	−76 27 36.4	M3.75	w	158 ± 33	35 ± 3	16.2 ± 0.4	0.7	1.6	5
Cha	Hn 21W	11 14 24.54	−77 33 06.2	M4	c	375 ± 31	19.1 ± 1.1	15.5 ± 0.3	0.4	0.1	4
Cha	B53	11 14 50.32	−77 33 39.0	M2.75	w	107 ± 18	8.3 ± 1.3	14.741 ± 0.017	0.070	0.039	4
Cha	T56	11 17 37.01	−77 04 38.1	M0.5	c	346 ± 41	7.2 ± 0.5	14.923 ± 0.013	0.189	0.165	6
Cha	CHXR 68 Aa+Ab	11 18 20.24	−76 21 57.6	K6	w	106 ± 22	8.8 ± 1.0	15.38 ± 0.04	0.23	0.26	4
Cha	CHXR 68 B	11 18 20.24	−76 21 57.6	M1	w	90 ± 17	8.3 ± 0.3	15.31 ± 0.05	0.11	0.09	4
Tau	NTTS 034903+2431	03 52 02.24	+24 39 47.9	K5	w	229 ± 31	36 ± 2	3.66 ± 0.10	0.23	0.22	4
Tau	NTTS 035120+3154SW	03 54 29.51	+32 03 01.4	G0	w	Absorp.	62 ± 3	10.7 ± 0.4	1.0	0.8	4
Tau	RX J0403.3+1725	04 03 24.95	+17 24 26.2	K3	?	···	111 ± 7	15.2 ± 0.7	2.8	2.8	4
Tau	RX J0405.1+2632	04 05 12.34	+26 32 43.9	K2	w	Absorp.	17.5 ± 1.3	7.091 ± 0.015	0.181	0.207	4
Tau	RX J0405.3+2009	04 05 19.59	+20 09 25.6	K1	w	Absorp.	24.1 ± 1.4	14.427 ± 0.012	0.187	0.190	4
Tau	HD284135	04 05 40.58	+22 48 12.2	G0	w	Absorp.	72 ± 4	14.23 ± 0.10	0.37	0.34	4
Tau	HD284149	04 06 38.79	+20 18 11.1	F8	w	Absorp.	27.0 ± 1.9	12.46 ± 0.03	0.30	0.15	5
Tau	RX J0406.8+2541 B	04 06 51.35	+25 41 28.3	K6.5	c	295	18 ± 2	16.01 ± 0.20	···	···	1
Tau	RX J0407.8+1750	04 07 53.99	+17 50 25.8	K4	w	115 ± 17	28.7 ± 1.0	12.47 ± 0.05	0.34	0.27	4

Table 4.1 (cont'd)

Region	Object	R.A. (J2000.0)	Dec. (J2000.0)	SpT	TTS[a]	10% width[bc] (km s^{-1})	$v \sin i$[de] (km s^{-1})	$\overline{RV}$ (km s^{-1})	σ_{RV}[f] (km s^{-1})	$\sigma_{\rm N}$[g] (km s^{-1})	# of obs.
Tau	RX J0409.1+2901..	04 09 09.74	+29 01 30.6	G8	w	Absorp.	24 ± 2	9.52 ± 0.03	0.13	0.14	4
Tau	RX J0409.2+1716..	04 09 17.00	+17 16 08.2	M1	w	223 ± 23	70.5 ± 1.1	16.1 ± 0.5	1.3	1.5	5
Tau	RX J0409.8+2446..	04 09 51.13	+24 46 21.1	M1	w	83 ± 8	5.9 ± 0.4	12.330 ± 0.012	0.170	0.208	4
Tau	RX J0412.8+1937..	04 12 50.64	+19 36 58.2	K6	w	96 ± 16	11.2 ± 0.8	16.37 ± 0.02	0.38	0.47	5
Tau	HD285579	04 12 59.88	+16 11 48.2	G0	w	Absorp.	9.6 ± 1.1	7.805 ± 0.006	0.142	0.142	6
Tau	LkCa 1	04 13 14.14	+28 19 10.8	M4	w	173	30.9 ± 1.1	9.57 ± 0.12	···	···	1
Tau	RX J0413.4+3352..	04 13 27.29	+33 52 41.7	K0	?	···	16.0 ± 1.7	18.13 ± 0.09	···	···	1
Tau	CW Tau	04 14 17.00	+28 10 57.8	K3	c	647 ± 7	33 ± 5	13.60 ± 0.10	3.01	2.55	5
Tau	FP Tau	04 14 47.31	+26 46 26.4	M4	c	378 ± 12	32 ± 2	16.26 ± 0.15	0.97	1.08	4
Tau	CX Tau	04 14 47.86	+26 48 11.0	M2	c	319	19.8 ± 0.6	16.63 ± 0.12	···	···	1
Tau	RX J0415.3+2044..	04 15 22.92	+20 44 17.0	K0	w	Absorp.	35 ± 3	13.84 ± 0.03	0.37	0.25	5
Tau	LkCa 4	04 16 28.11	+28 07 35.8	K7	w	198 ± 30	30 ± 2	15.77 ± 0.11	3.34	4.00	4
Tau	CY Tau	04 17 33.73	+28 20 46.9	M1.5	c	415 ± 28	10.6 ± 0.4	16.68 ± 0.02	1.06	1.21	4
Tau	LkCa 5	04 17 38.94	+28 33 00.5	M2	w	163	38.3 ± 1.1	15.83 ± 0.16	···	···	1
Tau	NTTS 041529+1652	04 18 21.47	+16 58 47.0	K5	w	Absorp.	5.1 ± 1.3	15.818 ± 0.020	0.180	0.202	5
Tau	V410 Tau	04 18 31.10	+28 27 16.2	K7	c	450 ± 106	83 ± 4	19.9 ± 0.3	1.3	1.5	4
Tau	DD Tau A	04 18 31.13	+28 16 29.0	M2	c	363	11.5 ± 1.4	13.9 ± 0.6	···	···	1
Tau	NTTS 041559+1716	04 18 51.70	+17 23 16.6	K7	w	210 ± 29	74 ± 4	15.5 ± 0.3	3.0	2.9	5
Tau	BP Tau	04 19 15.84	+29 06 26.9	K5	c	458 ± 28	13.1 ± 1.6	15.24 ± 0.04	0.09	0.10	4
Tau	V819 Tau	04 19 26.26	+28 26 14.3	K7	w	166 ± 41	9.1 ± 0.6	16.64 ± 0.02	0.77	0.94	5
Tau	LkCa 7	04 19 41.27	+27 49 48.5	K7	w	154 ± 7	14.7 ± 1.2	17.98 ± 0.04	0.21	0.21	2
Tau	RX J0420.3+3123..	04 20 24.12	+31 23 23.7	K4	?	···	9.6 ± 0.6	13.99 ± 0.03	···	···	1
Tau	DE Tau	04 21 55.64	+27 55 06.1	M1	c	453 ± 6	9.7 ± 0.3	15.402 ± 0.018	0.105	0.126	4
Tau	HD283572	04 21 58.84	+28 18 06.6	G2	w	Absorp.	79 ± 3	14.22 ± 0.08	0.94	1.30	4
Tau	T Tau A	04 21 59.43	+19 32 06.4	K1.5	c	430 ± 23	23.0 ± 1.2	19.23 ± 0.02	0.30	0.06	3
Tau	LkCa 21	04 22 03.14	+28 25 39.0	M3	c	277	46 ± 3	14.3 ± 0.3	···	···	1
Tau	HD285751	04 23 41.33	+15 37 54.9	G5	w	125	26.6 ± 1.4	15.22 ± 0.03	0.27	0.27	5
Tau	BD +26 718B	04 24 49.04	+26 43 10.4	K0	w	Absorp.	32.4 ± 1.8	16.23 ± 0.04	1.12	1.17	4
Tau	IP Tau	04 24 57.08	+27 11 56.5	M0	c	333 ± 54	12.3 ± 0.8	16.24 ± 0.03	0.62	0.73	5
Tau	DG Tau	04 27 04.70	+26 06 16.3	K6	c	484	24.7 ± 0.7	15.4 ± 0.6	···	···	1
Tau	BD +17 724B	04 27 05.97	+18 12 37.2	G5	w	Absorp.	49 ± 3	16.97 ± 0.06	0.14	0.18	4
Tau	NTTS 042417+1744	04 27 10.56	+17 50 42.6	K1	w	Absorp.	17.6 ± 1.5	15.324 ± 0.015	0.241	0.214	4
Tau	DH Tau	04 29 41.56	+26 32 58.3	M1	c	348	10.9 ± 0.6	16.52 ± 0.04	···	···	1
Tau	DI Tau	04 29 42.48	+26 32 49.3	M0	w	120 ± 19	12.5 ± 0.6	15.103 ± 0.020	0.266	0.192	4
Tau	IQ Tau	04 29 51.56	+26 06 44.9	M0.5	c	411 ± 48	14.4 ± 0.3	15.83 ± 0.03	0.25	0.27	5
Tau	UX Tau	04 30 04.00	+18 13 49.4	K2	c	513 ± 44	23.6 ± 1.8	15.45 ± 0.02	2.28	2.90	4
Tau	FX Tau A	04 30 29.61	+24 26 45.0	M2	c	281 ± 67	9.61 ± 0.19	16.363 ± 0.013	0.179	0.223	4
Tau	FX Tau B	04 30 29.61	+24 26 45.0	M1	c	413 ± 53	7.9 ± 0.3	17.332 ± 0.015	0.236	0.185	4

Table 4.1 (cont'd)

Region	Object	R.A. (J2000.0)	Dec. (J2000.0)	SpT	TTS[a]	10% width[bc] (km s^{-1})	$v \sin i$[de] (km s^{-1})	$\overline{RV}$ (km s^{-1})	σ_{RV}[f] (km s^{-1})	$\sigma_{\rm N}$[g] (km s^{-1})	# of obs.
Tau	DK Tau A	04 30 44.25	+26 01 24.5	K7	c	461 ± 54	17.5 ± 1.2	16.29 ± 0.05	0.42	0.29	4
Tau	DK Tau B	04 30 44.25	+26 01 24.5	M1	c	397 ± 35	14.0 ± 0.8	14.70 ± 0.10	0.85	0.78	5
Tau	RX J0430.8+2113	04 30 49.18	+21 14 10.6	G8	w	Absorp.	41 ± 4	15.09 ± 0.03	0.55	0.30	4
Tau	HD284496	04 31 16.86	+21 50 25.3	G0	w	Absorp.	20.0 ± 1.0	14.414 ± 0.019	0.329	0.307	4
Tau	NTTS 042835+1700	04 31 27.17	+17 06 24.9	K5	w	84 ± 7	14.8 ± 1.3	16.63 ± 0.04	0.38	0.43	4
Tau	XZ Tau	04 31 40.07	+18 13 57.2	M3	c	341 ± 13	15.0 ± 1.2	18.30 ± 0.04	0.18	0.20	4
Tau	V710 Tau A	04 31 57.79	+18 21 38.1	M0.5	w	192	21.5 ± 0.4	15.75 ± 0.15	···	···	1
Tau	V710 Tau B	04 31 57.79	+18 21 38.1	M2	c	371	18.31 ± 0.19	17.72 ± 0.09	···	···	1
Tau	L1551-51	04 32 09.27	+17 57 22.8	K7	w	146 ± 26	32.1 ± 1.4	18.39 ± 0.10	0.63	0.59	4
Tau	V827 Tau	04 32 14.57	+18 20 14.7	K7	w	168 ± 15	20.9 ± 1.3	17.77 ± 0.05	1.67	1.91	4
Tau	V928 Tau	04 32 18.86	+24 22 27.1	M0.5	w	178 ± 60	31.6 ± 0.7	15.38 ± 0.16	1.67	2.02	4
Tau	GG Tau A	04 32 30.35	+17 31 40.6	K7	c	512 ± 10	11.5 ± 0.7	18.08 ± 0.03	0.16	0.19	4
Tau	RX J0432.7+1853	04 32 42.43	+18 55 10.2	K1	w	Absorp.	25.2 ± 1.6	21.834 ± 0.013	0.128	0.106	4
Tau	UZ Tau A	04 32 43.04	+25 52 31.1	M1	c	438 ± 41	19.3 ± 0.5	18.03 ± 0.08	0.57	0.58	6
Tau	L1551-55	04 32 43.73	+18 02 56.3	K7	w	94 ± 9	7.7 ± 0.7	18.264 ± 0.013	0.158	0.120	4
Tau	RX J0432.8+1735	04 32 53.24	+17 35 33.8	M2	w	105 ± 4	11.18 ± 0.11	18.039 ± 0.015	0.243	0.344	5
Tau	GH Tau	04 33 06.22	+24 09 34.0	M1.5	c	472 ± 38	30.3 ± 0.7	16.70 ± 0.10	1.01	1.12	4
Tau	V807 Tau	04 33 06.64	+24 09 55.0	K7	c	408 ± 18	13.6 ± 0.7	16.85 ± 0.03	0.32	0.30	4
Tau	V830 Tau	04 33 10.03	+24 33 43.4	K7	w	121	32.0 ± 1.5	18.2 ± 0.2	···	···	1
Tau	GI Tau	04 33 34.06	+24 21 17.0	K7	c	302 ± 45	12.7 ± 1.9	17.29 ± 0.04	1.08	1.00	4
Tau	RX J0433.5+1916	04 33 34.67	+19 16 48.9	G6	w	Absorp.	58 ± 3	21.9 ± 0.4	4.1	4.1	5
Tau	DL Tau	04 33 39.06	+25 20 38.2	G	c	581 ± 6	19 ± 4	13.94 ± 0.14	0.86	1.03	5
Tau	HN Tau A	04 33 39.35	+17 51 52.4	K5	c	595 ± 48	39 ± 10	4.6 ± 0.6	11.6	12.6	4
Tau	DM Tau	04 33 48.72	+18 10 10.0	M1	c	376 ± 27	4.0 ± 0.7	18.607 ± 0.011	0.100	0.109	4
Tau	HBC 407	04 34 18.04	+18 30 06.7	G8	w	Absorp.	8.8 ± 1.8	17.75 ± 0.03	···	···	1
Tau	AA Tau	04 34 55.42	+24 28 53.2	K7	c	402 ± 89	12.8 ± 1.1	16.98 ± 0.04	0.62	0.26	4
Tau	FF Tau	04 35 20.90	+22 54 24.2	K7	w	160 ± 86	5.6 ± 0.8	14.165 ± 0.015	0.141	0.139	5
Tau	HBC 412 A	04 35 24.51	+17 51 43.0	M1.5	w	105 ± 4	4.9 ± 0.3	18.587 ± 0.012	0.024	0.024	2
Tau	HBC 412 B	04 35 24.51	+17 51 43.0	M1.5	w	104 ± 6	4.1 ± 0.2	18.295 ± 0.012	0.168	0.168	2
Tau	DN Tau	04 35 27.37	+24 14 58.9	M0	c	336 ± 16	12.3 ± 0.6	16.30 ± 0.02	0.24	0.32	5
Tau	HQ Tau	04 35 47.34	+22 50 21.7	K0	c	442 ± 93	48 ± 2	16.65 ± 0.11	0.85	0.81	4
Tau	HP Tau/G2	04 35 54.15	+22 54 13.5	G0	w	Absorp.	127 ± 4	16.6 ± 1.0	1.4	1.3	4
Tau	RX J0435.9+2352	04 35 56.83	+23 52 05.0	M1	w	125 ± 21	4.2 ± 0.5	16.605 ± 0.011	0.129	0.139	4
Tau	LkCa 14	04 36 19.09	+25 42 59.0	M0	w	122 ± 20	22.7 ± 1.0	16.65 ± 0.04	0.32	0.36	5
Tau	HD283759	04 36 49.12	+24 12 58.8	F2	w	Absorp.	57 ± 6	32.1 ± 0.2	1.2	1.5	4
Tau	RX J0437.2+3108	04 37 16.86	+31 08 19.5	K4	w	82 ± 9	11.3 ± 0.8	15.718 ± 0.016	0.441	0.417	4
Tau	RX J0438.2+2023	04 38 13.04	+20 22 47.1	K2	w	Absorp.	16.1 ± 1.7	14.954 ± 0.016	0.519	0.579	4
Tau	RX J0438.2+2302	04 38 15.62	+23 02 27.6	M1	w	111 ± 29	4.5 ± 0.4	16.493 ± 0.009	0.201	0.318	4

Table 4.1 (cont'd)

Region	Object	R.A. (J2000.0)	Dec. (J2000.0)	SpT	TTS[a]	10% width[bc] (km s^{-1})	v sin i[de] (km s^{-1})	$\overline{RV}$ (km s^{-1})	σ_{RV}[f] (km s^{-1})	$\sigma_{\rm N}$[g] (km s^{-1})	# of obs.
Tau	RX J0438.4+1543..	04 38 27.66	+15 43 38.0	K3	?	···	6 ± 2	15.211 ± 0.009	0.126	0.126	5
Tau	DO Tau	04 38 28.58	+26 10 49.4	M0	c	480 ± 56	10.5 ± 1.0	16.04 ± 0.17	1.86	2.00	5
Tau	HD285957.....	04 38 39.07	+15 46 13.7	K2	w	Absorp.	22.5 ± 1.2	17.991 ± 0.015	0.370	0.385	4
Tau	VY Tau	04 39 17.41	+22 47 53.4	M0	w	124 ± 16	5.8 ± 1.0	17.716 ± 0.016	0.320	0.357	5
Tau	LkCa 15	04 39 17.80	+22 21 03.5	K5	c	451 ± 51	13.9 ± 1.2	17.65 ± 0.03	0.65	0.69	5
Tau	IW Tau	04 41 04.71	+24 51 06.2	K7	w	170 ± 32	8.7 ± 0.8	15.880 ± 0.010	0.259	0.264	5
Tau	CoKu Tau/4.....	04 41 16.81	+28 40 00.1	M1	w	185 ± 33	25.8 ± 0.4	15.98 ± 0.04	0.42	0.40	7
Tau	HD283798.....	04 41 55.16	+26 58 49.5	G2	w	Absorp.	25.2 ± 1.2	13.774 ± 0.014	0.140	0.082	4
Tau	RX J0444.3+2017..	04 44 23.55	+20 17 17.5	K1	?	···	60 ± 3	15.09 ± 0.16	0.90	0.94	5
Tau	HD30171.....	04 45 51.29	+15 55 49.7	G5	w	Absorp.	108 ± 4	21.13 ± 0.17	1.37	1.24	4
Tau	V1001 Tau A.....	04 46 58.98	+17 02 38.2	K6	c	525 ± 48	12.1 ± 1.2	22.45 ± 0.05	0.72	···	2
Tau	V1001 Tau B.....	04 46 58.98	+17 02 38.2	K6	c	405 ± 24	7.0 ± 0.3	21.74 ± 0.08	0.50	1.41	3
Tau	DR Tau	04 47 06.21	+16 58 42.8	K4	c	370 ± 7	6.26 ± 0.12	21.10 ± 0.04	0.19	0.16	5
Tau	RX J0447.9+2755 A	04 48 00.44	+27 56 19.6	G2.5	w	Absorp.	30.5 ± 1.8	16.29 ± 0.10	1.03	1.03	2
Tau	RX J0447.9+2755 B	04 48 00.44	+27 56 19.6	G2	w	Absorp.	27.9 ± 1.4	15.67 ± 0.04	0.97	0.97	3
Tau	RX J0450.0+2230..	04 50 00.20	+22 29 57.5	K1	?	···	57 ± 3	15.04 ± 0.08	0.13	0.12	4
Tau	UY Aur A	04 51 47.38	+30 47 13.5	K7	c	324 ± 19	23.8 ± 1.3	13.92 ± 0.07	0.87	0.97	5
Tau	RX J0452.5+1730..	04 52 30.75	+17 30 25.8	K4	w	89	8.8 ± 0.6	16.820 ± 0.010	0.196	0.222	4
Tau	RX J0452.8+1621..	04 52 50.15	+16 22 09.2	K6	w	123 ± 12	24.9 ± 1.2	19.28 ± 0.06	0.40	0.40	4
Tau	RX J0452.9+1920..	04 52 57.08	+19 19 50.4	K5	w	89 ± 8	4.8 ± 1.3	14.699 ± 0.010	0.117	0.107	4
Tau	HD31281.....	04 55 09.62	+18 26 30.9	G0	w	Absorp.	79 ± 4	14.57 ± 0.12	0.26	0.20	4
Tau	GM Aur	04 55 10.98	+30 21 59.5	K7	c	505 ± 11	14.8 ± 0.9	15.15 ± 0.04	0.50	0.41	4
Tau	LkCa 19	04 55 36.96	+30 17 55.3	K0	w	154 ± 40	20.1 ± 1.1	13.578 ± 0.013	1.120	0.674	4
Tau	SU Aur	04 55 59.38	+30 34 01.6	G2	c	561 ± 58	59 ± 2	14.26 ± 0.05	0.40	0.25	4
Tau	RX J0456.2+1554..	04 56 13.57	+15 54 22.0	K7	w	106 ± 20	9.7 ± 0.6	18.966 ± 0.016	0.092	0.106	4
Tau	HD286179.....	04 57 00.65	+15 17 53.1	G0	w	Absorp.	17.1 ± 1.2	10.069 ± 0.009	0.211	0.090	4
Tau	RX J0457.2+1524..	04 57 17.67	+15 25 09.4	K1	w	Absorp.	42 ± 2	19.77 ± 0.03	0.70	0.75	4
Tau	RX J0458.7+2046..	04 58 39.74	+20 46 44.1	K7	w	Absorp.	7.8 ± 0.5	19.043 ± 0.013	0.108	0.124	5
Tau	RX J0459.7+1430..	04 59 46.17	+14 30 55.4	K4	w	53	14.5 ± 0.6	19.875 ± 0.012	0.150	0.092	4
Tau	V836 Tau	05 03 06.60	+25 23 19.7	K7	c	403 ± 58	13.4 ± 1.1	18.15 ± 0.03	0.53	0.44	4
Tau	RX J0507.2+2437..	05 07 12.07	+24 37 16.4	K6	w	126 ± 14	19.7 ± 1.0	18.74 ± 0.04	1.24	1.45	5
Tau	RW Aur B	05 07 49.54	+30 24 05.1	K1	c	618 ± 78	14.5 ± 1.8	15.00 ± 0.03	0.66	0.54	4

[a]c: Classical T Tauri star, w: Weak-lined T Tauri star, ?: Unknown.

[b]The Hα 10% widths were adopted from Nguyen et al. (2009b) where available, or measured using the same method otherwise.

[c]The Hα 10% width uncertainty does not correspond to the measurement uncertainty, but to the scatter in our multi-epoch data.

[d]The v sin i were adopted from Nguyen et al. (2009b) where available, or measured using the same method otherwise.

[e]The v sin i uncertainty represents the combined measurement scatter between results using different template spectra, and over different epochs.

[f]This is the weighted standard deviation of the radial velocity as described in §4.5.2.

[g]This is the systematic noise of the radial velocity as described in §4.5.2.

Table 4.2. Measurements of Stars with Close Companions in Cha I & Tau-Aur

SB[a] type	Region	Object	R.A. (J2000.0)	Dec. (J2000.0)	SpT	TTS[b]	10% width[cd] (km s^{-1})	# of obs.	Comp.	v sin i[ef] (km s^{-1})	Flux[g] ratio
SB1	Cha	T39 B	11 09 11.72	−77 29 12.5	M1.5	w	106 ± 13	5		12.8 ± 0.4	···
SB1	Tau	RX J0415.8+3100	04 15 51.38	+31 00 35.6	G6	w	Absorp.	4		31.7 ± 1.9	···
SB1	Tau	RX J0457.5+2014	04 57 30.66	+20 14 29.7	K3	w	Absorp.	4		33 ± 3	···
SB1?	Cha	T7	10 59 01.09	−77 22 40.7	K8	c	365 ± 76	6		11.3 ± 0.8	···
SB1?	Cha	CHXR 28 B	11 07 55.89	−77 27 25.8	G9	w	175	2		61 ± 4	···
SB1?	Tau	RY Tau	04 21 57.40	+28 26 35.5	F8	c	600 ± 24	4		48 ± 3	···
SB1?	Tau	CI Tau	04 33 52.00	+22 50 30.2	G	c	572 ± 9	4		13 ± 2	···
SB2	Cha	CHXR 12	11 03 56.83	−77 21 33.0	M3.5	w	101 ± 8	6	A	8.99 ± 0.14	···
									B	8 ± 2	0.20 ± 0.08
SB2	Cha	T42	11 09 53.41	−76 34 25.5	K5	c	543 ± 83	7	A	11.4 ± 1.1	···
									B	11.5 ± 1.5	0.8 ± 0.3
SB2	Tau	V826 Tau	04 32 15.84	+18 01 38.7	K7	w	139 ± 13	5	A	8.5 ± 0.5	···
									B	9.3 ± 0.7	0.88 ± 0.06
SB2	Tau	DQ Tau	04 46 53.05	+17 00 00.2	M0	c	340 ± 22	4	A	14.7 ± 1.6	···
									B	11.3 ± 0.7	0.78 ± 0.18
SB2	Tau	HBC 427	04 56 02.02	+30 21 03.8	K5	w	145 ± 13	4	A	9.9 ± 0.3	···
									B	14.5 ± 0.5	0.157 ± 0.014
SB2†	Cha	Hn 4	11 05 14.67	−77 11 29.1	M3.25	w	176 ± 126	4	A	9.0 ± 0.5	···
									B	90 ± 15	0.62 ± 0.09
SB2†	Cha	T21	11 06 15.41	−77 21 56.8	G5	w	Absorp.	1	A	94.1 ± 0.7	···
									B	14.5 ± 0.3	0.101 ± 0.005
SB2†	Cha	CHXR 47	11 10 38.02	−77 32 39.9	K3	w	Absorp.	2	A	59.5 ± 0.4	···
									B	24 ± 3	0.24 ± 0.06
SB2†	Tau	HD285281	04 00 31.07	+19 35 20.7	K0	w	Absorp.	4	A	78.0 ± 0.3	···
									B	17.0 ± 1.9	0.07 ± 0.05
SB2†	Tau	RX J0406.8+2541 A	04 06 51.35	+25 41 28.3	K4.5	c	277 ± 74	2	a	47 ± 4	···
									b	9.8 ± 0.3	0.32 ± 0.07
SB2†	Tau	DF Tau	04 27 02.80	+25 42 22.3	M3	c	369 ± 19	4	A	46.6 ± 1.8	···
									B	9.8 ± 0.6	0.49 ± 0.11
SB2†	Tau	RX J0441.4+2715	04 41 24.00	+27 15 12.4	G8	w	Absorp.	4	A	37.0 ± 0.6	···
									B	12.6 ± 1.5	0.32 ± 0.07
SB2†	Tau	RX J0443.4+1546	04 43 25.97	+15 46 03.9	G7	w	Absorp.	4	A	86.5 ± 1.6	···
									B	24.0 ± 0.8	0.83 ± 0.10
SB2†	Tau	RX J0455.7+1742	04 55 47.67	+17 42 02.0	K3	w	Absorp.	4	A	8 ± 2	···
									B	9.5 ± 0.4	0.337 ± 0.014
SB2?	Cha	T11	11 02 24.91	−77 33 35.7	K6	c	367 ± 38	4	A	11.2 ± 0.3	···
									B	13.0 ± 0.3	1.0 ± 0.4
SB2?	Cha	T31 A	11 08 01.49	−77 42 28.9	K3	c	471 ± 55	3	a	13 ± 2	···

Table 4.2 (cont'd)

SB[a] type	Region	Object	R.A. (J2000.0)	Dec. (J2000.0)	SpT	TTS[b]	10% width[cd] (km s^{-1})	# of obs.	Comp.	v sin i[ef] (km s^{-1})	Flux[g] ratio
									b	13 ± 3	0.7 ± 0.3
SB2?	Tau	Hubble 4	04 18 47.04	+28 20 07.3	K7	w	188 ± 16	4	A	12.1 ± 0.3	···
									B	13.1 ± 1.9	0.20 ± 0.05
SB3	Cha	T55	11 13 33.57	−76 35 37.4	M4.5	w	165 ± 59	5	A	23 ± 2	···
									B	34 ± 4	0.38 ± 0.08
									C	31.0 ± 1.6	0.19 ± 0.08
SB3	Tau	RX J0412.8+2442	04 12 51.22	+24 41 44.3	G9	w	Absorp.	3	A	28.50 ± 0.12	···
									B	15.1 ± 1.5	0.88 ± 0.12
									C	7.4 ± 0.3	0.36 ± 0.04
SB3	Tau	V773 Tau	04 14 12.92	+28 12 12.4	K3	c	433 ± 51	4	A	27 ± 4	···
									B	28 ± 4	1.0 ± 0.3
									C	21 ± 7	0.09 ± 0.06
SB3	Tau	LkCa 3	04 14 47.97	+27 52 34.7	M1	w	187 ± 25	4	Aa	12.0 ± 1.0	···
									Ab1	16 ± 2	0.75 ± 0.13
									Ab2	14 ± 4	0.21 ± 0.05

[a]SB1: Single-lined spectroscopic binary, SB2: Double-lined spectroscopic binary, SB3: Triple-lined spectroscopic binary; ?: suspected, †: long-period.

[b]c: Classical T Tauri star, w: Weak-lined T Tauri star, ?: Unknown.

[c]The Hα 10% widths were adopted from Nguyen et al. (2009b) where available, or measured using the same method otherwise.

[d]The Hα 10% width uncertainty does not correspond to the measurement uncertainty, but to the scatter in our multi-epoch data.

[e]The v sin i were adopted from Nguyen et al. (2009b) where available, or measured using the same method otherwise.

[f]The v sin i uncertainty represents the combined measurement scatter between results using different template spectra, and over different epochs.

[g]The flux ratio is between the companion and the primary star.

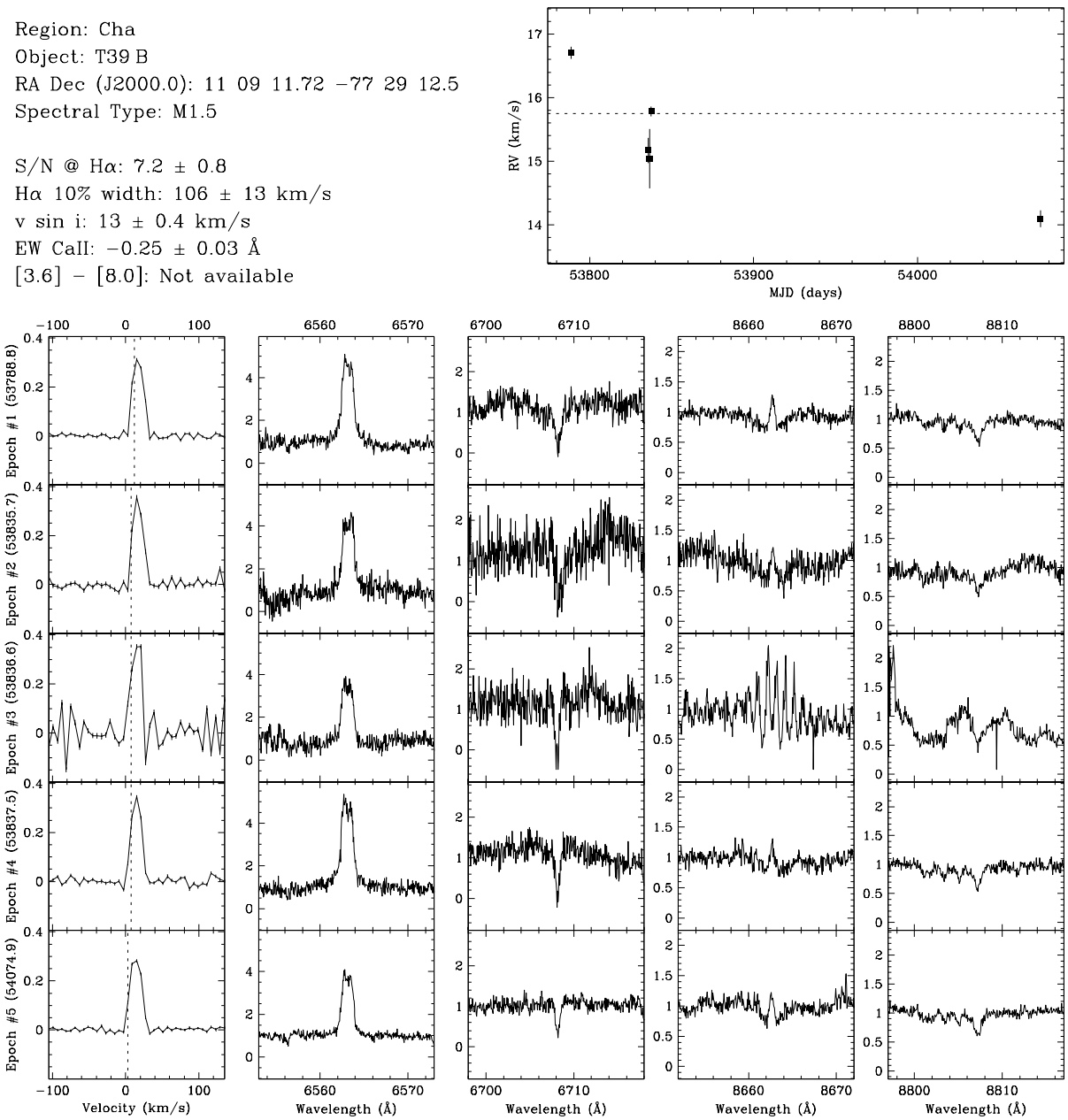

Figure 4.9 T39 B is an SB1. The overall radial velocity scatter is significant relative to the measurement uncertainties and to scatter observed within each observing run. The radial velocity scatter is larger than expected for a star with a v sin i of $13\,\mathrm{km\,s^{-1}}$, and thus is unlikely to be due to star spots. The lack of radial velocity offset from the cluster velocity ($\sim 16\,\mathrm{km\,s^{-1}}$) implies a long orbital period and a small velocity amplitude. If star spots are responsible for the changes in radial velocity, based on observed v sin i ($\sim 13\,\mathrm{km\,s^{-1}}$) and model stellar radius ($\sim 1.3\,R_\odot$), one would expect variations on a maximum timescale of ~ 5.1 days. From the stable results of the second observing run (epoch #2, #3 and #4) which spans 2.8 days compared to the overall range of radial velocities, it is unlikely that the radial velocity trends are the result of star spots. This target has been previously reported by Lafrenière et al. (2008) to be a component star of a resolved triple system (T39 Aa,Ab,B) with a separation of $\sim 4\farcs497$ (~ 630 AU) at a position angle of $\sim 70\fdg8$, and a B–Aa R-band flux ratio of ~ 0.13 ($\Delta K \sim 0.77$). Given the separation, the expected contribution to the line profile from the resolved companion is negligible.

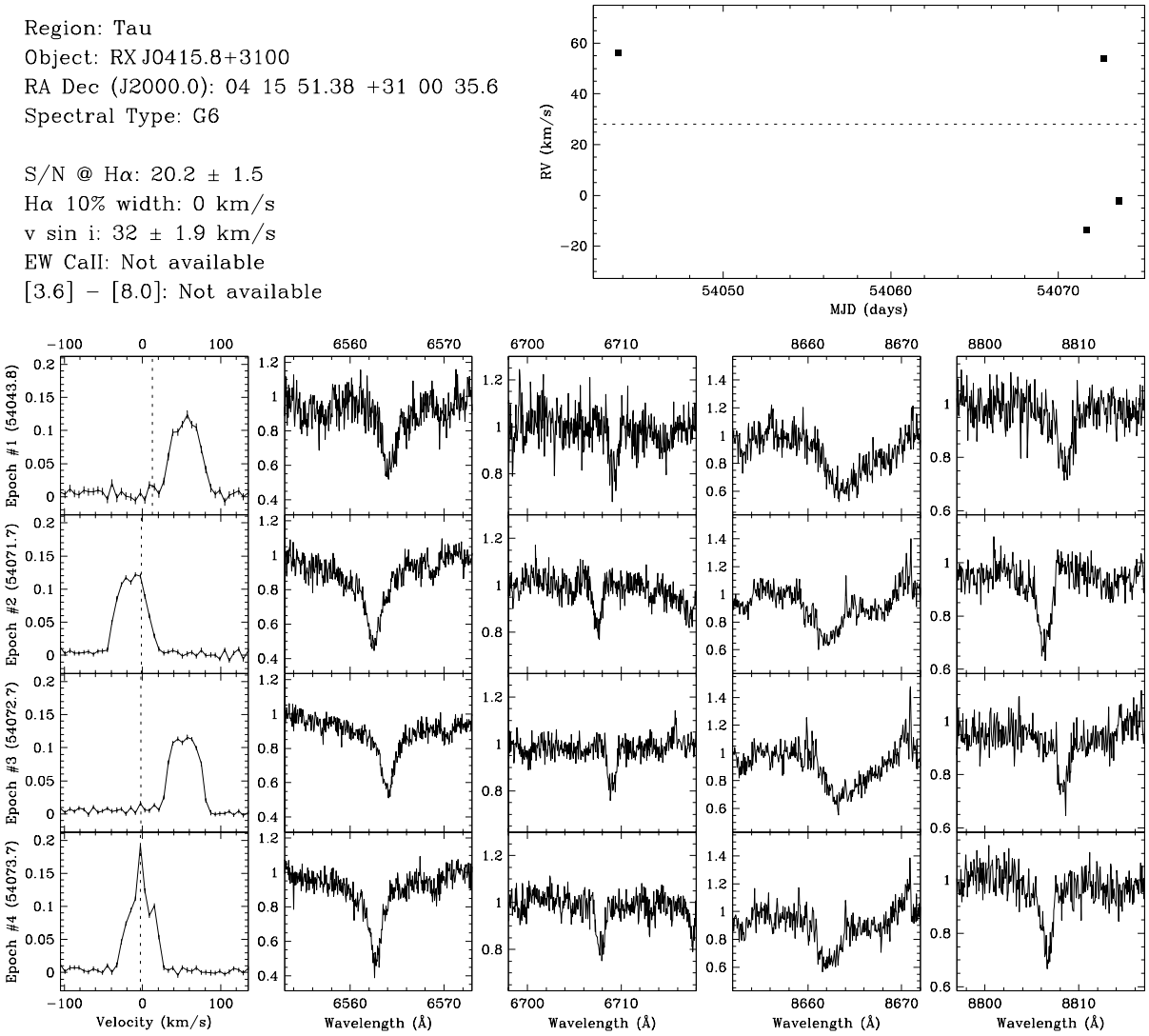

Figure 4.10 RX J0415.8+3100 is an SB1. The overall radial velocity scatter is significant relative to the measurement uncertainties. For epoch #4, the strong sharp peak in the line profile at the observer's rest frame is due to moonlight, and may have biased the radial velocity estimate toward the observer's rest frame. This target has been previously reported by Köhler & Leinert (1998) to have a resolved companion with a separation of $\sim 0\farcs94$ (~ 130 AU) at a position angle of $\sim 147\fdg2$, and an R-band flux ratio of ~ 0.19 ($\Delta K \sim 1.45$). Given the separation, the expected contribution to the line profile from the resolved companion is small.

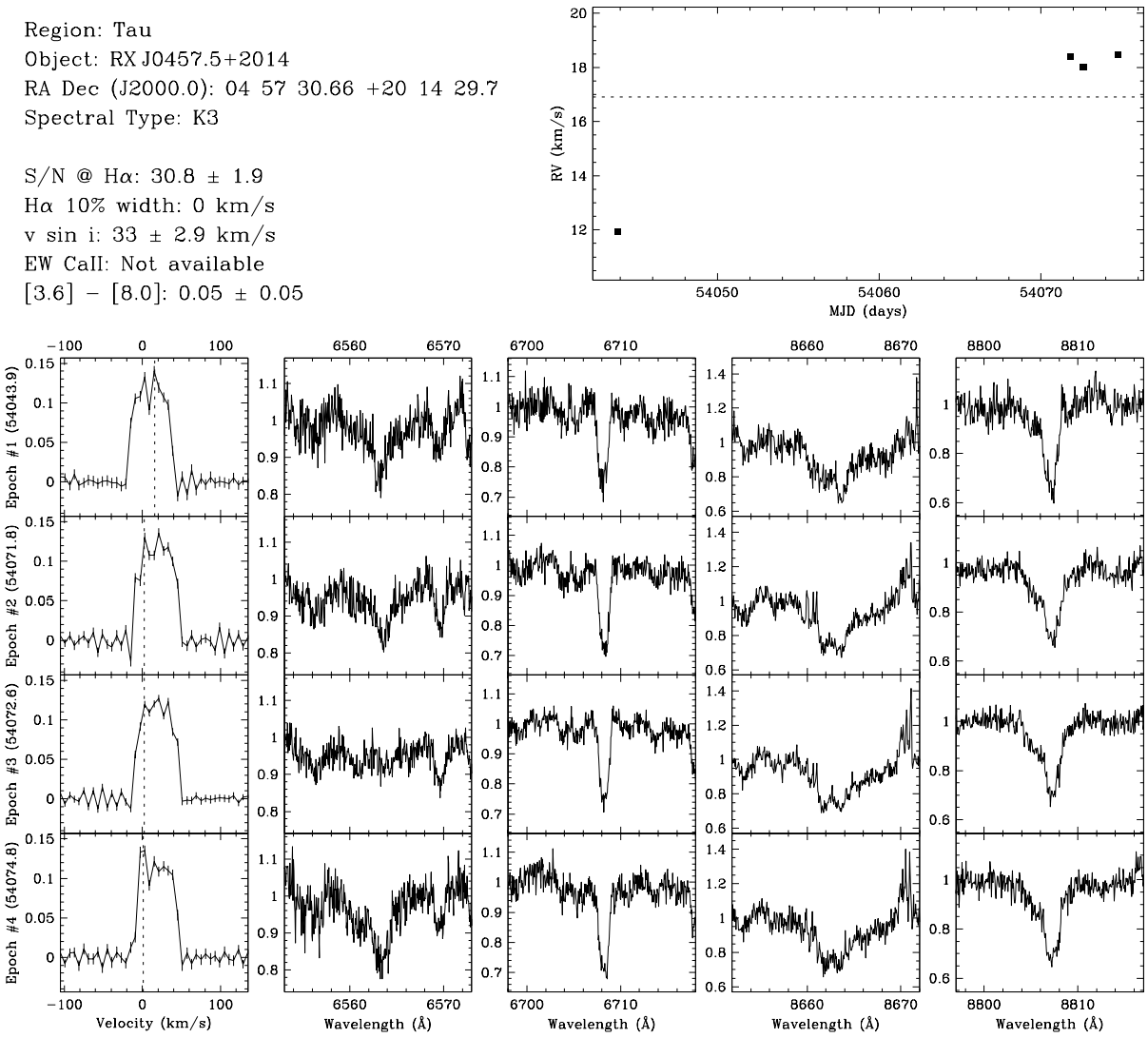

Figure 4.11 RX J0457.5+2014 is an SB1. The overall radial velocity scatter is significant relative to the measurement uncertainties and to scatter observed within each observing run. If star spots are responsible for the changes in radial velocity, based on observed $v \sin i$ ($\sim$33 km s^{-1}) and model stellar radius ($\sim 1.7\,R_{\odot}$), one would expect variations on a maximum timescale of $\sim$2.6 days. From the stable results of the second observing run (epochs #2, #3 and #4) which span 3.0 days, it is unlikely that the radial velocity trends are the result of star spots. For epoch #4, the sharp peak in the line profile at the observer's rest frame is due to moonlight, and may have biased the radial velocity estimate toward the observer's rest frame. This target has been previously reported by Köhler & Leinert (1998) to have a resolved companion with a separation of 6.″865–6.″867 ($\sim$960 AU) at a position angle of 204.°8–205.°5, and an R-band flux ratio of $\lesssim$0.01 ($\Delta K \sim$2.20–2.42). Given the flux ratio and separation, the expected contribution to the line profile from the resolved companion is negligible.

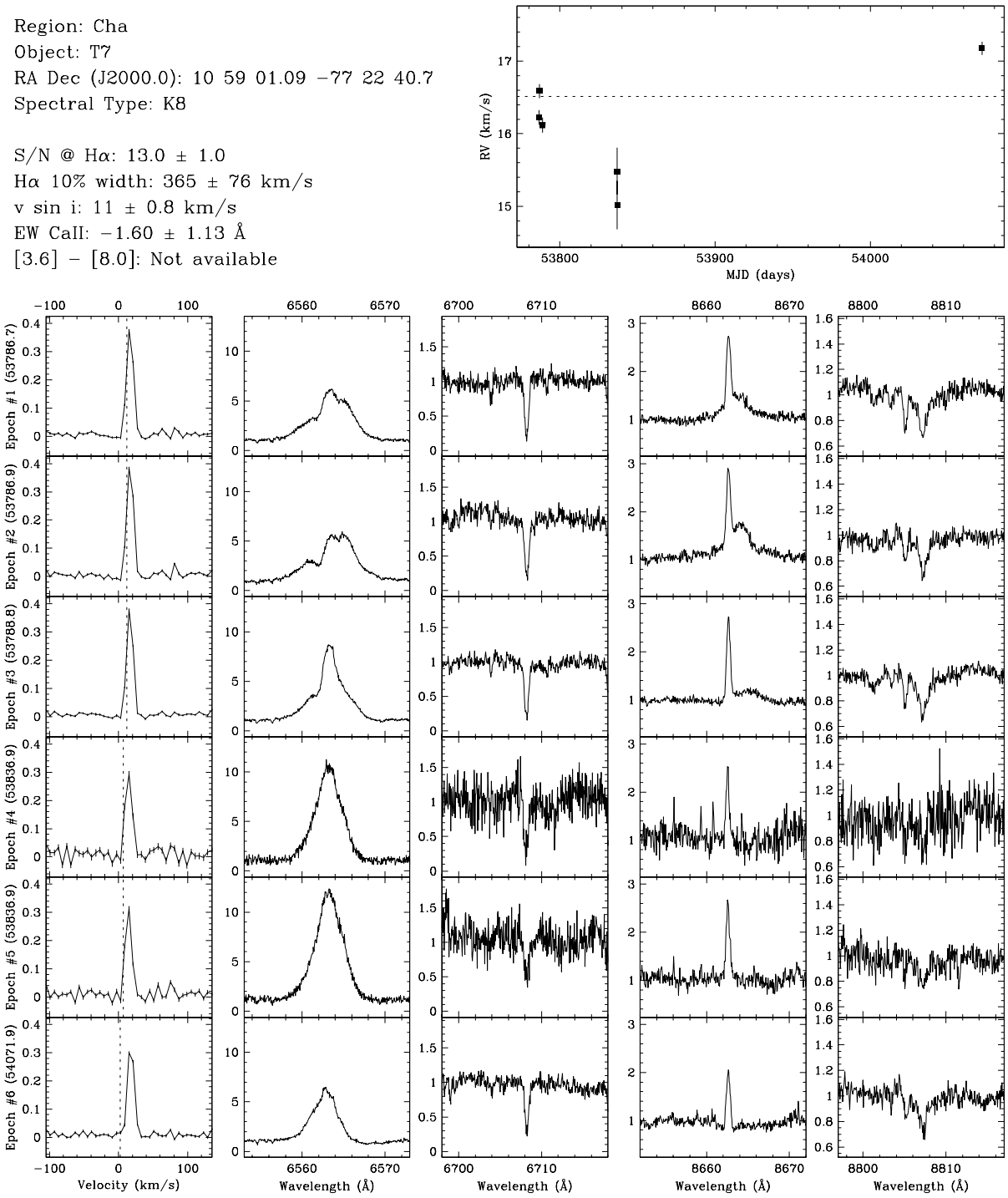

Figure 4.12 T7 is a suspected SB1. The overall radial velocity scatter is larger than expected from non-companion influences, e.g., star spots. If star spots are responsible for the changes in radial velocity, based on observed $v \sin i$ ($\sim 11\,\mathrm{km\,s^{-1}}$) and model stellar radius ($\sim 1.4\,R_\odot$), one would expect variations on a maximum timescale of ~ 6.1 days. From the stable results of the first observing run (epoch #1, #2 and #3) which spans 2.1 days, there is doubt that that the radial velocity trends are the result of star spots. This target has been previously reported by Lafrenière et al. (2008) to have no resolved companions.

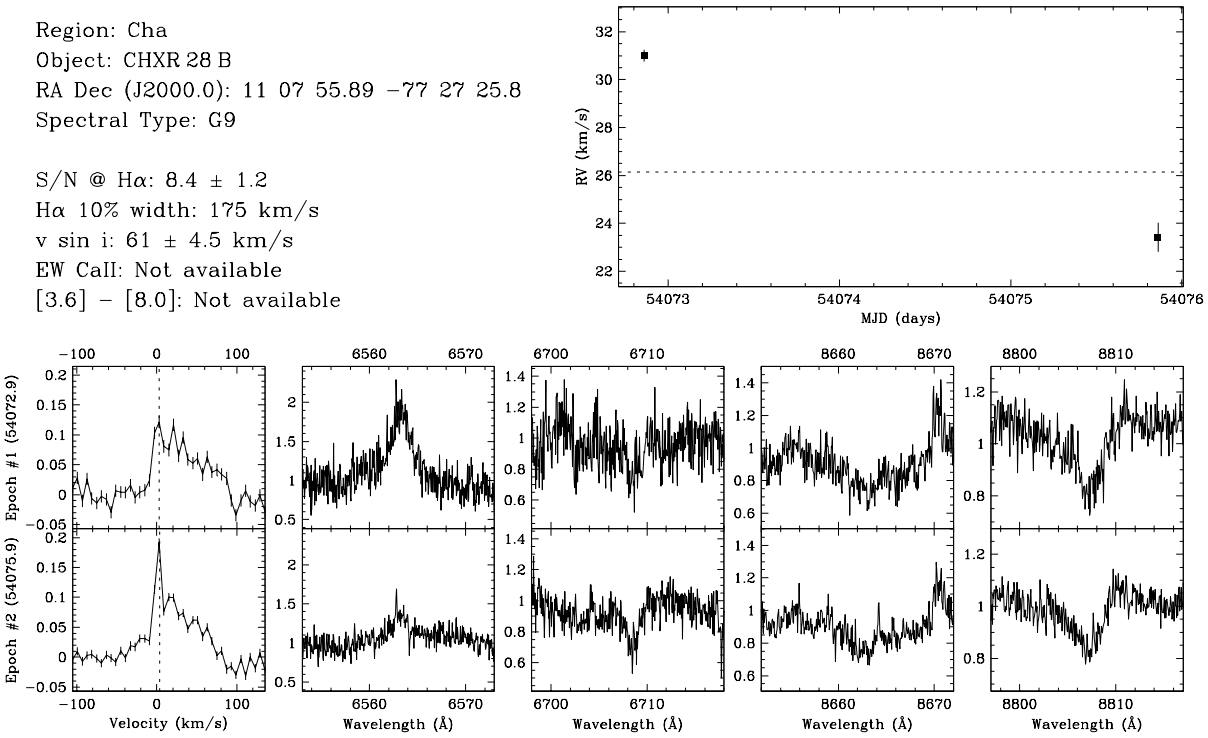

Figure 4.13 CHXR 28 B is a suspected SB1. The overall radial velocity scatter is larger than expected from non-companion influences, e.g., star spots. We derived the radial velocities from fits to the line profile rather than from direct fits to the spectra (see §4.4.2). The strong sharp peaks in the line profiles at the observer's rest frame are due to dawn twilight, and was included in the line profile fits. This target has been previously reported by Lafrenière et al. (2008) to have a resolved companion with a separation of $\sim 1\farcs818$ (~ 250 AU) at a position angle of $\sim 115\fdg9$, and an R-band flux ratio of ~ 0.68 ($\Delta K \sim 0.32$). Given the separation, the expected contribution to the line profile from the resolved companion is negligible.

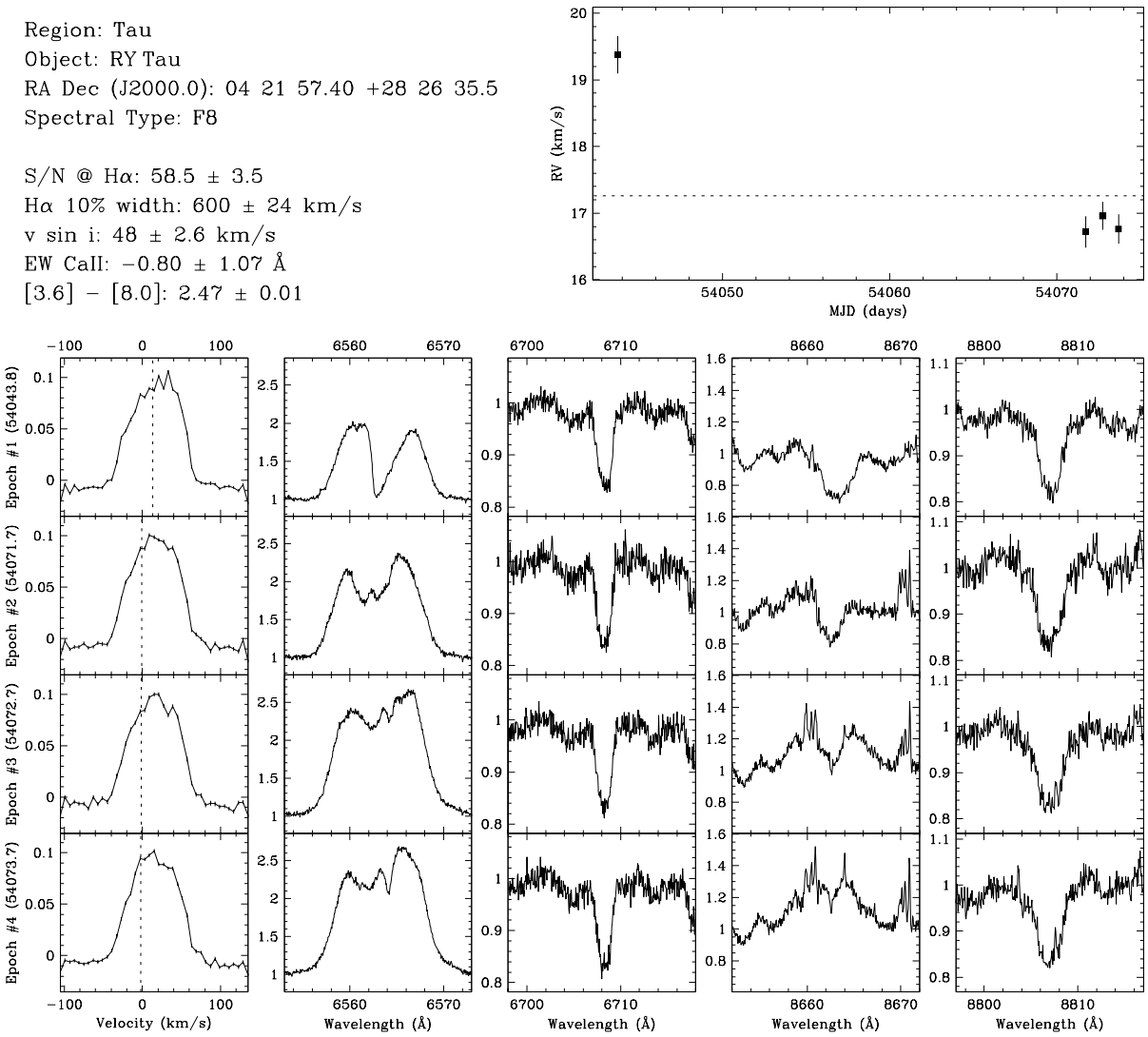

Figure 4.14 RY Tau is a suspected SB1. The overall radial velocity scatter is larger than expected from non-companion influences, e.g., star spots. If star spots are responsible for the changes in radial velocity, based on observed $v \sin i$ ($\sim 48\,\mathrm{km\,s^{-1}}$) and model stellar radius ($\sim 4.6\,R_\odot$), one would expect variations on a maximum timescale of ~ 4.9 days. From the stable results of the second observing run (epochs #2, #3 and #4) which span 2.0 days, it is unlikely that the radial velocity trends are the result of star spots. This target has been previously reported by Leinert et al. (1993), and Ghez et al. (1993) to have no resolved companions.

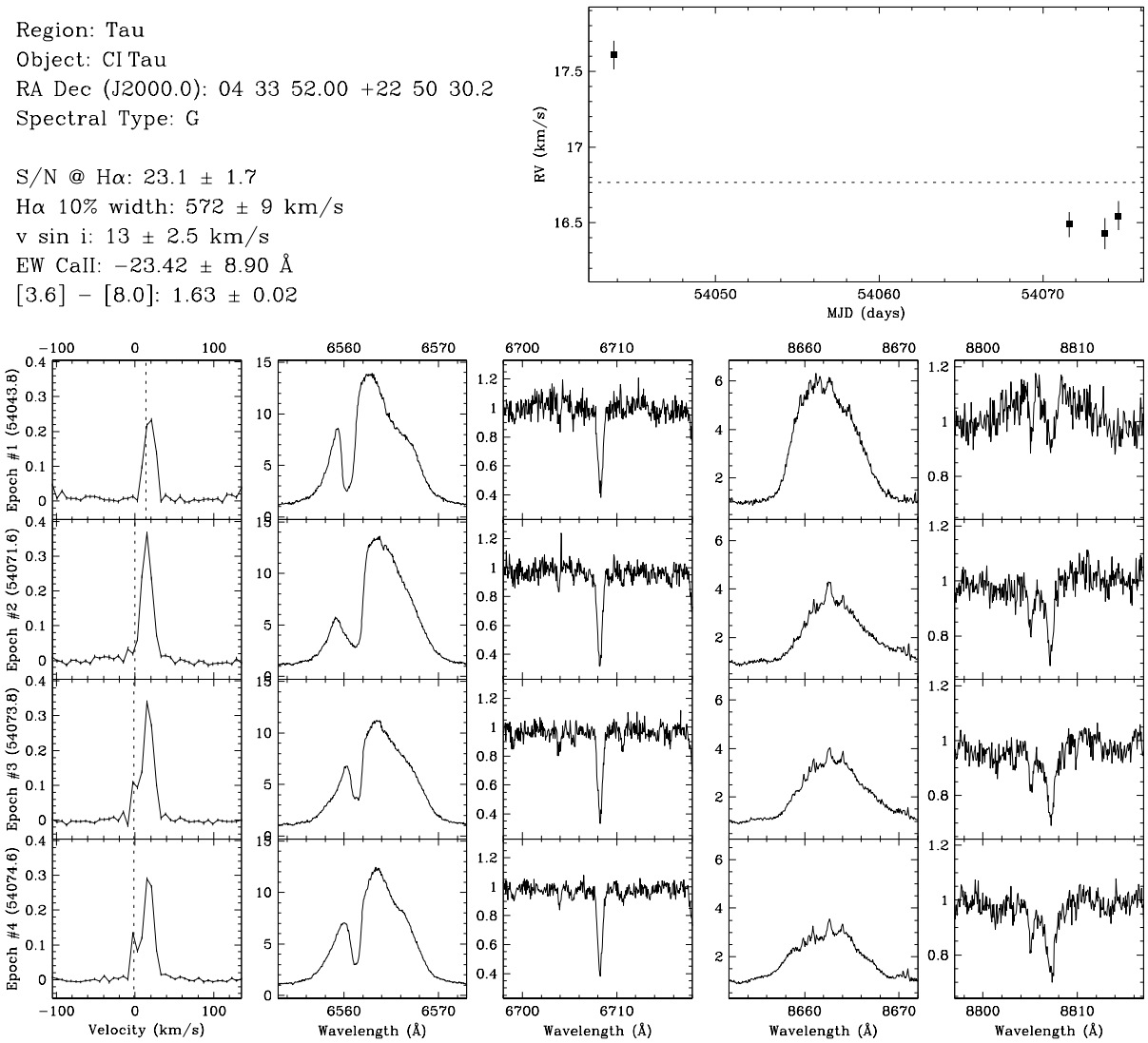

Figure 4.15 CI Tau is a suspected SB1. The overall radial velocity scatter is larger than expected from non-companion influences, e.g., star spots. If star spots were responsible for the changes in radial velocity, based on observed $v \sin i$ ($\sim$13 km s^{-1}) and model stellar radius ($\sim$4.0 $R_{\odot}$), one would expect variations on a maximum timescale of $\sim$15.5 days. From the stable results of the second observing run (epochs #2, #3 and #4) which span 3.0 days, it is unlikely that the radial velocity trends are the result of star spots. For epoch #3 and #4, the peaks in the line profile at the observer's rest frame are due to moonlight, and may have biased the radial velocity estimates toward the observer's rest frame. This target has been previously reported by Leinert et al. (1993), Ghez et al. (1993), and Simon et al. (1995) to have no resolved companions.

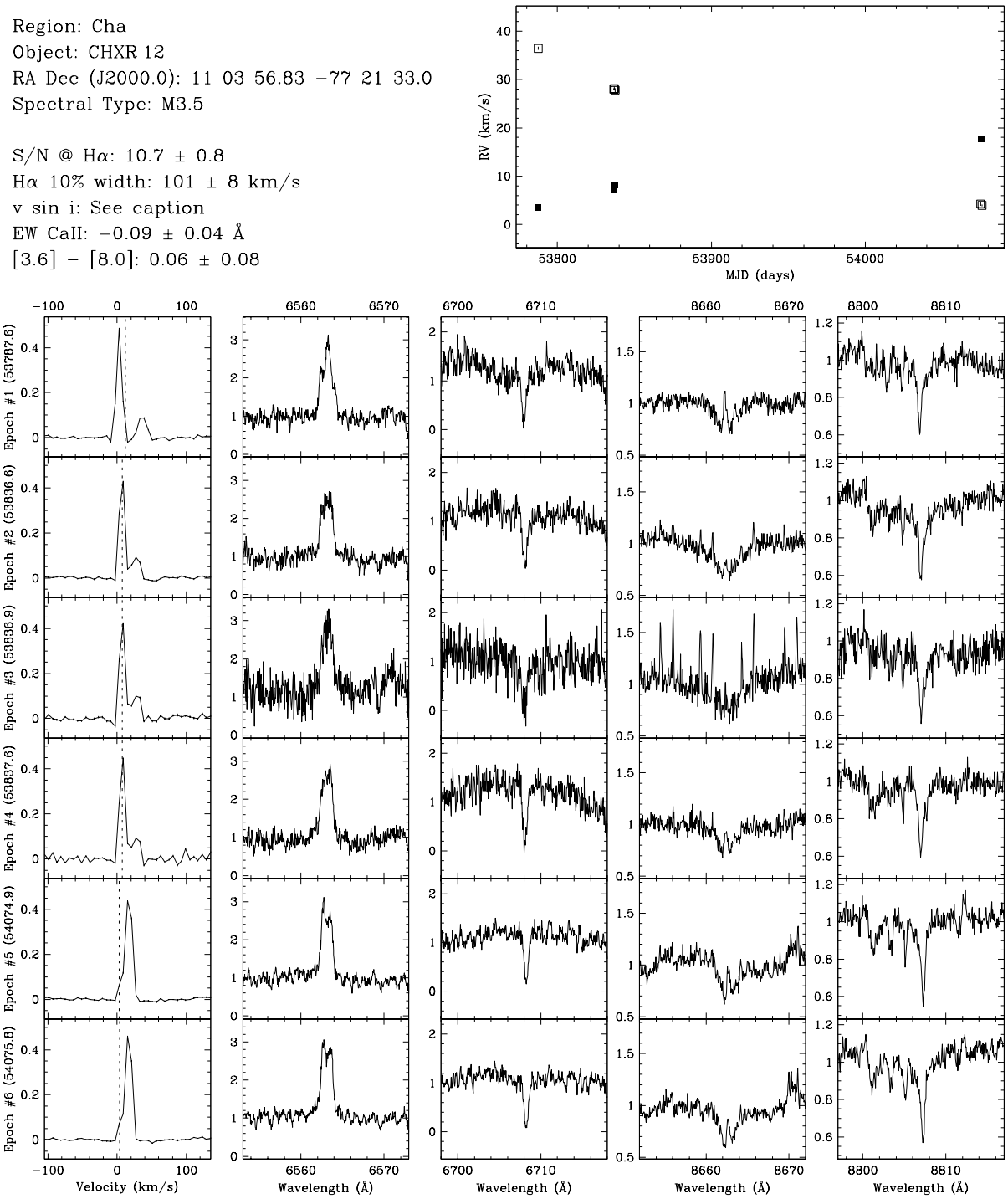

Figure 4.16 CHXR 12 is an SB2. Two sources can be seen in the line profile, and both show acceleration. By fitting the line profile to two rotational broadening functions, we estimate the two sources have a flux ratio of 0.20 ± 0.08, and the A and B sources have v sin i of 8.99 ± 0.14 km s^{-1} and 8 ± 2 km s^{-1}, respectively. For epoch #3, the narrow emission lines in the spectrum near 8662 Å are from the night sky. This target has been previously reported by Lafrenière et al. (2008) to have no resolved companions.

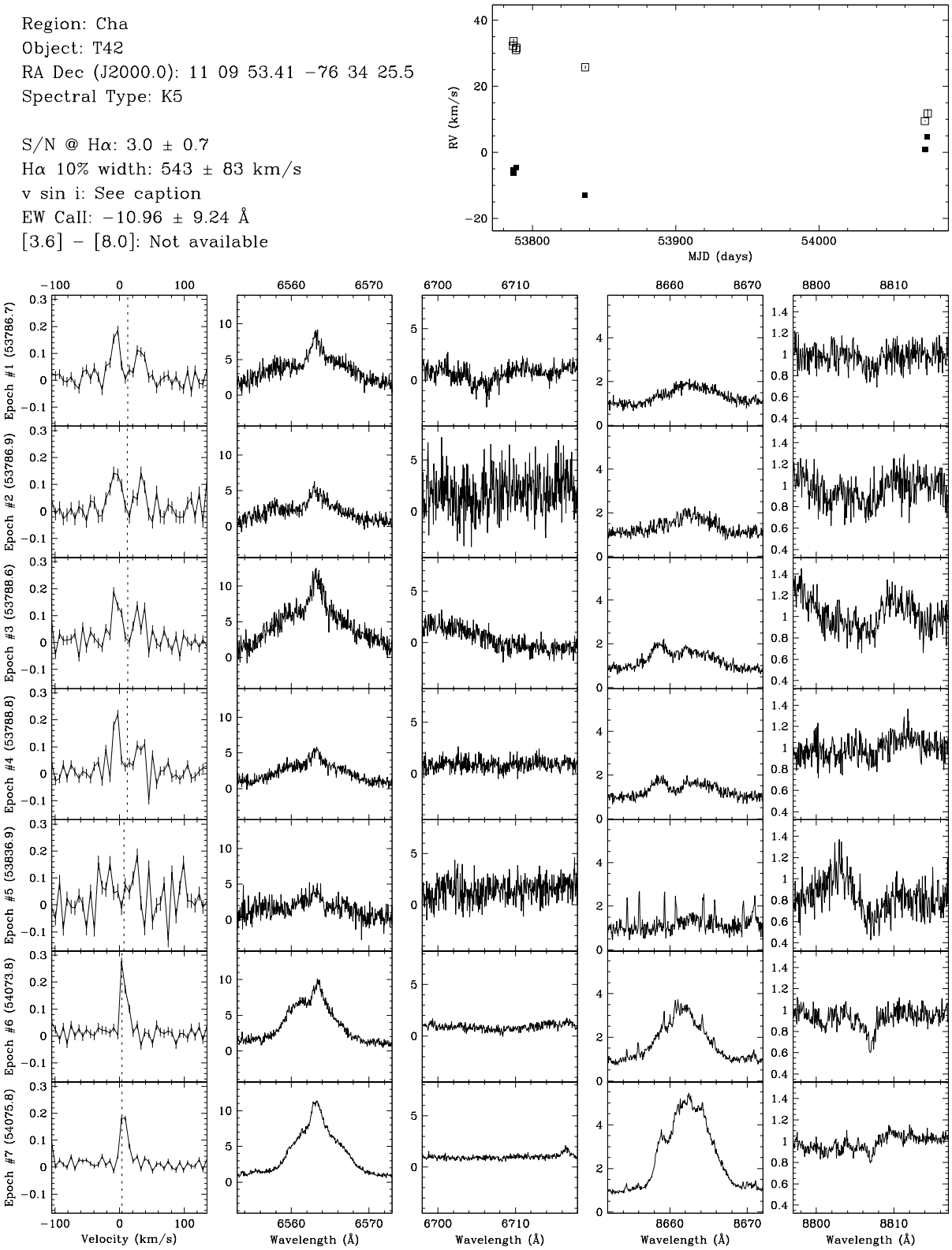

Figure 4.17 T42 is an SB2. The radial velocity estimate for epoch #5 is unreliable due to poor S/N. By fitting the line profile to two rotational broadening functions, we estimate the two sources have a flux ratio of 0.8 ± 0.3, and the A and B sources have $v \sin i$ of $11.4 \pm 1.1\,\mathrm{km\ s^{-1}}$ and $11.5 \pm 1.5\,\mathrm{km\ s^{-1}}$, respectively. For epoch #5, the narrow emission lines in the spectrum near 8662 Å are from the night sky. This target has been previously reported by Lafrenière et al. (2008) to have no resolved companions.

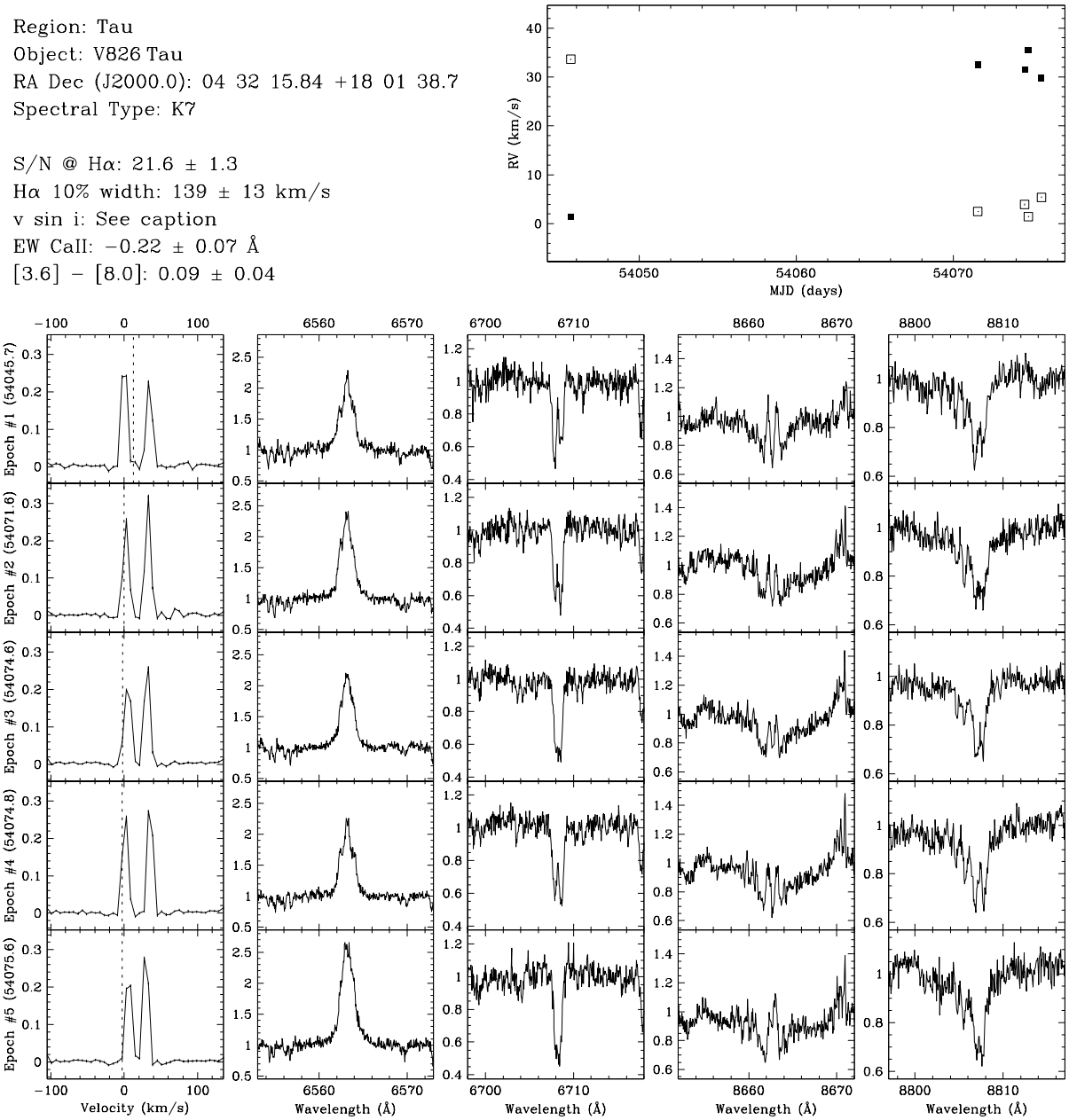

Figure 4.18 V826 Tau is an SB2. Two sources can be seen in the line profile, and both show acceleration. By fitting the line profile to two rotational broadening functions, we estimate the two sources have a flux ratio of 0.88 ± 0.06, and the A and B sources have $v \sin i$ of $8.5 \pm 0.5\,\mathrm{km\ s^{-1}}$ and $9.3 \pm 0.7\,\mathrm{km\ s^{-1}}$, respectively. This target has been previously reported by Leinert et al. (1993) as a spectroscopic binary (V826 Tau A+B) with a period of $\sim$3.9 days.

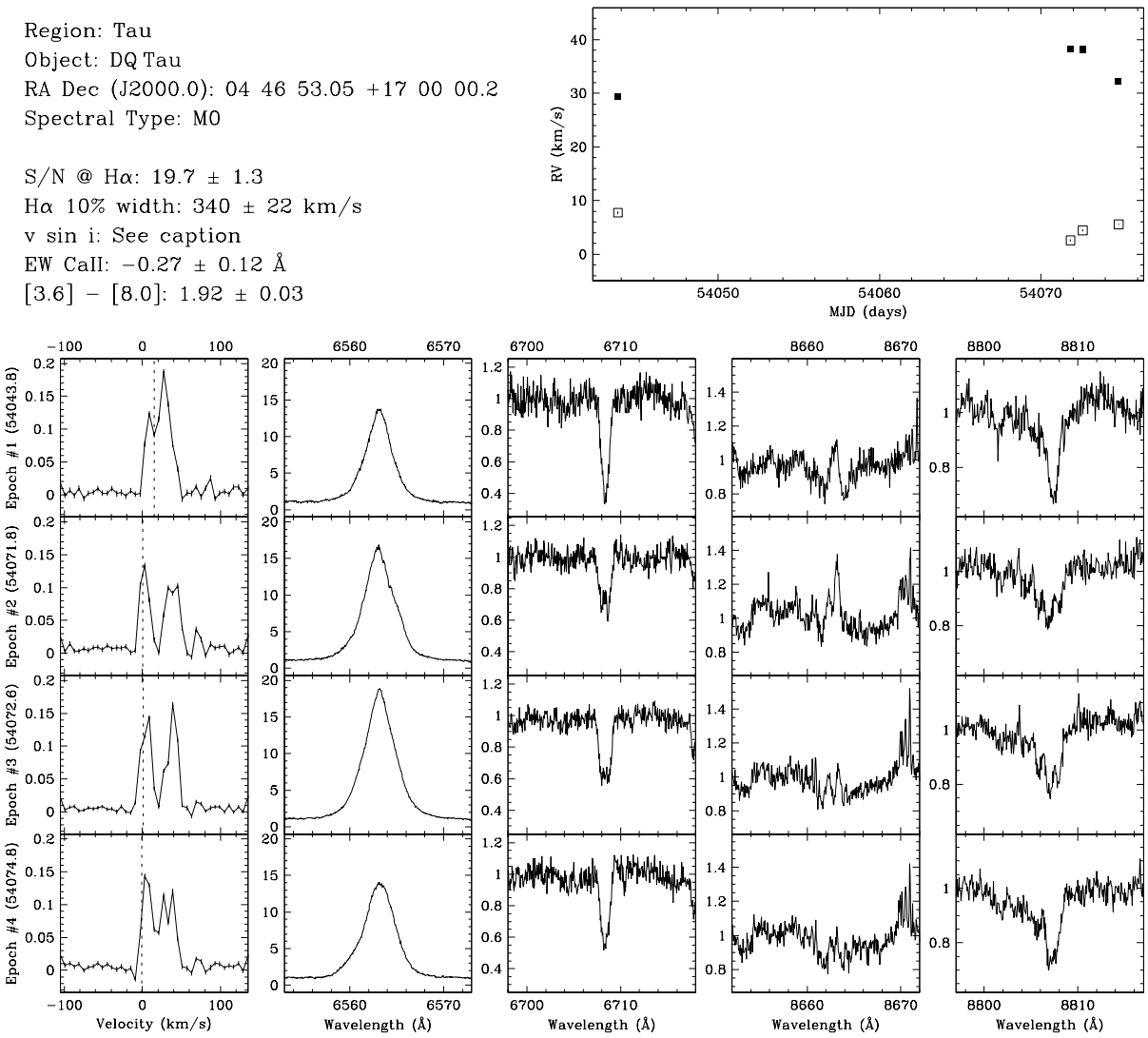

Figure 4.19 DQ Tau is an SB2. The two sources show radial acceleration. By fitting the line profile to two rotational broadening functions, we estimate the two sources have a flux ratio of 0.78 ± 0.18, and the A and B sources have $v \sin i$ of 14.7 ± 1.6 km s^{-1} and 11.3 ± 0.7 km s^{-1}, respectively. This target has been previously reported by Mathieu et al. (1997) as a spectroscopic binary with a period of 15.8 days.

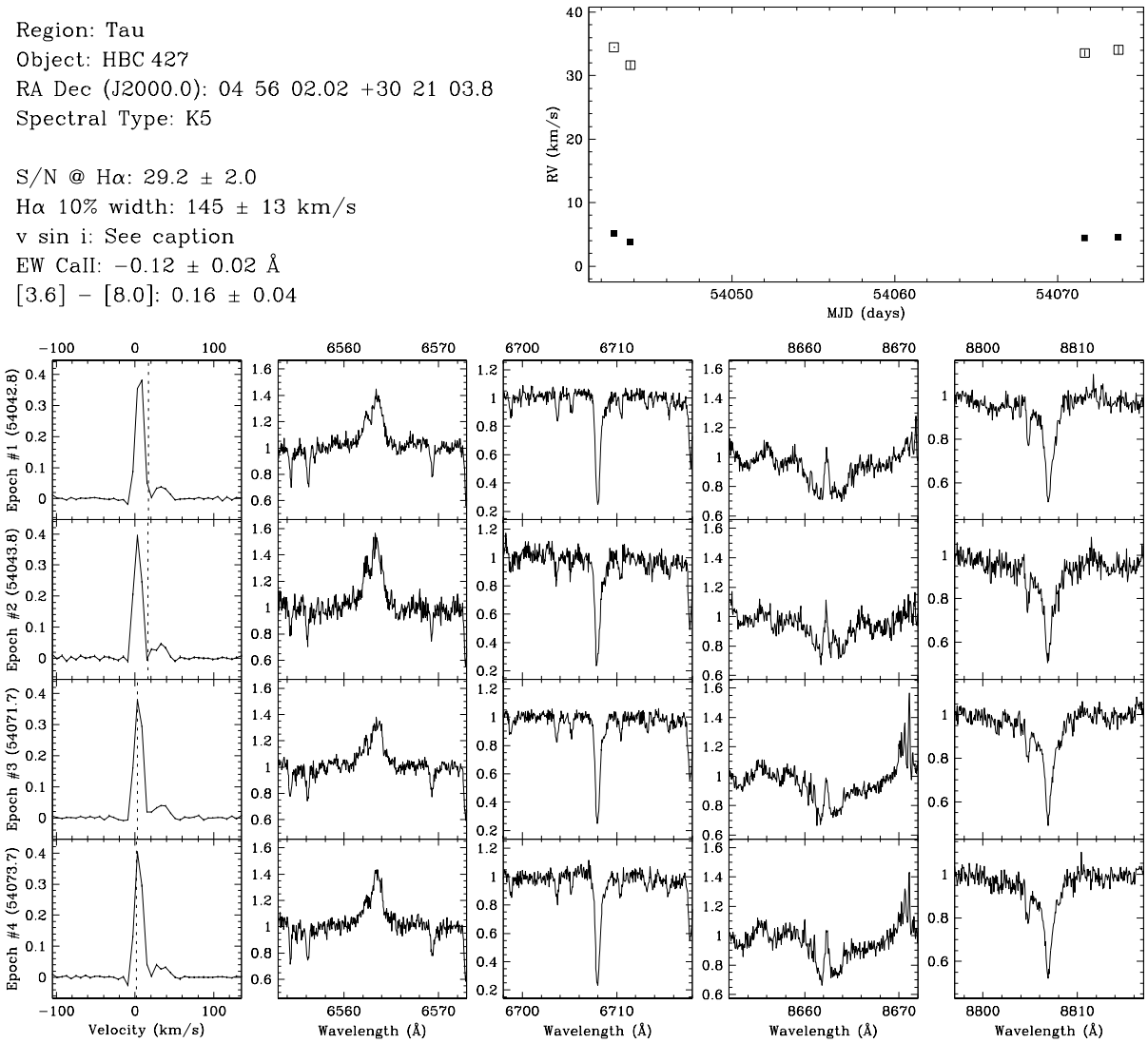

Figure 4.20 HBC 427 is an SB2. Two sources can be seen in the profile: a peak at $\sim 5\,\mathrm{km\,s^{-1}}$ and another peak at $\sim 30\,\mathrm{km\,s^{-1}}$. By fitting the line profile to two rotational broadening functions, we estimate the two sources have a flux ratio of 0.157 ± 0.014, and the A and B sources have $v \sin i$ of $9.9 \pm 0.3\,\mathrm{km\ s^{-1}}$ and $14.5 \pm 0.5\,\mathrm{km\ s^{-1}}$, respectively. This target has been previously reported by Steffen et al. (2001) as a spectroscopic binary with a period of 2500 days.

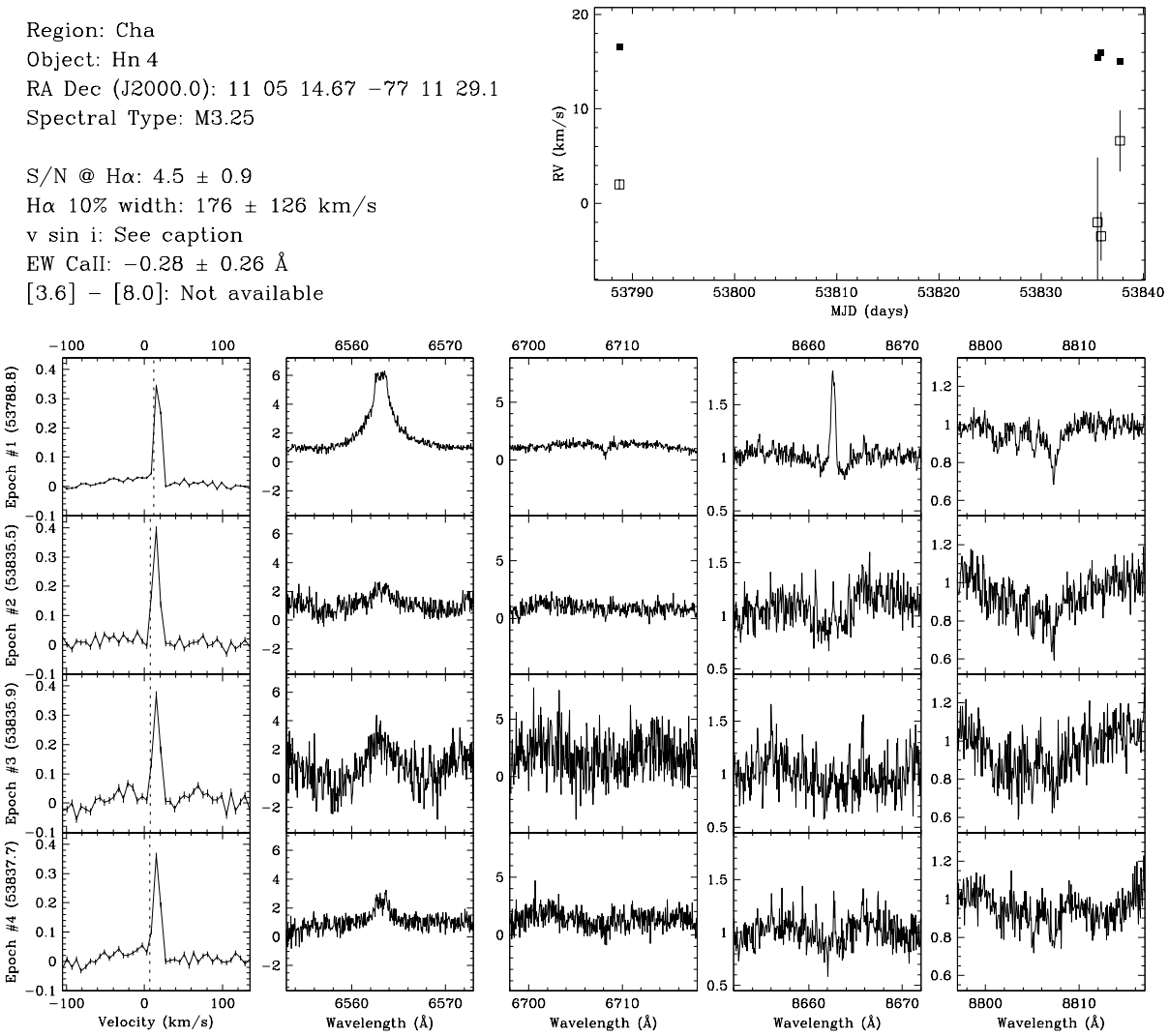

Figure 4.21 Hn 4 is a long-period SB2. Two sources can be seen in the line profile: a strong peak and a very shallow broad feature. By fitting the line profile to two rotational broadening functions, we estimate the two sources have a flux ratio of 0.62 ± 0.09, and the A and B sources have $v \sin i$ of $9.0 \pm 0.5\,\mathrm{km\ s^{-1}}$ and $90 \pm 15\,\mathrm{km\ s^{-1}}$, respectively. This target has been previously reported by Lafrenière et al. (2008) to have a resolved companion with a separation of $\sim 0\farcs211$ (~ 30 AU) at a position angle of $\sim 296\fdg1$, and an R-band flux ratio of ~ 0.89 ($\Delta K \sim 0.04$). This flux ratio is similar to that estimated between the SB2 components. Furthermore, the resolved companion has an expected circular orbital speed of $\sim 4\,\mathrm{km\ s^{-1}}$ which is compatible with the radial velocity separations of the SB2 components star if we consider the large uncertainties due to rapid rotation. Therefore, the resolved companion is likely the SB2 secondary star.

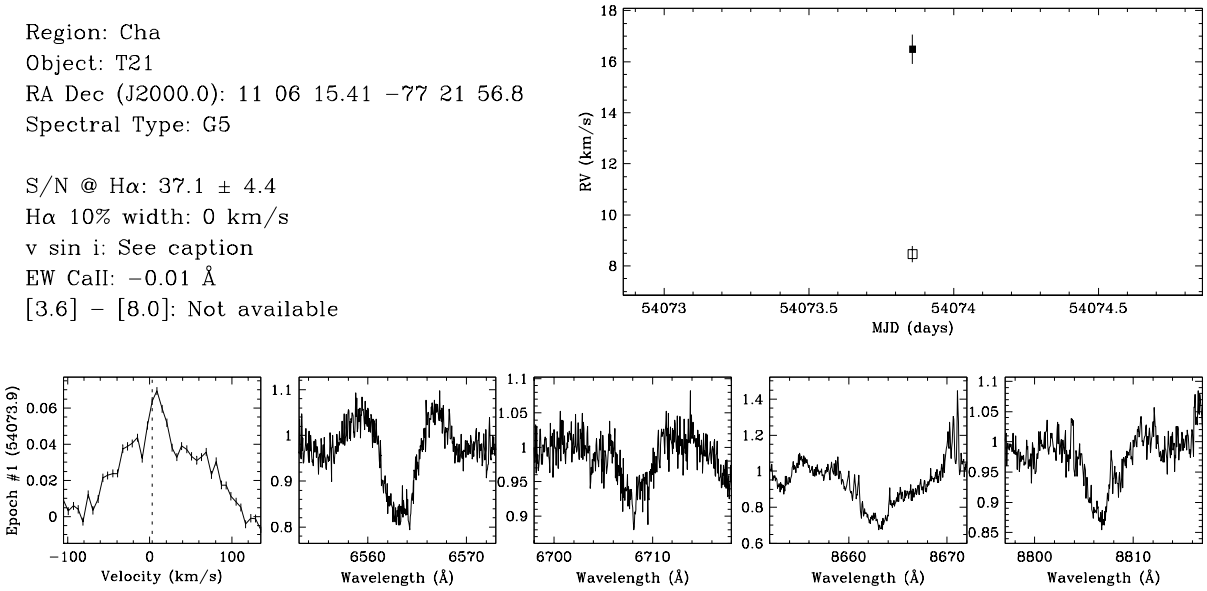

Figure 4.22 T21 is a long-period SB2. Two sources can be seen in the line profile: a strong peak and a shallower broad feature. By fitting the line profile to two rotational broadening functions, we estimate the two sources have a flux ratio of 0.101 ± 0.005, and the A and B sources have v sin i of 94.1 ± 0.7 km s^{-1} and 14.5 ± 0.3 km s^{-1}, respectively. This target has been previously reported by Lafrenière et al. (2008) to have a resolved companion with a separation of ∼0.″14 (∼20 AU) at a position angle of ∼126.°1, and an R-band flux ratio of ∼0.08 ($\Delta K \sim 2.16$). This flux ratio is similar to that estimated between the SB2 components. Furthermore, the resolved companion has an expected circular orbital speed of ∼13 km s^{-1} which is compatible with the radial velocity separations of the SB2 components star if we consider the large uncertainties due to rapid rotation. Therefore, the resolved companion is likely the SB2 secondary star.

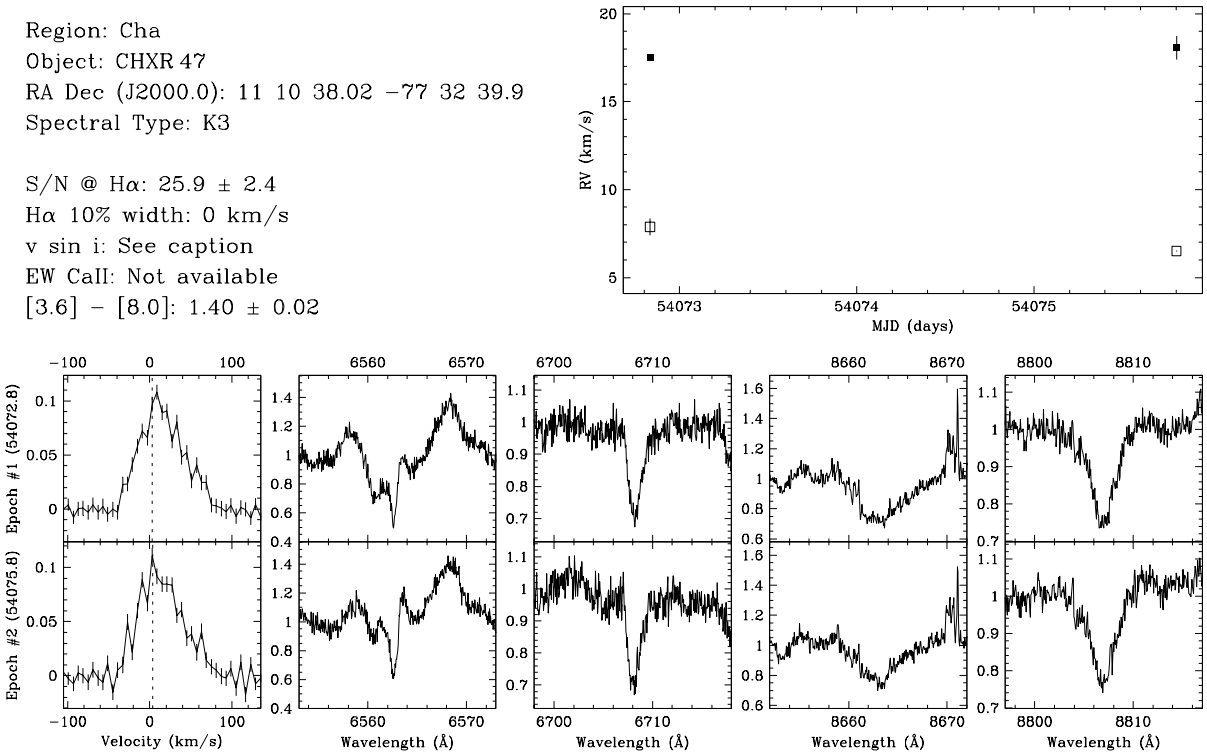

Figure 4.23 CHXR 47 is a long-period SB2. By fitting the line profile to two rotational broadening functions, we estimate the two sources have a flux ratio of 0.24 ± 0.06, and the A and B sources have $v \sin i$ of 59.5 ± 0.4 km s^{-1} and 24 ± 3 km s^{-1}, respectively. This target has been previously reported by Lafrenière et al. (2008) to have a resolved companion with a separation of ∼0.″175 (∼25 AU) at a position angle of ∼334.°8, and an R-band flux ratio of ∼0.49 ($\Delta K \sim 0.47$). This flux ratio is comparable to that estimated between the SB2 components. Furthermore, the resolved companion has an expected circular orbital speed of ∼8 km s^{-1} which is compatible with the estimated radial velocity separations of the SB2 component stars. Therefore, the resolved companion is likely the SB2 secondary star.

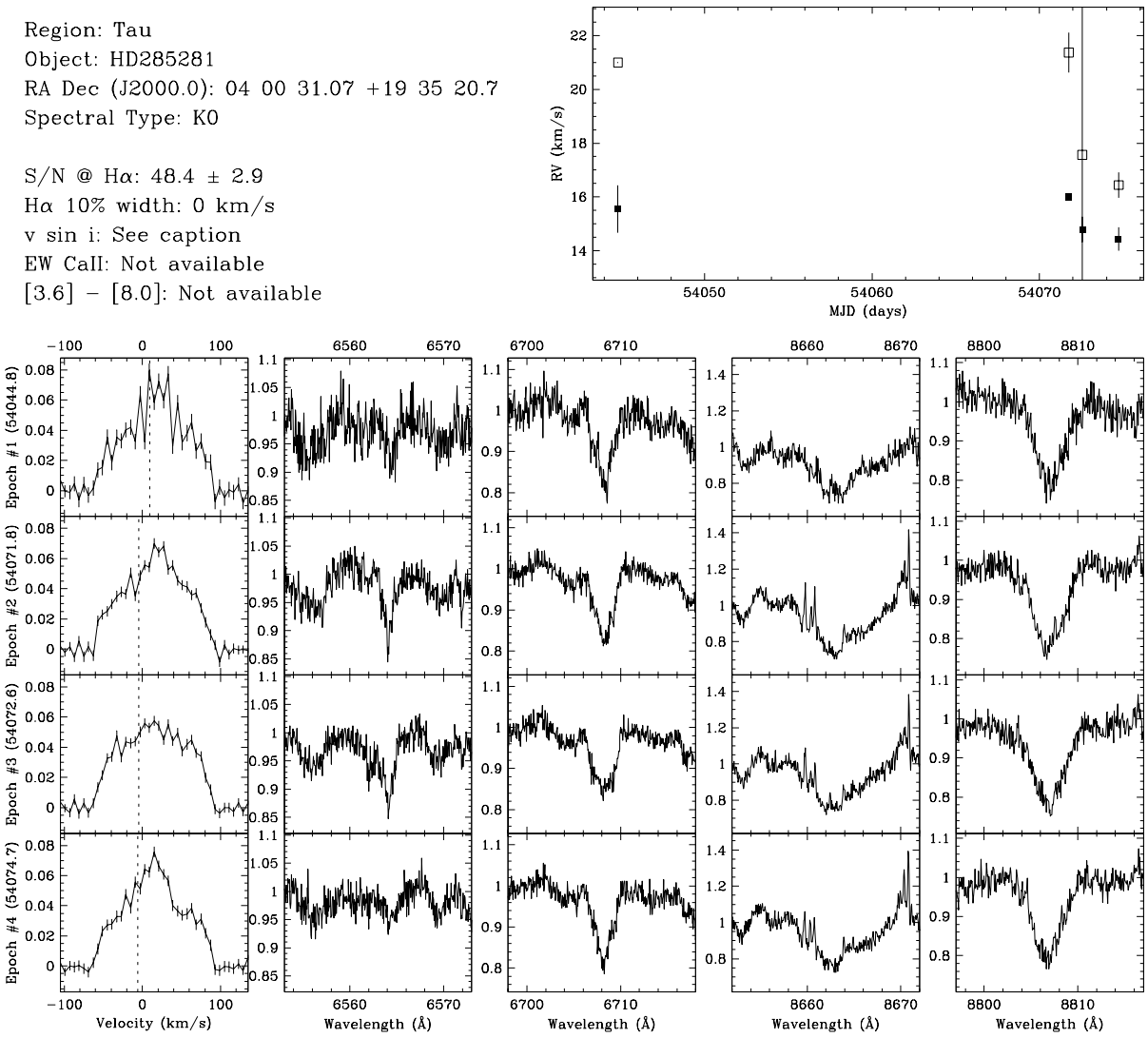

Figure 4.24 HD285281 is a long-period SB2. Two sources can be seen in the profile: a peak (at $\sim 20\,\mathrm{km\,s^{-1}}$) on top of a broad feature. By fitting the line profile to two rotational broadening functions, we estimate the two sources have a flux ratio of 0.07 ± 0.05, and the A and B sources have $v \sin i$ of 78.0 ± 0.3 km s^{-1} and 17.0 ± 1.9 km s^{-1}, respectively. The radial velocity estimates for epoch #3 are inaccurate because the fitting routine could not delineate the two individual profiles. This target has been previously reported by Köhler & Leinert (1998) to have a resolved companion with a separation of $\sim 0\farcs773$ (~ 110 AU) at a position angle of $\sim 190\fdg7$, and an R-band flux ratio of ~ 0.21 ($\Delta K \sim 1.23$). This flux ratio is comparable to that estimated between the SB2 components. Furthermore, the resolved companion has an expected circular orbital speed of $\sim 5\,\mathrm{km\,s^{-1}}$ which is consistent with the radial velocity separations of the SB2 component stars. Therefore, the resolved companion is likely the SB2 secondary star.

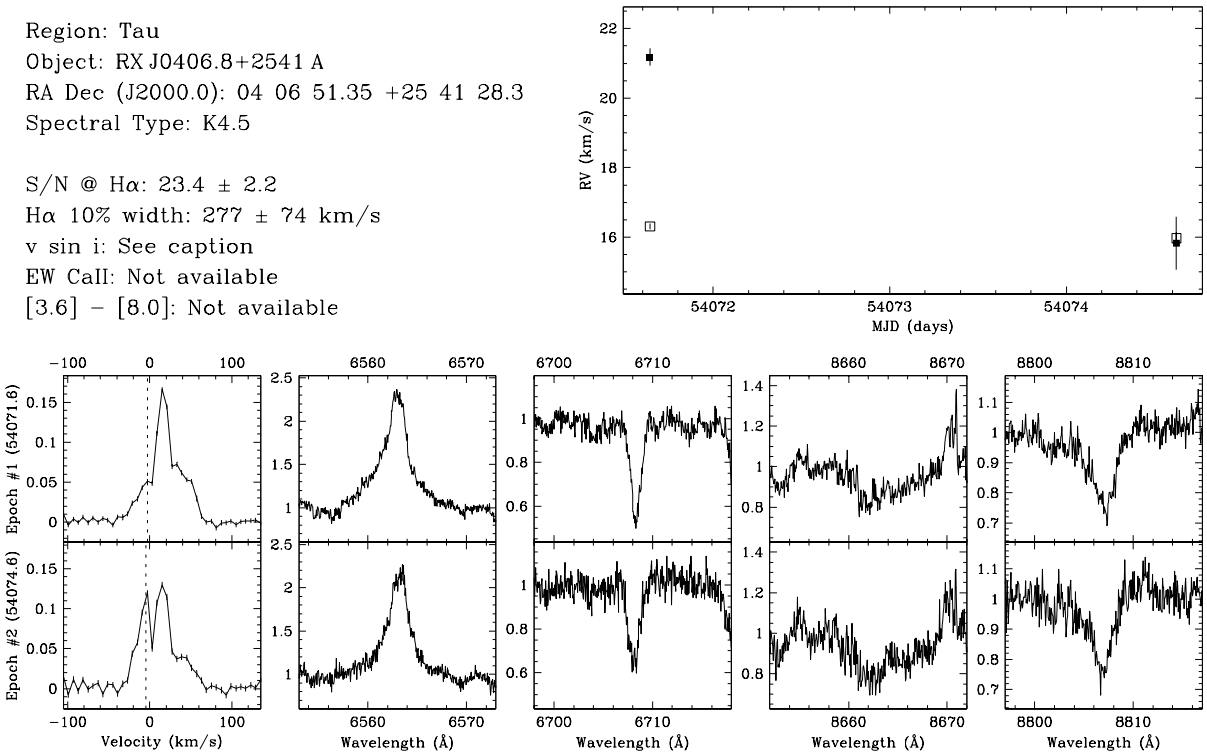

Figure 4.25 RX J0406.8+2541 A is a long-period SB2. Two sources can be seen in the line profile: a strong peak and a shallower broad feature. By fitting the line profile to two rotational broadening functions, we estimate the two sources have a flux ratio of 0.32 ± 0.07, and the a and b sources have $v \sin i$ of 47 ± 4 km s^{-1} and 9.8 ± 0.3 km s^{-1}, respectively. For epoch #2, the strong peak in the line profile at the observer's rest frame is due to moonlight, and biased the radial velocity estimates in the fits. This target has been previously reported by Köhler & Leinert (1998) to have a resolved companion (RX J0406.8+2541 B) with a separation of $\sim 0\farcs977$ (~ 140 AU) at a position angle of $\sim 12\fdg3$, and an R-band flux ratio of ~ 0.95 ($\Delta K \sim 0.04$). This flux ratio is comparable to that estimated between the SB2 components if one accounts for the diminished light from the companion at that distance from the slit. Furthermore, the resolved companion has an expected circular orbital speed of ~ 3 km s^{-1} which is similar to the radial velocity separations of the SB2 component stars. Furthermore, the radial velocity estimates of the SB2 secondary star is consistent with that of RX J0406.8+2541 B. Therefore, the resolved companion is likely the SB2 secondary star.

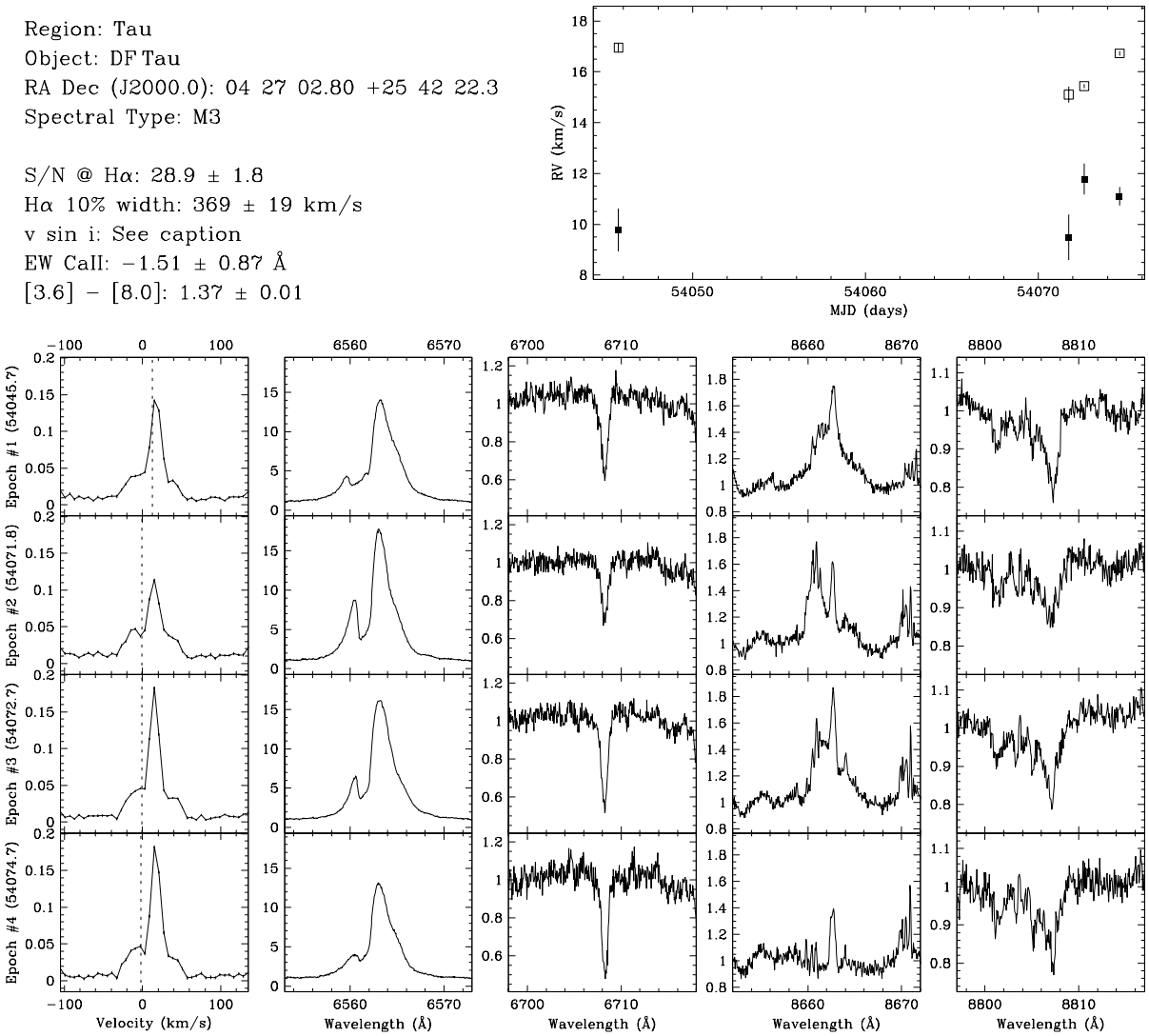

Figure 4.26 DF Tau is a long-period SB2. Two sources can be seen in the line profile: a strong peak and a shallower broad feature. By fitting the line profile to two rotational broadening functions, we estimate the two sources have a flux ratio of 0.49 ± 0.11, and the A and B sources have $v \sin i$ of 46.6 ± 1.8 km s^{-1} and 9.8 ± 0.6 km s^{-1}, respectively. This target has been previously reported by Ghez et al. (1993), Simon et al. (1995), and Ghez et al. (1997b) as a resolved binary (DF Tau A+B) with a separation of 0.″0871–0.″088 (∼12 AU) at a position angle of 301.°2–329°, and an R-band flux ratio of 0.05–0.24 ($\Delta K \sim 0.41$–0.90). This flux ratio is comparable to that estimated between the SB2 components with we consider the uncertainties in the models. Furthermore, the resolved secondary star has an expected circular orbital speed of ∼5 km s^{-1} which is consistent with the radial velocity separations of the SB2 component stars. Therefore, the resolved secondary star is likely the SB2 secondary star.

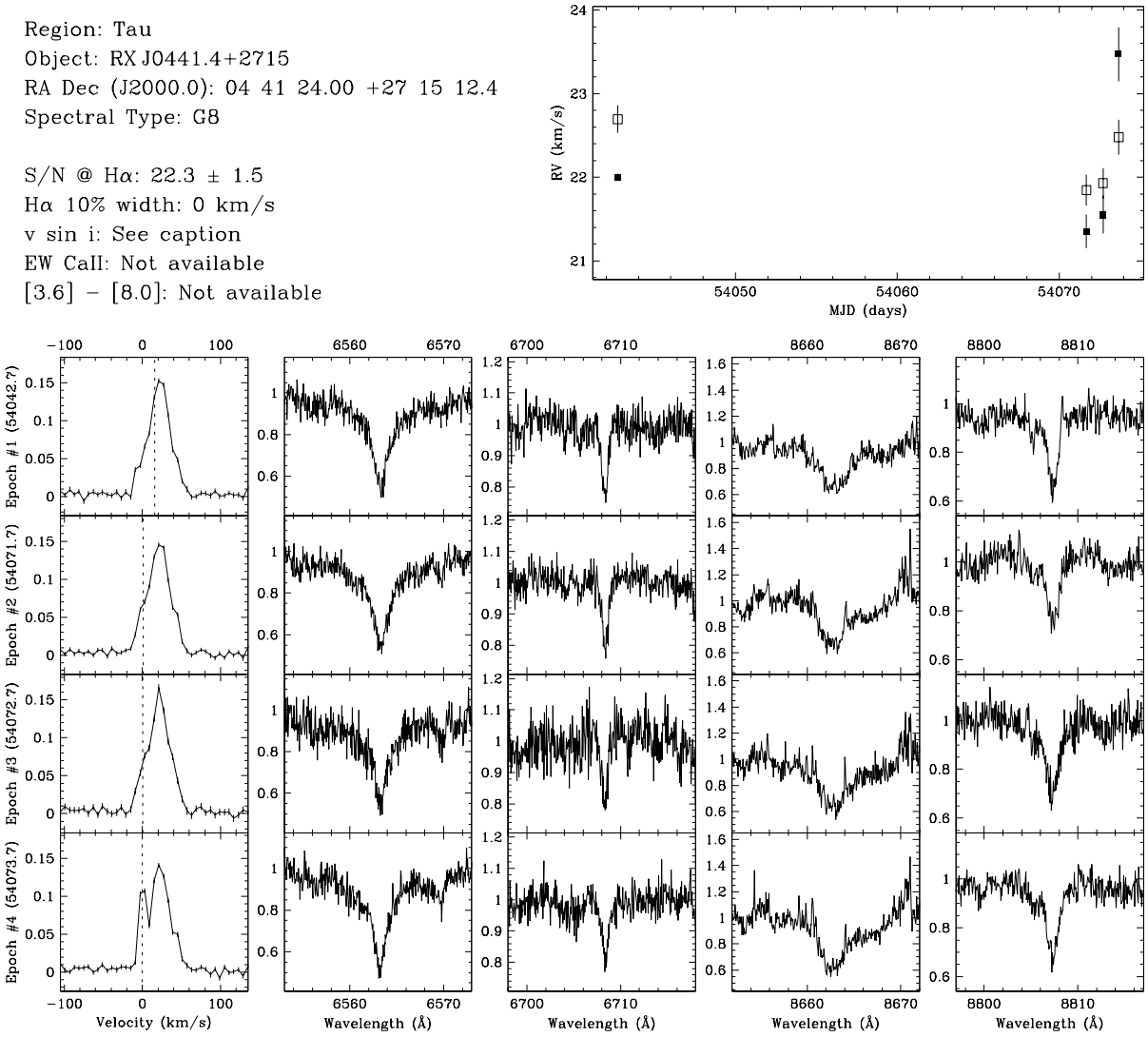

Figure 4.27 RX J0441.4+2715 is a long-period SB2. Two sources can be seen in the line profile: a strong peak and a shallower broad feature. By fitting the line profile to two rotational broadening functions, we estimate the two sources have a flux ratio of 0.32 ± 0.07, and the A and B sources have $v \sin i$ of $37.0 \pm 0.6\,\mathrm{km\,s^{-1}}$ and $12.6 \pm 1.5\,\mathrm{km\,s^{-1}}$, respectively. The overall radial velocity deviates from that of the star forming region. However, cluster membership is supported by Li-λ6708 absorption. For epoch #4, the sharp peak in the line profile at the observer's rest frame is due to moonlight, and biased the radial velocity estimates in the fits. This target has been previously reported by Köhler & Leinert (1998) to have a resolved companion with a separation of $\sim 0\farcs065$ ($\sim 9.1\,\mathrm{AU}$) at a position angle of $\sim 216°$, and an R-band flux ratio of ~ 0.49 ($\Delta K \sim 0.63$). This flux ratio is comparable to that estimated between the SB2 components. Furthermore, the resolved companion has an expected circular orbital speed of $\sim 21\,\mathrm{km\,s^{-1}}$ which is consistent with the radial velocity separations of the SB2 component stars. Therefore, the resolved companion is likely the SB2 secondary star.

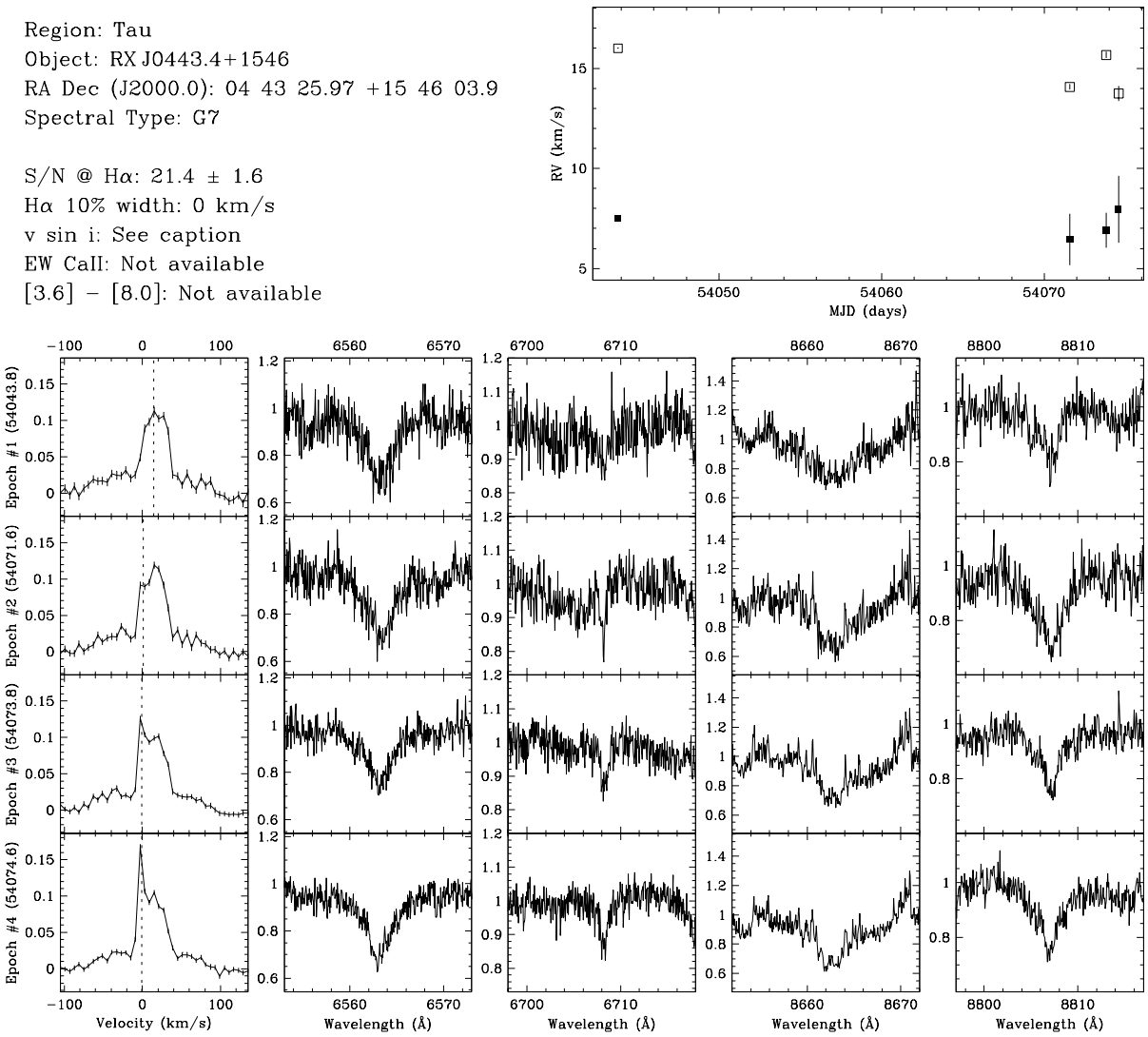

Figure 4.28 RX J0443.4+1546 is a long-period SB2. Two sources can be seen in the line profile: a strong peak and a shallower broad feature. By fitting the line profile to two rotational broadening functions, we estimate the two sources have a flux ratio of 0.83 ± 0.10, and the A and B sources have $v \sin i$ of 86.5 ± 1.6 km s^{-1} and 24.0 ± 0.8 km s^{-1}, respectively. For epochs #3 and #4, the peaks in the line profile at the observer's rest frame are due to moonlight, and have been accounted for in the radial velocity estimates. This target has been previously reported by Köhler & Leinert (1998) to have no resolved companions.

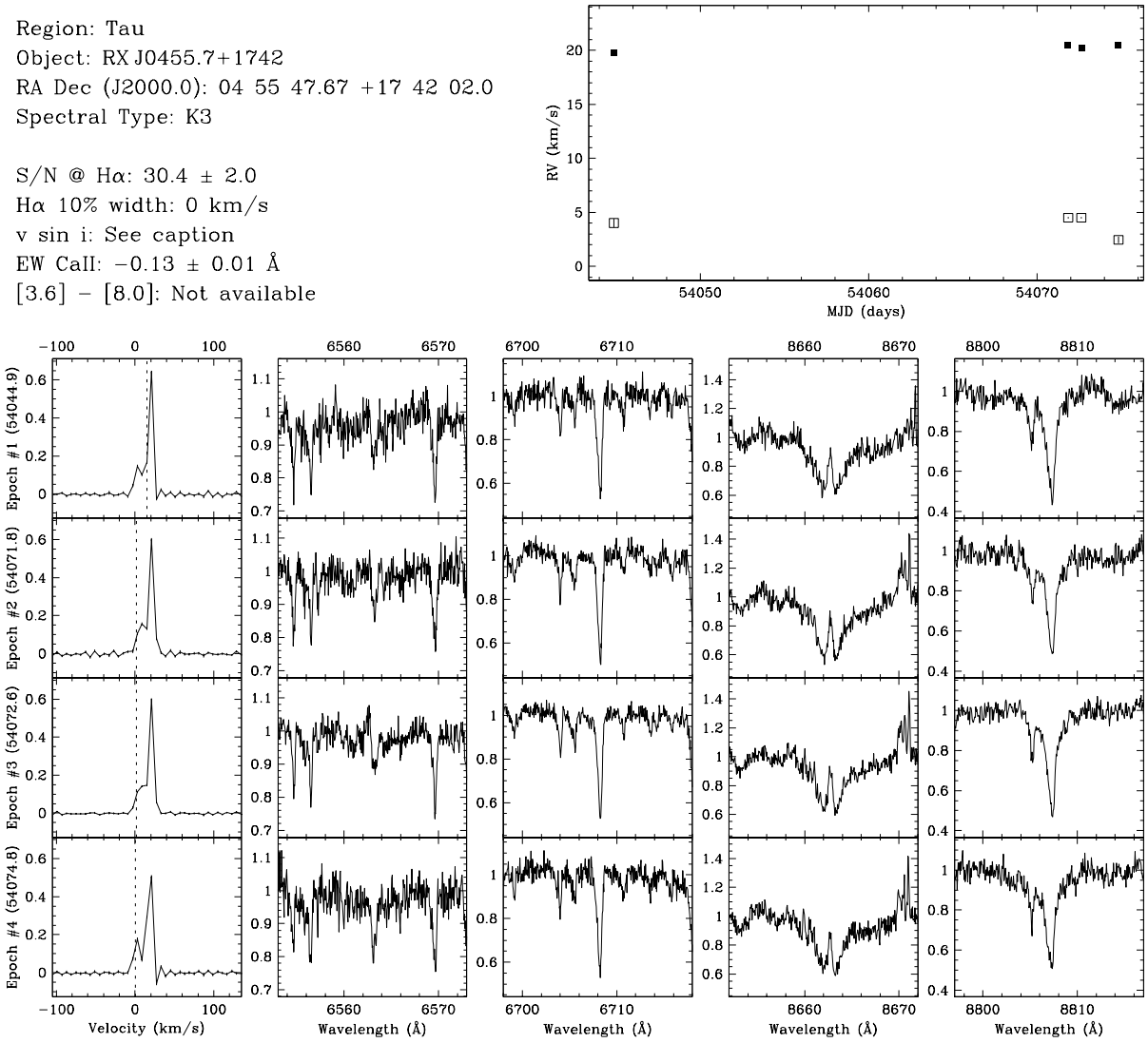

Figure 4.29 RX J0455.7+1742 is a long-period SB2. By fitting the line profile to two rotational broadening functions, we estimate the two sources have a flux ratio of 0.337 ± 0.014, and the A and B sources have $v \sin i$ of 8 ± 2 km s^{-1} and 9.5 ± 0.4 km s^{-1}, respectively. For epoch #4, the small peak in the line profile at the observer's rest frame has contribution from moonlight, and may have biased the radial velocity estimate toward the observer's rest frame. This target has been previously reported by Köhler & Leinert (1998) to have a resolved companion with a separation of ∼ 0.″093 (∼ 13 AU) at a position angle of ∼ 254.°6, and an R-band flux ratio of ∼ 0.53 ($\Delta K \sim 0.41$). This flux ratio is similar to that estimated between the SB2 components. Furthermore, the resolved companion has an expected circular orbital speed of ∼ 11 km s^{-1} which is comparable with the radial velocity separation of the SB2 component stars if we consider the large uncertainties due to rapid rotation. Therefore, the resolved companion is likely the SB2 secondary star.

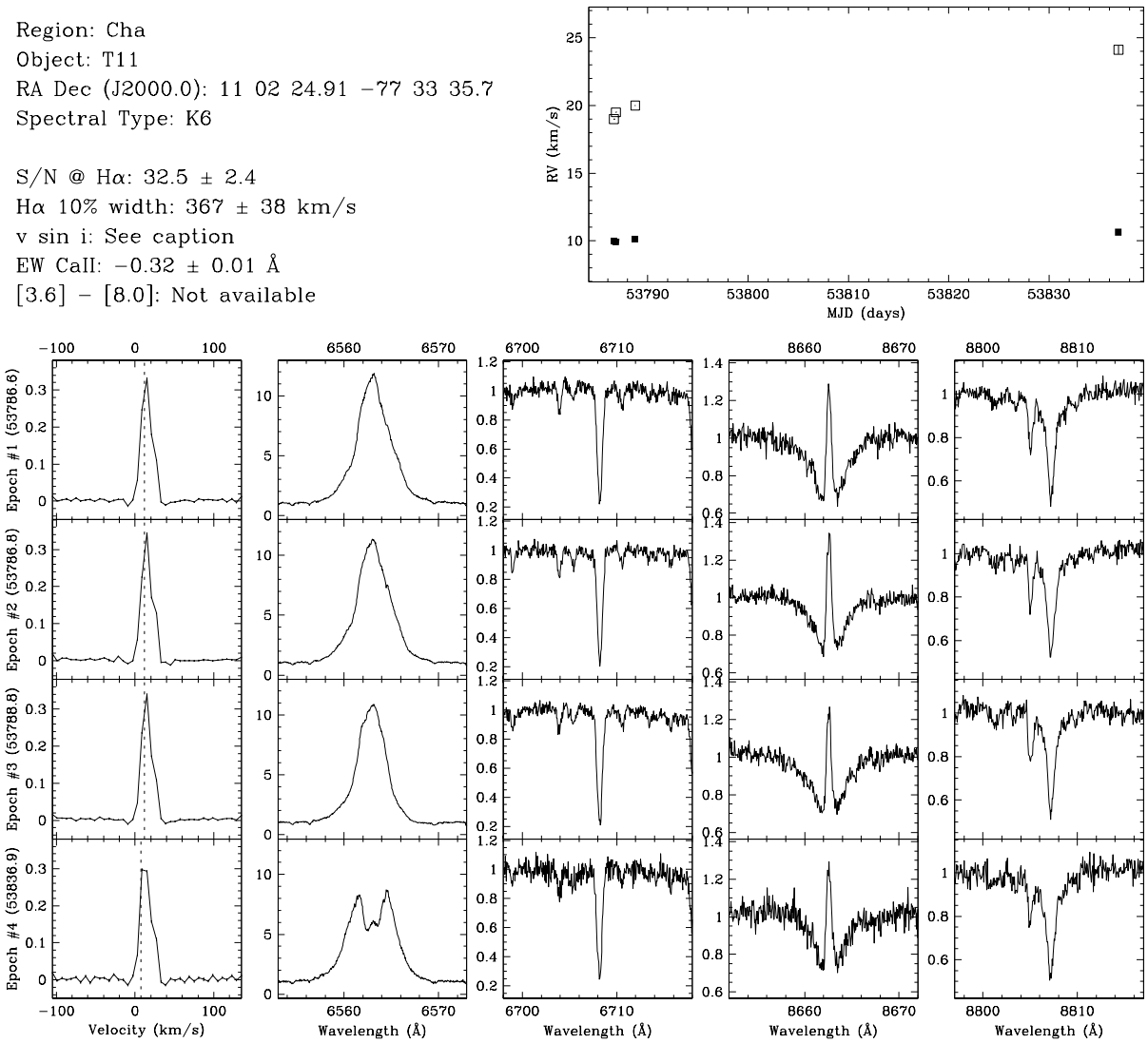

Figure 4.30 T11 is a suspected SB2. The line profile is unusually asymmetrical, and has both a strong peak and a shallower slightly broader feature. If star spots are responsible for the asymmetries in the line profile, based on observed $v \sin i$ ($\sim 14\,\mathrm{km\,s^{-1}}$) and model stellar radius ($\sim 1.4\,R_{\odot}$), one would expect variations on a maximum timescale of ~ 5.1 days. From the constant line profiles of the first observing run (epochs #1, #2 and #3) which span 2.2 days, it is unlikely that the line profile irregularities are the result of star spots. By fitting the line profile to two rotational broadening functions, we estimate the two sources have a flux ratio of 1.0 ± 0.4, and the A and B sources have $v \sin i$ of 11.2 ± 0.3 km s^{-1} and 13.0 ± 0.3 km s^{-1}, respectively. This target has been previously reported by Lafrenière et al. (2008) to have no resolved companions.

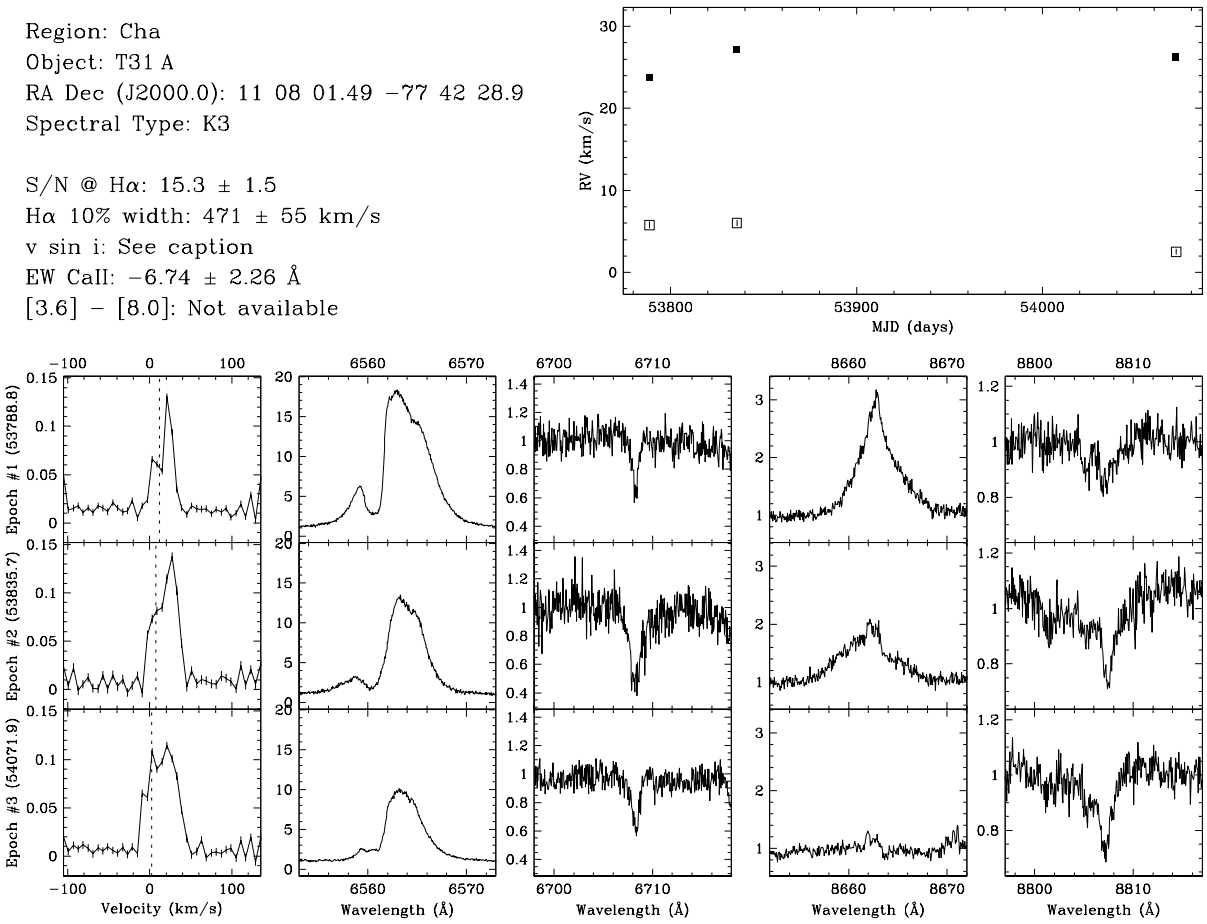

Figure 4.31 T31 A is a suspected SB2. Two sources can be seen in the profile: a peak at $\sim 25\,\mathrm{km\,s^{-1}}$ and another peak at $\sim 5\,\mathrm{km\,s^{-1}}$. By fitting the line profile to two rotational broadening functions, we estimate the two sources have a flux ratio of 0.7 ± 0.3, and the a and b sources have $v \sin i$ of 13 ± 2 km s^{-1} and 13 ± 3 km s^{-1}, respectively. This target has been previously reported by Lafrenière et al. (2008) to have a resolved companion with a separation of $\sim 0\farcs652$ (~ 91 AU) at a position angle of $\sim 178\fdg7$, and an R-band flux ratio of ~ 0.03 ($\Delta K \sim 1.74$). Given the flux ratio, the expected contribution to the line profile from the resolved companion is negligible. The companion was resolved in the guide camera during good seeing conditions and was indeed faint, so it cannot have contributed to the profile.

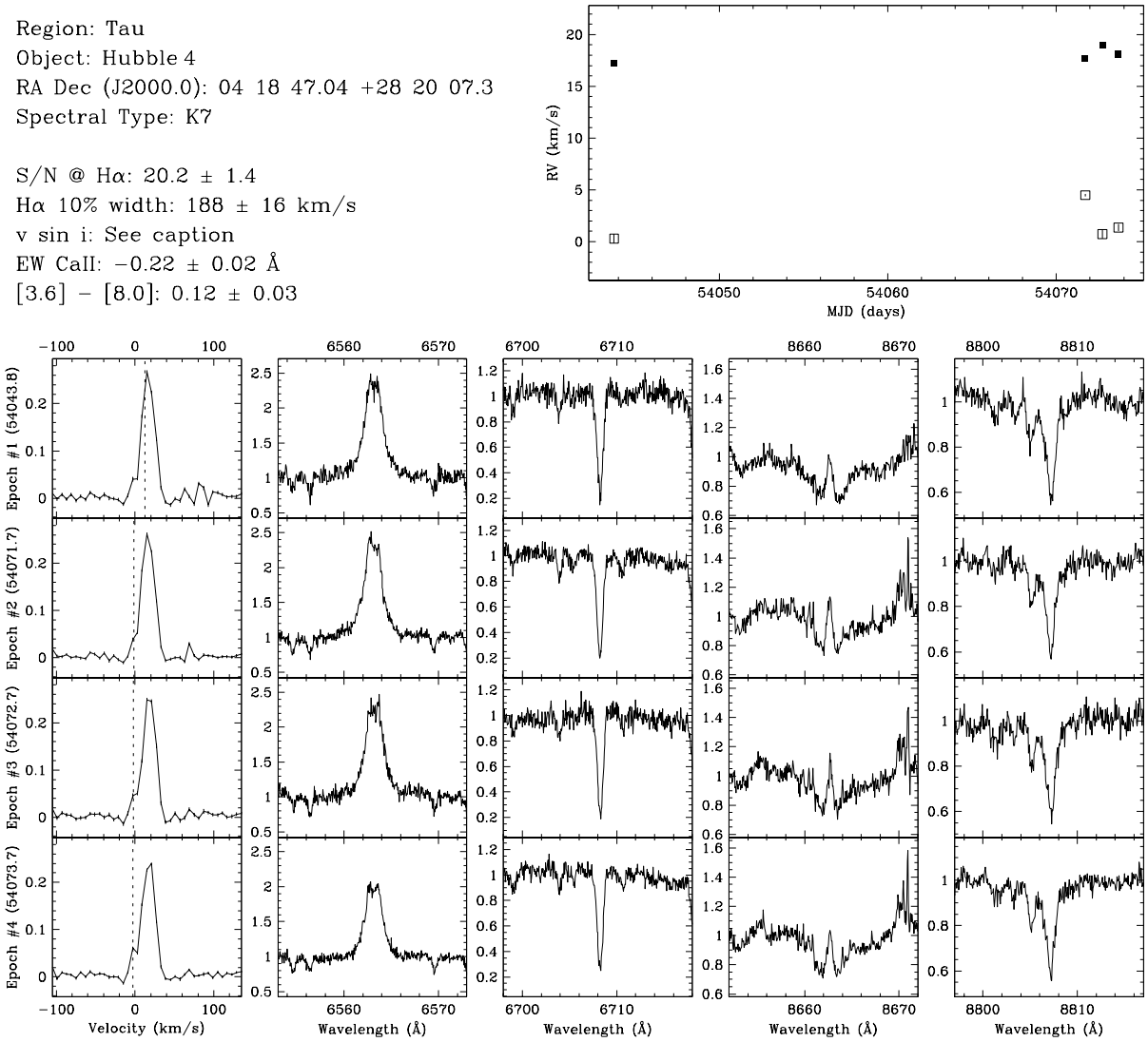

Figure 4.32 Hubble 4 is a suspected SB2. If star spots are responsible for the asymmetries in the line profile, based on observed $v \sin i$ ($\sim 16\,\mathrm{km\,s^{-1}}$) and model stellar radius ($\sim 1.4\,R_\odot$), one would expect variations on a maximum timescale of ~ 4.3 days. From the constant line profiles of the second observing run (epochs #2, #3 and #4) which span 2.0 days, it is unlikely that the line profile irregularities are the result of star spots. By fitting the line profile to two rotational broadening functions, we estimate the two sources have a flux ratio of 0.20 ± 0.05, and the A and B sources have $v \sin i$ of 12.1 ± 0.3 km s^{-1} and 13.1 ± 1.9 km s^{-1}, respectively. This target has been previously reported by Leinert et al. (1993), and Ghez et al. (1993) to have no resolved companions.

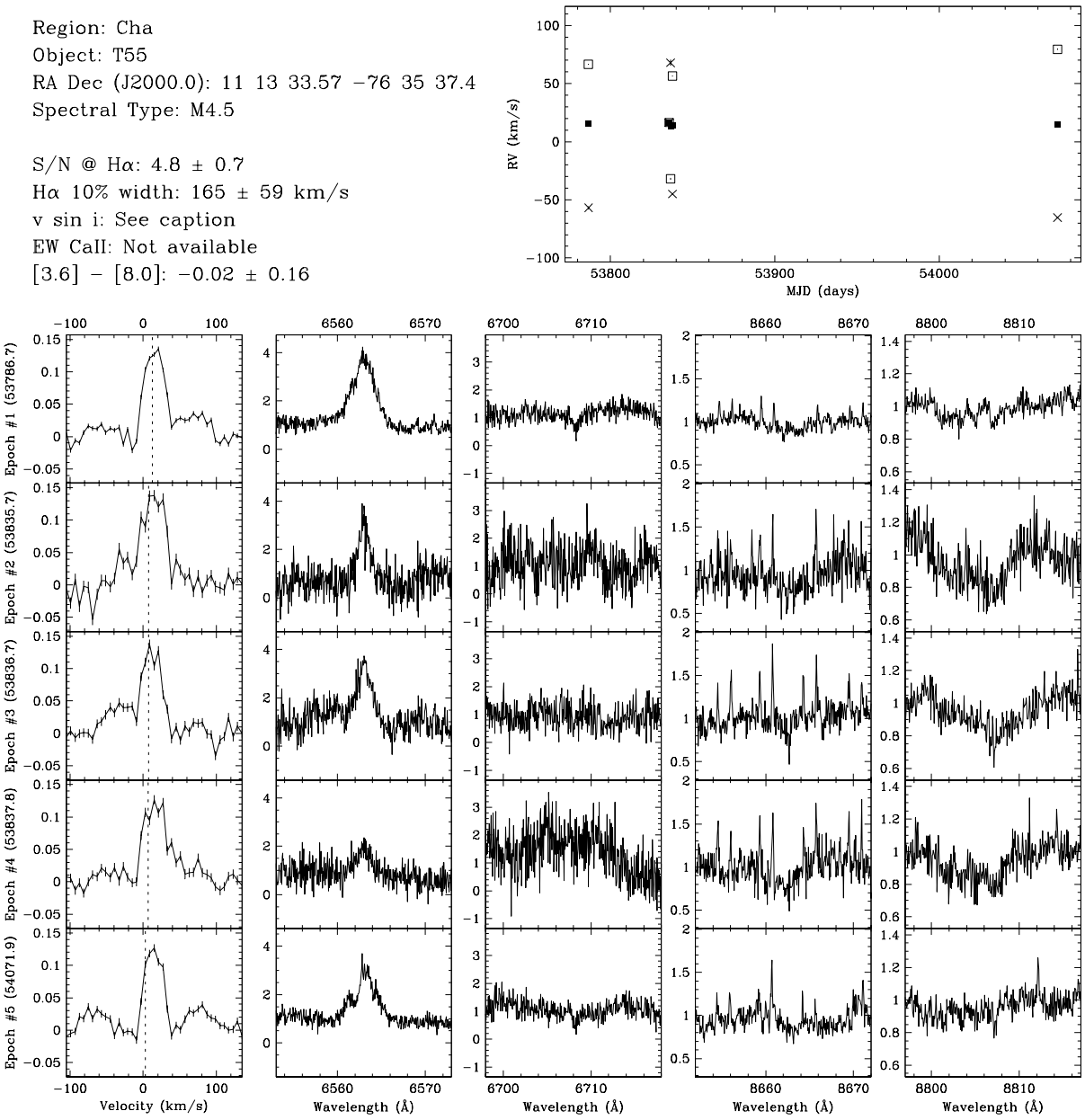

Figure 4.33 T55 is an SB3. The two fainter sources show large accelerations while the radial velocity of the brighter source is stable. This suggests a triple system comprised of a close binary in orbit with a farther away more massive star. By fitting the line profile fits to three rotational broadening functions, we estimate the sources have an A–B flux ratio of 0.38 ± 0.08, an A–C flux ratio of 0.19 ± 0.08, and the A, B and C sources have $v \sin i$ of $23 \pm 2\,\mathrm{km\ s^{-1}}$, $34 \pm 4\,\mathrm{km\ s^{-1}}$ and $31.0 \pm 1.6\,\mathrm{km\ s^{-1}}$, respectively. The narrow emission lines in the spectra near 8662 Å are from the night sky. This target has been previously reported by Lafrenière et al. (2008) to have no resolved companions.

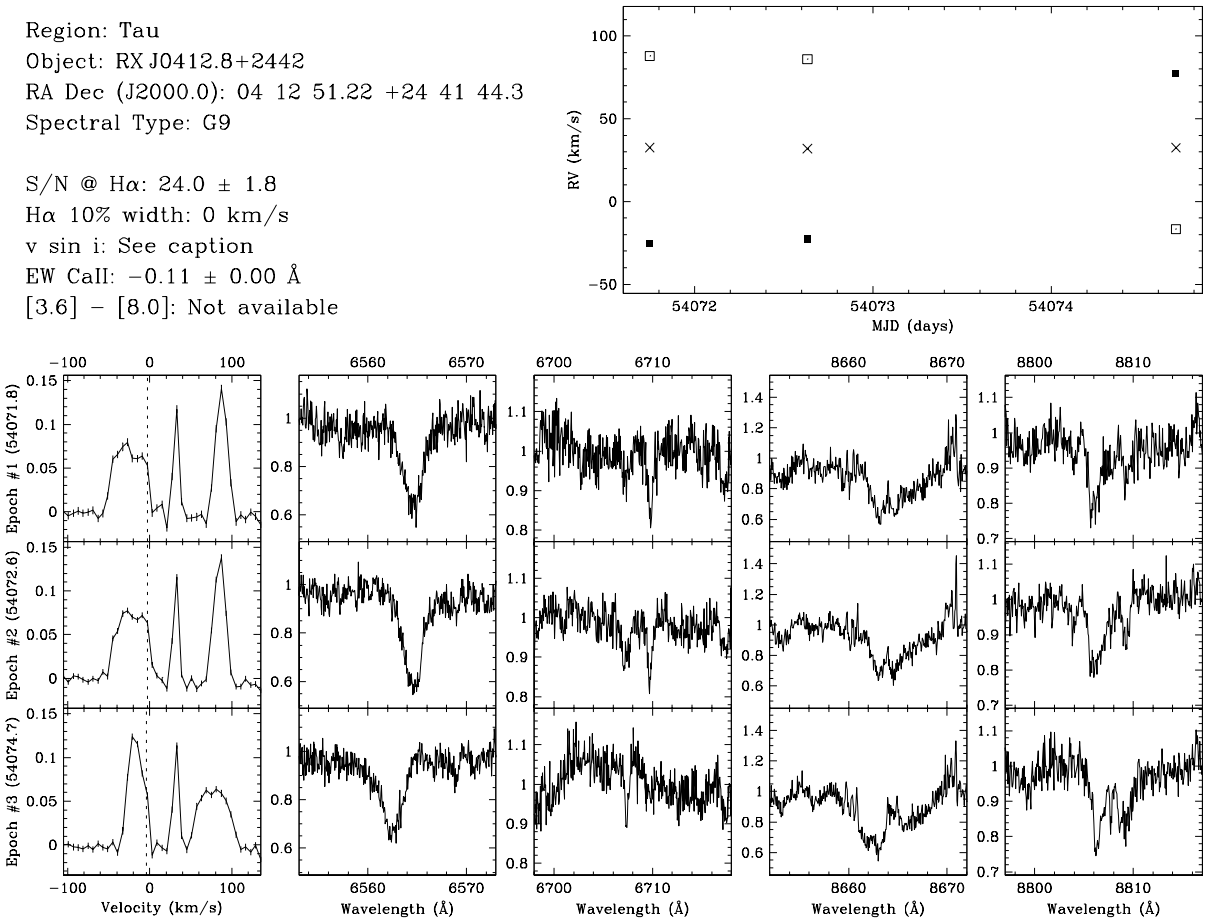

Figure 4.34 RX J0412.8+2442 is an SB3. The two of the sources show rapid radial acceleration. The radial velocity stable source has much less flux, and is likely a relatively farther away lower-mass companion. By fitting the line profile fits to three rotational broadening functions, we estimate the sources have an A–B flux ratio of 0.88 ± 0.12, an A–C flux ratio of 0.36 ± 0.04, and the A, B and C sources have v sin i of 28.50 ± 0.12 km s^{-1}, 15.1 ± 1.5 km s^{-1} and 7.4 ± 0.3 km s^{-1}, respectively. This target has been previously reported by Köhler & Leinert (1998) to have no resolved companions.

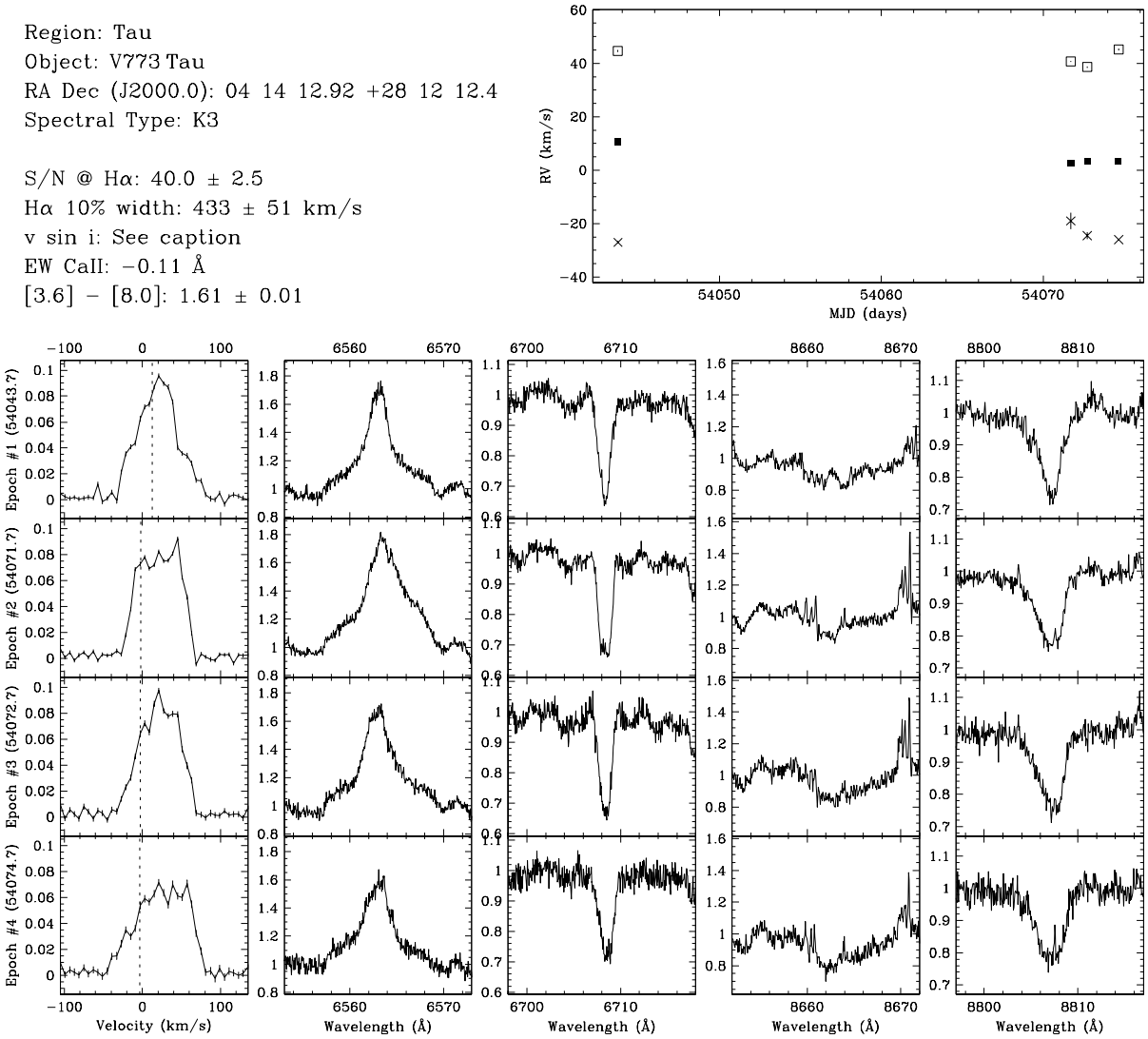

Figure 4.35 V773 Tau is an SB3. The line profile appears to consist of three sources that fluctuate over time. By fitting the line profile fits to three rotational broadening functions, we estimate the sources have an A–B flux ratio of 1.0 ± 0.3, an A–C flux ratio of 0.09 ± 0.06, and the A, B and C sources have $v \sin i$ of 27 ± 4 km s^{-1}, 28 ± 4 km s^{-1} and 21 ± 7 km s^{-1}, respectively. This target has been previously reported by Duchêne et al. (2003), and Woitas (2003) as a quadruple system consisting of a spectroscopic binary (V773 Tau Aa,Ab) with a period of ∼51 days and two wide companions (V773 Tau B,C) with an A–B and A–C separations of ∼0.″1 (∼14 AU) and ∼0.″2 (∼28 AU) with an A–B $\Delta K \sim 0.33 - -2.22$ and an A–C $\Delta K \sim 1.84 - -2.85$.

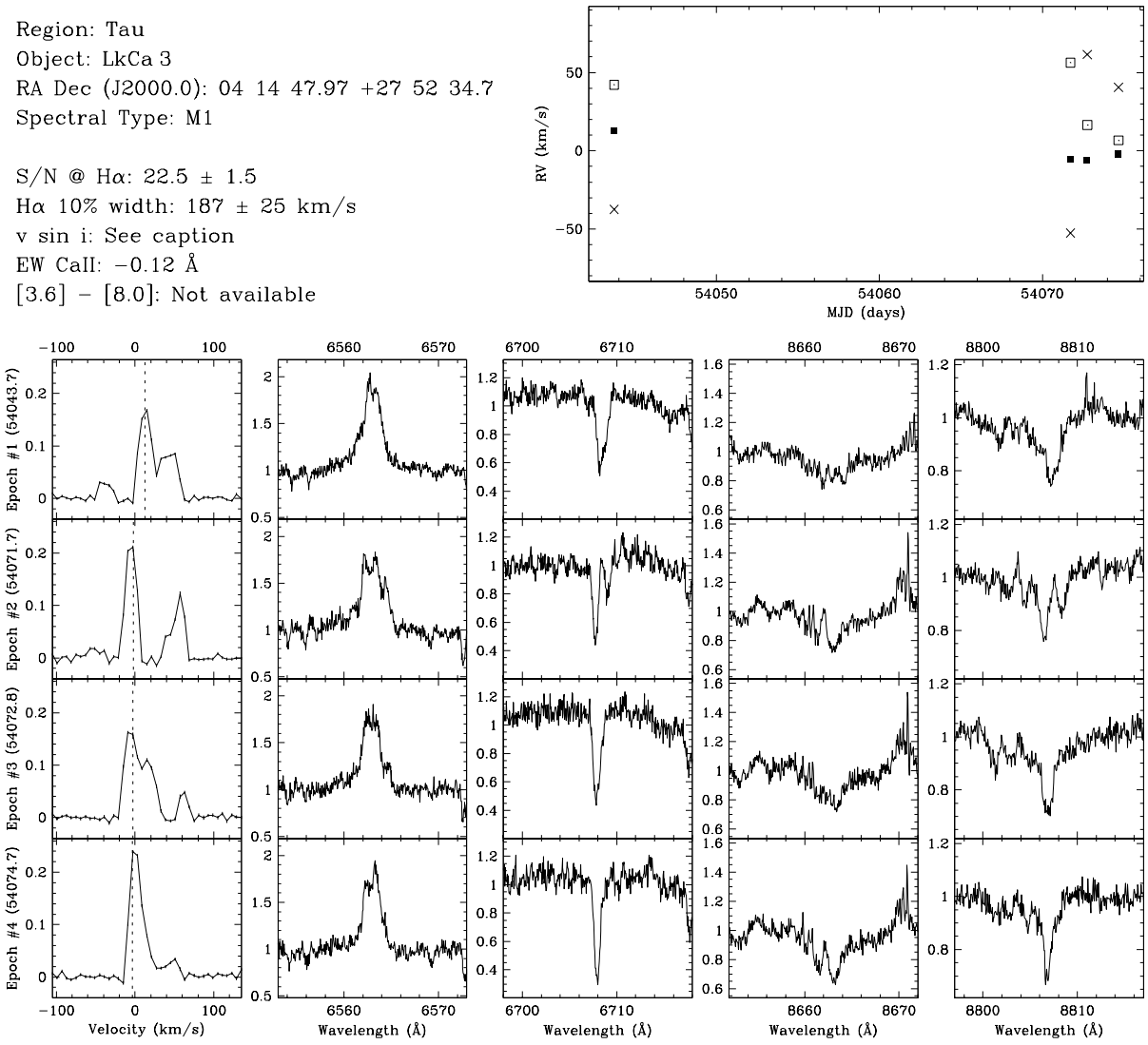

Figure 4.36 LkCa 3 is an SB3. The three sources also show radial acceleration and are very close companions. Therefore, the companions are not likely to be the previously resolved companion. By fitting the line profile fits to three rotational broadening functions, we estimate the sources have an Aa–Ab1 flux ratio of 0.75 ± 0.13, an Aa–Ab2 flux ratio of 0.21 ± 0.05, and the Aa, Ab1 and Ab2 sources have $v \sin i$ of 12.0 ± 1.0 km s^{-1}, 16 ± 2 km s^{-1} and 14 ± 4 km s^{-1}, respectively. This target has been previously reported by Leinert et al. (1993), and Ghez et al. (1993) to have a resolved companion with a separation of 0.″47–0.″491 (66–69 AU) at a position angle of 77°–78°, and an R-band flux ratio of 0.47–0.92 ($\Delta K \sim$ 0.05–0.42). However, there is no clear evidence in the line profile of the resolved companion. Since the resolved companion has an expected circular orbital speed of $\sim$3 km s^{-1}, another profile could be obscured if the central star and the resolved companion have similar projected rotational velocities. Therefore, the system is possibly a quadruple system consisting of a spectroscopic binary in orbit with another spectroscopic companion and a resolved companion.

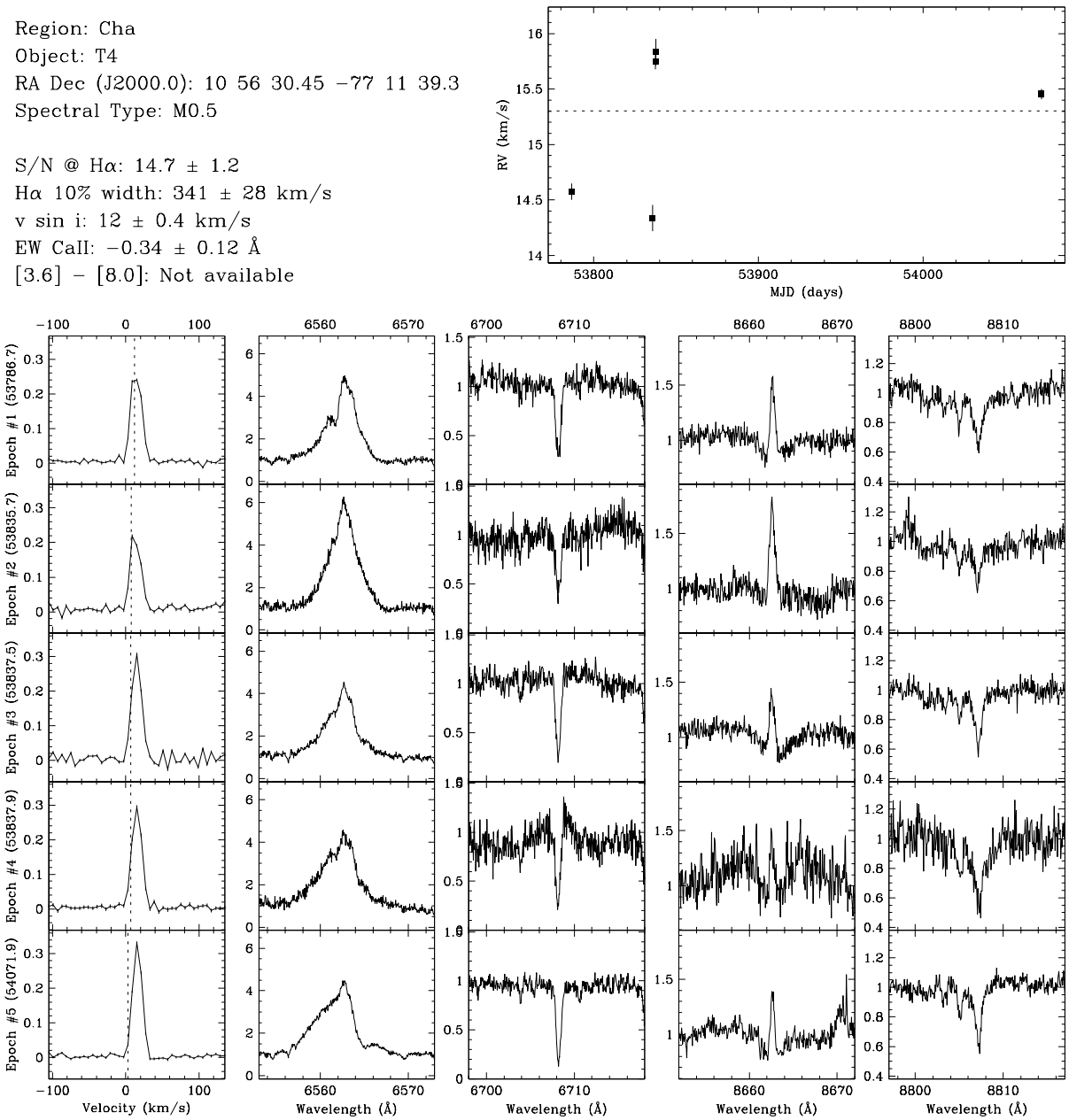

Figure 4.37 T4 shows no clear evidence of a close companion. The star has a single-line profile, and a radial velocity scatter not significant relative to variations observed within each observing run. The radial velocity scatter within the second observing run (epochs #2, #3 and #4) is consistent with that expected from systematic line profile variations, e.g. from star spots rotating with the star. This target has been previously reported by Lafrenière et al. (2008) to have no resolved companions.

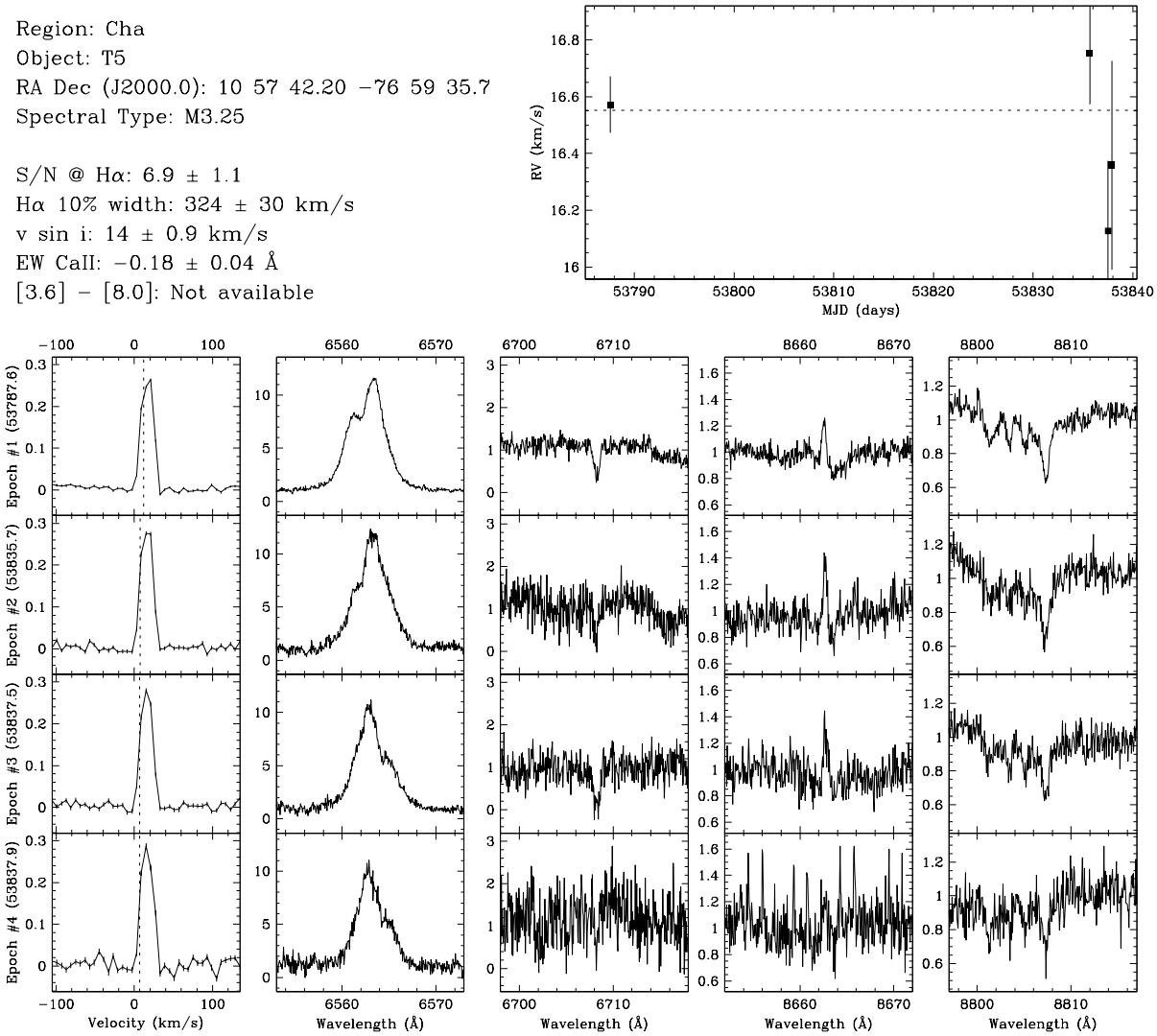

Figure 4.38 T5 shows no evidence of a close companion. The star has a single-line profile, and the radial velocity scatter is not significant relative to the measurement uncertainties. For epoch #4, the narrow emission lines in the spectrum near 8662 Å are from the night sky. This target has been previously reported by Lafrenière et al. (2008) to have a resolved companion with a separation of $\sim$0.″159 ($\sim$22 AU) at a position angle of $\sim$342.°9, and an R-band flux ratio of $\sim$0.87 ($\Delta K \sim 0.05$). However, there is no clear evidence in the line profile of the resolved companion. Since the resolved companion has an expected circular orbital speed of $\sim 4\,\mathrm{km\,s^{-1}}$, a second profile could be obscured if the primary star and the resolved companion have similar projected rotational velocities.

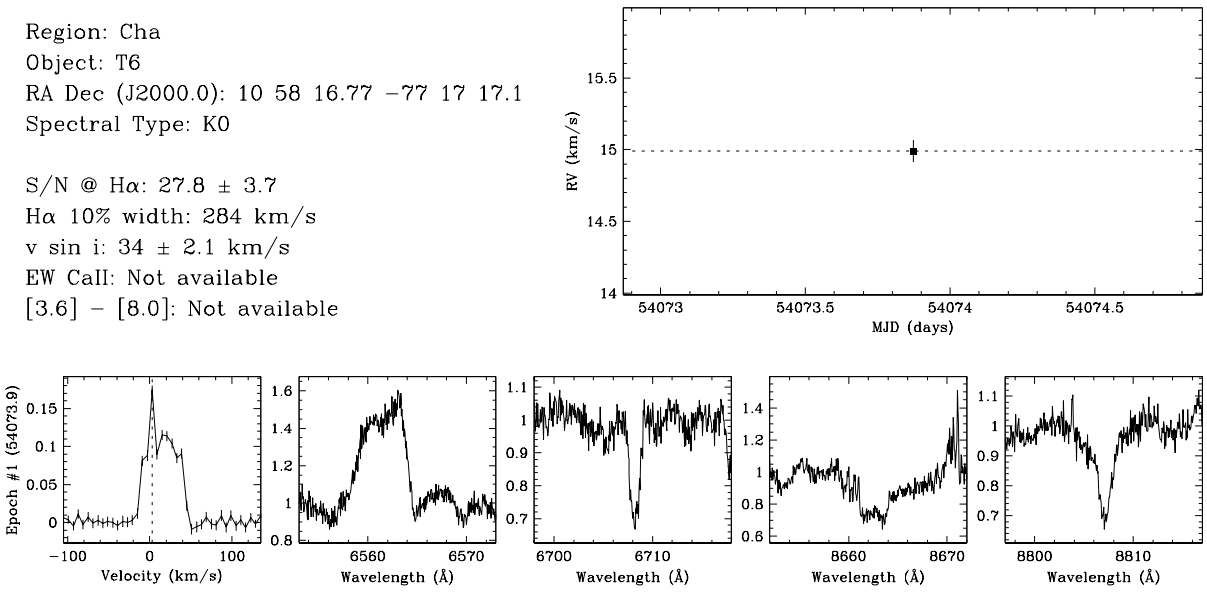

Figure 4.39 T6 has a single-line profile, and is therefore not an SB2. The radial velocity scatter cannot be determined because the target was observed for a single epoch. Hence, it is undetermined if the target is an SB1 or a single star. The strong peak in the line profile at the observer's rest frame is due to dawn twilight, and may have biased the radial velocity estimates toward the observer's rest frame. This target has been previously reported by Lafrenière et al. (2008) to have a resolved companion with a separation of $\sim 5\farcs122$ (~ 720 AU) at a position angle of $\sim 122\fdg9$, and an R-band flux ratio of $\lesssim 0.01$ ($\Delta K \sim 3.79$). Given the flux ratio and separation, the expected contribution to the line profile from the resolved companion is negligible.

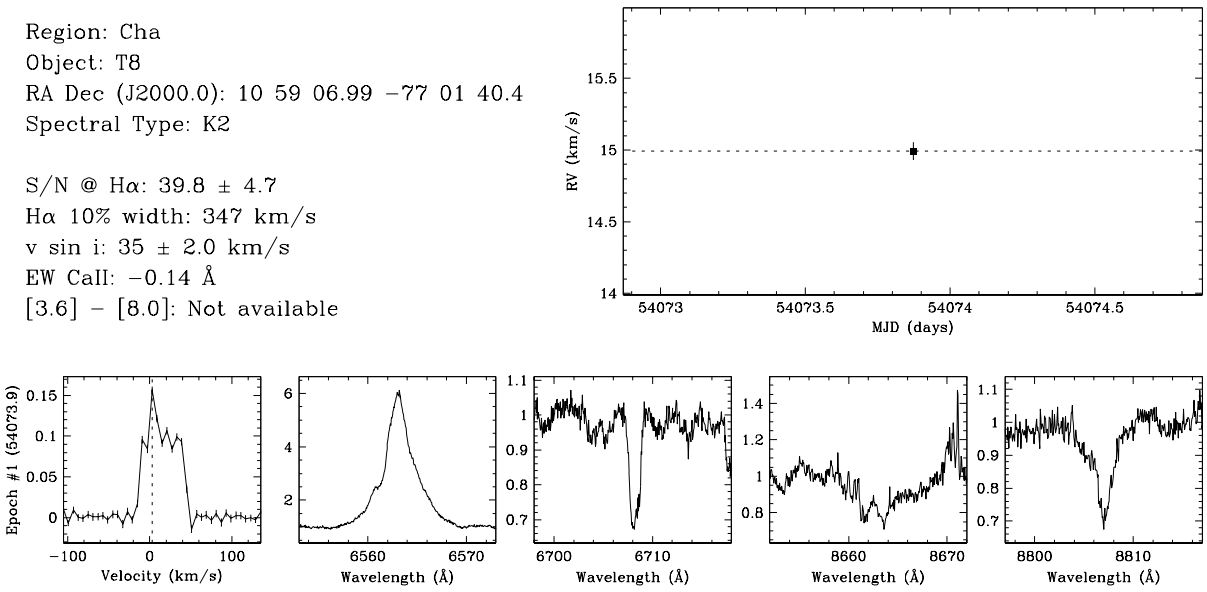

Figure 4.40 T8 has a single-line profile, and is therefore not an SB2. The radial velocity scatter cannot be determined because the target was observed for a single epoch. Hence, it is undetermined if the target is an SB1 or a single star. The strong sharp peak in the line profile at the observer's rest frame is due to dawn twilight, and may have biased the radial velocity estimate toward the observer's rest frame. This target has been previously reported by Lafrenière et al. (2008) to have no resolved companions.

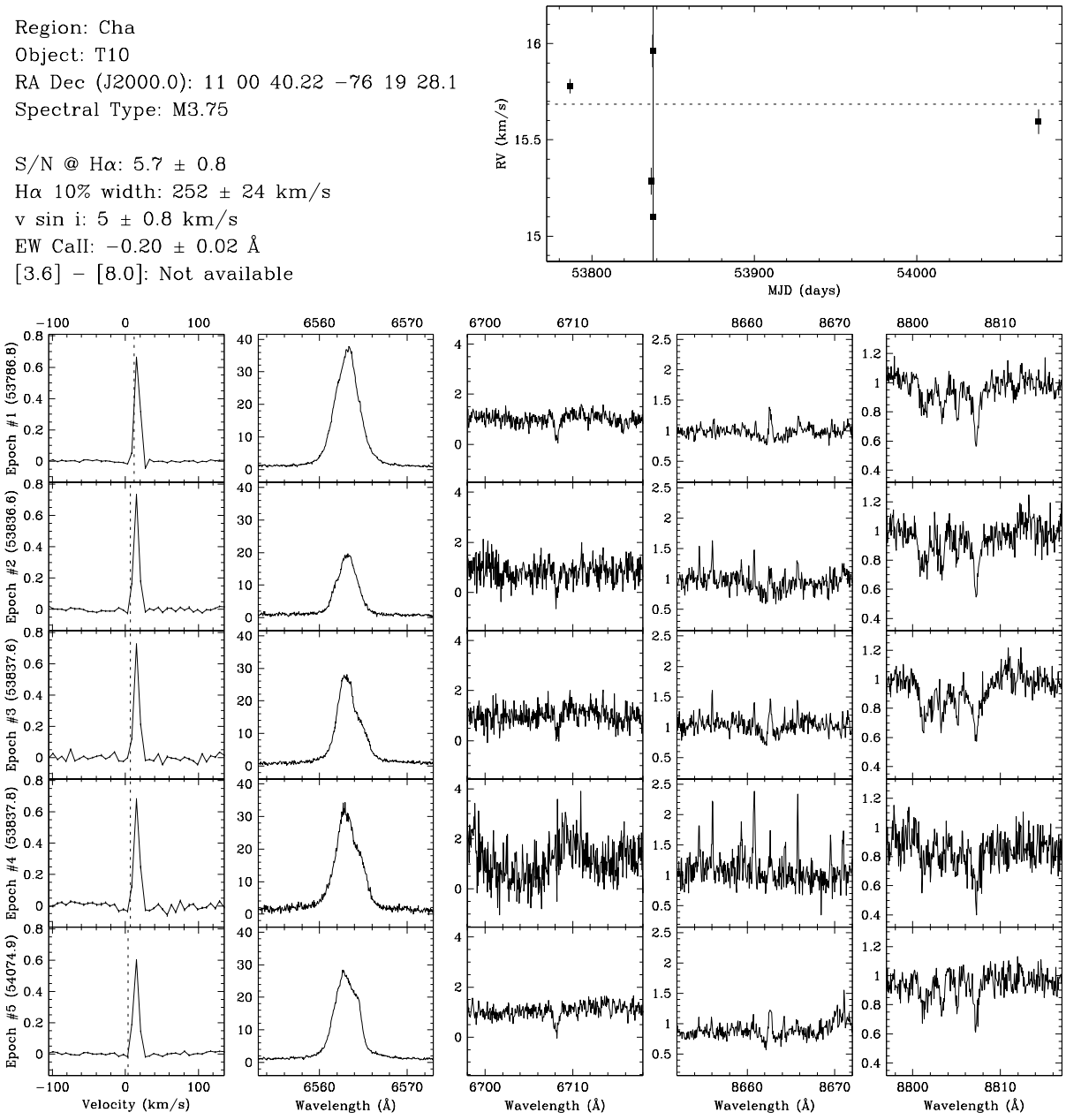

Figure 4.41 T10 shows no clear evidence of a close companion. The star has a single-line profile, and a radial velocity scatter not significant relative to variations observed within each observing run. The radial velocity scatter within the second observing run (epochs #2, #3 and #4) is consistent with that expected from systematic line profile variations, e.g. from star spots rotating with the star. The narrow emission lines in the spectra, especially for epoch #4, near 8662 Å are from the night sky. This target has been previously reported by Lafrenière et al. (2008) to have no resolved companions.

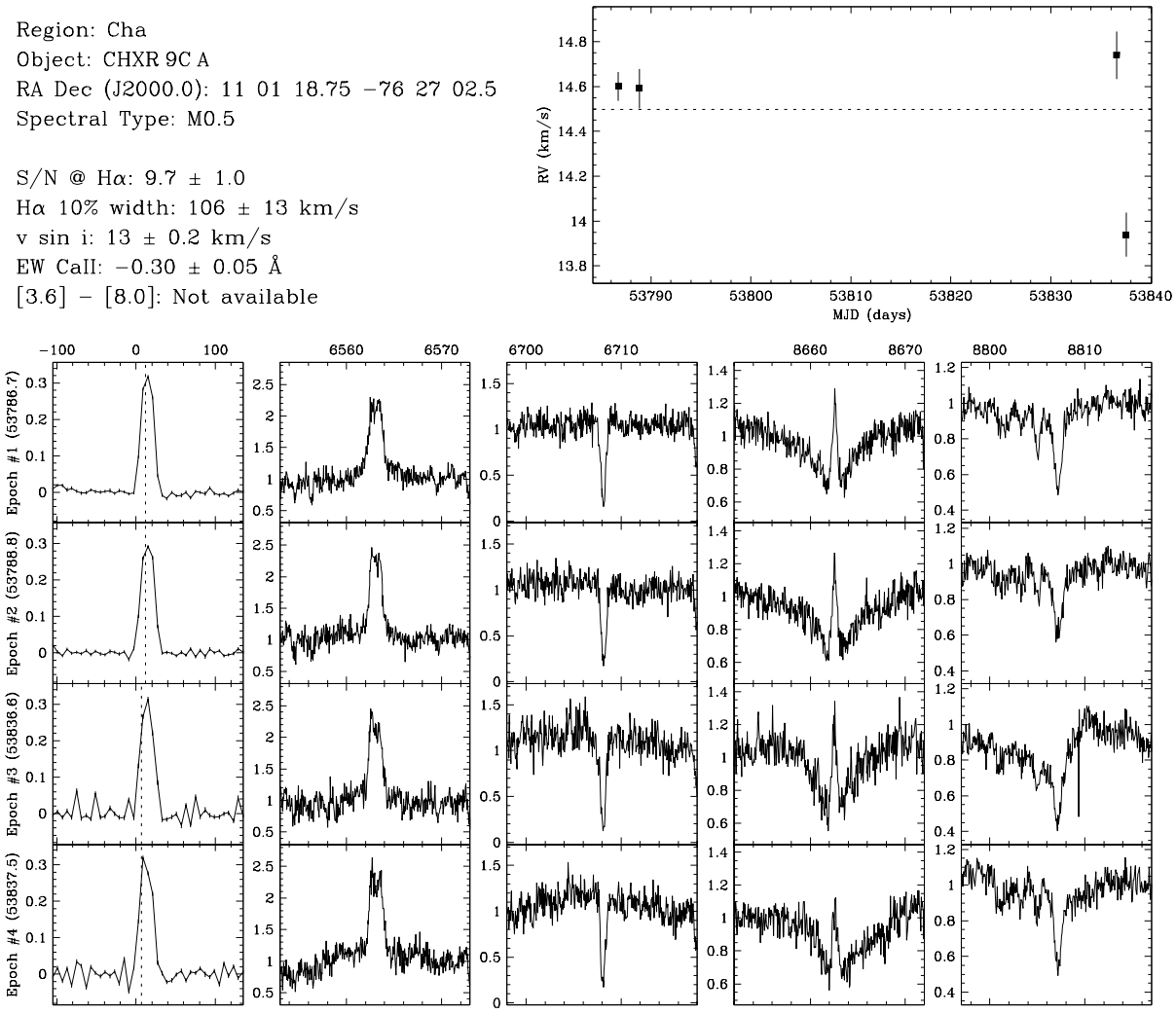

Figure 4.42 CHXR 9C A shows no clear evidence of a close companion. The star has a single-line profile, and a radial velocity scatter not significant relative to variations observed within each observing run. The radial velocity scatter within the second observing run (epochs #3 and #4) is consistent with that expected from systematic line profile variations, e.g. from star spots rotating with the star. This target has been previously reported by Lafrenière et al. (2008) to have a resolved companion with a separation of $\sim 0\farcs852$ (~ 120 AU) at a position angle of $\sim 81\fdg3$, and an R-band flux ratio of ~ 0.56 ($\Delta K \sim 0.36$). However, there is no clear evidence in the line profile of the resolved companion. Since the resolved companion has an expected circular orbital speed of $\sim 3\,\mathrm{km\,s^{-1}}$, a second profile could be obscured if the primary star and the resolved companion have similar projected rotational velocities.

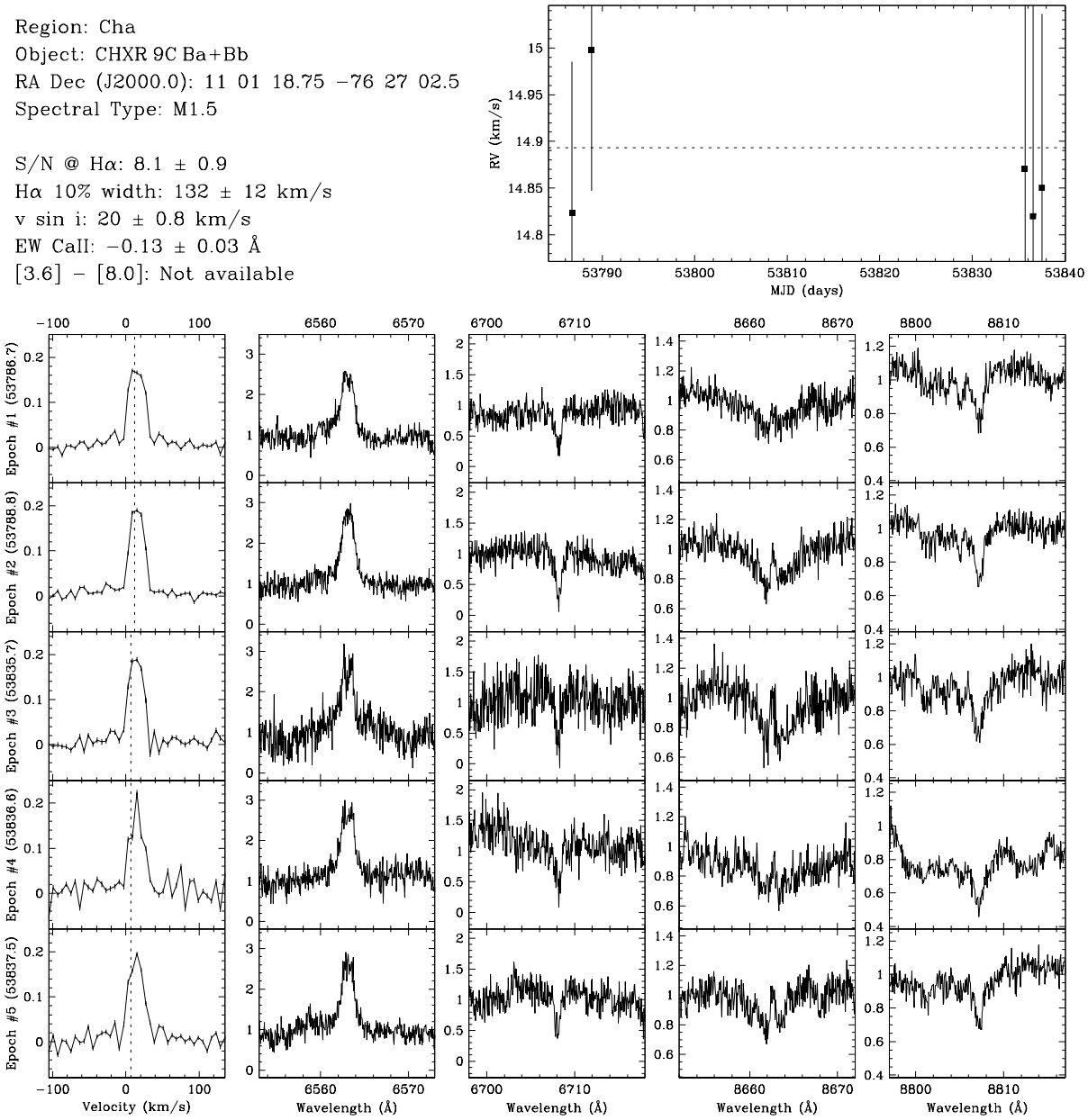

Figure 4.43 CHXR 9C Ba+Bb shows no evidence of a close companion. The star has a single-line profile, and the radial velocity scatter is not significant relative to the measurement uncertainties. This target has been previously reported by Lafrenière et al. (2008) to have a resolved companion with a separation of $\sim 0\farcs13$ (~ 18 AU) at a position angle of $\sim 76\fdg1$, and an R-band flux ratio of ~ 0.18 ($\Delta K \sim 0.70$). However, there is no clear evidence in the line profile of the resolved companion. Since the resolved companion has an expected circular orbital speed of $\sim 5\,\mathrm{km\,s^{-1}}$, a second profile could be obscured if the primary star and the resolved companion have similar projected rotational velocities.

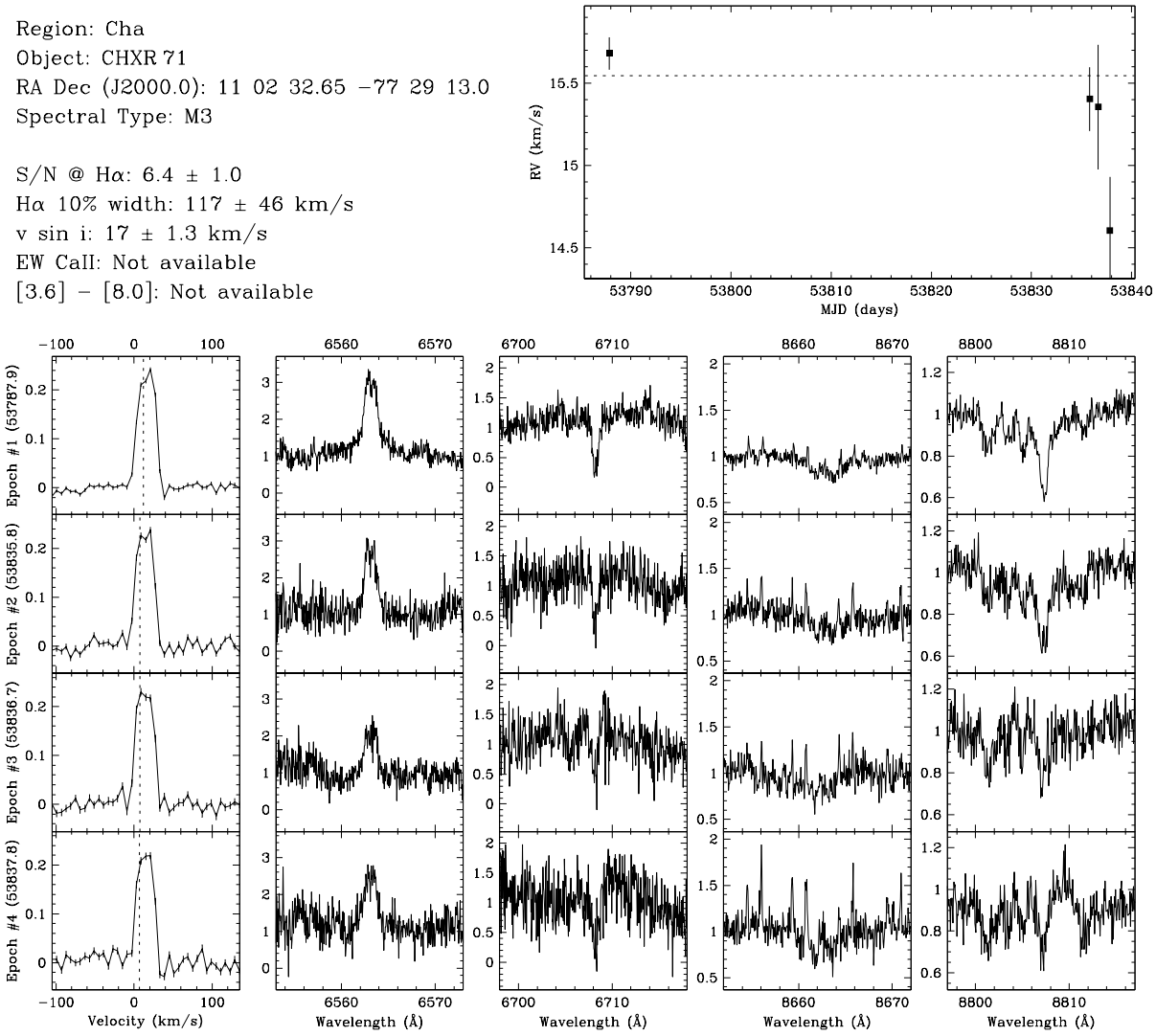

Figure 4.44 CHXR 71 shows no evidence of a close companion. The star has a single-line profile, and the radial velocity scatter is not significant relative to the measurement uncertainties. The narrow emission lines in the spectra near 8662 Å are from the night sky. This target has been previously reported by Lafrenière et al. (2008) to have a resolved companion with a separation of $\sim 0\farcs572$ (~ 80 AU) at a position angle of $\sim 70°$, and an R-band flux ratio of ~ 0.02 ($\Delta K \sim 1.63$). Given the flux ratio, the expected contribution to the line profile from the resolved companion is negligible.

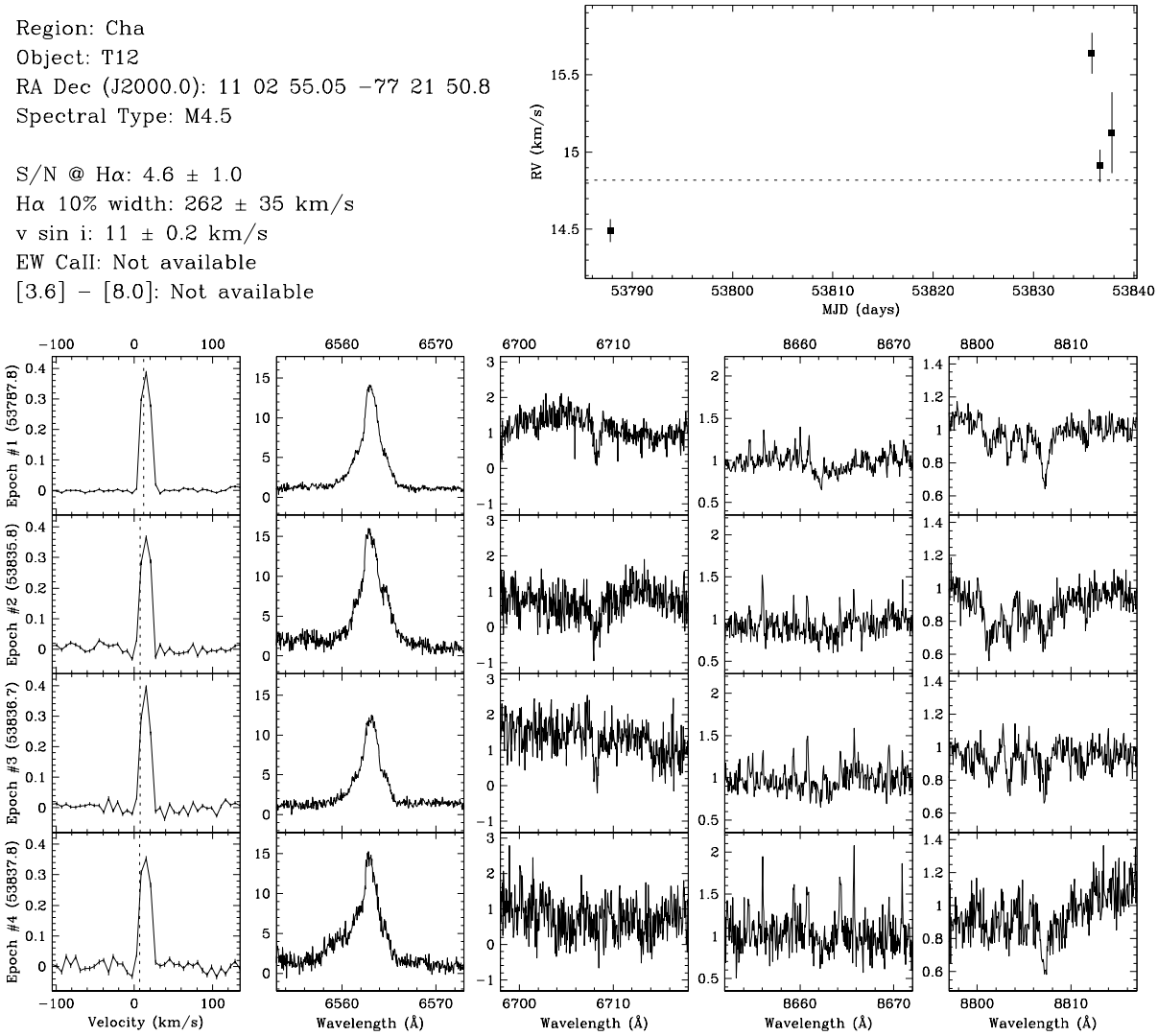

Figure 4.45 T12 shows no clear evidence of a close companion. The star has a single-line profile, and a radial velocity scatter not significant relative to variations observed within each observing run. The radial velocity scatter within the second observing run (epochs #2, #3 and #4) is consistent with that expected from systematic line profile variations, e.g. from star spots rotating with the star. The narrow emission lines in the spectra near 8662 Å are from the night sky. This target has been previously reported by Lafrenière et al. (2008) to have no resolved companions.

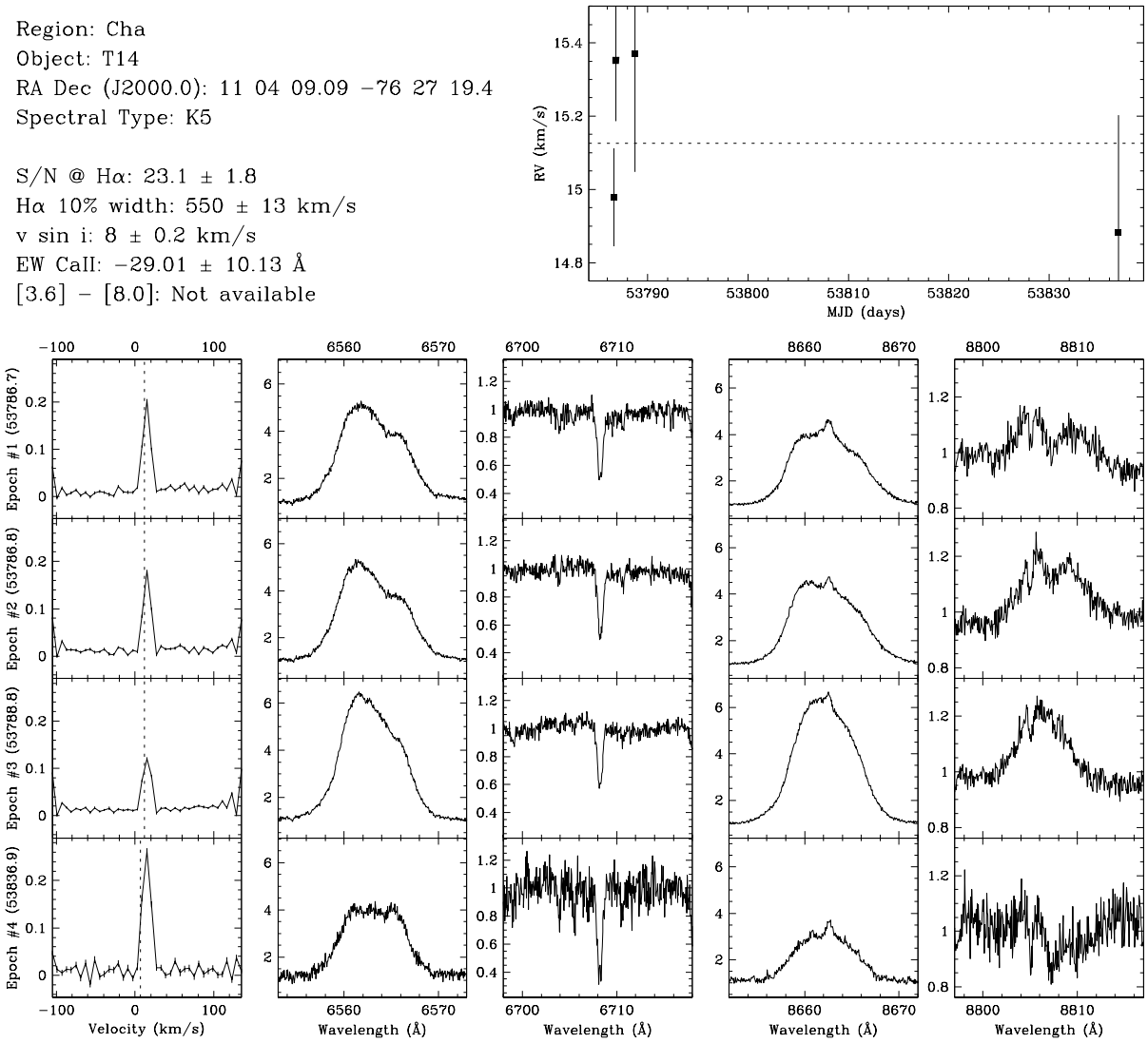

Figure 4.46 T14 shows no evidence of a close companion. The star has a single-line profile, and the radial velocity scatter is not significant relative to the measurement uncertainties. The spectrum is heavily veiled, and we derived the radial velocities from fits to the line profile rather than from direct fits to the spectra (see §4.4.2). This target has been previously reported by Lafrenière et al. (2008) to have no resolved companions.

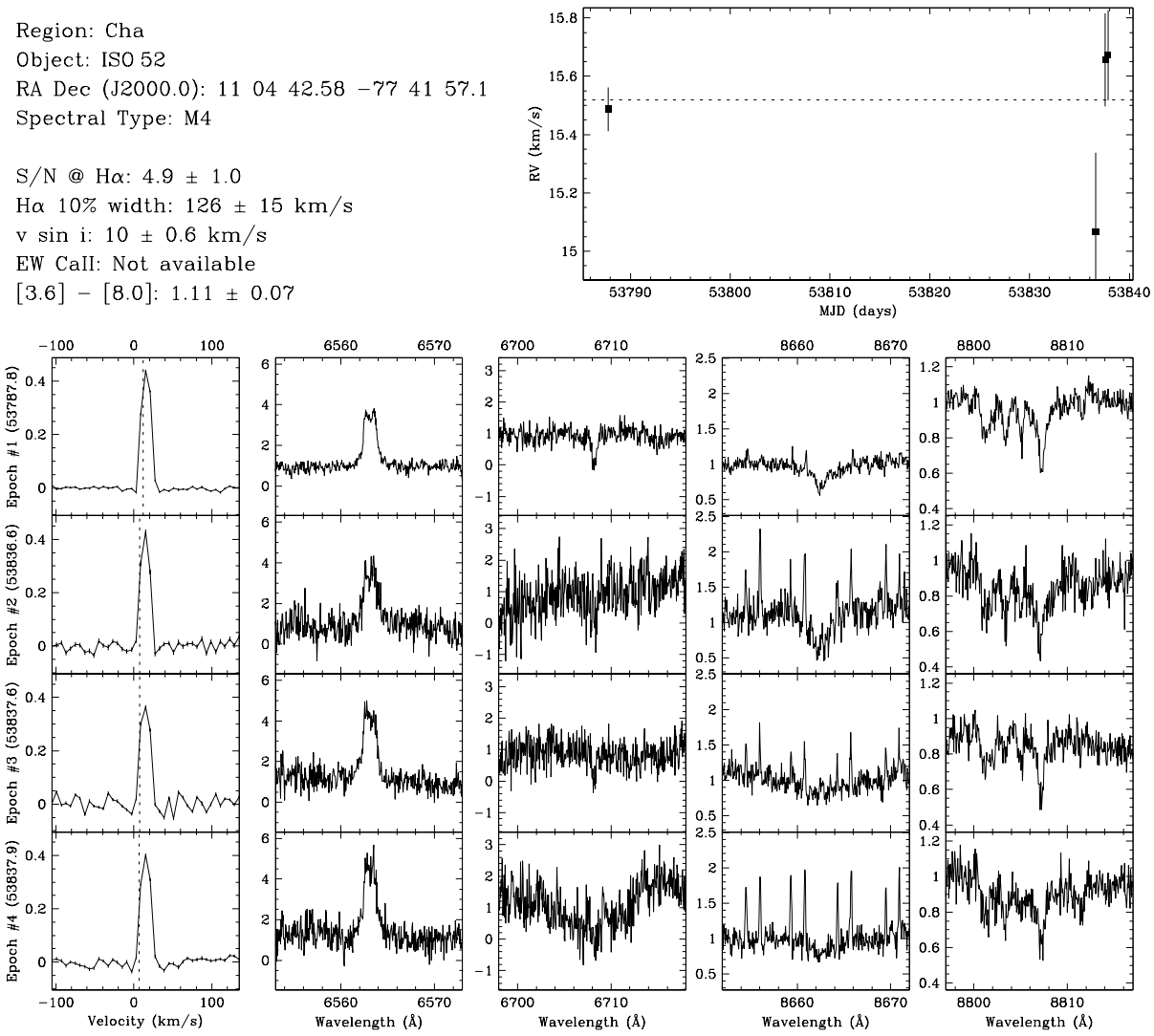

Figure 4.47 ISO 52 shows no evidence of a close companion. The star has a single-line profile, and the radial velocity scatter is not significant relative to the measurement uncertainties. The narrow emission lines in the spectra near 8662 Å are from the night sky. This target has been previously reported by Lafrenière et al. (2008) to have no resolved companions.

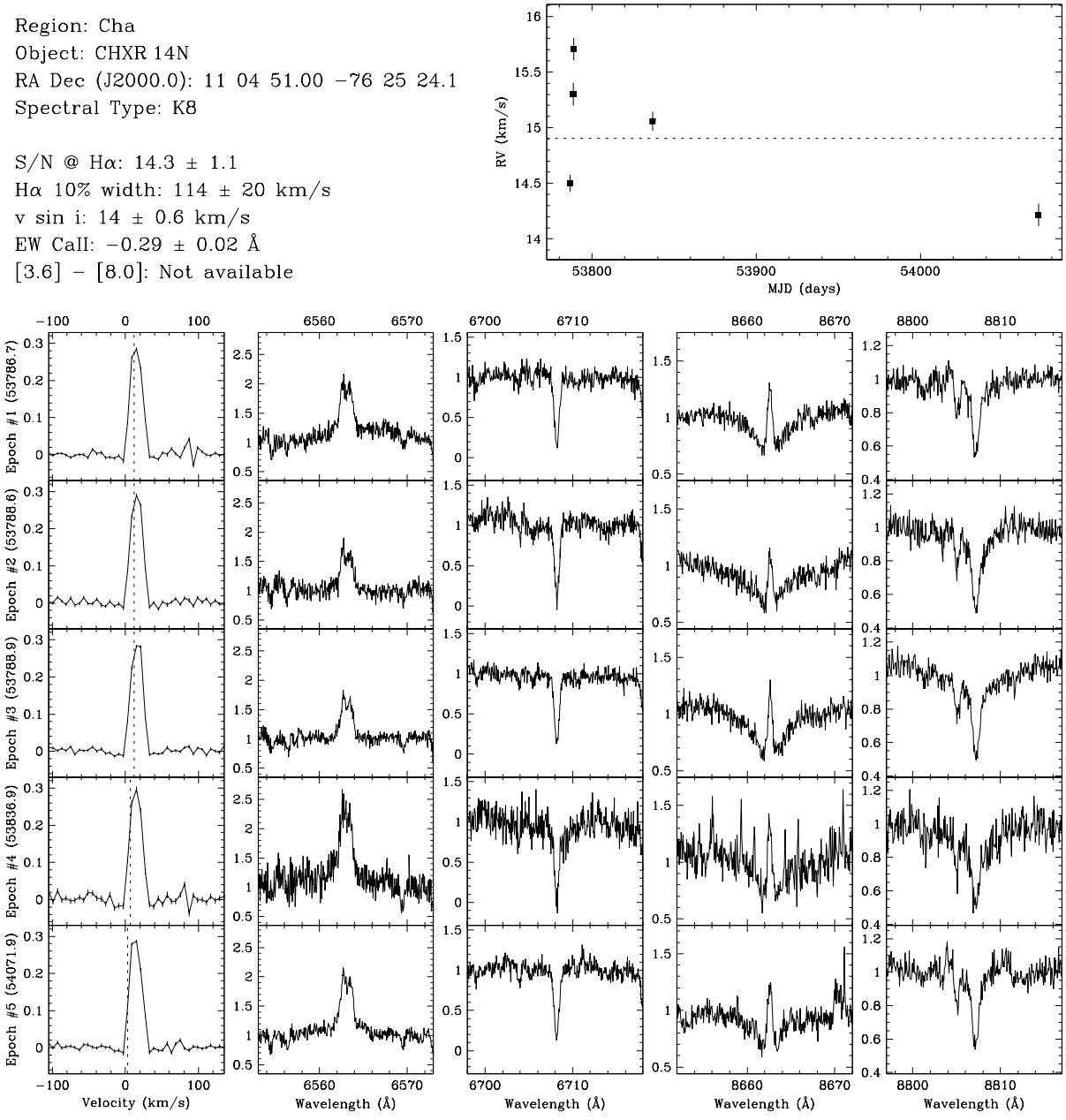

Figure 4.48 CHXR 14N shows no clear evidence of a close companion. The star has a single-line profile, and a radial velocity scatter not significant relative to variations observed within each observing run. The radial velocity scatter within the first observing run (epochs #1, #2 and #3) is consistent with that expected from systematic line profile variations, e.g. from star spots rotating with the star. For epoch #4, the narrow emission lines in the spectrum near 8662 Å are from the night sky. This target has been previously reported by Lafrenière et al. (2008) to have no resolved companions.

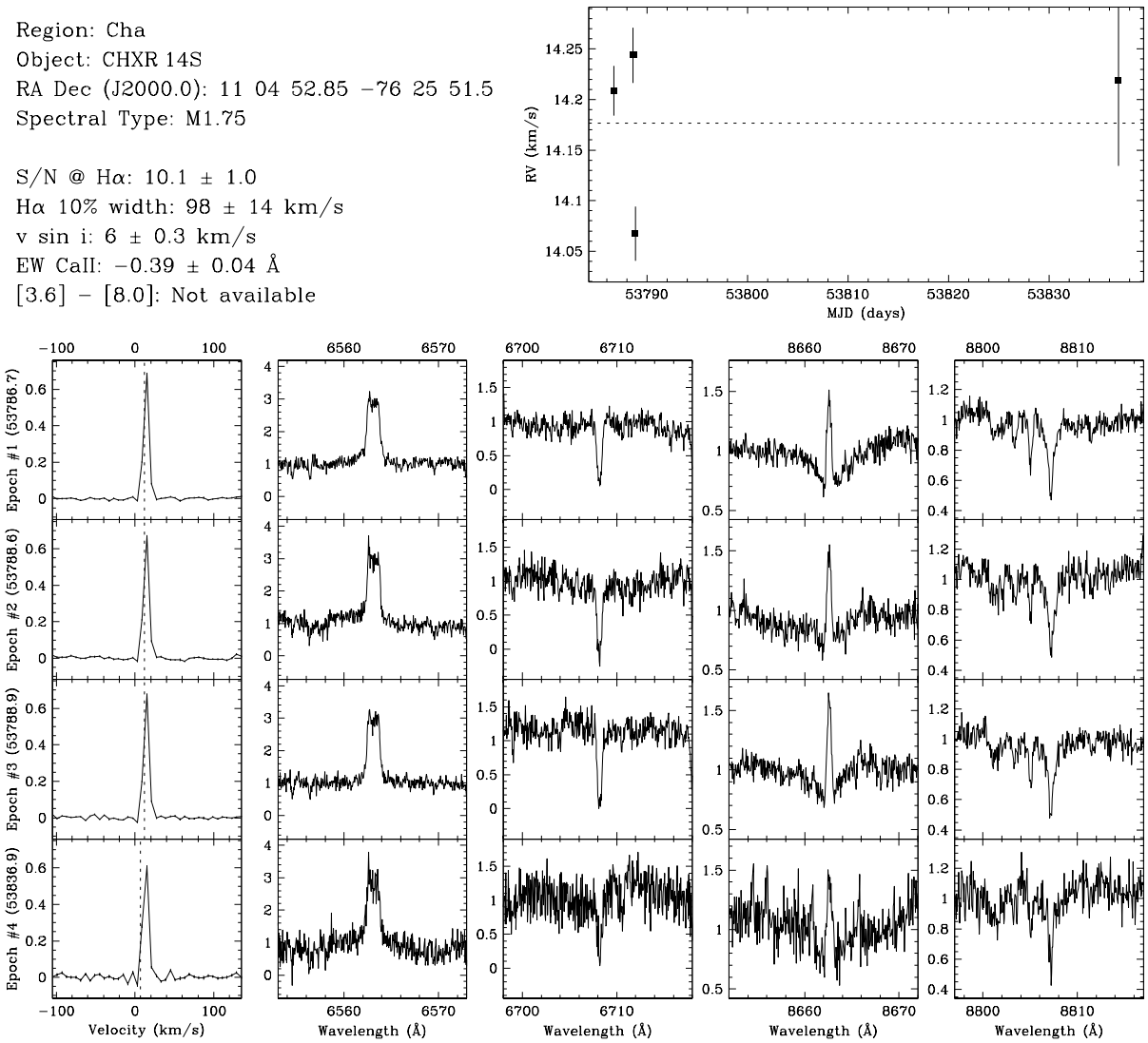

Figure 4.49 CHXR 14S shows no clear evidence of a close companion. The star has a single-line profile, and a radial velocity scatter not significant relative to variations observed within each observing run. The radial velocity scatter within the first observing run (epochs #1, #2 and #3) is consistent with that expected from systematic line profile variations, e.g. from star spots rotating with the star. This target has been previously reported by Lafrenière et al. (2008) to have no resolved companions.

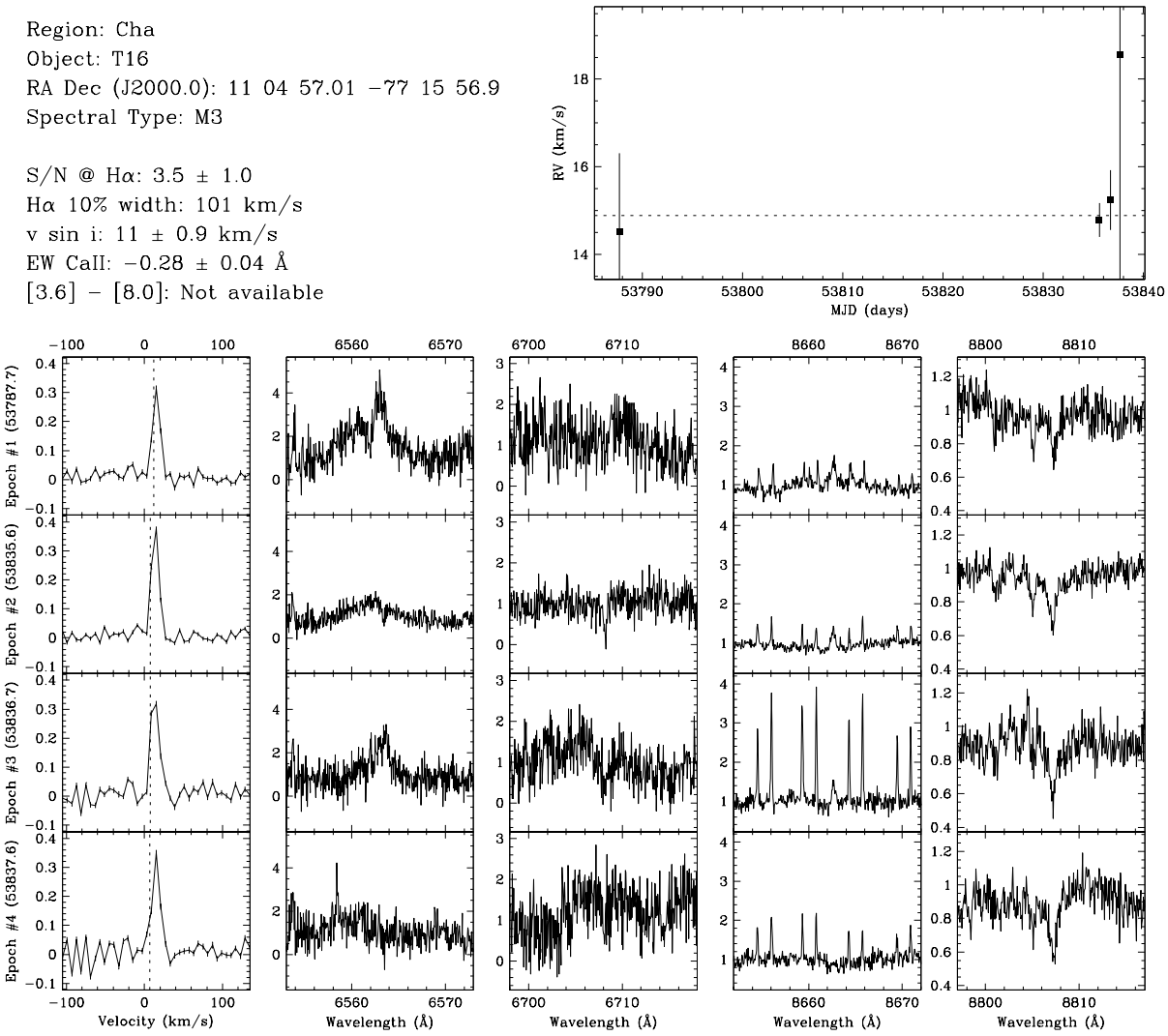

Figure 4.50 T16 shows no evidence of a close companion. The star has a single-line profile, and the radial velocity scatter is not significant relative to the measurement uncertainties. The narrow emission lines in the spectra near 8662 Å are from the night sky. This target has been previously reported by Lafrenière et al. (2008) to have no resolved companions.

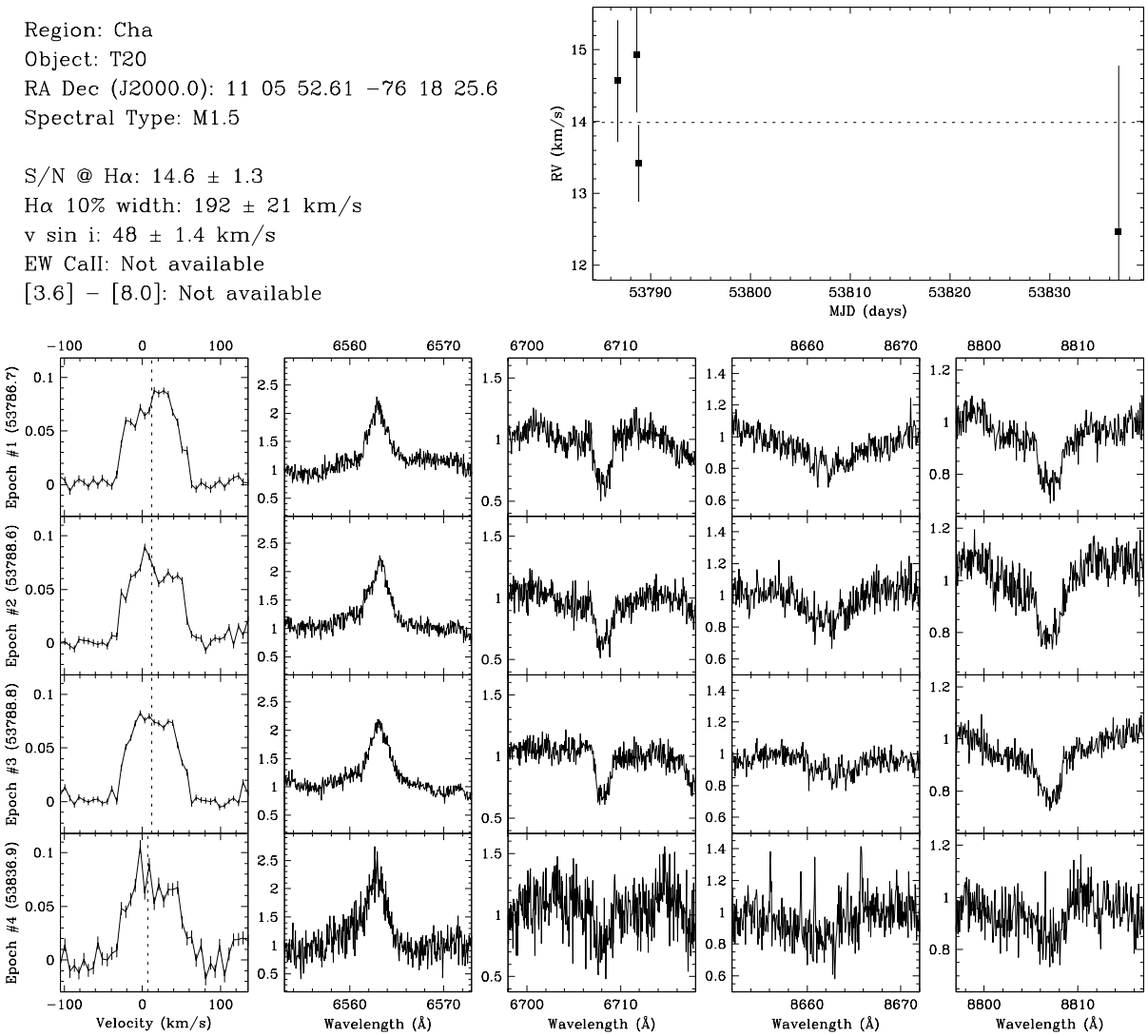

Figure 4.51 T20 shows no evidence of a close companion. The star has a single-line profile, and the radial velocity scatter is not significant relative to the measurement uncertainties. The line profile seems more consistent with a single, rapidly rotating star, with the variability likely due to noise. For epoch #4, the narrow emission lines in the spectrum near 8662 Å are from the night sky. This target has been previously reported by Lafrenière et al. (2008) to have no resolved companions.

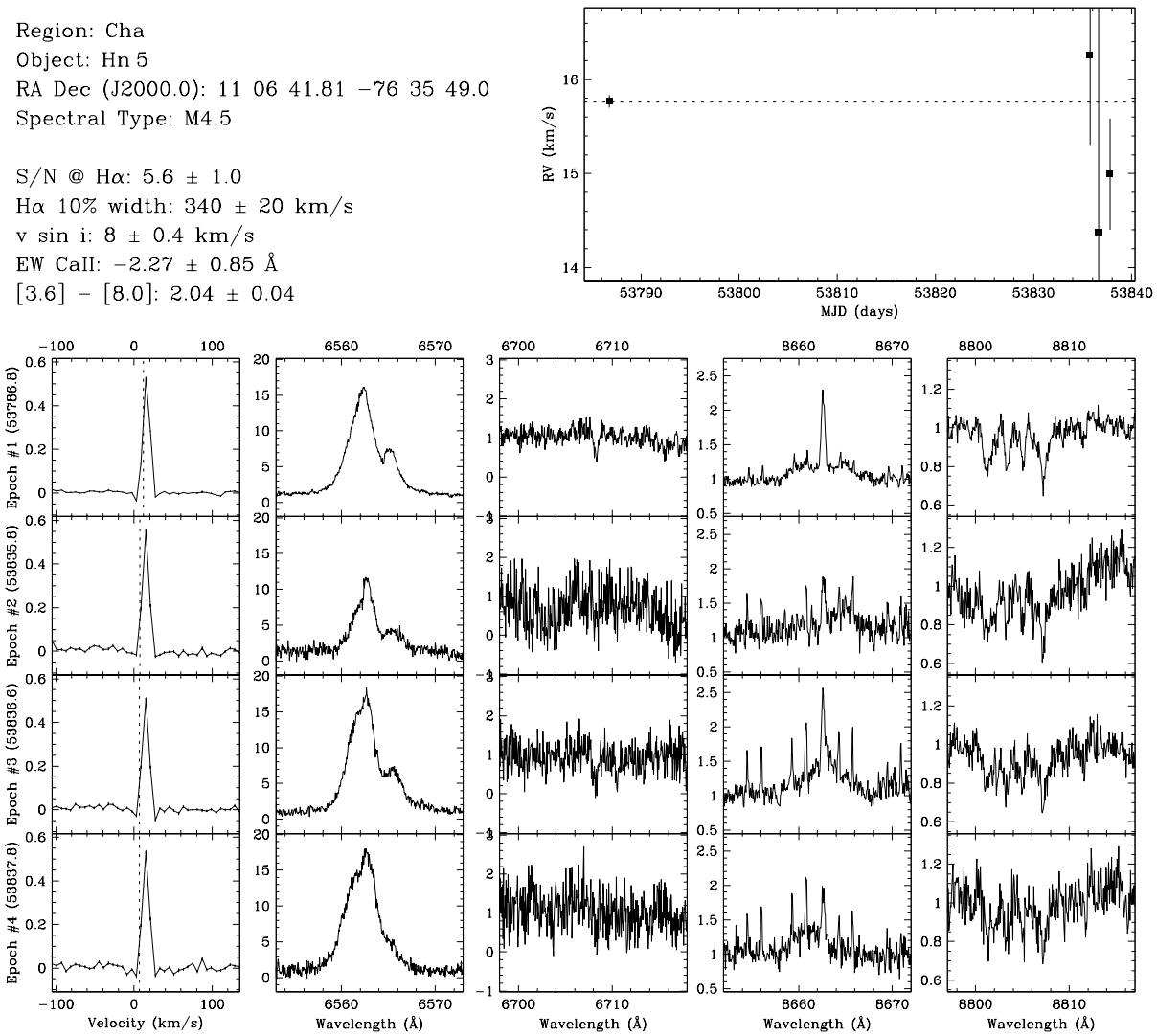

Figure 4.52 Hn 5 shows no evidence of a close companion. The star has a single-line profile, and the radial velocity scatter is not significant relative to the measurement uncertainties. The narrow emission lines in the spectra near 8662 Å are from the night sky. This target has been previously reported by Lafrenière et al. (2008) to have no resolved companions.

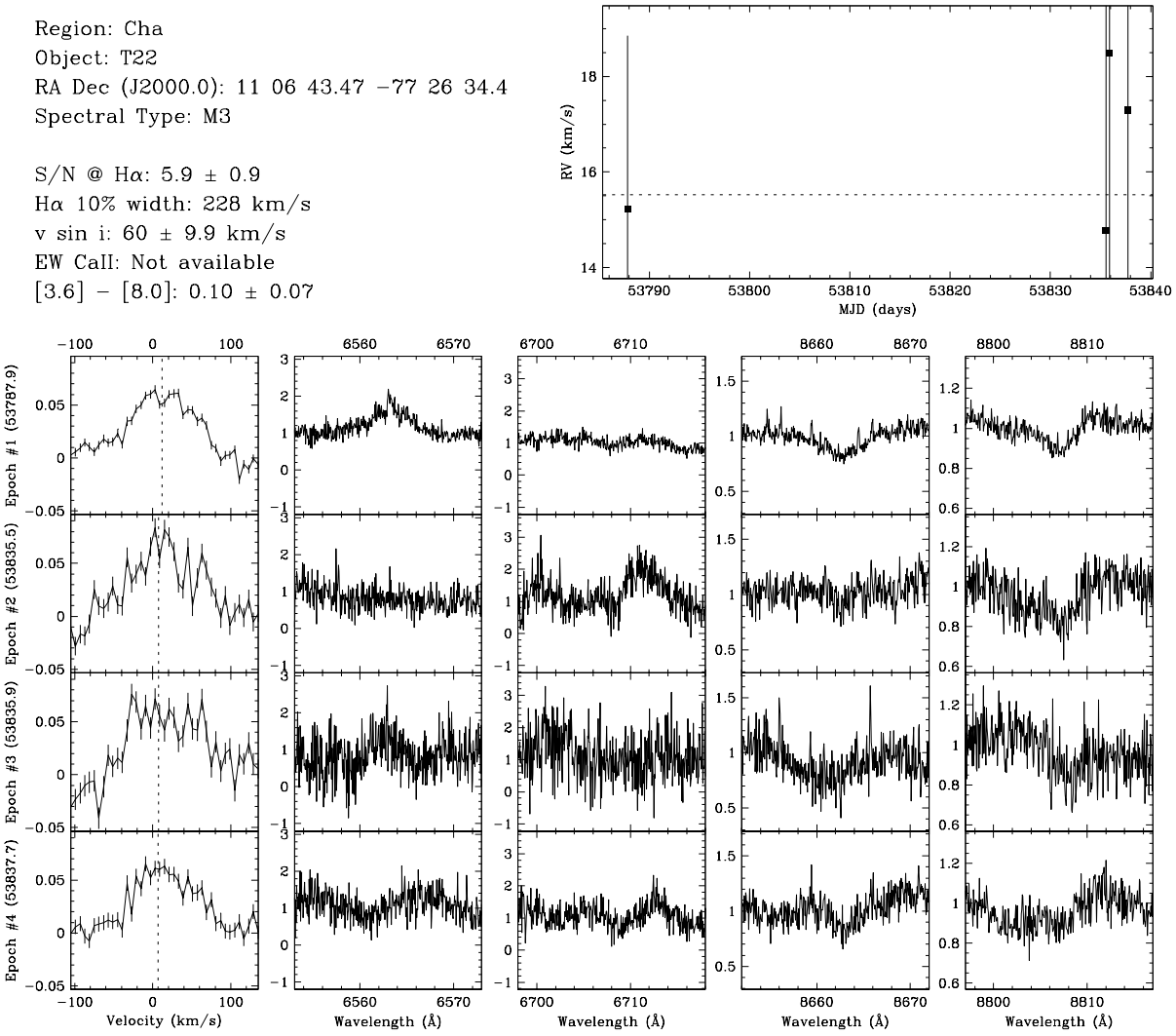

Figure 4.53 T22 shows no evidence of a close companion. The star has a single-line profile, and the radial velocity scatter is not significant relative to the measurement uncertainties. This target has been previously reported by Lafrenière et al. (2008) to have no resolved companions.

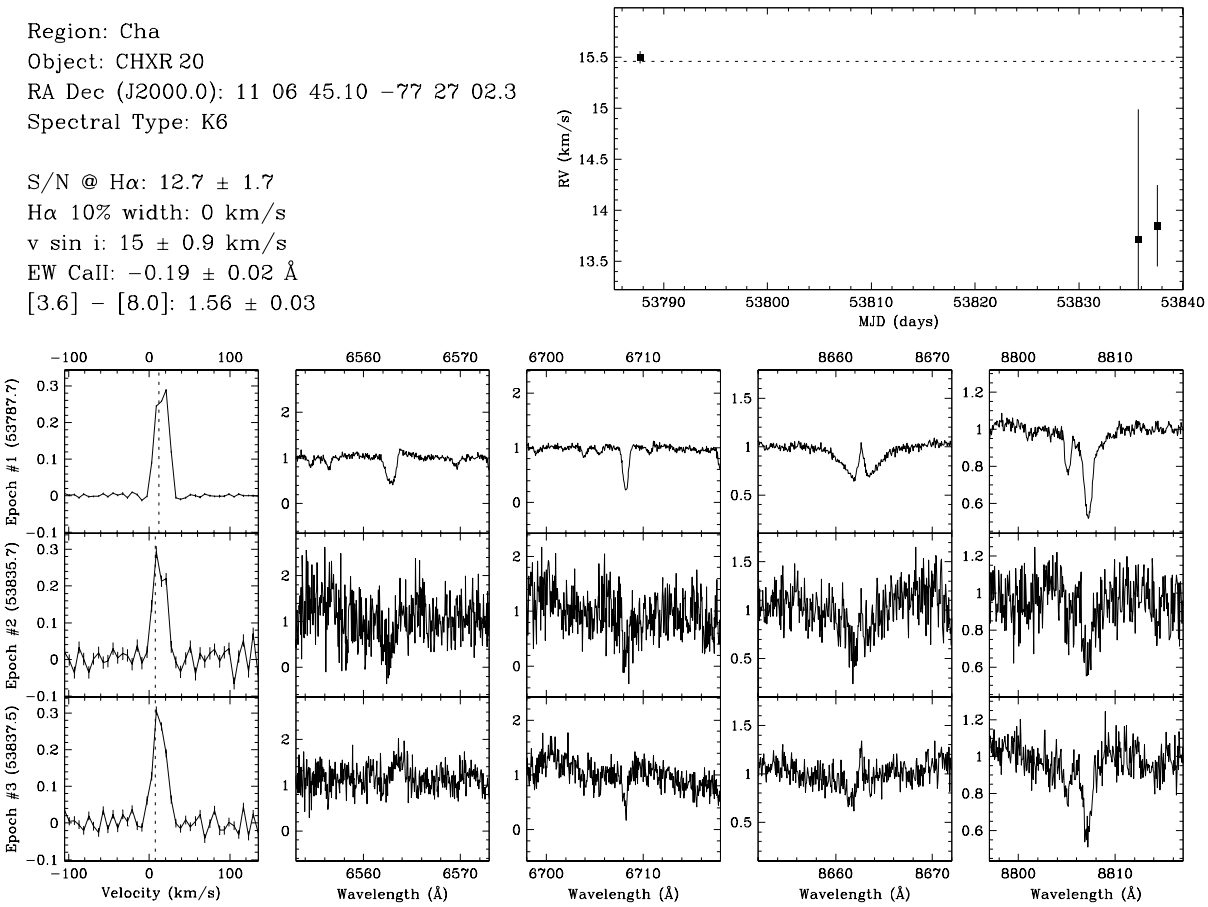

Figure 4.54 CHXR 20 shows no clear evidence of a close companion. The star has a single-line profile, and a radial velocity scatter not significant relative to variations observed within each observing run. The radial velocity displacement between observing runs is consistent with variations caused by the presence of star spots rotating with the star. This target has been previously reported by Lafrenière et al. (2008) to have no resolved companions.

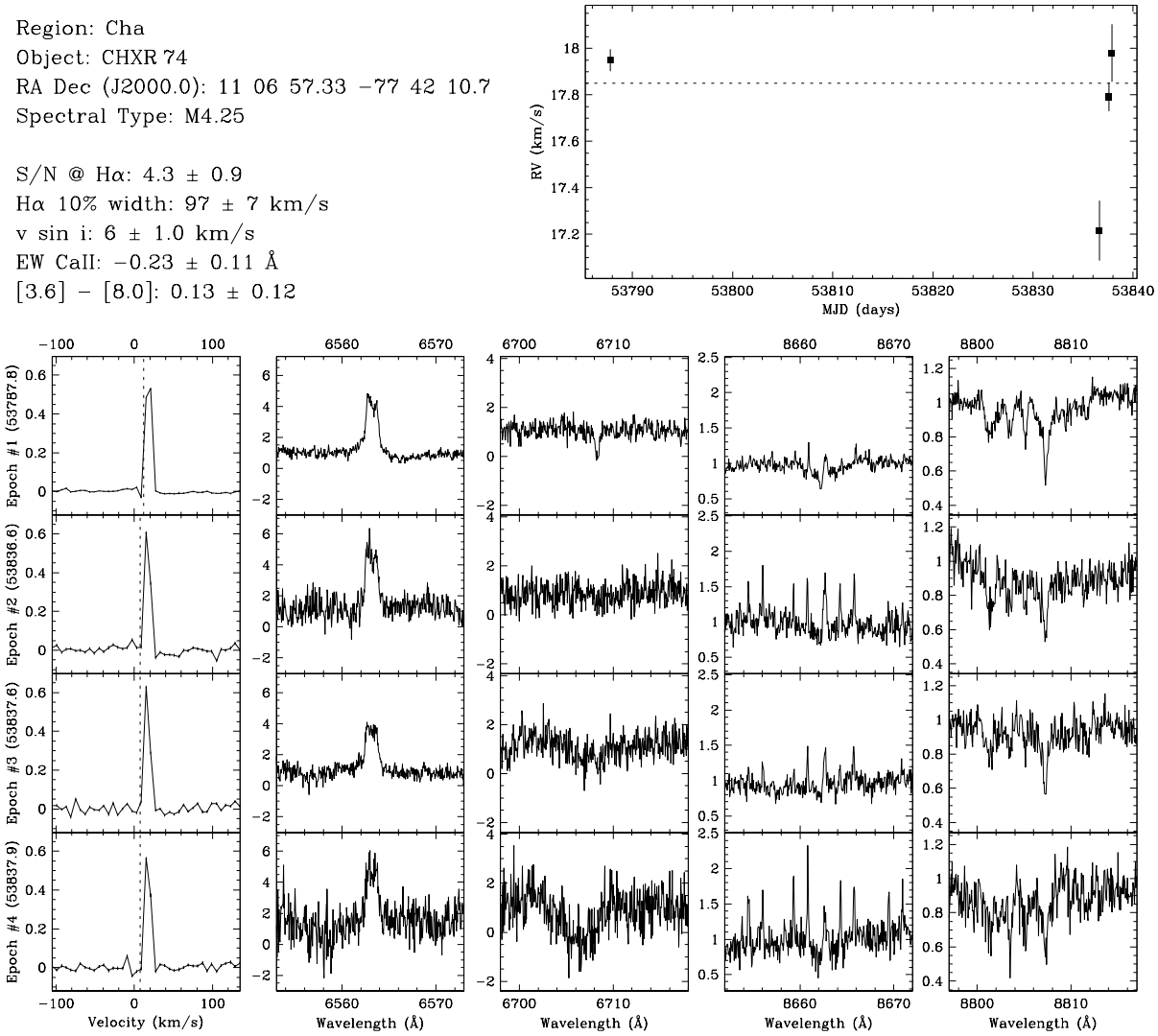

Figure 4.55 CHXR 74 shows no clear evidence of a close companion. The star has a single-line profile, and a radial velocity scatter not significant relative to variations observed within each observing run. The radial velocity scatter within the second observing run (epochs #2, #3 and #4) is consistent with that expected from systematic line profile variations, e.g. from star spots rotating with the star. The overall radial velocity deviates from that of the star forming region. However, cluster membership is supported by Li-λ6708 absorption. The absorption is prominent in the first, best S/N spectrum. The narrow emission lines in the spectra near 8662 Å are from the night sky. This target has been previously reported by Lafrenière et al. (2008) to have no resolved companions.

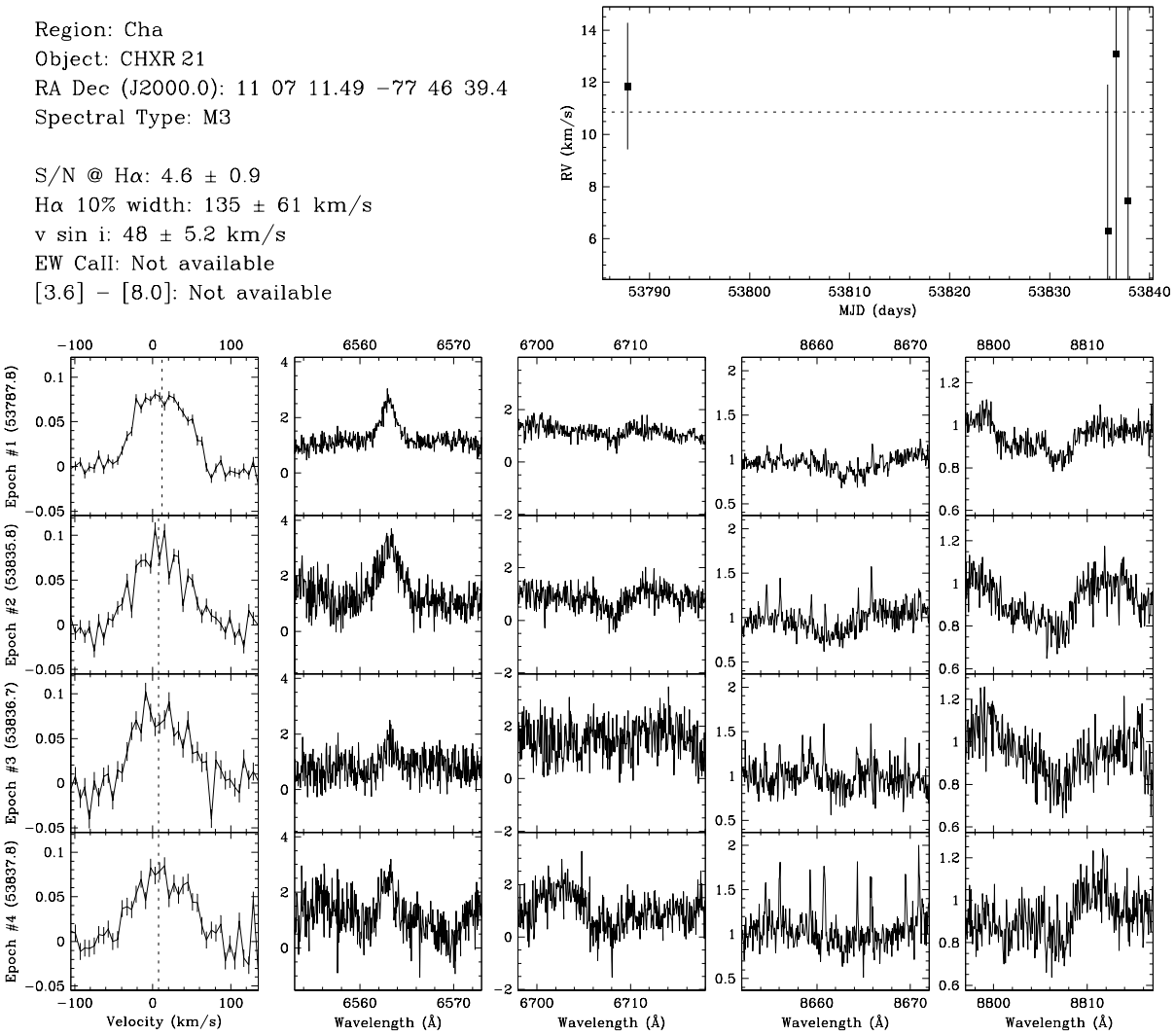

Figure 4.56 CHXR 21 shows no evidence of a close companion. The star has a single-line profile, and the radial velocity scatter is not significant relative to the measurement uncertainties. The overall radial velocity deviates from that of the star forming region. However, cluster membership is supported by Li-λ6708 absorption. The narrow emission lines in the spectra near 8662 Å are from the night sky. This target has been previously reported by Lafrenière et al. (2008) to have no resolved companions.

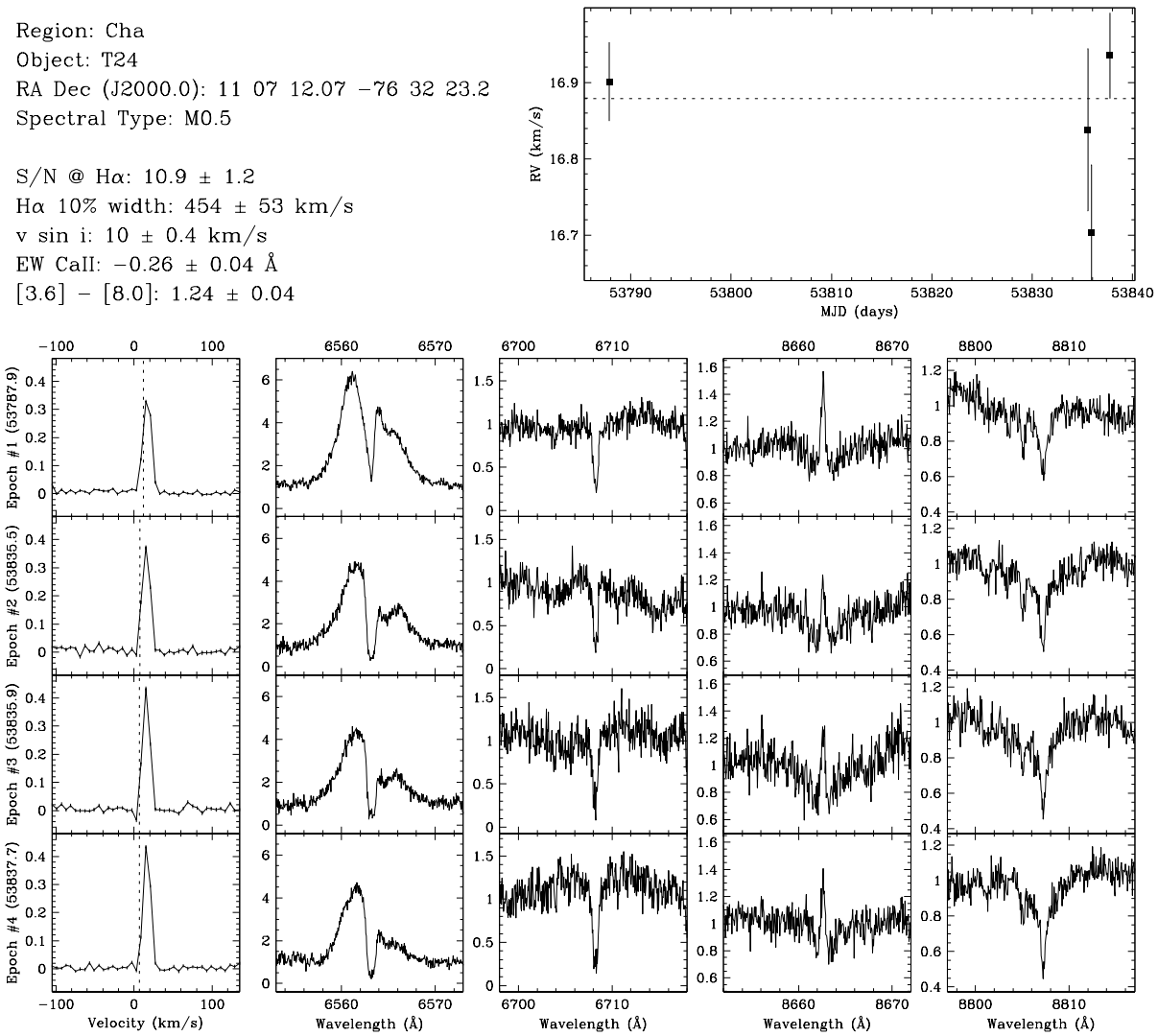

Figure 4.57 T24 shows no evidence of a close companion. The star has a single-line profile, and the radial velocity scatter is not significant relative to the measurement uncertainties. This target has been previously reported by Lafrenière et al. (2008) to have no resolved companions.

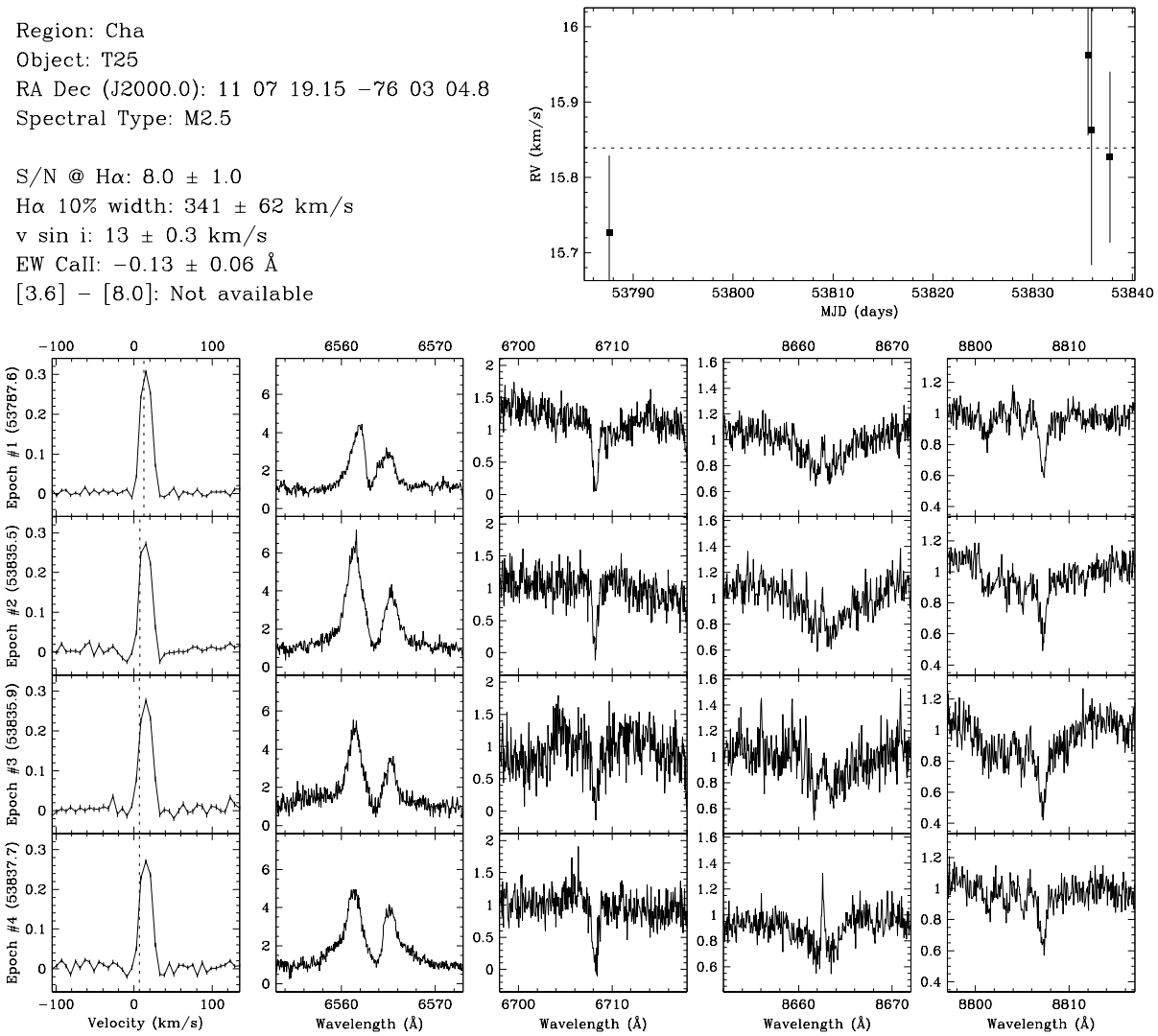

Figure 4.58 T25 shows no evidence of a close companion. The star has a single-line profile, and the radial velocity scatter is not significant relative to the measurement uncertainties. This target has been previously reported by Lafrenière et al. (2008) to have no resolved companions.

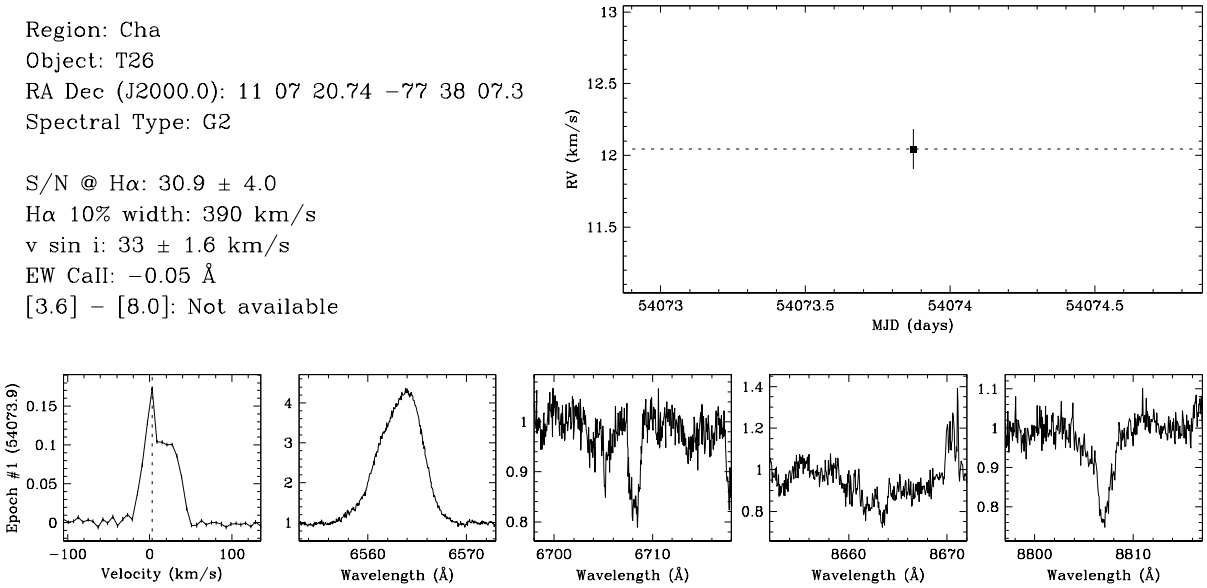

Figure 4.59 T26 has a single-line profile, and is therefore not an SB2. The radial velocity scatter cannot be determined because the target was observed for a single epoch. Hence, it is undetermined if the target is an SB1 or a single star. The overall radial velocity deviates from that of the star forming region. However, cluster membership is supported by Li-λ6708 absorption. The strong sharp peak in the line profile at the observer's rest frame is due to dawn twilight, and likely biased the radial velocity estimate toward the observer's rest frame. This target has been previously reported by Lafrenière et al. (2008) to have a resolved companion with a separation of $\sim 0\farcs066$ (~ 9.2 AU) at a position angle of $\sim 177\fdg9$, and an R-band flux ratio of ~ 0.86 ($\Delta K \sim 0.06$). However, there is no clear evidence in the line profile of the resolved companion. Since the resolved companion has an expected circular orbital speed of $\sim 22\,\mathrm{km\,s^{-1}}$, a second profile could be obscured if the primary star and the resolved companion have similar projected rotational velocities.

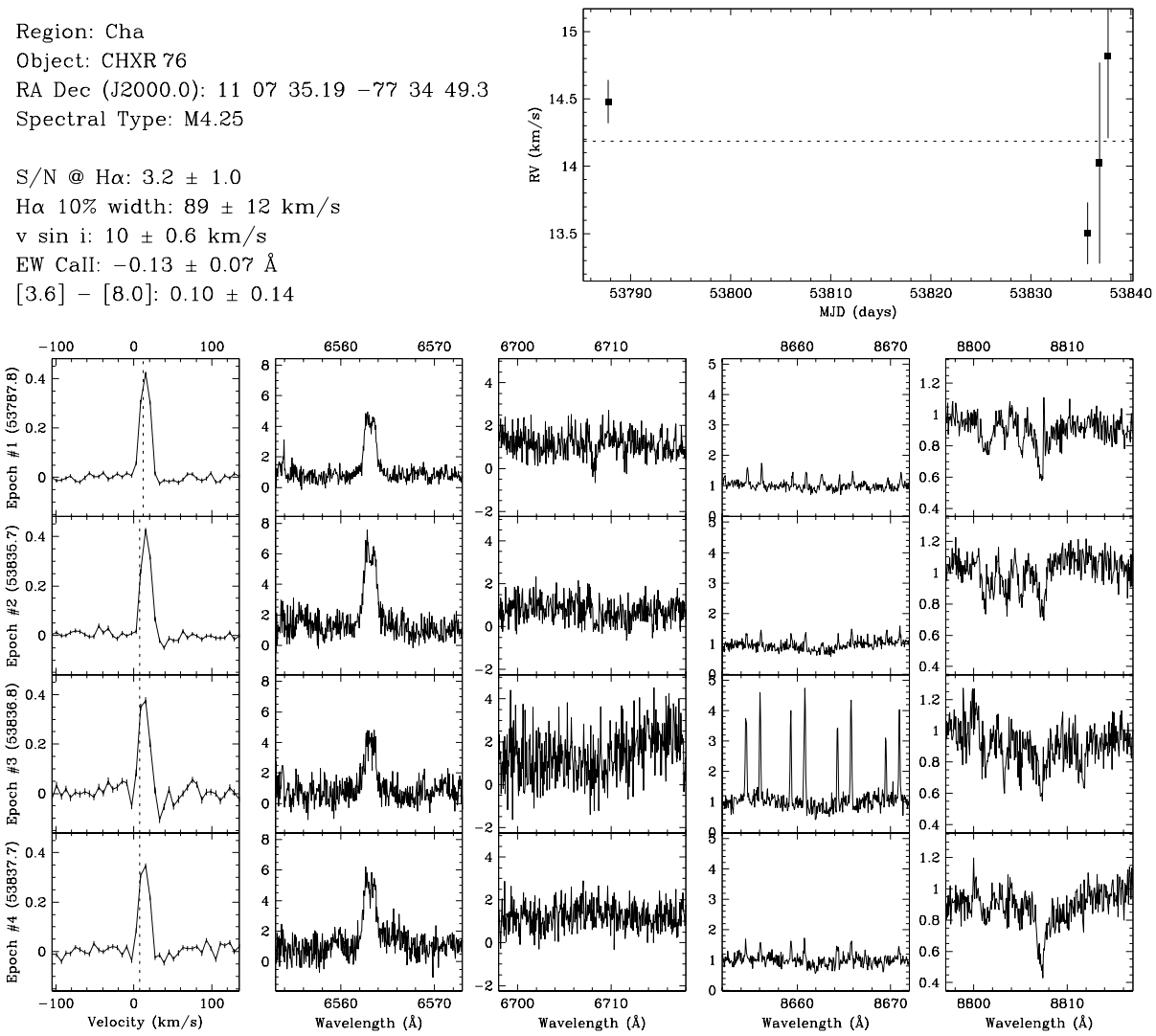

Figure 4.60 CHXR 76 shows no evidence of a close companion. The star has a single-line profile, and the radial velocity scatter is not significant relative to the measurement uncertainties. The narrow emission lines in the spectra, especially for epoch #3, near 8662 Å are from the night sky. This target has been previously reported by Lafrenière et al. (2008) to have no resolved companions.

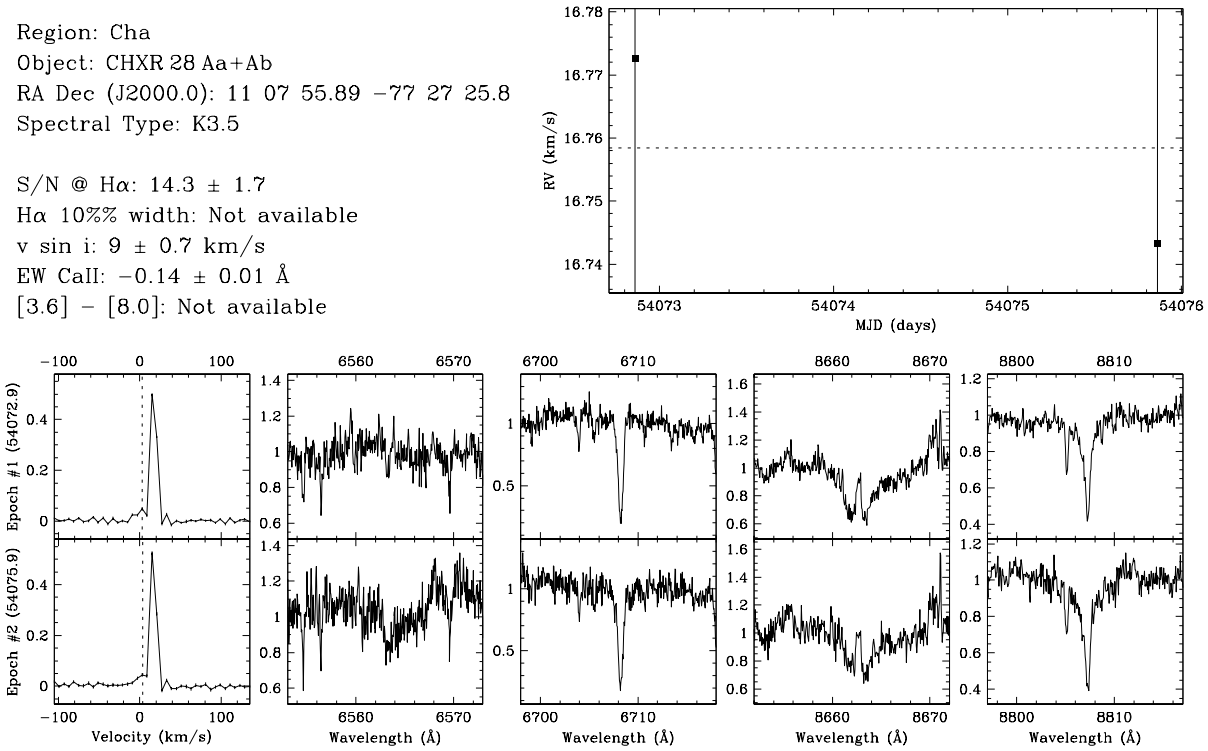

Figure 4.61 CHXR 28 Aa+Ab has a single-line profile, and is therefore not an SB2. The radial velocity scatter over the short baseline available does not conclusively indicate if the target is an SB1 or a single star. The small peaks in the line profiles at the observer's rest frame are due to dawn twilight, and was included in the line profile fits. This target has been previously reported by Lafrenière et al. (2008) to have a resolved companion with a separation of $\sim 0\farcs143$ (~ 20 AU) at a position angle of $\sim 356\fdg6$, and an R-band flux ratio of ~ 0.55 ($\Delta K \sim 0.40$). However, there is no clear evidence in the line profile of the resolved companion. Since the resolved companion has an expected circular orbital speed of $\sim 8\,\mathrm{km\,s^{-1}}$, a second profile could be obscured if the primary star and the resolved companion have similar projected rotational velocities.

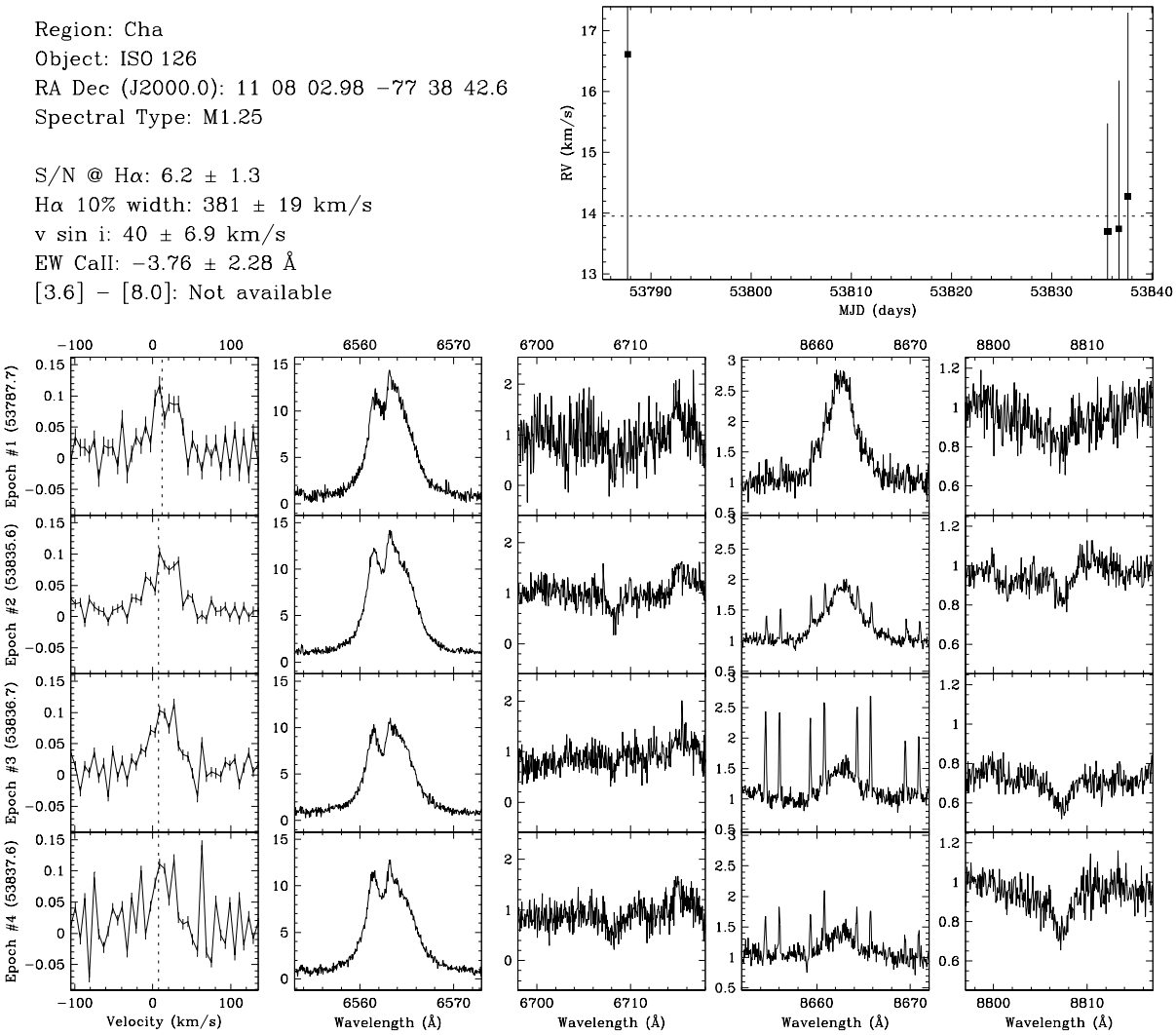

Figure 4.62 ISO 126 shows no evidence of a close companion. The star has a single-line profile, and the radial velocity scatter is not significant relative to the measurement uncertainties. The narrow emission lines in the spectra near 8662 Å are from the night sky. This target has been previously reported by Lafrenière et al. (2008) to have a resolved companion with a separation of $\sim 0\farcs292$ (~ 41 AU) at a position angle of $\sim 232\fdg4$, and an R-band flux ratio of ~ 0.23 ($\Delta K \sim 0.66$). However, there is no clear evidence in the line profile of the resolved companion. Since the resolved companion has an expected circular orbital speed of $\sim 4\,\mathrm{km\,s^{-1}}$, a second profile could be obscured if the primary star and the resolved companion have similar projected rotational velocities.

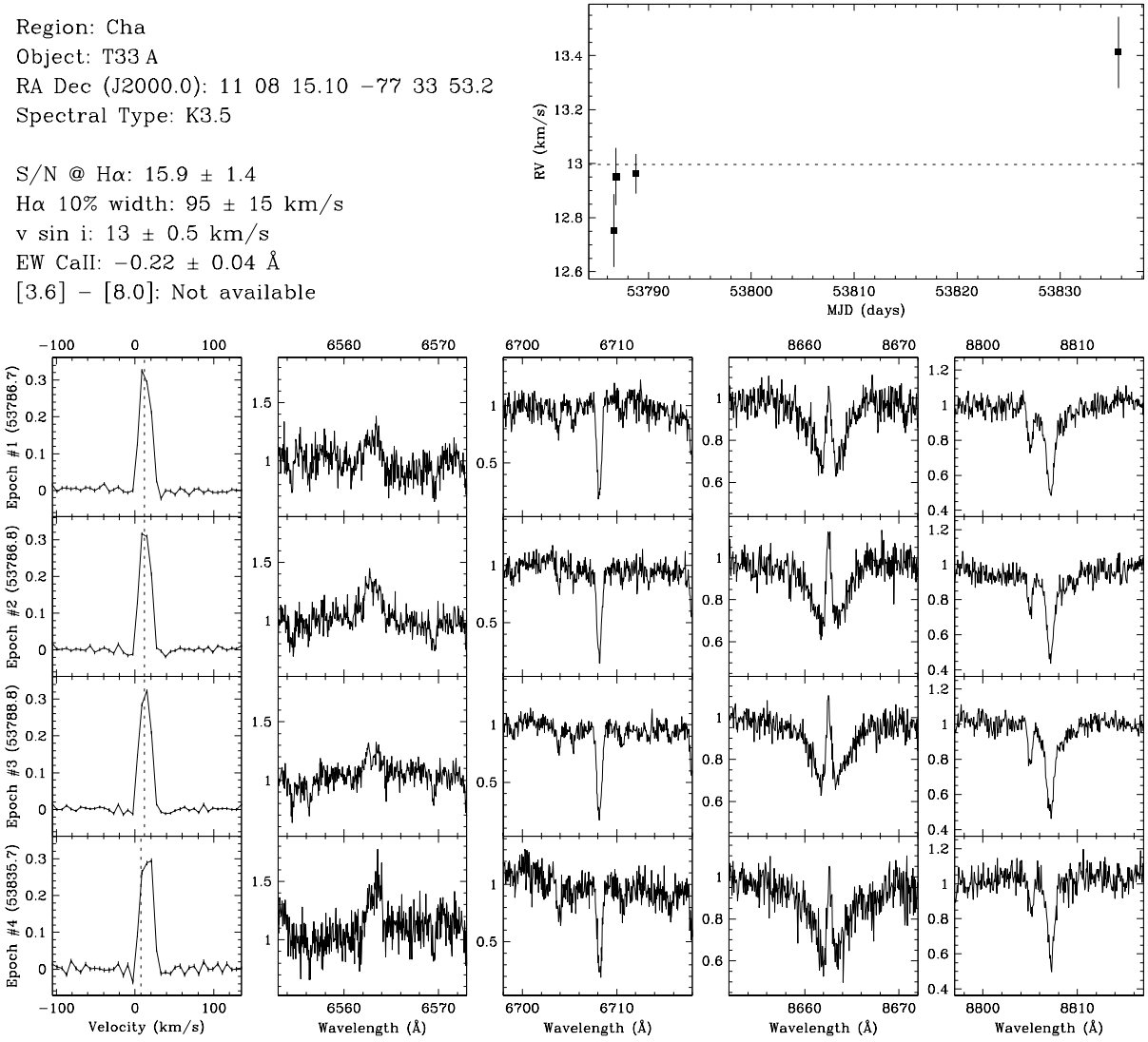

Figure 4.63 T33 A shows no evidence of a close companion. The star has a single-line profile, and the radial velocity scatter is not significant relative to the measurement uncertainties. This target has been previously reported by Lafrenière et al. (2008) to have a resolved companion with a separation of $\sim 2\farcs434$ (~ 340 AU) at a position angle of $\sim 284\fdg8$, and an R-band flux ratio of ~ 0.01 ($\Delta K \sim 1.93$). Given the flux ratio and separation, the expected contribution to the line profile from the resolved companion is negligible.

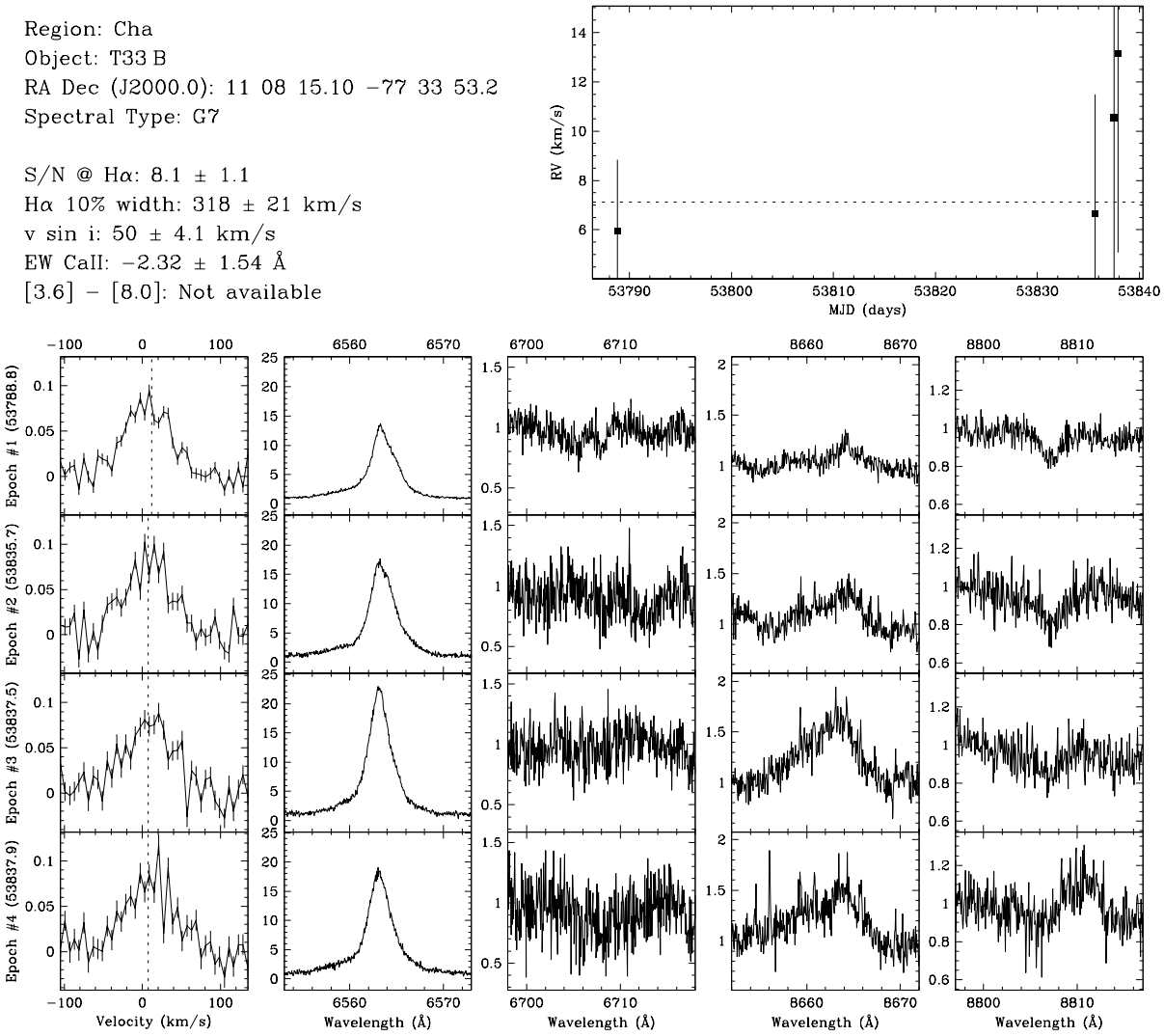

Figure 4.64 T33 B shows no evidence of a close companion. The star has a single-line profile, and the radial velocity scatter is not significant relative to the measurement uncertainties. The overall radial velocity deviates from that of the star forming region. We do not see evidence of Li-λ6708 absorption. However, cluster membership was previously established by Luhman (2004a) based on reddening, emission lines, and IR excess emssion. This target has been previously reported by Lafrenière et al. (2008) to have a resolved companion with a separation of $\sim$2.″434 ($\sim$340 AU) at a position angle of $\sim$284.°8, and an R-band flux ratio of $\sim$0.11 ($\Delta K \sim 1.93$). Given the separation, the expected contribution to the line profile from the resolved companion is negligible.

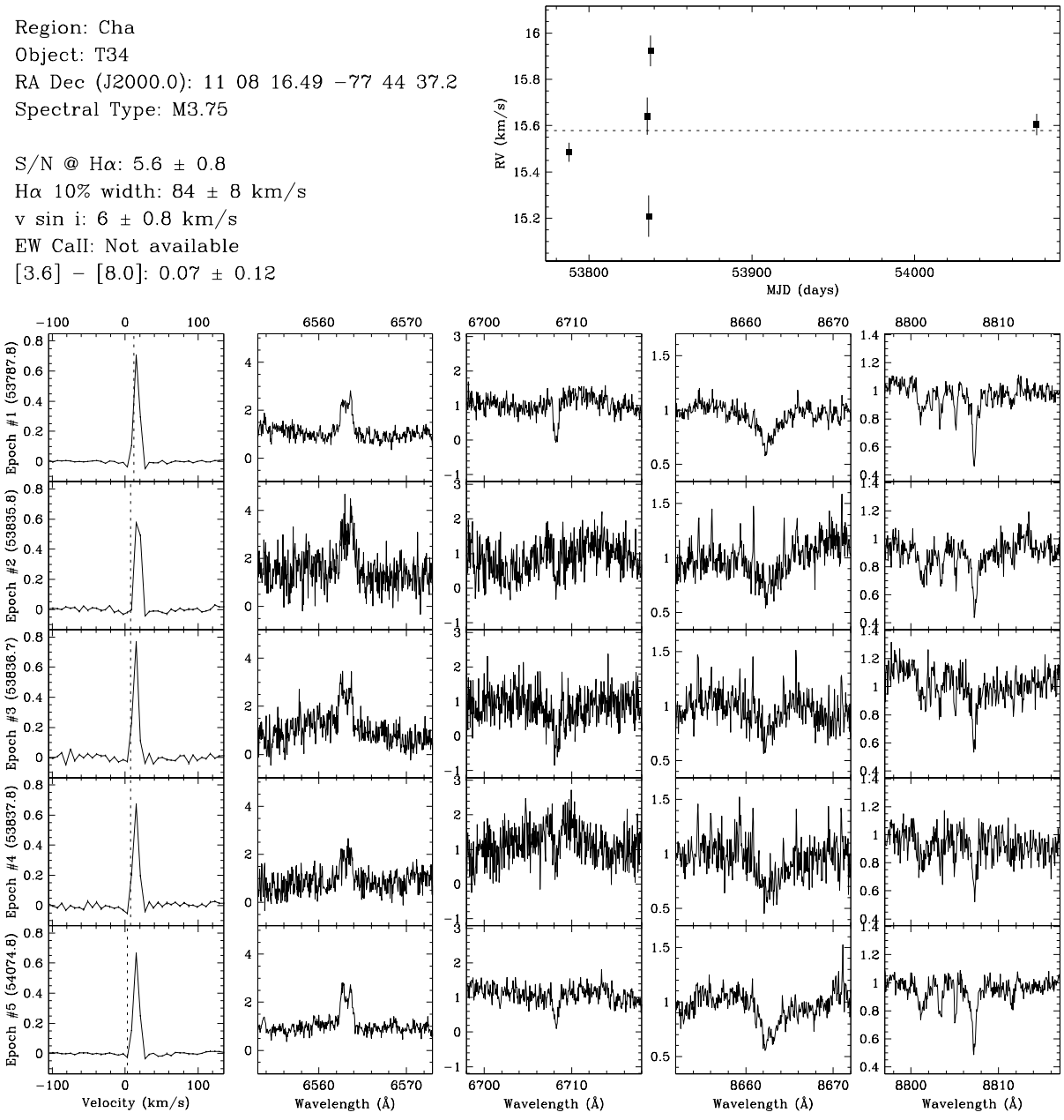

Figure 4.65 T34 shows no clear evidence of a close companion. The star has a single-line profile, and a radial velocity scatter not significant relative to variations observed within each observing run. The radial velocity scatter within the second observing run (epochs #2, #3 and #4) is consistent with that expected from systematic line profile variations, e.g. from star spots rotating with the star. The narrow emission lines in the spectra near 8662 Å are from the night sky. This target has been previously reported by Lafrenière et al. (2008) to have no resolved companions.

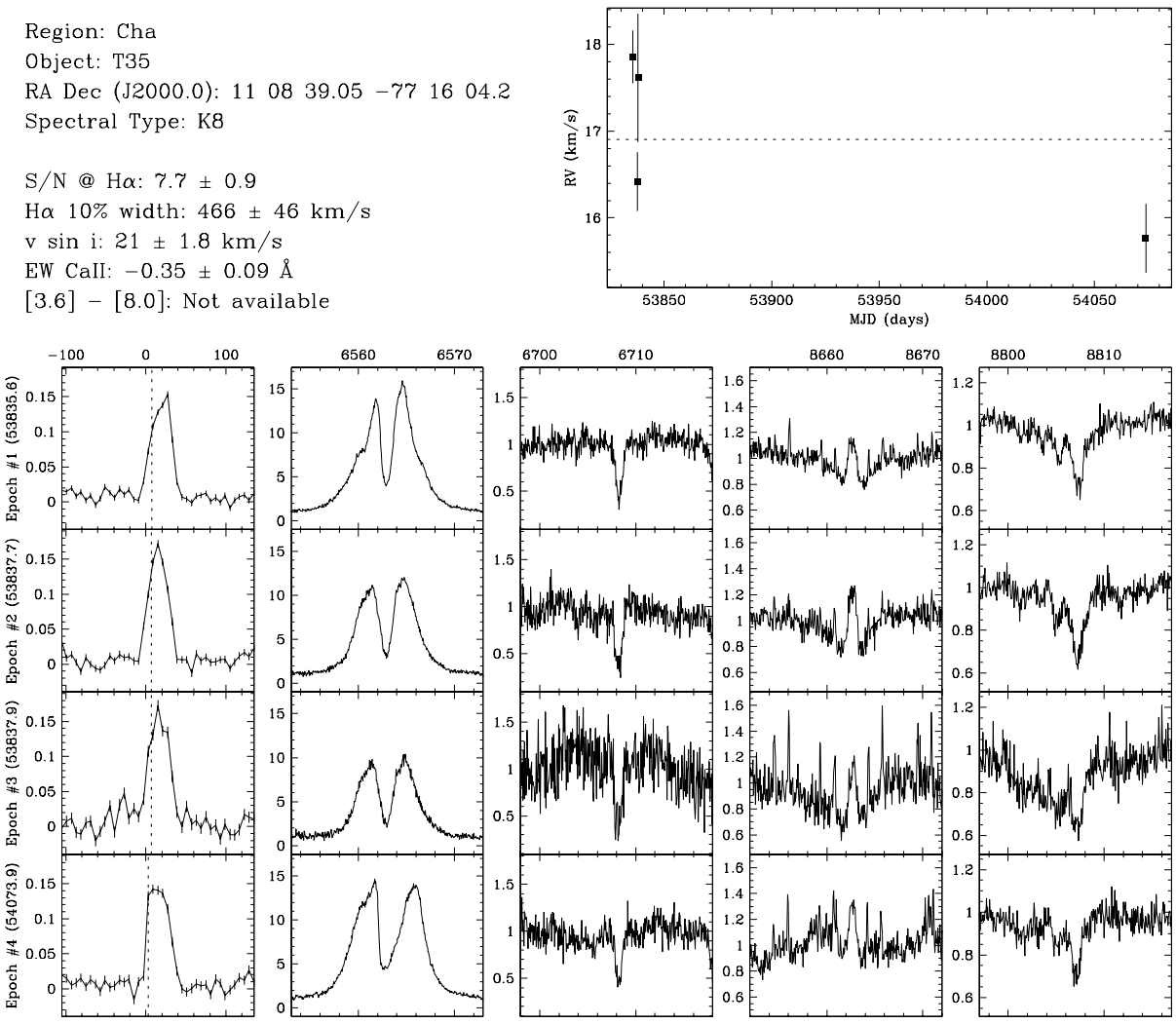

Figure 4.66 T35 shows no evidence of a close companion. The star has a single-line profile, and the radial velocity scatter is not significant relative to the measurement uncertainties. For epoch #3, the narrow emission lines in the spectrum near 8662 Å are from the night sky. This target has been previously reported by Lafrenière et al. (2008) to have no resolved companions.

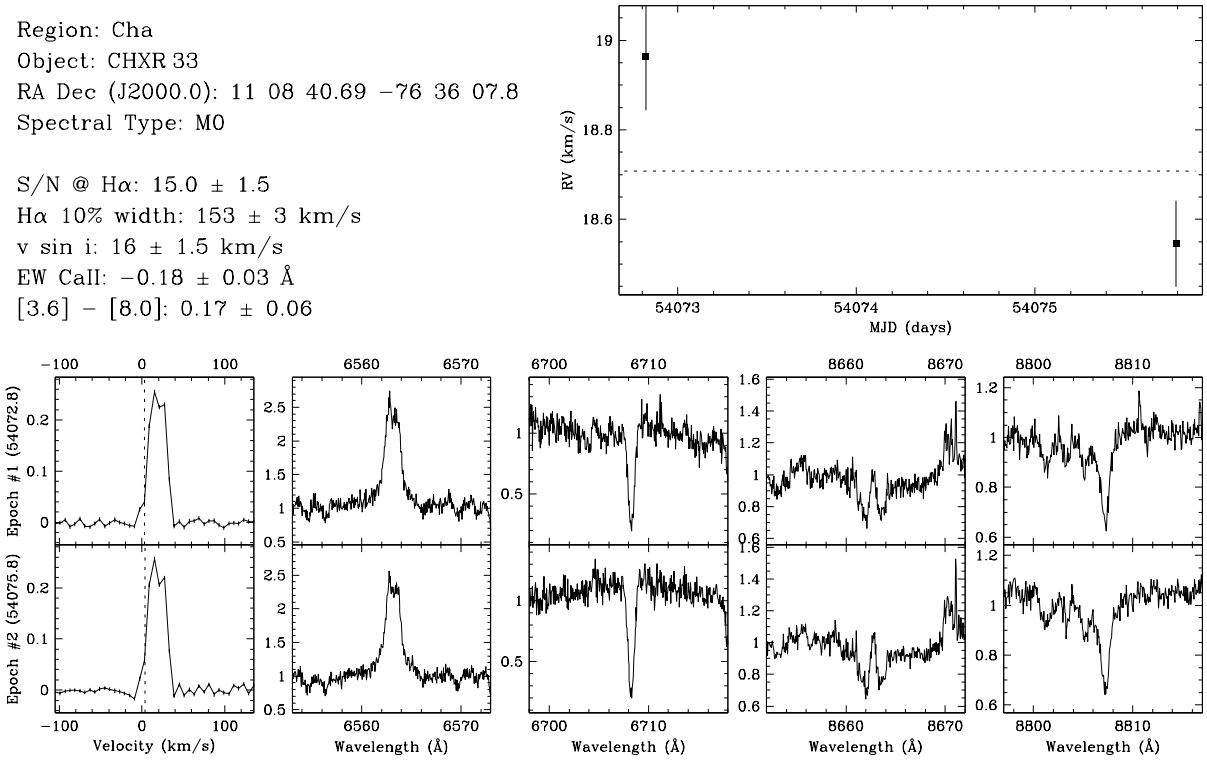

Figure 4.67 CHXR 33 has a single-line profile, and is therefore not an SB2. The radial velocity scatter over the short baseline available does not conclusively indicate if the target is an SB1 or a single star. The overall radial velocity deviates from that of the star forming region. However, cluster membership is supported by Li-λ6708 absorption. This target has been previously reported by Lafrenière et al. (2008) to have no resolved companions.

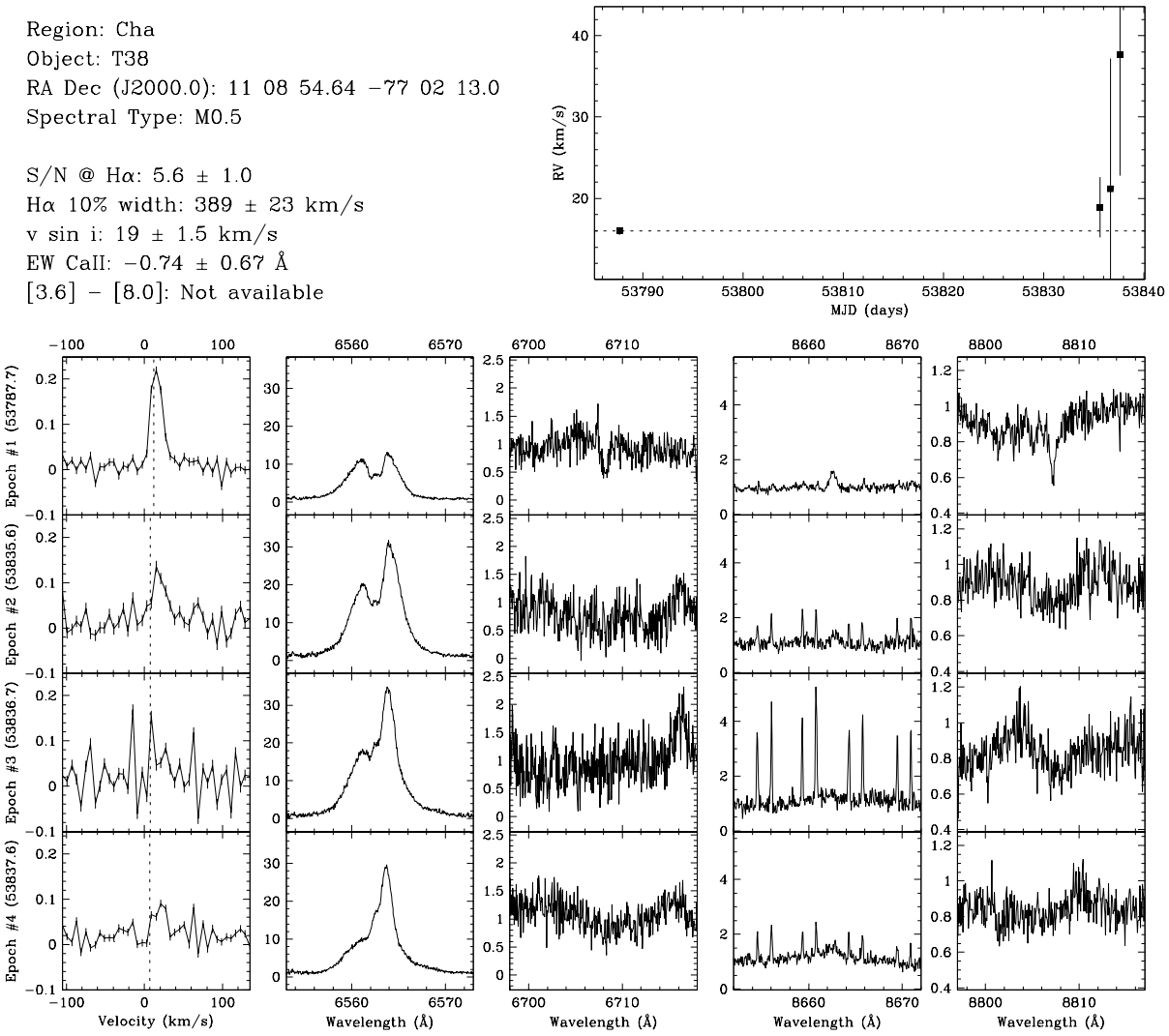

Figure 4.68 T38 shows no evidence of a close companion. The star has a single-line profile, and the radial velocity scatter is not significant relative to the measurement uncertainties. The two reliable radial velocity estimates for epochs #1 and #2 are stable. The narrow emission lines in the spectra near 8662 Å are from the night sky. This target has been previously reported by Lafrenière et al. (2008) to have no resolved companions.

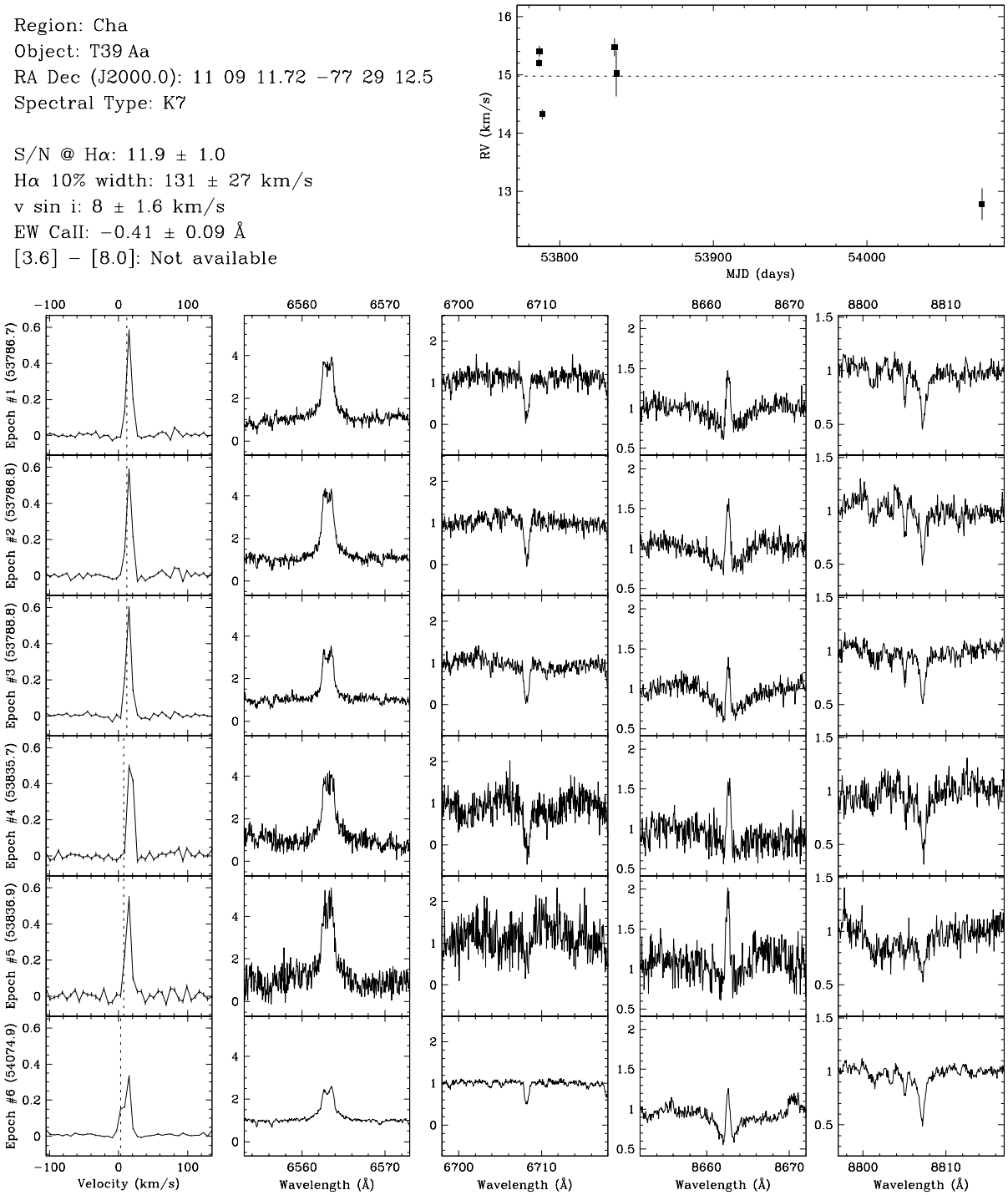

Figure 4.69 T39 Aa shows no clear evidence of a close companion. The star has a single-line profile, and a radial velocity scatter not significant relative to variations observed within each observing run. The radial velocity scatter within the first observing run (epochs #1, #2 and #3) and the second observing run (epochs #4, #5 and #6) are consistent with that expected from systematic line profile variations, e.g. from star spots rotating with the star. For epoch #6, the peak in the line profile at the observer's rest frame is due to dawn twilight, and likely biased the radial velocity estimate toward the observer's rest frame. This target has been previously reported by Lafrenière et al. (2008) to have a resolved companion (T39 Ab) with a separation of $\sim 1\farcs242$ (~ 170 AU) at a position angle of $\sim 19\fdg2$, and an R-band flux ratio of ~ 0.44 ($\Delta K \sim 0.31$). Given the separation, the expected contribution to the line profile from the resolved companion is small.

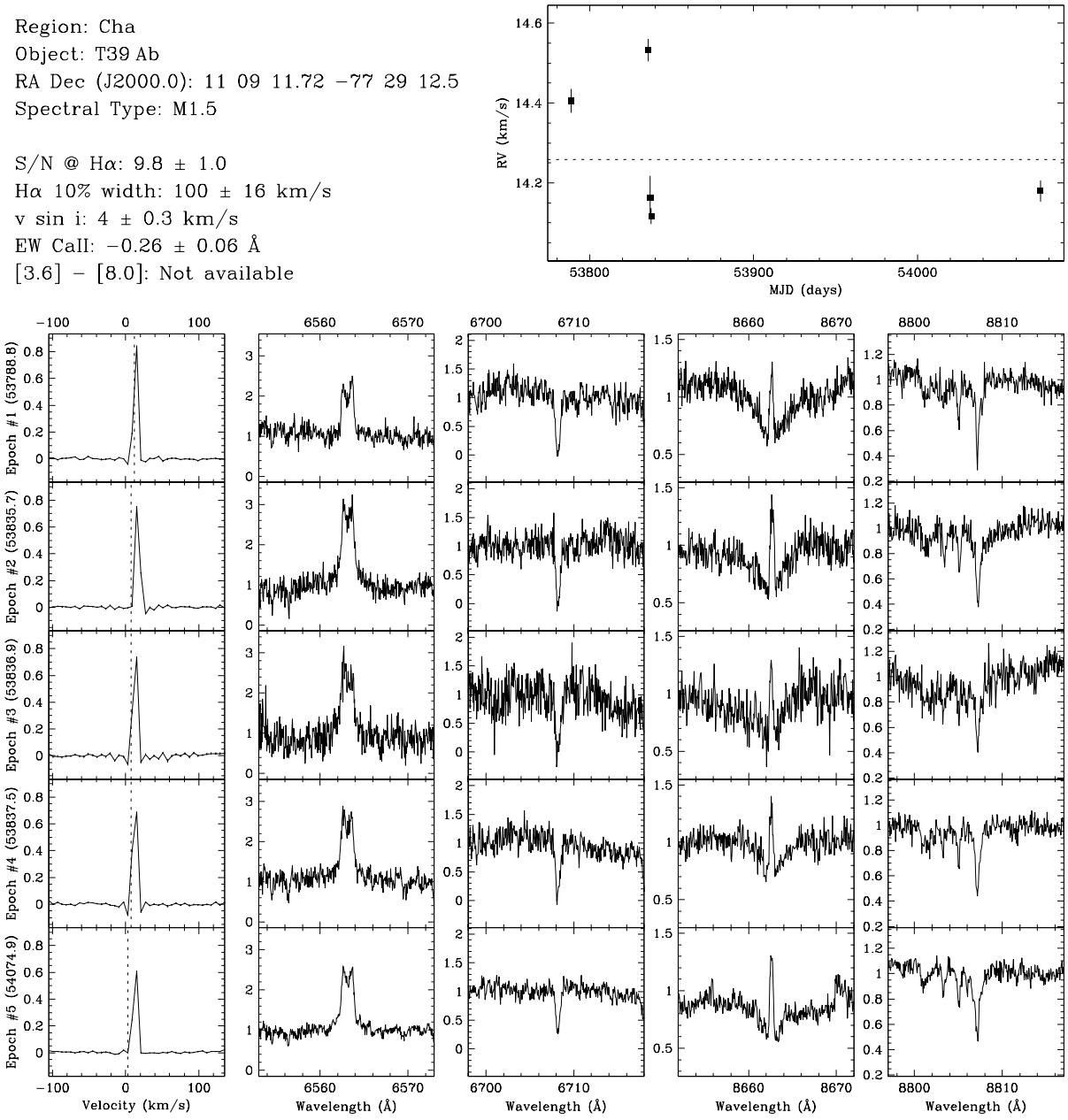

Figure 4.70 T39 Ab shows no clear evidence of a close companion. The star has a single-line profile, and a radial velocity scatter not significant relative to variations observed within each observing run. The radial velocity scatter within the second observing run (epochs #2, #3 and #4) is consistent with that expected from systematic line profile variations, e.g. from star spots rotating with the star. This target has been previously reported by Lafrenière et al. (2008) to be the secondary star of a resolved binary (T39 Aa,Ab) with a separation of $\sim$1.″242 ($\sim$170 AU) at a position angle of $\sim$19.°2, and an R-band flux ratio of $\sim$0.55 ($\Delta K \sim 0.31$). Given the separation, the expected contribution to the line profile from the resolved companion is small.

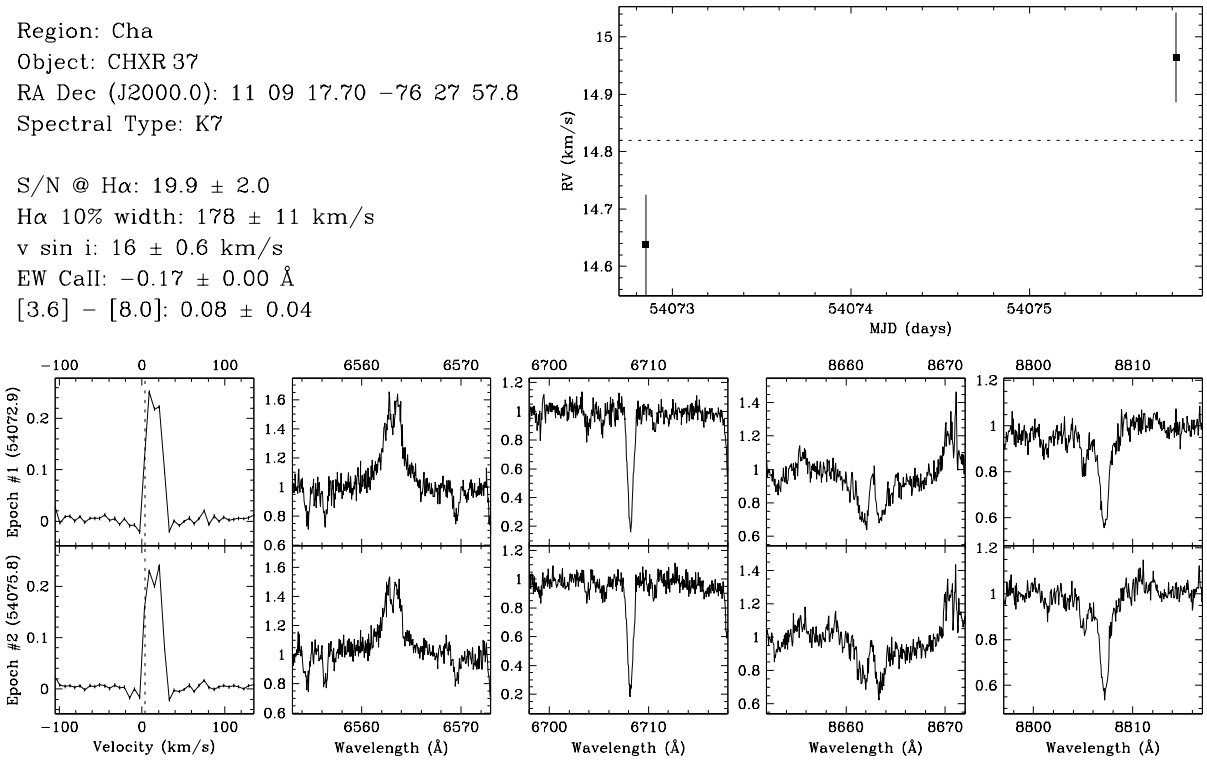

Figure 4.71 CHXR 37 has a single-line profile, and is therefore not an SB2. The radial velocity scatter over the short baseline available does not conclusively indicate if the target is an SB1 or a single star. This target has been previously reported by Lafrenière et al. (2008) to have a resolved companion with a separation of $\sim 0\farcs079$ (~ 11 AU) at a position angle of $\sim 81°$, and an R-band flux ratio of ~ 0.08 ($\Delta K \sim 1.07$). Given the flux ratio, the expected contribution to the line profile from the resolved companion is small.

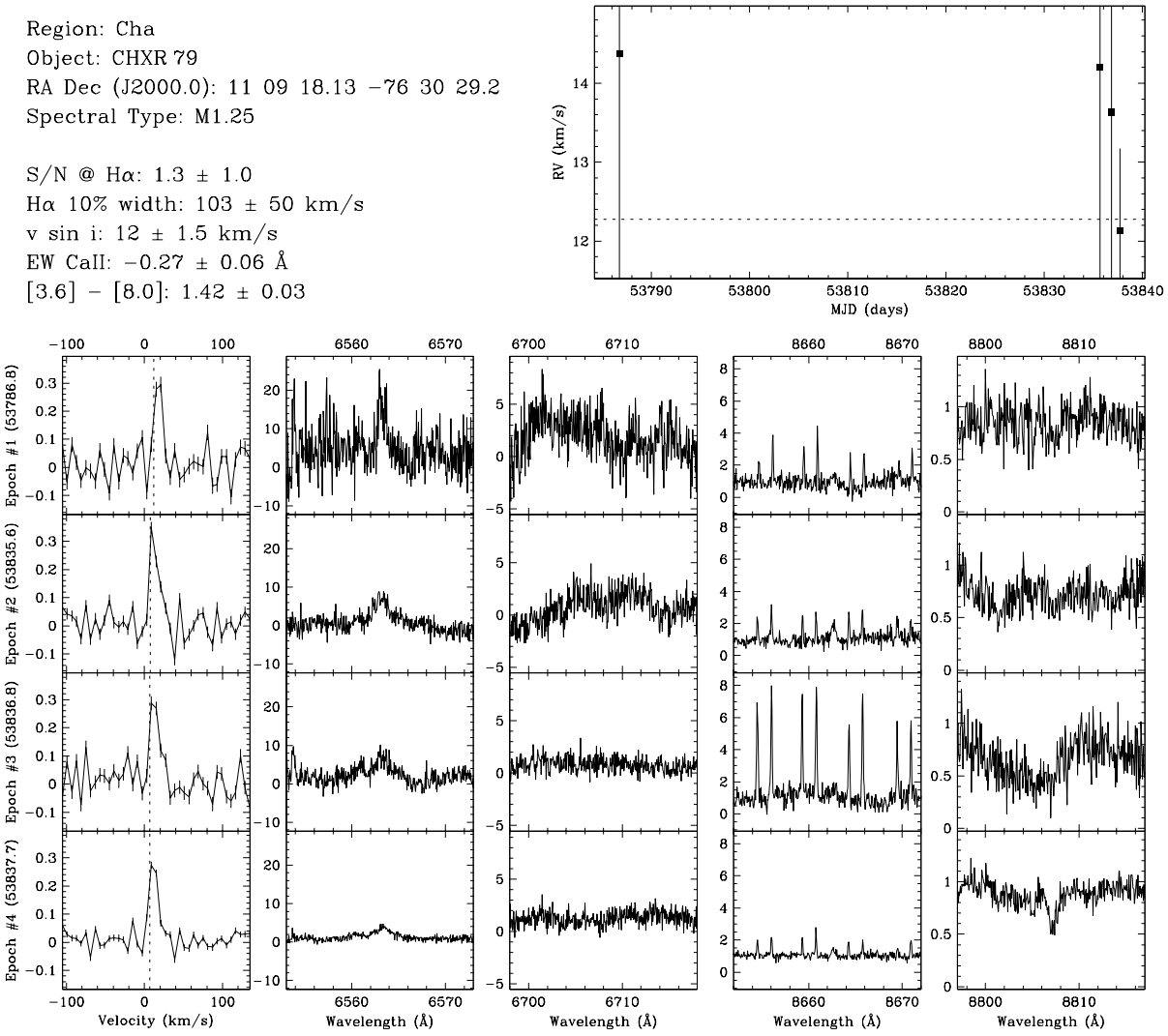

Figure 4.72 CHXR 79 shows no evidence of a close companion. The star has a single-line profile, and the radial velocity scatter is not significant relative to the measurement uncertainties. The overall radial velocity deviates from that of the star forming region. We do not see evidence of Li-λ6708 absorption. However, cluster membership was previously established by Luhman (2004a) based on reddening, emission lines, and IR excess emssion. The narrow emission lines in the spectra near 8662 Å are from the night sky. This target has been previously reported by Lafrenière et al. (2008) to have a resolved companion with a separation of $\sim$0.″885 ($\sim$120 AU) at a position angle of $\sim$211.°2, and an R-band flux ratio of $\sim$0.01 ($\Delta K \sim 2.45$). Given the flux ratio, the expected contribution to the line profile from the resolved companion is negligible.

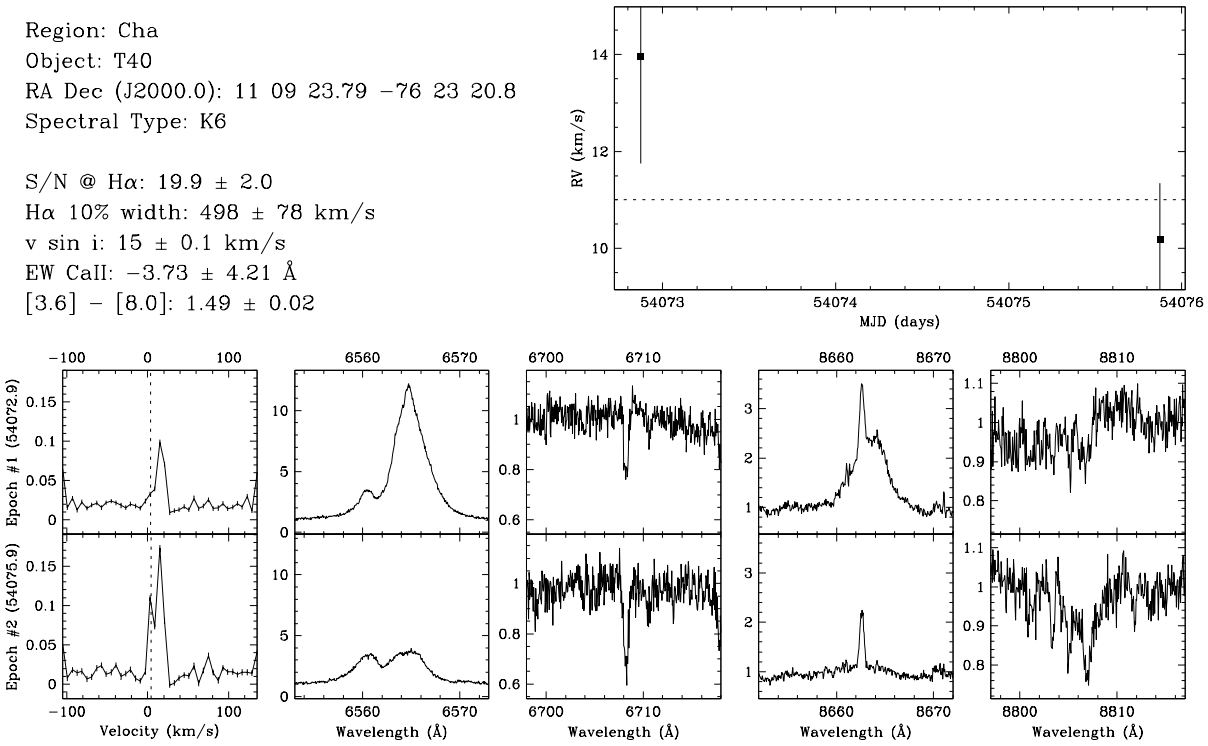

Figure 4.73 T40 has a single-line profile, and is therefore not an SB2. The radial velocity scatter over the short baseline available does not conclusively indicate if the target is an SB1 or a single star. The overall radial velocity deviates from that of the star forming region. However, cluster membership is supported by Li-λ6708 absorption. The small bulge and the peak in the line profiles at the observer's rest frame is due to dawn twilight, and likely biased the radial velocity estimates toward the observer's rest frame. This target has been previously reported by Lafrenière et al. (2008) to have no resolved companions.

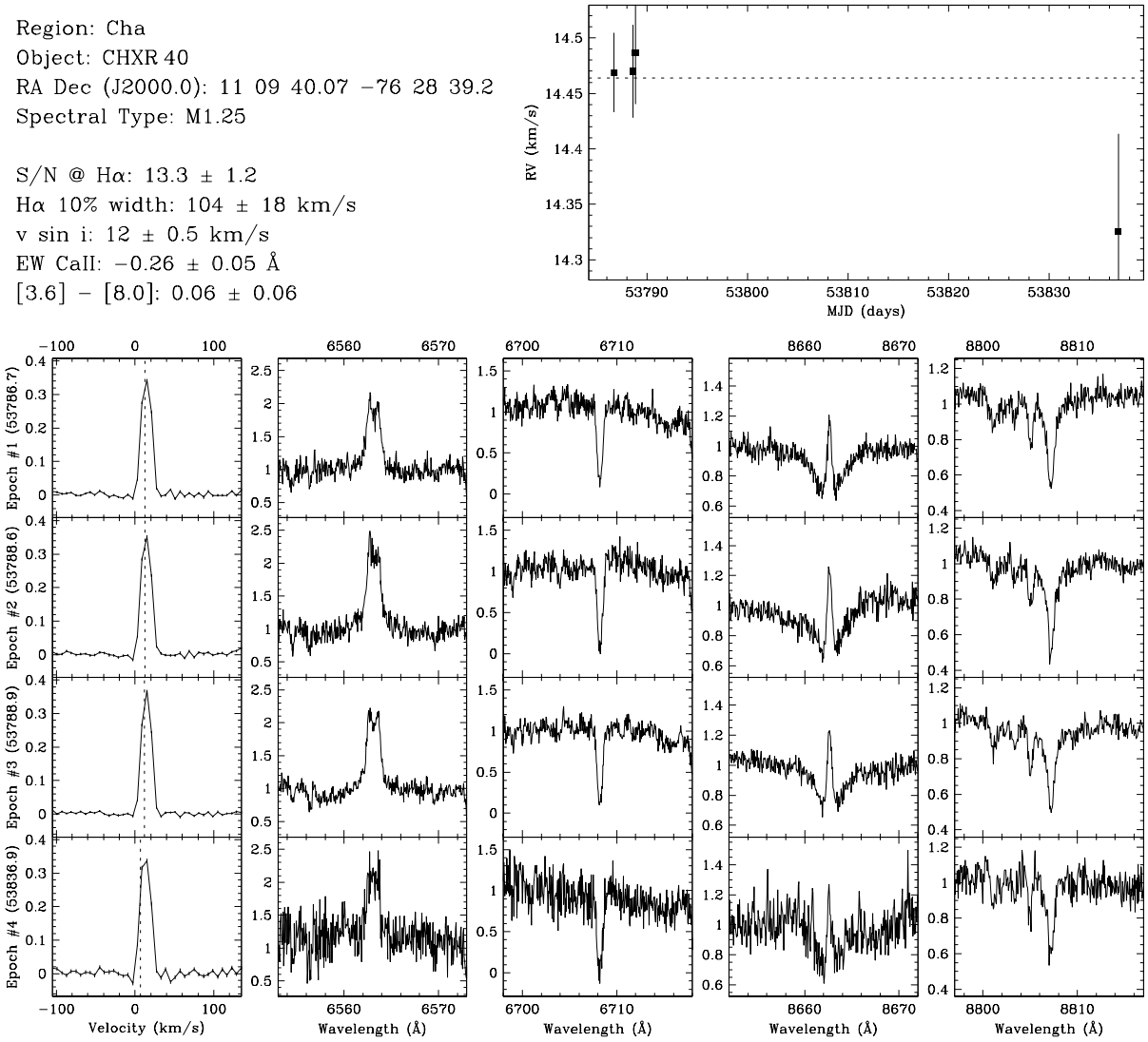

Figure 4.74 CHXR 40 shows no evidence of a close companion. The star has a single-line profile, and the radial velocity scatter is not significant relative to the measurement uncertainties. This target has been previously reported by Lafrenière et al. (2008) to have a resolved companion with a separation of $\sim 0\farcs151$ (~ 21 AU) at a position angle of $\sim 66\fdg1$, and an R-band flux ratio of ~ 0.83 ($\Delta K \sim 0.12$). However, there is no clear evidence in the line profile of the resolved companion. Since the resolved companion has an expected circular orbital speed of $\sim 6\,\mathrm{km\,s^{-1}}$, a second profile could be obscured if the primary star and the resolved companion have similar projected rotational velocities.

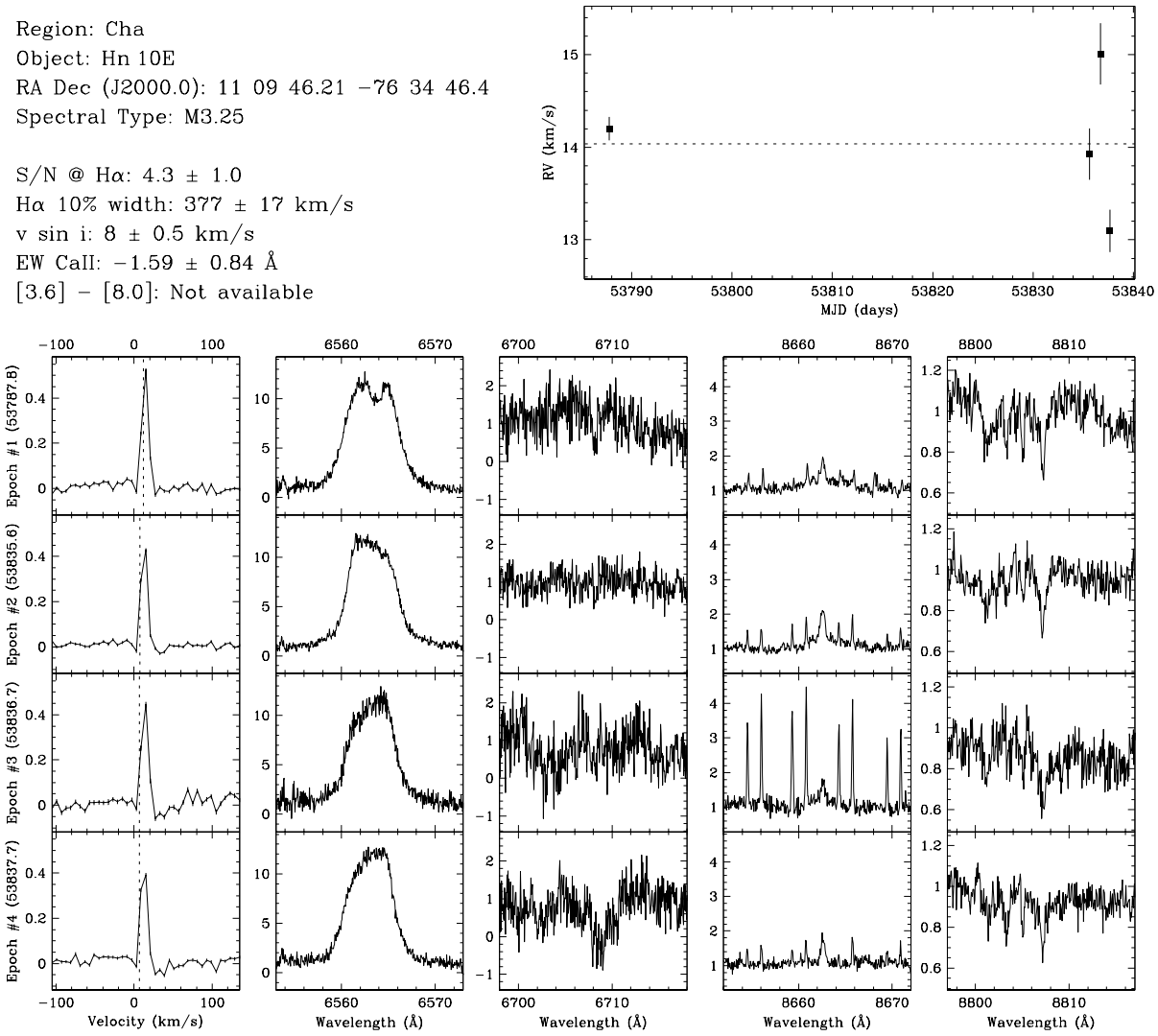

Figure 4.75 Hn 10E shows no clear evidence of a close companion. The star has a single-line profile, and a radial velocity scatter not significant relative to variations observed within each observing run. The radial velocity scatter within the second observing run (epochs #2, #3 and #4) is large but consistent with that expected from systematic line profile variations, e.g. from star spots rotating with the star. The narrow emission lines in the spectra, especially for epoch #3, near 8662 Å are from the night sky. This target has been previously reported by Lafrenière et al. (2008) to have no resolved companions.

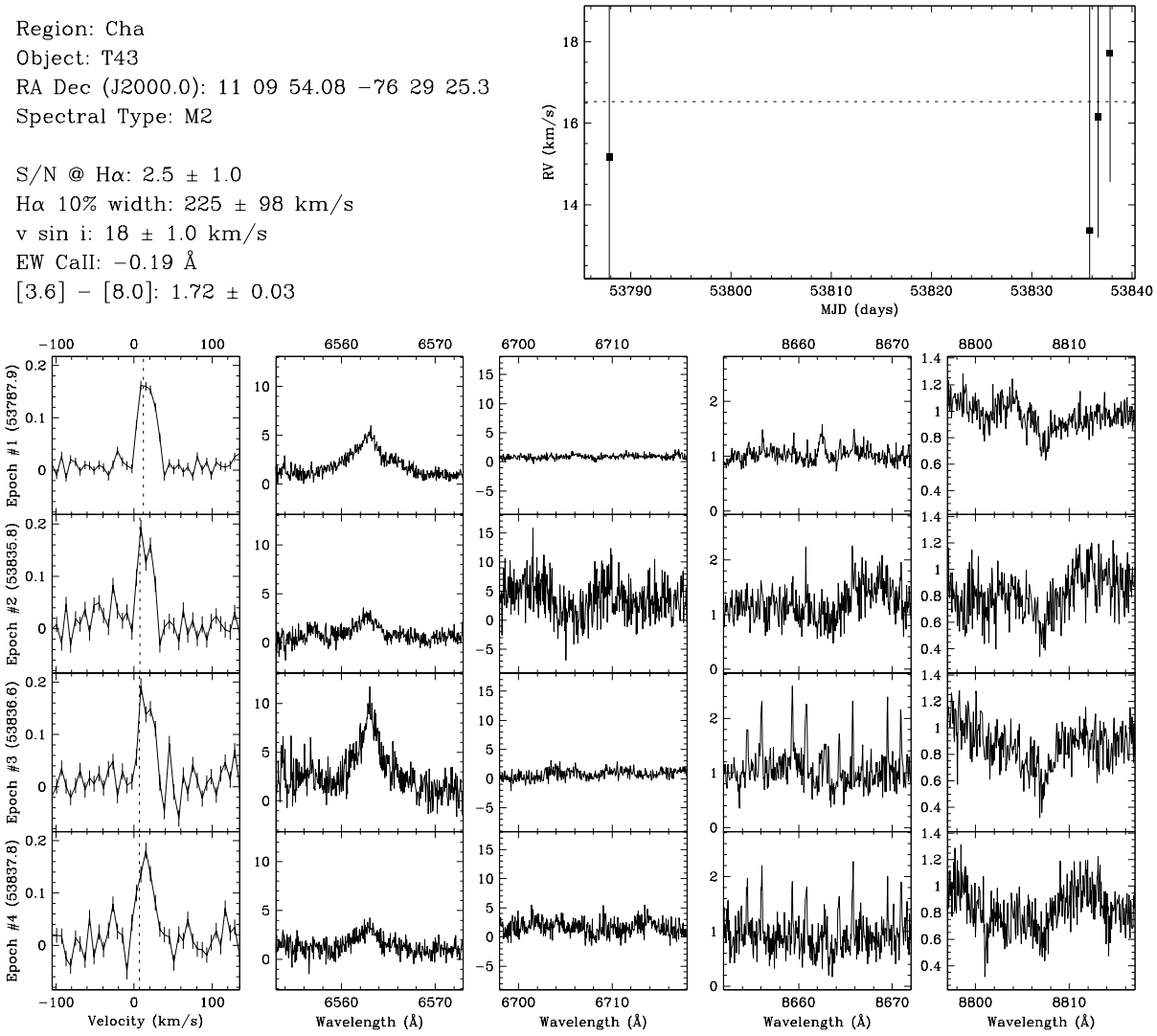

Figure 4.76 T43 shows no evidence of a close companion. The star has a single-line profile, and the radial velocity scatter is not significant relative to the measurement uncertainties. The narrow emission lines in the spectra near 8662 Å are from the night sky. This target has been previously reported by Lafrenière et al. (2008) to have a resolved companion with a separation of $\sim 0\farcs796$ (~ 110 AU) at a position angle of $\sim 352\fdg2$, and an R-band flux ratio of ~ 0.02 ($\Delta K \sim 1.41$). Given the flux ratio, the expected contribution to the line profile from the resolved companion is negligible.

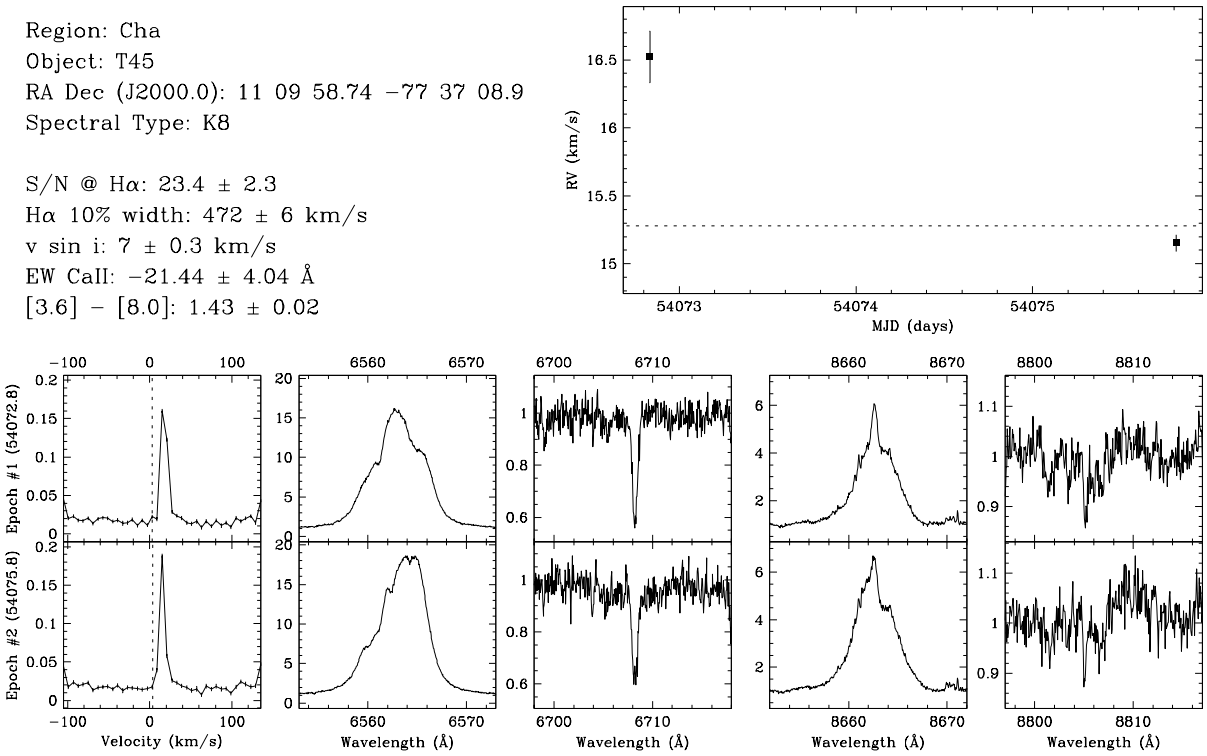

Figure 4.77 T45 has a single-line profile, and is therefore not an SB2. The radial velocity scatter over the short baseline available does not conclusively indicate if the target is an SB1 or a single star. The radial velocity displacement is consistent with variations caused by the presence of star spots rotating with the star. The spectrum is heavily veiled, and we derived the radial velocities from fits to the line profile rather than from direct fits to the spectra (see §4.4.2). This target has been previously reported by Lafrenière et al. (2008) to have a resolved companion with a separation of $\sim 0\farcs752$ (~ 110 AU) at a position angle of $\sim 52\fdg2$, and an R-band flux ratio of $\lesssim 0.01$ ($\Delta K \sim 2.67$). Given the flux ratio, the expected contribution to the line profile from the resolved companion is negligible.

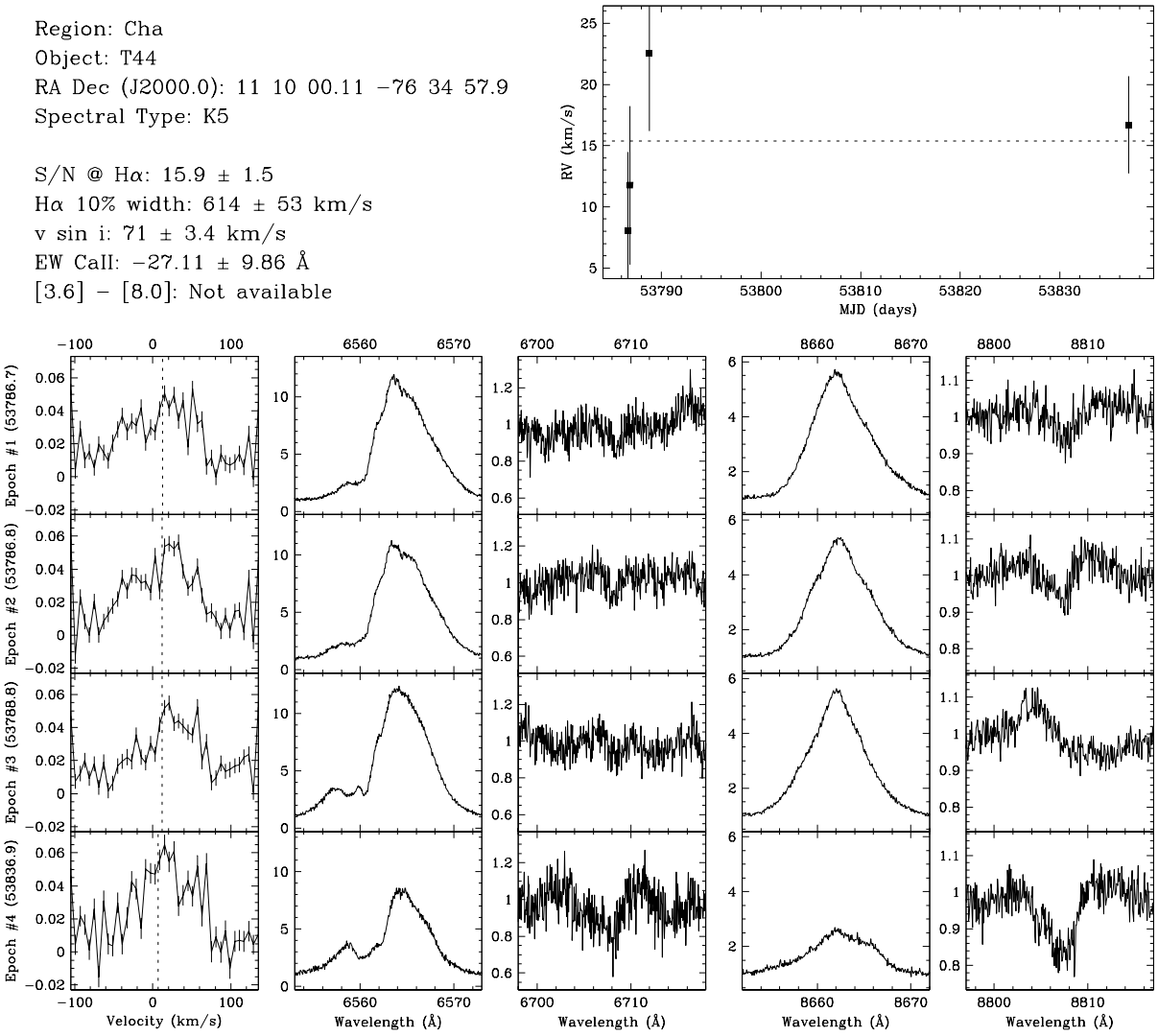

Figure 4.78 T44 shows no evidence of a close companion. The star has a single-line profile, and the radial velocity scatter is not significant relative to the measurement uncertainties. The spectrum is heavily veiled, and we derived the radial velocities from fits to the line profile rather than from direct fits to the spectra (see §4.4.2). The radial velocity scatter within the first observing run (epochs #1, #2 and #3) is consistent with that expected from systematic line profile variations, e.g. from star spots rotating with the star. This target has been previously reported by Lafrenière et al. (2008) to have no resolved companions.

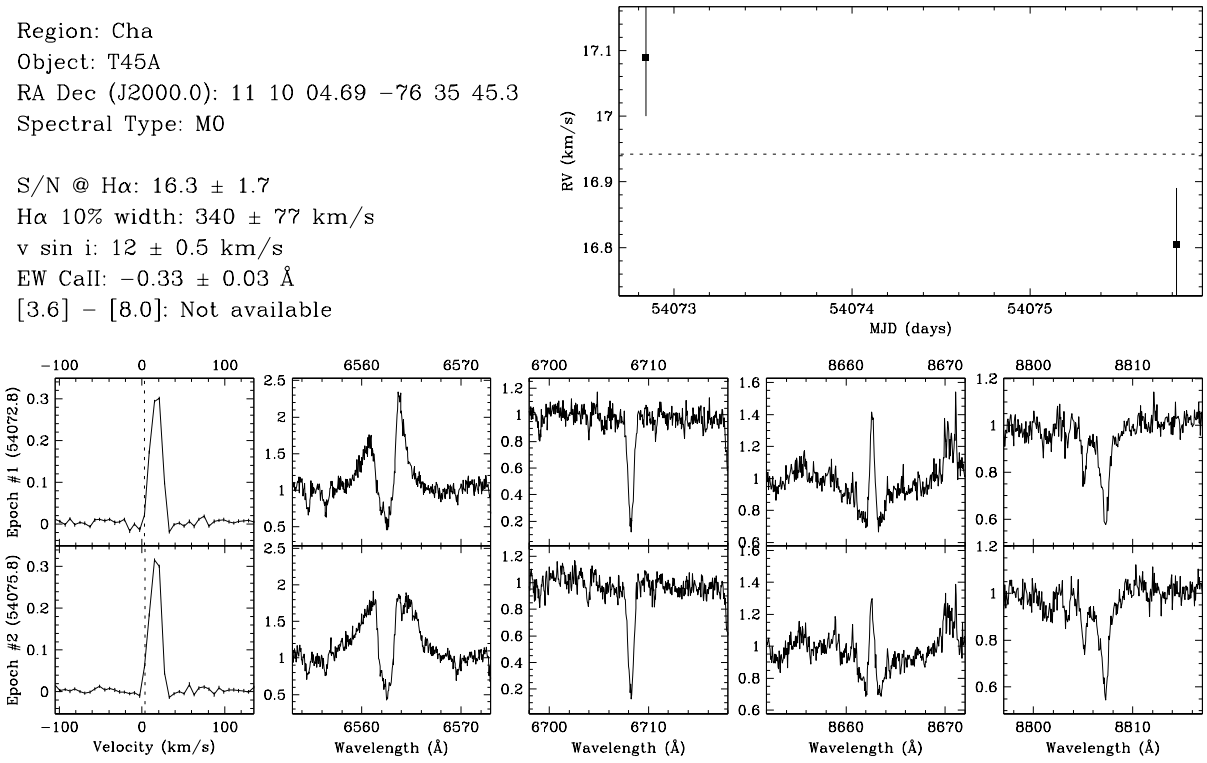

Figure 4.79 T45A has a single-line profile, and is therefore not an SB2. The radial velocity scatter over the short baseline available does not conclusively indicate if the target is an SB1 or a single star. This target has been previously reported by Lafrenière et al. (2008) to have no resolved companions.

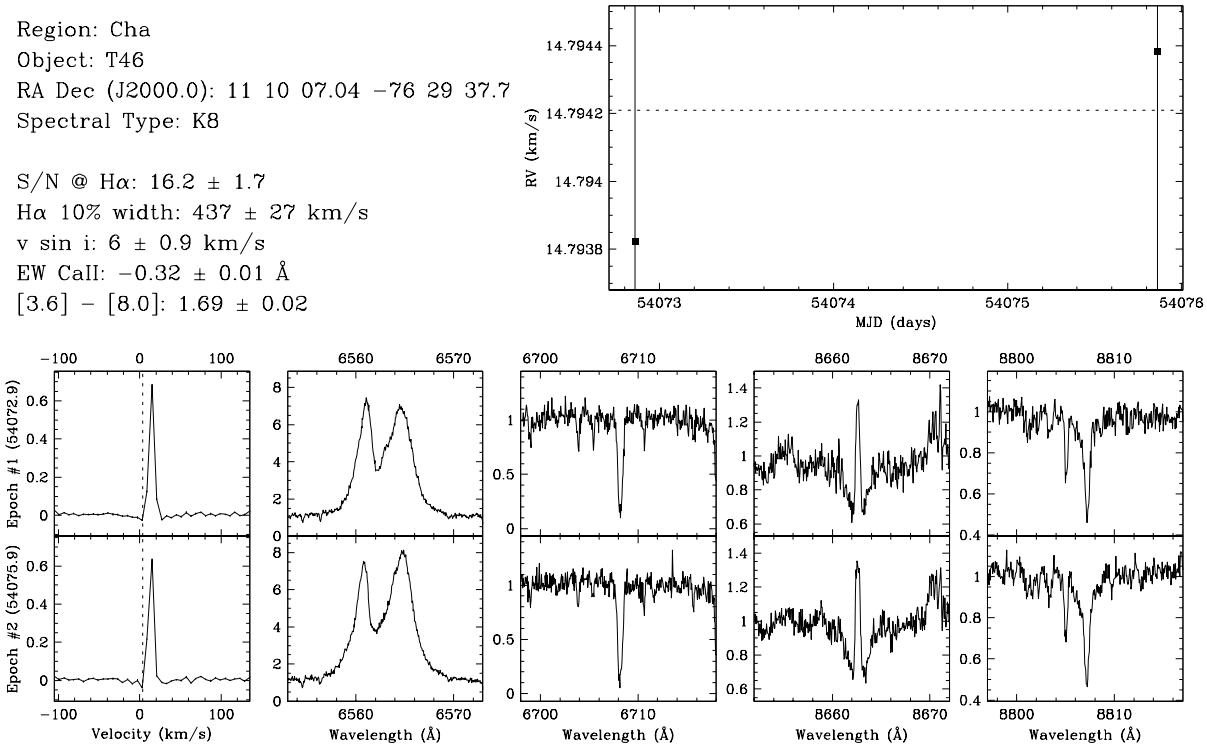

Figure 4.80 T46 has a single-line profile, and is therefore not an SB2. The radial velocity scatter over the short baseline available does not conclusively indicate if the target is an SB1 or a single star. This target has been previously reported by Lafrenière et al. (2008) to have a resolved companion with a separation of $\sim 0\farcs123$ (~ 17 AU) at a position angle of $\sim 241\fdg6$, and an R-band flux ratio of $\sim$0.01 ($\Delta K \sim 1.57$). Given the flux ratio, the expected contribution to the line profile from the resolved companion is negligible.

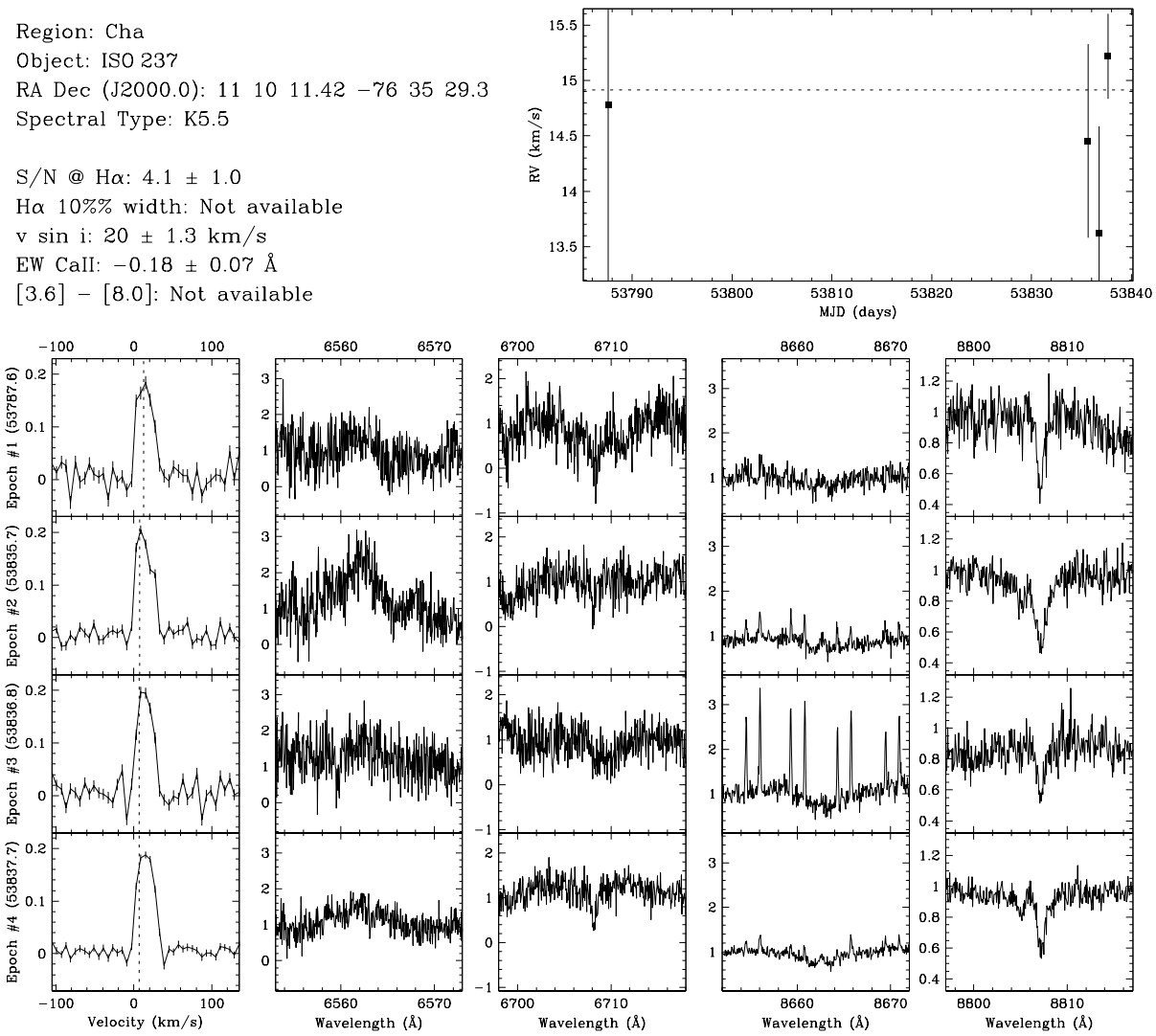

Figure 4.81 ISO 237 shows no evidence of a close companion. The star has a single-line profile, and the radial velocity scatter is not significant relative to the measurement uncertainties. The narrow emission lines in the spectra, especially for epoch #3, near 8662 Å are from the night sky. This target has been previously reported by Lafrenière et al. (2008) to have no resolved companions.

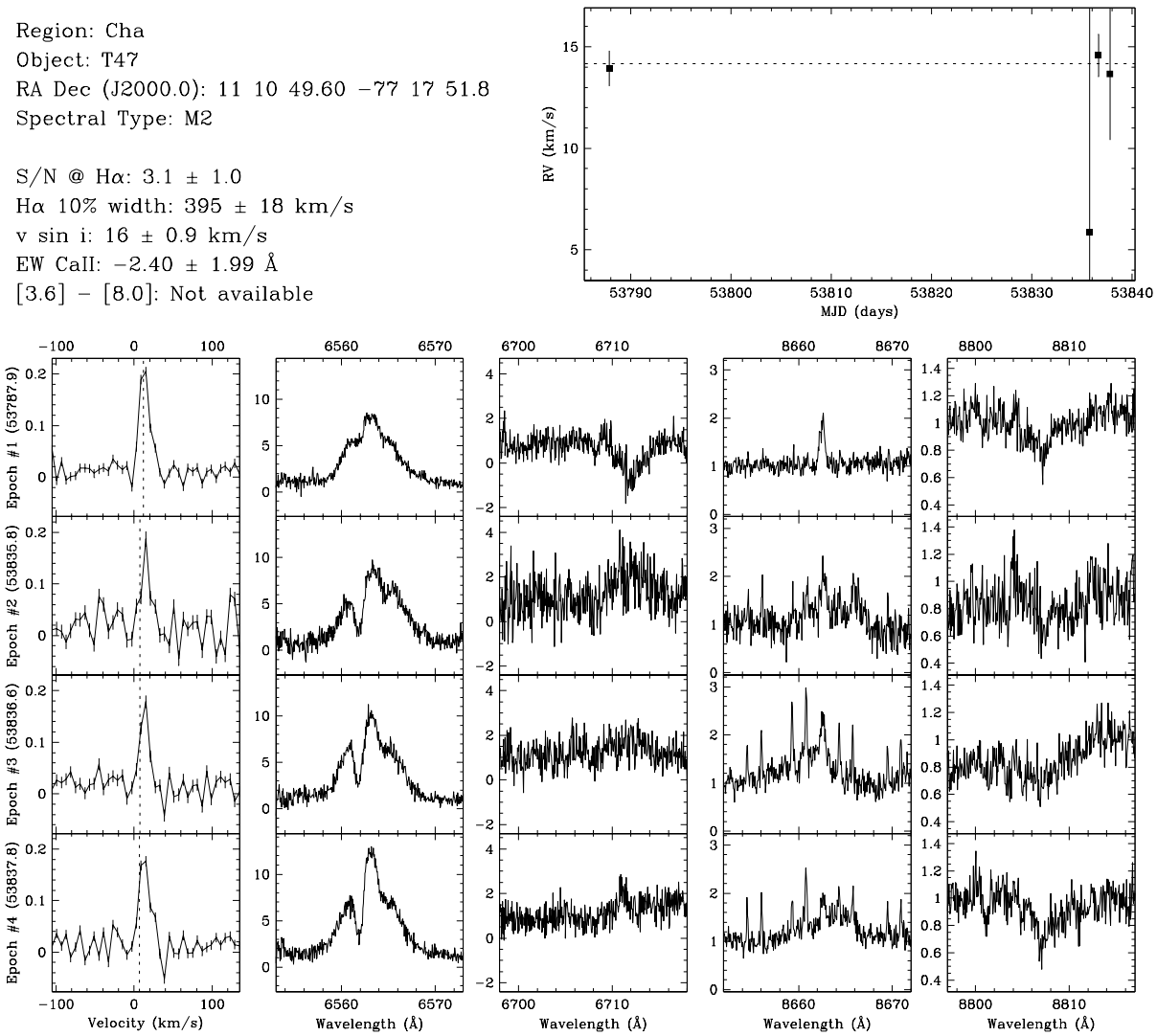

Figure 4.82 T47 shows no evidence of a close companion. The star has a single-line profile, and the radial velocity scatter is not significant relative to the measurement uncertainties. The narrow emission lines in the spectra near 8662 Å are from the night sky. This target has been previously reported by Lafrenière et al. (2008) to have no resolved companions.

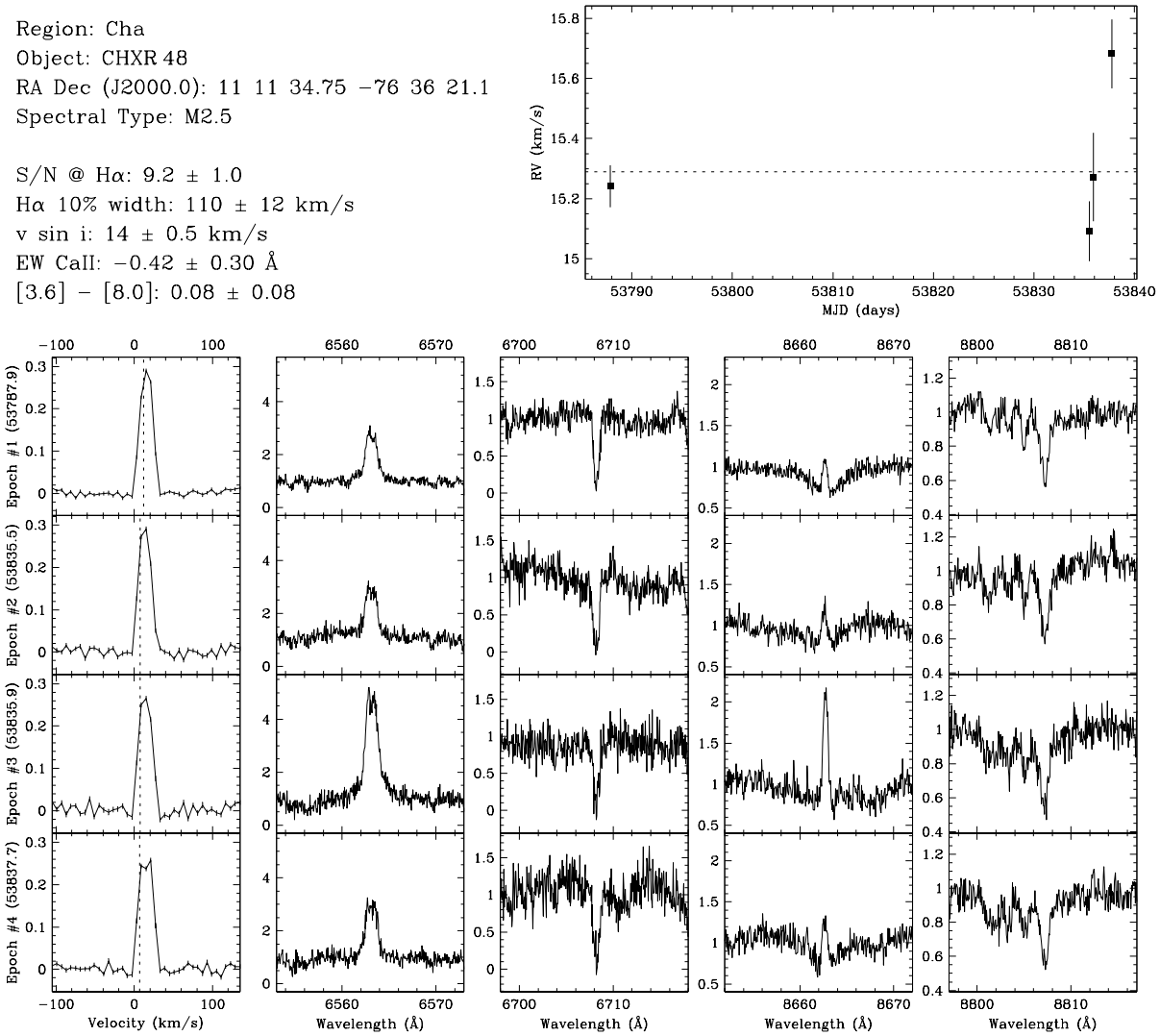

Figure 4.83 CHXR 48 shows no evidence of a close companion. The star has a single-line profile, and the radial velocity scatter is not significant relative to the measurement uncertainties. This target has been previously reported by Lafrenière et al. (2008) to have no resolved companions.

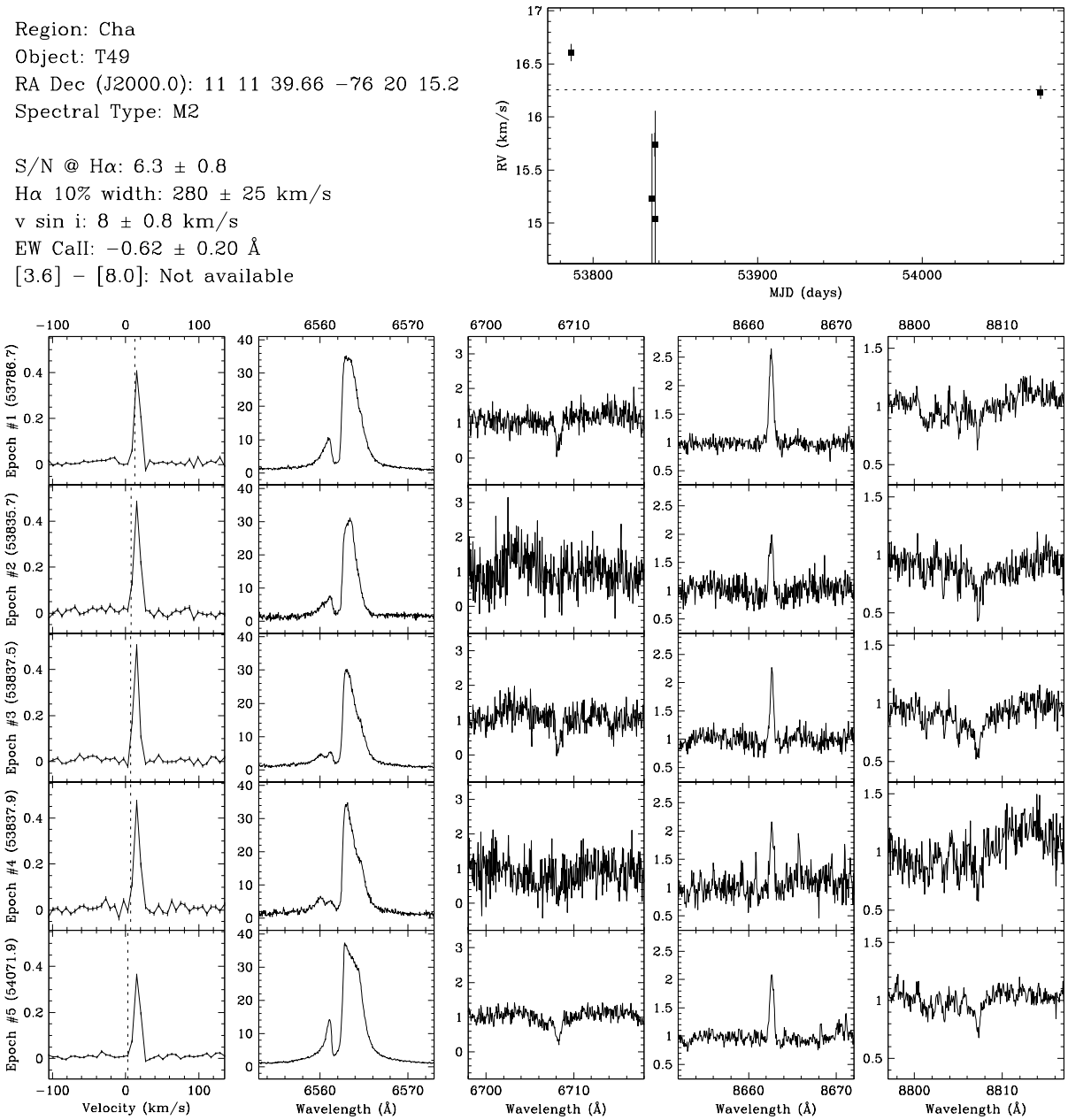

Figure 4.84 T49 shows no clear evidence of a close companion. The star has a single-line profile, and a radial velocity scatter not significant relative to variations observed within each observing run. The radial velocity scatter within the second observing run (epochs #2, #3 and #4) is consistent with that expected from systematic line profile variations, e.g. from star spots rotating with the star. This target has been previously reported by Lafrenière et al. (2008) to have no resolved companions.

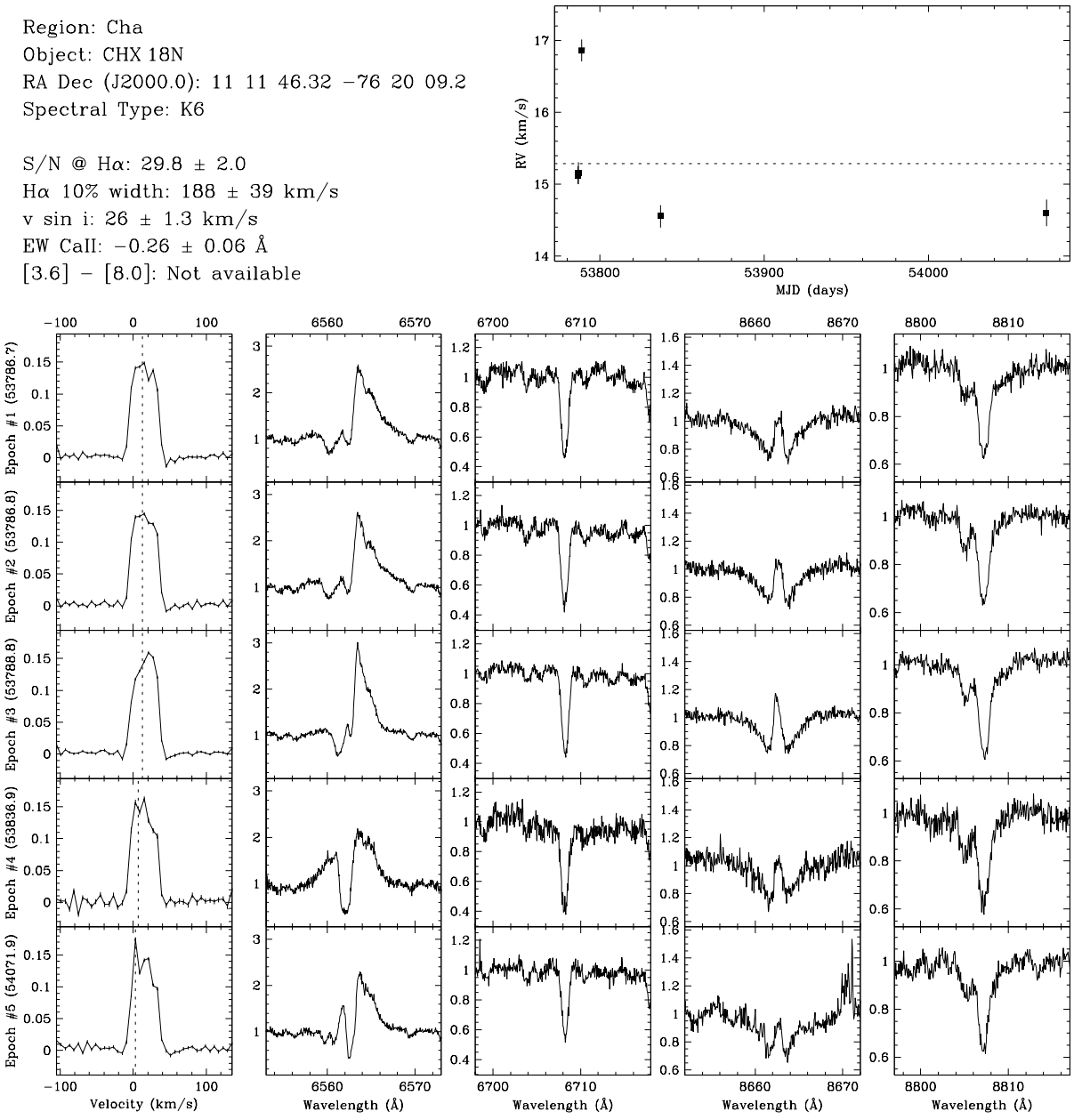

Figure 4.85 CHX 18N shows no clear evidence of a close companion. The star has a single-line profile, and a radial velocity scatter not significant relative to variations observed within each observing run. For epochs #3, #4 and #5, the line profiles show weak evidence for a double source. The radial velocity scatter within the first observing run (epochs #1, #2 and #3) is consistent with that expected from systematic line profile variations, e.g. from star spots rotating with the star. For epoch #5, the peak in the line profile at the observer's rest frame is due to dawn twilight, and likely biased the radial velocity estimate toward the observer's rest frame. This target has been previously reported by Lafrenière et al. (2008) to have no resolved companions.

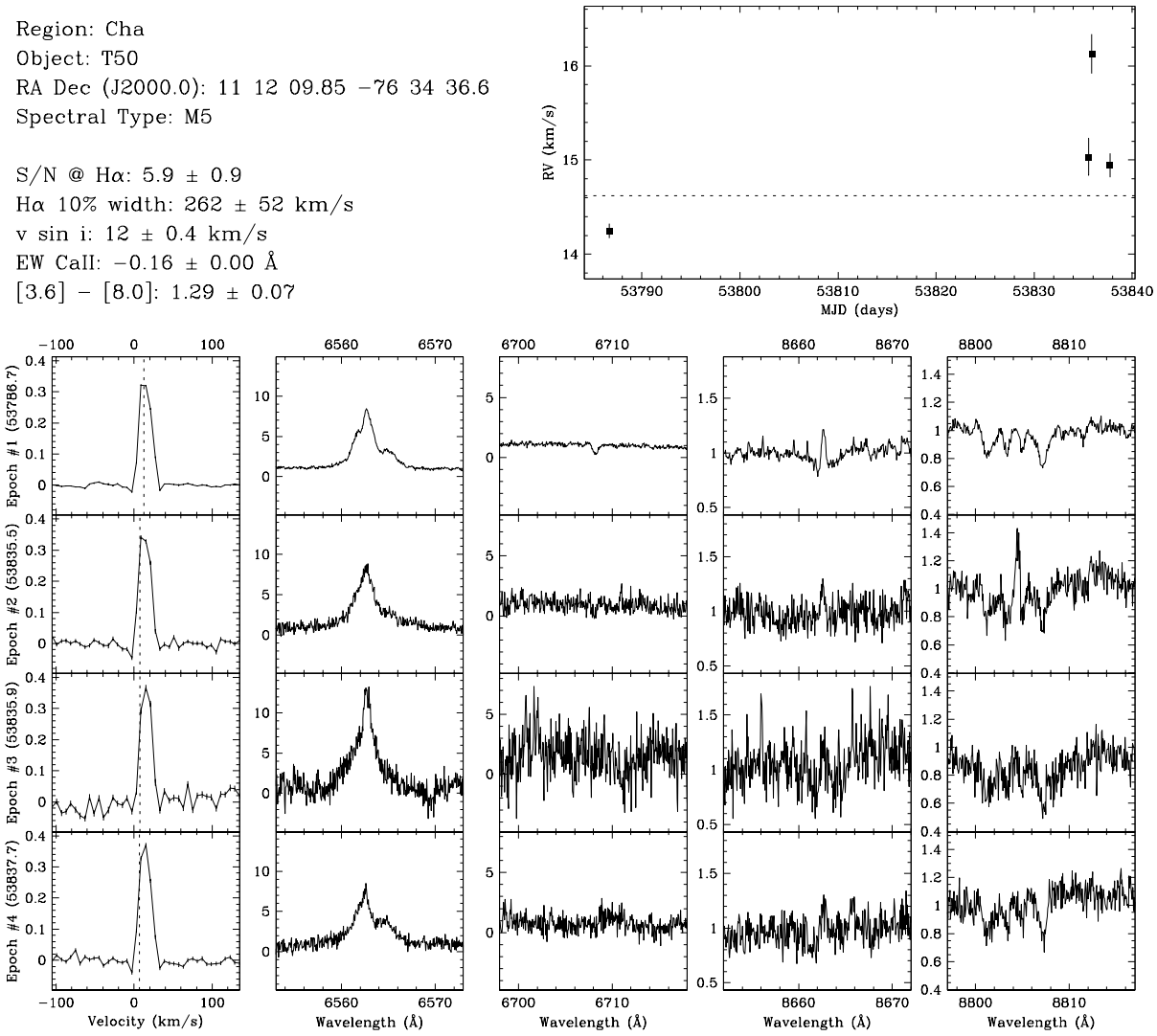

Figure 4.86 T50 shows no clear evidence of a close companion. The star has a single-line profile, and a radial velocity scatter not significant relative to variations observed within each observing run. The radial velocity scatter within the second observing run (epochs #2, #3 and #4) is consistent with that expected from systematic line profile variations, e.g. from star spots rotating with the star. This target has been previously reported by Lafrenière et al. (2008) to have no resolved companions.

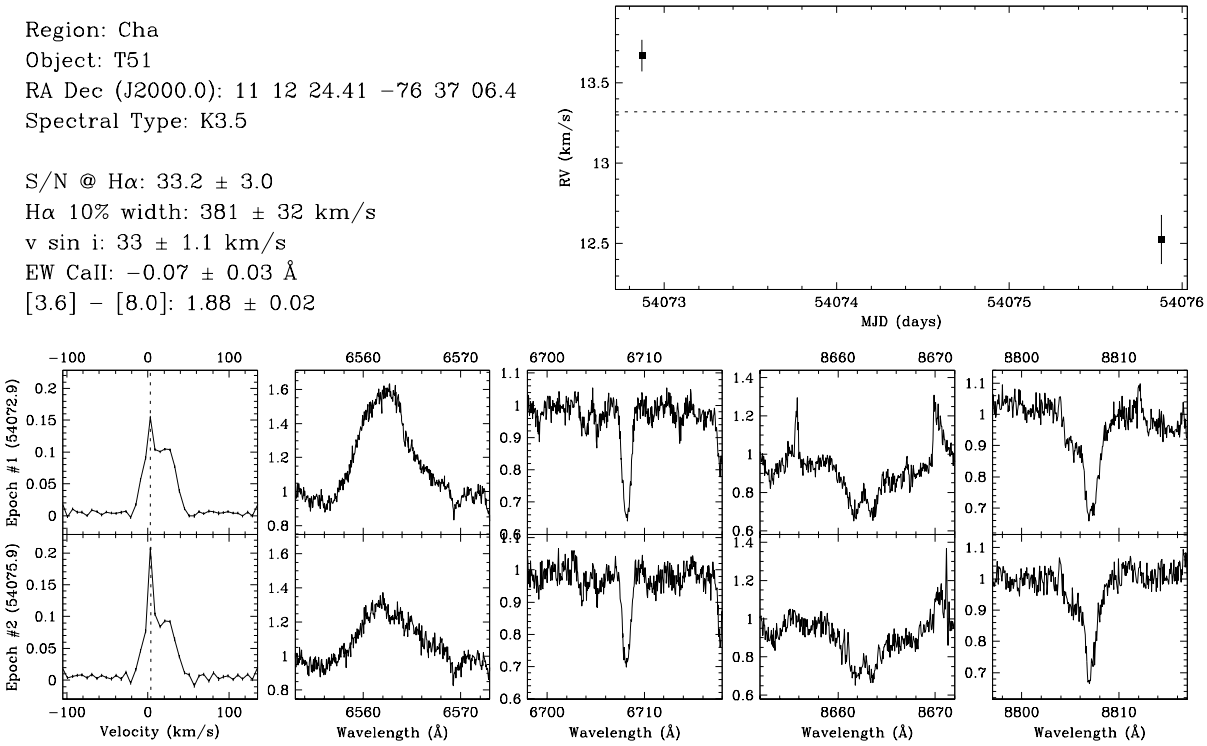

Figure 4.87 T51 has a single-line profile, and is therefore not an SB2. The radial velocity scatter over the short baseline available does not conclusively indicate if the target is an SB1 or a single star. The strong peaks in the line profiles at the observer's rest frame are due to dawn twilight, and likely biased the radial velocity estimates toward the observer's rest frame. This target has been previously reported by Lafrenière et al. (2008) to have a resolved companion with a separation of $\sim 1\farcs977$ (~ 280 AU) at a position angle of $\sim 162\fdg5$, and an R-band flux ratio of $\lesssim 0.01$ ($\Delta K \sim 2.35$). Given the flux ratio and separation, the expected contribution to the line profile from the resolved companion is negligible.

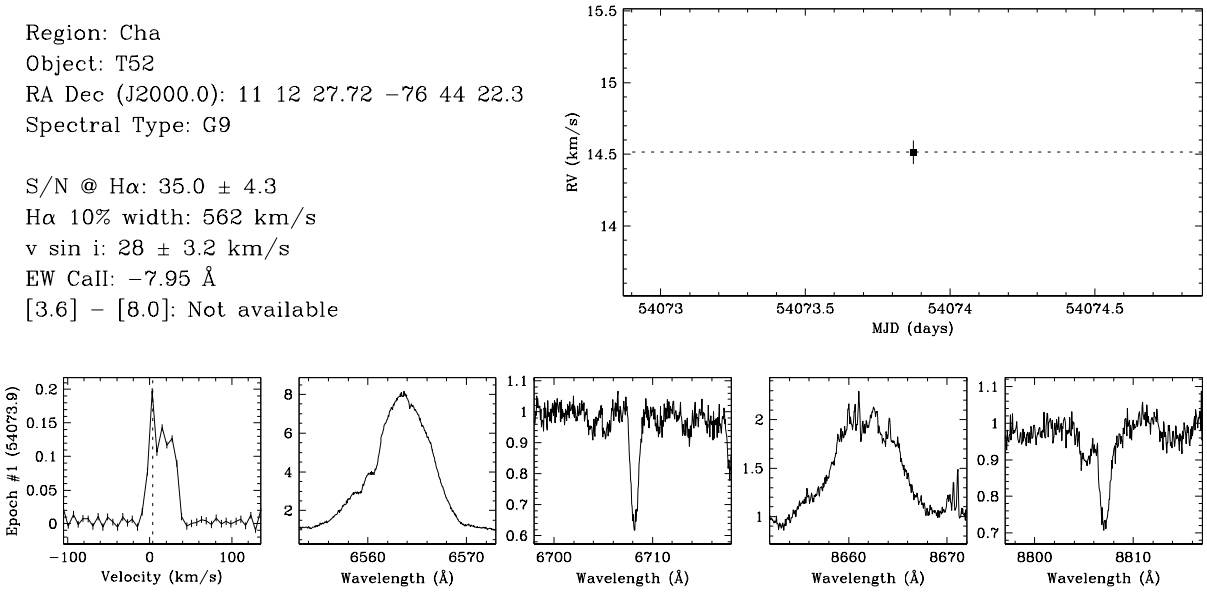

Figure 4.88 T52 has a single-line profile, and is therefore not an SB2. The radial velocity scatter cannot be determined because the target was observed for a single epoch. Hence, it is undetermined if the target is an SB1 or a single star. The strong peak in the line profiles at the observer's rest frame is due to dawn twilight, and may have biased the radial velocity estimate toward the observer's rest frame. This target has been previously reported by Lafrenière et al. (2008) to have no resolved companions.

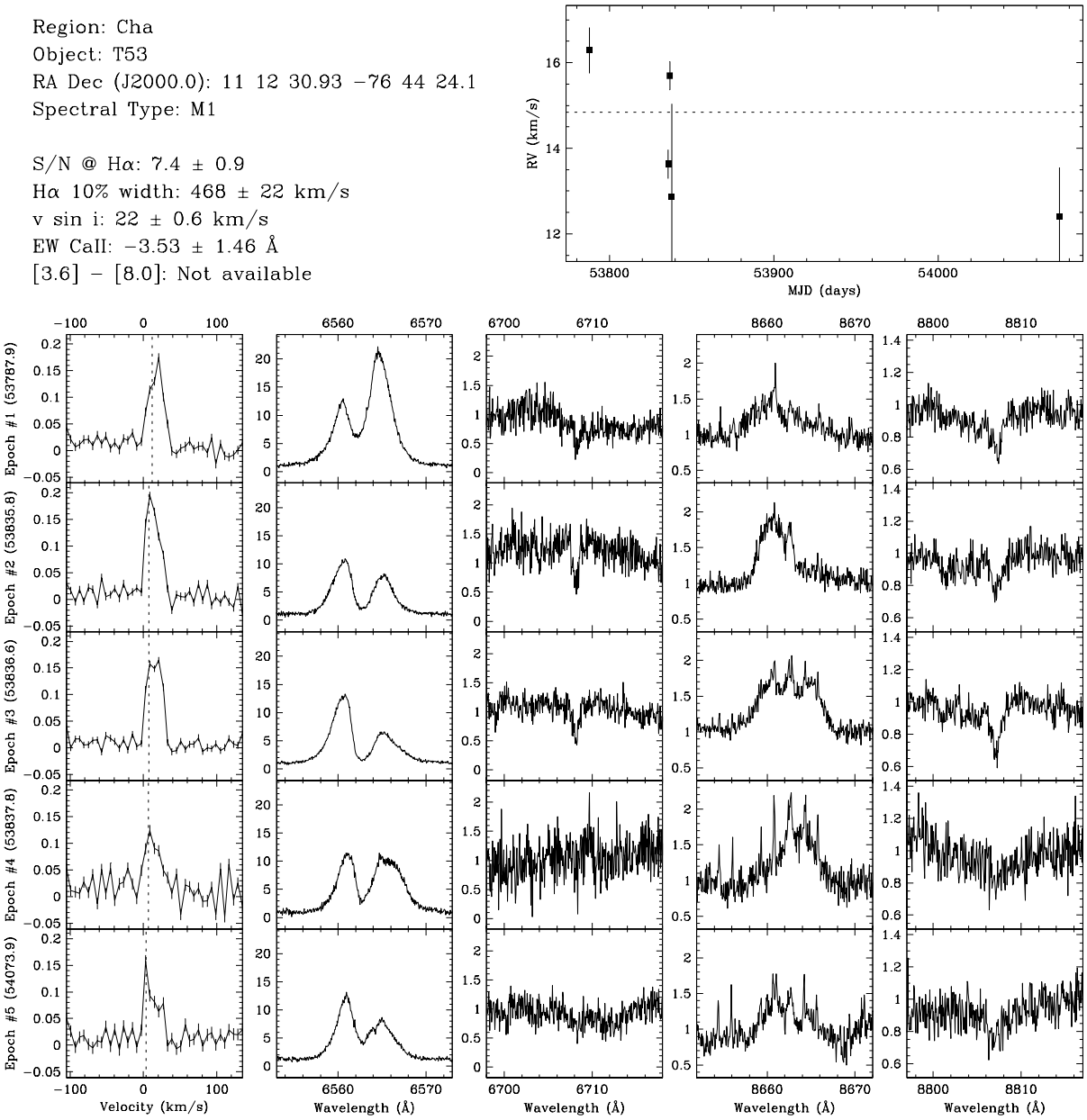

Figure 4.89 T53 shows no clear evidence of a close companion. The star has a single-line profile, and a radial velocity scatter not significant relative to variations observed within each observing run. The radial velocity scatter within the second observing run (epochs #2, #3 and #4) is consistent with that expected from systematic line profile variations, e.g. from star spots rotating with the star. For epoch #5, the peak in the line profile at the observer's rest frame is due to dawn twilight, and likely biased the radial velocity estimate toward the observer's rest frame. For epoch #4, the narrow emission lines in the spectrum near 8662 Å are from the night sky. This target has been previously reported by Lafrenière et al. (2008) to have no resolved companions.

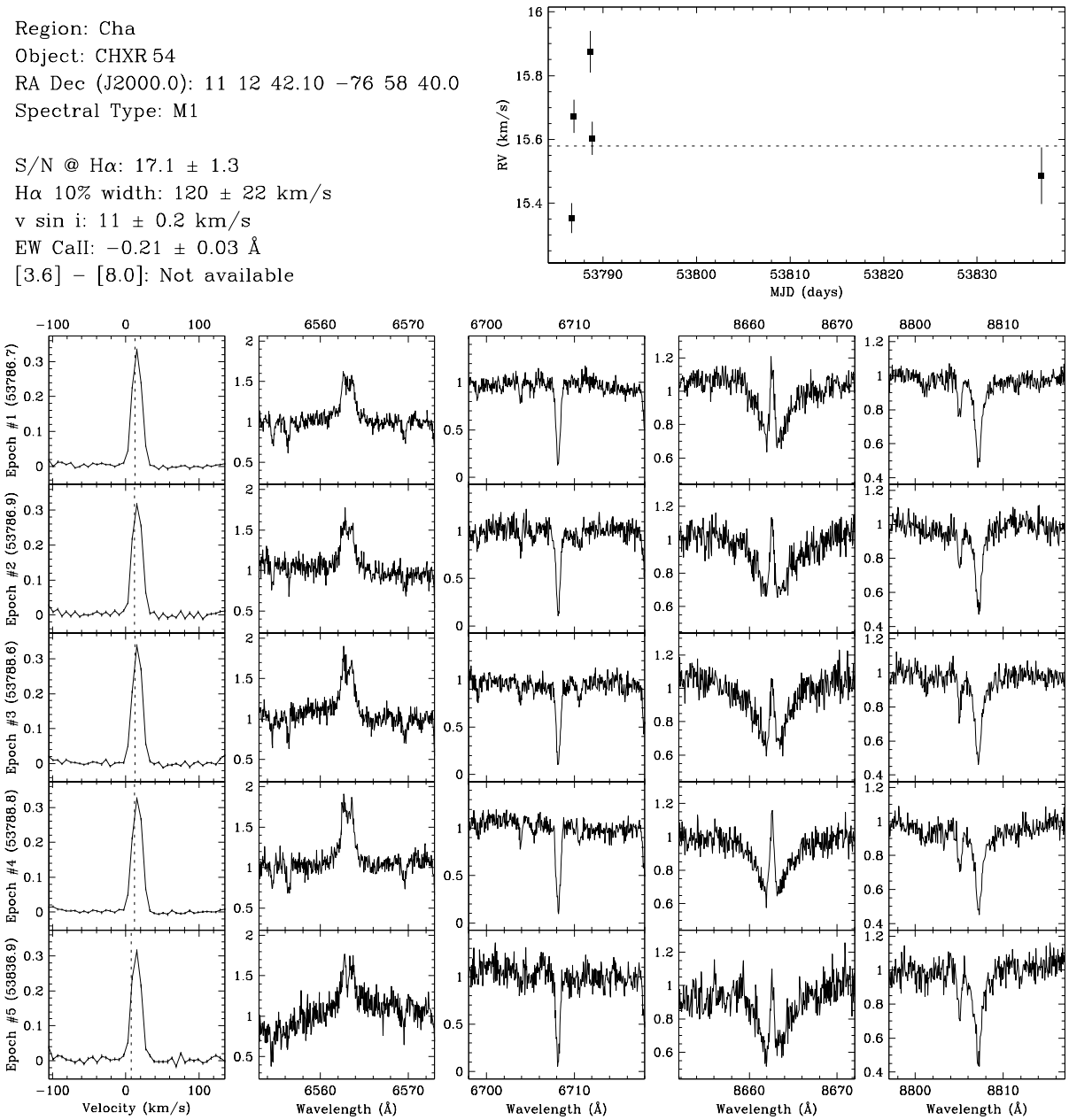

Figure 4.90 CHXR 54 shows no clear evidence of a close companion. The star has a single-line profile, and a radial velocity scatter not significant relative to variations observed within each observing run. The radial velocity scatter within the first observing run (epochs #1, #2, #3 and #4) is consistent with that expected from systematic line profile variations, e.g. from star spots rotating with the star. This target has been previously reported by Lafrenière et al. (2008) to have no resolved companions.

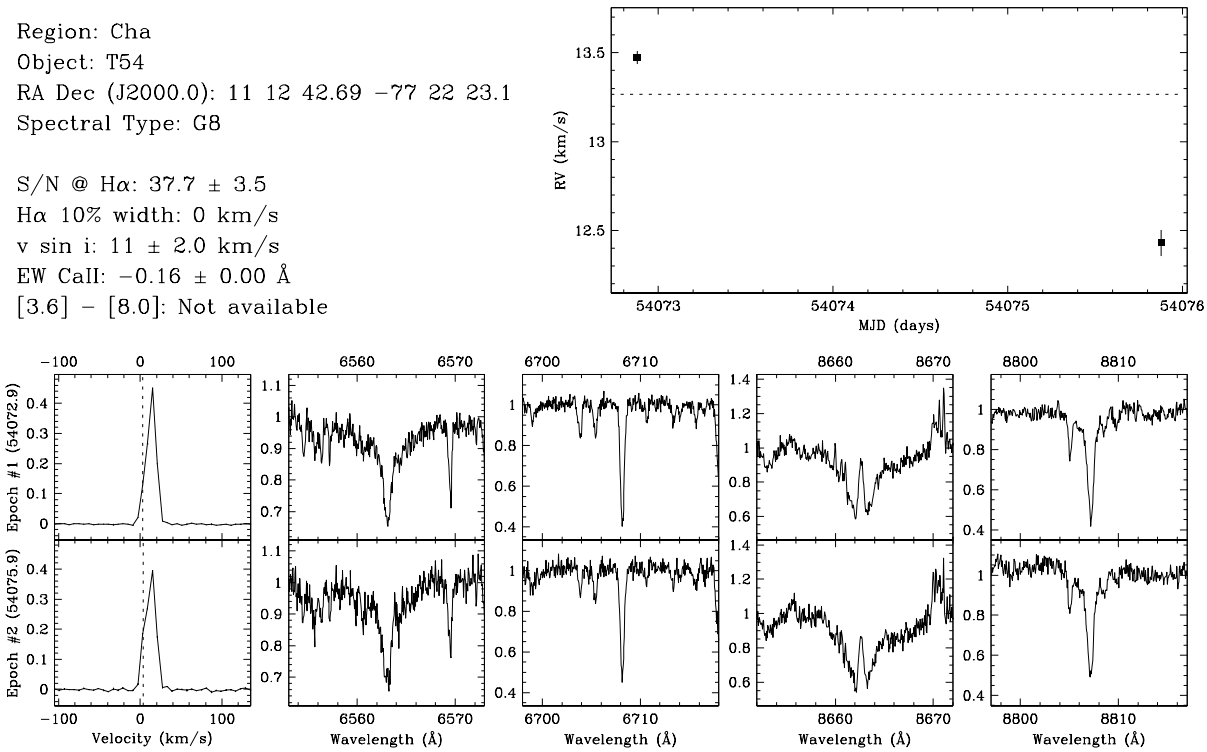

Figure 4.91 T54 has a single-line profile, and is therefore not an SB2. The radial velocity scatter over the short baseline available does not conclusively indicate if the target is an SB1 or a single star. The slight bulges in the line profiles at the observer's rest frame are due to dawn twilight, and likely biased the radial velocity estimates toward the observer's rest frame. This target has been previously reported by Lafrenière et al. (2008) to have a resolved companion with a separation of $\sim 0\farcs247$ (~ 35 AU) at a position angle of $\sim 246\fdg5$, and an R-band flux ratio of ~ 0.19 ($\Delta K \sim 1.45$). However, there is no clear evidence in the line profile of the resolved companion. Since the resolved companion has an expected circular orbital speed of $\sim 10\,\mathrm{km\,s^{-1}}$, a second profile could be obscured if the primary star and the resolved companion have similar projected rotational velocities.

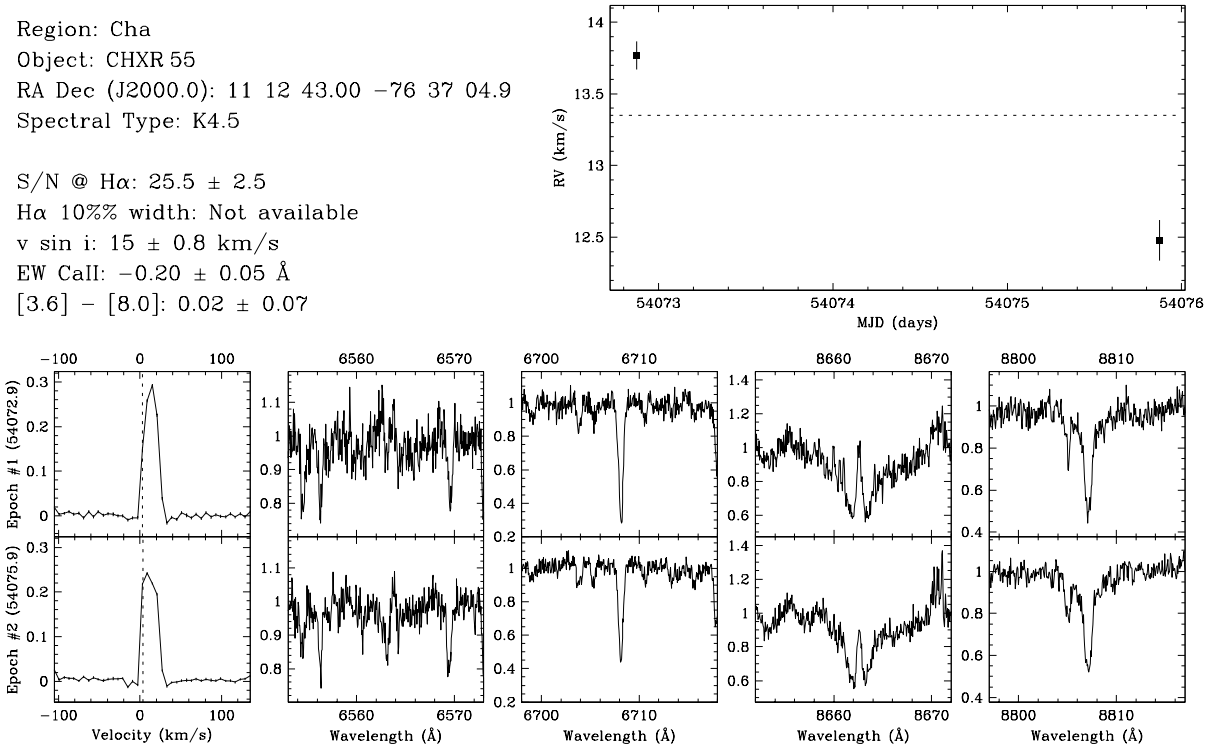

Figure 4.92 CHXR 55 has a single-line profile, and is therefore not an SB2. The radial velocity scatter over the short baseline available does not conclusively indicate if the target is an SB1 or a single star. The radial velocity scatter is large but consistent with that expected from systematic line profile variations, e.g. from star spots rotating with the star. This target has been previously reported by Lafrenière et al. (2008) to have no resolved companions.

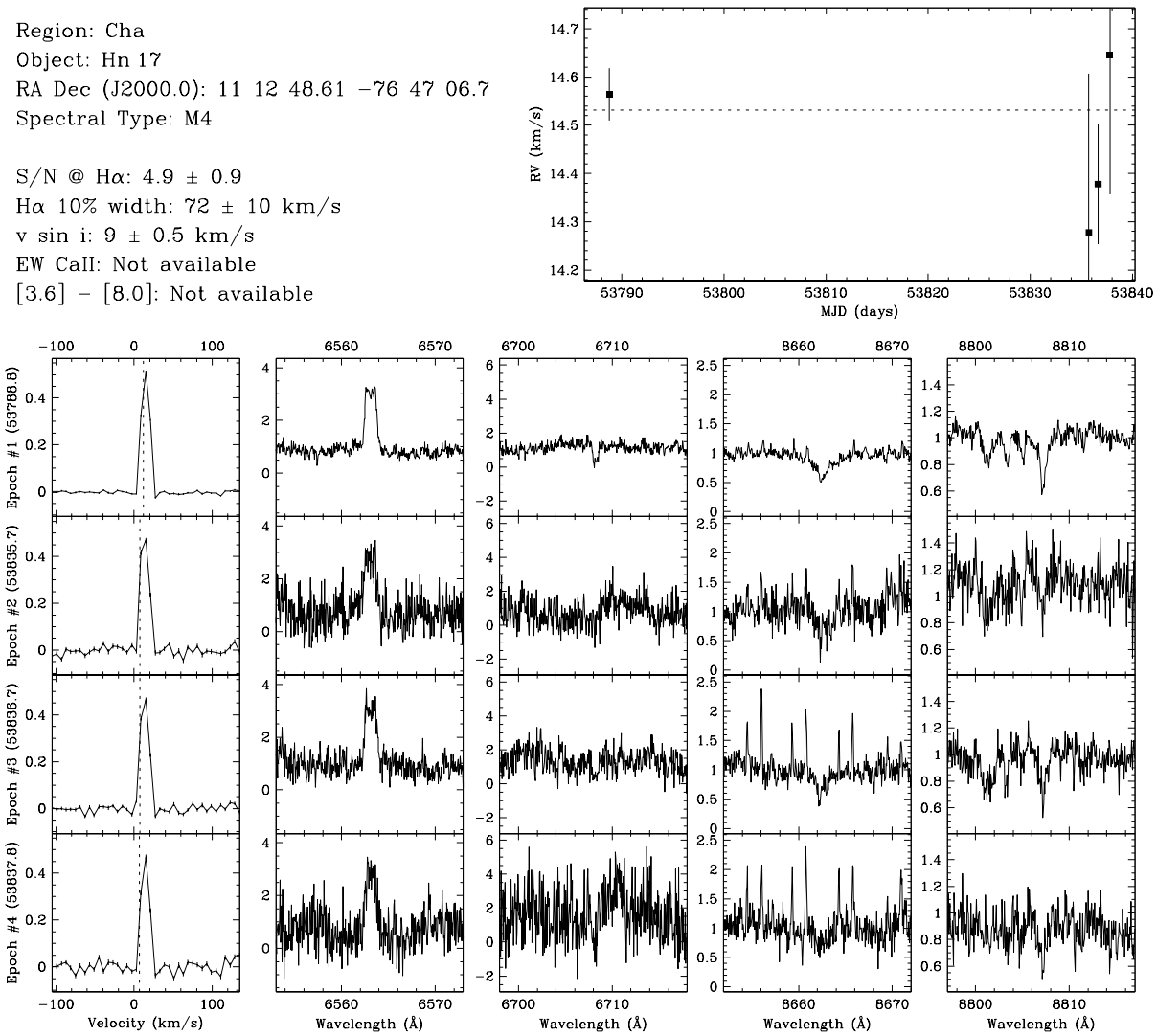

Figure 4.93 Hn 17 shows no evidence of a close companion. The star has a single-line profile, and the radial velocity scatter is not significant relative to the measurement uncertainties. The narrow emission lines in the spectra near 8662 Å are from the night sky. This target has been previously reported by Lafrenière et al. (2008) to have no resolved companions.

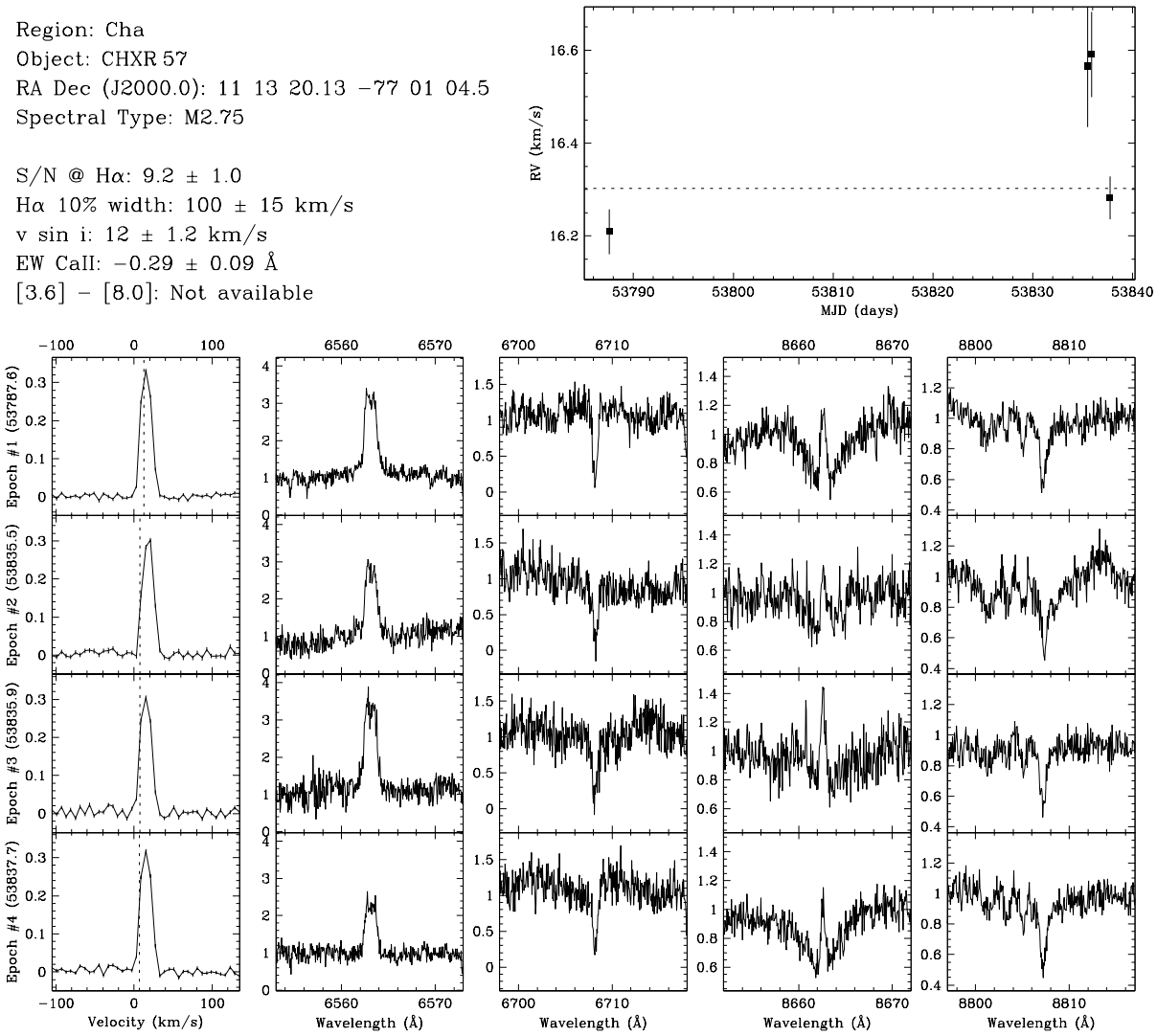

Figure 4.94 CHXR 57 shows no evidence of a close companion. The star has a single-line profile, and the radial velocity scatter is not significant relative to the measurement uncertainties. This target has been previously reported by Lafrenière et al. (2008) to have no resolved companions.

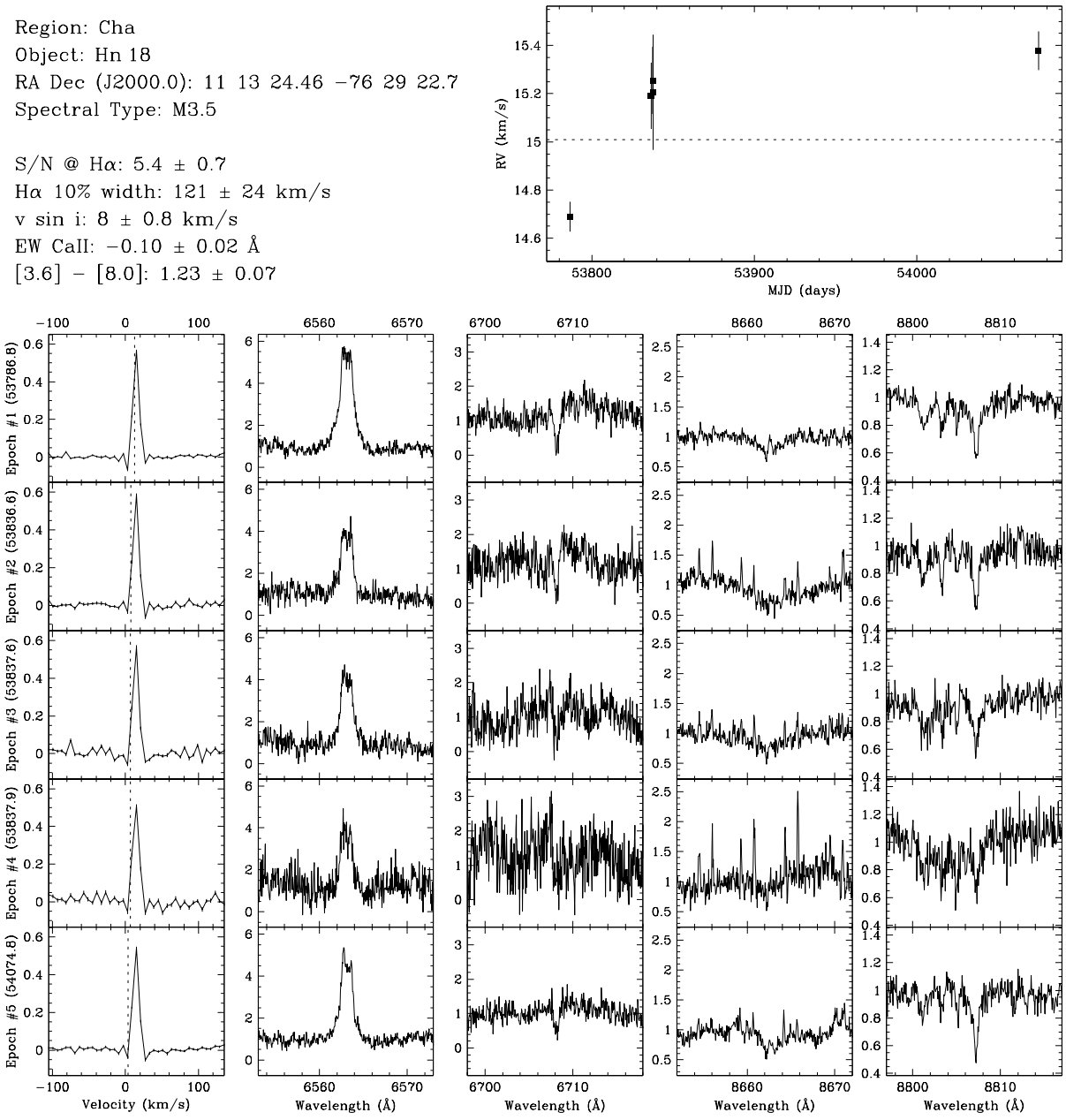

Figure 4.95 Hn 18 shows no clear evidence of a close companion. The overall radial velocity is close to that of the star forming region, and the possible changes in radial velocity imply that if a close companion exists, it would have a mass below the hydrogen burning limit. The overall radial velocity scatter is comparable to that expected from line profile variations, e.g. from star spots rotating with the star. The narrow emission lines in the spectra near 8662 Å are from the night sky. This target has been previously reported by Lafrenière et al. (2008) to have no resolved companions.

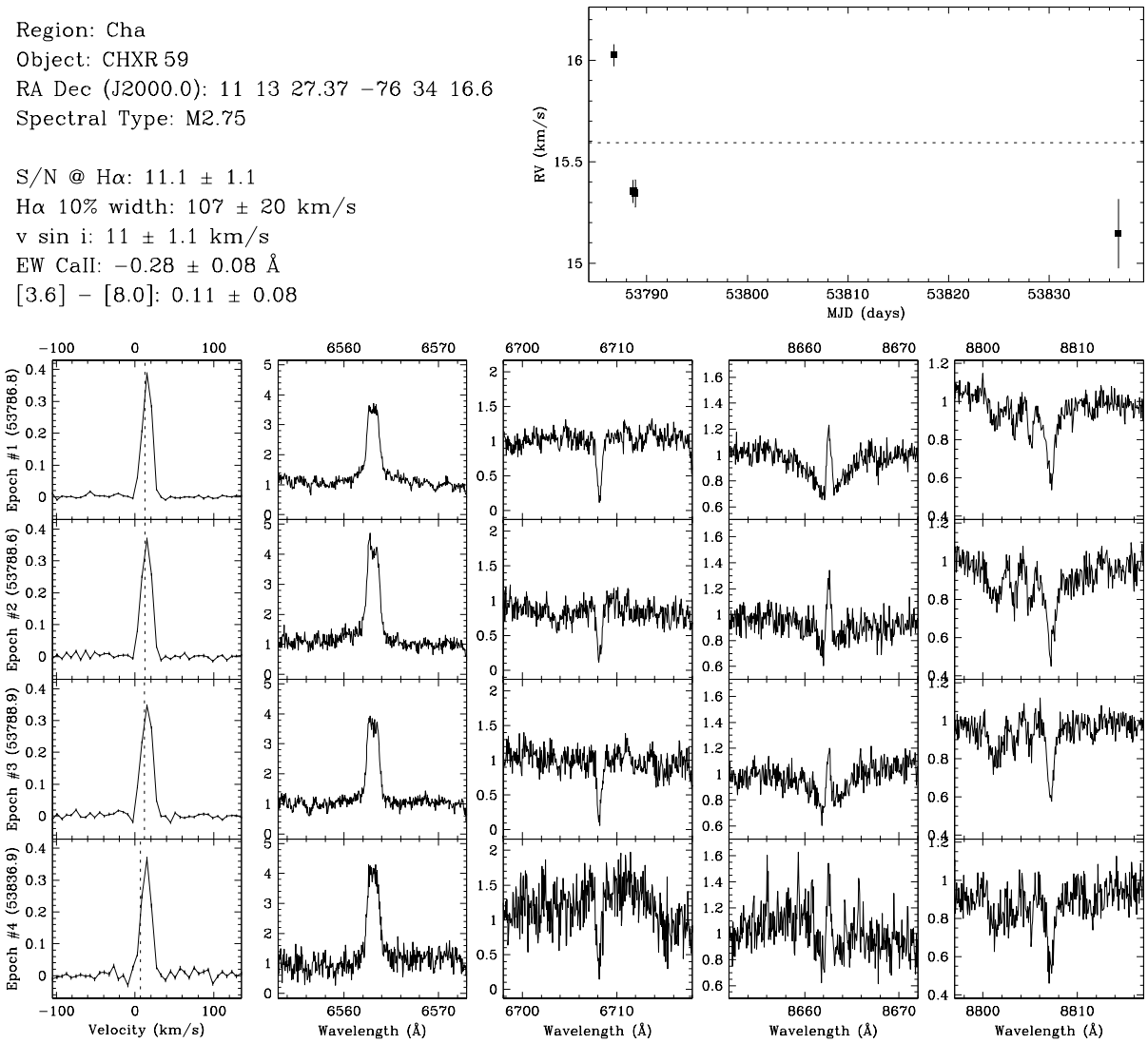

Figure 4.96 CHXR 59 shows no clear evidence of a close companion. The star has a single-line profile, and a radial velocity scatter not significant relative to variations observed within each observing run. The radial velocity scatter within the first observing run (epochs #1, #2 and #3) is consistent with that expected from systematic line profile variations, e.g. from star spots rotating with the star. This target has been previously reported by Lafrenière et al. (2008) to have a resolved companion with a separation of $\sim 0\farcs148$ (~ 21 AU) at a position angle of $\sim 347\fdg4$, and an R-band flux ratio of ~ 0.95 ($\Delta K \sim 0.02$). However, there is no clear evidence in the line profile of the resolved companion. Since the resolved companion has an expected circular orbital speed of $\sim 5\,\mathrm{km\,s^{-1}}$, a second profile could be obscured if the primary star and the resolved companion have similar projected rotational velocities.

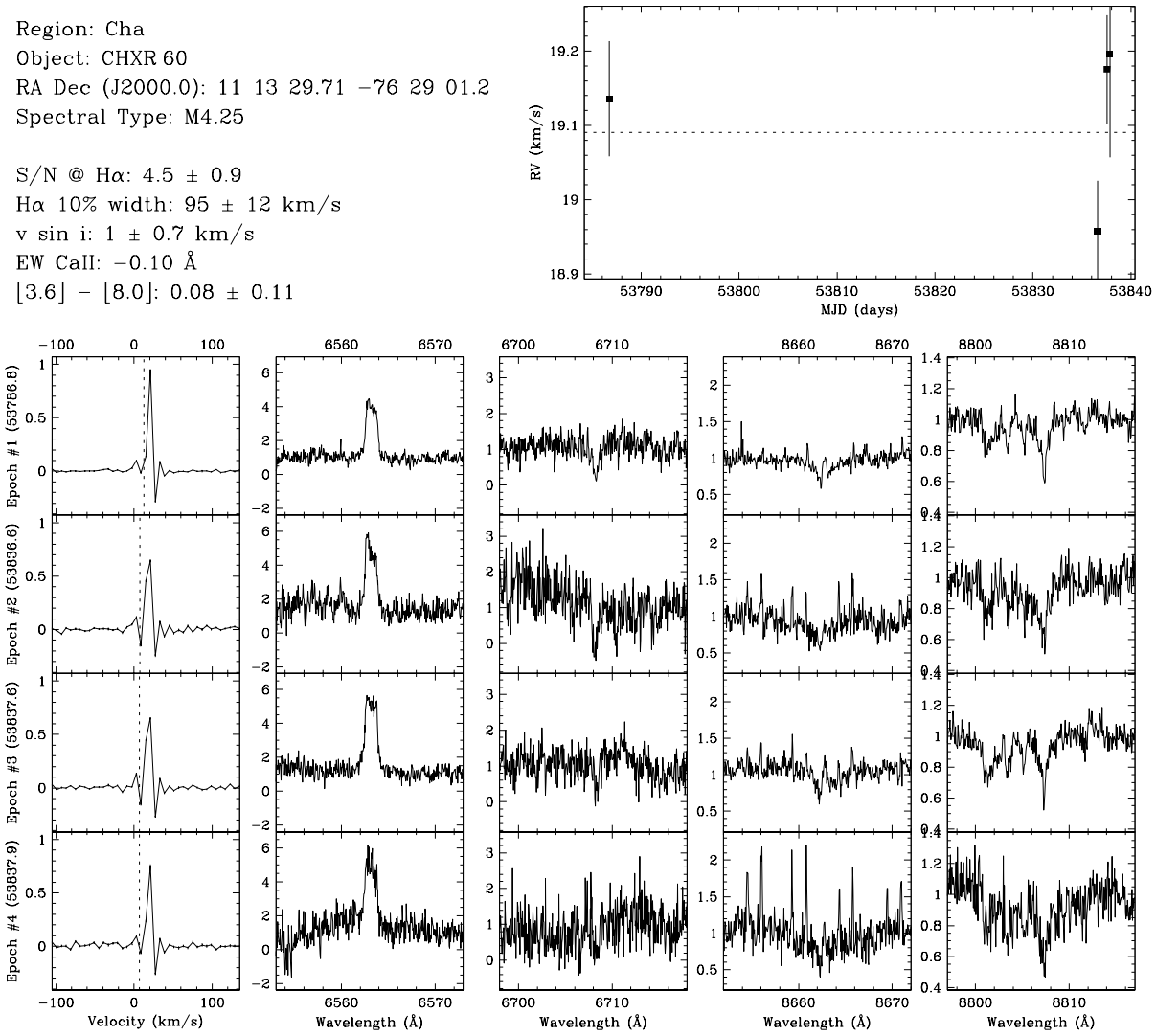

Figure 4.97 CHXR 60 shows no evidence of a close companion. The star has a single-line profile, and the radial velocity scatter is not significant relative to the measurement uncertainties. The overall radial velocity deviates from that of the star forming region. However, cluster membership is supported by Li-λ6708 absorption. The narrow emission lines in the spectra near 8662 Å are from the night sky. This target has been previously reported by Lafrenière et al. (2008) to have no resolved companions.

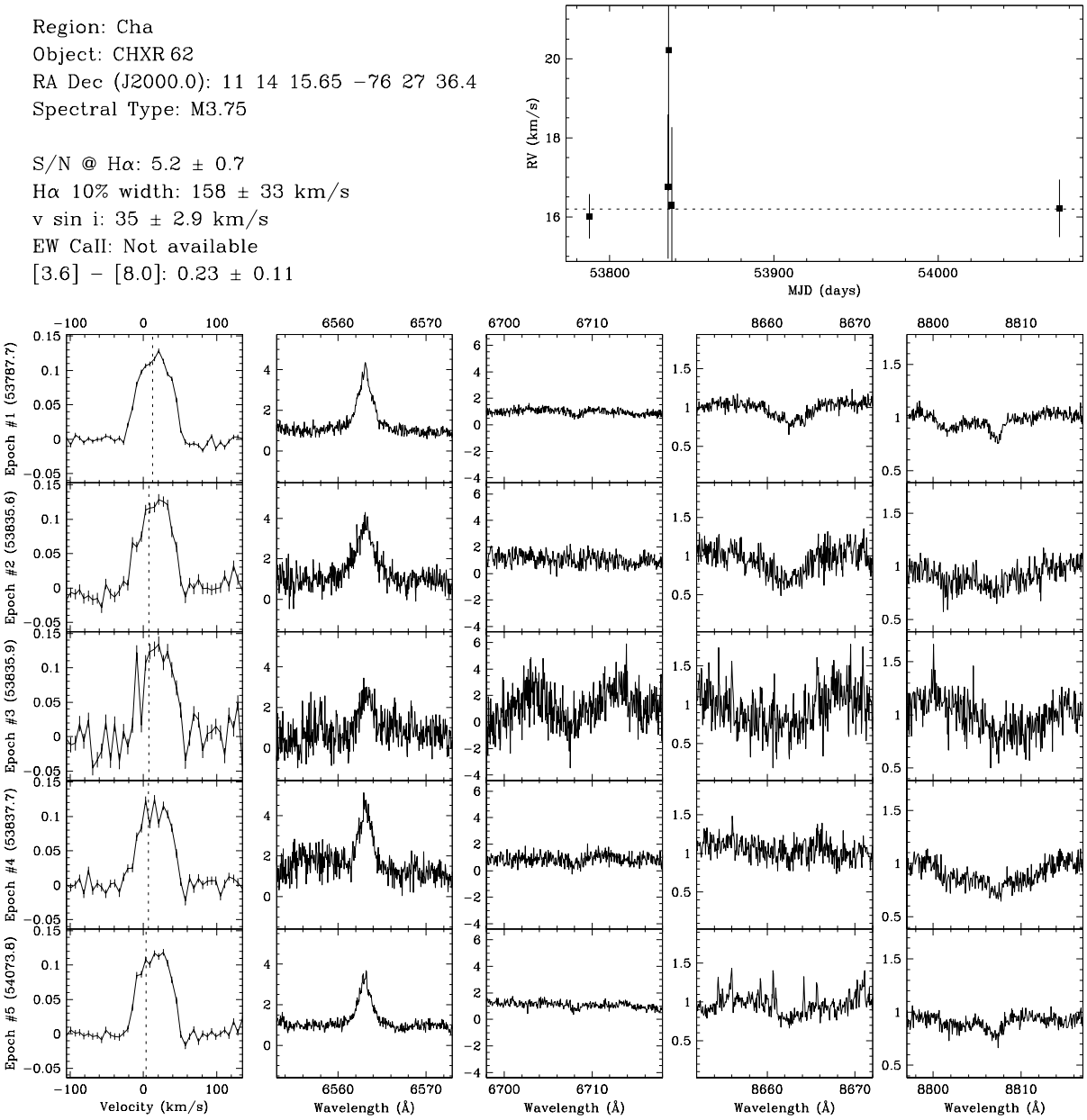

Figure 4.98 CHXR 62 shows no evidence of a close companion. The star has a single-line profile, and the radial velocity scatter is not significant relative to the measurement uncertainties. This target has been previously reported by Lafrenière et al. (2008) to have a resolved companion with a separation of $\sim 0\farcs12$ (~ 17 AU) at a position angle of $\sim 135\fdg1$, and an R-band flux ratio of ~ 0.86 ($\Delta K \sim 0.06$). However, there is no clear evidence in the line profile of the resolved companion. Since the resolved companion has an expected circular orbital speed of $\sim 5\,\mathrm{km\,s^{-1}}$, a second profile could be obscured if the primary star and the resolved companion have similar projected rotational velocities.

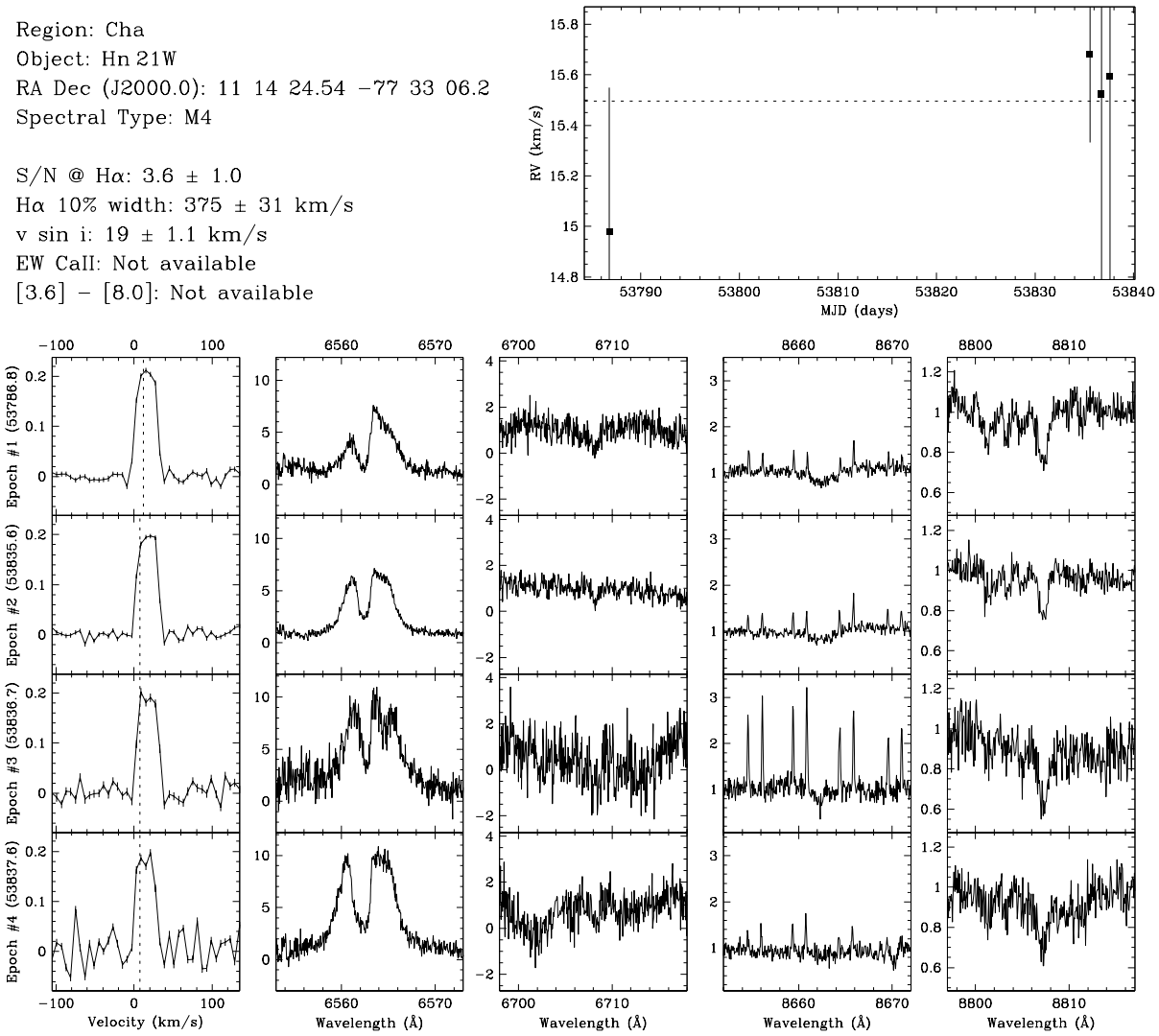

Figure 4.99 Hn 21W shows no evidence of a close companion. The star has a single-line profile, and the radial velocity scatter is not significant relative to the measurement uncertainties. The narrow emission lines in the spectra near 8662 Å are from the night sky. This target has been previously reported by Lafrenière et al. (2008) to have a resolved companion with a separation of $\sim 5\farcs495$ (~ 770 AU) at a position angle of $\sim 69\fdg2$, and an R-band flux ratio of ~ 0.07 ($\Delta K \sim 0.95$). Given the flux ratio and separation, the expected contribution to the line profile from the resolved companion is negligible.

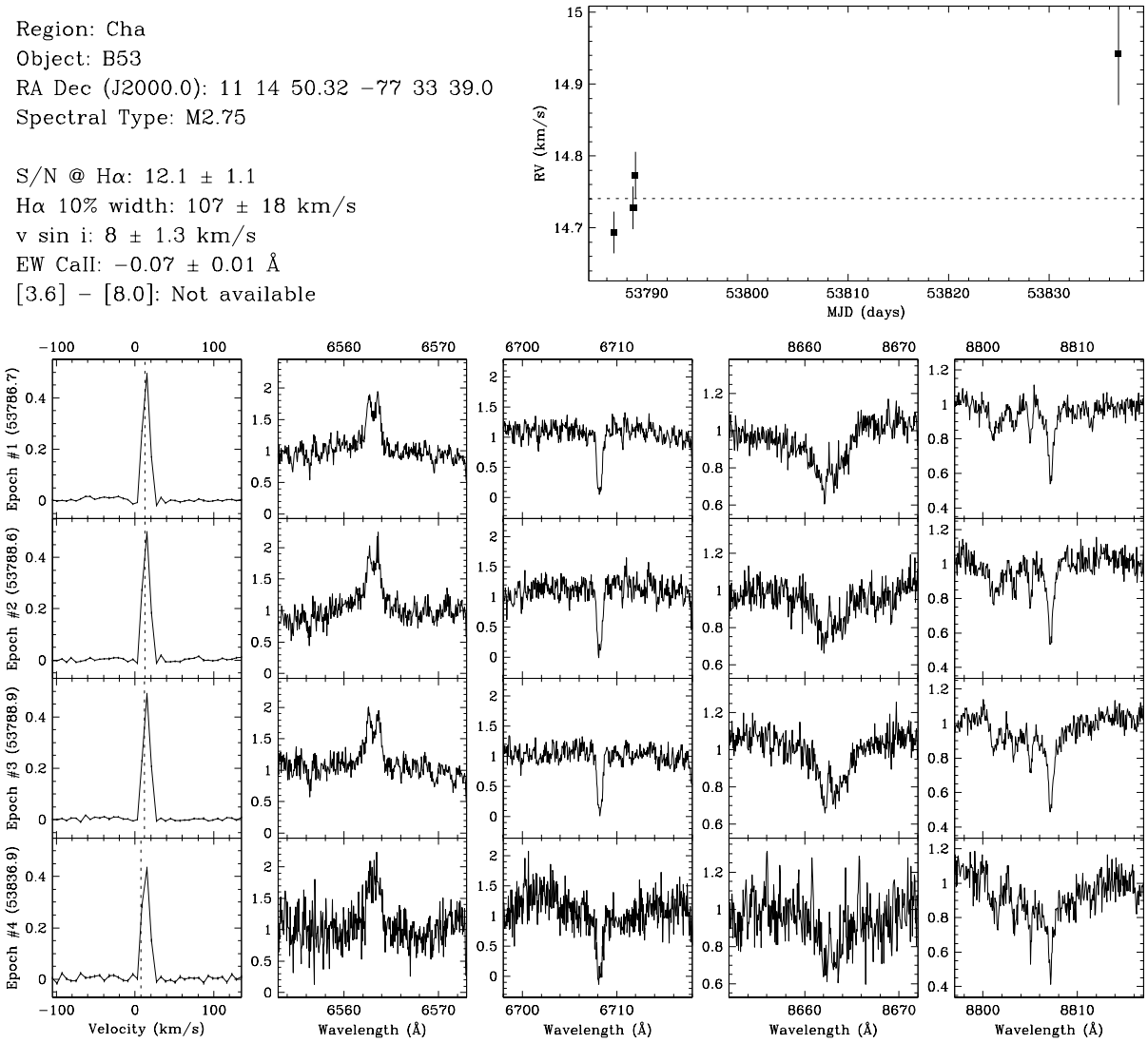

Figure 4.100 B53 shows no evidence of a close companion. The star has a single-line profile, and the radial velocity scatter is not significant relative to the measurement uncertainties. This target has been previously reported by Lafrenière et al. (2008) to have a resolved companion with a separation of $\sim$0.″295 ($\sim$41 AU) at a position angle of $\sim$235.°2, and an R-band flux ratio of $\sim$0.02 ($\Delta K \sim 1.52$). Given the flux ratio, the expected contribution to the line profile from the resolved companion is negligible.

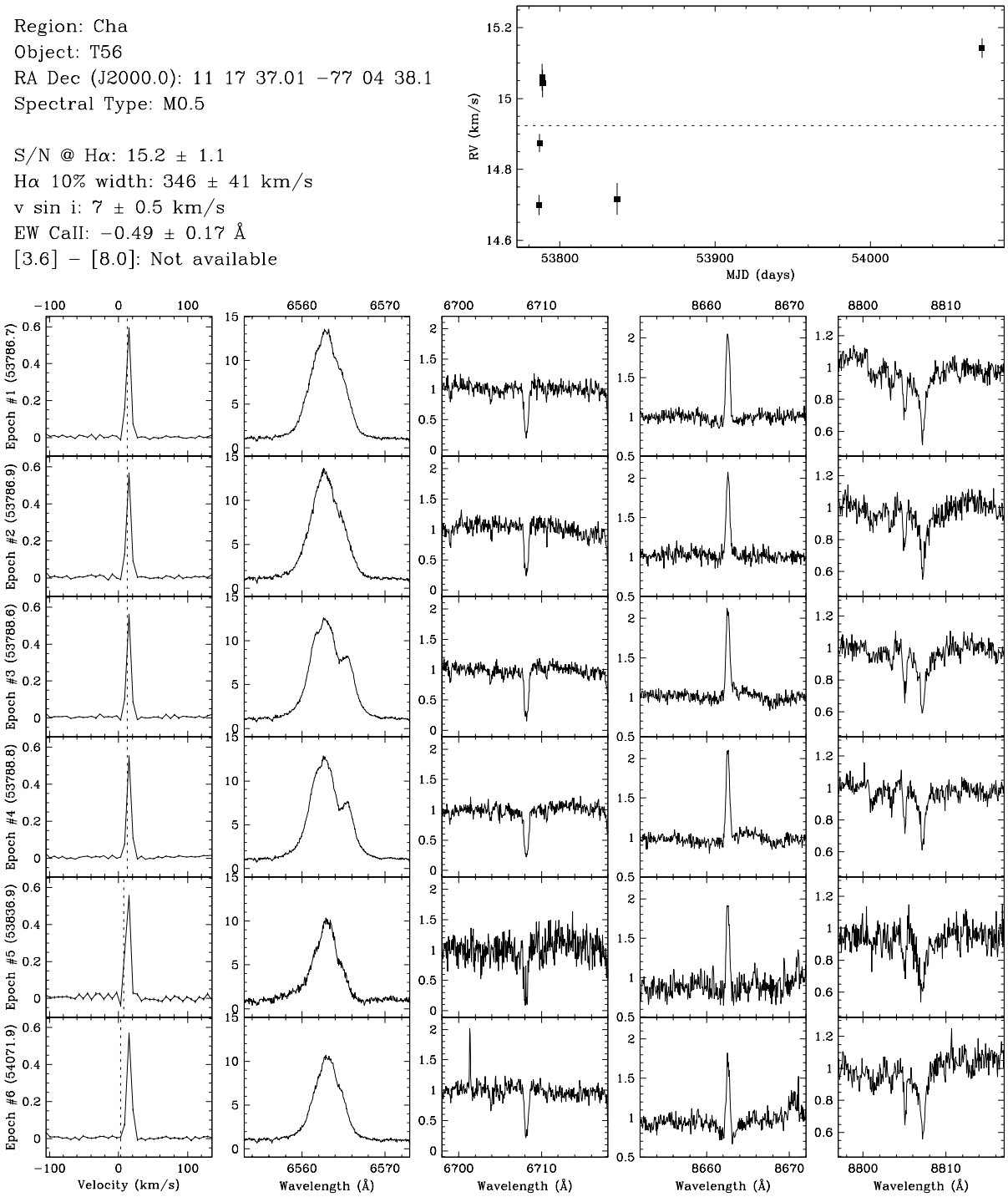

Figure 4.101 T56 shows no clear evidence of a close companion. The star has a single-line profile, and a radial velocity scatter not significant relative to variations observed within each observing run. The radial velocity scatter within the first observing run (epochs #1, #2, #3 and #4) is consistent with that expected from systematic line profile variations, e.g. from star spots rotating with the star. This target has been previously reported by Lafrenière et al. (2008) to have no resolved companions.

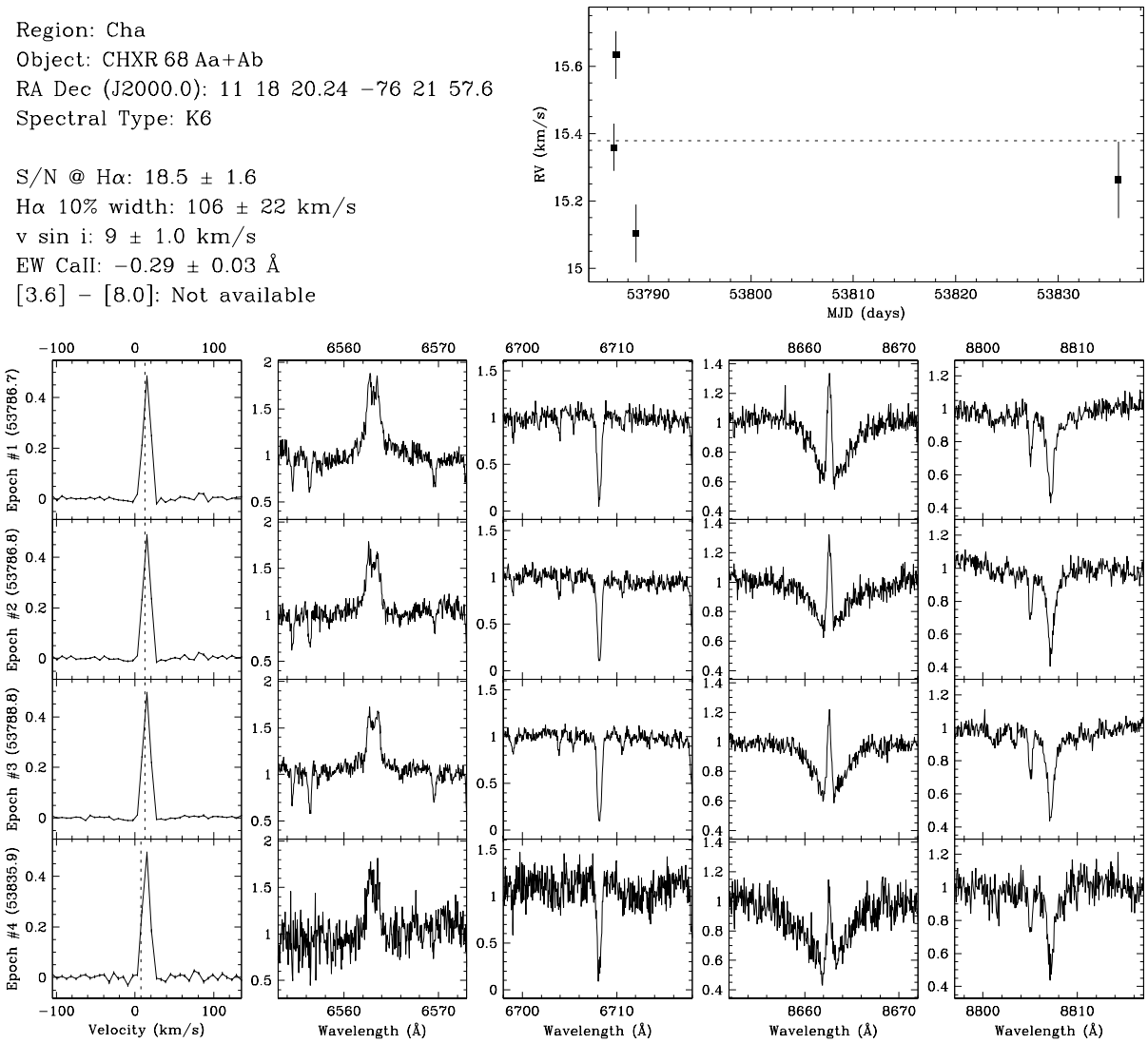

Figure 4.102 CHXR 68 Aa+Ab shows no clear evidence of a close companion. The star has a single-line profile, and a radial velocity scatter not significant relative to variations observed within each observing run. The radial velocity scatter within the first observing run (epochs #1, #2 and #3) is consistent with that expected from systematic line profile variations, e.g. from star spots rotating with the star. This target has been previously reported by Lafrenière et al. (2008) to have a resolved companion with a separation of $\sim 0\farcs101$ (~ 14 AU) at a position angle of $\sim 13\fdg6$, and an R-band flux ratio of ~ 0.60 ($\Delta K \sim 0.22$). However, there is no clear evidence in the line profile of the resolved companion. Since the resolved companion has an expected circular orbital speed of $\sim 9\,\mathrm{km\,s^{-1}}$, a second profile could be obscured if the primary star and the resolved companion have similar projected rotational velocities.

Region: Cha
Object: CHXR 68 B
RA Dec (J2000.0): 11 18 20.24 −76 21 57.6
Spectral Type: M1

S/N @ Hα: 7.8 ± 1.0
Hα 10% width: 90 ± 17 km/s
v sin i: 8 ± 0.3 km/s
EW CaII: Not available
[3.6] − [8.0]: Not available

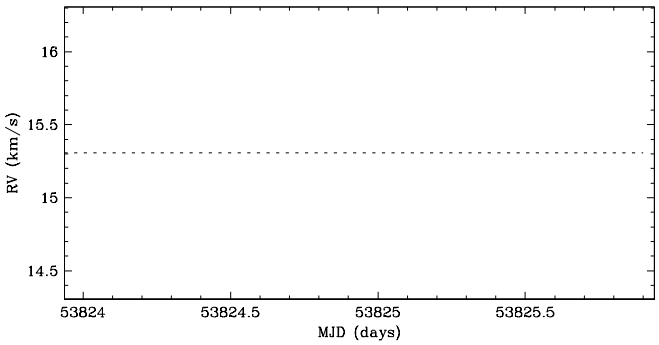

Figure 4.103 CHXR 68 B shows no evidence of a close companion. The star has a single-line profile, and the radial velocity scatter is not significant relative to the measurement uncertainties. This target has been previously reported by Lafrenière et al. (2008) to have a resolved companion with a separation of $\sim$4.″367 ($\sim$610 AU) at a position angle of $\sim$213°, and an R-band flux ratio of $\sim$0.08 ($\Delta K \sim 0.95$). Given the flux ratio and separation, the expected contribution to the line profile from the resolved companion is negligible.

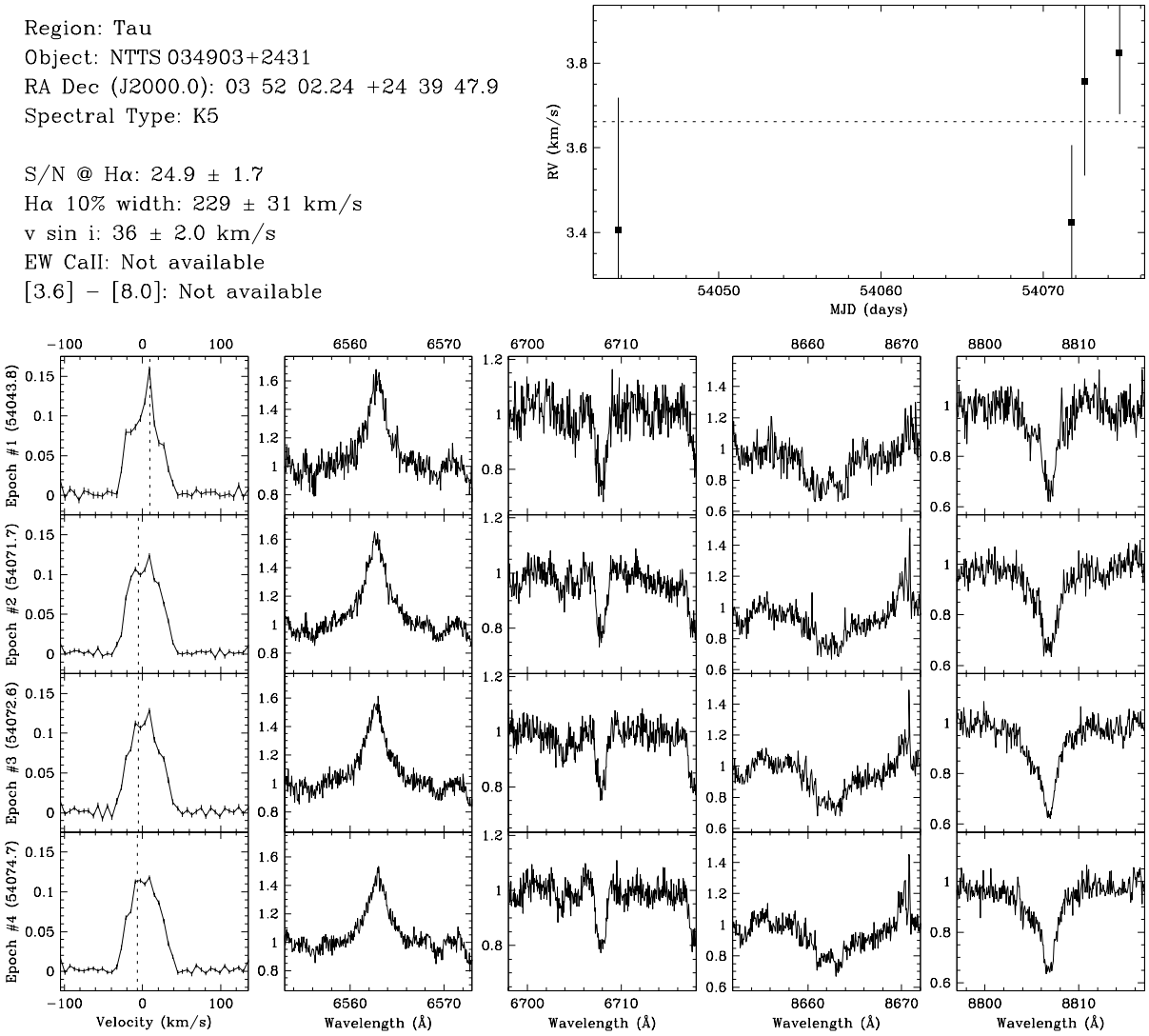

Figure 4.104 NTTS 034903+2431 shows no clear evidence of a close companion. The star has a single-line profile, and a radial velocity scatter not significant relative to variations observed within each observing run. The line profiles show significant deviation from the shape expected from pure rotational broadening. To see if these irregularities are from close companions, we fitted multiple broadening functions to the line profiles. The resultant radial velocities were not consistent with those expected from close companions: the radial velocity separations were $\sim 20\,\mathrm{km\,s^{-1}}$ with no acceleration. Therefore, we suspect the variations in the line profile are the result of star spots. The overall radial velocity deviates from that of the star forming region. However, cluster membership is supported by Li-λ6708 absorption. This target has been previously reported by Leinert et al. (1993) to have a resolved companion with a separation of $\sim 0\farcs61$ ($\sim 85\,\mathrm{AU}$) at a position angle of $\sim 317°$, and an R-band flux ratio of ~ 0.01 ($\Delta K \sim 1.64$). Given the flux ratio, the expected contribution to the line profile from the resolved companion is negligible.

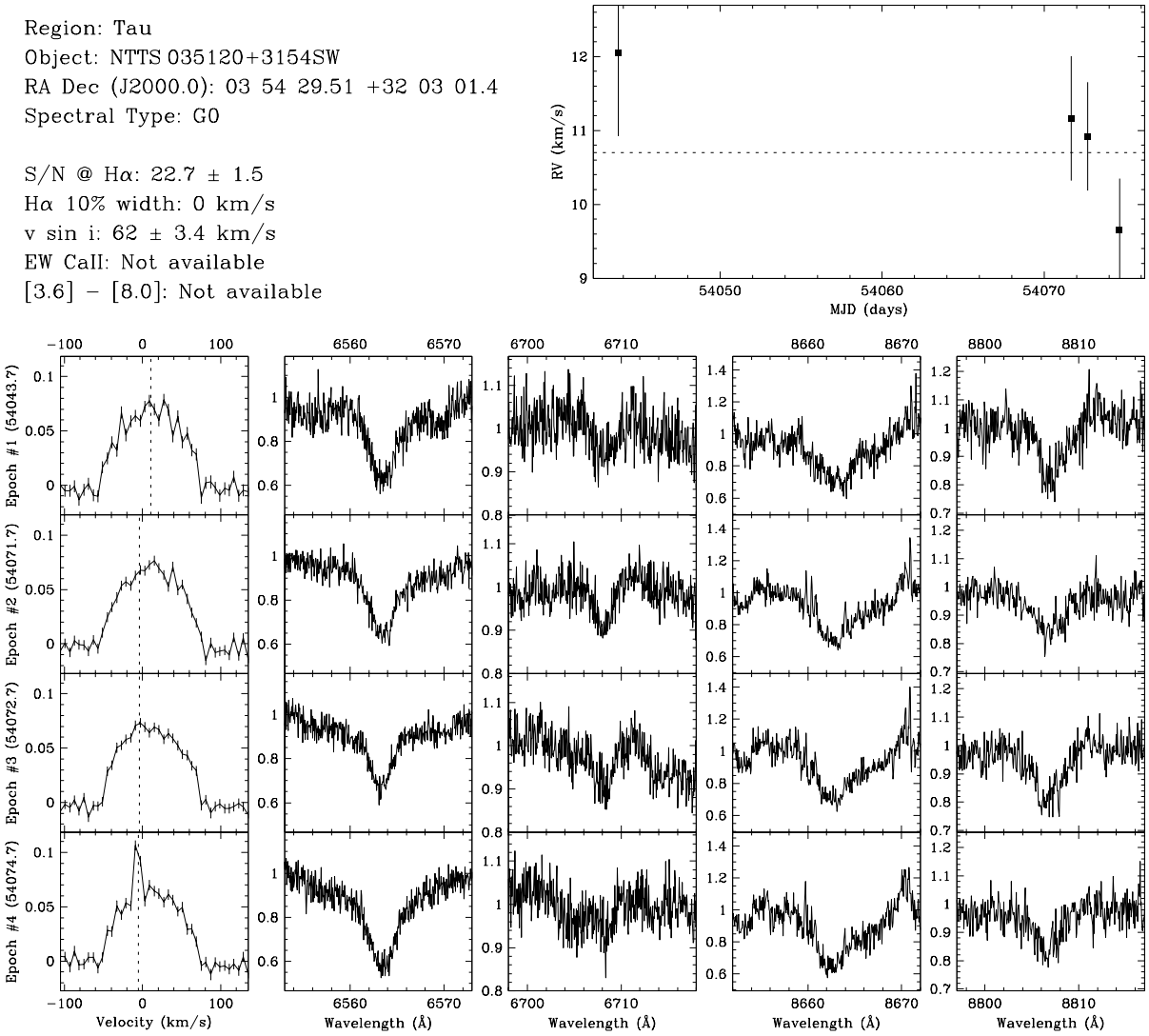

Figure 4.105 NTTS 035120+3154SW shows no evidence of a close companion. The star has a single-line profile, and the radial velocity scatter is not significant relative to the measurement uncertainties. For epoch #4, the sharp peak in the line profile at the observer's rest frame is due to moonlight, and may have biased the radial velocity estimate toward the observer's rest frame. This target has been previously reported by Leinert et al. (1993) to have a resolved companion with a separation of $\sim 8\farcs6$ (~ 1200 AU) at a position angle of $\sim 62°$, and an R-band flux ratio of ~ 0.67 ($\Delta K \sim 0.28$). Given the separation, the expected contribution to the line profile from the resolved companion is negligible.

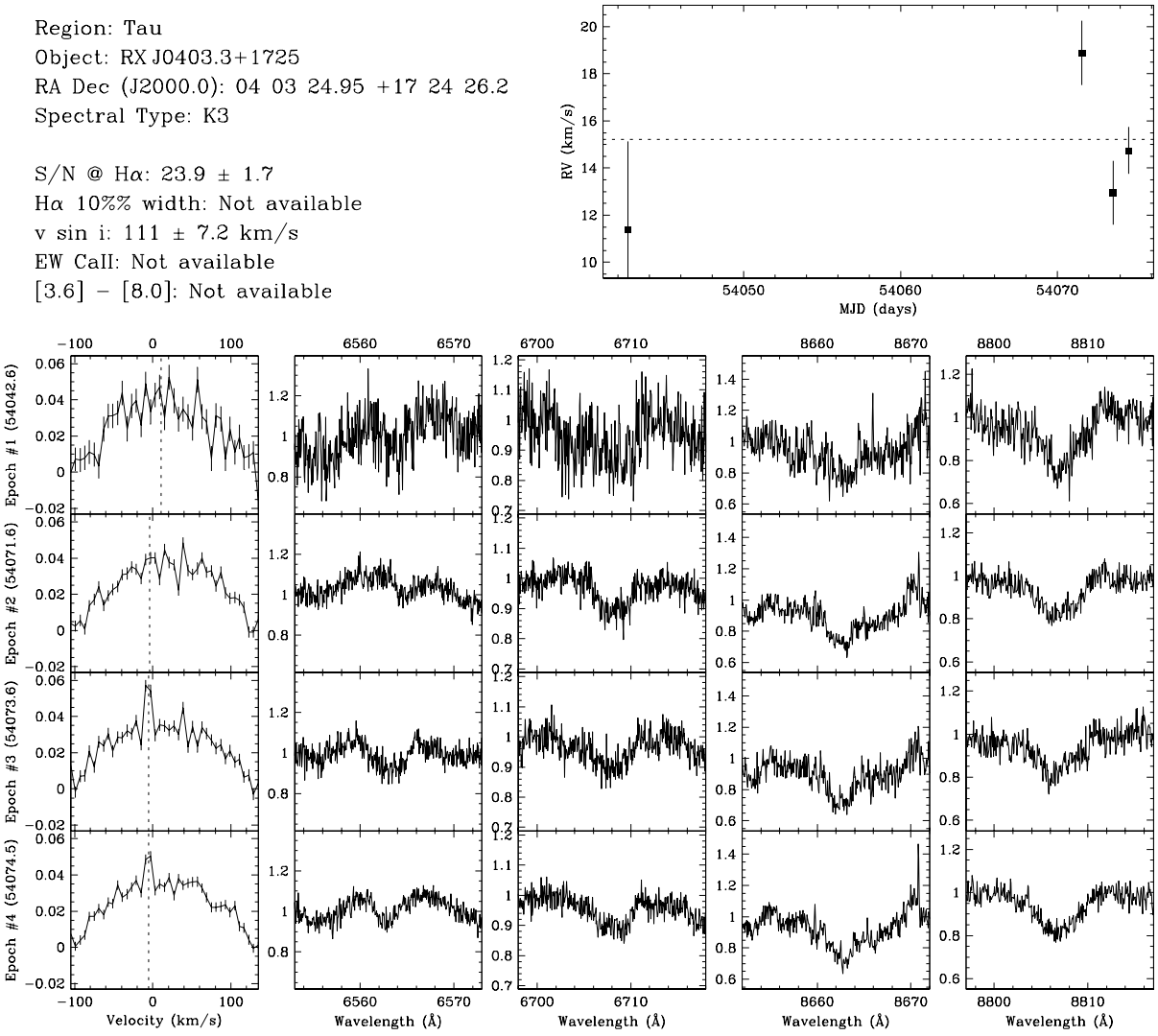

Figure 4.106 RX J0403.3+1725 shows no evidence of a close companion. The star has a single-line profile, and the radial velocity scatter is not significant relative to the measurement uncertainties. For epochs #3 and #4, the sharp peaks in the line profile at the observer's rest frame are due to moonlight, and may have biased the radial velocity estimates toward the observer's rest frame. This target has been previously reported by Köhler & Leinert (1998) to have no resolved companions.

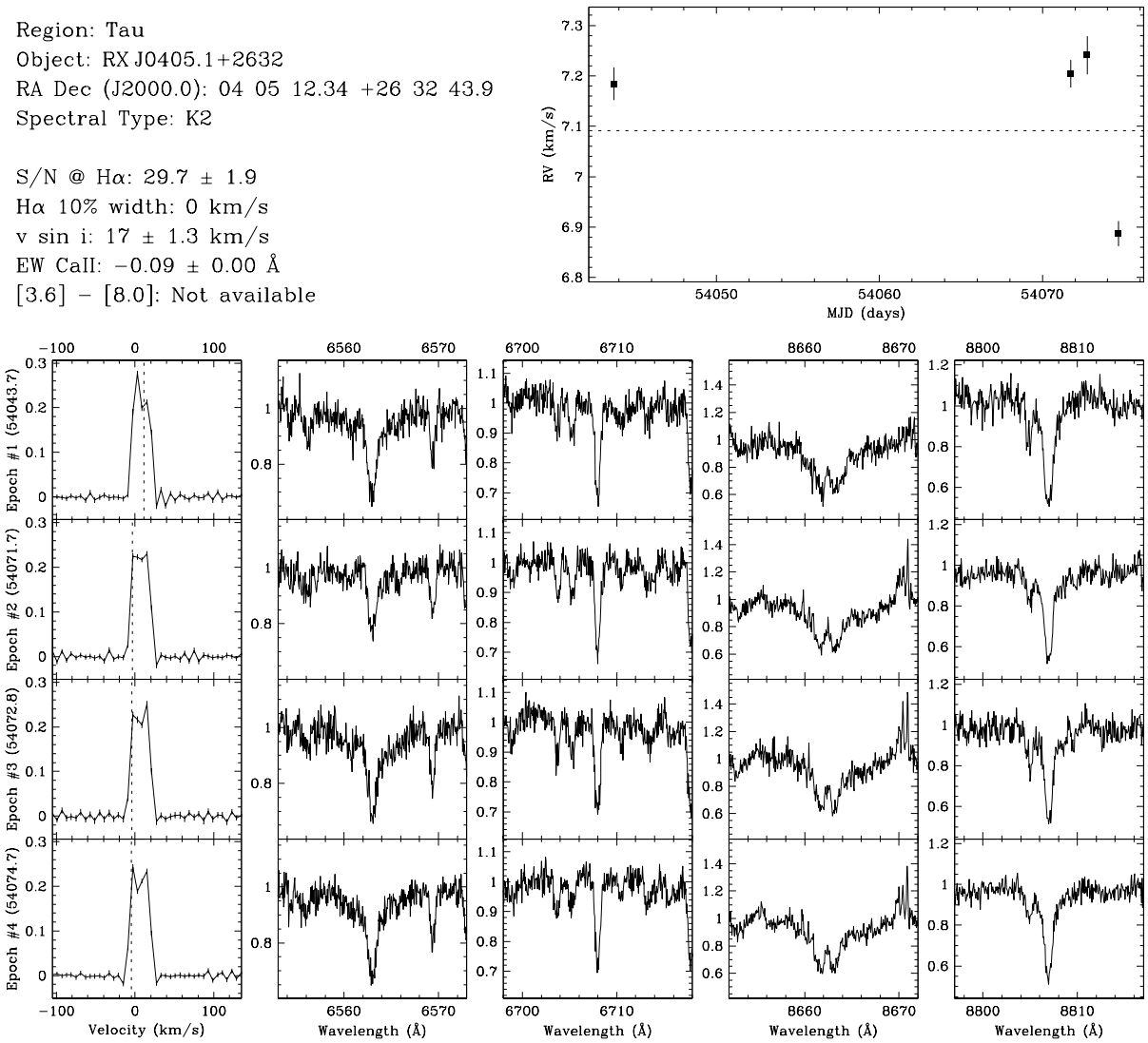

Figure 4.107 RX J0405.1+2632 shows no clear evidence of a close companion. The star has a single-line profile, and a radial velocity scatter not significant relative to variations observed within each observing run. The radial velocity scatter within the second observing run (epochs #2, #3 and #4) is consistent with that expected from systematic line profile variations, e.g. from star spots rotating with the star. The overall radial velocity deviates from that of the star forming region. However, cluster membership is supported by Li-λ6708 absorption. For epoch #4, the asymmetry in the line profile at the observer's rest frame is due to moonlight, and may have biased the radial velocity estimate toward the observer's rest frame. This target has been previously reported by Köhler & Leinert (1998) to have no resolved companions.

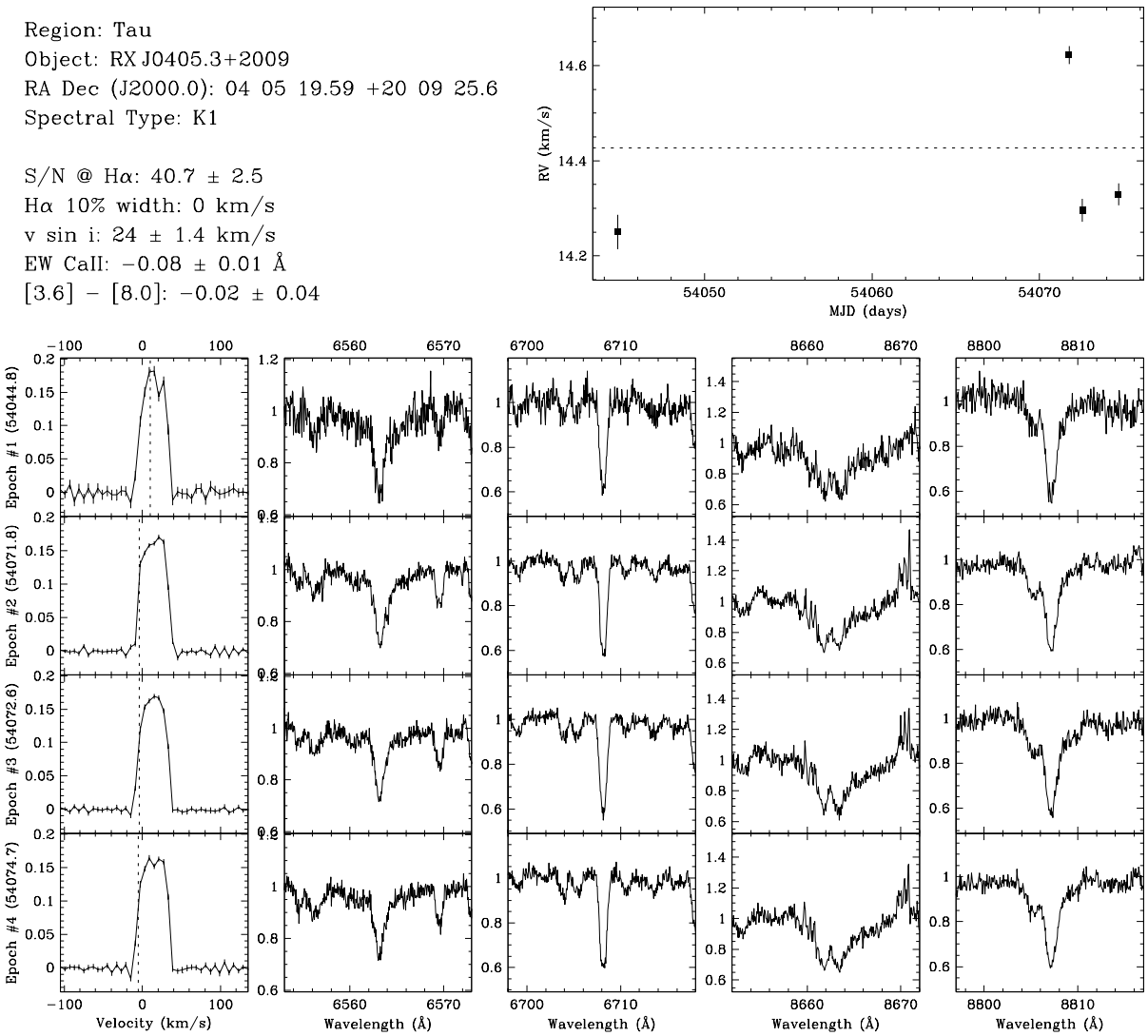

Figure 4.108 RX J0405.3+2009 shows no clear evidence of a close companion. The star has a single-line profile, and a radial velocity scatter not significant relative to variations observed within each observing run. The radial velocity scatter within the second observing run (epochs #2, #3 and #4) is consistent with that expected from systematic line profile variations, e.g. from star spots rotating with the star. This target has been previously reported by Köhler & Leinert (1998) to have no resolved companions.

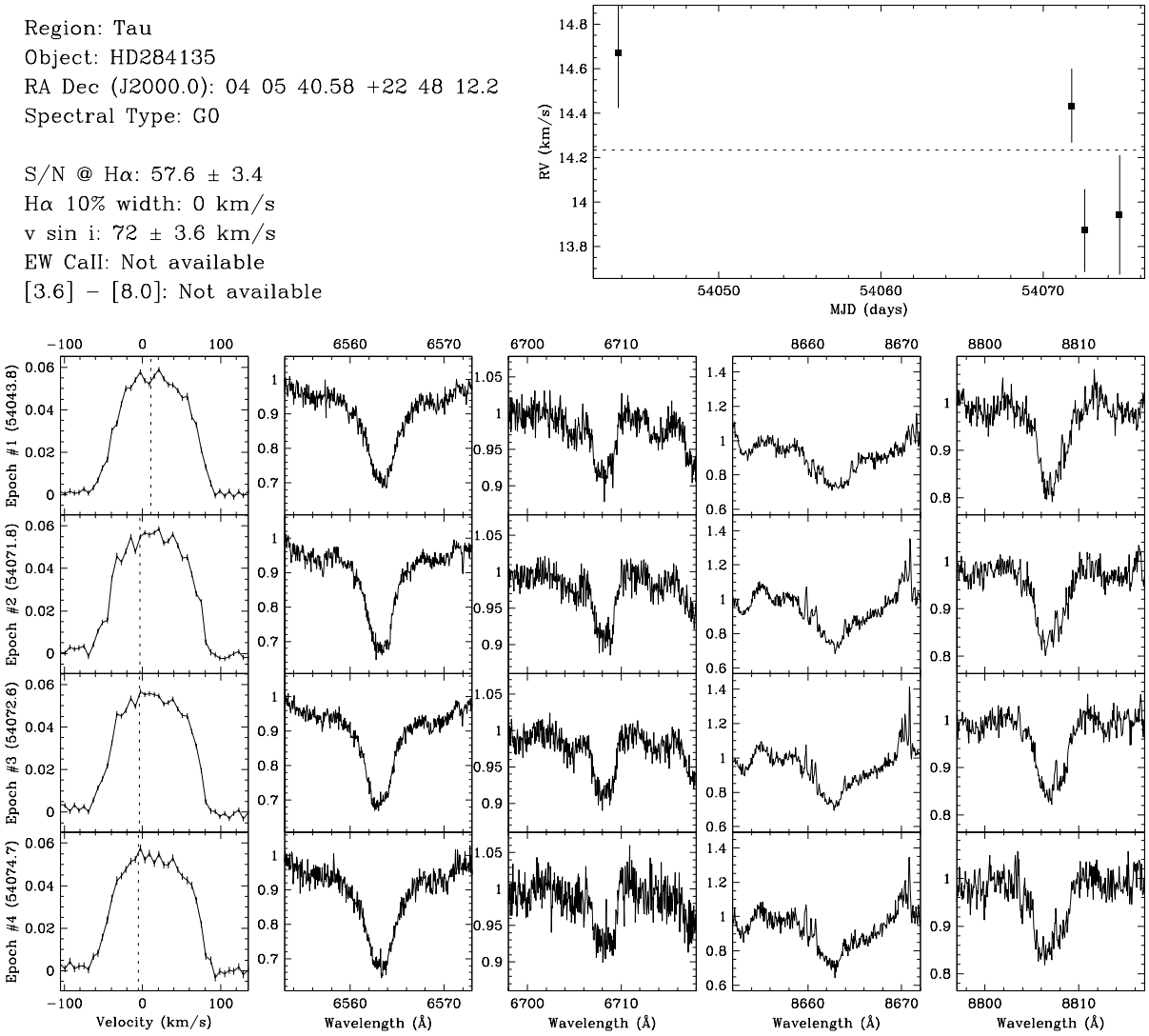

Figure 4.109 HD284135 shows no evidence of a close companion. The star has a single-line profile, and the radial velocity scatter is not significant relative to the measurement uncertainties. This target has been previously reported by Köhler & Leinert (1998) to have a resolved companion with a separation of $\sim 0\farcs378$ (~ 53 AU) at a position angle of $\sim 75\fdg2$, and an R-band flux ratio of ~ 0.80 ($\Delta K \sim 0.21$). However, there is no clear evidence in the line profile of the resolved companion. Since the resolved companion has an expected circular orbital speed of $\sim 9\,\mathrm{km\,s^{-1}}$, a second profile could be obscured if the primary star and the resolved companion have similar projected rotational velocities.

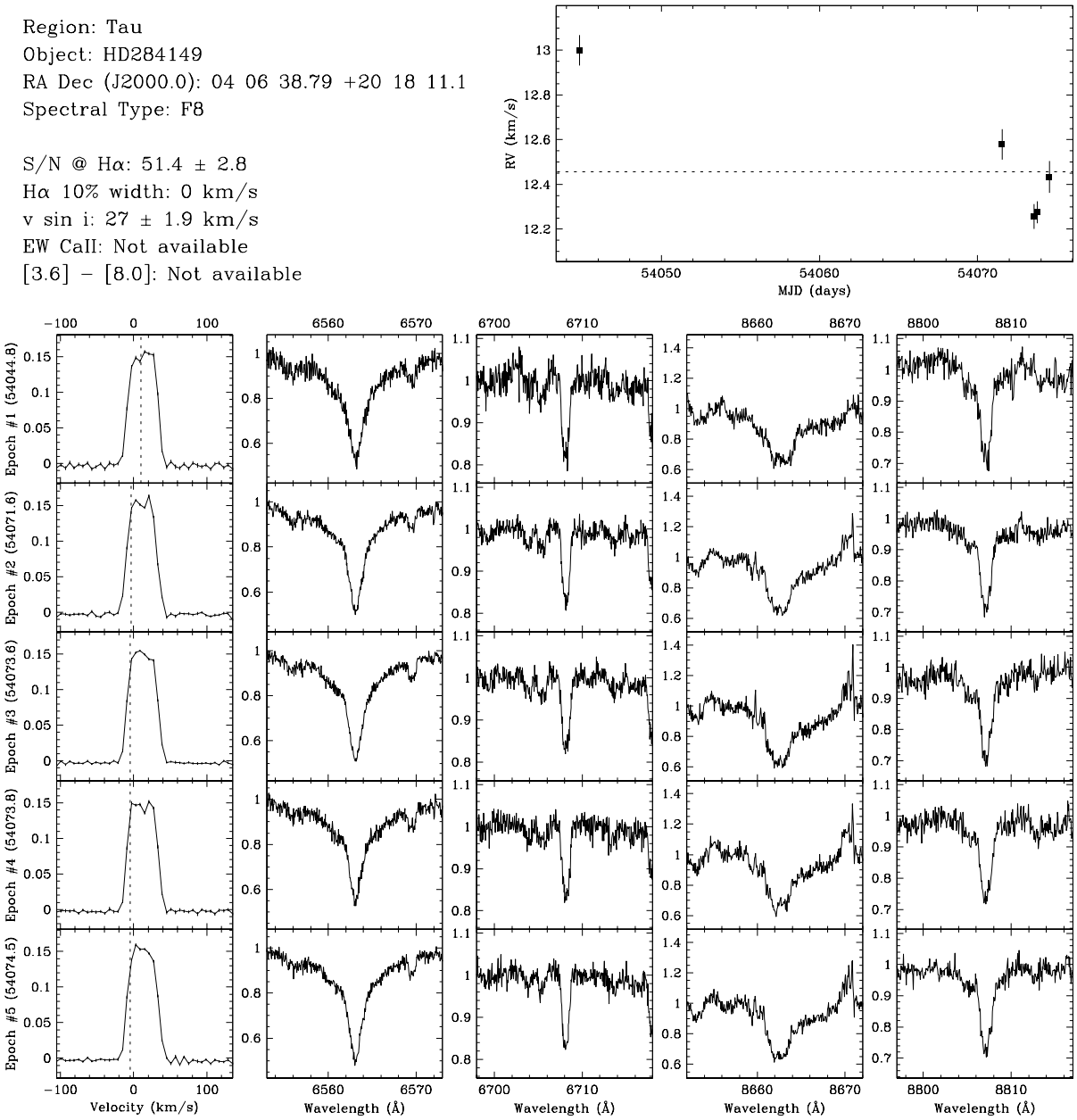

Figure 4.110 HD284149 shows no clear evidence of a close companion. The overall radial velocity scatter is consistent with that expected from systematic line profile variations, e.g. from star spots rotating with the star. This target has been previously reported by Köhler & Leinert (1998) to have no resolved companions.

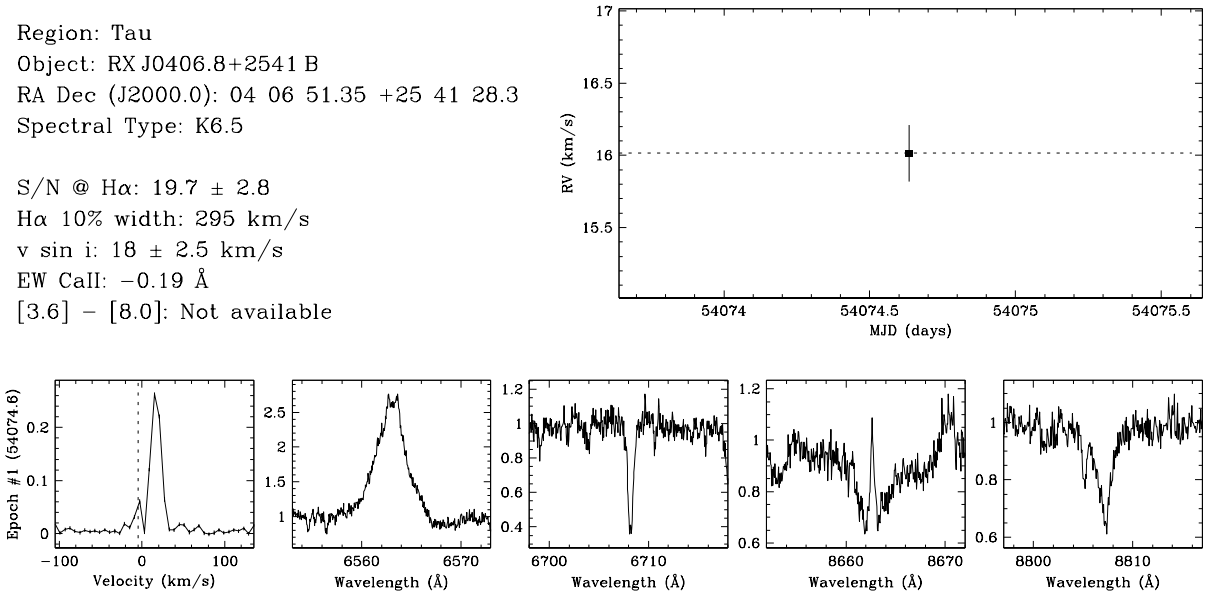

Figure 4.111 RX J0406.8+2541 B has a single-line profile, and is therefore not an SB2. The radial velocity scatter cannot be determined because the target was observed for a single epoch. Hence, it is undetermined if the target is an SB1 or a single star. The small peak in the line profile at the observer's rest frame is due to moonlight, and may have biased the radial velocity estimate toward the observer's rest frame. This target has been previously reported by Köhler & Leinert (1998) to be the secondary star of a resolved binary (RX J0406.8+2541 A+B) with a separation of $\sim 0\farcs977$ (~ 140 AU) at a position angle of $\sim 12\fdg3$, and an R-band flux ratio of ~ 0.95 ($\Delta K \sim 0.04$). However, there is no clear evidence in the line profile of the resolved companion. Since the resolved companion has an expected circular orbital speed of $\sim 3\,\mathrm{km\,s^{-1}}$, a second profile could be obscured if the primary star and the resolved companion have similar projected rotational velocities.

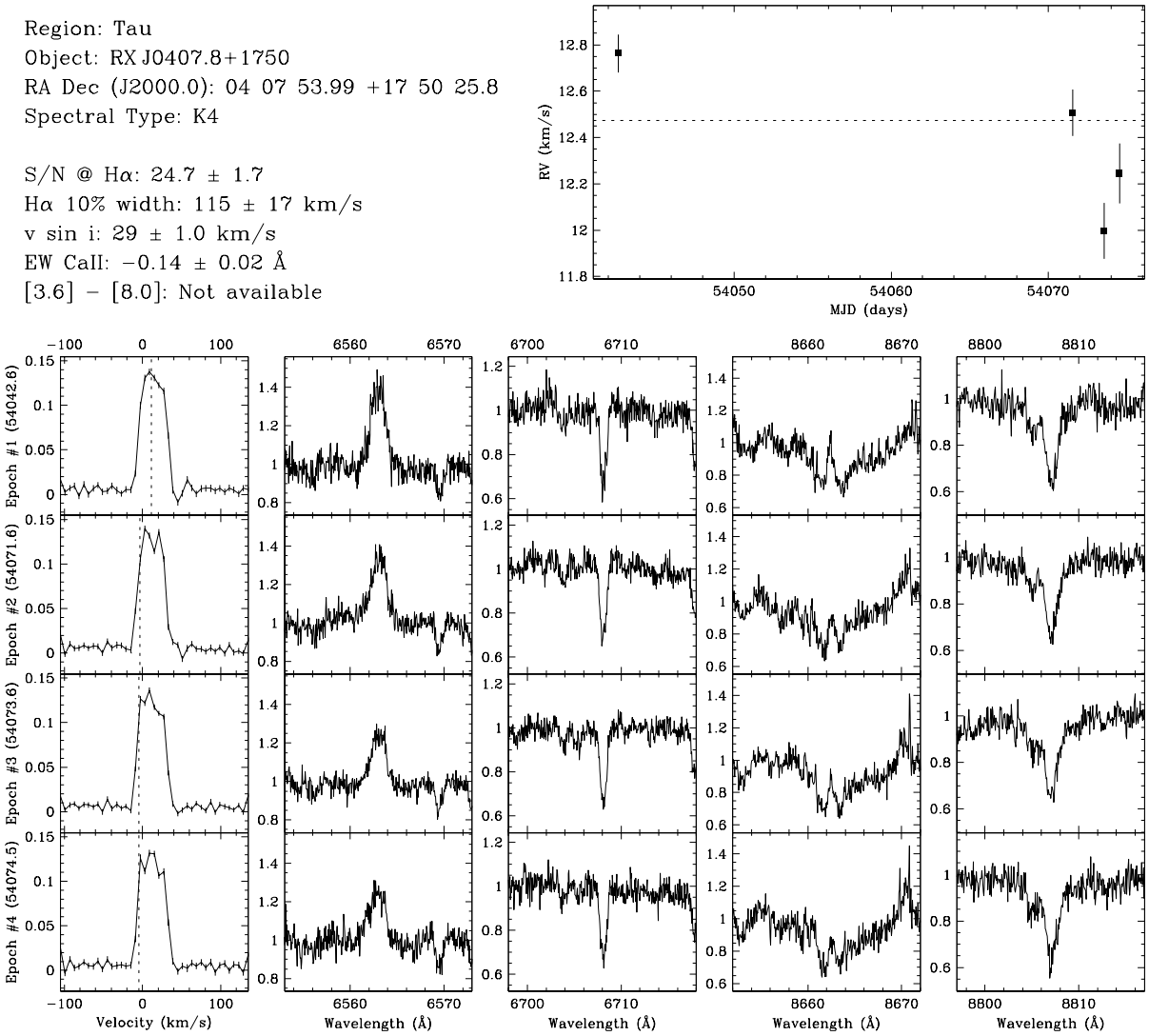

Figure 4.112 RX J0407.8+1750 shows no clear evidence of a close companion. The star has a single-line profile, and a radial velocity scatter not significant relative to variations observed within each observing run. The line profiles show significant deviation from the shape expected from pure rotational broadening. To see if these irregularities are from close companions, we fitted multiple broadening functions to the line profiles. The resultant radial velocities were not consistent with those expected from close companions: the radial velocity separations were $\sim 20\,\mathrm{km\,s^{-1}}$ with no acceleration. Therefore, we suspect the variations in the line profile are the result of star spots. The radial velocity scatter within the second observing run (epochs #2, #3 and #4) is consistent with that expected from systematic line profile variations, e.g. from star spots rotating with the star. This target has been previously reported by Köhler & Leinert (1998) to have no resolved companions.

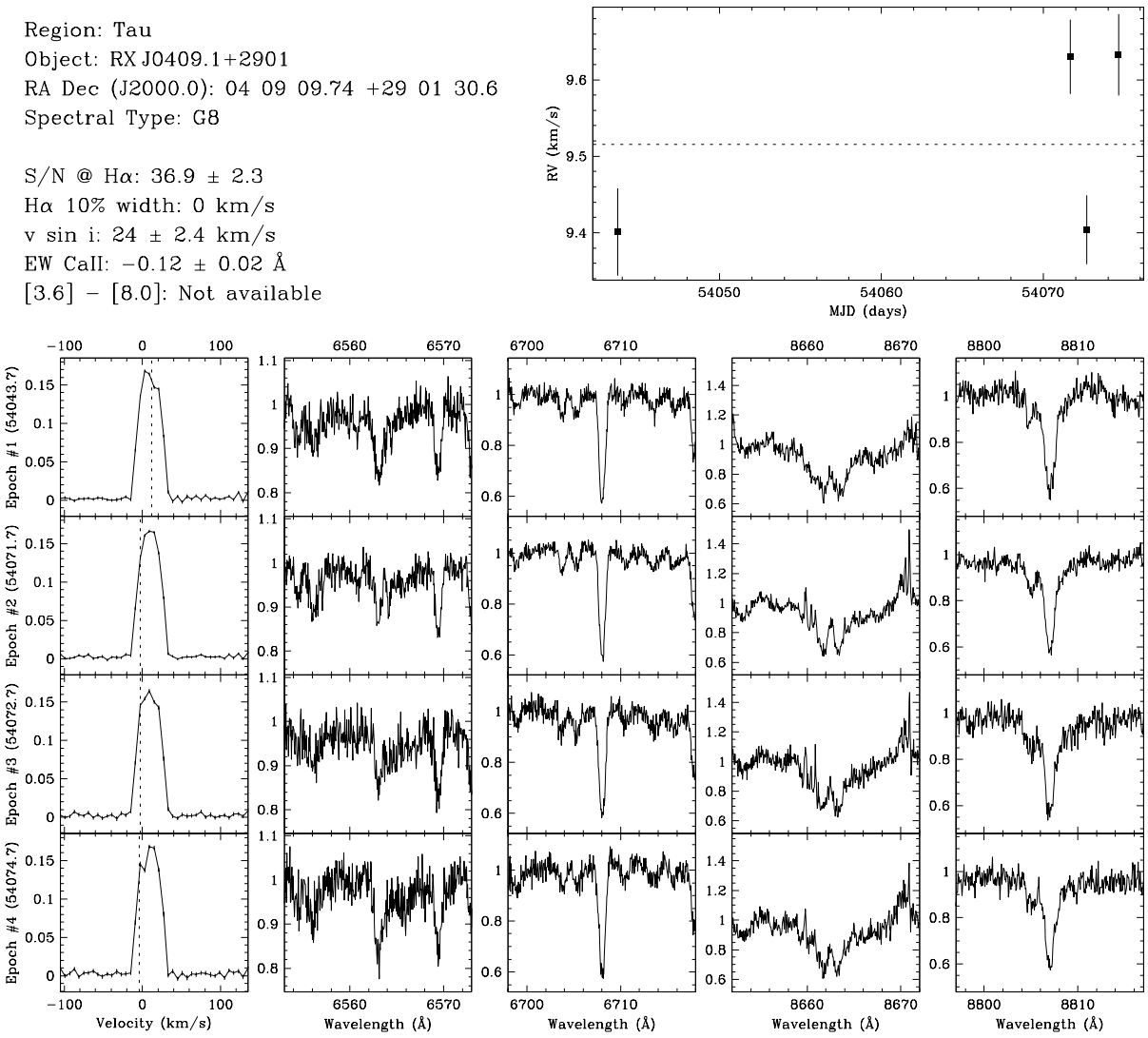

Figure 4.113 RX J0409.1+2901 shows no clear evidence of a close companion. The star has a single-line profile, and a radial velocity scatter not significant relative to variations observed within each observing run. The radial velocity scatter within the second observing run (epochs #2, #3 and #4) is consistent with that expected from systematic line profile variations, e.g. from star spots rotating with the star. The overall radial velocity deviates from that of the star forming region. However, cluster membership is supported by Li-λ6708 absorption. For epoch #4, the asymmetry in the line profile at the observer's rest frame is due to moonlight, and may have biased the radial velocity estimate toward the observer's rest frame. This target has been previously reported by Köhler & Leinert (1998) to have a resolved companion with a separation of 6.″764–6.″786 ($\sim$ 950 AU) at a position angle of 138.°7–138.°9, and an R-band flux ratio of 0.16–0.17 ($\Delta K \sim$ 1.53–1.59). Given the separation, the expected contribution to the line profile from the resolved companion is negligible.

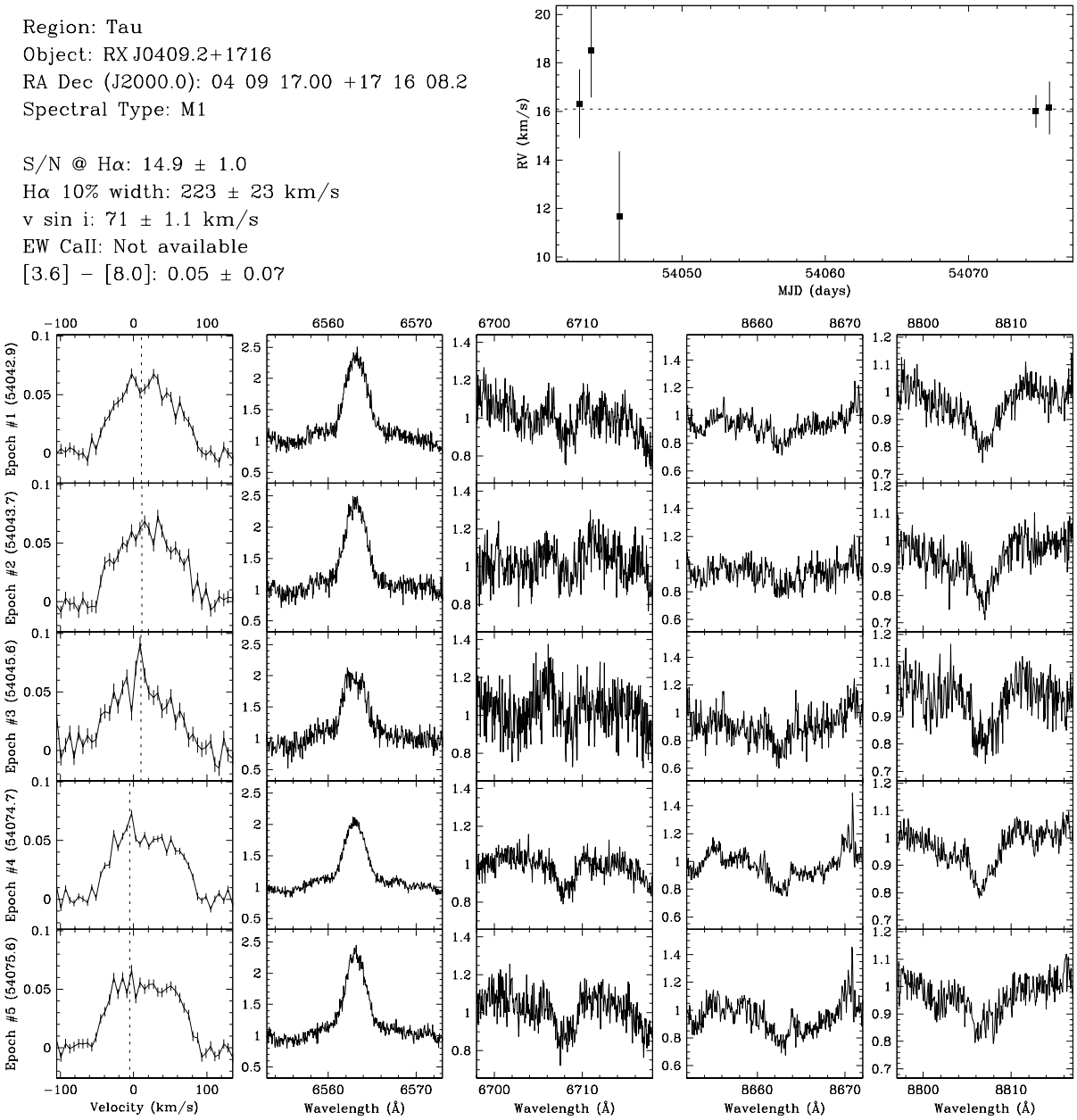

Figure 4.114 RX J0409.2+1716 shows no evidence of a close companion. The star has a single-line profile, and the radial velocity scatter is not significant relative to the measurement uncertainties. For epochs #3 and #4, the peaks in the line profile at the observer's rest frame are due to moonlight, and may have biased the radial velocity estimates toward the observer's rest frame. This target has been previously reported by Köhler & Leinert (1998) to have no resolved companions.

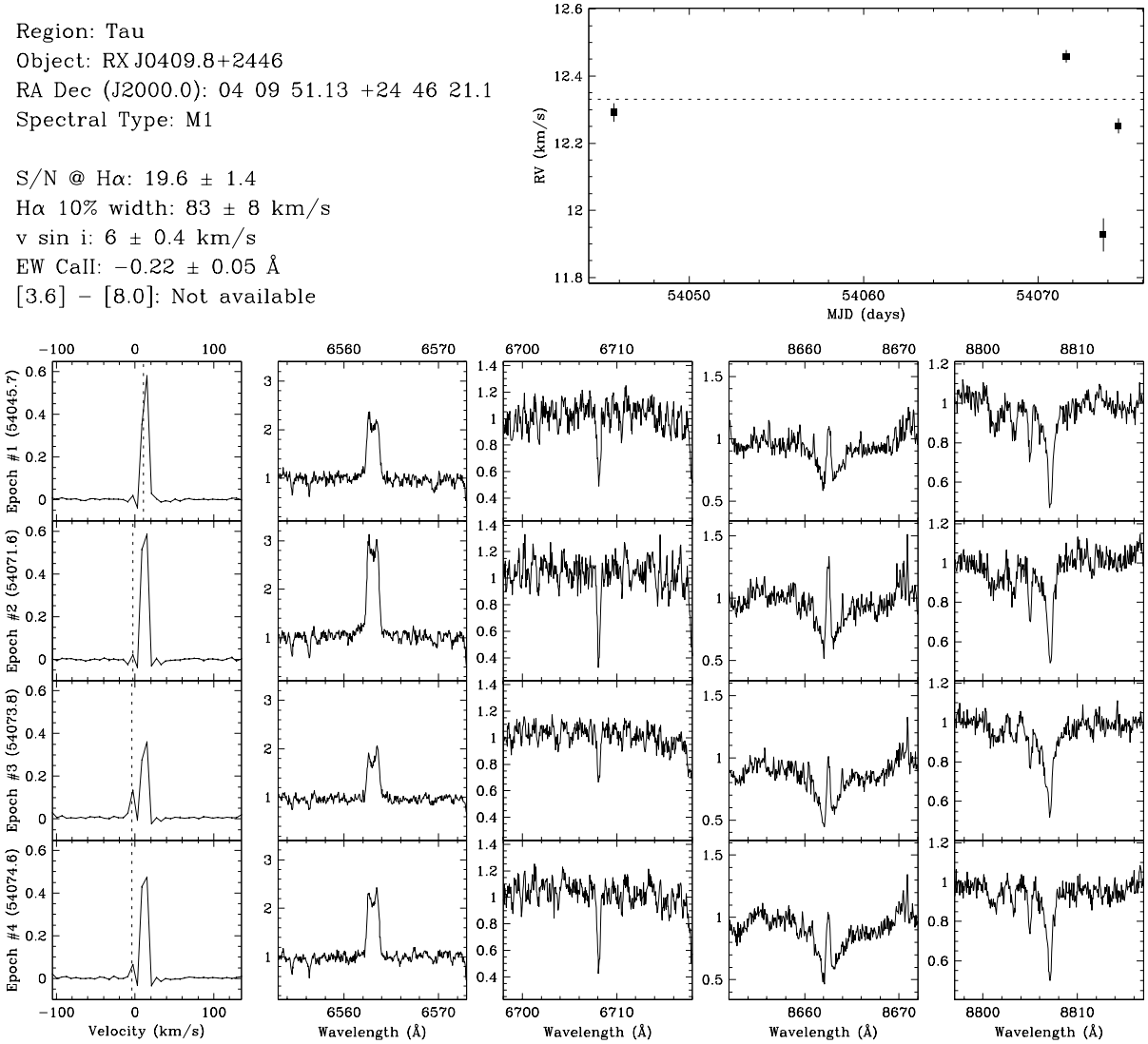

Figure 4.115 RX J0409.8+2446 shows no clear evidence of a close companion. The star has a single-line profile, and a radial velocity scatter not significant relative to variations observed within each observing run. The radial velocity scatter within the second observing run (epochs #2, #3 and #4) is consistent with that expected from systematic line profile variations, e.g. from star spots rotating with the star. For epochs #3 and #4, the small peaks in the line profile at the observer's rest frame are due to moonlight, and likely biased the radial velocity estimates toward the observer's rest frame. This target has been previously reported by Köhler & Leinert (1998) to have no resolved companions.

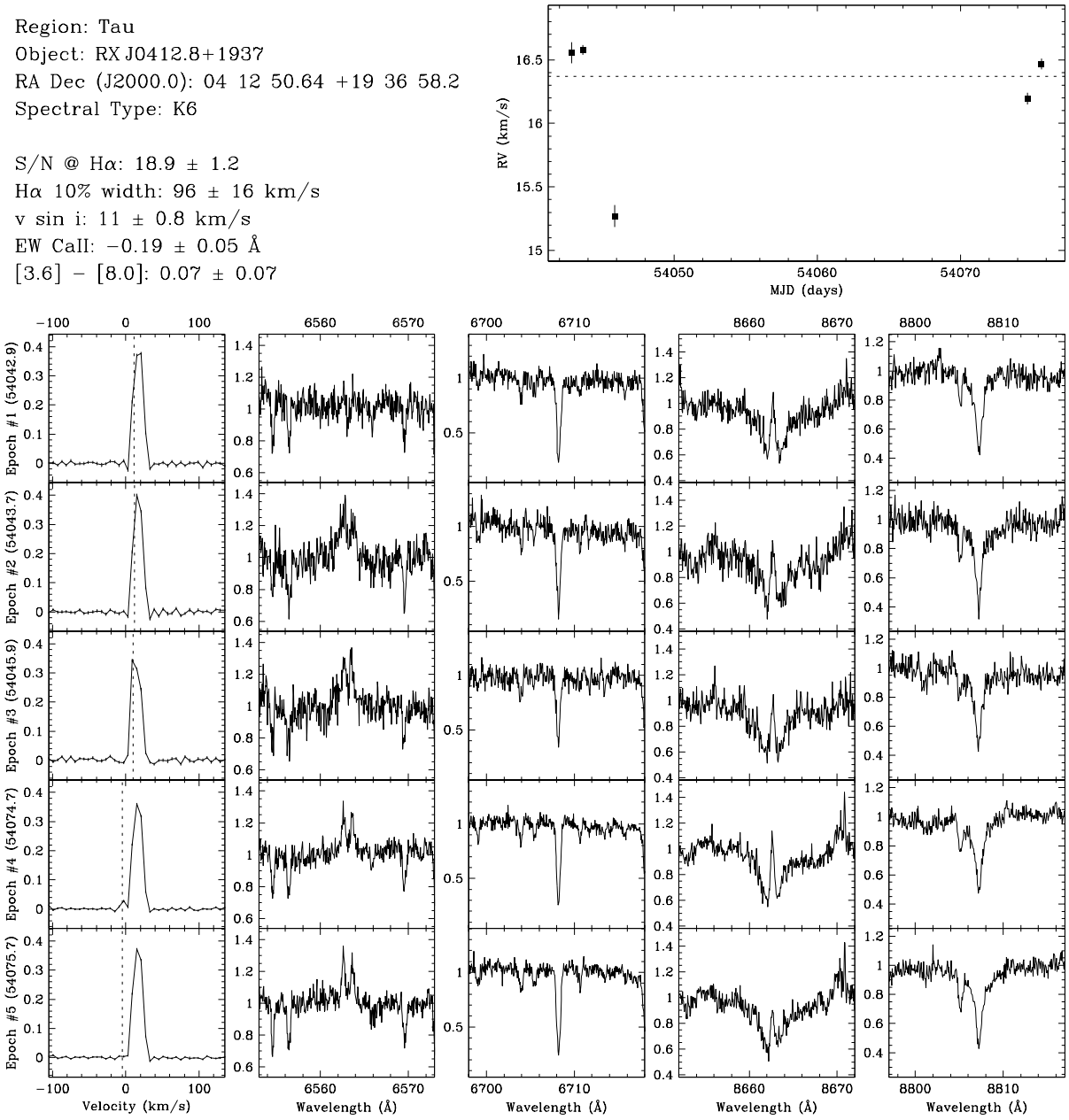

Figure 4.116 RX J0412.8+1937 shows no clear evidence of a close companion. The star has a single-line profile, and a radial velocity scatter not significant relative to variations observed within each observing run. The radial velocity scatter within each observing run is consistent with that expected from systematic line profile variations, e.g. from star spots rotating with the star. For epochs #3 and #4, the asymmetry and small peak in the line profile at the observer's rest frame is due to moonlight, and likely biased the radial velocity estimate toward the observer's rest frame. This target has been previously reported by Köhler & Leinert (1998) to have a resolved companion with a separation of $\sim 2\farcs568$ ($\sim$360 AU) at a position angle of $\sim 35\fdg3$, and an R-band flux ratio of $\sim$0.10 ($\Delta K \sim 1.05$). Given the separation, the expected contribution to the line profile from the resolved companion is negligible.

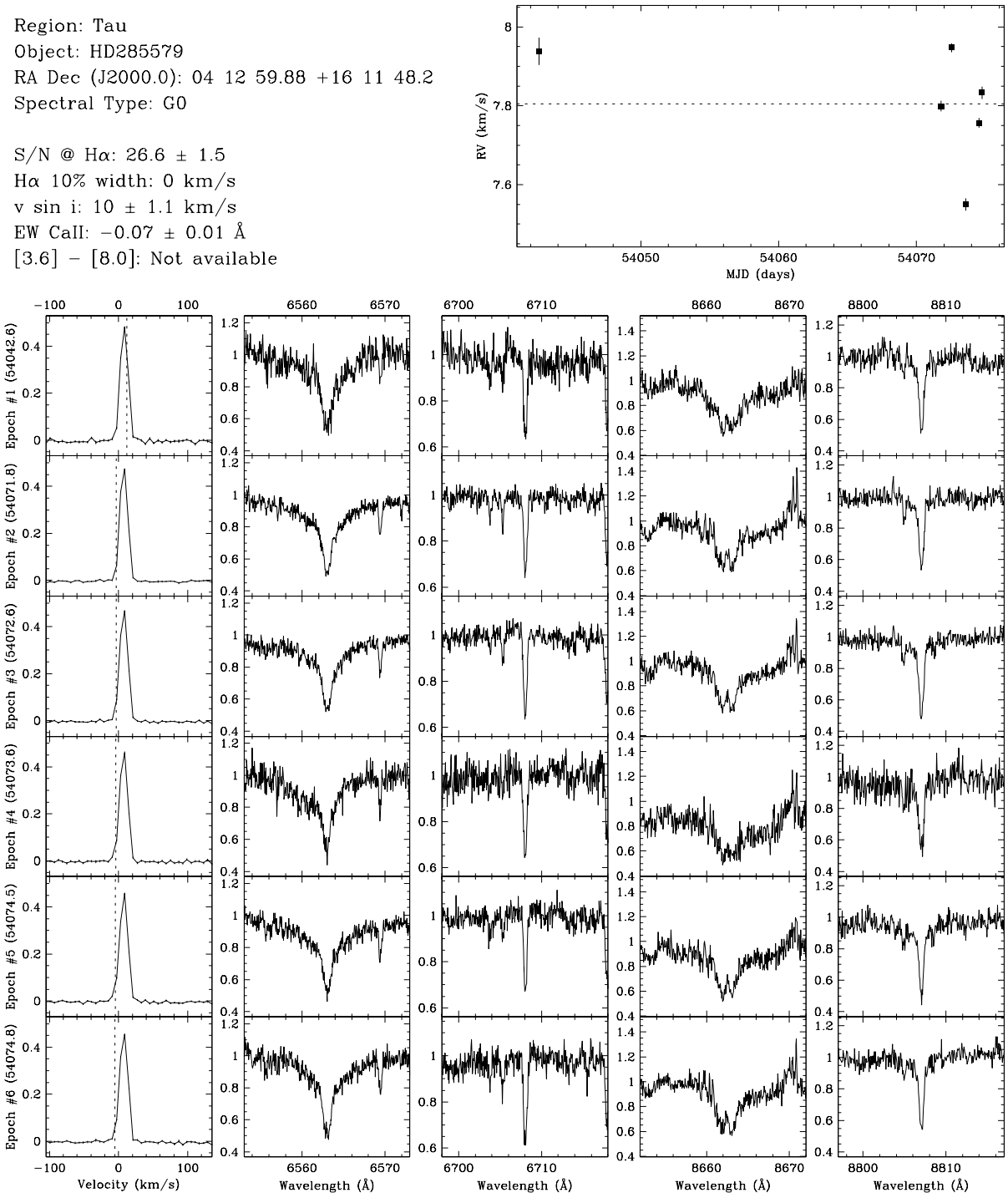

Figure 4.117 HD285579 shows no clear evidence of a close companion. The star has a single-line profile, and a radial velocity scatter not significant relative to variations observed within each observing run. The radial velocity scatter within the second observing run (epochs #2, #3, #4, #5 and #6) is consistent with that expected from systematic line profile variations, e.g. from star spots rotating with the star. The overall radial velocity deviates from that of the star forming region. However, cluster membership is supported by Li-λ6708 absorption. This target has been previously reported by Köhler & Leinert (1998) to have no resolved companions.

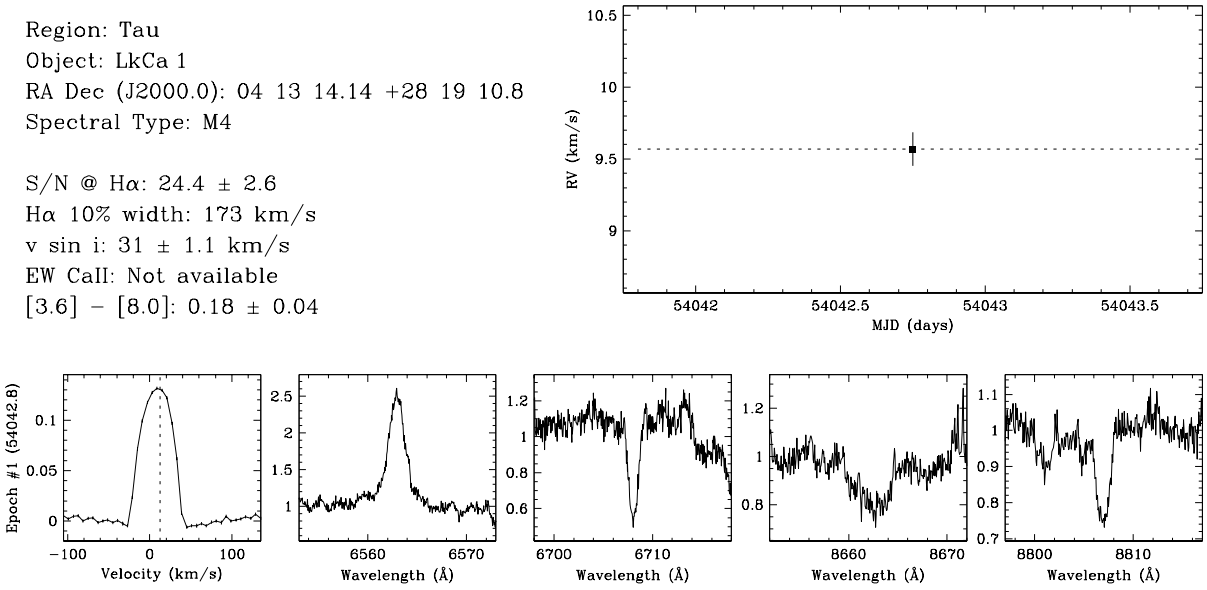

Figure 4.118 LkCa 1 has a single-line profile, and is therefore not an SB2. The radial velocity scatter cannot be determined because the target was observed for a single epoch. Hence, it is undetermined if the target is an SB1 or a single star. The overall radial velocity deviates from that of the star forming region. However, cluster membership is supported by Li-λ6708 absorption. This target has been previously reported by Leinert et al. (1993) to have no resolved companions.

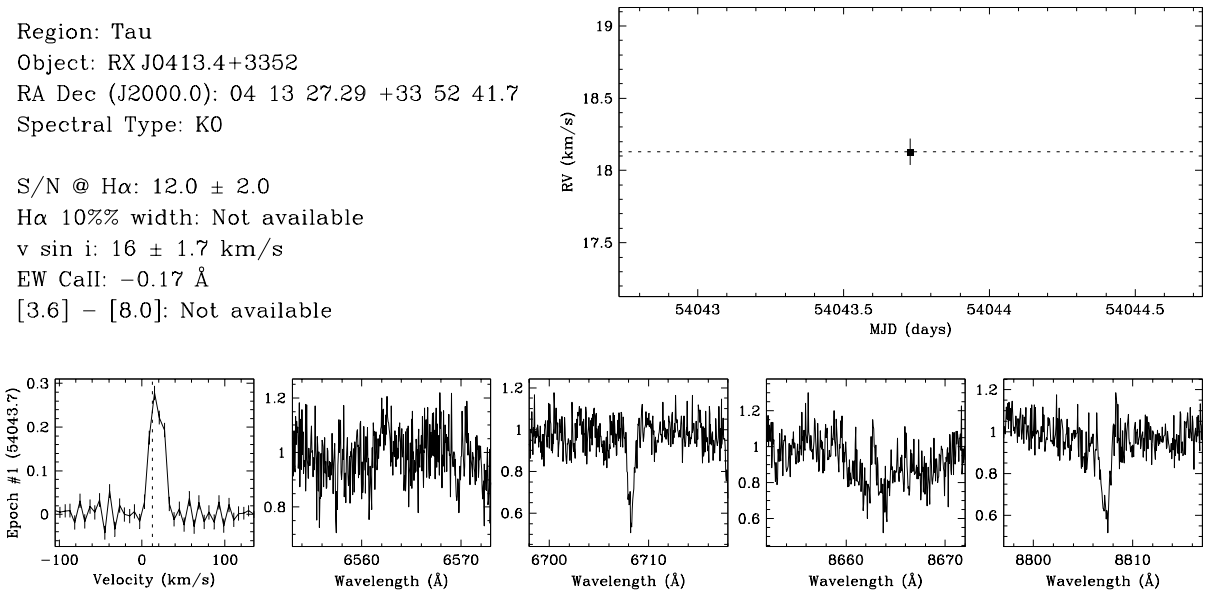

Figure 4.119 RX J0413.4+3352 has a single-line profile, and is therefore not an SB2. The radial velocity scatter cannot be determined because the target was observed for a single epoch. Hence, it is undetermined if the target is an SB1 or a single star. This target has been previously reported by Köhler & Leinert (1998) to have a resolved companion with a separation of $\sim 1\farcs008$ (~ 140 AU) at a position angle of $\sim 247\fdg9$, and an R-band flux ratio of $\lesssim 0.01$ ($\Delta K \sim 3.13$). Given the flux ratio, the expected contribution to the line profile from the resolved companion is negligible.

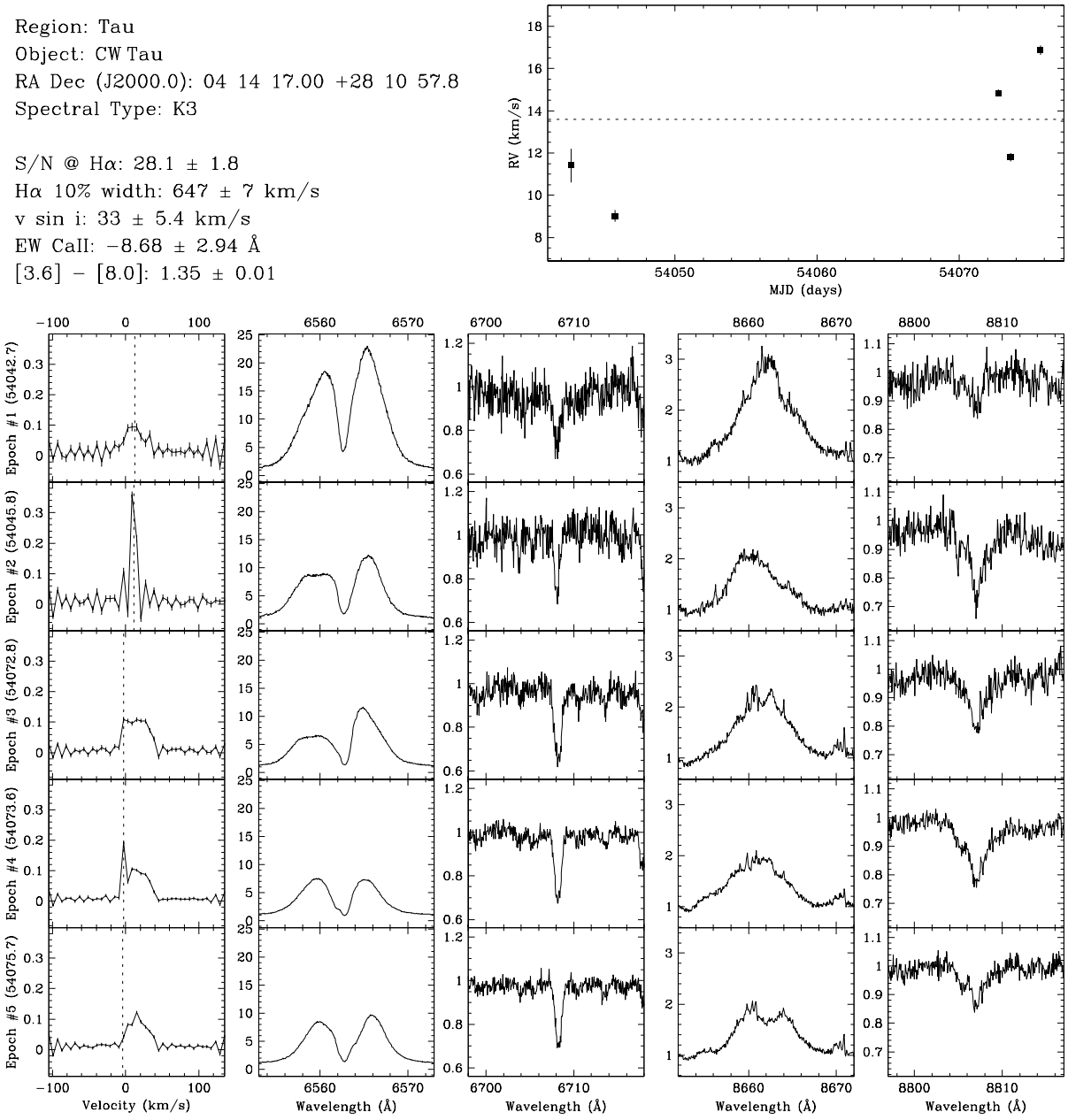

Figure 4.120 CW Tau shows no clear evidence of a close companion. The star has a single-line profile, and a radial velocity scatter not significant relative to variations observed within each observing run. The radial velocity scatter within each observing run is large but consistent with that expected from systematic line profile variations, e.g. from star spots rotating with the star. For epochs #2 and #4, the sharp peaks in the line profile at the observer's rest frame are due to moonlight, and likely biased the radial velocity estimates toward the observer's rest frame. This target has been previously reported by Leinert et al. (1993), and Ghez et al. (1993) to have no resolved companions.

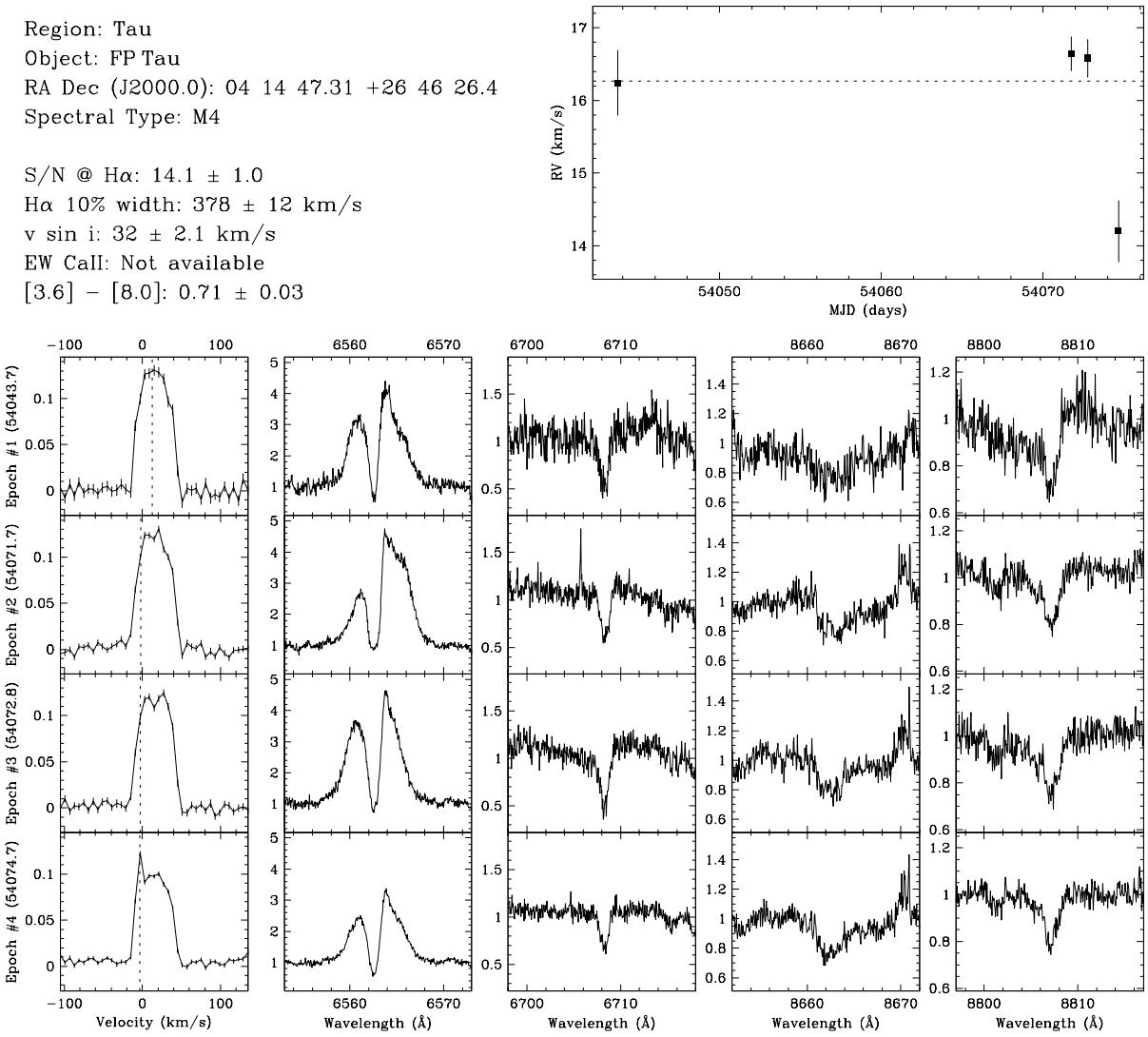

Figure 4.121 FP Tau shows no clear evidence of a close companion. The star has a single-line profile, and a radial velocity scatter not significant relative to variations observed within each observing run. The radial velocity scatter within the second observing run (epochs #2, #3 and #4) is consistent with that expected from systematic line profile variations, e.g. from star spots rotating with the star. For epoch #4, the sharp peak in the line profile at the observer's rest frame is due to moonlight, and likely biased the radial velocity estimate toward the observer's rest frame. This target has been previously reported by Leinert et al. (1993) to have no resolved companions.

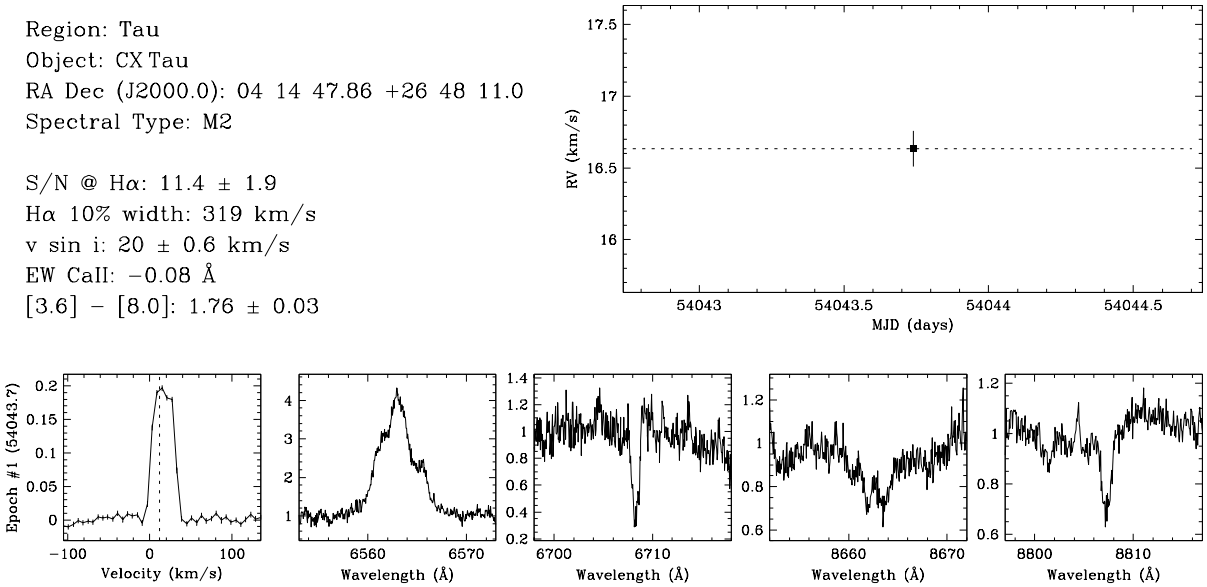

Figure 4.122 CX Tau has a single-line profile, and is therefore not an SB2. The radial velocity scatter cannot be determined because the target was observed for a single epoch. Hence, it is undetermined if the target is an SB1 or a single star. This target has been previously reported by Leinert et al. (1993) to have no resolved companions.

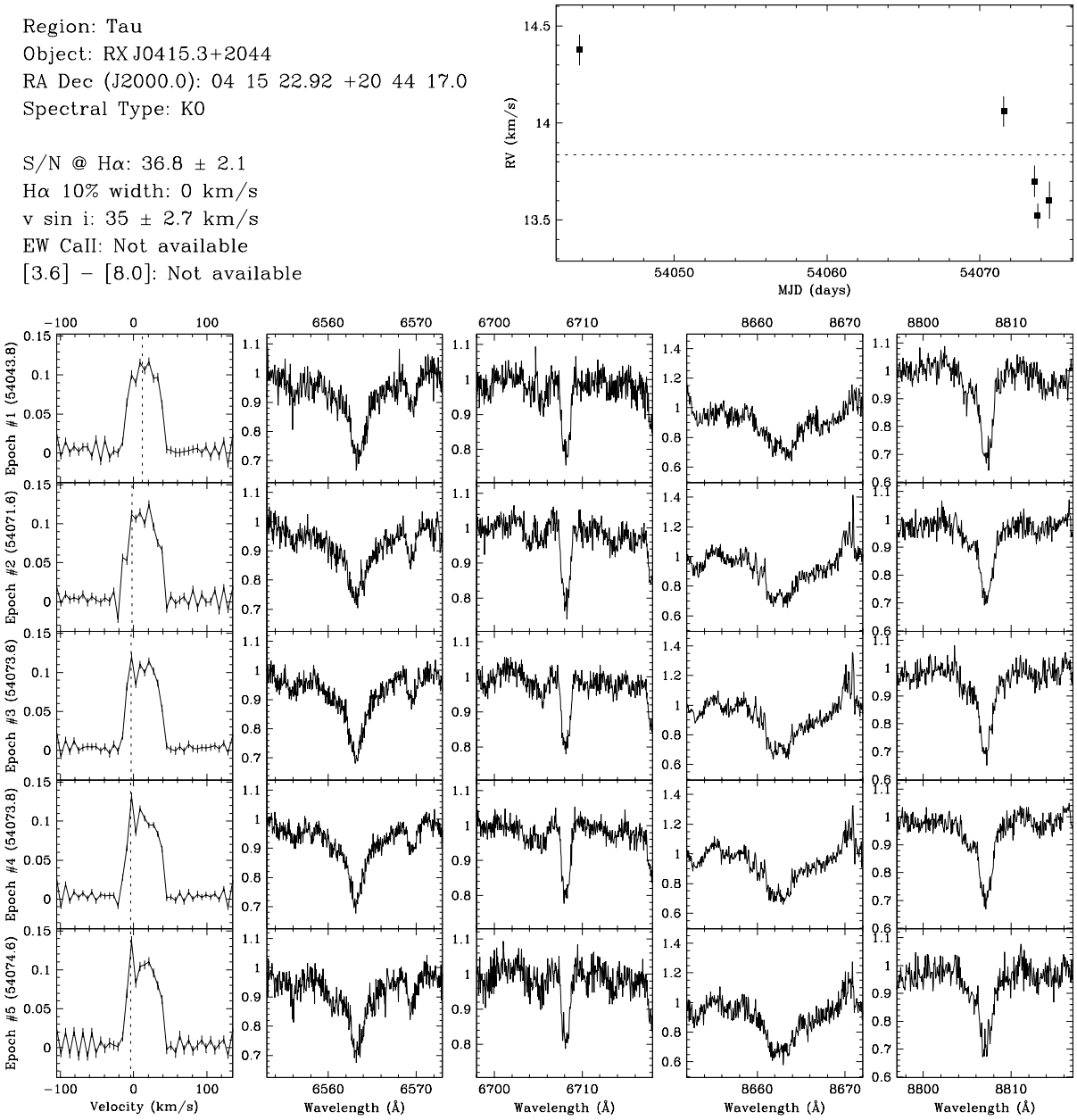

Figure 4.123 RX J0415.3+2044 shows no clear evidence of a close companion. The star has a single-line profile, and a radial velocity scatter not significant relative to variations observed within each observing run. The radial velocity scatter within the second observing run (epochs #2, #3, #4 and #5) is consistent with that expected from systematic line profile variations, e.g. from star spots rotating with the star. For epochs #3, #4 and #5, the sharp peaks in the line profile at the observer's rest frame are due to moonlight, and may have biased the radial velocity estimates toward the observer's rest frame. This target has been previously reported by Köhler & Leinert (1998) to have a resolved companion with a separation of $\sim 0\farcs589$ (~ 82 AU) at a position angle of $\sim 356\fdg8$, and an R-band flux ratio of ~ 0.06 ($\Delta K \sim 1.92$). Given the flux ratio, the expected contribution to the line profile from the resolved companion is negligible.

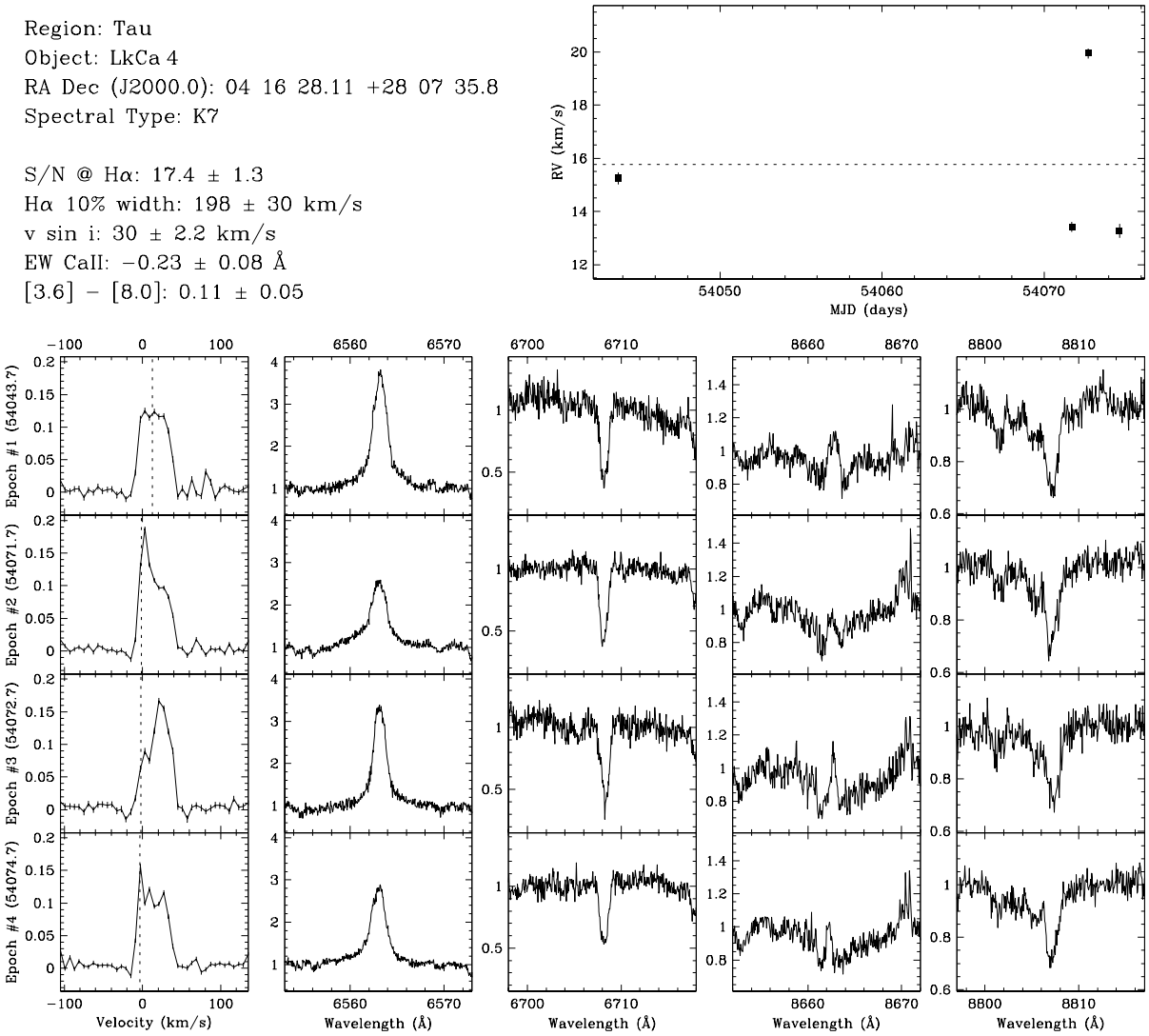

Figure 4.124 LkCa 4 shows no clear evidence of a close companion. The star has a single-line profile, and a radial velocity scatter not significant relative to variations observed within each observing run. For epochs #2, #3 and #4, the line profiles show significant deviation from the shape expected from pure rotational broadening and suggests a possible close companion. To see if these irregularities are from close companions, we fitted two broadening functions to the line profiles which give an estimate flux ratio of $\sim$0.9. For epoch #1, however, the line profile is not consistent with that expected from two sources with that flux ratio. Therefore, we suspect the variations in the line profile are the result of star spots. For epoch #4, the sharp peak in the line profile at the observer's rest frame is due to moonlight, and may have biased the radial velocity estimates toward the observer's rest frame. This target has been previously reported by Leinert et al. (1993) to have no resolved companions.

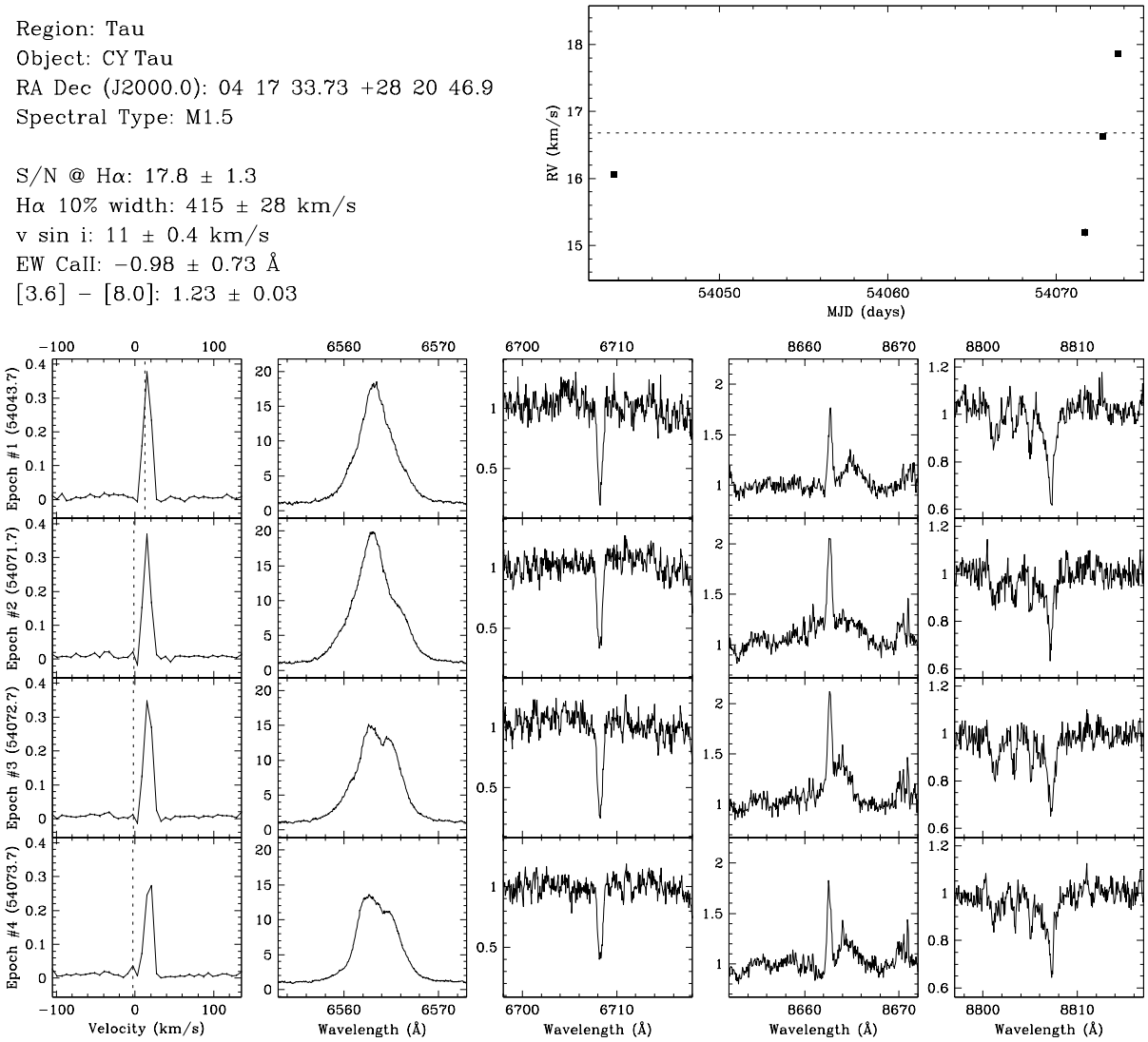

Figure 4.125 CY Tau shows no clear evidence of a close companion. The star has a single-line profile, and a radial velocity scatter not significant relative to variations observed within each observing run. The radial velocity scatter within the second observing run (epochs #2, #3 and #4) is large. To see the likelihood of a close companion contributing to this radial velocity trend, we fitted sinusoidal orbits to the radial velocities. The orbit that best fits velocities from all four epochs in one cycle has a period of ~ 46 days with an semi-amplitude of $\sim 11\,\mathrm{km\,s^{-1}}$. For this amplitude, it is unlikely that we would observe similar radial velocities between the first and second observing runs. If star spots are responsible for the trend, based on observed $v \sin i$ ($\sim 11\,\mathrm{km\,s^{-1}}$) and model stellar radius ($\sim 1.3\,R_{\odot}$), one would expect variations on a maximum timescale of ~ 2.5 days. This timescale is compatible with the second observing run span of 3.0 days. Therefore, although a close companion may be cause the radial velocity changes during the second observing run, we suspect the trend is the result of star spots. The radial velocity scatter within the second observing run (epochs #2, #3 and #4) is large. This target has been previously reported by Leinert et al. (1993), and Ghez et al. (1993) to have no resolved companions.

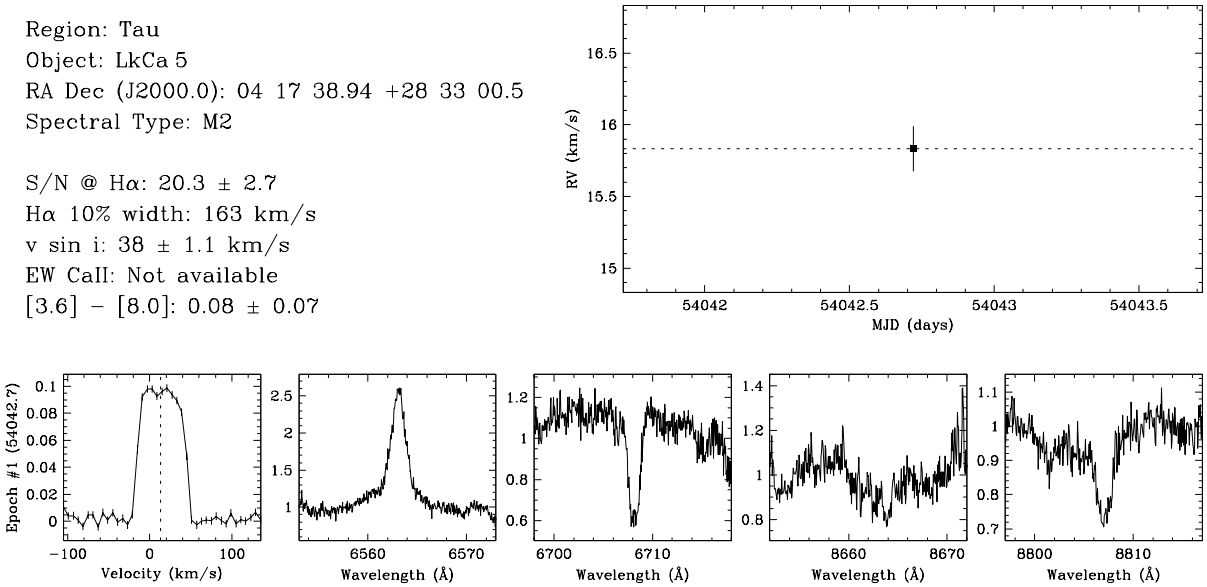

Figure 4.126 LkCa 5 has a single-line profile, and is therefore not an SB2. The radial velocity scatter cannot be determined because the target was observed for a single epoch. Hence, it is undetermined if the target is an SB1 or a single star. This target has been previously reported by Leinert et al. (1993) to have no resolved companions.

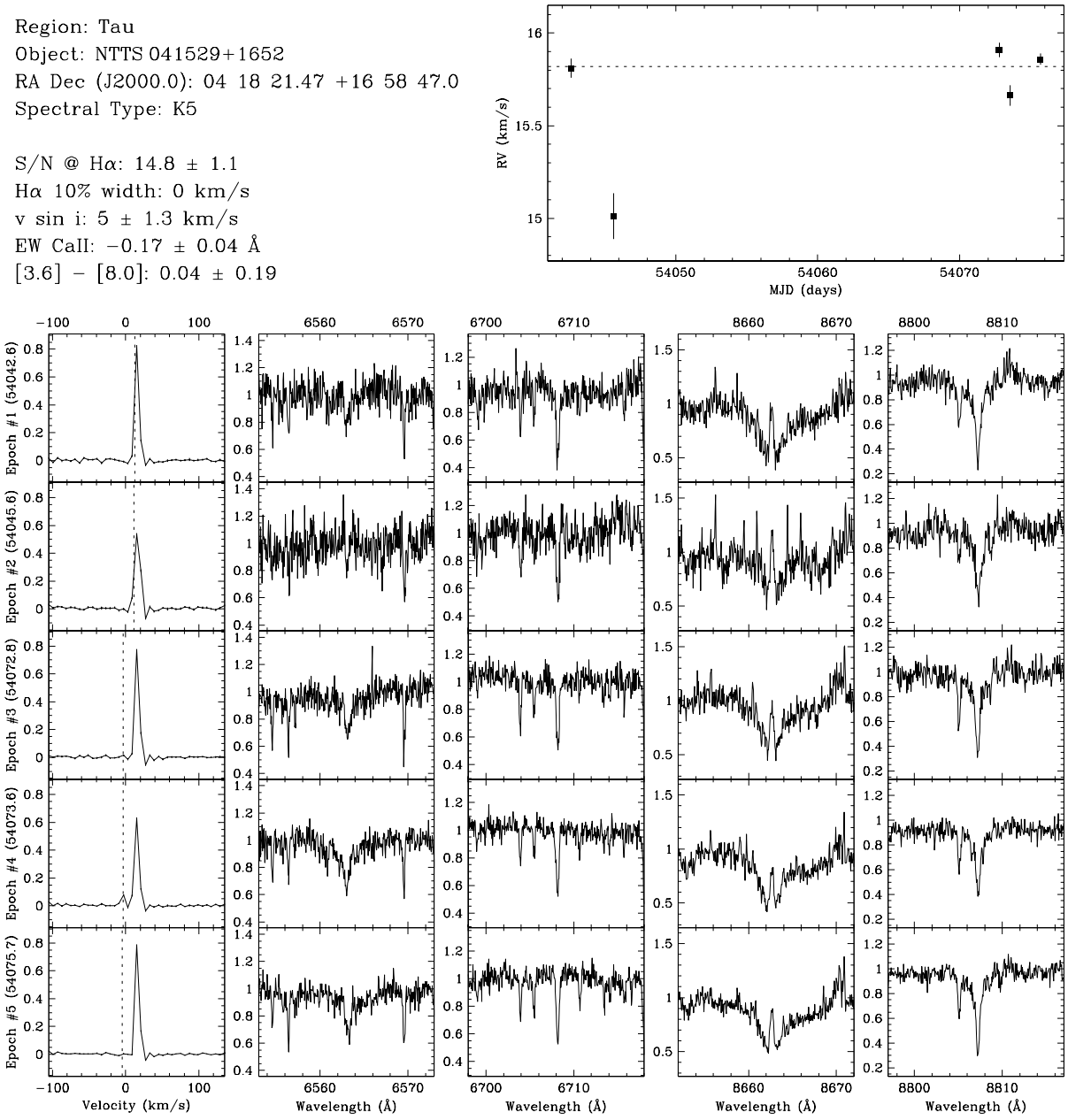

Figure 4.127 NTTS 041529+1652 shows no clear evidence of a close companion. The star has a single-line profile, and a radial velocity scatter not significant relative to variations observed within each observing run. The radial velocity scatter within each observing run is consistent with that expected from systematic line profile variations, e.g. from star spots rotating with the star. For epoch #4, the small peak in the line profile at the observer's rest frame is due to moonlight, and may have biased the radial velocity estimate toward the observer's rest frame. This target has been previously reported by Leinert et al. (1993) to have no resolved companions.

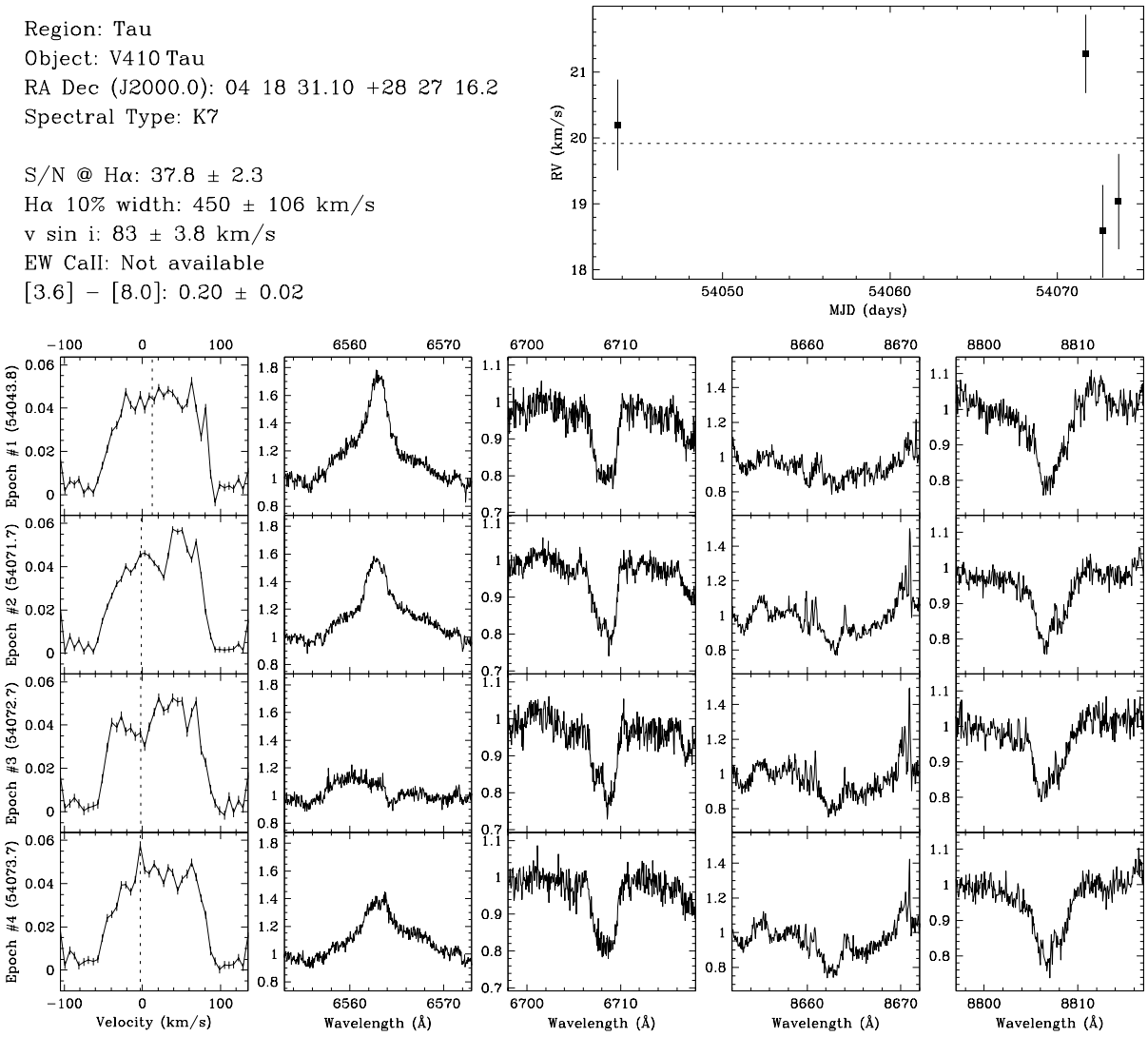

Figure 4.128 V410 Tau shows no evidence of a close companion. The star has a single-line profile, and the radial velocity scatter is not significant relative to the measurement uncertainties. For epoch #4, the sharp peak in the line profile at the observer's rest frame is due to moonlight, and may have biased the radial velocity estimate toward the observer's rest frame. This target has been previously reported by Ghez et al. (1993), and Ghez et al. (1997b) as a resolved triple (V410 Tau A+B+C) with an A–B and AB–C separation of $\sim 0\farcs123$ (~ 17 AU) and $\sim 0\farcs2871$ (~ 40 AU) at position angles of $\sim 218°$ and $\sim 132°$, and an A–B R-band flux ratio of 0.00–0.01 ($\Delta K \sim 1.94$–2.50). Given the flux ratio, the expected contribution to the line profile from the resolved companion is negligible.

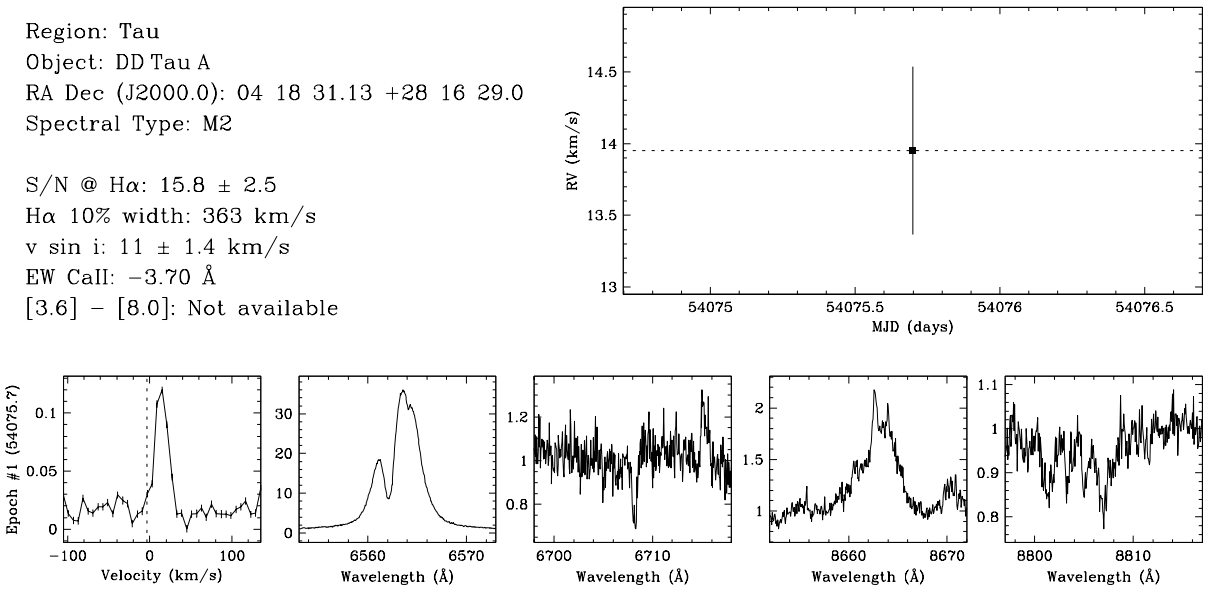

Figure 4.129 DD Tau A has a single-line profile, and is therefore not an SB2. The radial velocity scatter cannot be determined because the target was observed for a single epoch. Hence, it is undetermined if the target is an SB1 or a single star. The spectrum is heavily veiled, and we derived the radial velocity from fits to the line profile rather than from direct fits to the spectra (see §4.4.2). This target has been previously reported by Leinert et al. (1993), and Ghez et al. (1993) to have a resolved companion (DD Tau B) with a separation of 0.″56–0.″57 (78–80 AU) at a position angle of 186°–188°, and an R-band flux ratio of 0.05–0.28 ($\Delta K \sim 0.48$–0.84). However, there is no clear evidence in the line profile of the resolved companion. Since the resolved companion has an expected circular orbital speed of $\sim 2\,\mathrm{km\,s^{-1}}$, a second profile could be obscured if the primary star and the resolved companion have similar projected rotational velocities.

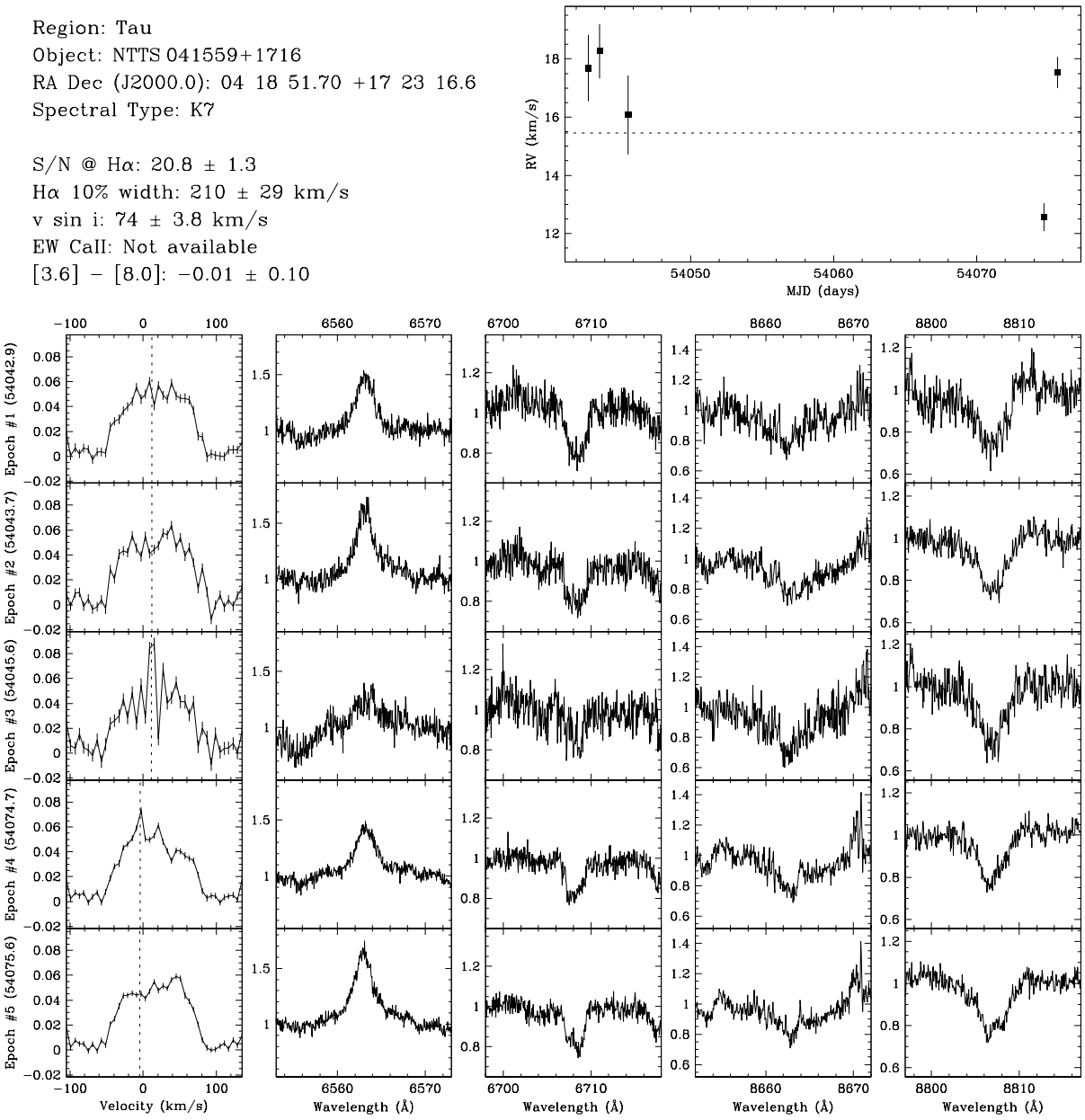

Figure 4.130 NTTS 041559+1716 shows no clear evidence of a close companion. The star has a single-line profile, and a radial velocity scatter not significant relative to variations observed within each observing run. The radial velocity scatter within each observing run is consistent with that expected from systematic line profile variations, e.g. from star spots rotating with the star. For epoch #3 and #4, the sharp peaks in the line profile at the observer's rest frame are due to moonlight, and may have biased the radial velocity estimates toward the observer's rest frame. This target has been previously reported by Leinert et al. (1993) to have no resolved companions.

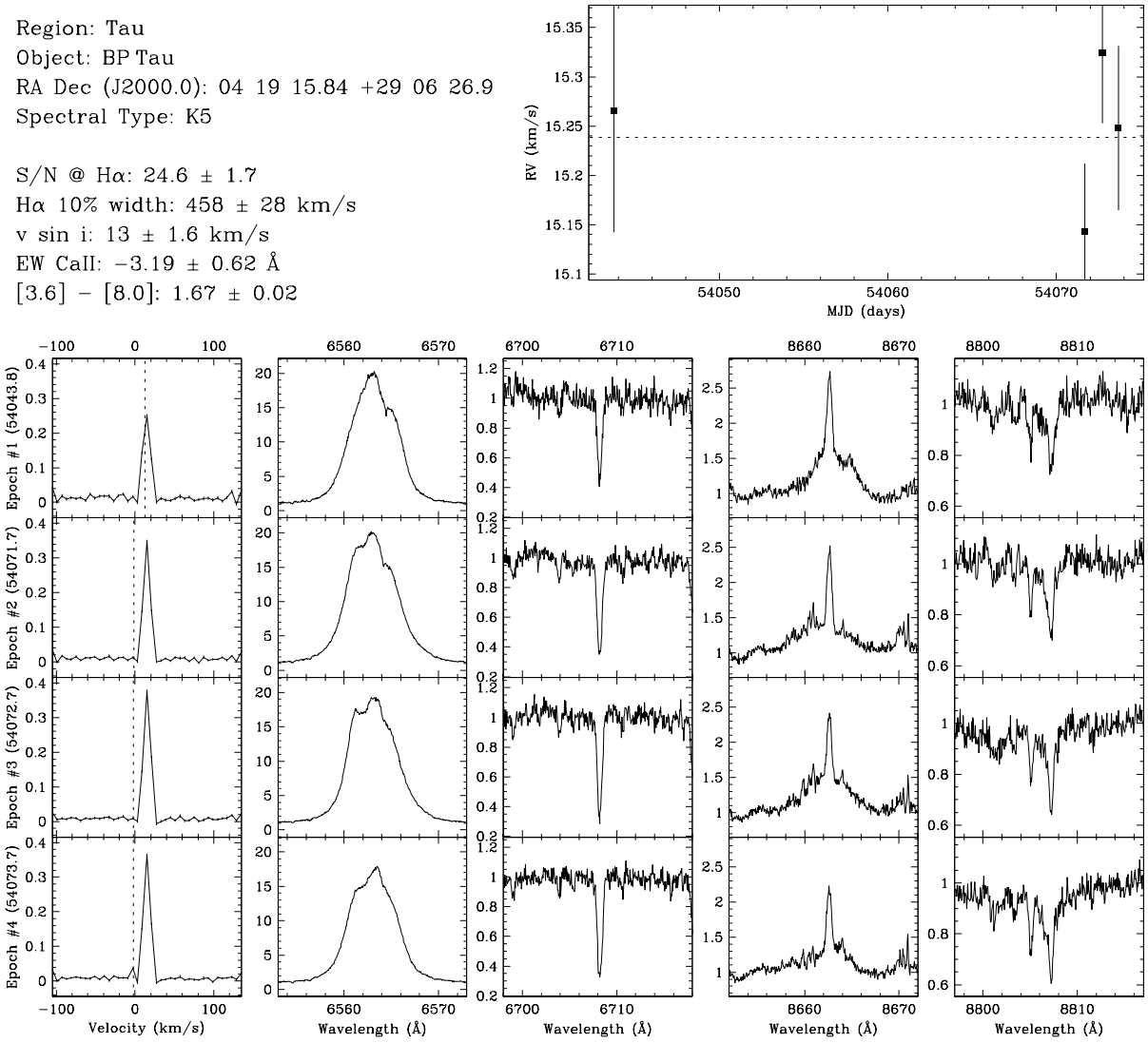

Figure 4.131 BP Tau shows no evidence of a close companion. The star has a single-line profile, and the radial velocity scatter is not significant relative to the measurement uncertainties. This target has been previously reported by Leinert et al. (1993), and Ghez et al. (1993) to have no resolved companions.

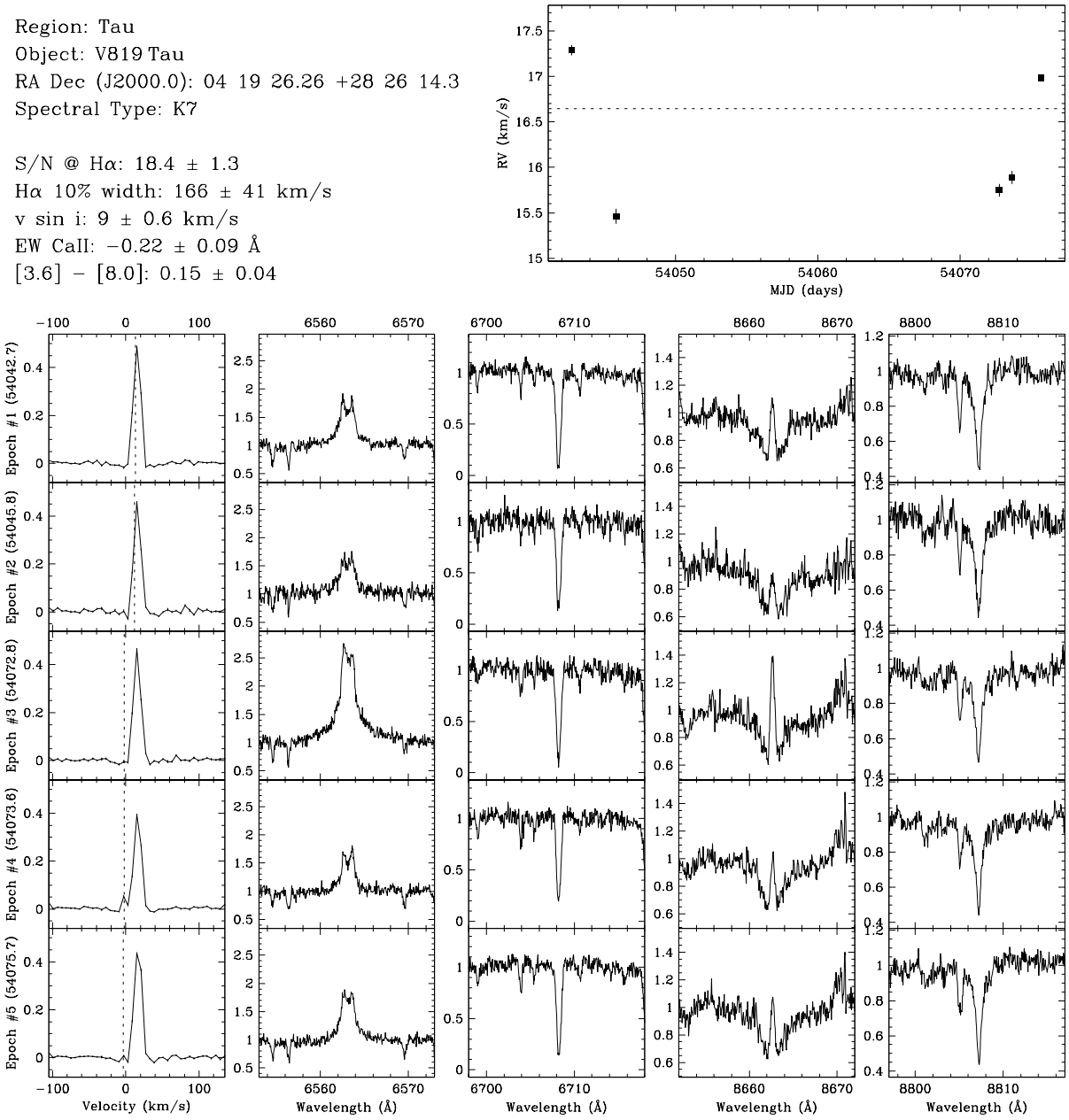

Figure 4.132 V819 Tau shows no clear evidence of a close companion. The star has a single-line profile, and a radial velocity scatter not significant relative to variations observed within each observing run. There are large variations in accretion signatures such as Hα 10% width and Ca II–λ8662 flux. These changes may contribute to the scatter in radial velocity estimates. The radial velocity scatter within the second observing run (epochs #2, #3 and #4) is large but consistent with that expected from systematic line profile variations, e.g. from star spots rotating with the star. For epoch #2, #4 and #5, the slight asymmetry and small peak in the line profile at the observer's rest frame is due to moonlight, and may have biased the radial velocity estimate toward the observer's rest frame. This target has been previously reported by Leinert et al. (1993) to have a resolved companion with a separation of $\sim$10.″5 ($\sim$1500 AU) at a position angle of $\sim$172°, and an R-band flux ratio of $\lesssim$0.01 ($\Delta K \sim 3.64$). Given the flux ratio and separation, the expected contribution to the line profile from the resolved companion is negligible.

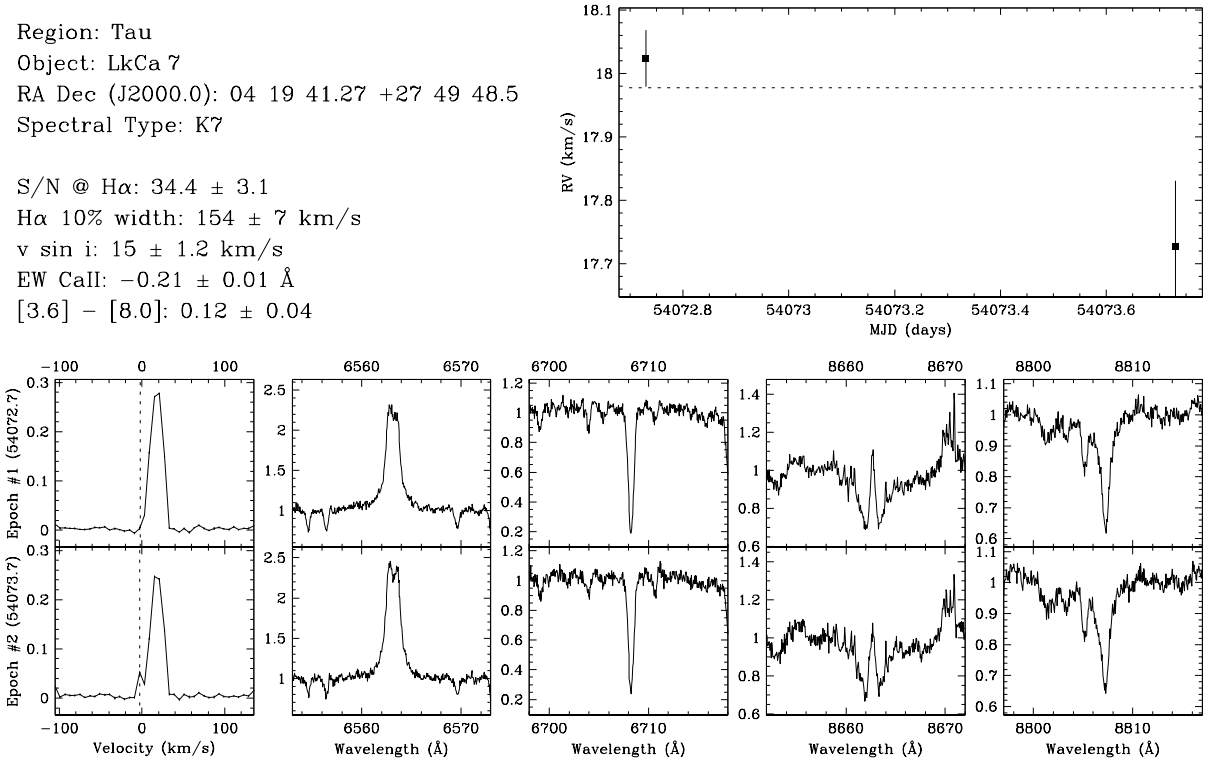

Figure 4.133 LkCa 7 has a single-line profile, and is therefore not an SB2. The radial velocity scatter over the short baseline available does not conclusively indicate if the target is an SB1 or a single star. For epoch #2, the small peak in the line profile at the observer's rest frame is due to moonlight, and may have biased the radial velocity estimate toward the observer's rest frame. This target has been previously reported by Leinert et al. (1993) to have a resolved companion with a separation of $\sim 1\farcs05$ (~ 150 AU) at a position angle of $\sim 25°$, and an R-band flux ratio of ~ 0.26 ($\Delta K \sim 0.63$). Given the separation, the expected contribution to the line profile from the resolved companion is small.

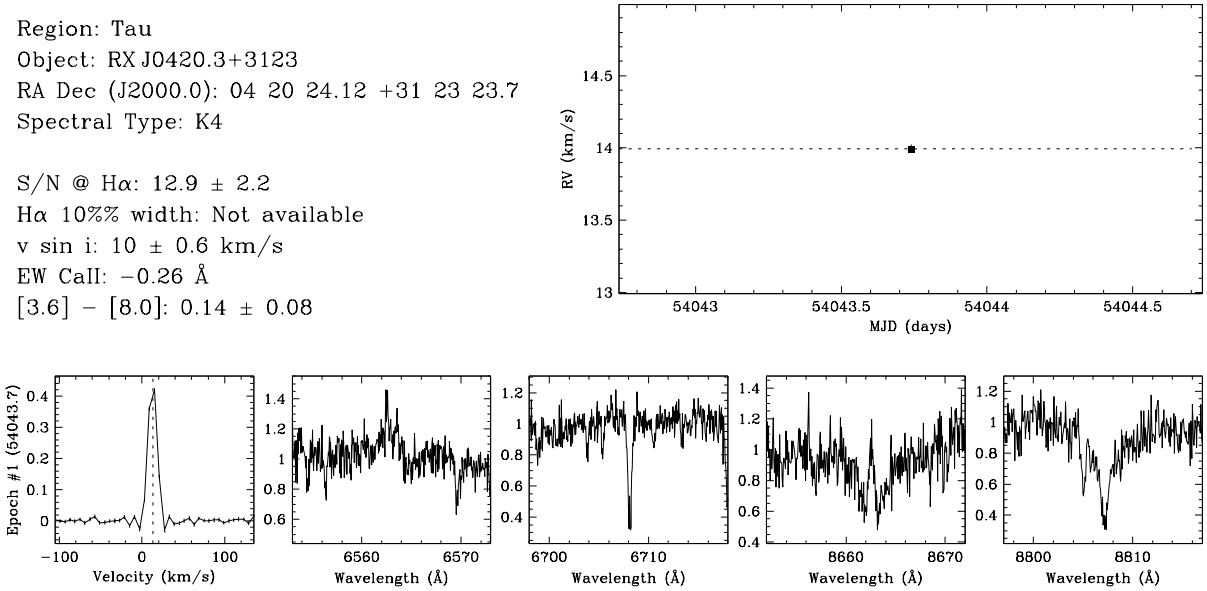

Figure 4.134 RX J0420.3+3123 has a single-line profile, and is therefore not an SB2. The radial velocity scatter cannot be determined because the target was observed for a single epoch. Hence, it is undetermined if the target is an SB1 or a single star. This target has been previously reported by Köhler & Leinert (1998) to have no resolved companions.

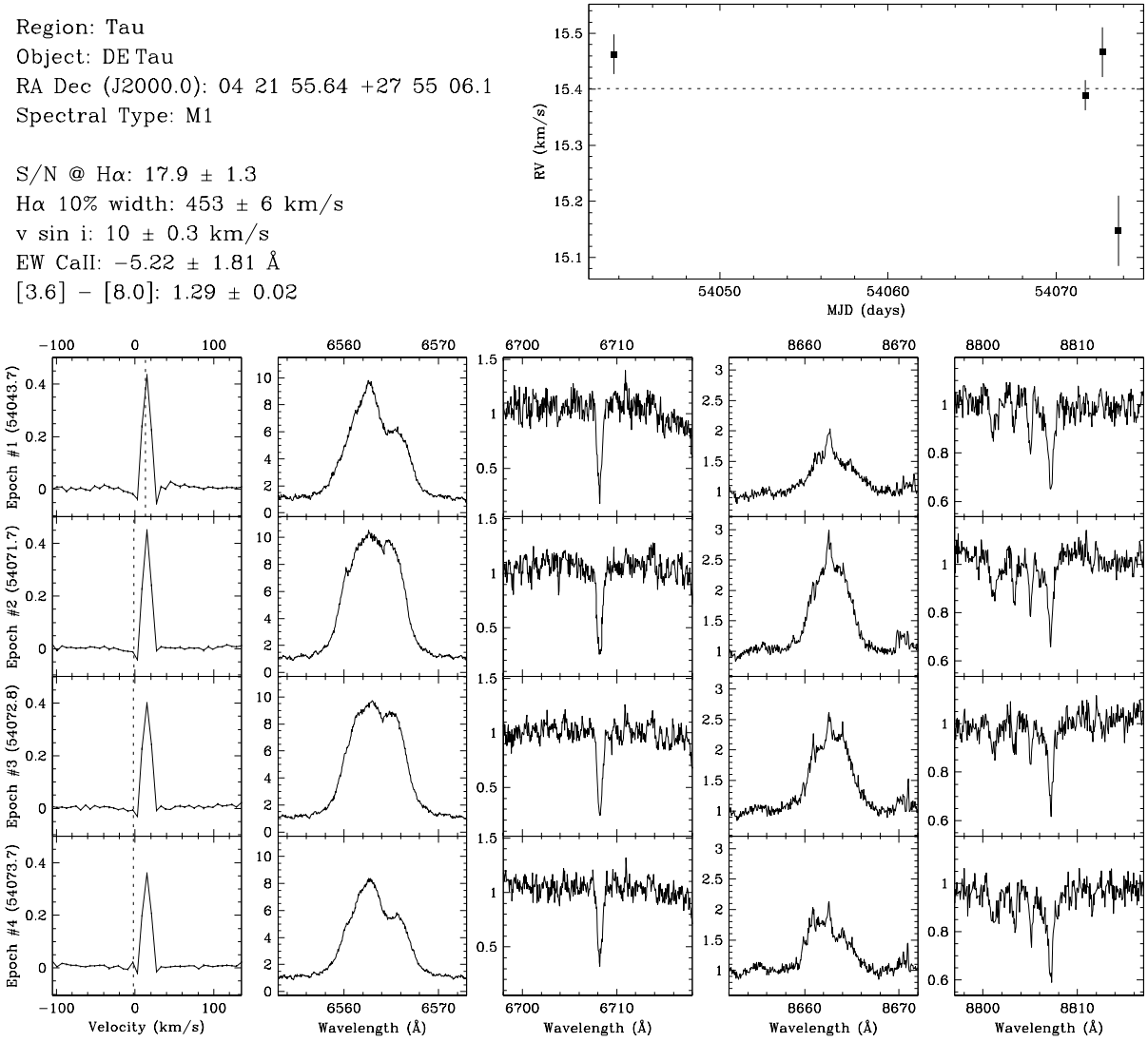

Figure 4.135 DE Tau shows no clear evidence of a close companion. The star has a single-line profile, and a radial velocity scatter not significant relative to variations observed within each observing run. The radial velocity scatter within the second observing run (epochs #2, #3 and #4) is consistent with that expected from systematic line profile variations, e.g. from star spots rotating with the star. This target has been previously reported by Leinert et al. (1993), and Ghez et al. (1993) to have no resolved companions.

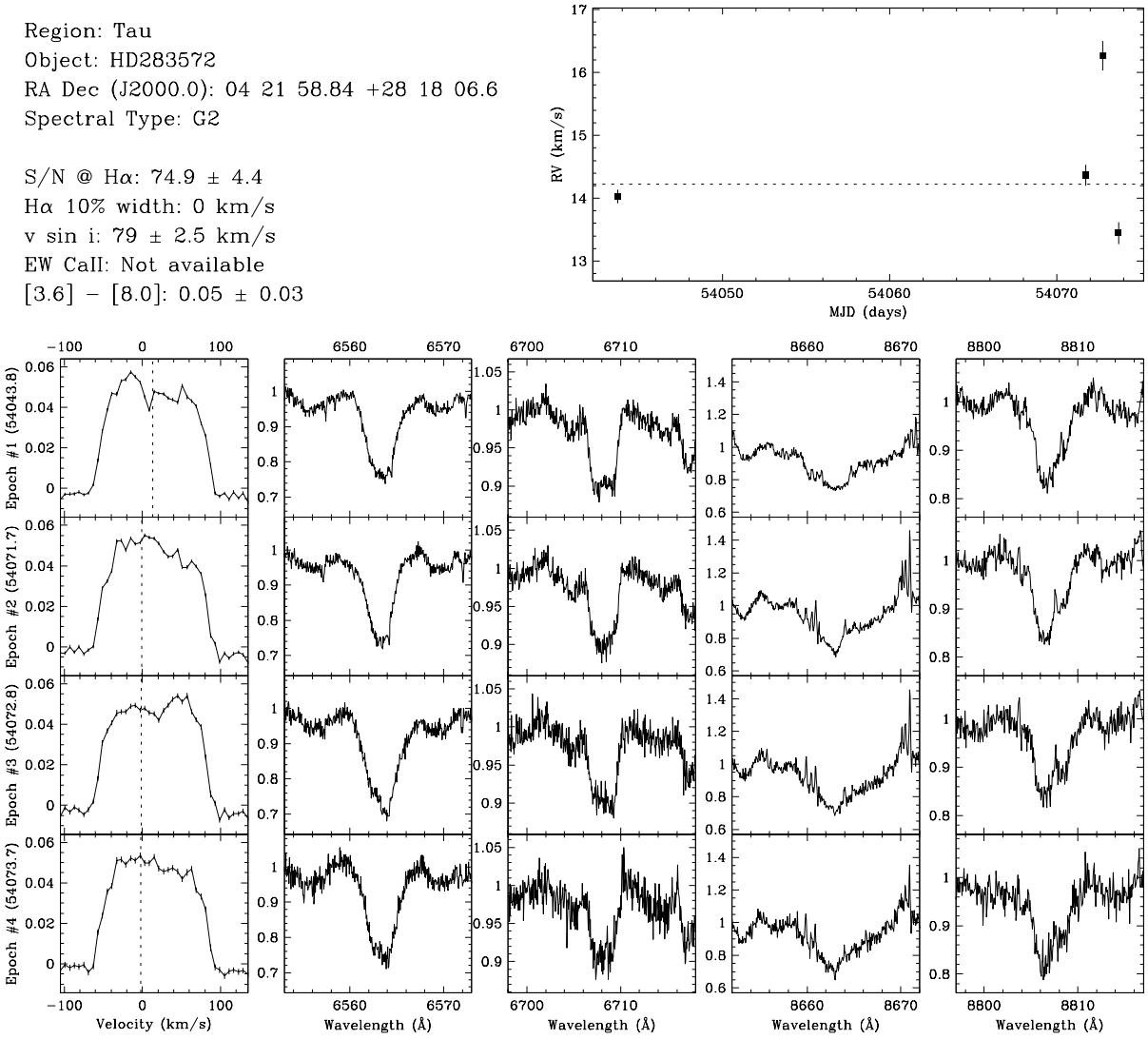

Figure 4.136 HD283572 shows no clear evidence of a close companion. The star has a single-line profile, and a radial velocity scatter not significant relative to variations observed within each observing run. The radial velocity scatter within the second observing run (epochs #2, #3 and #4) is consistent with that expected from systematic line profile variations, e.g. from star spots rotating with the star. This target has been previously reported by Leinert et al. (1993), and Ghez et al. (1993) to have no resolved companions.

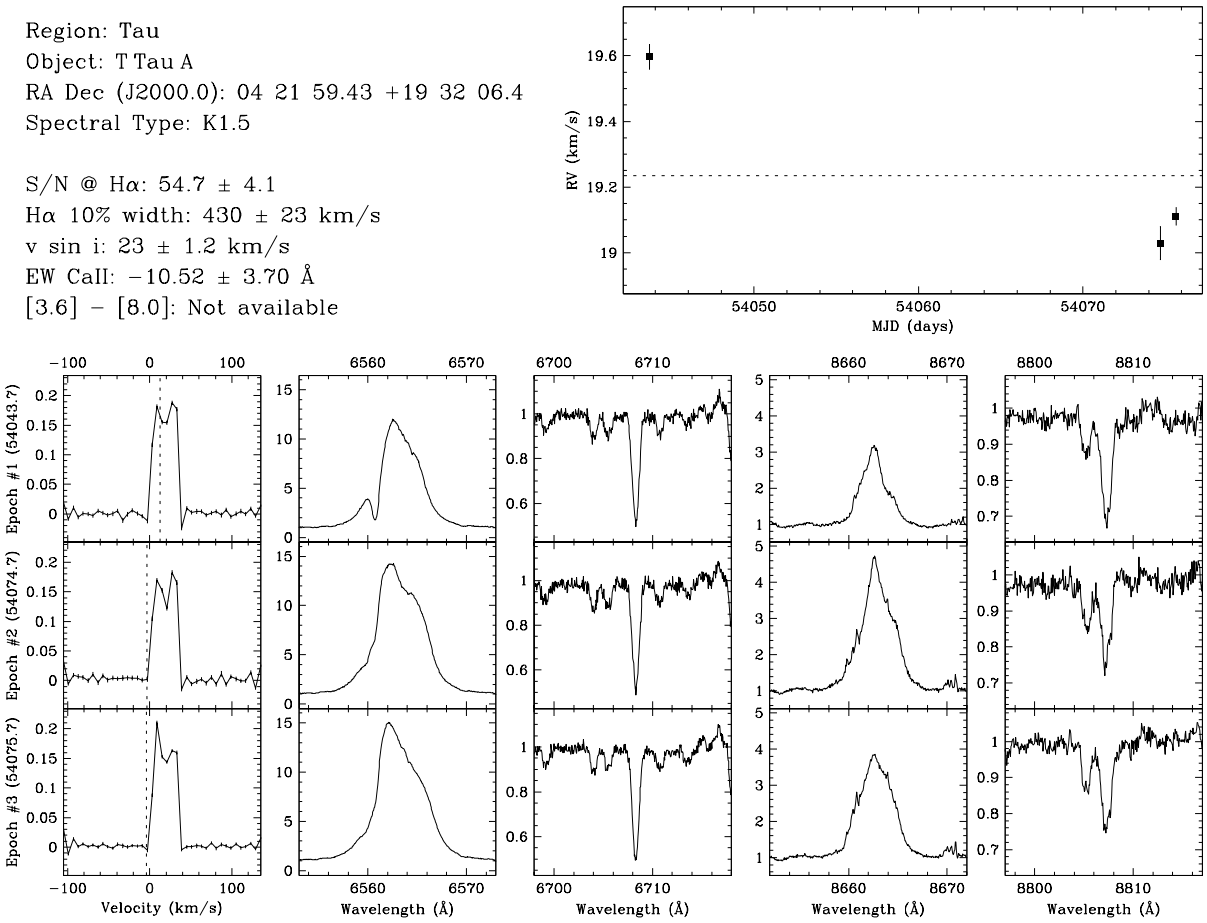

Figure 4.137 T Tau A shows no clear evidence of a close companion. The star has a single-line profile, and a radial velocity scatter not significant relative to variations observed within each observing run. The line profiles show significant deviation from the shape expected from pure rotational broadening. To see if these irregularities are from close companions, we fitted multiple broadening functions to the line profiles. The resultant radial velocities were not consistent with those expected from close companions: the radial velocity separations were $\sim 20\,\mathrm{km\,s^{-1}}$ with no acceleration. Therefore, we suspect the variations in the line profile are the result of star spots. This target has been previously reported by Leinert et al. (1993), and Ghez et al. (1993) to have a resolved companion (T Tau B) with a separation of 0.″71–0.″73 (99–100 AU) at a position angle of $\sim 176°$, and an R-band flux ratio of 0.00–0.04 ($\Delta K \sim 1.99$–2.60). Given the flux ratio, the expected contribution to the line profile from the resolved companion is negligible.

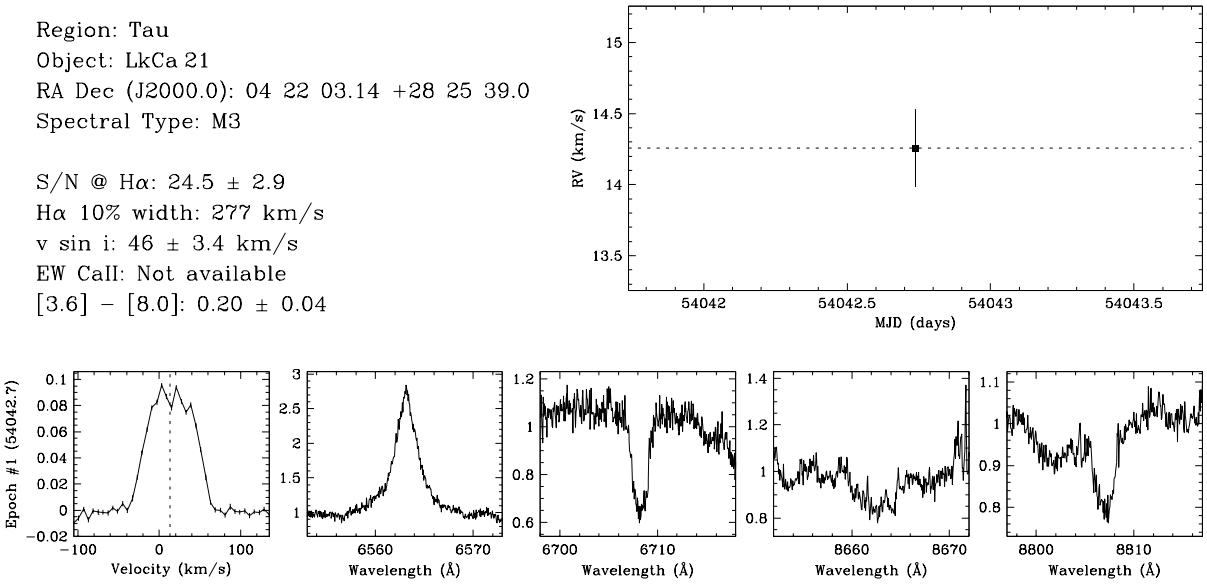

Figure 4.138 LkCa 21 has a single-line profile, and is therefore not an SB2. The radial velocity scatter cannot be determined because the target was observed for a single epoch. Hence, it is undetermined if the target is an SB1 or a single star. This target has been previously reported by Leinert et al. (1993) to have no resolved companions.

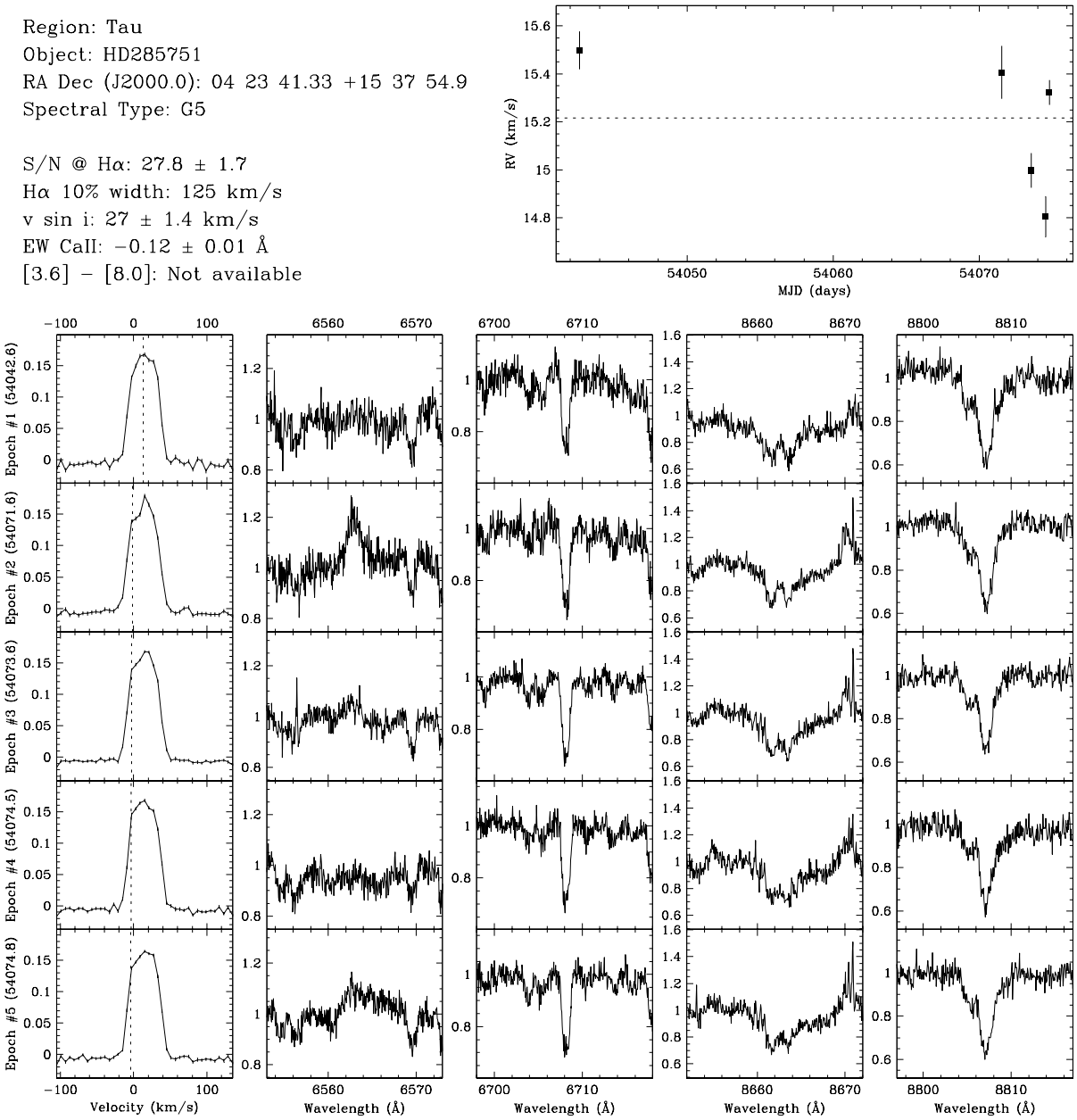

Figure 4.139 HD285751 shows no clear evidence of a close companion. The star has a single-line profile, and a radial velocity scatter not significant relative to variations observed within each observing run. The radial velocity scatter within the second observing run (epochs #2, #3, #4 and #5) is consistent with that expected from systematic line profile variations, e.g. from star spots rotating with the star. This target has been previously reported by Köhler & Leinert (1998) to have no resolved companions.

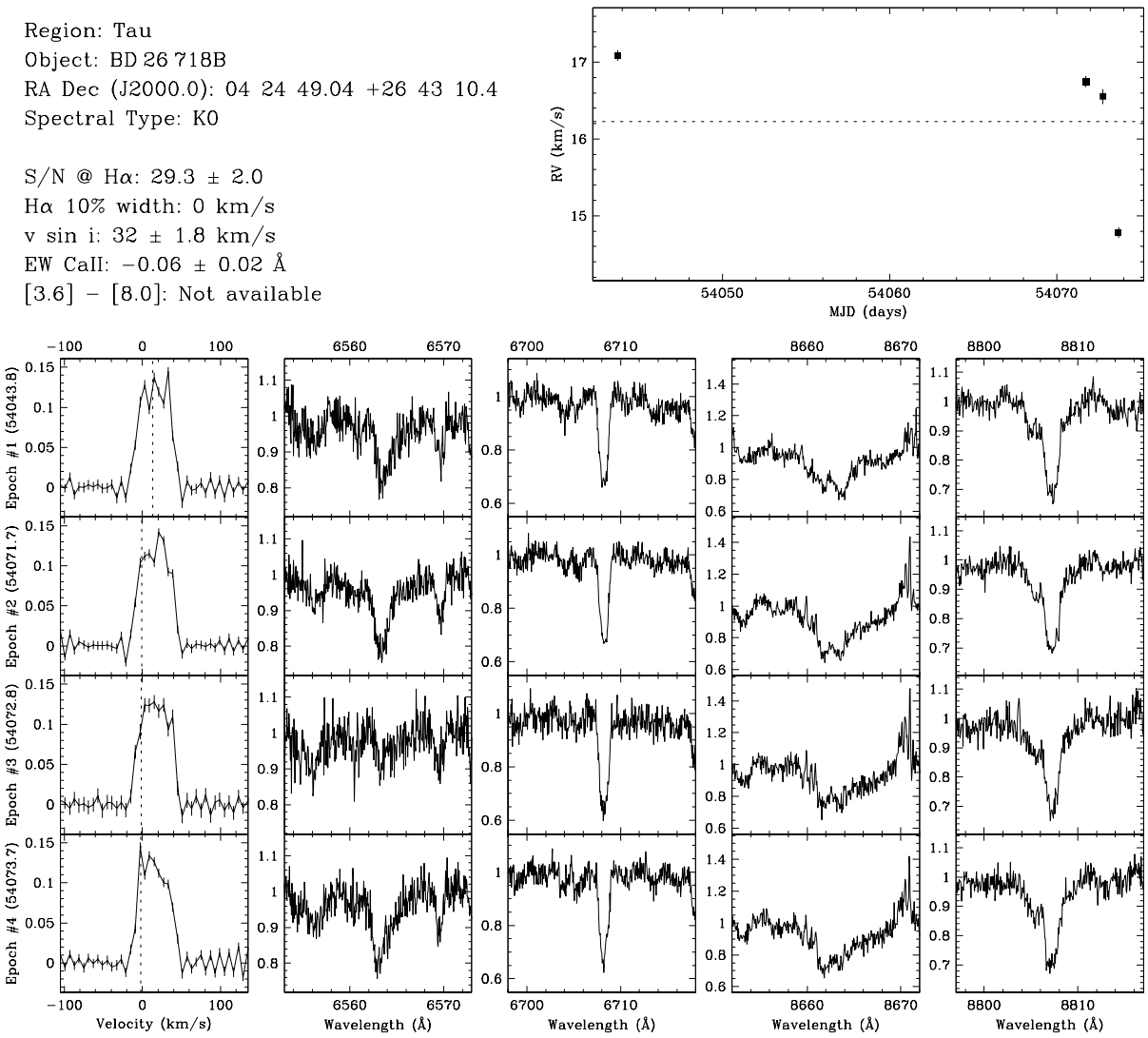

Figure 4.140 BD +26 718B shows no clear evidence of a close companion. The star has a single-line profile, and a radial velocity scatter not significant relative to variations observed within each observing run. The line profiles show significant deviation from the shape expected from pure rotational broadening. To see if these irregularities are from close companions, we fitted multiple broadening functions to the line profiles. The resultant radial velocities were not consistent with those expected from close companions: the radial velocity separations were $\sim 20\,\mathrm{km\,s^{-1}}$ with no acceleration. Therefore, we suspect the variations in the line profile are the result of star spots. The radial velocity scatter within the second observing run (epochs #2, #3 and #4) is consistent with that expected from systematic line profile variations, e.g. from star spots rotating with the star. For epoch #4, the peak in the line profile at the observer's rest frame is due to moonlight, and likely biased the radial velocity estimate toward the observer's rest frame. This target is near the star BD +26 718 with a separation of $\sim 13''$ and has been previously reported by Köhler & Leinert (1998) to have a resolved companion with a separation of 0.″155–0.″166 (22–23 AU) at a position angle of 133.°4–136.°8, and an R-band flux ratio of 0.43–0.54 ($\Delta K \sim 0.53$–0.73). This flux ratio is consistent with that estimated from fitting the line profile with multiple broadening functions (~ 0.5). Furthermore, the resolved companion has an expected circular orbital speed of $\sim 12\,\mathrm{km\,s^{-1}}$, which is similar to the radial velocity separations estimated from the fits if we consider uncertainties due to the models. Therefore, the resolved companion may also be a source of the irregularities in the line profile.

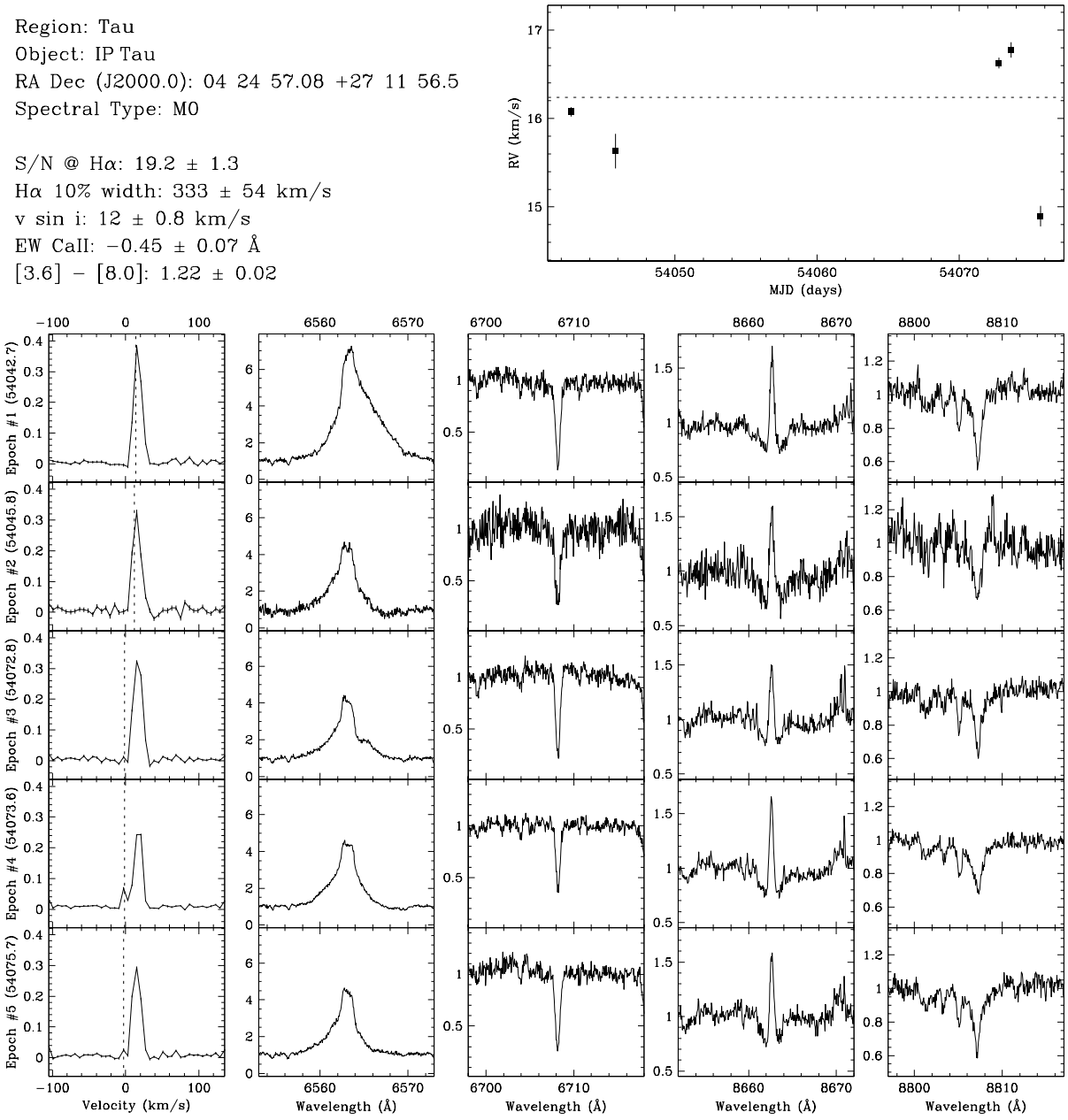

Figure 4.141 IP Tau shows no clear evidence of a close companion. The star has a single-line profile, and a radial velocity scatter not significant relative to variations observed within each observing run. The radial velocity scatter within each observing run is large but consistent with that expected from systematic line profile variations, e.g. from star spots rotating with the star. For epochs #4 and #5, the sharp peaks in the line profile at the observer's rest frame are due to moonlight, and may have biased the radial velocity estimates toward the observer's rest frame. This target has been previously reported by Leinert et al. (1993) to have no resolved companions.

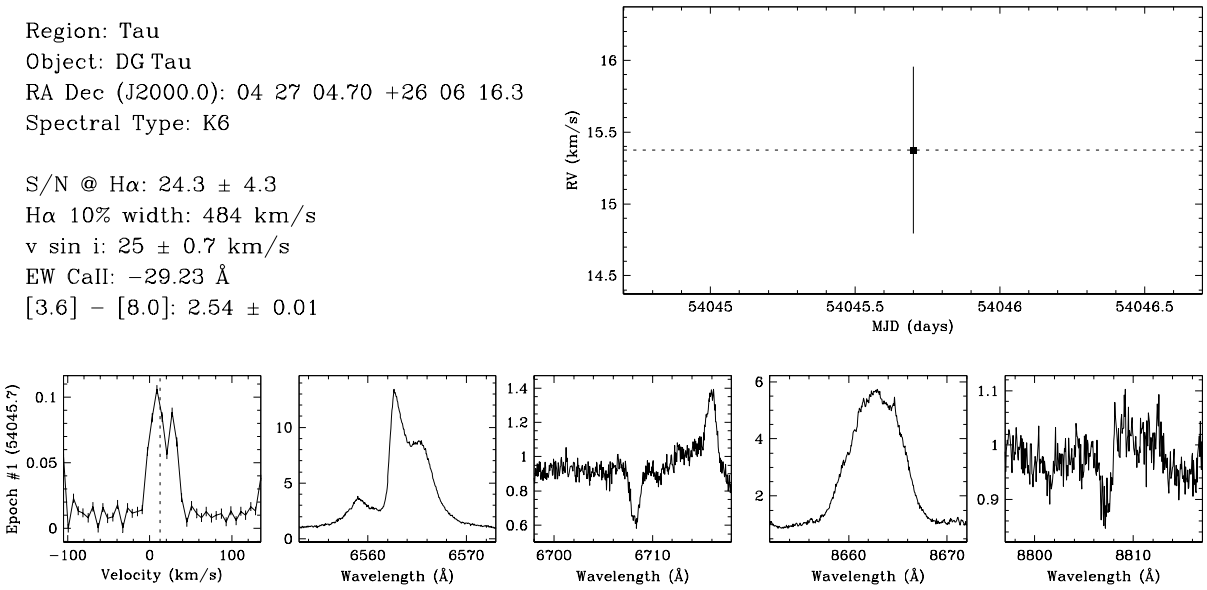

Figure 4.142 DG Tau has a single-line profile, and is therefore not an SB2. The radial velocity scatter cannot be determined because the target was observed for a single epoch. Hence, it is undetermined if the target is an SB1 or a single star. The sharp indentation in the line profile is consistent with star spots. The spectrum is heavily veiled, and we derived the radial velocity from fits to the line profile rather than from direct fits to the spectra (see §4.4.2). This target has been previously reported by Leinert et al. (1993), Ghez et al. (1993), and Simon et al. (1995) to have no resolved companions.

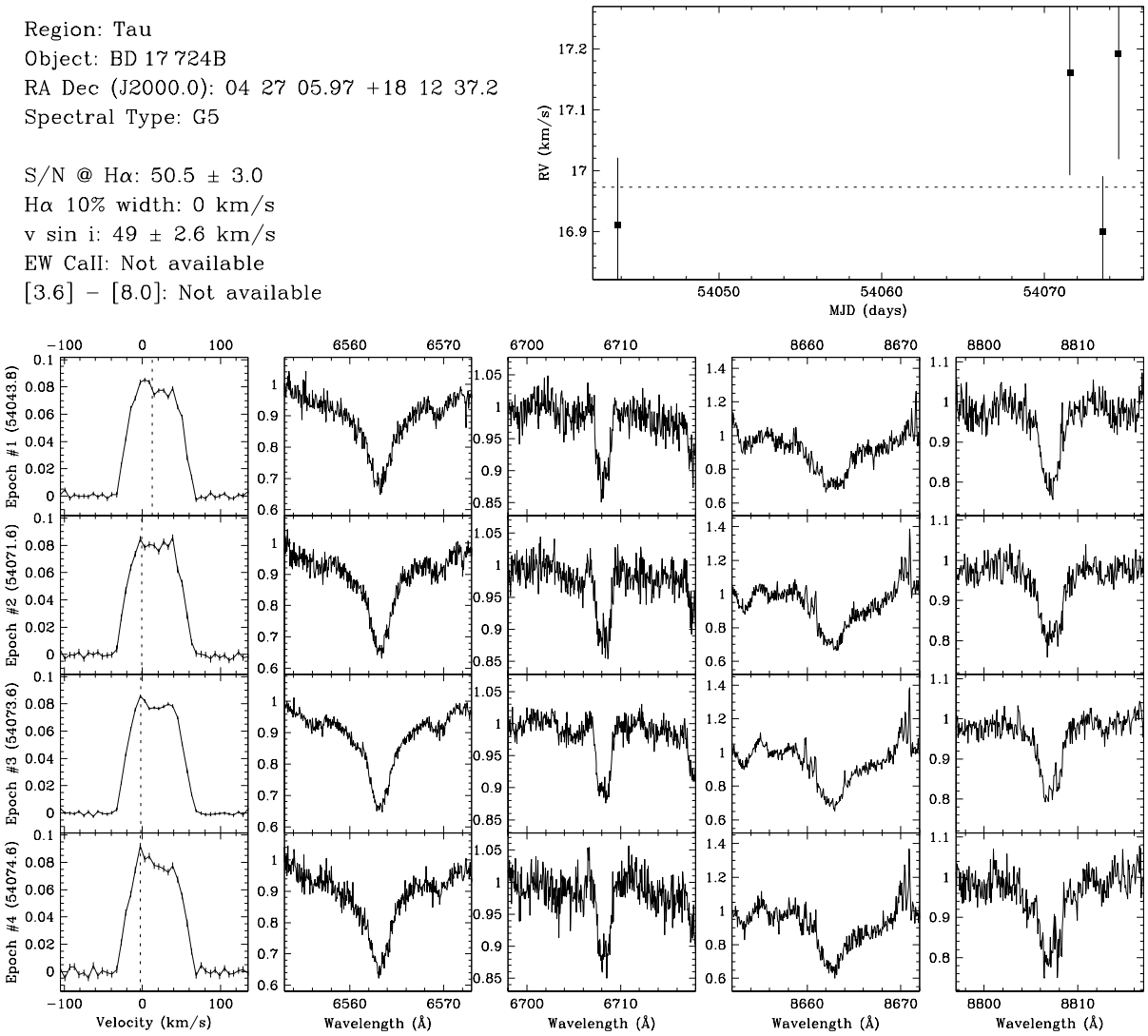

Figure 4.143 BD +17 724B shows no clear evidence of a close companion. The star has a single-line profile, and a radial velocity scatter not significant relative to variations observed within each observing run. The line profiles show significant deviation from the shape expected from pure rotational broadening. To see if these irregularities are from close companions, we fitted multiple broadening functions to the line profiles. The resultant radial velocities were not consistent with those expected from close companions: the radial velocity separations were $\sim 20\,\mathrm{km\,s^{-1}}$ with no acceleration. Therefore, we suspect the variations in the line profile are the result of star spots. The radial velocity scatter within the second observing run (epochs #2, #3 and #4) is consistent with that expected from systematic line profile variations, e.g. from star spots rotating with the star. For epochs #3 and #4, the peaks in the line profile at the observer's rest frame is due to moonlight, and likely biased the radial velocity estimate toward the observer's rest frame. This target is in a double system (with BD +17 724) with a separation of $\sim 19''$ and has been previously reported by Köhler & Leinert (1998) to have a resolved companion with a separation of $0\overset{''}{.}083$–$0\overset{''}{.}1$ (12–14 AU) at a position angle of 193°.5–208°.7, and an R-band flux ratio of 0.07–0.16 ($\Delta K \sim 1.55$–2.28). This flux ratio is similar to that estimated from fitting the line profile with multiple broadening functions (~ 0.05). Furthermore, the resolved companion has an expected circular orbital speed of $\sim 16\,\mathrm{km\,s^{-1}}$, which is comparable with the radial velocity separations estimated from the fits. Therefore, the resolved companion may also be a source of the irregularities in the line profile.

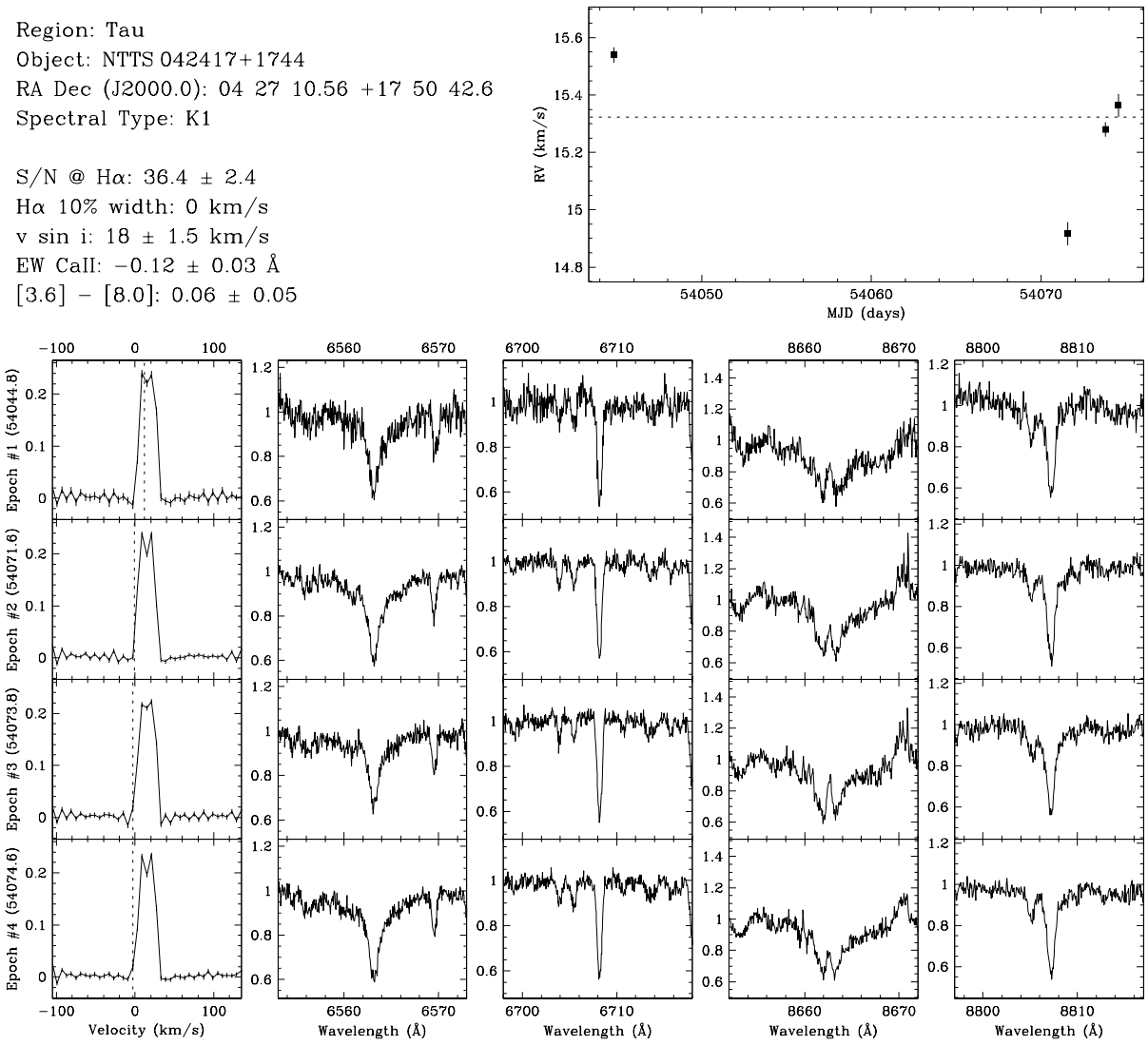

Figure 4.144 NTTS 042417+1744 shows no clear evidence of a close companion. The star has a single-line profile, and a radial velocity scatter not significant relative to variations observed within each observing run. The radial velocity scatter within the second observing run (epochs #2, #3 and #4) is consistent with that expected from systematic line profile variations, e.g. from star spots rotating with the star. This target has been previously reported by Leinert et al. (1993), and Ghez et al. (1993) to have no resolved companions.

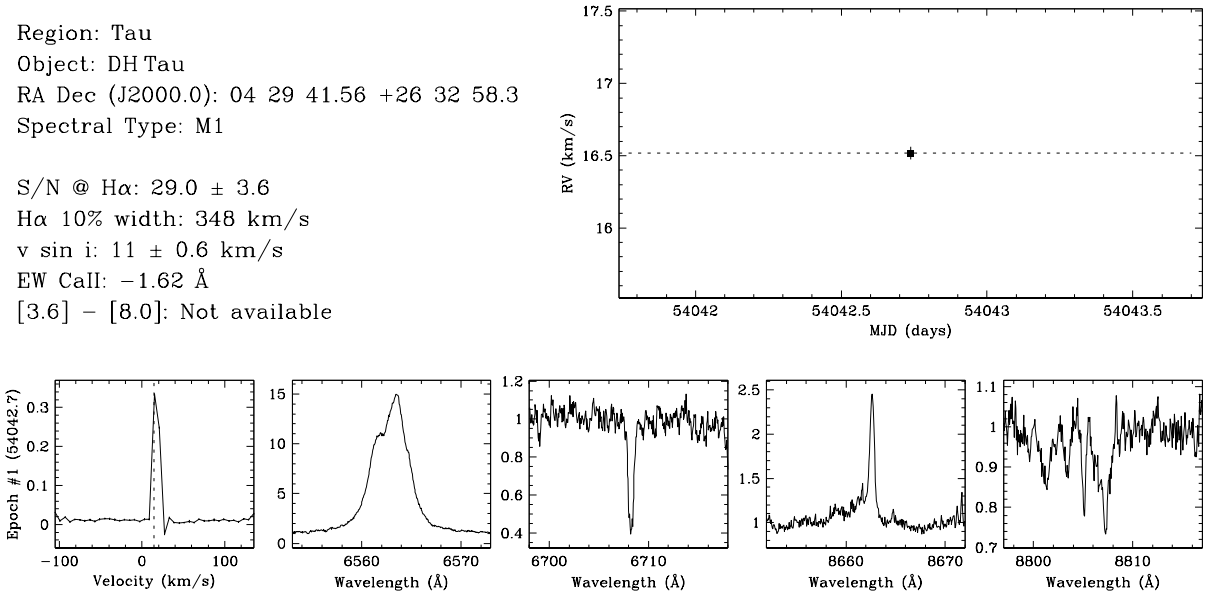

Figure 4.145 DH Tau has a single-line profile, and is therefore not an SB2. The radial velocity scatter cannot be determined because the target was observed for a single epoch. Hence, it is undetermined if the target is an SB1 or a single star. This target has been previously reported by Leinert et al. (1993), and Simon et al. (1995) to have no resolved companions.

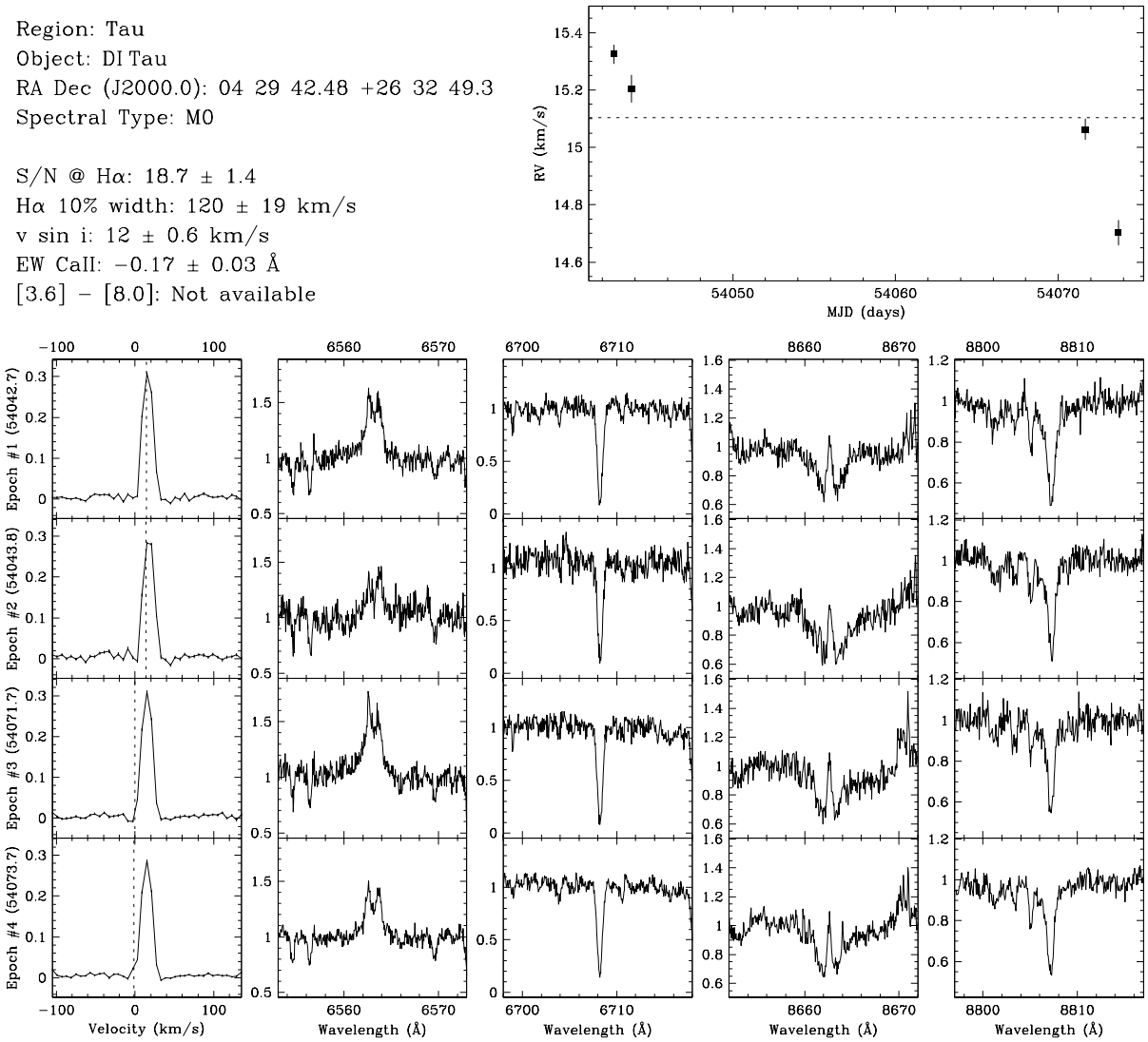

Figure 4.146 DI Tau shows no clear evidence of a close companion. The star has a single-line profile, and a radial velocity scatter not significant relative to variations observed within each observing run. The radial velocity scatter within each observing run is consistent with that expected from systematic line profile variations, e.g. from star spots rotating with the star. This target has been previously reported by Ghez et al. (1993), and Simon et al. (1995) as a resolved binary (DI Tau A+B) with a separation of $\sim 0\farcs12$ (~ 17 AU) at a position angle of $\sim 294°$, and an R-band flux ratio of ~ 0.01 ($\Delta K \sim 2.26$–2.30). Given the flux ratio, the expected contribution to the line profile from the resolved secondary star is negligible.

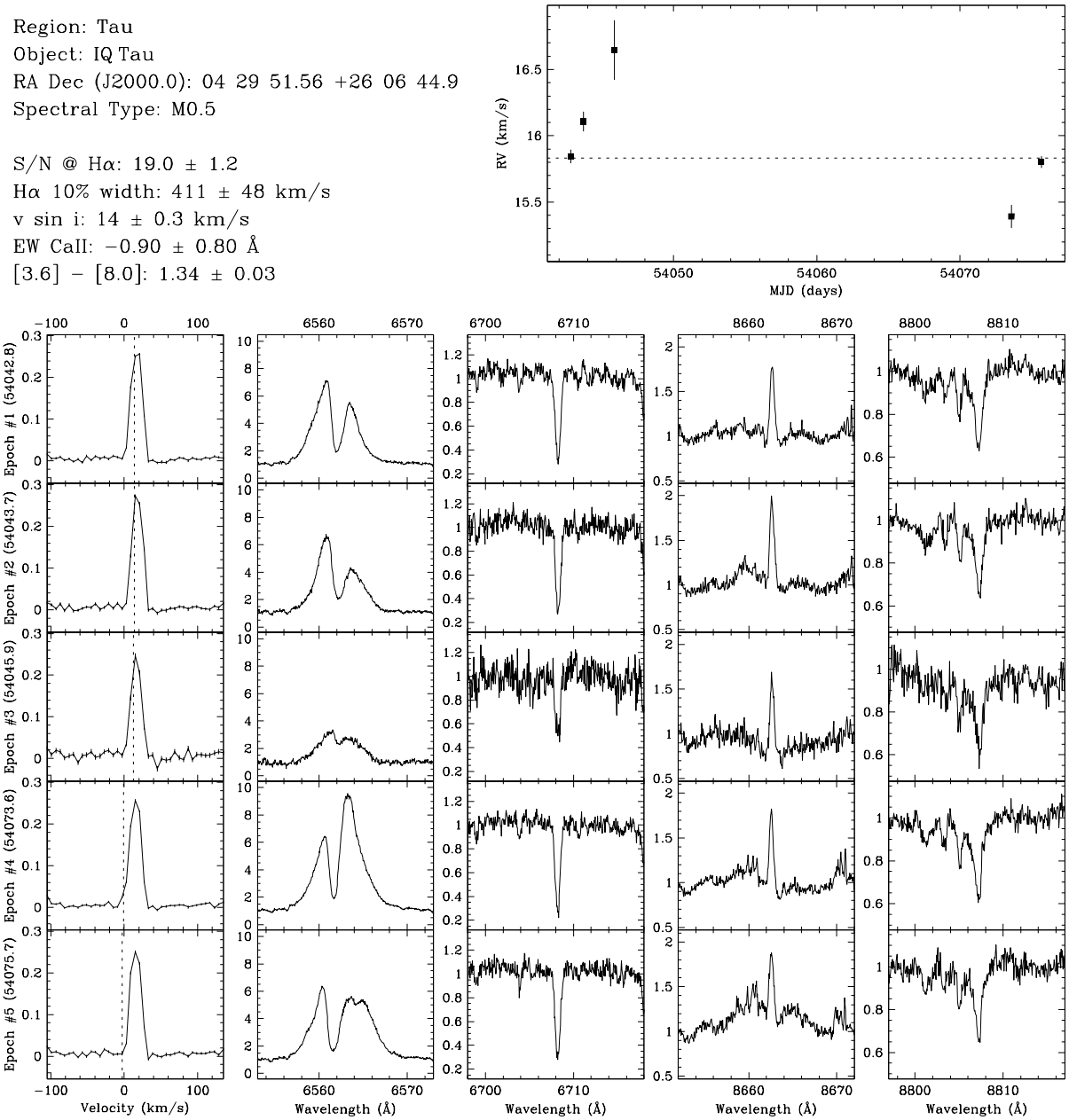

Figure 4.147 IQ Tau shows no clear evidence of a close companion. The star has a single-line profile, and a radial velocity scatter not significant relative to variations observed within each observing run. The radial velocity scatter within each observing run is consistent with that expected from systematic line profile variations, e.g. from star spots rotating with the star. This target has been previously reported by Leinert et al. (1993), Ghez et al. (1993), and Simon et al. (1995) to have no resolved companions.

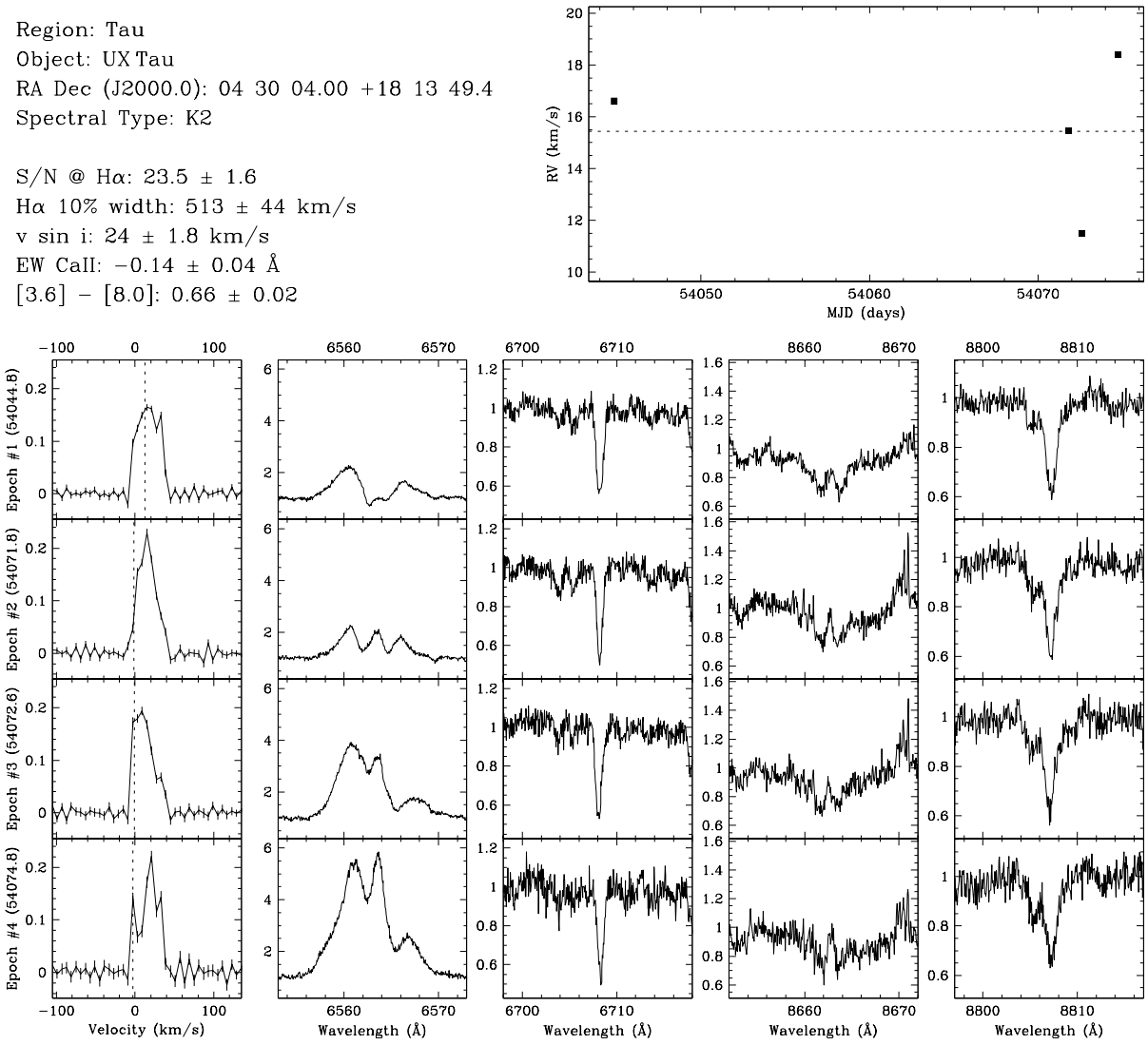

Figure 4.148 UX Tau shows no clear evidence of a close companion. The star has a single-line profile, and a radial velocity scatter not significant relative to variations observed within each observing run. The line profiles show significant deviation from the shape expected from pure rotational broadening. To see if these irregularities are from close companions, we fitted multiple broadening functions to the line profiles. The resultant radial velocities were not consistent with those expected from close companions: the radial velocity separations were $\sim 20\,\mathrm{km\,s^{-1}}$ with no acceleration. If star spots were responsible for these irregularities, based on observed $v \sin i$ ($\sim 24\,\mathrm{km\,s^{-1}}$) and model stellar radius ($\sim 2.0\,R_\odot$), one would expect variations on a maximum timescale of ~ 4.2 days. The line profiles are similar between epochs #2 and #3 which are separated by ~ 1 day, whereas epoch #4 two days later is quite different. Furthermore, the Hα profile changes significantly between epochs. Therefore, we suspect the asymmetries in the line profile are the result of star spots. The radial velocity scatter within the second observing run (epochs #2, #3 and #4) is large but is consistent with the observed line profile variations. For epoch #4, the sharp peak in the line profile at the observer's rest frame is due to moonlight, and may have biased the radial velocity estimates toward the observer's rest frame. This target has been previously reported by Leinert et al. (1993) to have a resolved companion with a separation of $\sim 5\farcs9$ (~ 830 AU) at a position angle of $\sim 269°$, and an R-band flux ratio of ~ 0.09 ($\Delta K \sim 1.42$). Given the flux ratio and separation, the expected contribution to the line profile from the resolved companion is negligible.

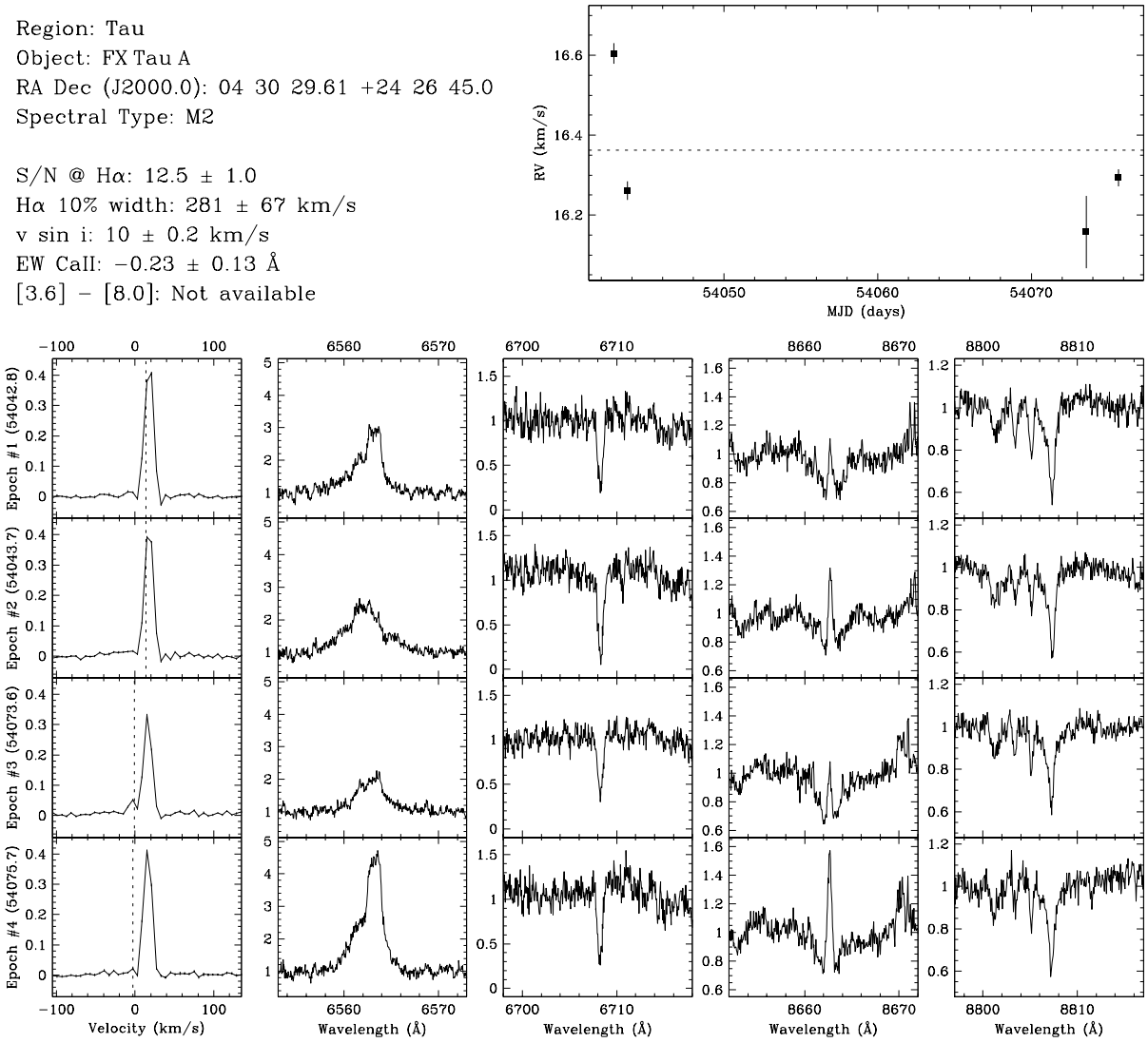

Figure 4.149 FX Tau A shows no clear evidence of a close companion. The star has a single-line profile, and a radial velocity scatter not significant relative to variations observed within each observing run. The radial velocity scatter within each observing run is consistent with that expected from systematic line profile variations, e.g. from star spots rotating with the star. For epoch #3, the small peak in the line profile at the observer's rest frame is due to moonlight, and may have biased the radial velocity estimates toward the observer's rest frame. This target has been previously reported by Leinert et al. (1993), Ghez et al. (1993), and Simon et al. (1995) to have a resolved companion (FX Tau B) with a separation of 0.″9–0.″91 ($\sim$130 AU) at a position angle of 291°–292°, and an R-band flux ratio of 0.20–0.49 ($\Delta K \sim 0.40$–0.73). However, there is no clear evidence in the line profile of the resolved companion. Since the resolved companion has an expected circular orbital speed of $\sim 2\,\mathrm{km\,s^{-1}}$, a second profile could be obscured if the primary star and the resolved companion have similar projected rotational velocities.

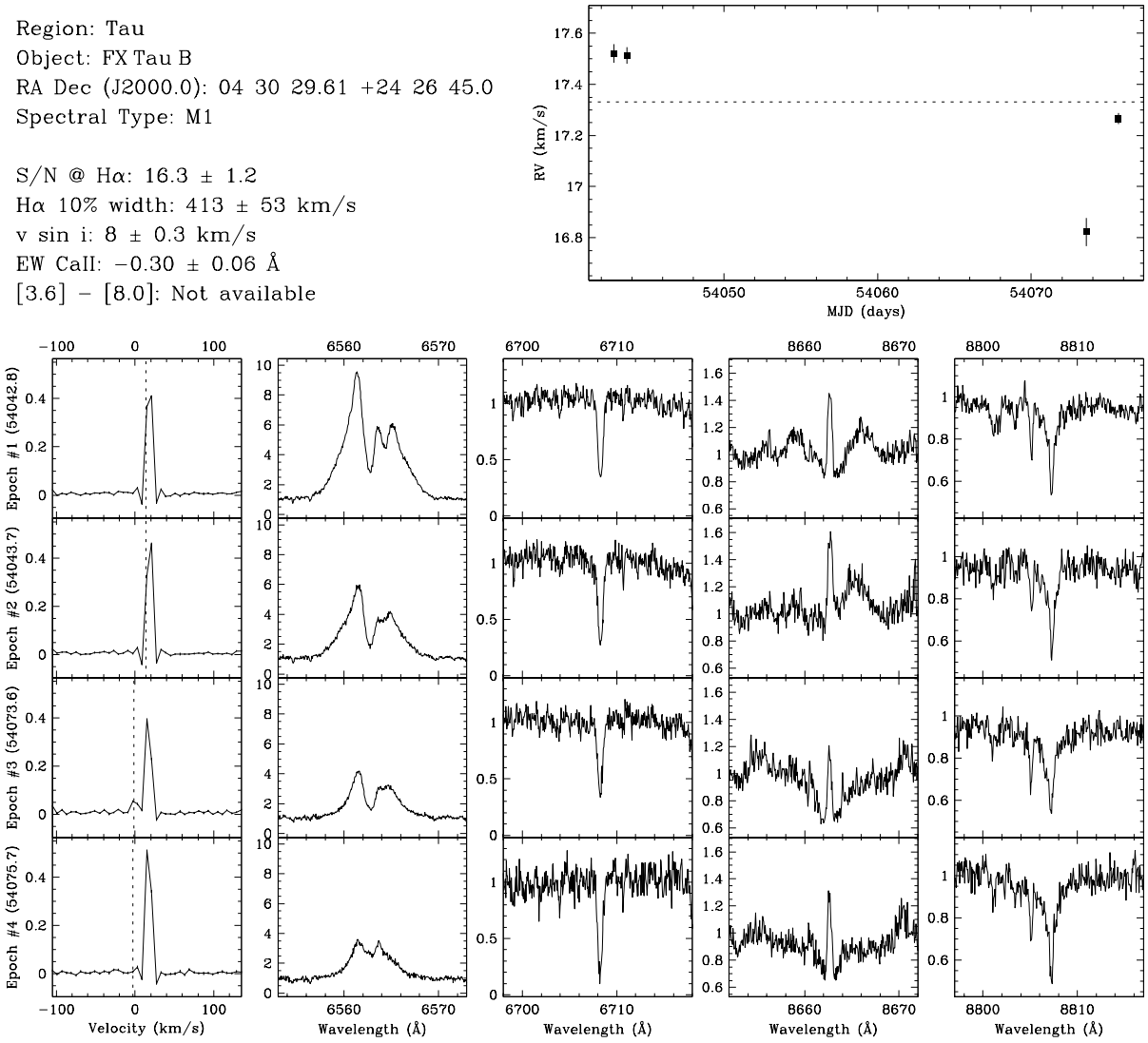

Figure 4.150 FX Tau B shows no clear evidence of a close companion. The star has a single-line profile, and a radial velocity scatter not significant relative to variations observed within each observing run. The radial velocity scatter within each observing run is consistent with that expected from systematic line profile variations, e.g. from star spots rotating with the star. For epoch #3, the small peak in the line profile at the observer's rest frame is due to moonlight, and likely biased the radial velocity estimates toward the observer's rest frame. This target has been previously reported by Leinert et al. (1993), Ghez et al. (1993), and Simon et al. (1995) to be the secondary star of a resolved binary (FX Tau A+B) with a separation of 0.″9–0.″91 ($\sim$130 AU) at a position angle of 291°–292°, and an R-band flux ratio of 0.20–0.49 ($\Delta K \sim 0.40$–0.73). However, there is no clear evidence in the line profile of the resolved companion. Since the resolved companion has an expected circular orbital speed of $\sim 2\,\mathrm{km\,s^{-1}}$, a second profile could be obscured if the primary star and the resolved companion have similar projected rotational velocities.

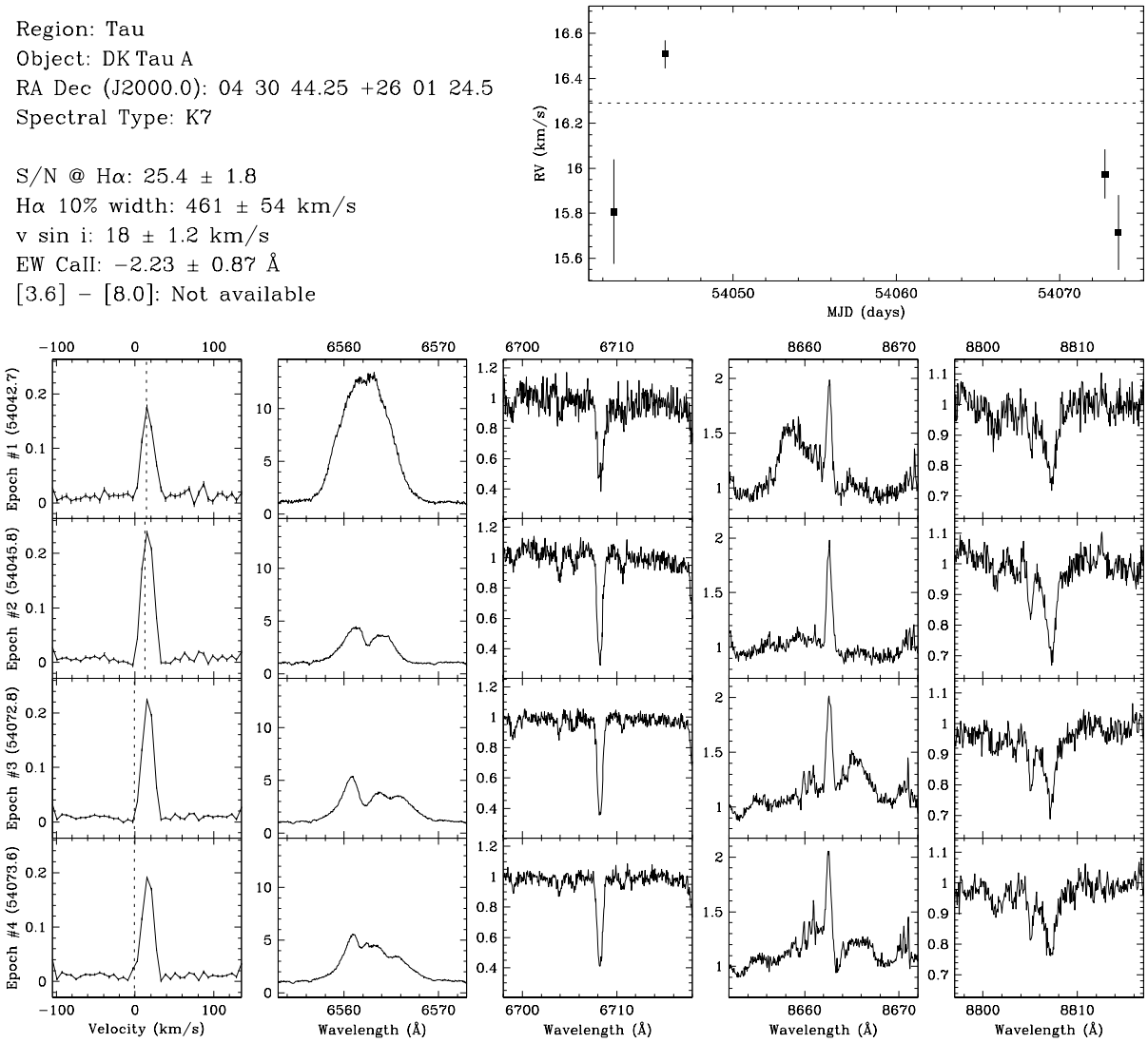

Figure 4.151 DK Tau A shows no clear evidence of a close companion. The star has a single-line profile, and a radial velocity scatter not significant relative to variations observed within each observing run. The radial velocity scatter within each observing run is consistent with that expected from systematic line profile variations, e.g. from star spots rotating with the star. For epoch #4, the small bulge in the line profile at the observer's rest frame is due to moonlight, and may have biased the radial velocity estimate toward the observer's rest frame. This target has been previously reported by Leinert et al. (1993), Ghez et al. (1993), and Simon et al. (1995) to have a resolved companion (DK Tau B) with a separation of 2.″53–2.″8 (350–390 AU) at a position angle of ∼115°, and an R-band flux ratio of 0.01–0.03 ($\Delta K \sim 1.30$–1.51). Given the flux ratio and separation, the expected contribution to the line profile from the resolved companion is negligible.

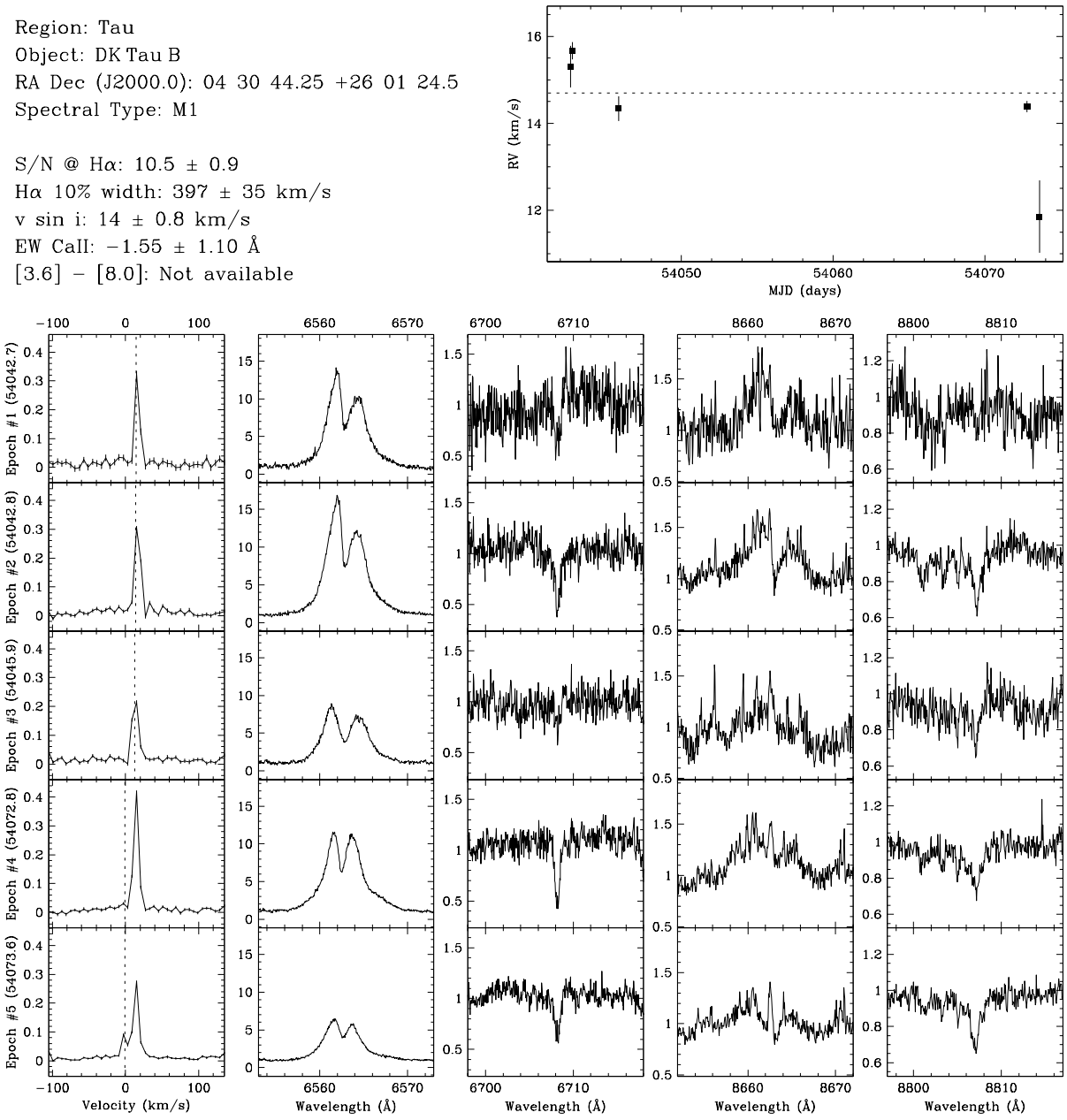

Figure 4.152 DK Tau B shows no clear evidence of a close companion. The star has a single-line profile, and a radial velocity scatter not significant relative to variations observed within each observing run. The radial velocity scatter within each observing run is consistent with that expected from systematic line profile variations, e.g. from star spots rotating with the star. For epoch #5, the small sharp peak in the line profile at the observer's rest frame is due to moonlight, and likely biased the radial velocity estimate toward the observer's rest frame. This target has been previously reported by Leinert et al. (1993), Ghez et al. (1993), and Simon et al. (1995) to be the secondary star of a resolved binary (DK Tau A+B) with a separation of 2.″53–2.″8 (350–390 AU) at a position angle of ∼115°, and an R-band flux ratio of ∼0.02 ($\Delta K \sim 1.30$–1.51). Given the flux ratio and separation, the expected contribution to the line profile from the resolved companion is negligible.

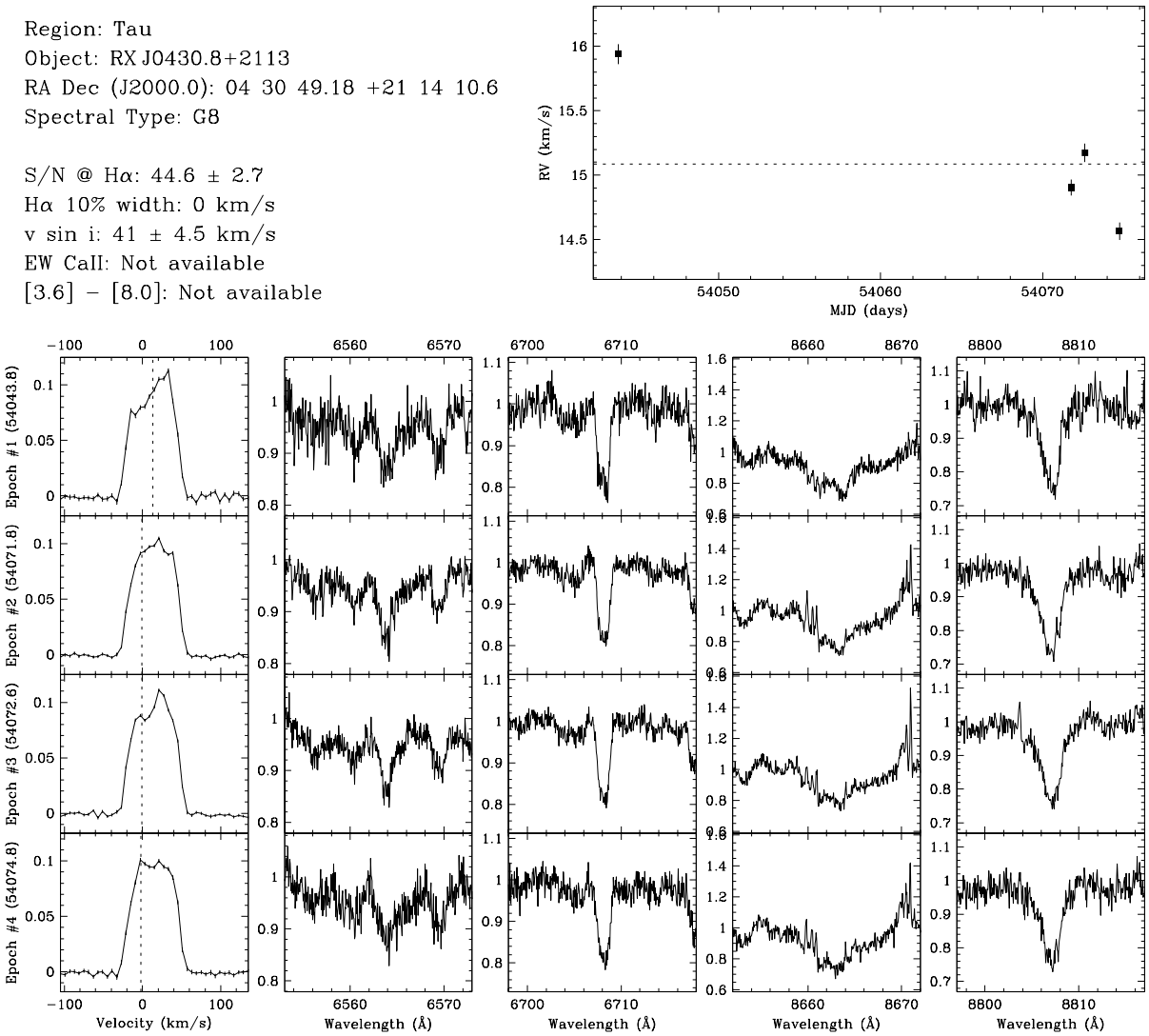

Figure 4.153 RX J0430.8+2113 shows no clear evidence of a close companion. The star has a single-line profile, and a radial velocity scatter not significant relative to variations observed within each observing run. The line profiles show significant deviation from the shape expected from pure rotational broadening. To see if these irregularities are from close companions, we fitted multiple broadening functions to the line profiles. The resultant radial velocities were not consistent with those expected from close companions: the radial velocity separations were $\sim 20\,\mathrm{km\,s^{-1}}$ with no acceleration. Therefore, we suspect the variations in the line profile are the result of star spots. This target has been previously reported by Köhler & Leinert (1998) to have a resolved companion with a separation of $\sim 0\farcs389$ (~ 54 AU) at a position angle of $\sim 151\fdg5$, and an R-band flux ratio of $\lesssim 0.01$ ($\Delta K \sim 3.58$). Given the flux ratio, the expected contribution to the line profile from the resolved companion is negligible.

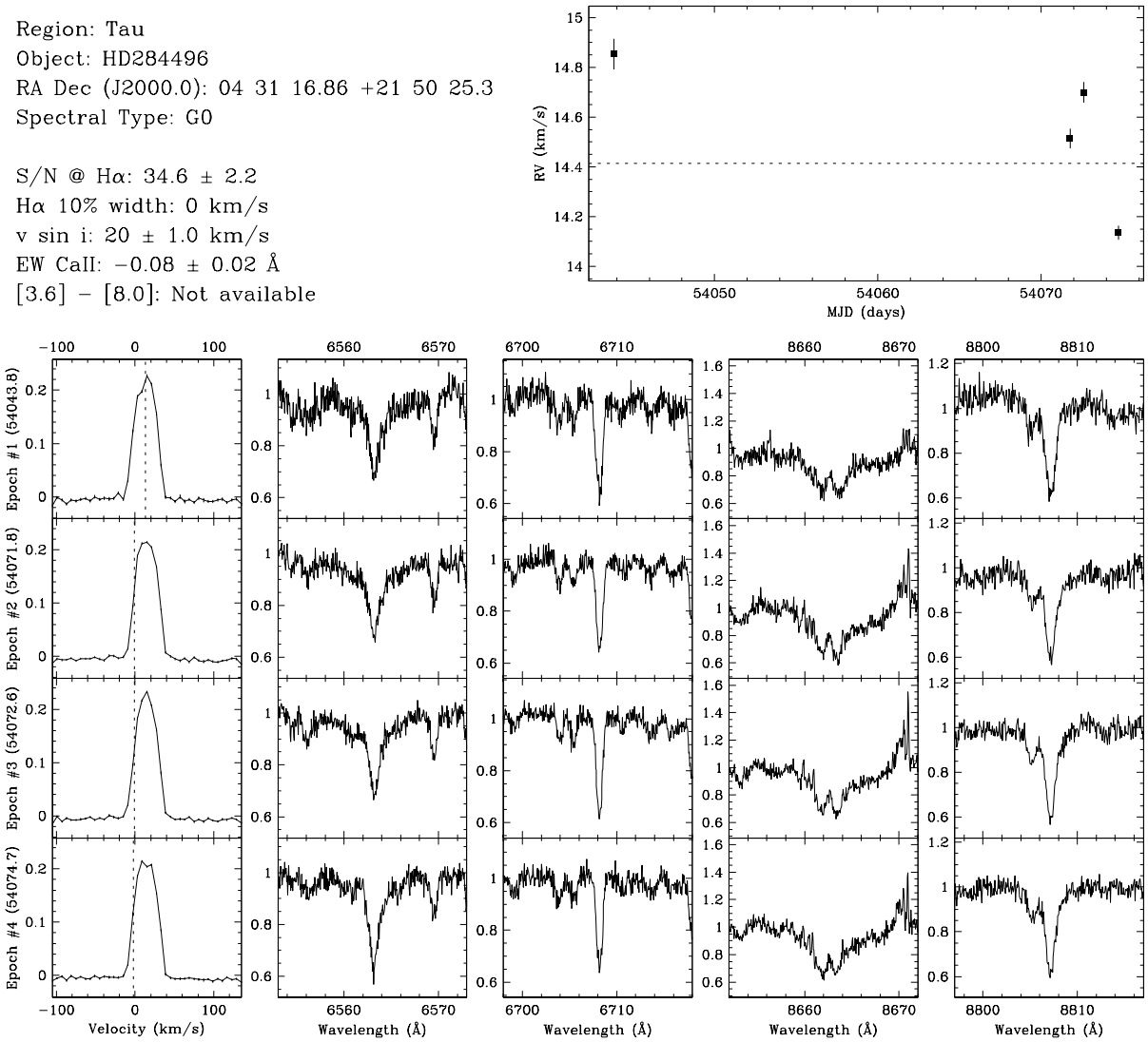

Figure 4.154 HD284496 shows no clear evidence of a close companion. The star has a single-line profile, and a radial velocity scatter not significant relative to variations observed within each observing run. The radial velocity scatter within the second observing run (epochs #2, #3 and #4) is consistent with that expected from systematic line profile variations, e.g. from star spots rotating with the star. This target has been previously reported by Köhler & Leinert (1998) to have a resolved companion with a separation of $\sim 4\farcs598$ (~ 640 AU) at a position angle of $\sim 337\fdg7$, and an R-band flux ratio of $\lesssim 0.01$ ($\Delta K \sim 4.25$). Given the flux ratio and separation, the expected contribution to the line profile from the resolved companion is negligible.

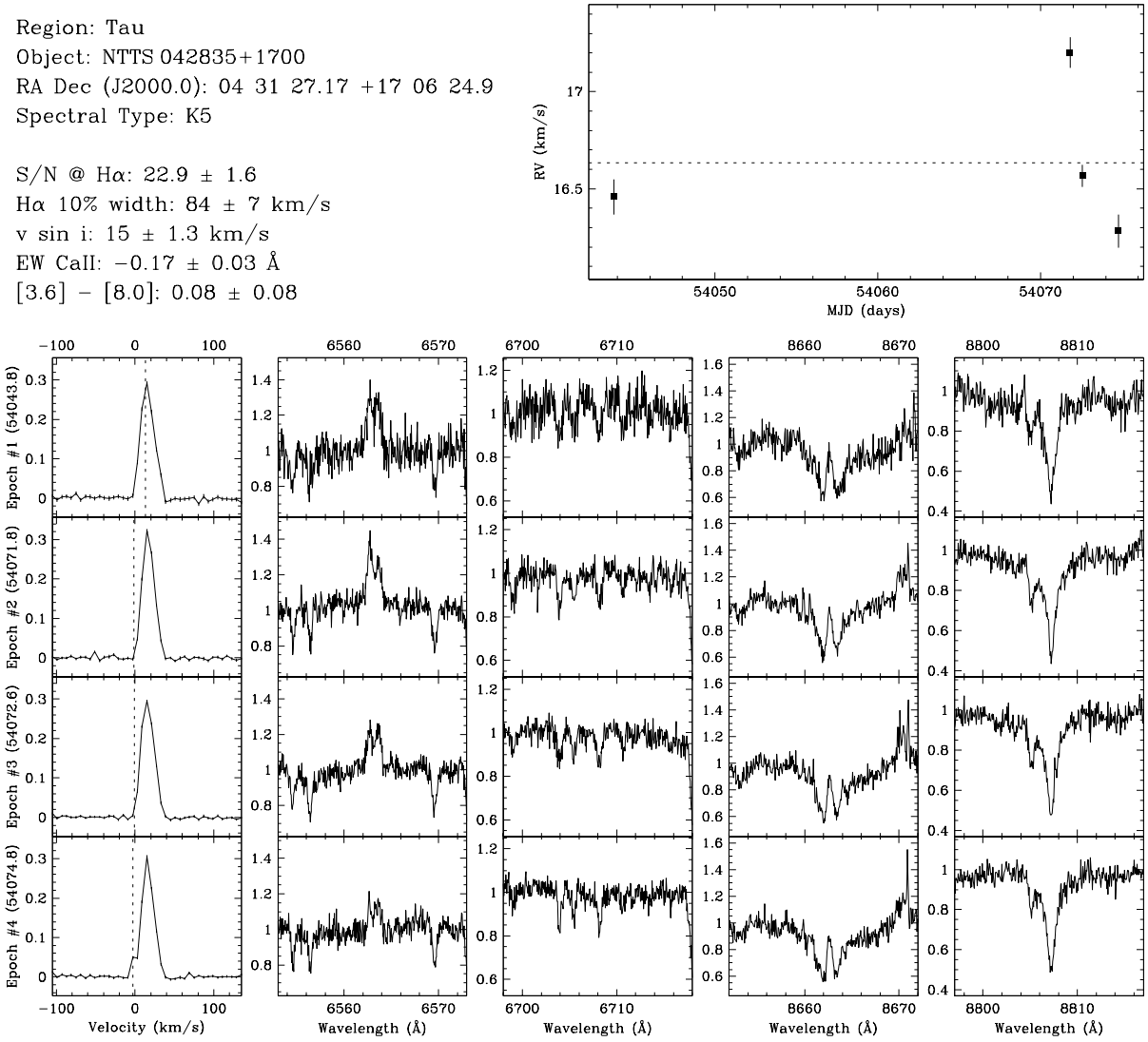

Figure 4.155 NTTS 042835+1700 shows no clear evidence of a close companion. The star has a single-line profile, and a radial velocity scatter not significant relative to variations observed within each observing run. The radial velocity scatter within the second observing run (epochs #2, #3 and #4) is consistent with that expected from systematic line profile variations, e.g. from star spots rotating with the star. For epoch #4, the small bulge in the line profile at the observer's rest frame is due to moonlight, and likely biased the radial velocity estimate toward the observer's rest frame. This target has been previously reported by Leinert et al. (1993) to have no resolved companions.

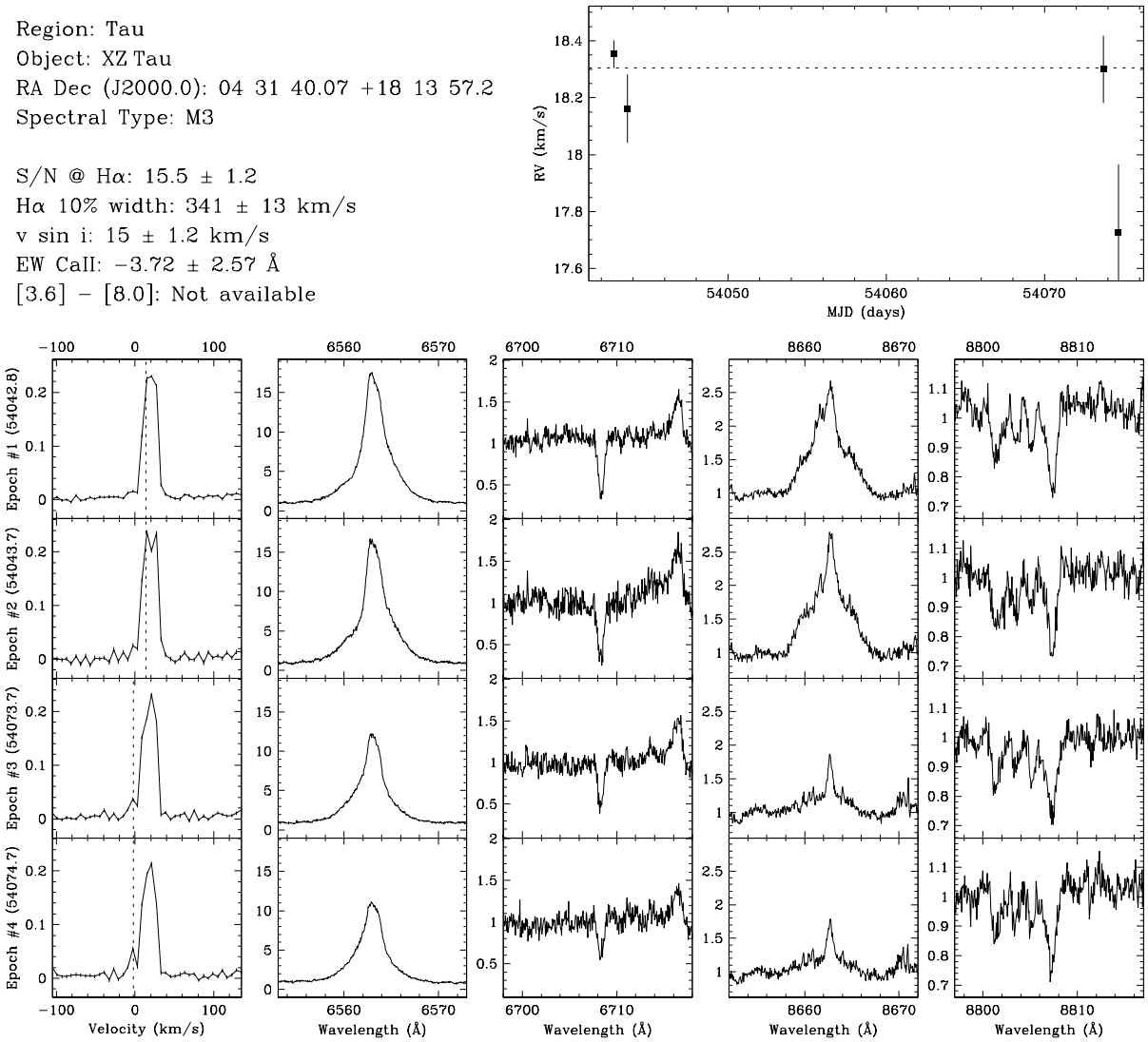

Figure 4.156 XZ Tau shows no evidence of a close companion. The star has a single-line profile, and the radial velocity scatter is not significant relative to the measurement uncertainties. For epochs #3 and #4, the small peaks in the line profile at the observer's rest frame are due to moonlight, and may have biased the radial velocity estimates toward the observer's rest frame. This target has been previously reported by Leinert et al. (1993), and Ghez et al. (1993) as a resolved binary (XZ Tau A+B) with a separation of 0.″3–0.″311 (42–44 AU) at a position angle of 153°–154°, and an R-band flux ratio of 0.04–0.07 ($\Delta K \sim 0.73$–1.14). Given the flux ratio, the expected contribution to the line profile from the resolved companion is small.

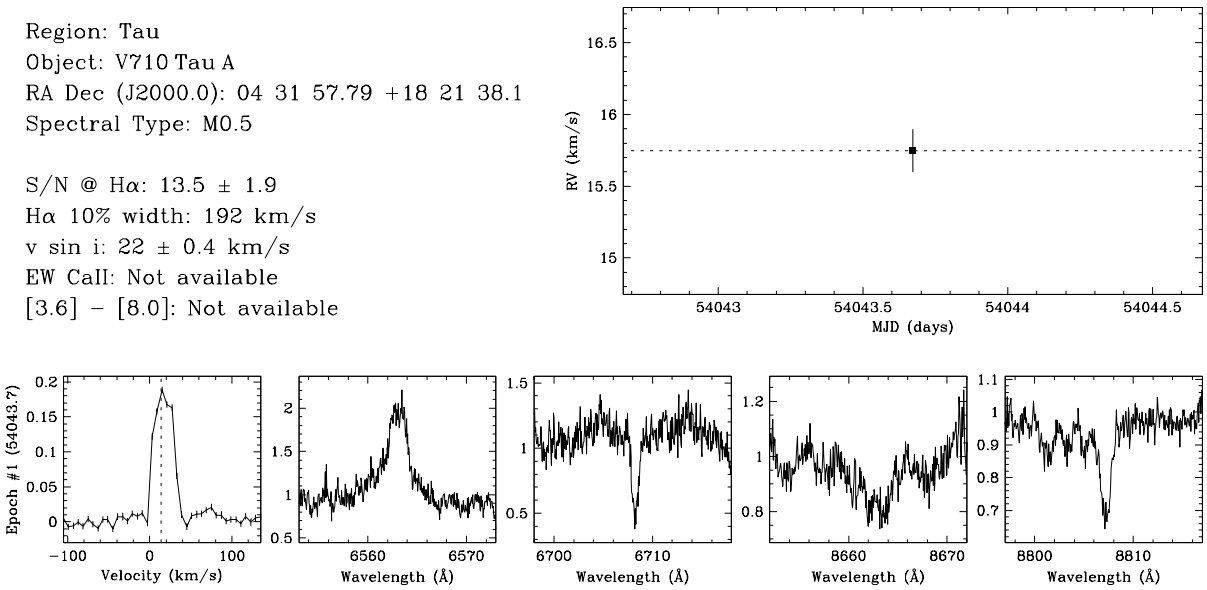

Figure 4.157 V710 Tau A has a single-line profile, and is therefore not an SB2. The radial velocity scatter cannot be determined because the target was observed for a single epoch. Hence, it is undetermined if the target is an SB1 or a single star. This target has been previously reported by Leinert et al. (1993) to have a resolved companion (V710 Tau B) with a separation of $\sim 3\farcs24$ (~ 450 AU) at a position angle of $\sim 357°$, and an R-band flux ratio of ~ 0.71 ($\Delta K \sim 0.20$). Given the separation, the expected contribution to the line profile from the resolved companion is negligible.

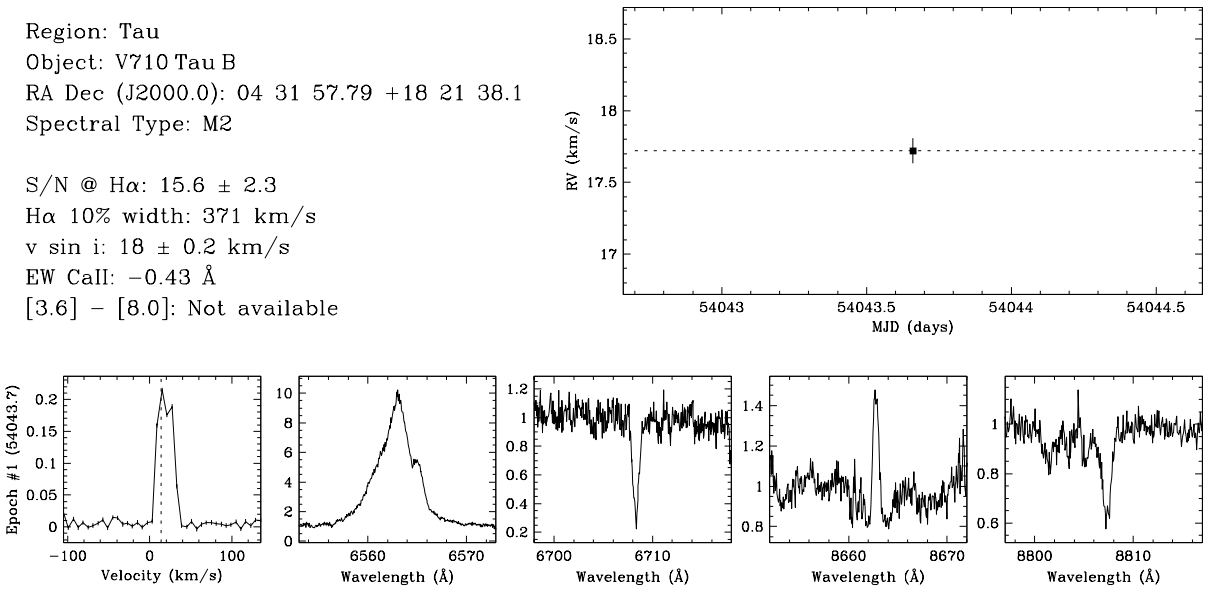

Figure 4.158 V710 Tau B has a single-line profile, and is therefore not an SB2. The radial velocity scatter cannot be determined because the target was observed for a single epoch. Hence, it is undetermined if the target is an SB1 or a single star. This target has been previously reported by Leinert et al. (1993) to be the secondary star of a resolved binary (V710 Tau A+B) with a separation of $\sim 3\farcs24$ (~ 450 AU) at a position angle of $\sim 357°$, and an R-band flux ratio of ~ 0.60 ($\Delta K \sim 0.20$). Given the separation, the expected contribution to the line profile from the resolved companion is negligible.

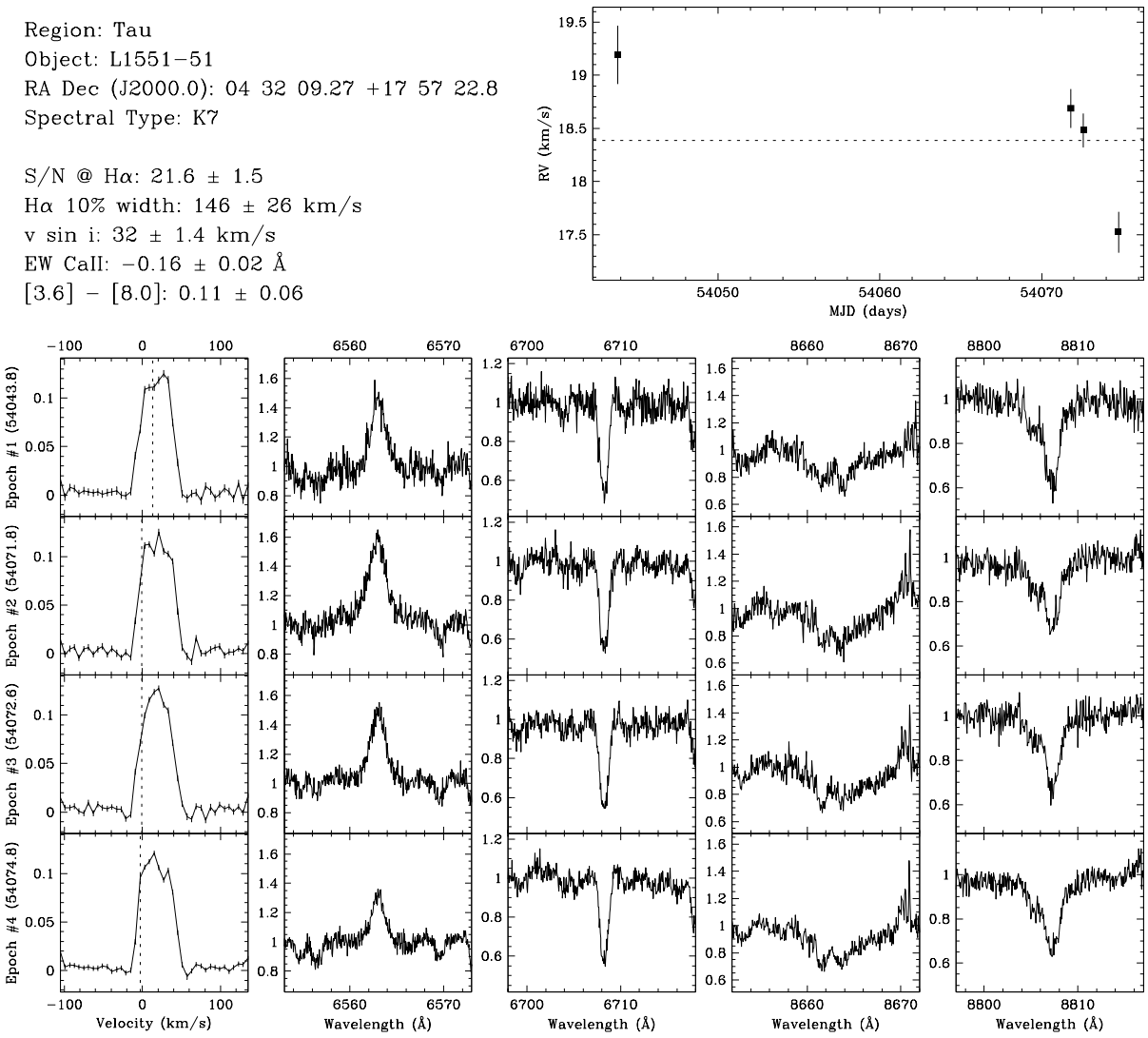

Figure 4.159 L1551-51 shows no clear evidence of a close companion. The star has a single-line profile, and a radial velocity scatter not significant relative to variations observed within each observing run. The radial velocity scatter within the second observing run (epochs #2, #3 and #4) is consistent with that expected from systematic line profile variations, e.g. from star spots rotating with the star. This target has been previously reported by Leinert et al. (1993) to have no resolved companions.

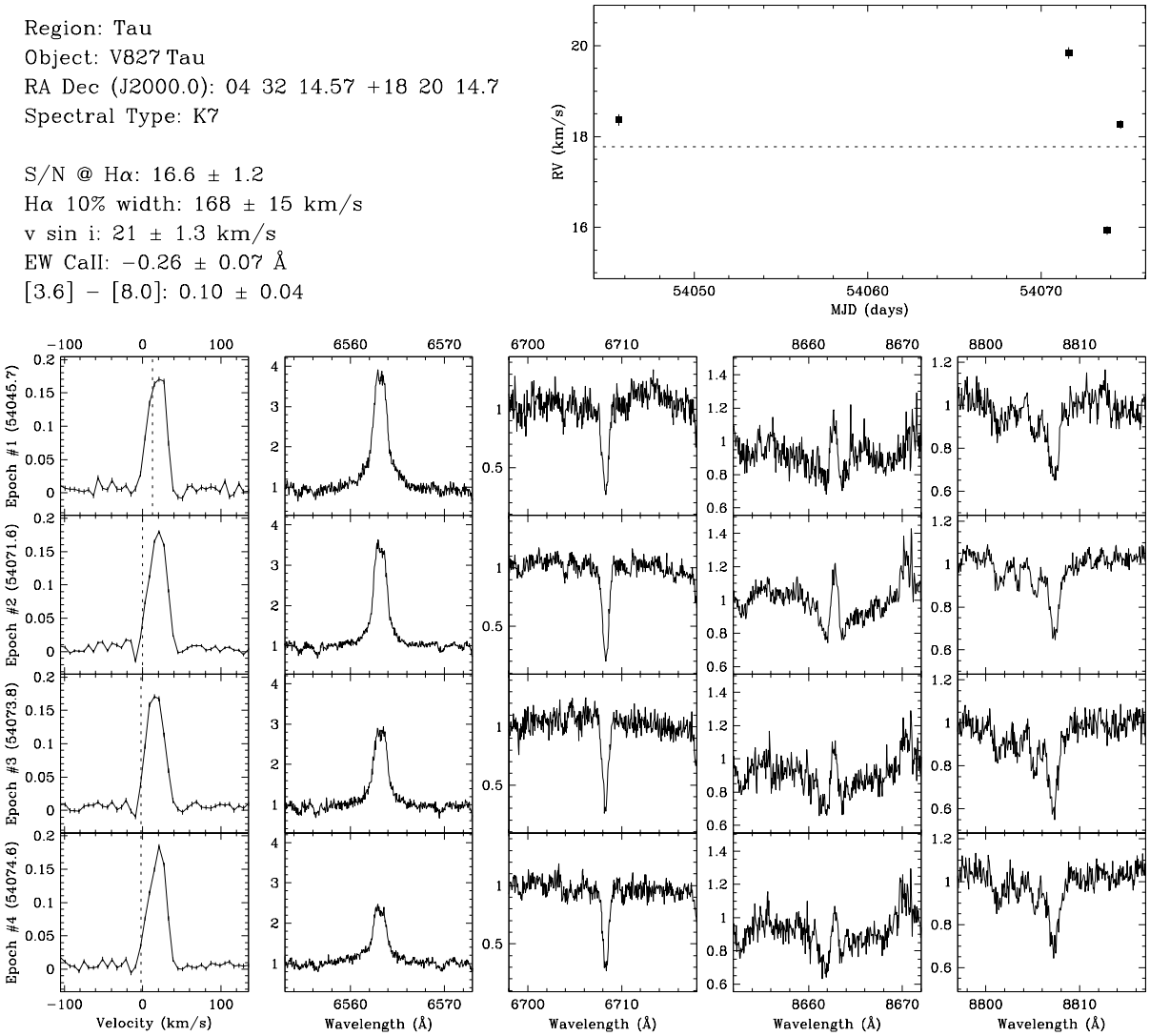

Figure 4.160 V827 Tau shows no clear evidence of a close companion. The star has a single-line profile, and a radial velocity scatter not significant relative to variations observed within each observing run. The radial velocity scatter within the second observing run (epochs #2, #3 and #4) is large but consistent with that expected from systematic line profile variations, e.g. from star spots rotating with the star. This target has been previously reported by (Lafrenière, priv. comm.) to have a resolved companion with a separation of $\sim 0\farcs09$ (~ 13 AU) at a position angle of $\sim 11.3°$, and an R-band flux ratio of ~ 0.31 ($\Delta K \sim 0.51$). However, there is no clear evidence in the line profile of the resolved companion. Since the resolved companion has an expected circular orbital speed of $\sim 8\,\mathrm{km\,s^{-1}}$, a second profile could be obscured if the primary star and the resolved companion have similar projected rotational velocities.

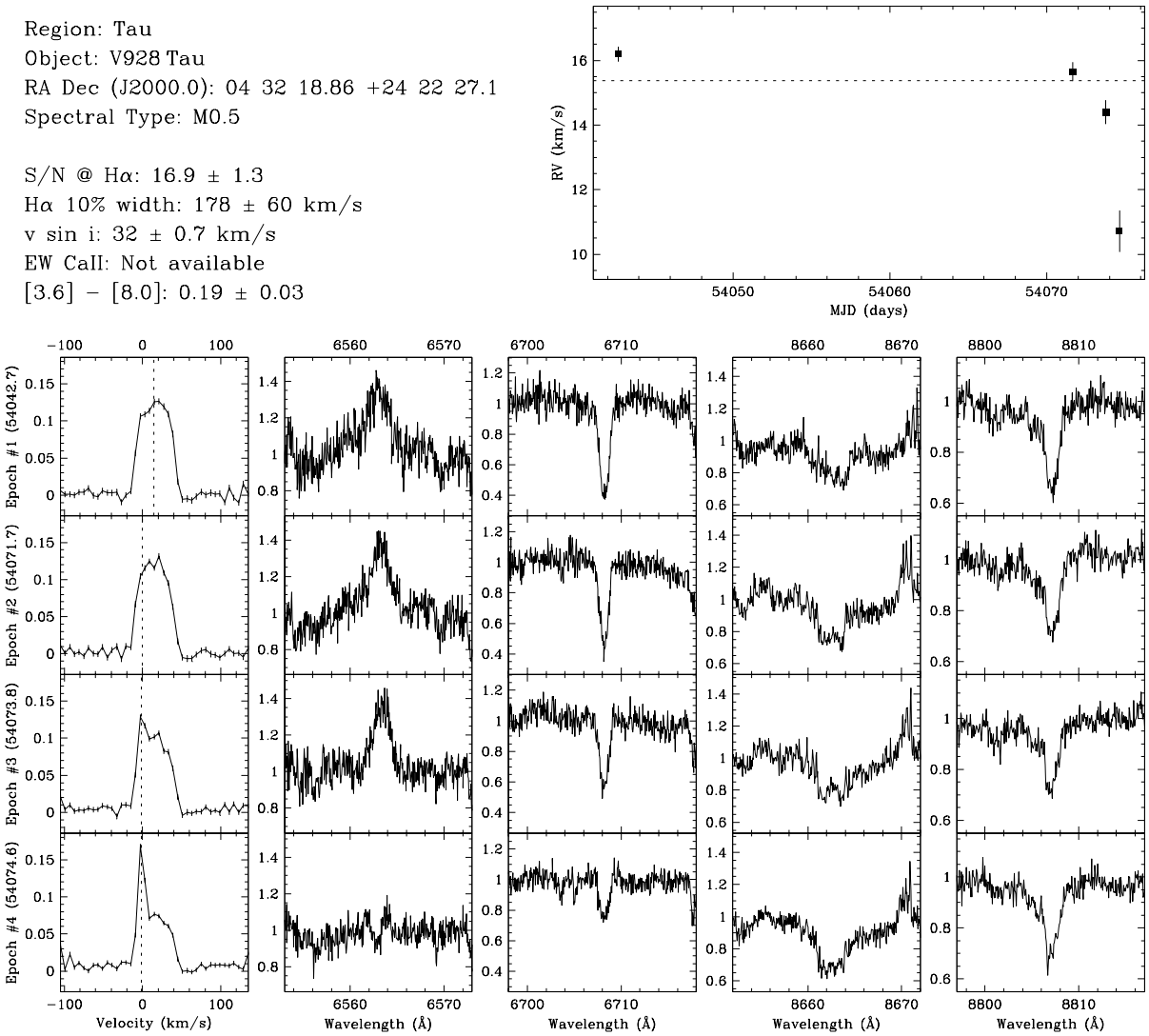

Figure 4.161 V928 Tau shows no clear evidence of a close companion. The star has a single-line profile, and a radial velocity scatter not significant relative to variations observed within each observing run. For epochs #3 and #4, the sharp peaks in the line profile at the observer's rest frame are due to moonlight, and biased the radial velocity estimates toward the observer's rest frame. This target has been previously reported by Leinert et al. (1993), Ghez et al. (1993), and Simon et al. (1995) as a resolved binary (V928 Tau A+B) with a separation of 0.″165–0.″18 (23–25 AU) at a position angle of $\sim$125° or $\sim$300°, and an R flux ratio of 0.31–0.79 ($\Delta K \sim 0.14$–0.60). However, there is no clear evidence in the line profile of the resolved companion. Since the resolved companion has an expected circular orbital speed of $\sim 6\,\mathrm{km\,s^{-1}}$, a second profile could be obscured if the primary star and the resolved companion have similar projected rotational velocities.

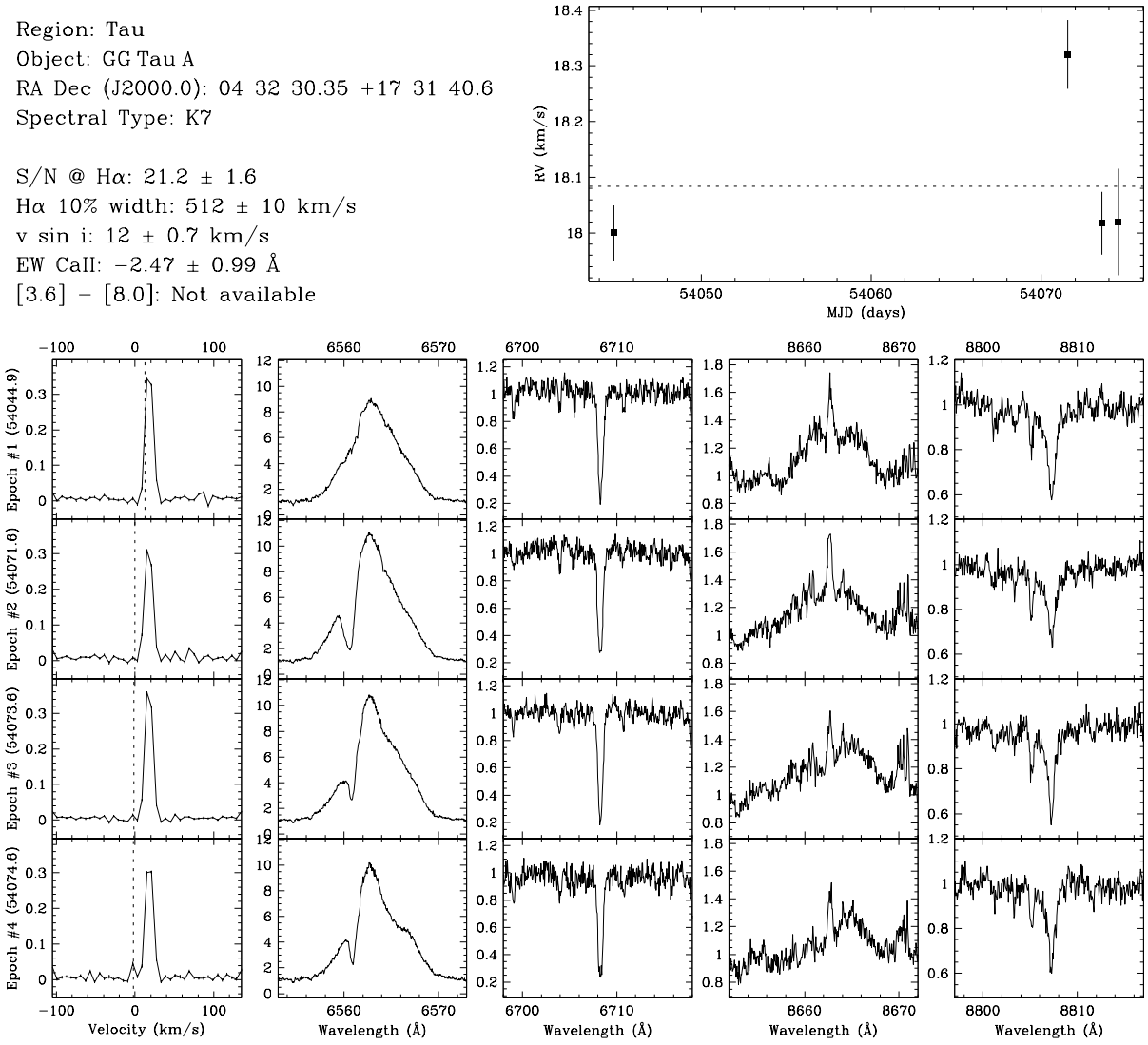

Figure 4.162 GG Tau A shows no clear evidence of a close companion. The star has a single-line profile, and a radial velocity scatter not significant relative to variations observed within each observing run. The radial velocity scatter within the second observing run (epochs #2, #3 and #4) is consistent with that expected from systematic line profile variations, e.g. from star spots rotating with the star. For epoch #4, the small peak in the line profile at the observer's rest frame is due to moonlight, and may have biased the radial velocity estimate toward the observer's rest frame. This target has been previously reported by Leinert et al. (1993), Ghez et al. (1993), and Ghez et al. (1997b) to have a resolved companion (GG Tau a) with a separation of $0\farcs2502$–$0\farcs288$ (35–40 AU) at a position angle of $358\fdg79$–$3°$, and an R-band flux ratio of 0.01–0.33 ($\Delta K \sim 0.48$–1.51). However, there is no clear evidence in the line profile of the resolved companion. Since the resolved companion has an expected circular orbital speed of $\sim 4\,\mathrm{km\,s^{-1}}$, a second profile could be obscured if the primary star and the resolved companion have similar projected rotational velocities.

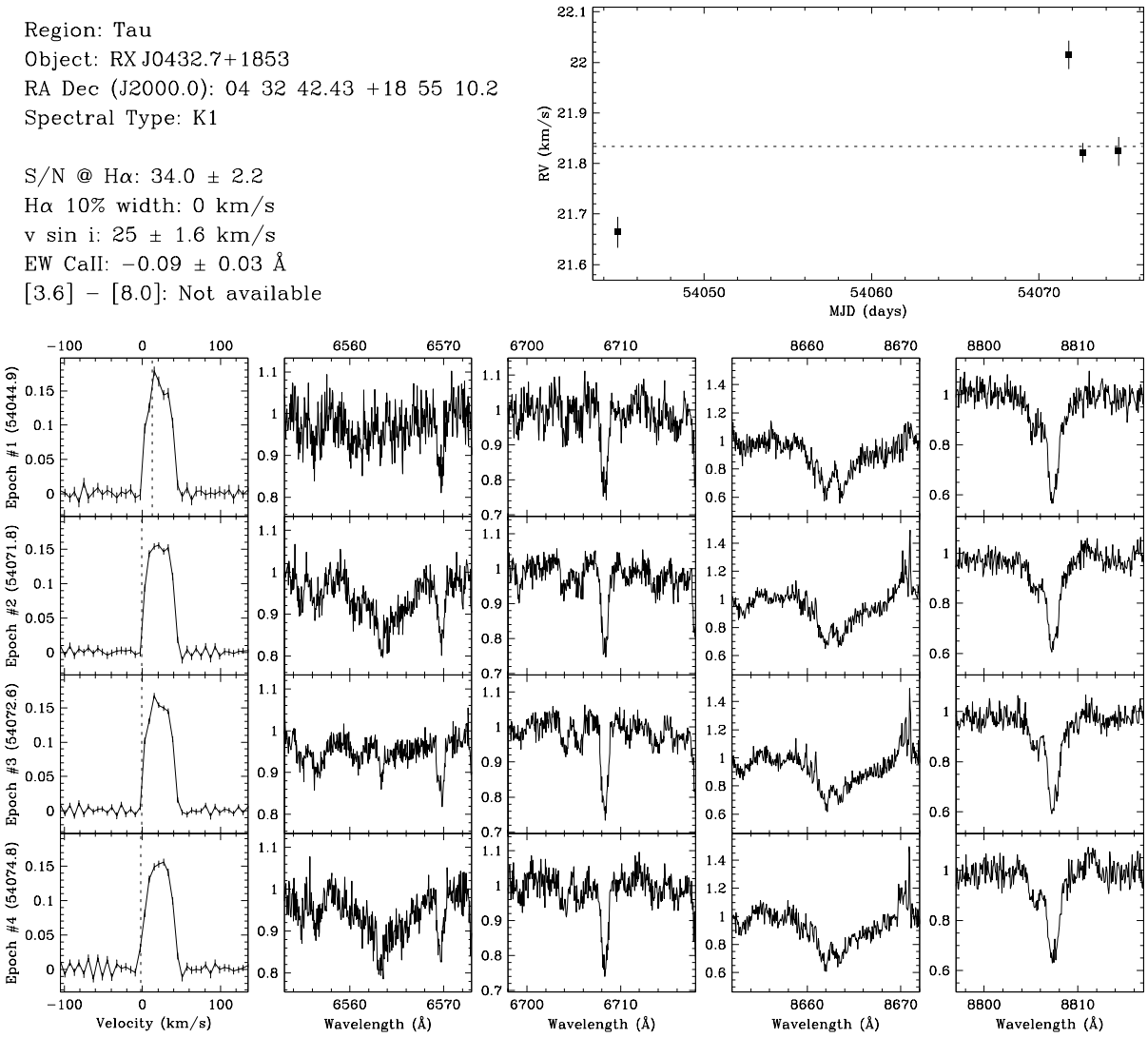

Figure 4.163 RX J0432.7+1853 shows no clear evidence of a close companion. The star has a single-line profile, and a radial velocity scatter not significant relative to variations observed within each observing run. The radial velocity scatter within the second observing run (epochs #2, #3 and #4) is consistent with that expected from systematic line profile variations, e.g. from star spots rotating with the star. This target has been previously reported by Köhler & Leinert (1998) to have no resolved companions.

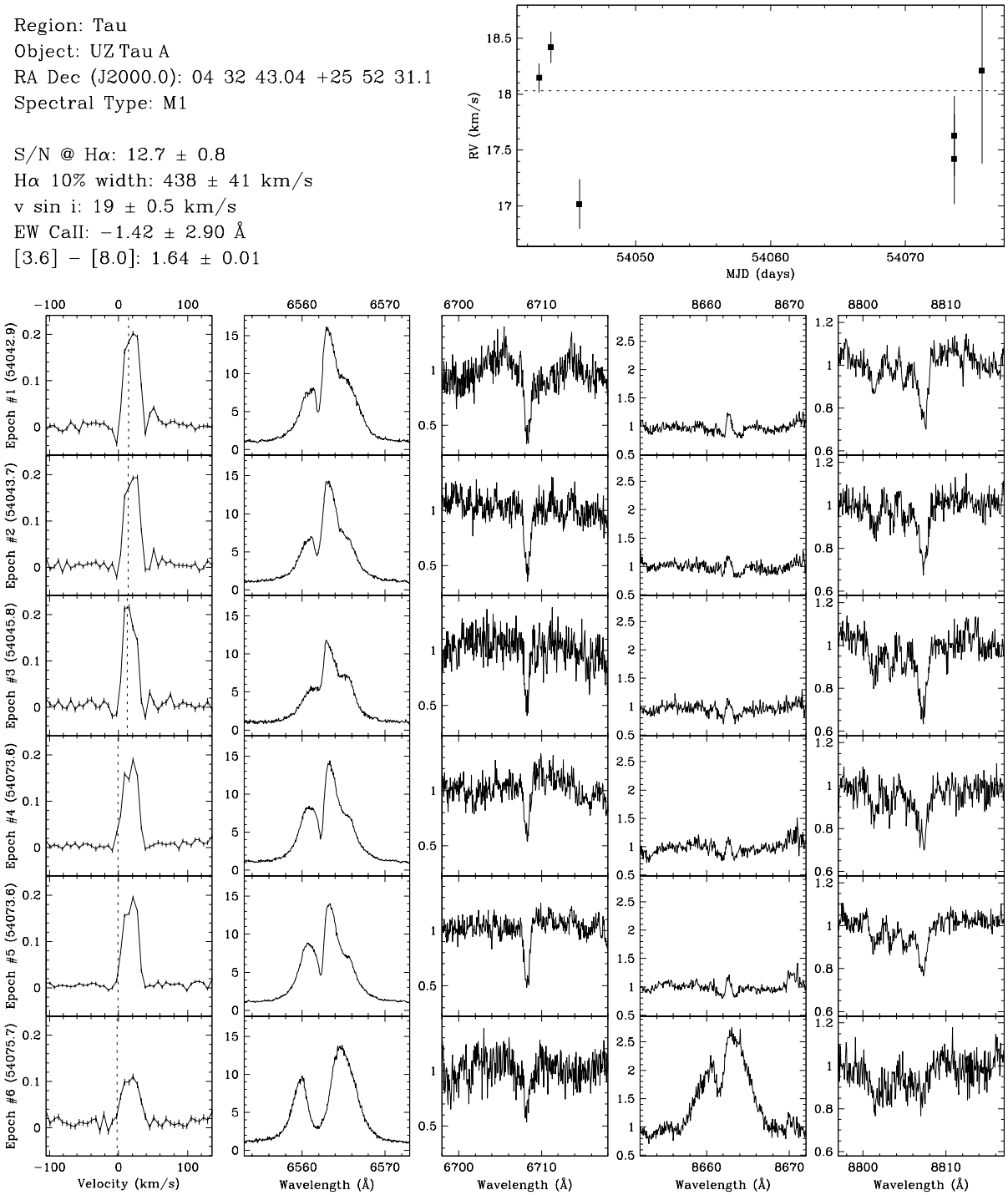

Figure 4.164 UZ Tau A shows no clear evidence of a close companion. The star has a single-line profile, and a radial velocity scatter not significant relative to variations observed within each observing run. The radial velocity scatter within each observing run is consistent with that expected from systematic line profile variations, e.g. from star spots rotating with the star. This target has been previously reported by Leinert et al. (1993), Ghez et al. (1993), Simon et al. (1995), and Ghez et al. (1997b) to have a resolved companion with a separation of 0.″34–0.″3678 (48–51 AU) at a position angle of 359°–0°, and an R-band flux ratio of 0.03–0.37 ($\Delta K \sim 0.50$–1.11). However, there is no clear evidence in the line profile of the resolved companion. Since the resolved companion has an expected circular orbital speed of $\sim 3\,\mathrm{km\,s^{-1}}$, a second profile could be obscured if the primary star and the resolved companion have similar projected rotational velocities.

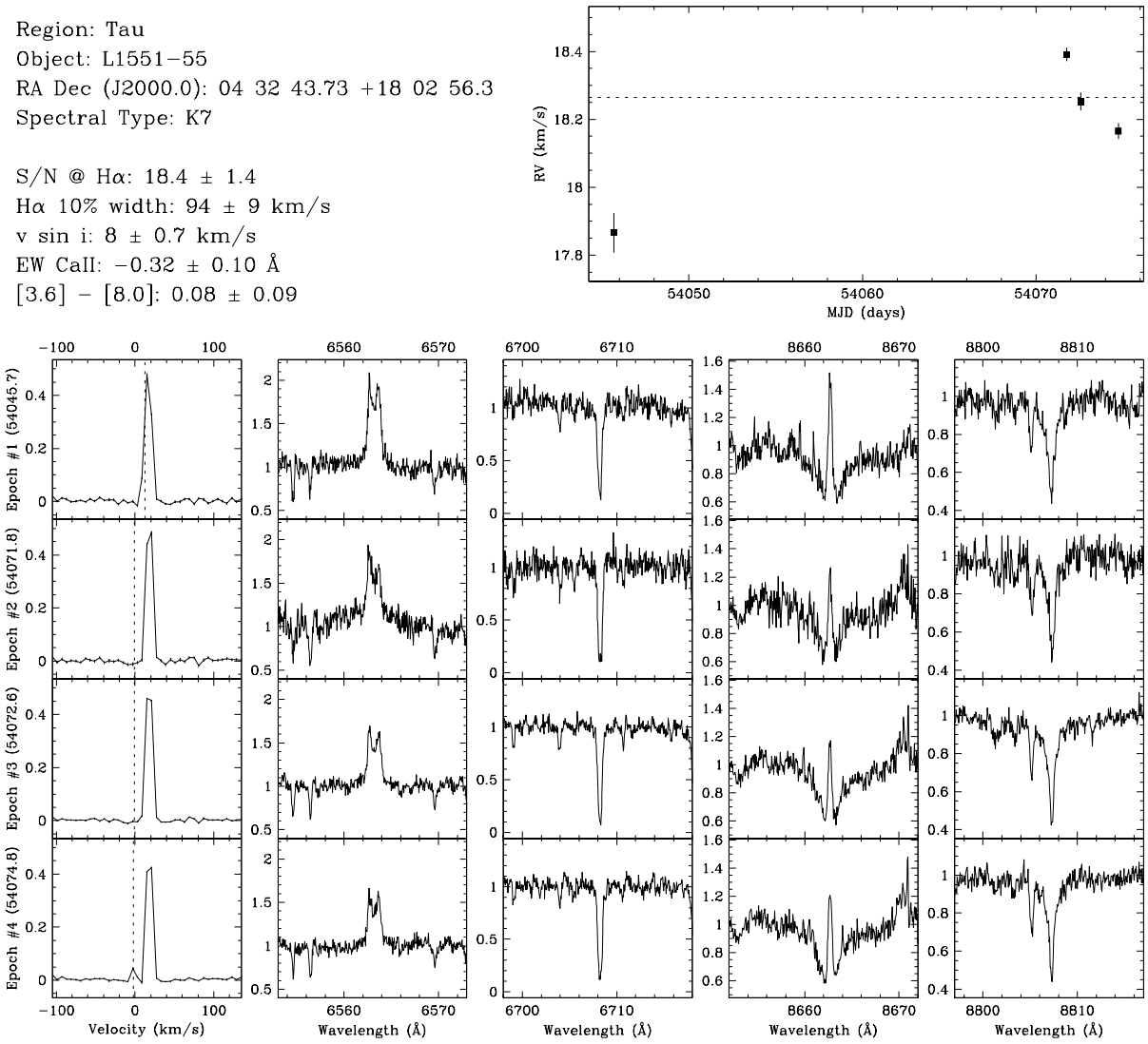

Figure 4.165 L1551-55 shows no clear evidence of a close companion. The star has a single-line profile, and a radial velocity scatter not significant relative to variations observed within each observing run. The radial velocity scatter within the second observing run (epochs #2, #3 and #4) is consistent with that expected from systematic line profile variations, e.g. from star spots rotating with the star. For epoch #4, the small peak in the line profile at the observer's rest frame is due to moonlight, and may have biased the radial velocity estimates toward the observer's rest frame. This target has been previously reported by Leinert et al. (1993) to have no resolved companions.

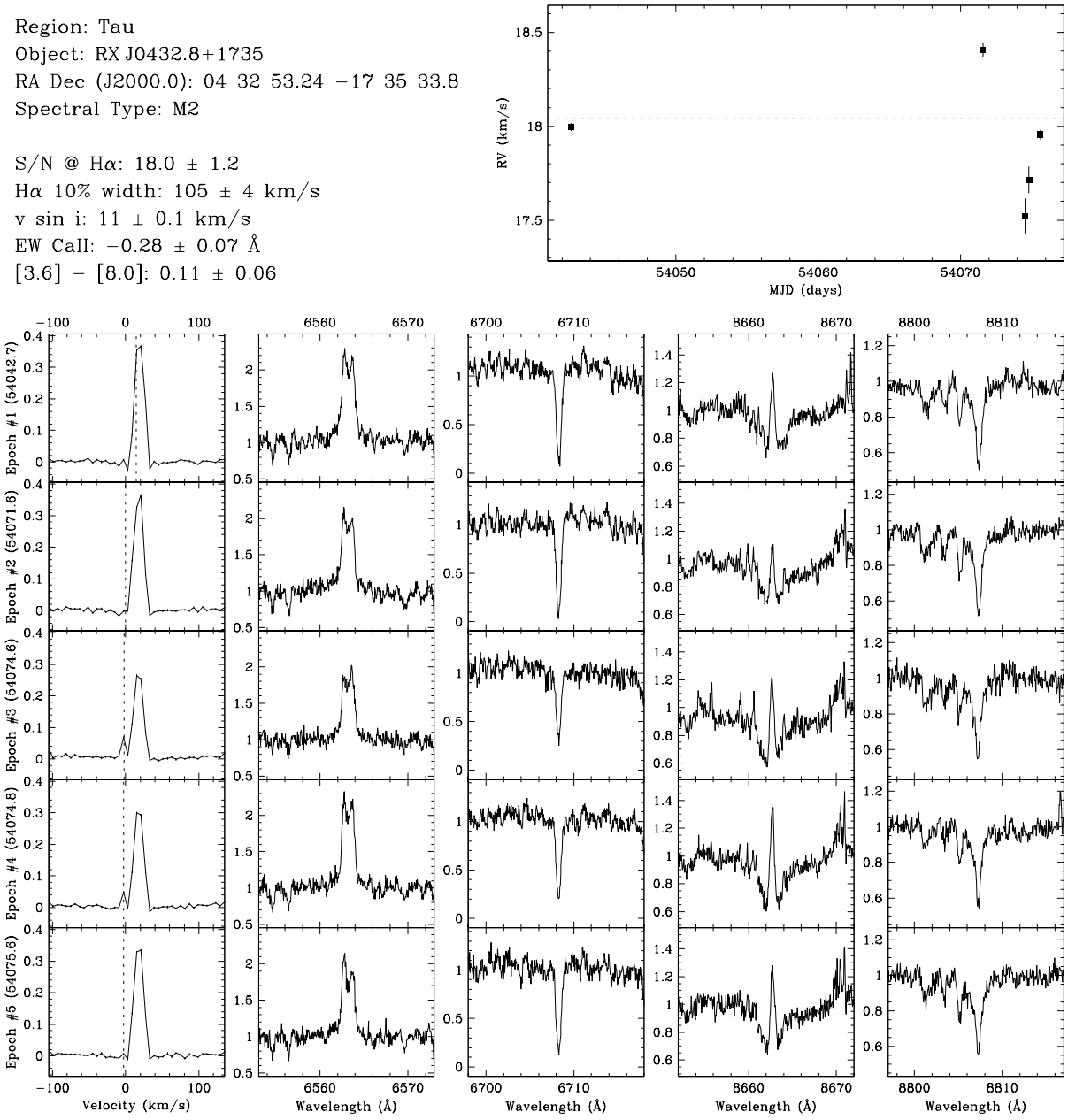

Figure 4.166 RX J0432.8+1735 shows no clear evidence of a close companion. The star has a single-line profile, and a radial velocity scatter not significant relative to variations observed within each observing run. The radial velocity scatter within the second observing run (epochs #2, #3, #4 and #5) is consistent with that expected from systematic line profile variations, e.g. from star spots rotating with the star. For epochs #3 and #4, the sharp peaks in the line profile at the observer's rest frame are due to moonlight, and likely biased the radial velocity estimates toward the observer's rest frame. This target has been previously reported by Köhler & Leinert (1998) to have no resolved companions.

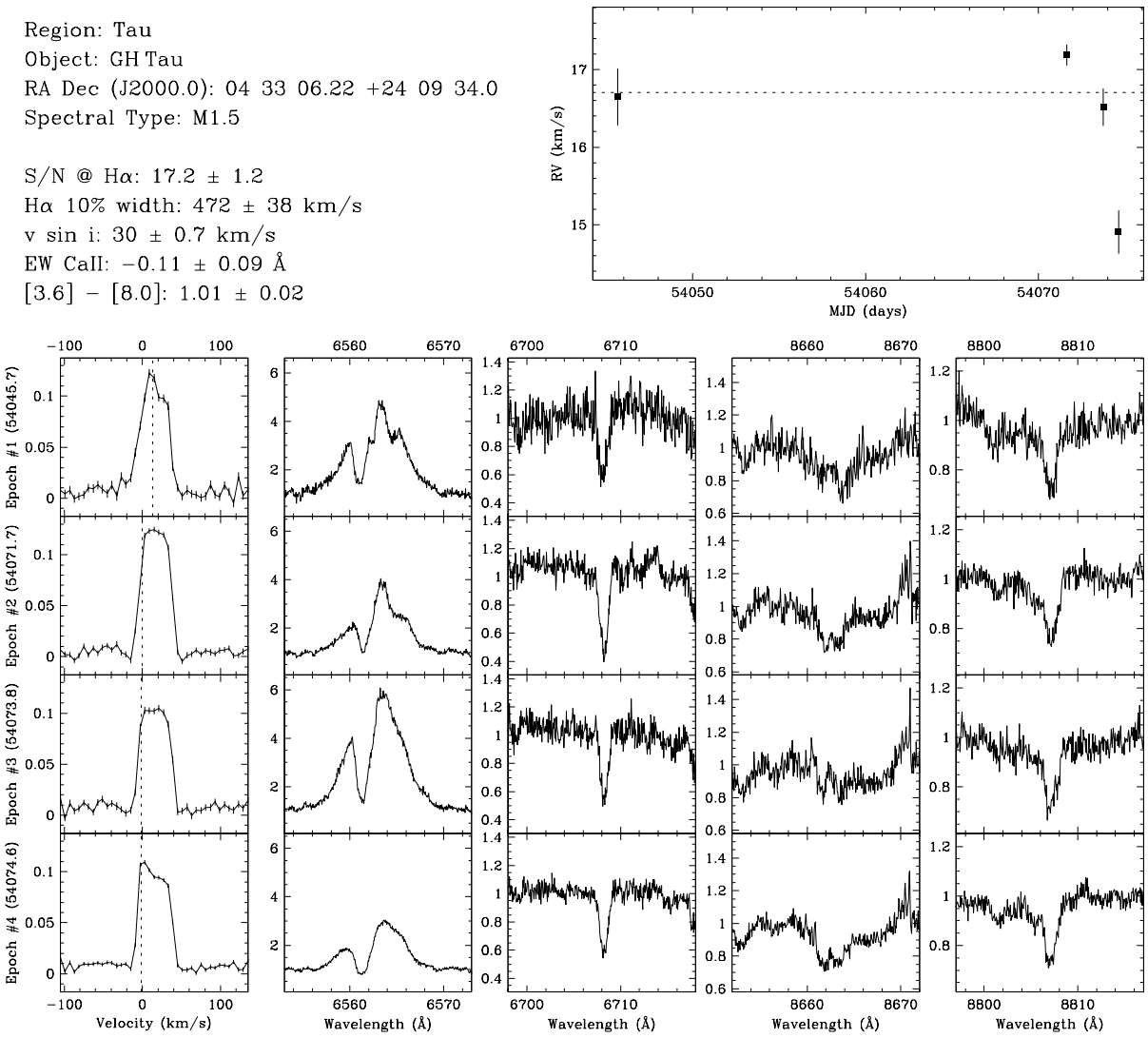

Figure 4.167 GH Tau shows no clear evidence of a close companion. The star has a single-line profile, and a radial velocity scatter not significant relative to variations observed within each observing run. The radial velocity scatter within the second observing run (epochs #2, #3 and #4) is consistent with that expected from systematic line profile variations, e.g. from star spots rotating with the star. For epochs #1 and #4, the peaks in the line profile at the observer's rest frame is due to moonlight, and likely biased the radial velocity estimate toward the observer's rest frame. This target has been previously reported by Leinert et al. (1993), and Ghez et al. (1993) as a resolved binary (GH Tau A+B) with a separation of 0.″314–0.″35 (44–49 AU) at a position angle of 120° or 299°, and an R-band flux ratio of 0.22–0.86 ($\Delta K \sim 0.10$–0.64). However, there is no clear evidence in the line profile of the resolved secondary star. Since the resolved secondary star has an expected circular orbital speed of $\sim 4\,\mathrm{km\,s^{-1}}$, a second profile could be obscured if the primary star and the secondary star have similar projected rotational velocities.

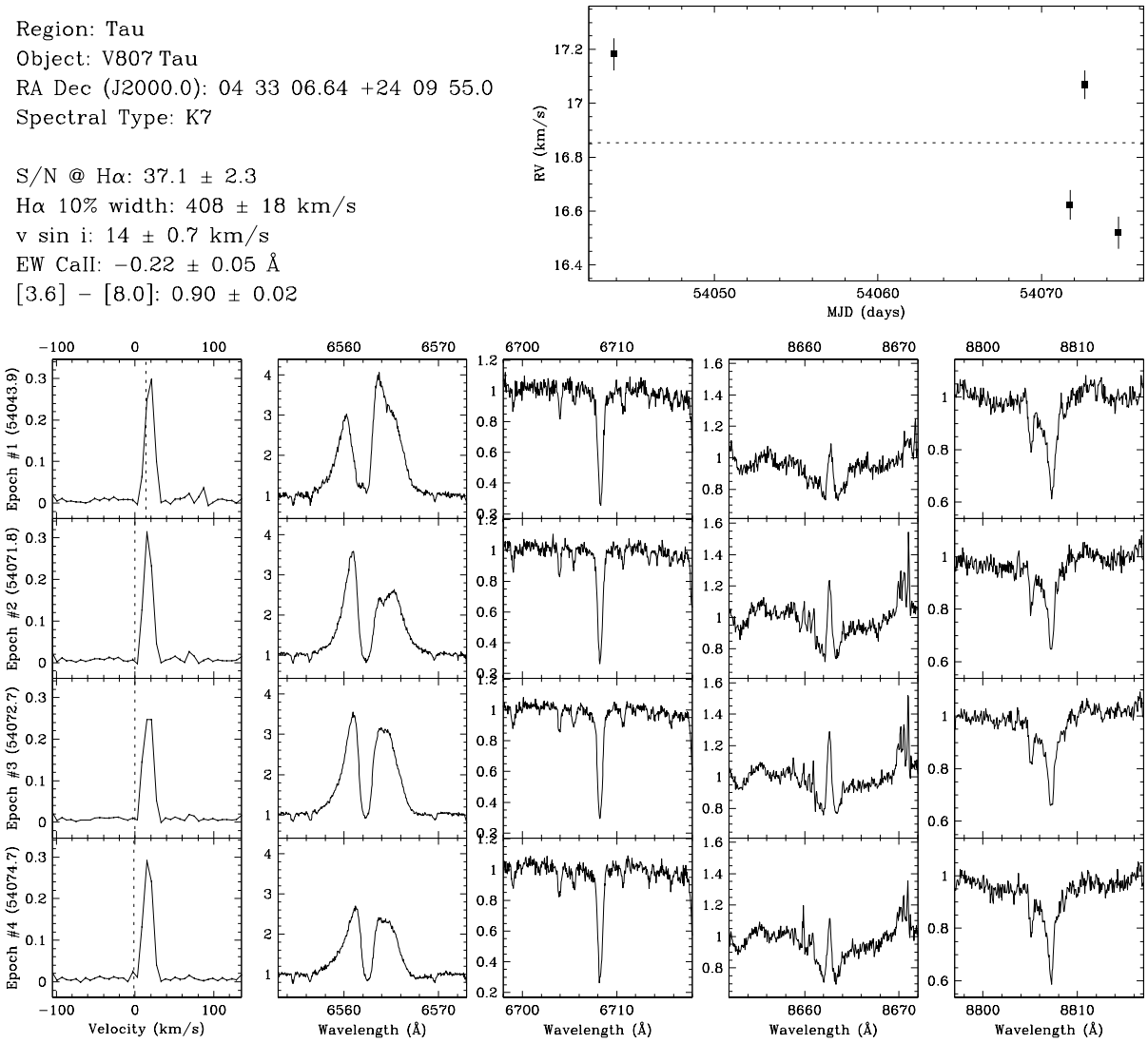

Figure 4.168 V807 Tau shows no clear evidence of a close companion. The star has a single-line profile, and a radial velocity scatter not significant relative to variations observed within each observing run. The radial velocity scatter within the second observing run (epochs #2, #3 and #4) is consistent with that expected from systematic line profile variations, e.g. from star spots rotating with the star. This target has been previously reported by Leinert et al. (1993), and Ghez et al. (1993) as a resolved binary (V807 Tau A+B) with a separation of 0.″375–0.″41 (53–57 AU) at a position angle of 330°–332°, and an R-band flux ratio of 0.08–0.15 ($\Delta K \sim 0.84$–1.07). However, there is no clear evidence in the line profile of the resolved companion. Since the resolved companion has an expected circular orbital speed of $\sim 4\,\mathrm{km\,s^{-1}}$, a second profile could be obscured if the primary star and the resolved companion have similar projected rotational velocities.

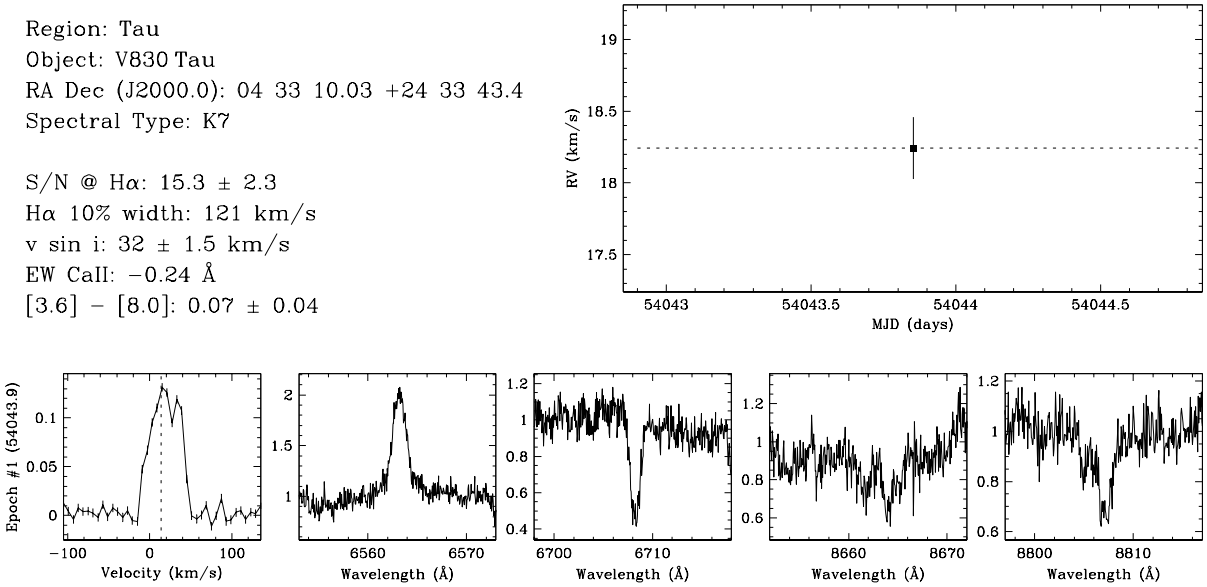

Figure 4.169 V830 Tau has a single-line profile, and is therefore not an SB2. The radial velocity scatter cannot be determined because the target was observed for a single epoch. Hence, it is undetermined if the target is an SB1 or a single star. The sharp indentation in the line profile is consistent with star spots. This target has been previously reported by Leinert et al. (1993) to have no resolved companions.

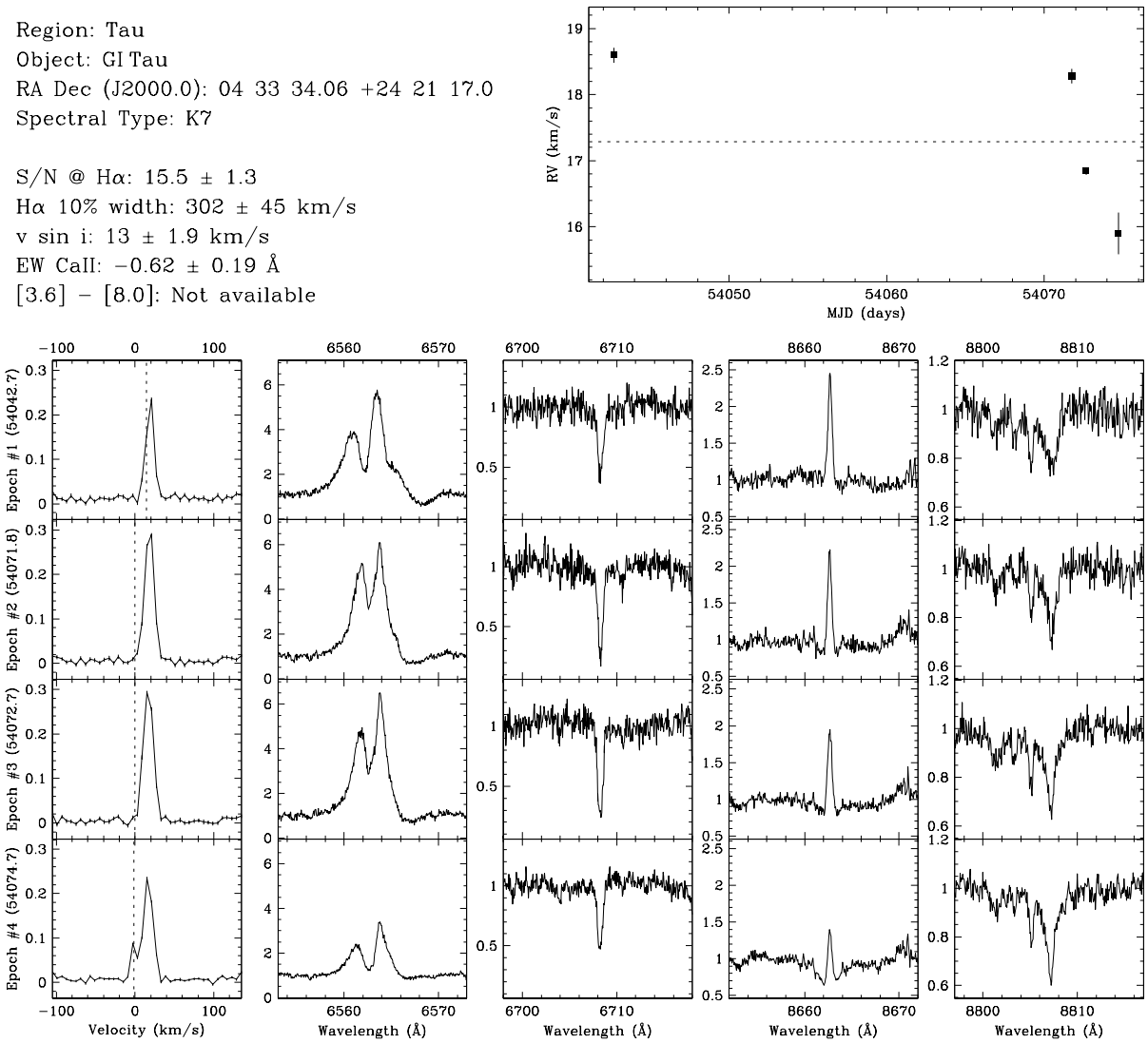

Figure 4.170 GI Tau shows no clear evidence of a close companion. The star has a single-line profile, and a radial velocity scatter not significant relative to variations observed within each observing run. The radial velocity scatter within the second observing run (epochs #2, #3 and #4) is large but consistent with that expected from systematic line profile variations, e.g. from star spots rotating with the star. For epoch #4, the sharp peak in the line profile at the observer's rest frame is due to moonlight, and likely biased the radial velocity estimate toward the observer's rest frame. This target has been previously reported by Leinert et al. (1993) to have a resolved companion with a separation of $\sim$12.″2 ($\sim$1700 AU) at a position angle of $\sim$151°, and an R-band flux ratio of $\sim$0.50 ($\Delta K \sim 0.23$). Given the separation, the expected contribution to the line profile from the resolved companion is negligible.

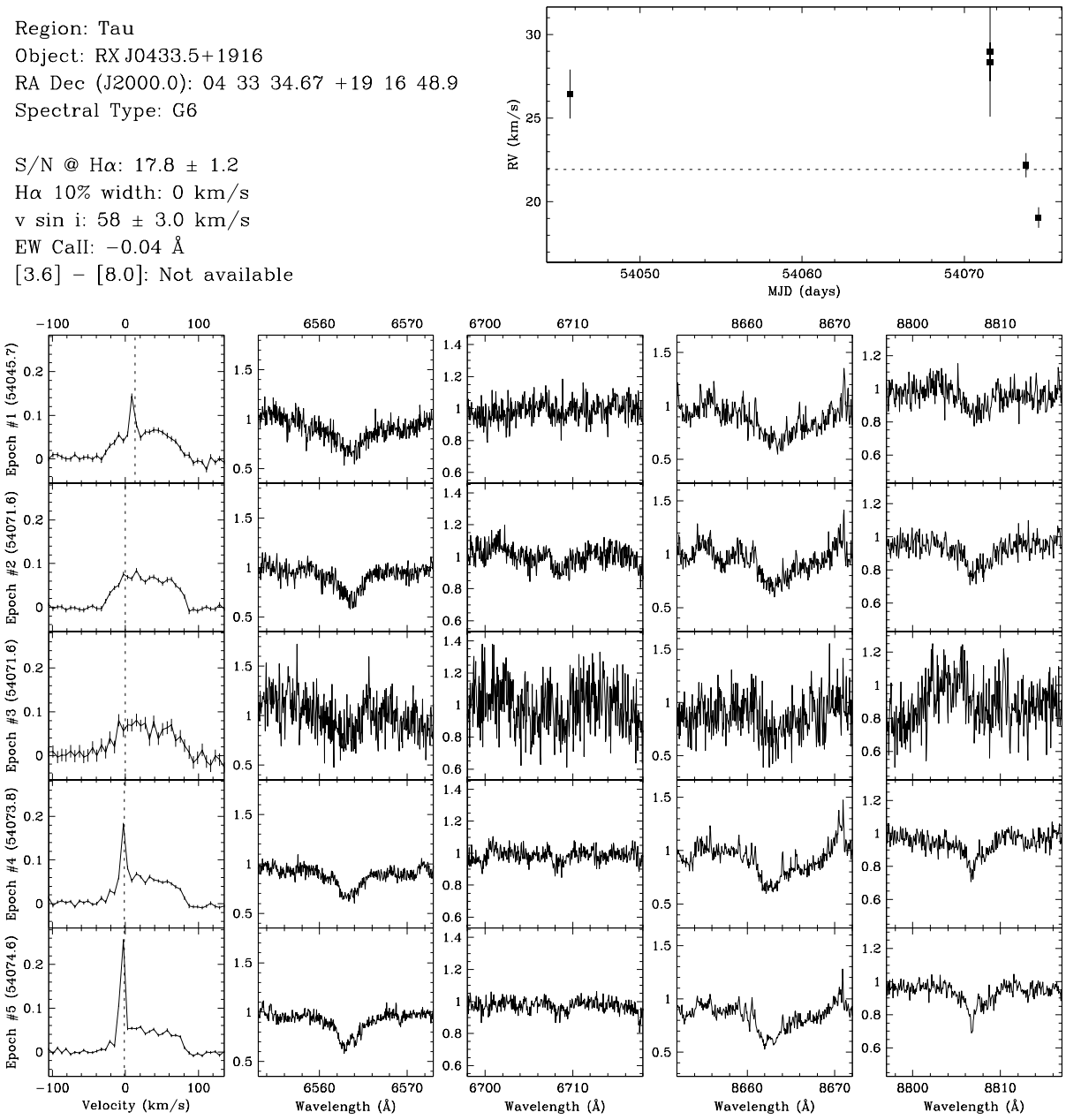

Figure 4.171 RX J0433.5+1916 shows no clear evidence of a close companion. The star has a single-line profile, and a radial velocity scatter not significant relative to variations observed within each observing run. The radial velocity scatter within the second observing run (epochs #2, #3, #4 and #5) is large but consistent with that expected from systematic line profile variations, e.g. from star spots rotating with the star. For epochs #1, #4 and #5, the sharp peaks in the line profile at the observer's rest frame are due to moonlight, and may have biased the radial velocity estimates toward the observer's rest frame. This target has been previously reported by Köhler & Leinert (1998) to have no resolved companions.

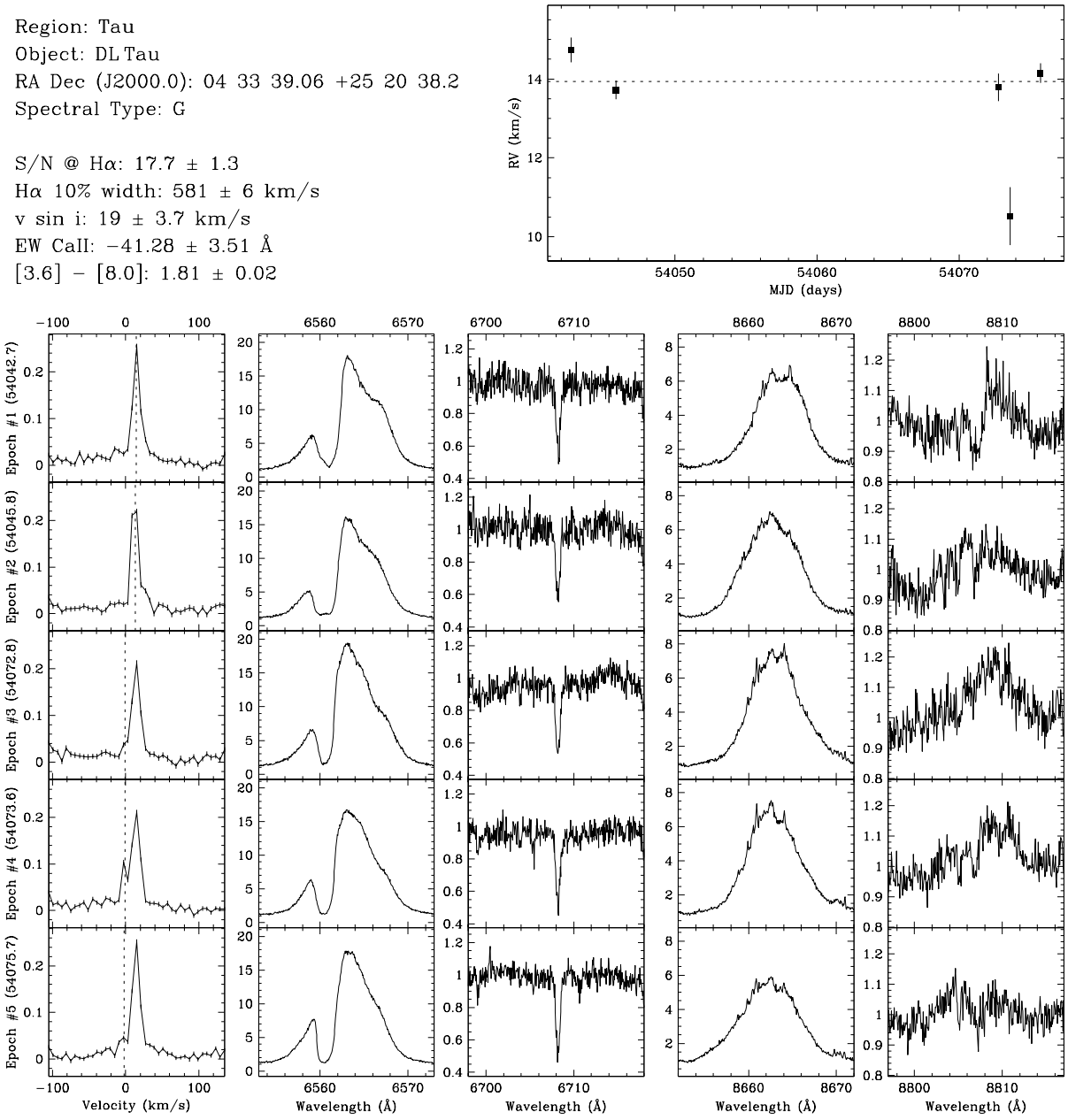

Figure 4.172 DL Tau shows no clear evidence of a close companion. The star has a single-line profile, and a radial velocity scatter not significant relative to variations observed within each observing run. The radial velocity scatter within each observing run, with the exception of epoch #4, is consistent with that expected from systematic line profile variations, e.g. from star spots rotating with the star. For epoch #4, the peak in the line profile at the observer's rest frame is due to moonlight, and likely biased the radial velocity estimate toward the observer's rest frame. This target has been previously reported by Leinert et al. (1993), and Simon et al. (1995) to have no resolved companions.

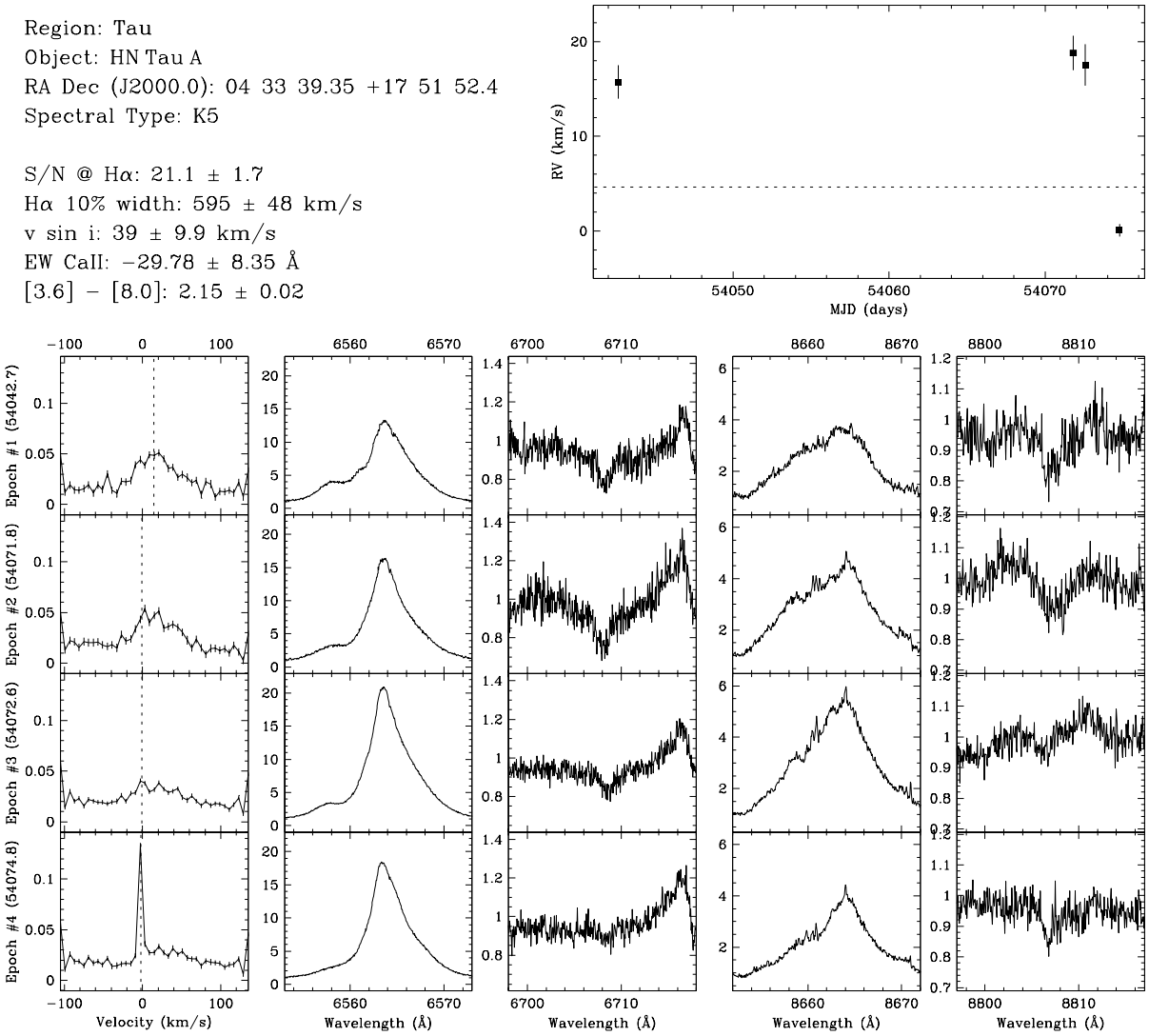

Figure 4.173 HN Tau A shows no clear evidence of a close companion. The star has a single-line profile, and a radial velocity scatter not significant relative to variations observed within each observing run. The spectrum is heavily veiled, and we derived the radial velocities from fits to the line profile rather than from direct fits to the spectra (see §4.4.2). Only the three reliable radial velocity estimates (epochs #1, #2 and #3) were evaluated for scatter, and are stable relative to the measurement uncertainties. The overall radial velocity deviates from that of the star forming region. However, cluster membership is supported by Li-λ6708 absorption. For epoch #4, the strong sharp peak in the line profile at the observer's rest frame is due to moonlight, and biased the radial velocity estimate toward the observer's rest frame. This target has been previously reported by Leinert et al. (1993) to have a resolved companion with a separation of $\sim 3\farcs1$ (~ 430 AU) at a position angle of $\sim 215°$, and an R-band flux ratio of $\lesssim 0.01$ ($\Delta K \sim 3.44$). Given the flux ratio and separation, the expected contribution to the line profile from the resolved companion is negligible.

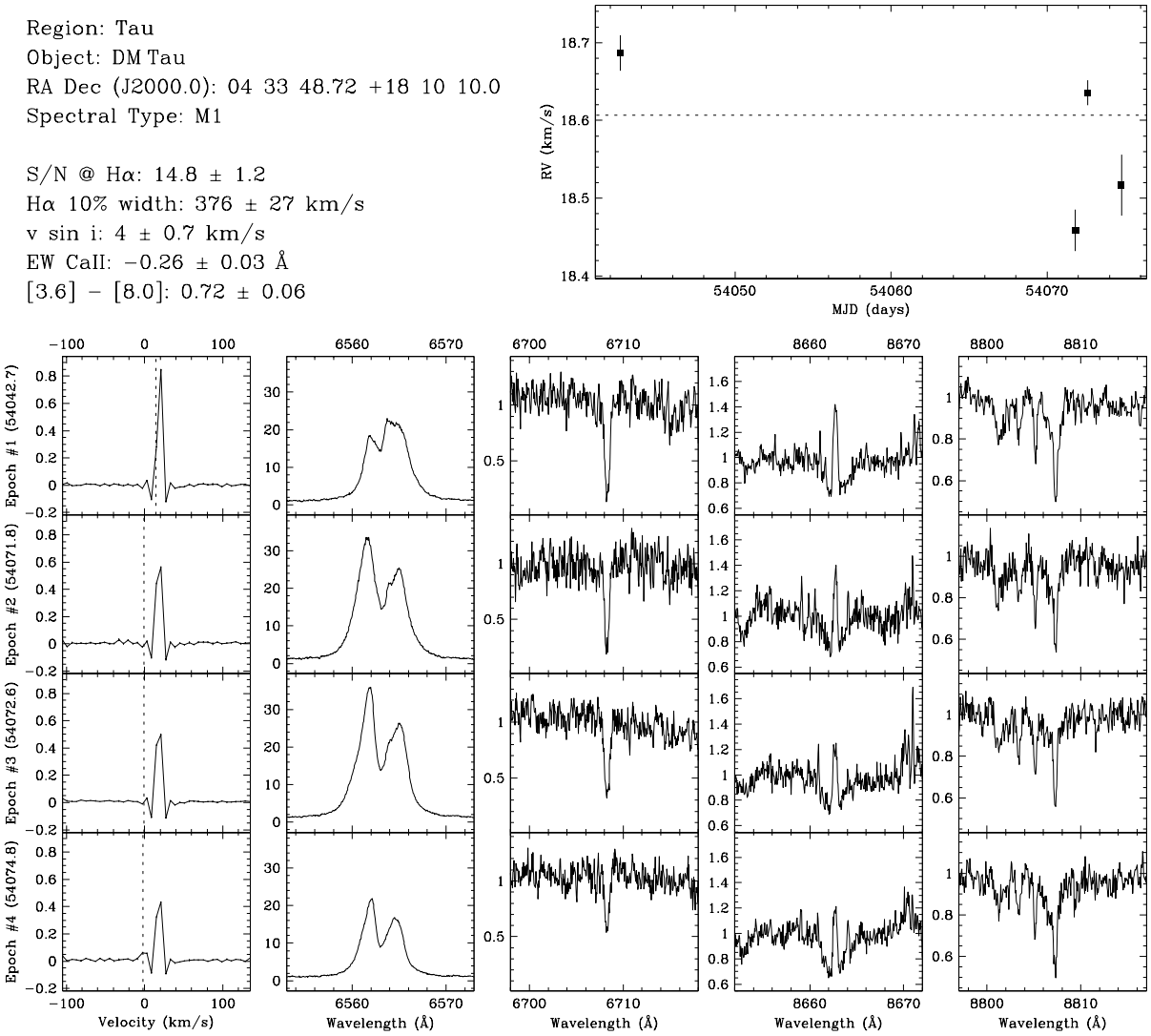

Figure 4.174 DM Tau shows no clear evidence of a close companion. The star has a single-line profile, and a radial velocity scatter not significant relative to variations observed within each observing run. The radial velocity scatter within the second observing run (epochs #2, #3 and #4) is consistent with that expected from systematic line profile variations, e.g. from star spots rotating with the star. This target has been previously reported by Leinert et al. (1993) to have no resolved companions.

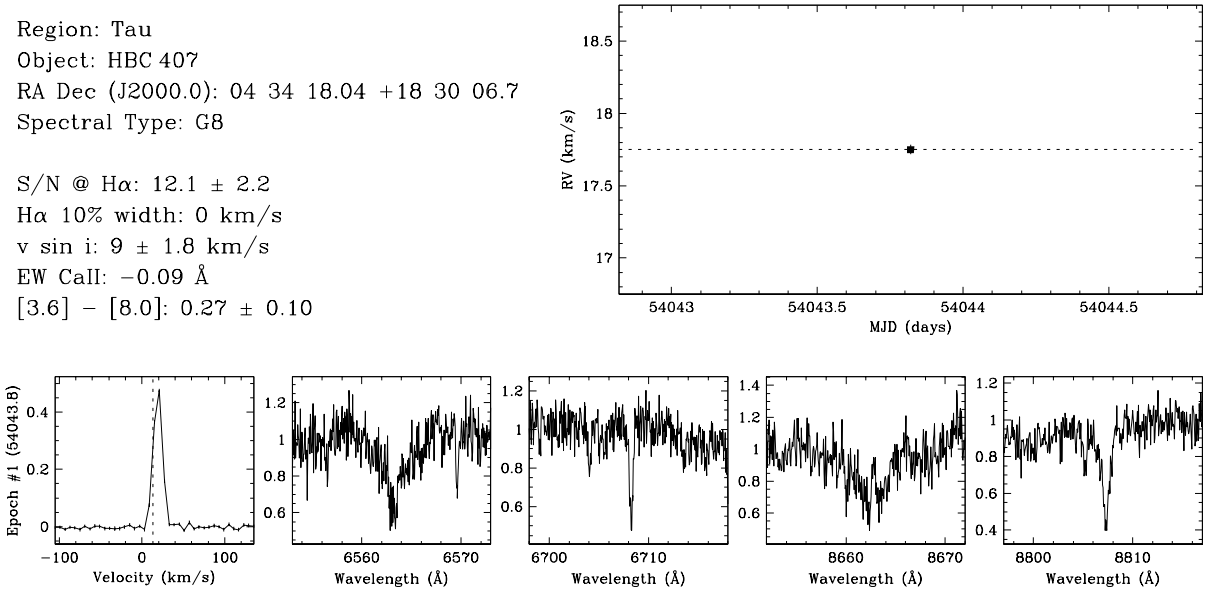

Figure 4.175 HBC 407 has a single-line profile, and is therefore not an SB2. The radial velocity scatter cannot be determined because the target was observed for a single epoch. Hence, it is undetermined if the target is an SB1 or a single star. This target has been previously reported by Leinert et al. (1993) to have no resolved companions.

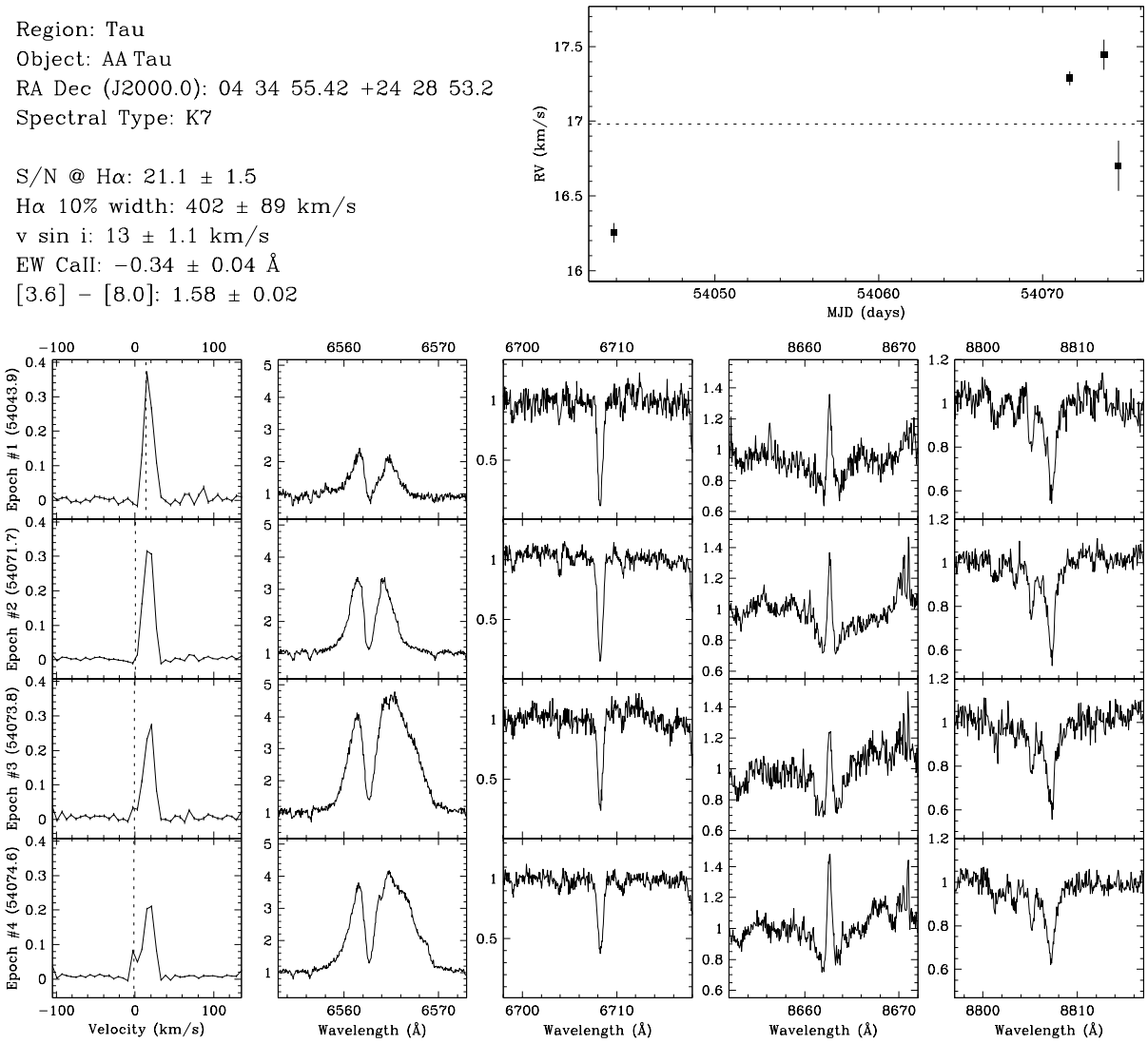

Figure 4.176 AA Tau shows no clear evidence of a close companion. The star has a single-line profile, and a radial velocity scatter not significant relative to variations observed within each observing run. The radial velocity scatter within the second observing run (epochs #2, #3 and #4) is consistent with that expected from systematic line profile variations, e.g. from star spots rotating with the star. For epochs #3 and #4, the peaks in the line profile at the observer's rest frame is due to moonlight, and likely biased the radial velocity estimate toward the observer's rest frame. This target has been previously reported by Leinert et al. (1993), and Simon et al. (1995) to have no resolved companions.

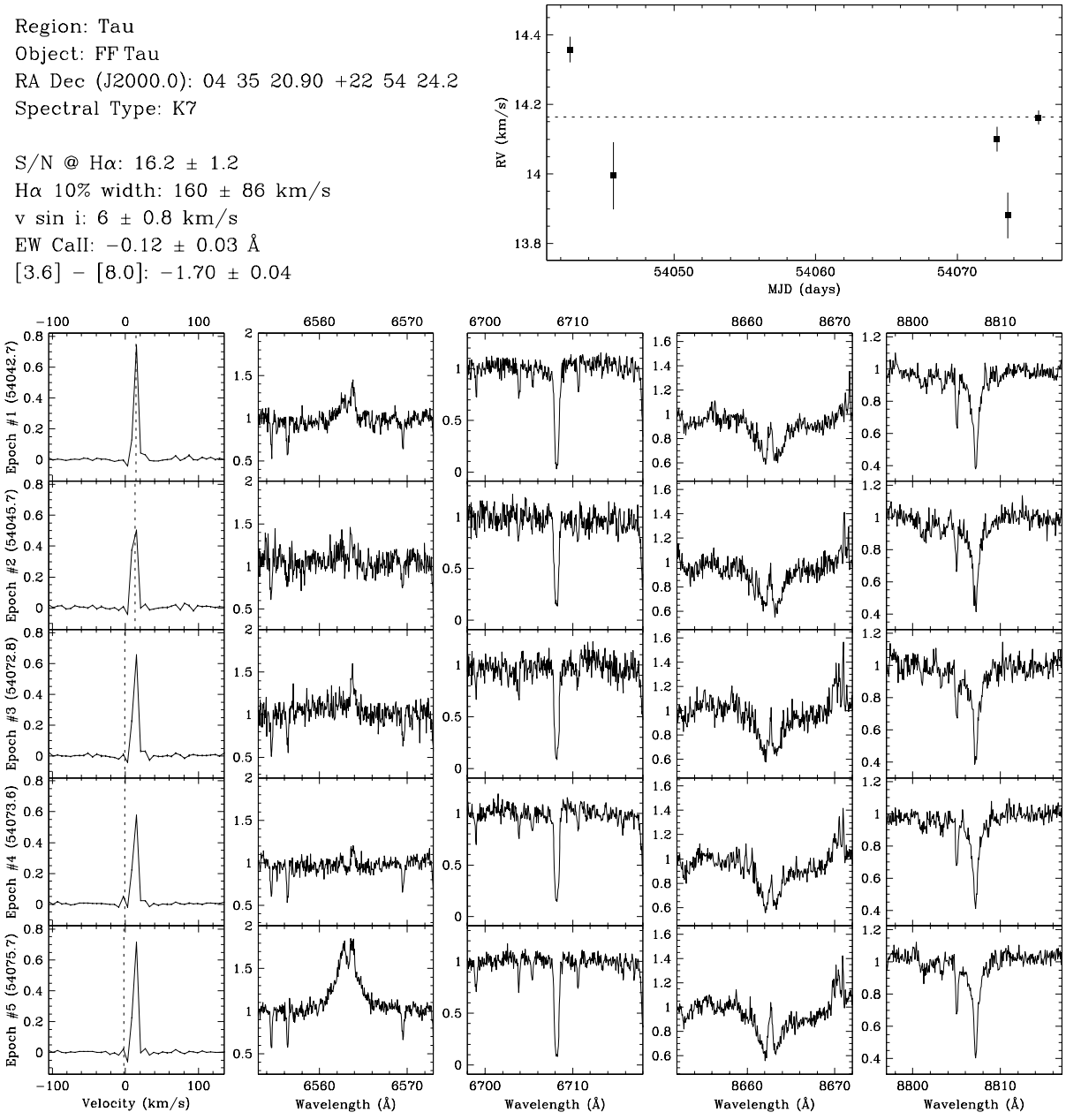

Figure 4.177 FF Tau shows no clear evidence of a close companion. The star has a single-line profile, and a radial velocity scatter not significant relative to variations observed within each observing run. This target has been previously reported by Simon et al. (1995) as a resolved binary (FF Tau A+B) with a separation of $\sim 0\farcs026$ (~ 3.6 AU) at a position angle of $\sim 46°$, and an R-band flux ratio of $\sim$0.10 ($\Delta K \sim 1.00$). Given the flux ratio, the expected contribution to the line profile from the resolved secondary star is small.

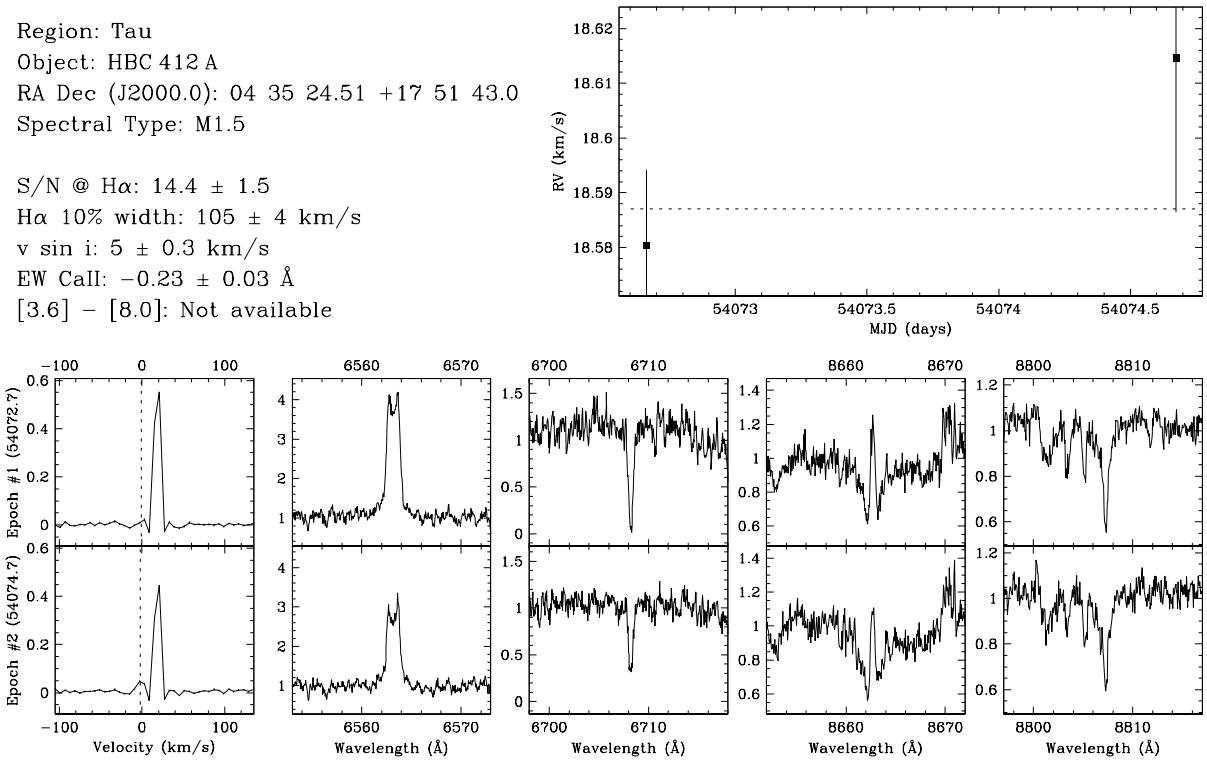

Figure 4.178 HBC 412 A has a single-line profile, and is therefore not an SB2. The radial velocity scatter over the short baseline available does not conclusively indicate if the target is an SB1 or a single star. For epoch #2, the small peak in the line profile at the observer's rest frame is due to moonlight, and may have biased the radial velocity estimate toward the observer's rest frame. This target has been previously reported by Leinert et al. (1993) to have a resolved companion (HBC 412 B) with a separation of $\sim$0.″7 ($\sim$98 AU) at a position angle of $\sim$68°, and an R-band flux ratio of $\sim$1.00 ($\Delta K \sim 0.00$). However, there is no clear evidence in the line profile of the resolved companion. Since HBC 412 B has an expected circular orbital speed of $\sim 3\,\mathrm{km\,s^{-1}}$, and a similar v sin i ($\sim 4\,\mathrm{km\,s^{-1}}$), a second profile is likely obscured.

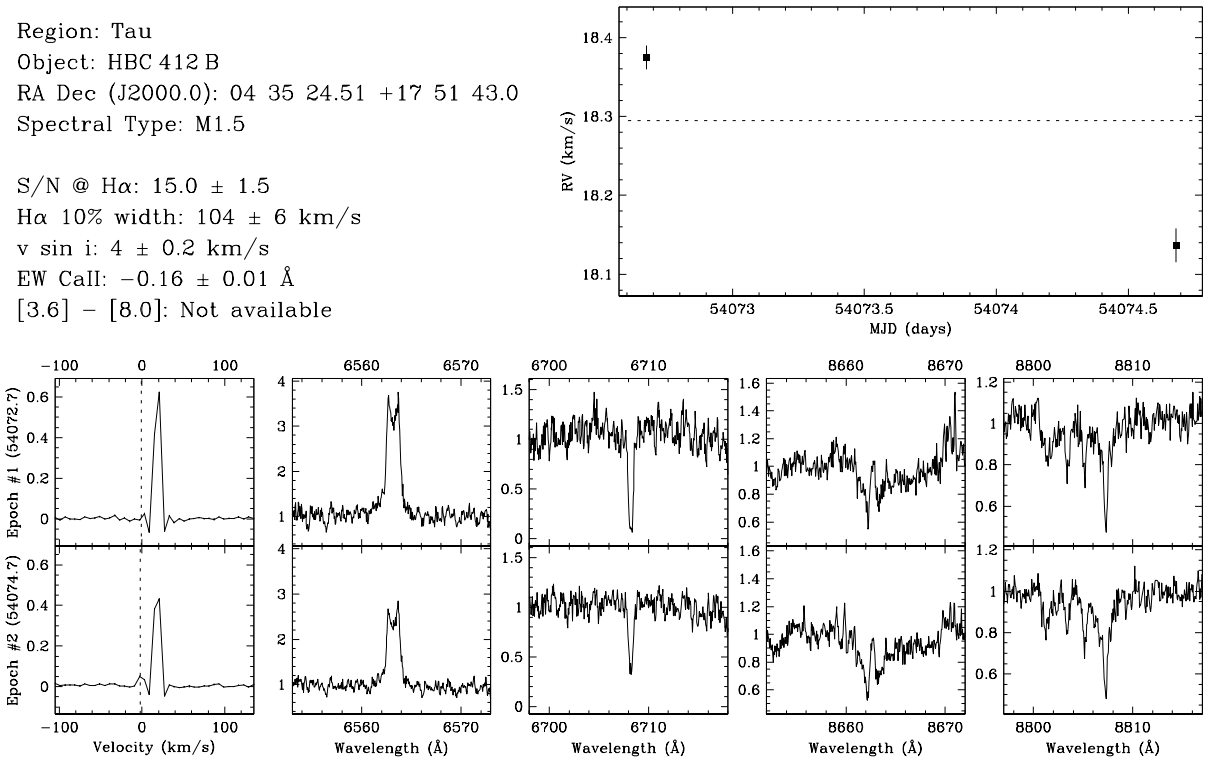

Figure 4.179 HBC 412 B has a single-line profile, and is therefore not an SB2. The radial velocity scatter over the short baseline available does not conclusively indicate if the target is an SB1 or a single star. For epoch #2, the small peak in the line profile at the observer's rest frame is due to moonlight, and may have biased the radial velocity estimate toward the observer's rest frame. This target has been previously reported by Leinert et al. (1993) to be the secondary star of a resolved binary (HBC 412 A+B) with a separation of $\sim 0\farcs7$ (~ 98 AU) at a position angle of $\sim 68°$, and an R-band flux ratio of ~ 1.00 ($\Delta K \sim 0.00$). However, there is no clear evidence in the line profile of the primary star. Since HBC 412 A has an expected circular orbital speed of $\sim 3\,\mathrm{km\,s^{-1}}$, and a similar $v \sin i$ ($\sim 5\,\mathrm{km\,s^{-1}}$), a second profile is likely obscured.

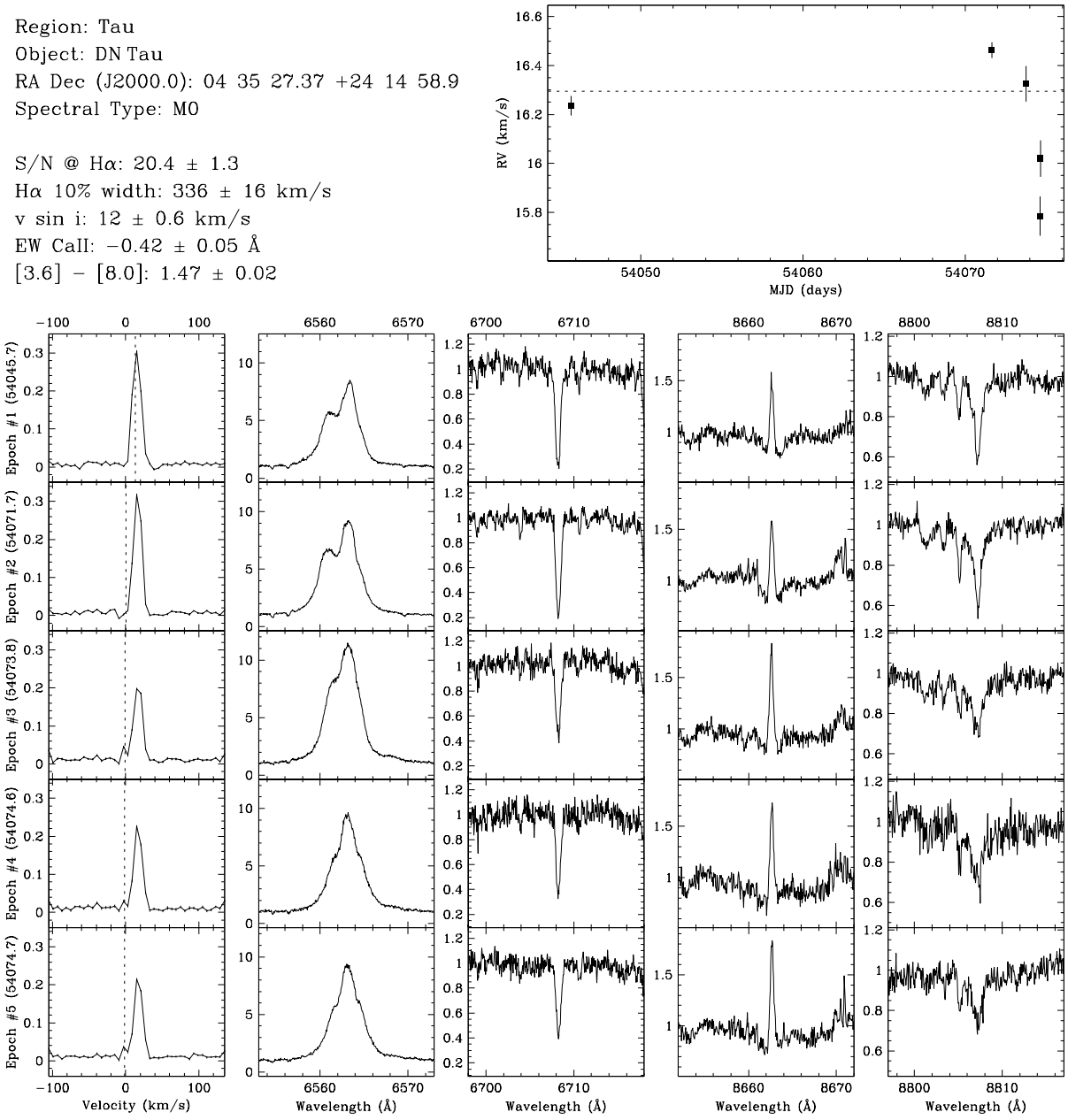

Figure 4.180 DN Tau shows no clear evidence of a close companion. The star has a single-line profile, and a radial velocity scatter not significant relative to variations observed within each observing run. The radial velocity scatter within the second observing run (epochs #2, #3, #4 and #5) is consistent with that expected from systematic line profile variations, e.g. from star spots rotating with the star. For epochs #3, #4 and #5, the small sharp peaks in the line profile at the observer's rest frame are due to moonlight, and may have biased the radial velocity estimates toward the observer's rest frame. This target has been previously reported by Leinert et al. (1993), and Simon et al. (1995) to have no resolved companions.

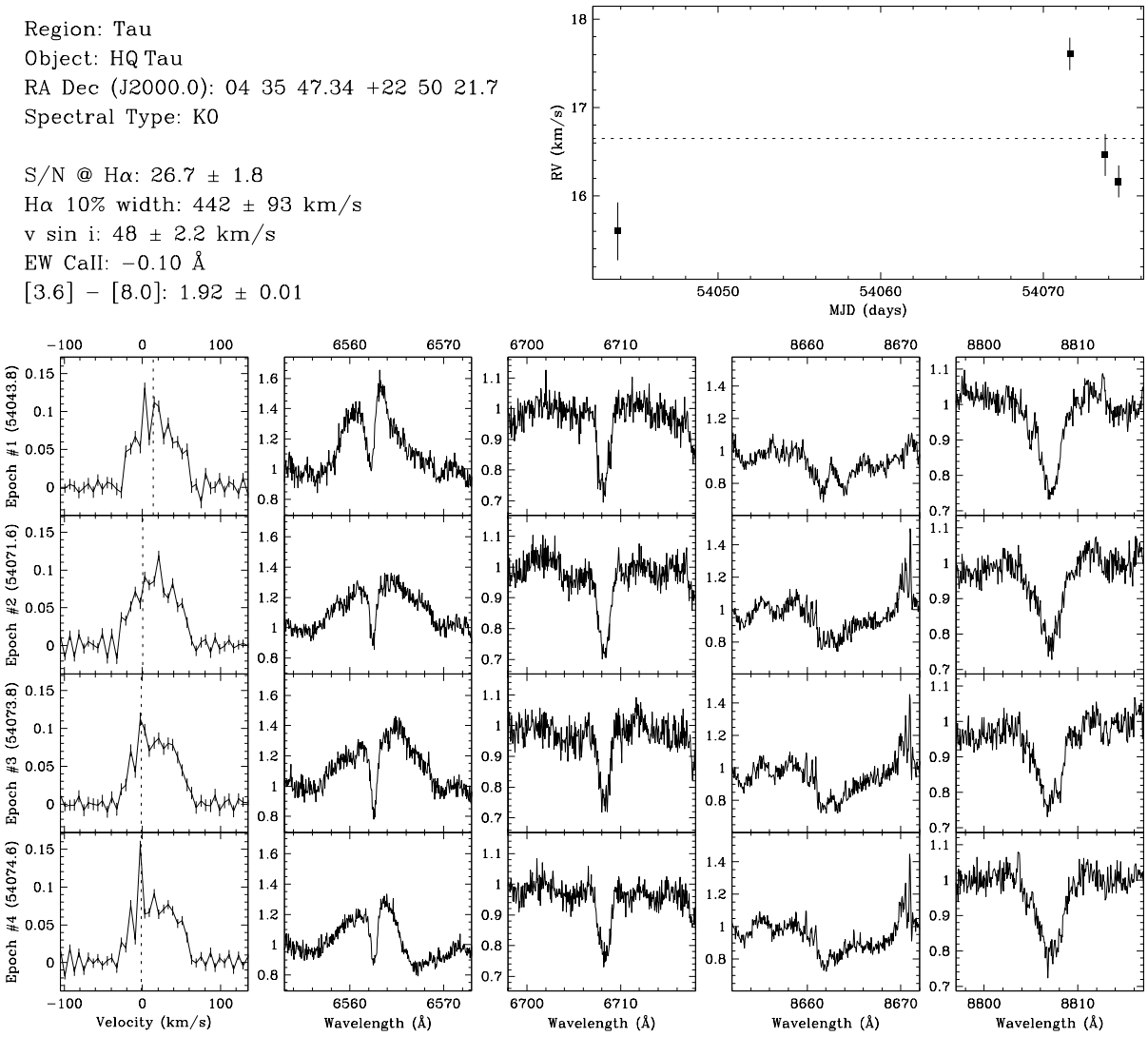

Figure 4.181 HQ Tau shows no clear evidence of a close companion. The star has a single-line profile, and a radial velocity scatter not significant relative to variations observed within each observing run. The radial velocity scatter within the second observing run (epochs #2, #3 and #4) is consistent with that expected from systematic line profile variations, e.g. from star spots rotating with the star. For epochs #3 and #4, the sharp peaks in the line profile at the observer's rest frame are due to moonlight, and likely biased the radial velocity estimates toward the observer's rest frame. This target has been previously reported by Simon et al. (1995) to have no resolved companions.

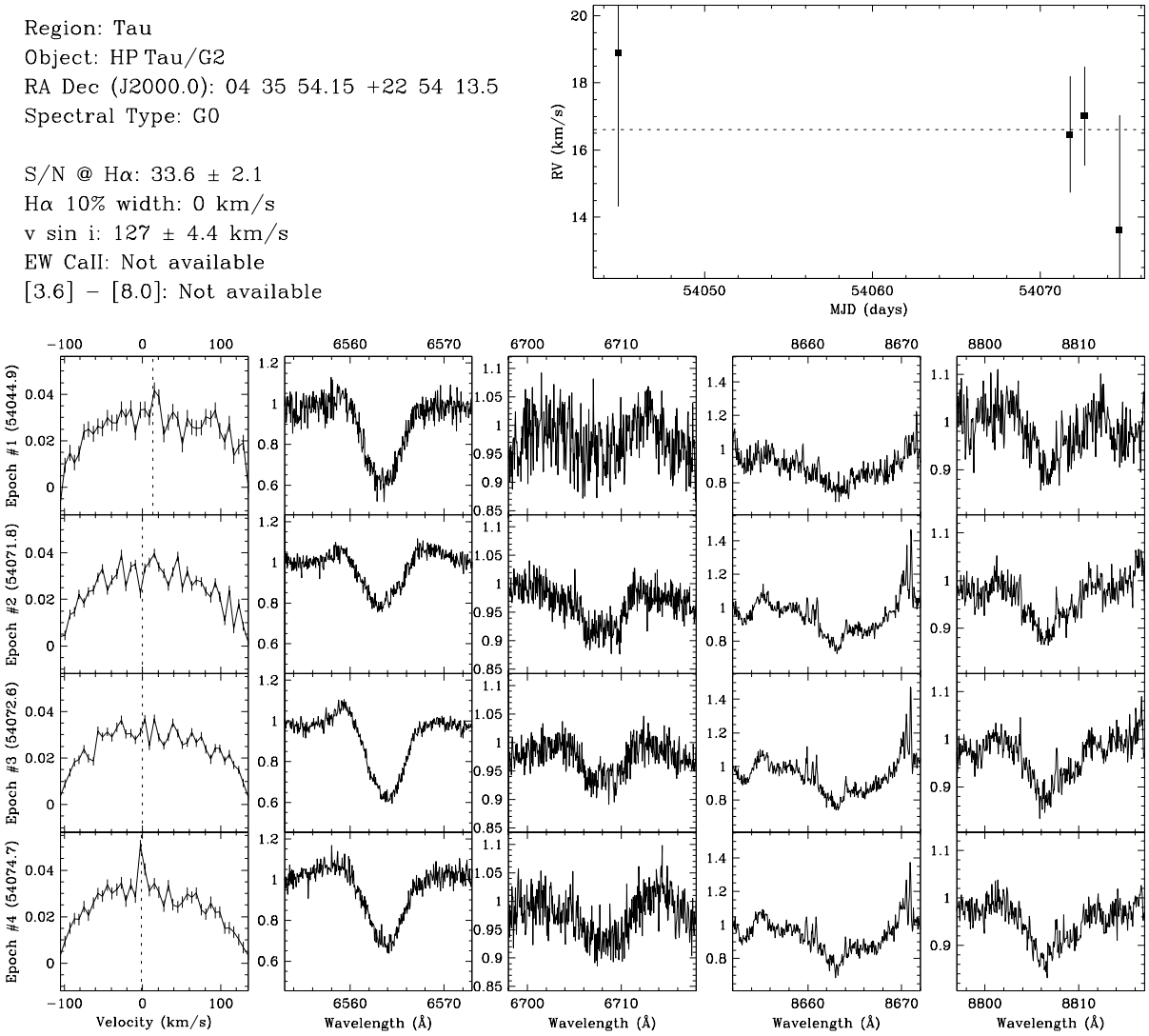

Figure 4.182 HP Tau/G2 shows no evidence of a close companion. The star has a single-line profile, and the radial velocity scatter is not significant relative to the measurement uncertainties. For epoch #4, the strong sharp peak in the line profile at the observer's rest frame is due to moonlight, and biased the radial velocity estimate toward the observer's rest frame. This target has been previously reported by Leinert et al. (1993), and Simon et al. (1995) to have a resolved companion with a separation of 9.″9–10.″ ($\sim$1400 AU) at a position angle of $\sim$243°, and an R-band flux ratio of $\sim$0.15 ($\Delta K \sim 1.55$). Given the separation, the expected contribution to the line profile from the resolved companion is negligible.

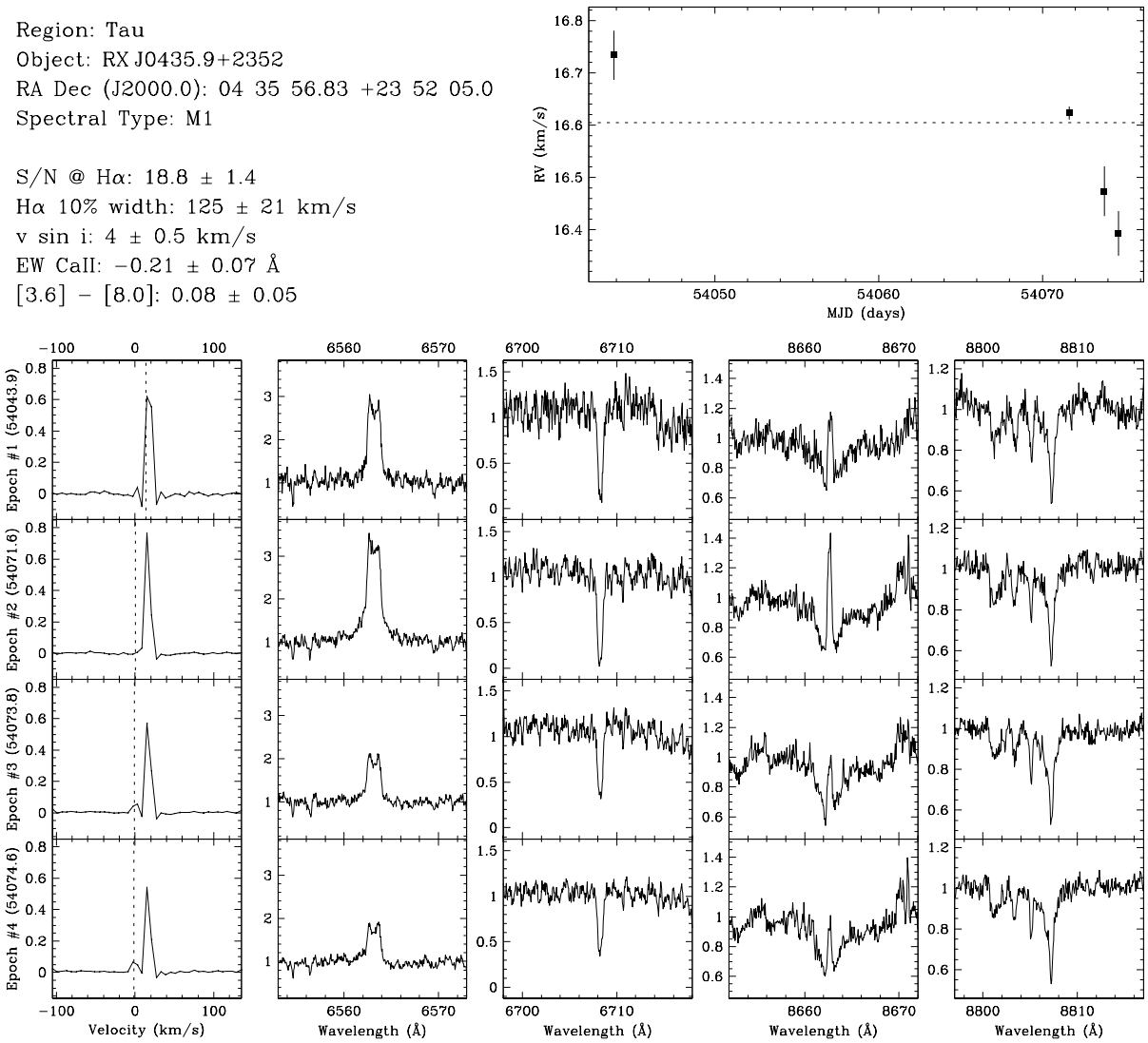

Figure 4.183 RX J0435.9+2352 shows no clear evidence of a close companion. The star has a single-line profile, and a radial velocity scatter not significant relative to variations observed within each observing run. The radial velocity scatter within the second observing run (epochs #2, #3 and #4) is consistent with that expected from systematic line profile variations, e.g. from star spots rotating with the star. For epochs #3 and #4, the small peaks in the line profile at the observer's rest frame are due to moonlight, and likely biased the radial velocity estimates toward the observer's rest frame. This target has been previously reported by Köhler & Leinert (1998) to have a resolved companion with a separation of $\sim 0\farcs069$ ($\sim$9.7 AU) at a position angle of $\sim 166\fdg8$, and an R-band flux ratio of $\sim$0.02 ($\Delta K \sim 1.28$). Given the flux ratio, the expected contribution to the line profile from the resolved companion is negligible.

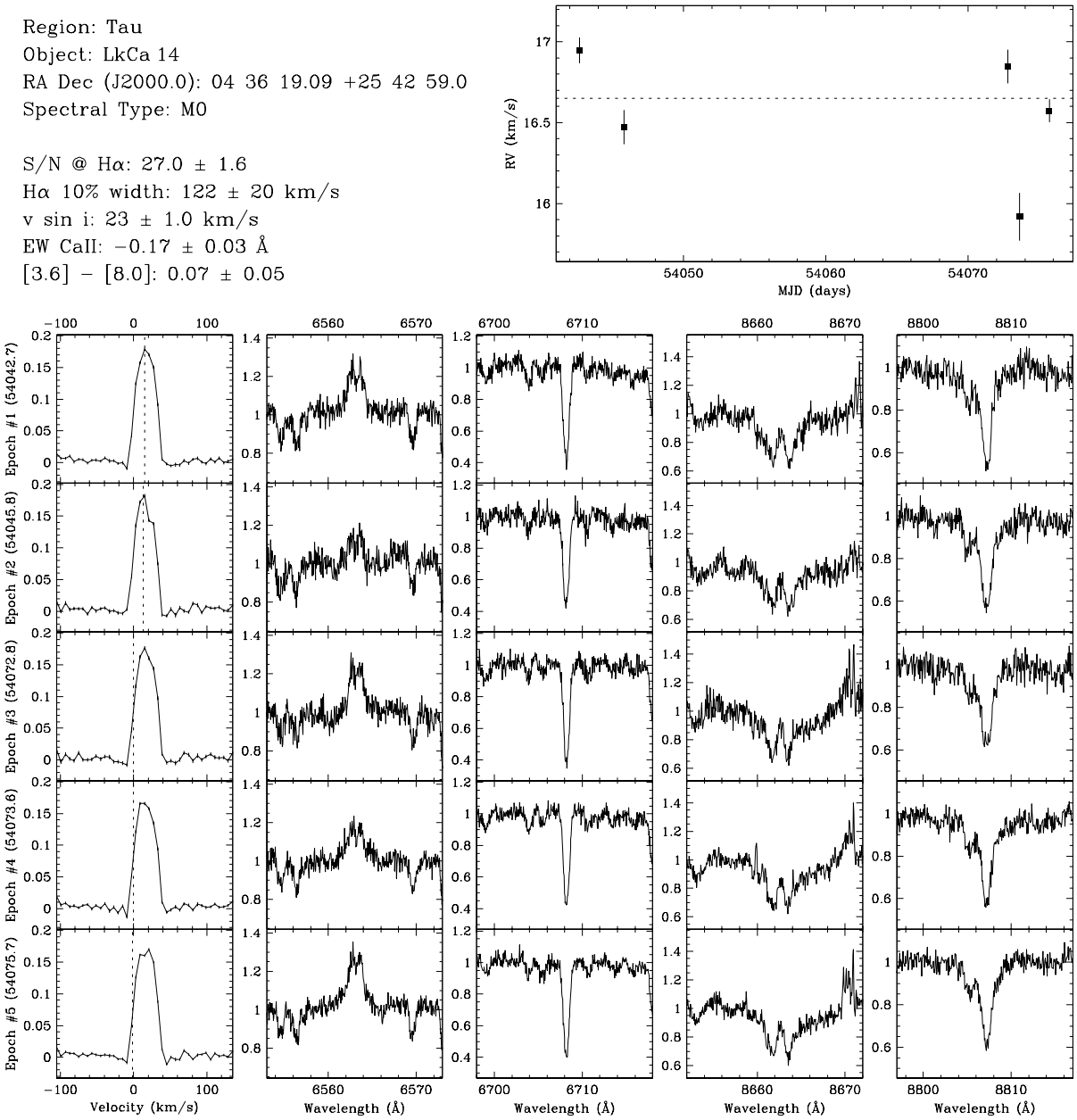

Figure 4.184 LkCa 14 shows no clear evidence of a close companion. The star has a single-line profile, and a radial velocity scatter not significant relative to variations observed within each observing run. The radial velocity scatter within each observing run is consistent with that expected from systematic line profile variations, e.g. from star spots rotating with the star. This target has been previously reported by Leinert et al. (1993) to have no resolved companions.

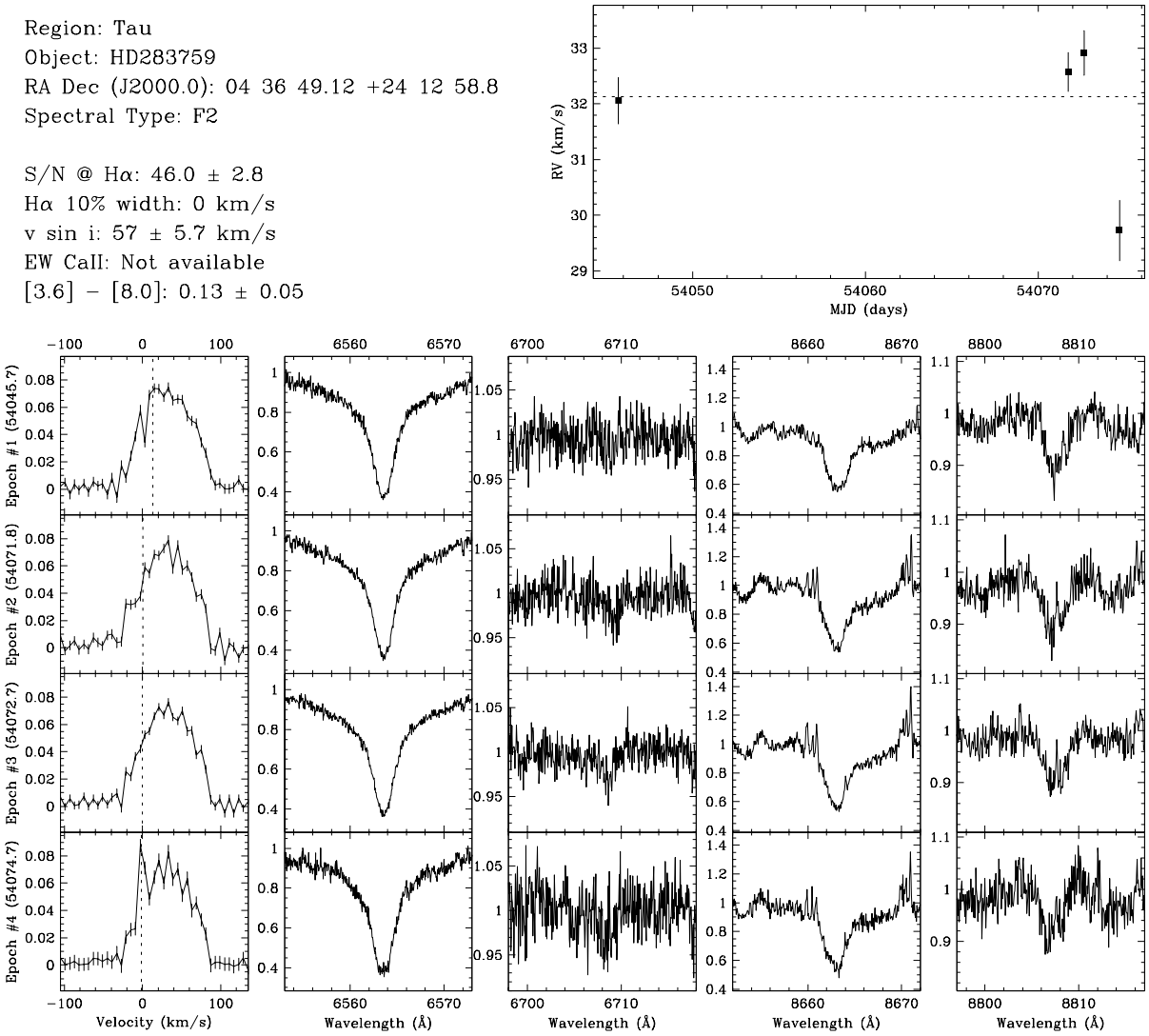

Figure 4.185 HD283759 shows no clear evidence of a close companion. The star has a single-line profile, and a radial velocity scatter not significant relative to variations observed within each observing run. The radial velocity scatter within the second observing run (epochs #2, #3 and #4) is consistent with that expected from systematic line profile variations, e.g. from star spots rotating with the star. The overall radial velocity deviates from that of the star forming region. However, cluster membership is supported by Li-λ6708 absorption. For epoch #4, the strong sharp peak in the line profile at the observer's rest frame is due to moonlight, and likely biased the radial velocity estimate toward the observer's rest frame. This target has been previously reported by Simon et al. (1995) to have no resolved companions.

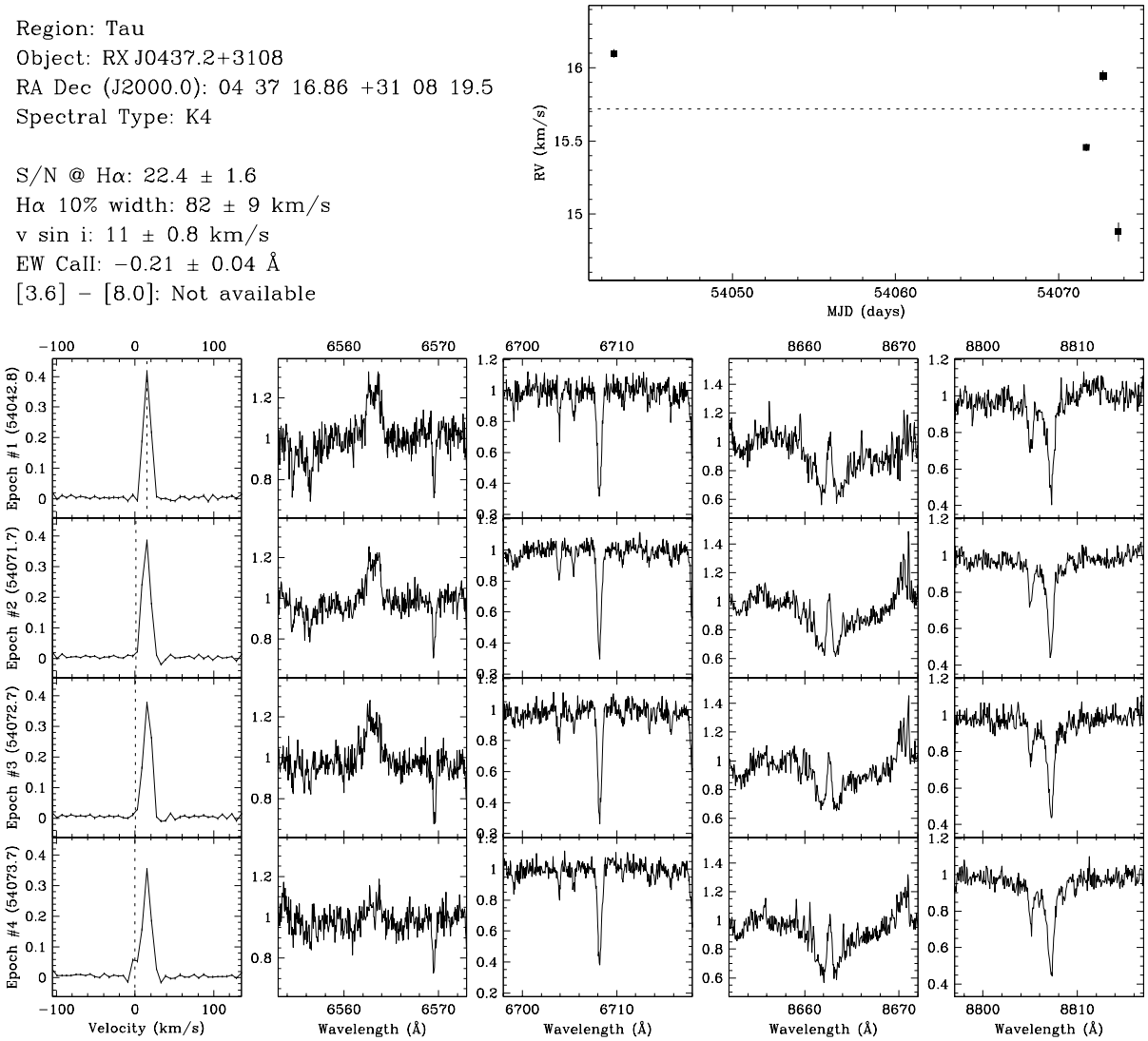

Figure 4.186 RX J0437.2+3108 shows no clear evidence of a close companion. The star has a single-line profile, and a radial velocity scatter not significant relative to variations observed within each observing run. The radial velocity scatter within the second observing run (epochs #2, #3 and #4) is consistent with that expected from systematic line profile variations, e.g. from star spots rotating with the star. For epochs #3 and #4, the small peaks in the line profile at the observer's rest frame are due to moonlight, and likely biased the radial velocity estimates toward the observer's rest frame. This target has been previously reported by Köhler & Leinert (1998) to have a resolved companion with a separation of $\sim 0\farcs109$ (~ 15 AU) at a position angle of $\sim 16\fdg3$, and an R-band flux ratio of ~ 0.15 ($\Delta K \sim 1.03$). However, there is no clear evidence in the line profile of the resolved companion. Since the resolved companion has an expected circular orbital speed of $\sim 9\,\mathrm{km\,s^{-1}}$, a second profile could be obscured for significant orbital fractions if the primary star and the resolved companion have similar projected rotational velocities.

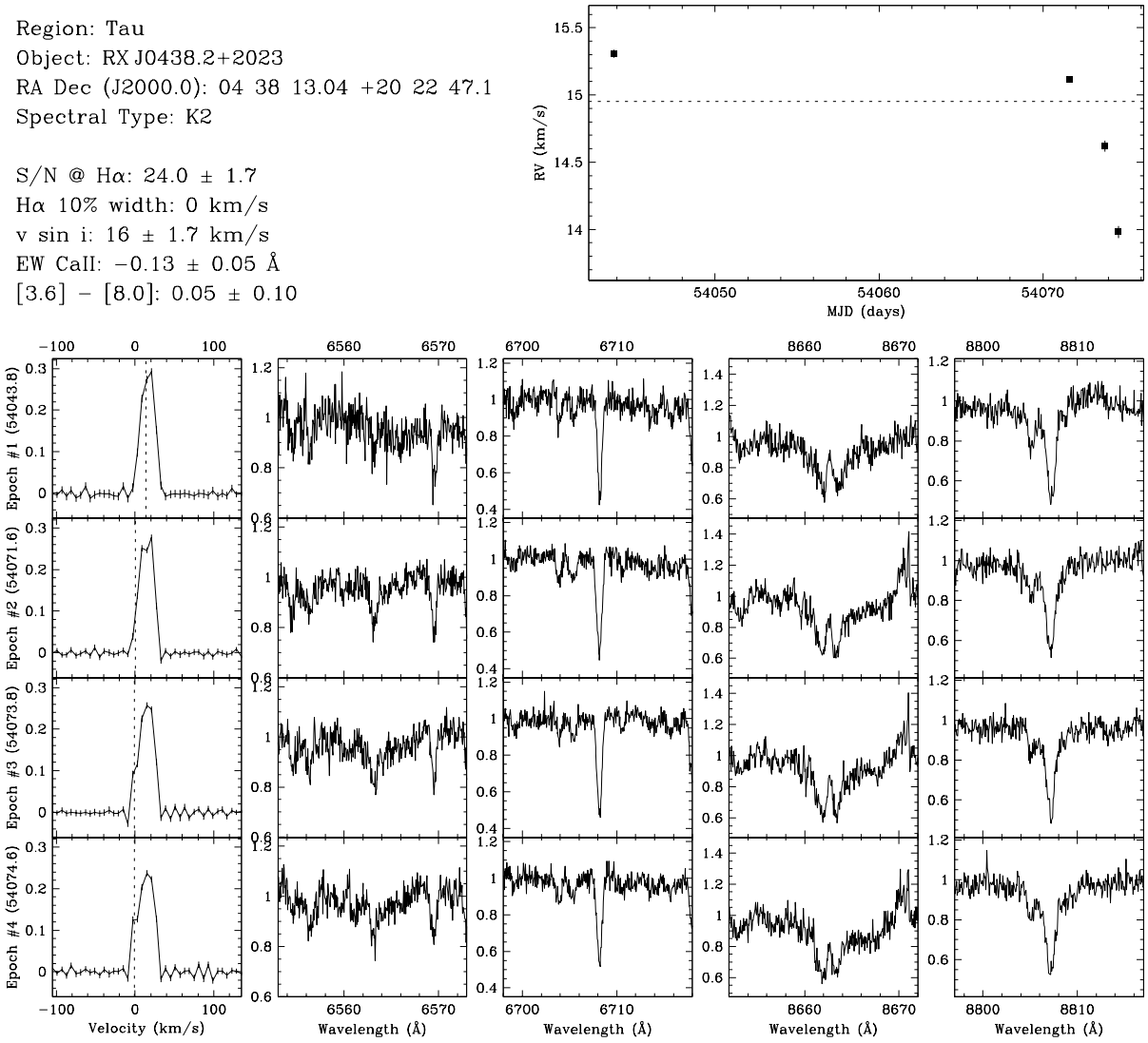

Figure 4.187 RX J0438.2+2023 shows no clear evidence of a close companion. The star has a single-line profile, and a radial velocity scatter not significant relative to variations observed within each observing run. The radial velocity scatter within the second observing run (epochs #2, #3 and #4) is consistent with that expected from systematic line profile variations, e.g. from star spots rotating with the star. For epochs #3 and #4, the bulges in the line profile at the observer's rest frame are due to moonlight, and likely biased the radial velocity estimates toward the observer's rest frame. This target has been previously reported by Köhler & Leinert (1998) to have a resolved companion with a separation of $\sim 0\farcs464$ (~ 65 AU) at a position angle of $\sim 352\fdg4$, and an R-band flux ratio of ~ 0.87 ($\Delta K \sim 0.10$). However, there is no clear evidence in the line profile of the resolved companion. Since the resolved companion has an expected circular orbital speed of $\sim 6\,\mathrm{km\,s^{-1}}$, a second profile could be obscured if the primary star and the resolved companion have similar projected rotational velocities.

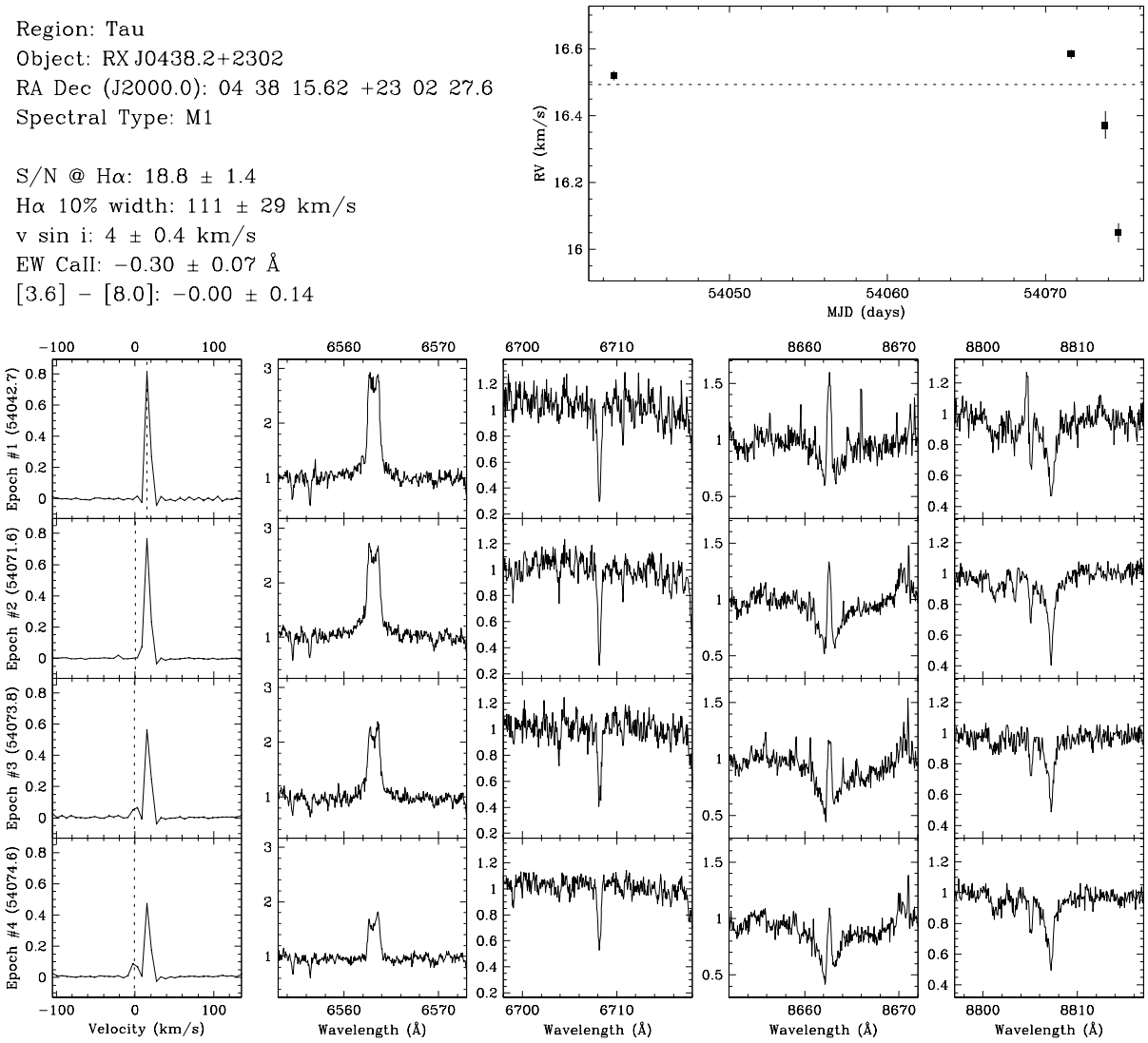

Figure 4.188 RX J0438.2+2302 shows no clear evidence of a close companion. The star has a single-line profile, and a radial velocity scatter not significant relative to variations observed within each observing run. The radial velocity scatter within the second observing run (epochs #2, #3 and #4) is consistent with that expected from systematic line profile variations, e.g. from star spots rotating with the star. For epochs #3 and #4, the small peaks in the line profile at the observer's rest frame are due to moonlight, and may have biased the radial velocity estimates toward the observer's rest frame. This target has been previously reported by Köhler & Leinert (1998) to have a resolved companion with a separation of $\sim 9\farcs19$ ($\sim$1300 AU) at a position angle of $\sim 93\fdg3$, and an R-band flux ratio of $\sim$0.01 ($\Delta K \sim 2.49$). Given the flux ratio and separation, the expected contribution to the line profile from the resolved companion is negligible.

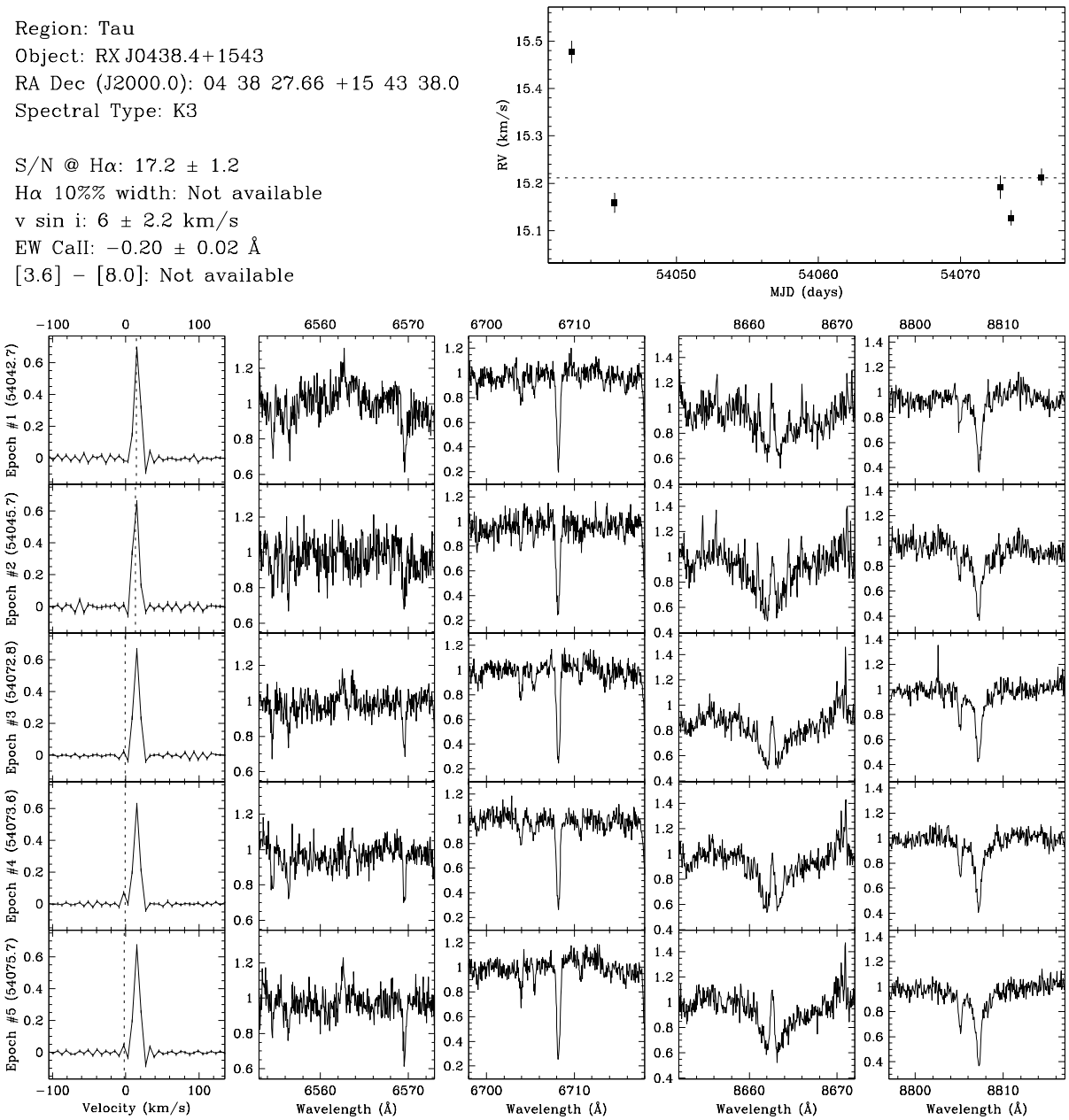

Figure 4.189 RX J0438.4+1543 shows no clear evidence of a close companion. The star has a single-line profile, and a radial velocity scatter not significant relative to variations observed within each observing run. The radial velocity scatter within each observing run is consistent with that expected from systematic line profile variations, e.g. from star spots rotating with the star. This target has been previously reported by Köhler & Leinert (1998) to have no resolved companions.

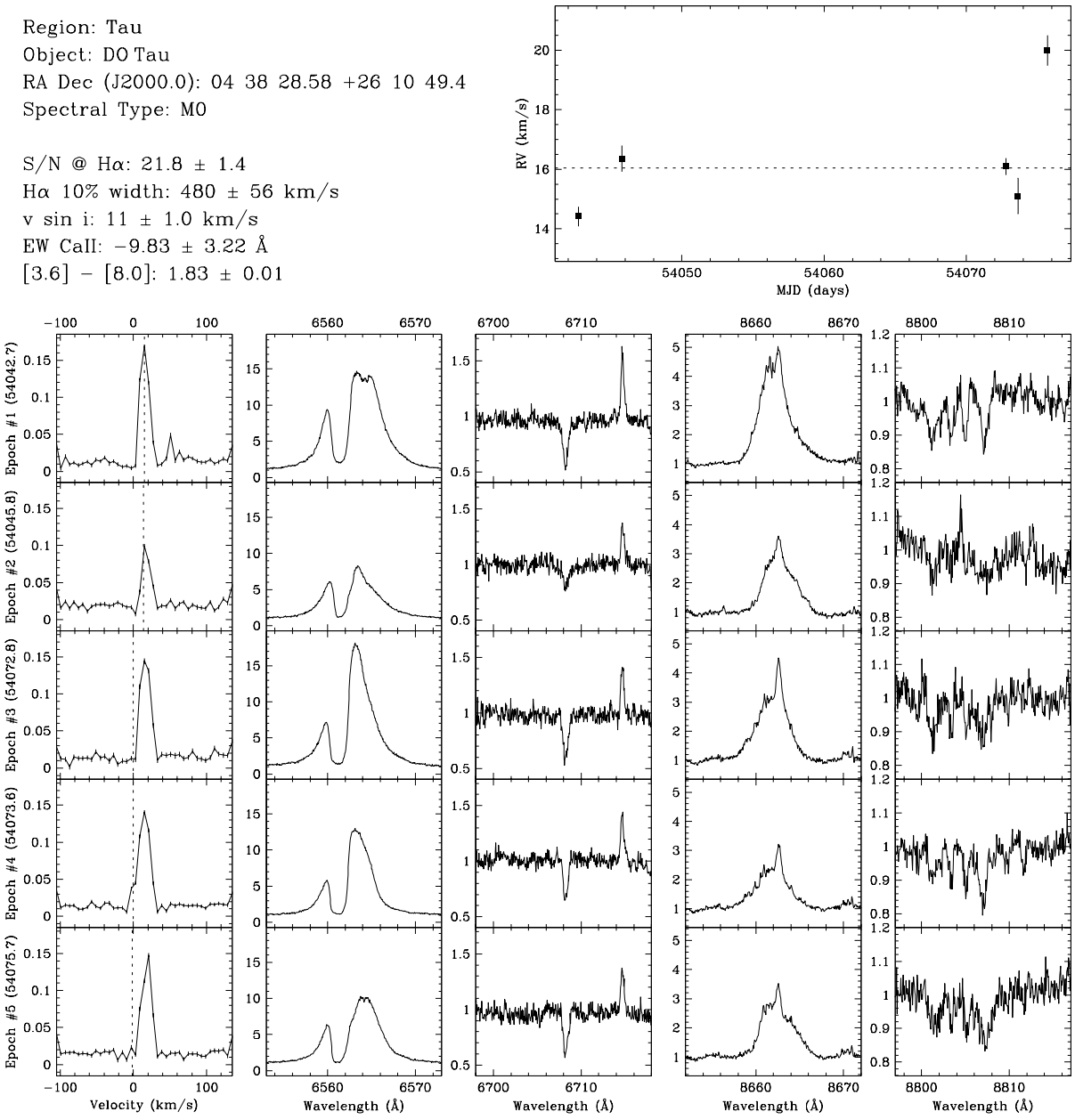

Figure 4.190 DO Tau shows no clear evidence of a close companion. The star has a single-line profile, and a radial velocity scatter not significant relative to variations observed within each observing run. The spectrum is heavily veiled, and we derived the radial velocities from fits to the line profile rather than from direct fits to the spectra (see §4.4.2). For epoch #4, the bulge in the line profile at the observer's rest frame is due to moonlight, and may have biased the radial velocity estimates toward the observer's rest frame. This target has been previously reported by Leinert et al. (1993), Ghez et al. (1993), and Simon et al. (1995) to have no resolved companions.

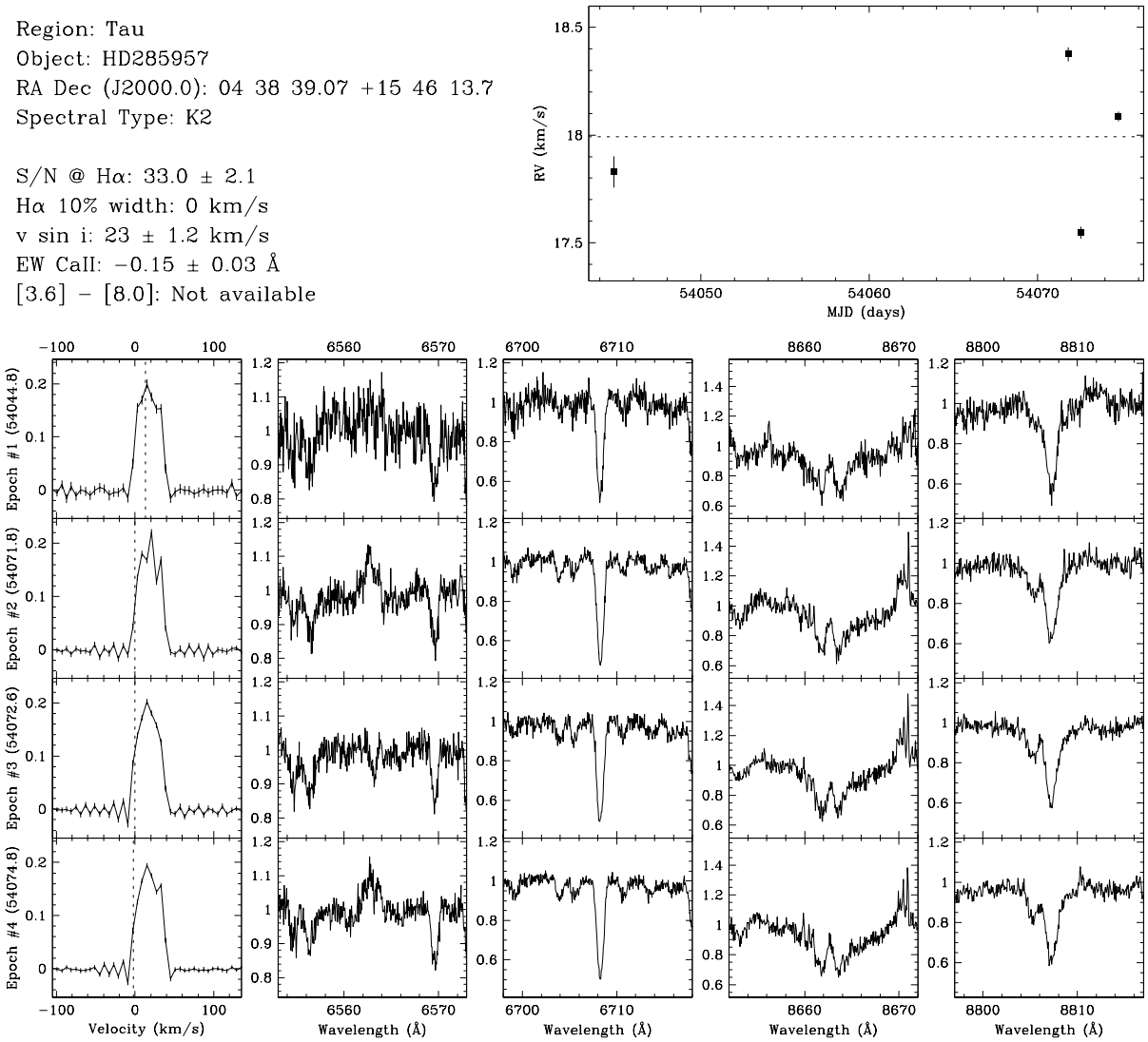

Figure 4.191 HD285957 shows no clear evidence of a close companion. The star has a single-line profile, and a radial velocity scatter not significant relative to variations observed within each observing run. The radial velocity scatter within the second observing run (epochs #2, #3 and #4) is consistent with that expected from systematic line profile variations, e.g. from star spots rotating with the star. This target has been previously reported by Köhler & Leinert (1998) to have a resolved companion with a separation of 9.″463–9.″504 ($\sim$1300 AU) at a position angle of 199°–200°, and an R-band flux ratio of 0.04–0.05 ($\Delta K \sim 1.74$–1.84). Given the flux ratio and separation, the expected contribution to the line profile from the resolved companion is negligible.

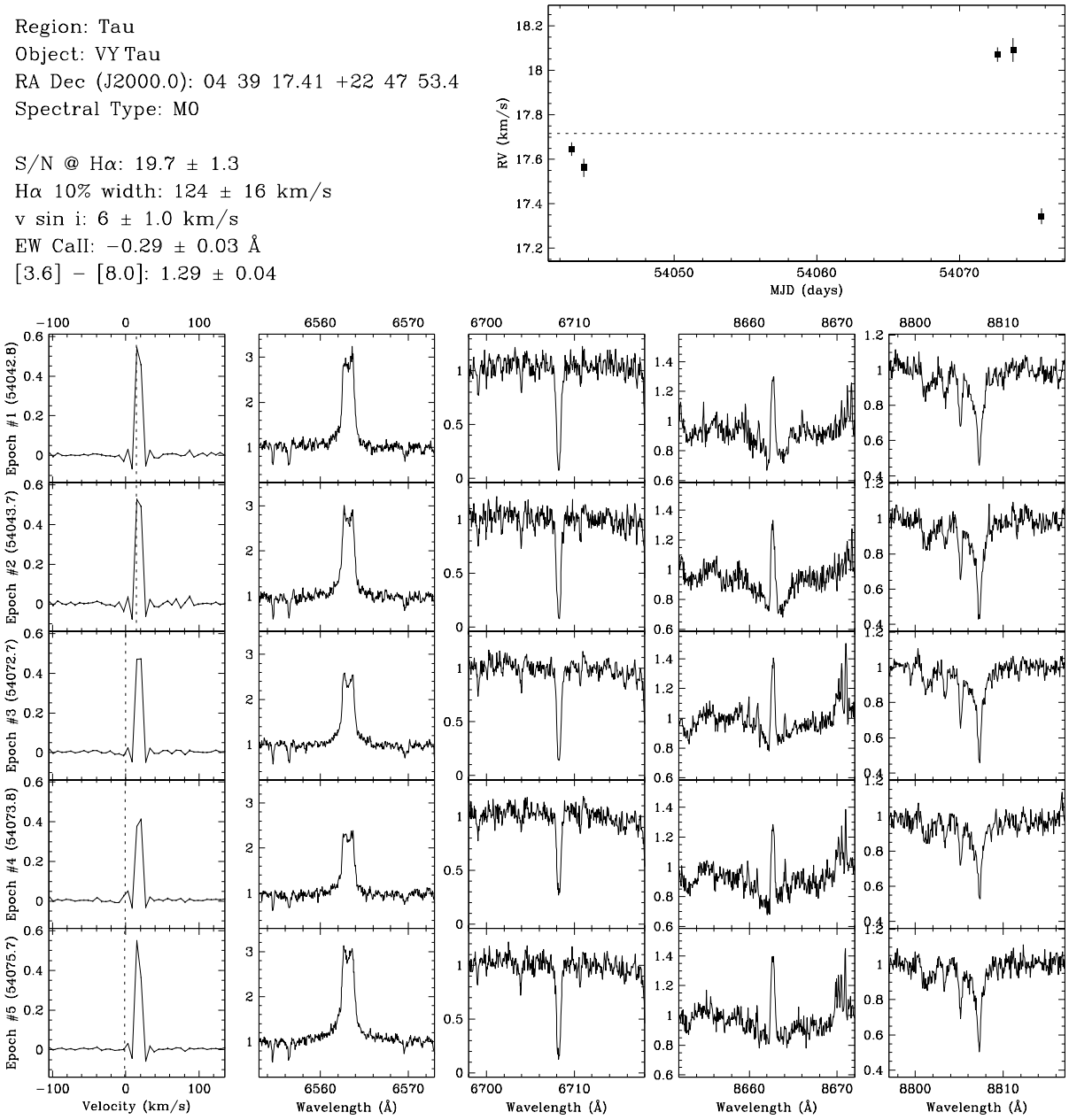

Figure 4.192 VY Tau shows no clear evidence of a close companion. The star has a single-line profile, and a radial velocity scatter not significant relative to variations observed within each observing run. The radial velocity scatter within each observing run is consistent with that expected from systematic line profile variations, e.g. from star spots rotating with the star. For epoch #4, the small peak in the line profile at the observer's rest frame is due to moonlight, and may have biased the radial velocity estimate toward the observer's rest frame. This target has been previously reported by Leinert et al. (1993), and Simon et al. (1995) to have a resolved companion with a separation of $\sim$0.″66 ($\sim$92 AU) at a position angle of $\sim$317°, and an R-band flux ratio of 0.01–0.02 ($\Delta K \sim$1.46–1.50). Given the flux ratio, the expected contribution to the line profile from the resolved companion is negligible.

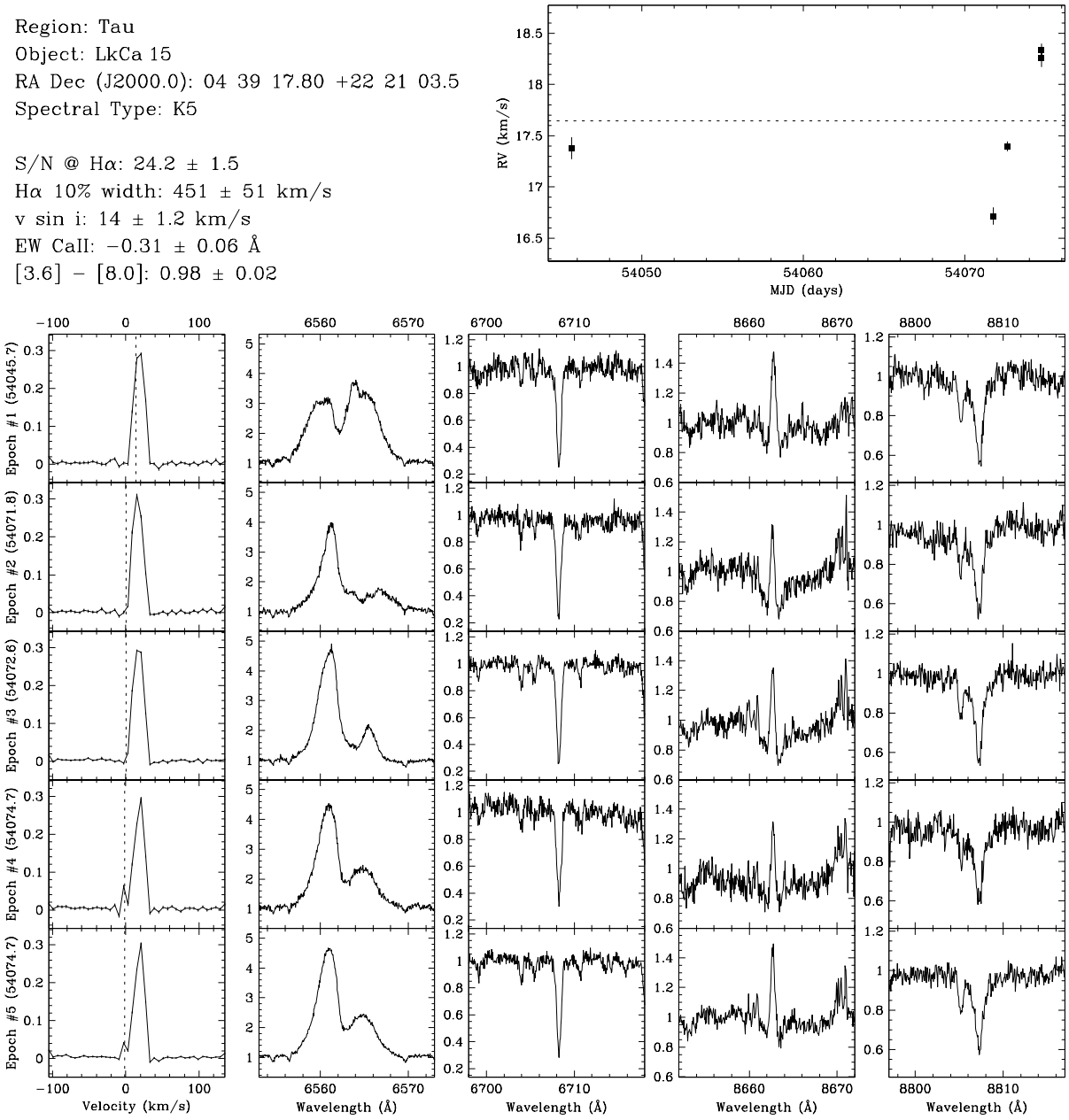

Figure 4.193 LkCa 15 shows no clear evidence of a close companion. The star has a single-line profile, and a radial velocity scatter not significant relative to variations observed within each observing run. The Hα profile changes significantly between epochs, and perhaps, implies the presence of non-companion influence, e.g. star spots. The radial velocity scatter within the second observing run (epochs #2, #3, #4 and #5) is large but consistent with that expected from systematic line profile variations, e.g. from star spots rotating with the star. For epoch #4 and #5, the sharp peaks in the line profile at the observer's rest frame are due to moonlight, and may have biased the radial velocity estimates toward the observer's rest frame. This target has been previously reported by Leinert et al. (1993) to have no resolved companions.

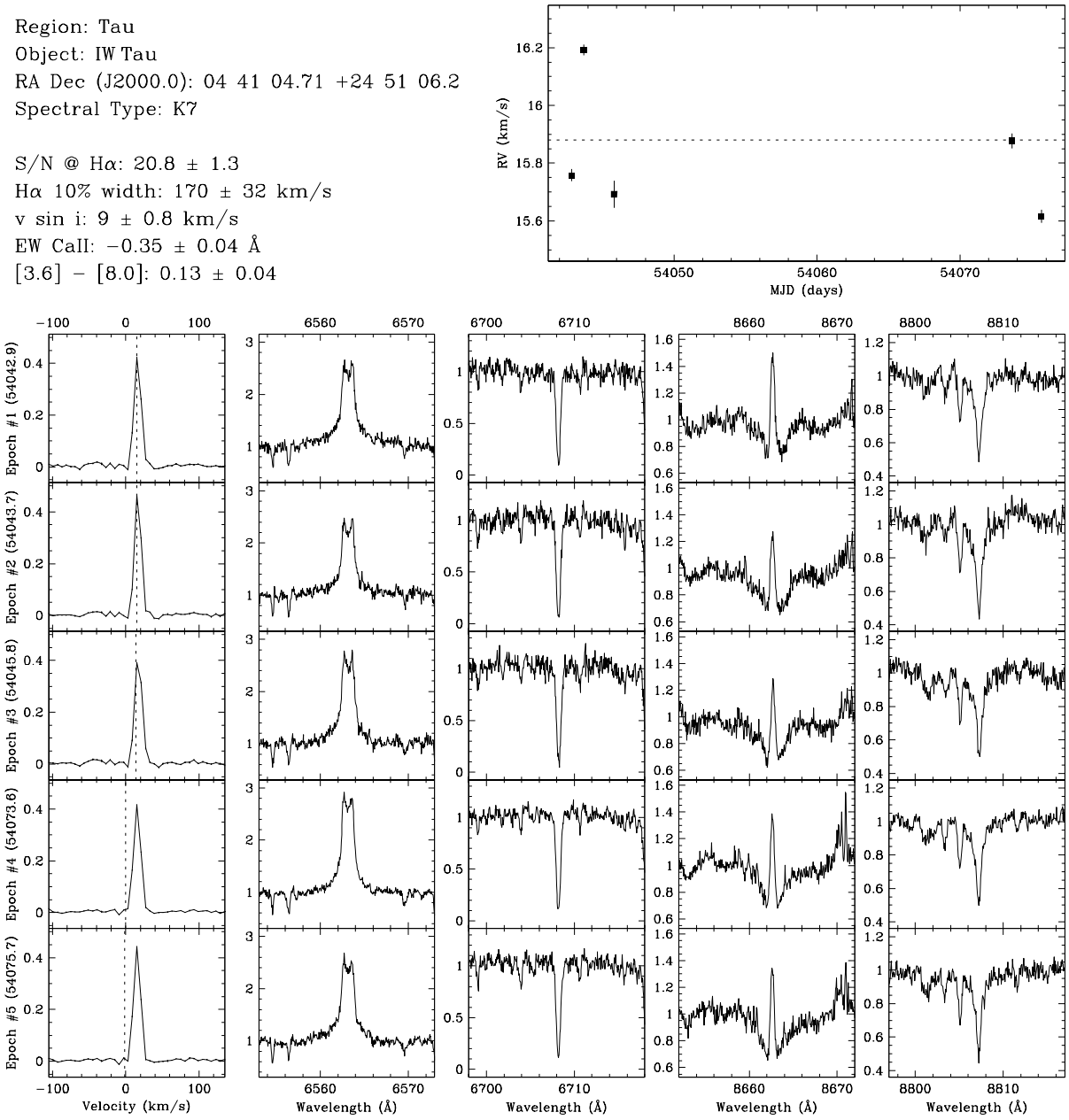

Figure 4.194 IW Tau shows no clear evidence of a close companion. The star has a single-line profile, and a radial velocity scatter not significant relative to variations observed within each observing run. The radial velocity scatter within each observing run is consistent with that expected from systematic line profile variations, e.g. from star spots rotating with the star. This target has been previously reported by Leinert et al. (1993), and Simon et al. (1995) to have a resolved companion with a separation of $\sim 0\farcs27$ (~ 38 AU) at a position angle of $\sim 177°$, and an R-band flux ratio of 0.66–1.00 ($\Delta K \sim 0.00$–0.10). However, there is no clear evidence in the line profile of the resolved companion. Since the resolved companion has an expected circular orbital speed of $\sim 5\,\mathrm{km\,s^{-1}}$, a second profile could be obscured if the primary star and the resolved companion have similar projected rotational velocities.

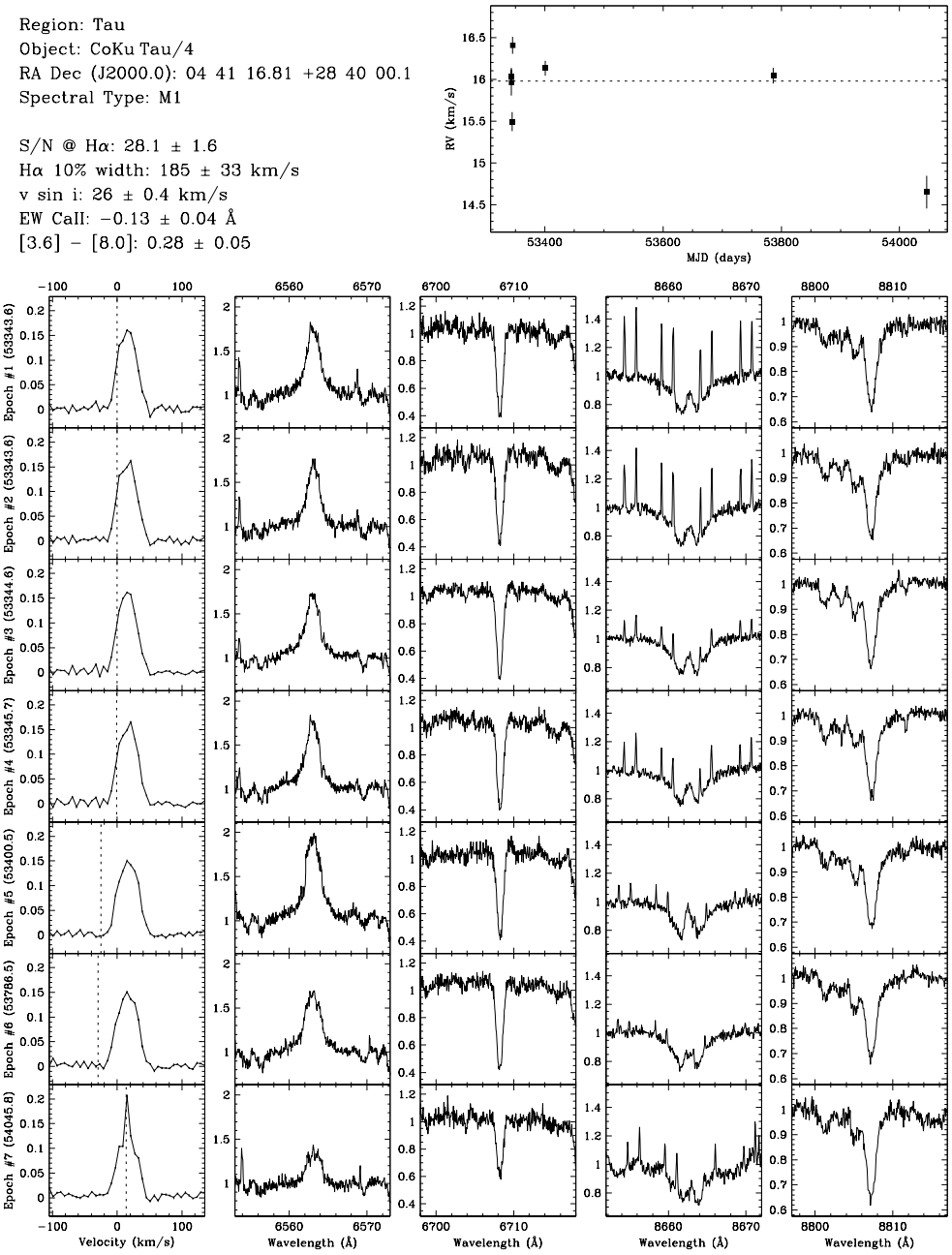

Figure 4.195 CoKu Tau/4 shows no clear evidence of a close companion. The star has a single-line profile, and a radial velocity scatter not significant relative to variations observed within each observing run. The radial velocity scatter within the first observing run (epochs #1, #2, #3 and #4) is consistent with that expected from systematic line profile variations, e.g. from star spots rotating with the star. For epoch #7, the strong sharp peak in the line profile at the observer's rest frame is due to moonlight, and likely biased the radial velocity estimate toward the observer's rest frame. The narrow emission lines in the spectra near 8662 Å are from the night sky. This target has been previously reported by Ireland & Kraus (2008) to have a resolved companion with a separation of $\sim 0\farcs0536$ (~ 7.5 AU) at a position angle of $\sim 306\fdg0$, and an R-band flux ratio of ~ 0.73 ($\Delta K \sim 0.20$). However, there is no clear evidence in the line profile of the resolved companion. Since the resolved companion has an expected circular orbital speed of $\sim 10\,\mathrm{km\,s^{-1}}$, a second profile could be obscured if the primary star and the resolved companion have similar projected rotational velocities.

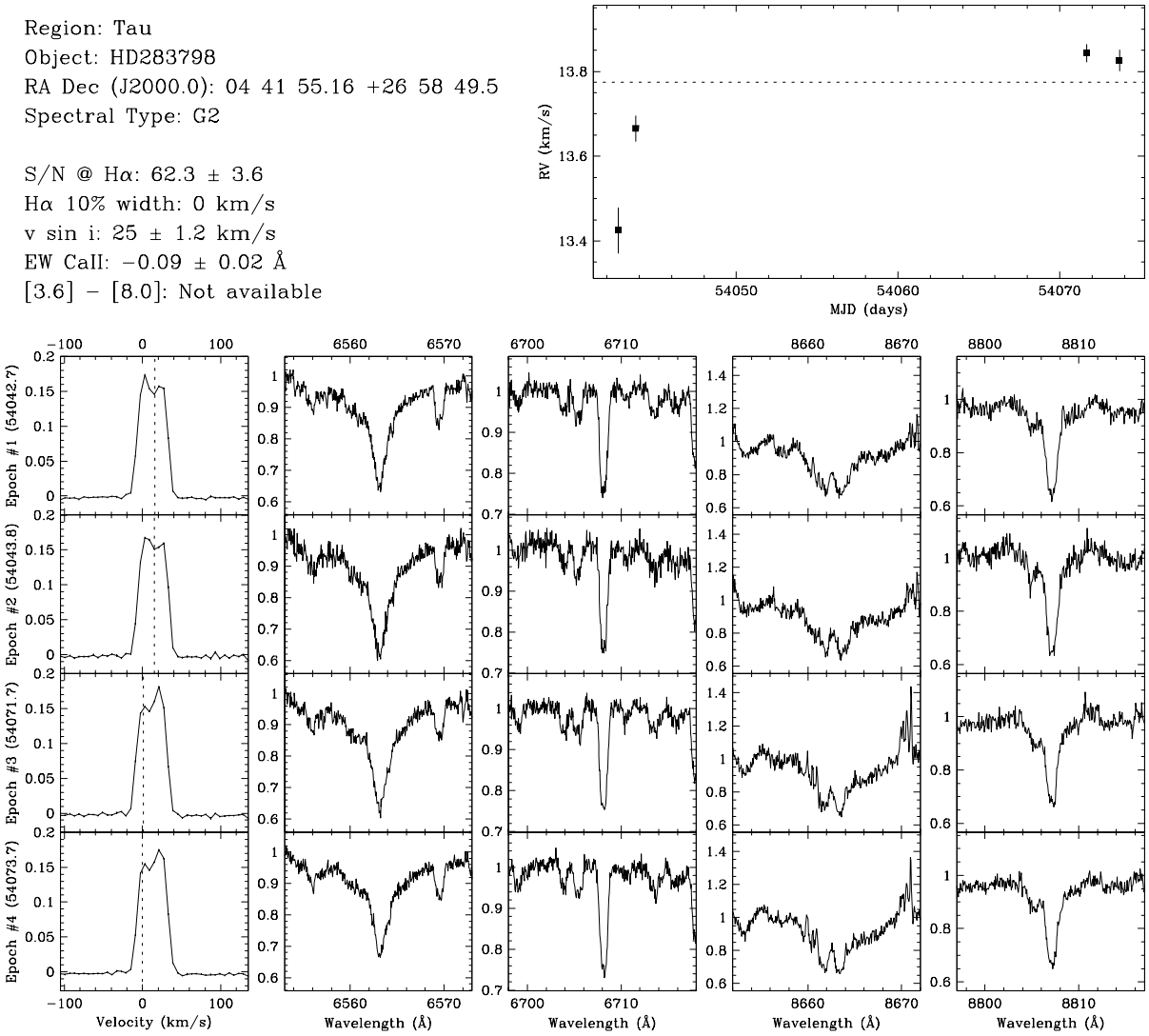

Figure 4.196 HD283798 shows no clear evidence of a close companion. The star has a single-line profile, and a radial velocity scatter not significant relative to variations observed within each observing run. The line profiles show significant deviation from the shape expected from pure rotational broadening. To see if these irregularities are from close companions, we fitted multiple broadening functions to the line profiles. The resultant radial velocities were not consistent with those expected from close companions: the radial velocity separations were $\sim 20\,\mathrm{km\,s^{-1}}$ with no acceleration. Therefore, we suspect the variations in the line profile are the result of star spots. The radial velocity scatter within each observing run is consistent with that expected from systematic line profile variations, e.g. from star spots rotating with the star. This target has been previously reported by Köhler & Leinert (1998) to have a resolved companion with a separation of $\sim 1\farcs631$ ($\sim 230\,\mathrm{AU}$) at a position angle of $\sim 303\fdg1$, and an R-band flux ratio of ~ 0.01 ($\Delta K \sim 3.42$). Given the flux ratio and separation, the expected contribution to the line profile from the resolved companion is negligible.

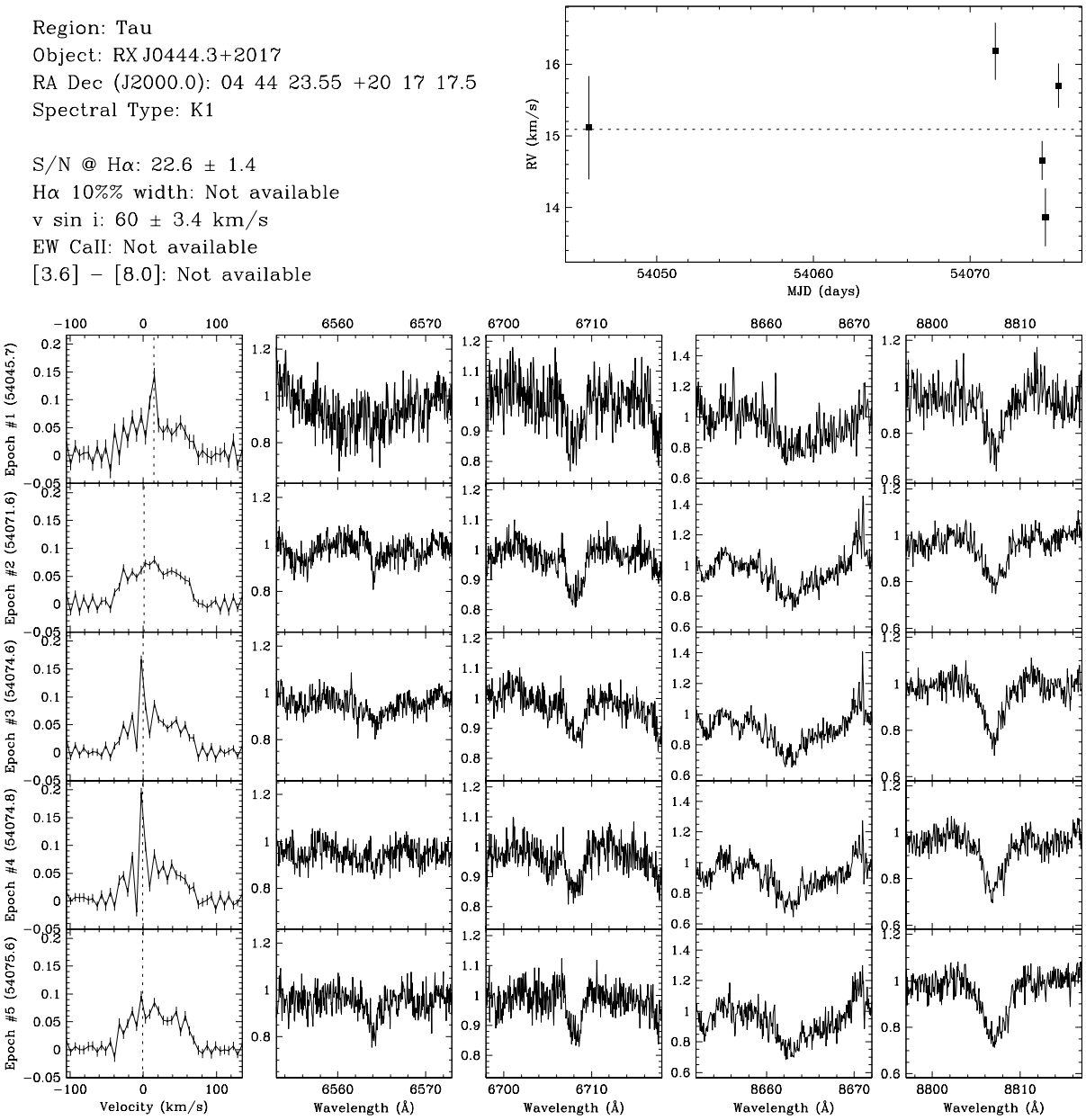

Figure 4.197 RX J0444.3+2017 shows no clear evidence of a close companion. The star has a single-line profile, and a radial velocity scatter not significant relative to variations observed within each observing run. The radial velocity scatter within the second observing run (epochs #2, #3, #4 and #5) is consistent with that expected from systematic line profile variations, e.g. from star spots rotating with the star. For epoch #1, #3 and #4, the sharp peaks in the line profile at the observer's rest frame are due to moonlight, and may have biased the radial velocity estimates toward the observer's rest frame. This target has been previously reported by Köhler & Leinert (1998) to have a resolved companion with a separation of $\sim 9\farcs868$ (~ 1400 AU) at a position angle of $\sim 159\fdg7$, and an R-band flux ratio of ~ 0.01 ($\Delta K \sim 2.45$). Given the flux ratio and separation, the expected contribution to the line profile from the resolved companion is negligible.

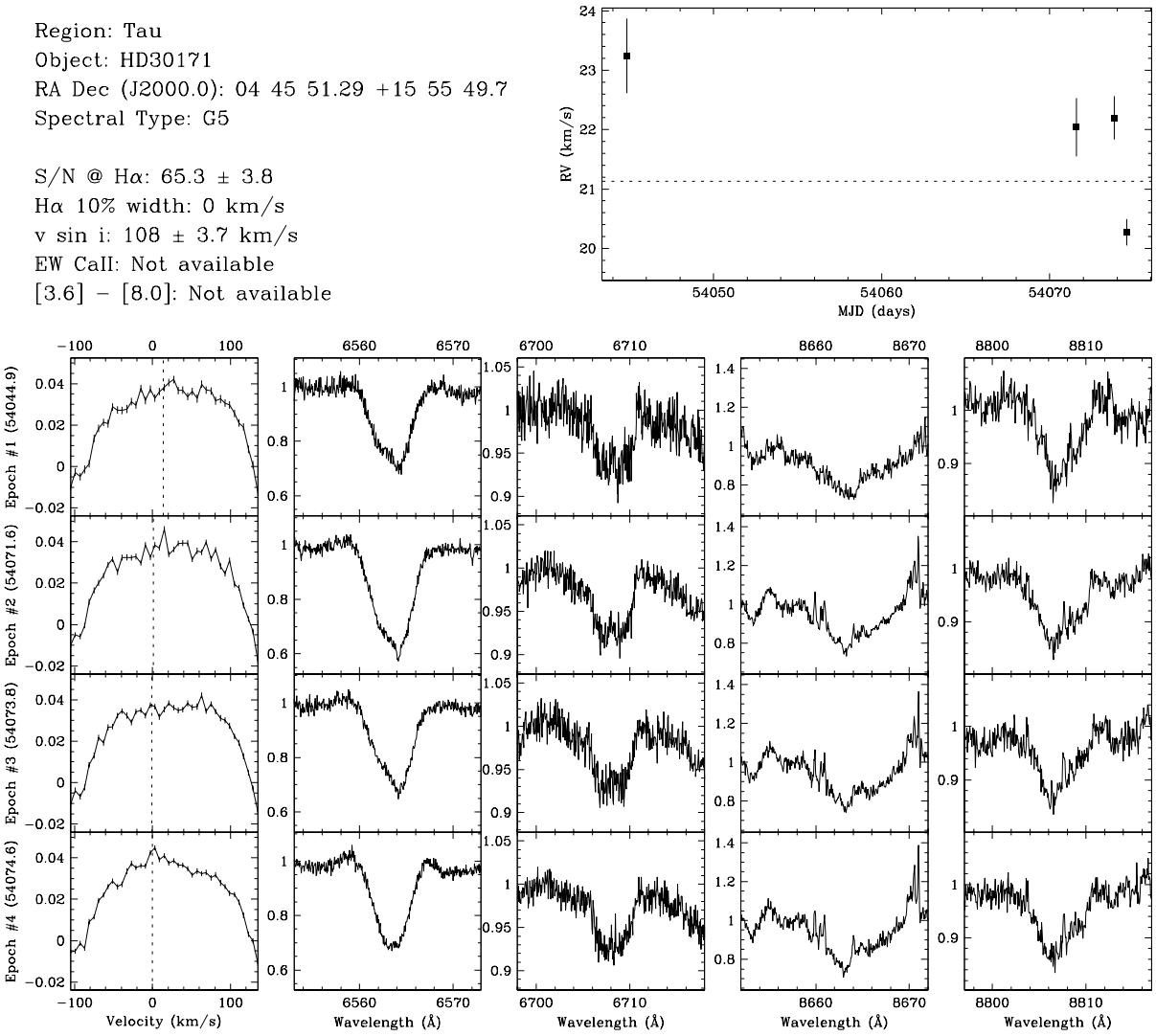

Figure 4.198 HD30171 shows no clear evidence of a close companion. The star has a single-line profile, and a radial velocity scatter not significant relative to variations observed within each observing run. The radial velocity scatter within the second observing run (epochs #2, #3 and #4) is consistent with that expected from systematic line profile variations, e.g. from star spots rotating with the star. This target has been previously reported by Köhler & Leinert (1998) to have a resolved companion with a separation of $\sim 12\farcs926$ (~ 1800 AU) at a position angle of $\sim 175\fdg8$, and an R-band flux ratio of ~ 0.14 ($\Delta K \sim 1.71$). Given the separation, the expected contribution to the line profile from the resolved companion is negligible.

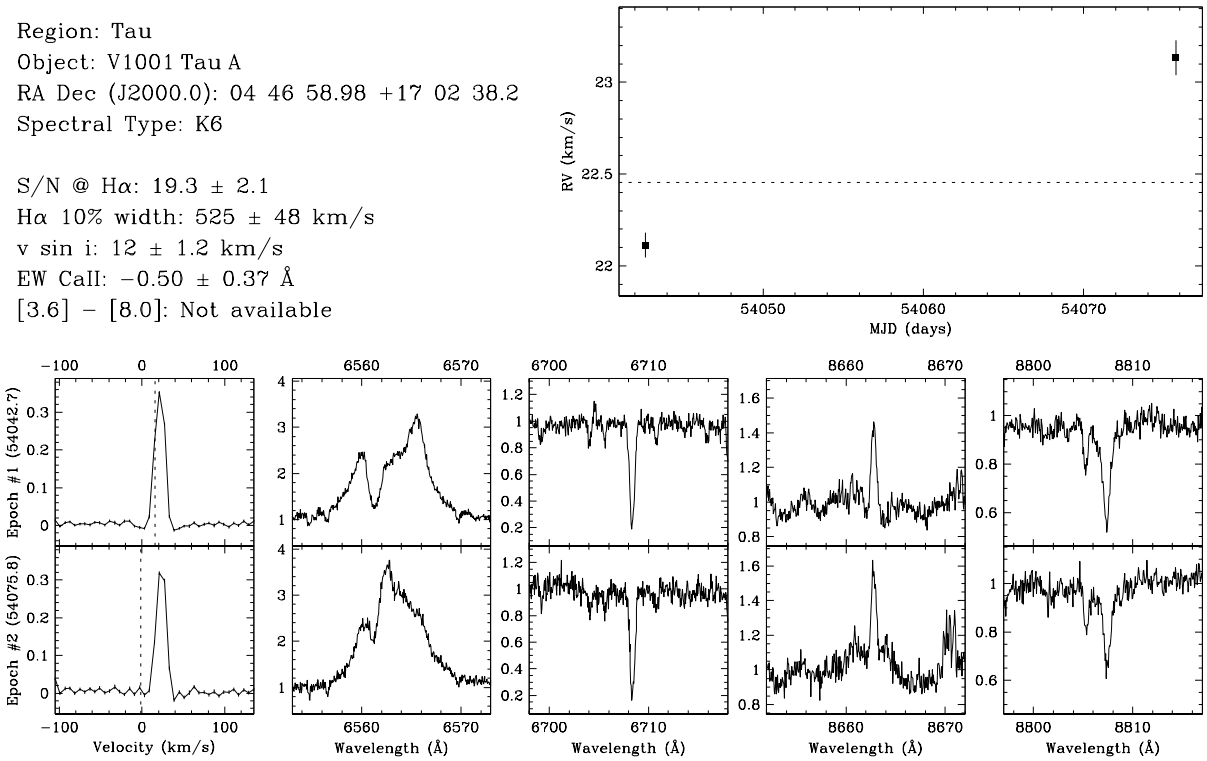

Figure 4.199 V1001 Tau A shows no clear evidence of a close companion. The Hα profile changes significantly between epochs, and perhaps, implies radial velocity influence from non-companion sources, e.g. star spots. The overall radial velocity deviates from that of the star forming region. However, cluster membership is supported by Li-λ6708 absorption. This target has been previously reported by Leinert et al. (1993) to have a resolved companion (V1001 Tau B) with a separation of $\sim 2\farcs7$ (~ 380 AU) at a position angle of $\sim 37°$, and an R-band flux ratio of ~ 0.17 ($\Delta K \sim 0.87$). Given the separation, the expected contribution to the line profile from the resolved companion is negligible.

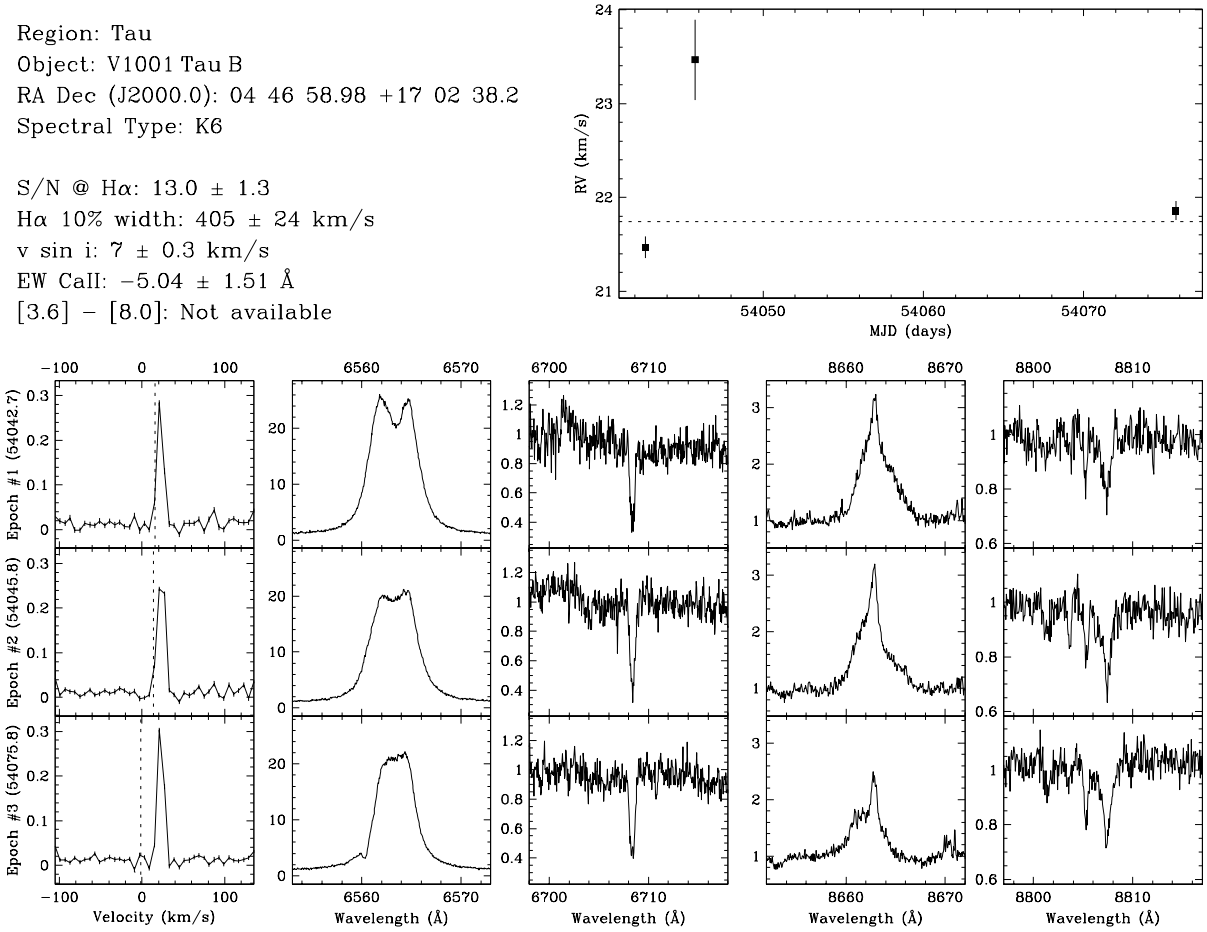

Figure 4.200 V1001 Tau B shows no clear evidence of a close companion. The star has a single-line profile, and a radial velocity scatter not significant relative to variations observed within each observing run. The spectrum is heavily veiled, and we derived the radial velocities from fits to the line profile rather than from direct fits to the spectra (see §4.4.2). This target has been previously reported by Leinert et al. (1993) to be the secondary star of a resolved binary (V1001 Tau A+B) with a separation of $\sim$2.″7 ($\sim$380 AU) at a position angle of $\sim$37°, and an R-band flux ratio of $\sim$0.17 ($\Delta K \sim 0.87$). Given the separation, the expected contribution to the line profile from the resolved companion is negligible.

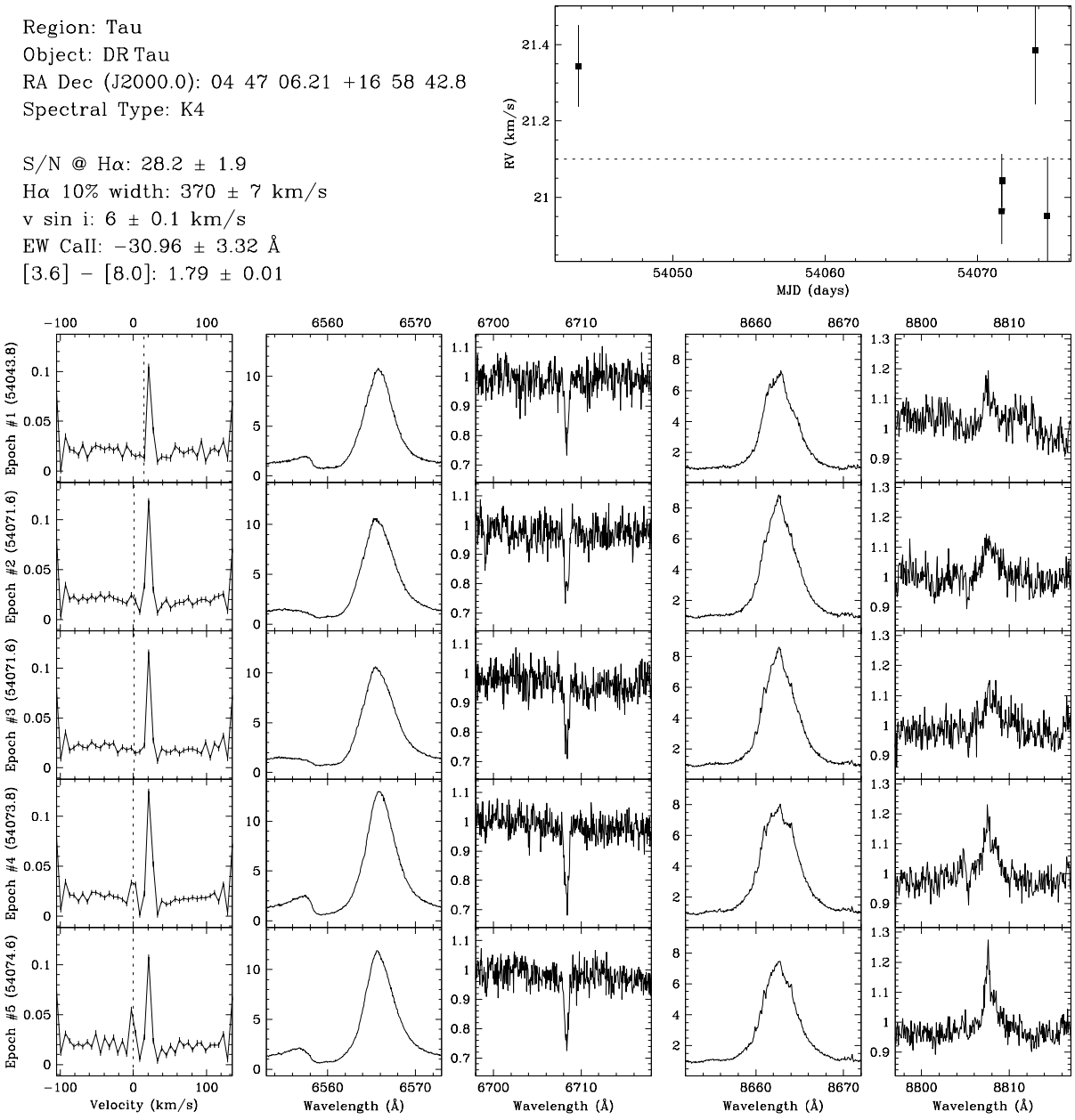

Figure 4.201 DR Tau shows no evidence of a close companion. The star has a single-line profile, and the radial velocity scatter is not significant relative to the measurement uncertainties. The spectrum is heavily veiled, and we derived the radial velocities from fits to the line profile rather than from direct fits to the spectra (see §4.4.2). For epochs #4 and #5, the small sharp peaks in the line profile at the observer's rest frame are due to moonlight, and may have biased the radial velocity estimates toward the observer's rest frame. This target has been previously reported by Leinert et al. (1993), and Ghez et al. (1993) to have no resolved companions.

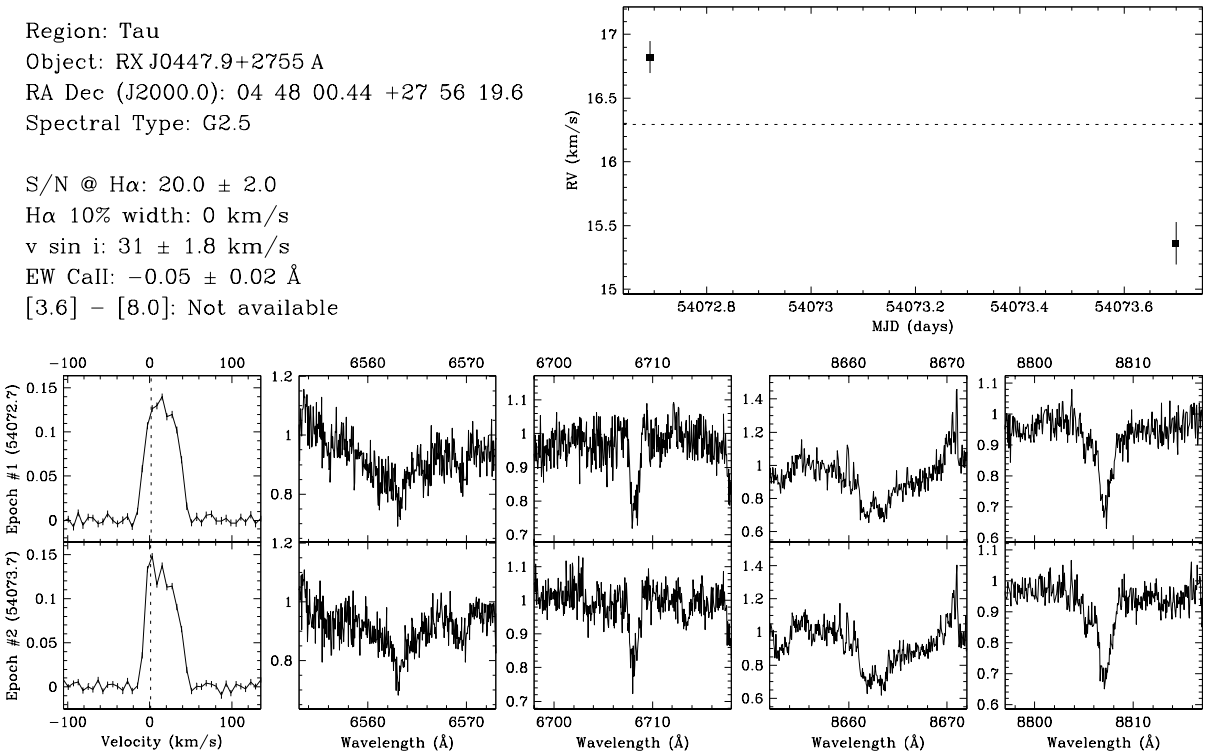

Figure 4.202 RX J0447.9+2755 A has a single-line profile, and is therefore not an SB2. The radial velocity scatter over the short baseline available does not conclusively indicate if the target is an SB1 or a single star. For epoch #2, the sharp peak in the line profile at the observer's rest frame is due to moonlight, and likely biased the radial velocity estimate toward the observer's rest frame. This target has been previously reported by Köhler & Leinert (1998) to have a resolved companion (RX J0447.9+2755 B) with a separation of $\sim 0\farcs639$ (~ 89 AU) at a position angle of $\sim 86\fdg5$, and an R-band flux ratio of ~ 0.79 ($\Delta K \sim 0.12$). However, there is no clear evidence in the line profile of the resolved companion. Since RX J0447.9+2755 B has an expected circular orbital speed of $\sim 7\,\mathrm{km\,s^{-1}}$, and a similar $v \sin i$ ($\sim 28\,\mathrm{km\,s^{-1}}$), a second profile is likely obscured.

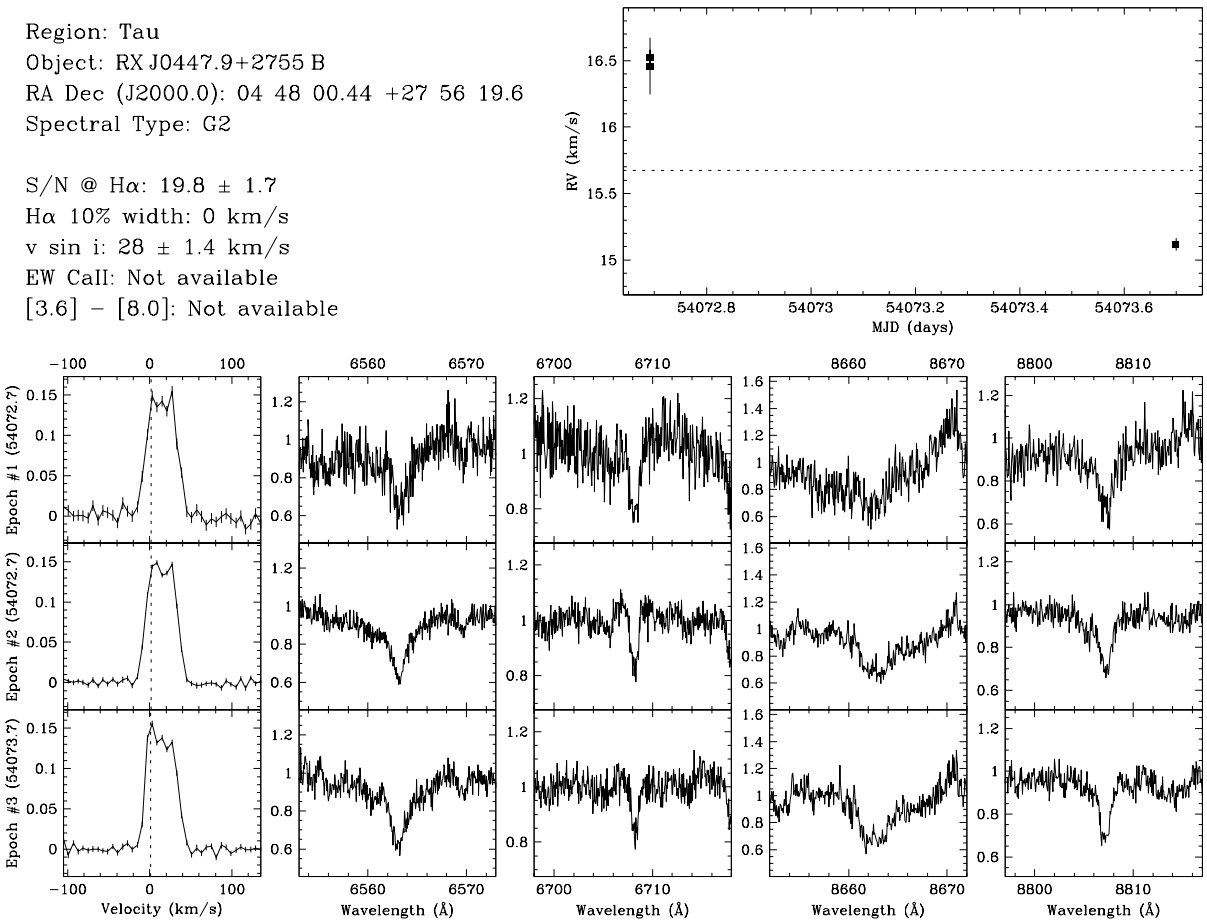

Figure 4.203 RX J0447.9+2755 B has a single-line profile, and is therefore not an SB2. The radial velocity scatter over the short baseline available does not conclusively indicate if the target is an SB1 or a single star. For epoch #3, the sharp peak in the line profile at the observer's rest frame is due to moonlight, and likely biased the radial velocity estimate toward the observer's rest frame. This target has been previously reported by Köhler & Leinert (1998) to be the secondary star of a resolved binary (RX J0447.9+2755 A+B) with a separation of $\sim 0\farcs639$ (~ 89 AU) at a position angle of $\sim 86\fdg5$, and an R-band flux ratio of ~ 0.79 ($\Delta K \sim 0.12$). However, there is no clear evidence in the line profile of the primary star. Since RX J0447.9+2755 A has an expected circular orbital speed of $\sim 7\,\mathrm{km\,s^{-1}}$, and a similar $v \sin i$ ($\sim 31\,\mathrm{km\,s^{-1}}$), a second profile is likely obscured.

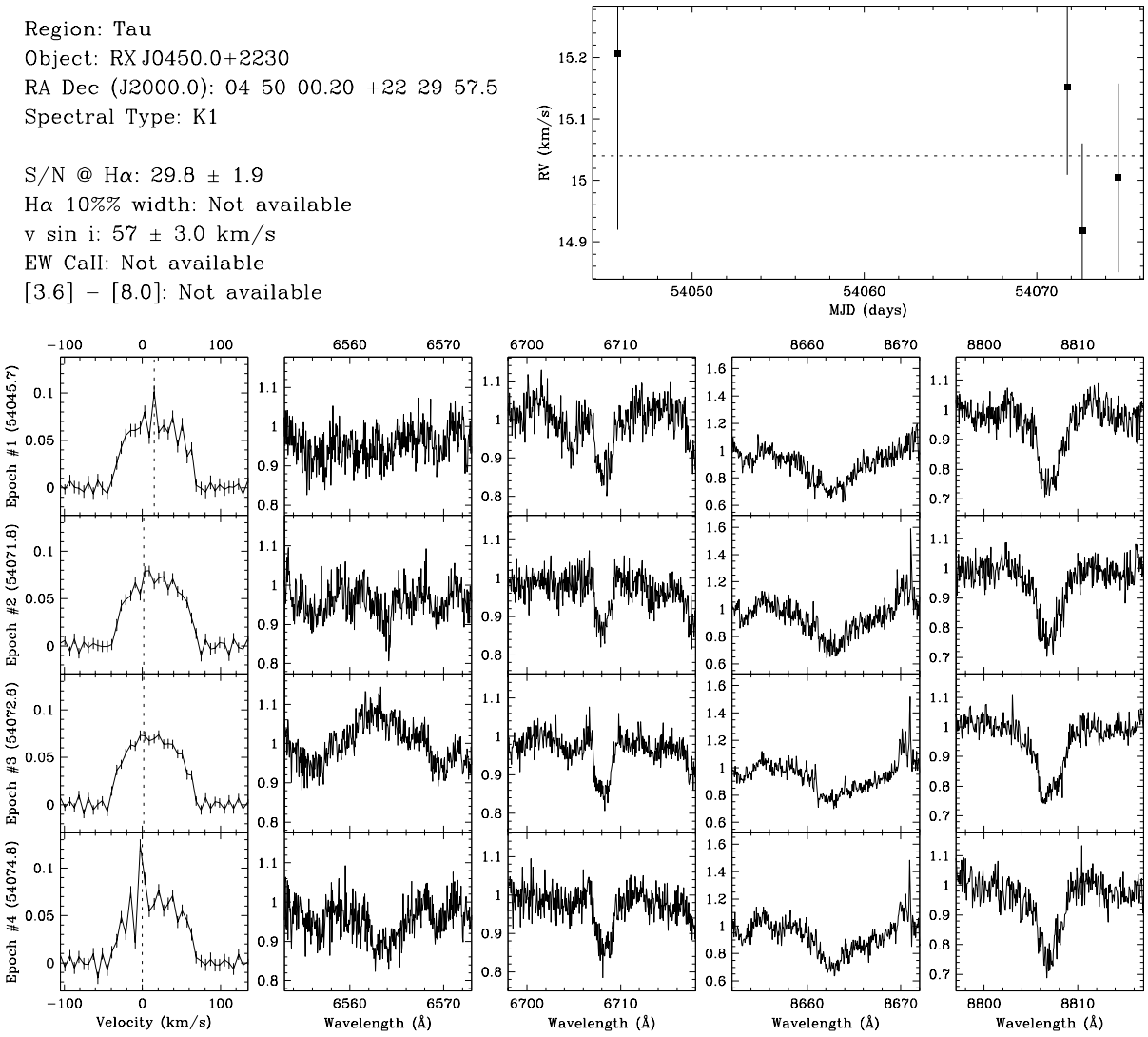

Figure 4.204 RX J0450.0+2230 shows no evidence of a close companion. The star has a single-line profile, and the radial velocity scatter is not significant relative to the measurement uncertainties. For epoch #4, the sharp peak in the line profile at the observer's rest frame is due to moonlight, and may have biased the radial velocity estimate toward the observer's rest frame. This target has been previously reported by Köhler & Leinert (1998) to have a resolved companion with a separation of $\sim$2.″072 ($\sim$290 AU) at a position angle of $\sim$84.°1, and an R-band flux ratio of $\lesssim$0.01 ($\Delta K \sim 3.74$). Given the flux ratio and separation, the expected contribution to the line profile from the resolved companion is negligible.

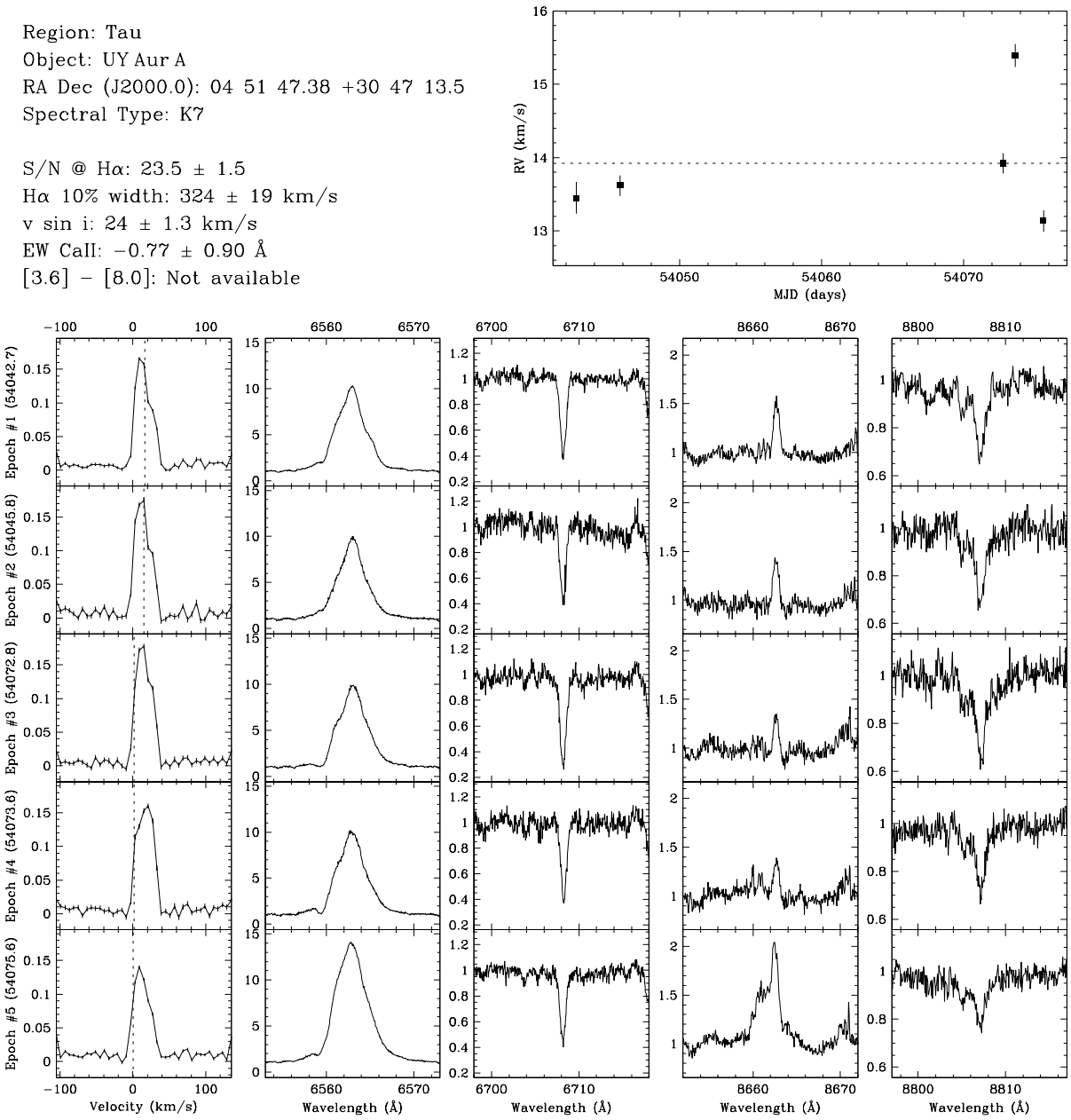

Figure 4.205 UY Aur A shows no clear evidence of a close companion. The star has a single-line profile, and a radial velocity scatter not significant relative to variations observed within each observing run. The line profiles show significant deviation from the shape expected from pure rotational broadening. To see if these irregularities are from close companions, we fitted multiple broadening functions to the line profiles. The resultant radial velocities were not consistent with those expected from close companions: the radial velocity separations were $\sim 15\,\mathrm{km\,s^{-1}}$ with no acceleration. Alternatively, if star spots are responsible for the unusual line profiles, based on observed $v \sin i$ ($\sim 24\,\mathrm{km\,s^{-1}}$) and model stellar radius ($\sim 1.4\,R_\odot$), one would expect variations on a maximum timescale of ~ 2.9 days. The line profiles are similar between epochs #1 and #2, and between epochs #3 and #5 which are both separated by ~ 3 days, whereas epoch #4 has a somewhat mirrored line profile which is consistent with the rotation timescale. Therefore, we suspect the asymmetries in the line profile are the result of star spots. The radial velocity scatter within each observing run is consistent with that expected from systematic line profile variations, e.g. from star spots rotating with the star. This target has been previously reported by Leinert et al. (1993), and Ghez et al. (1993) to have a resolved companion (UY Aur B) with a separation of 0.″88–0.″89 (~ 120 AU) at a position angle of 225°–227°, and an R-band flux ratio of 0.02–0.06 ($\Delta K \sim 1.14$–1.38). Given the flux ratio, the expected contribution to the line profile from the resolved companion is negligible.

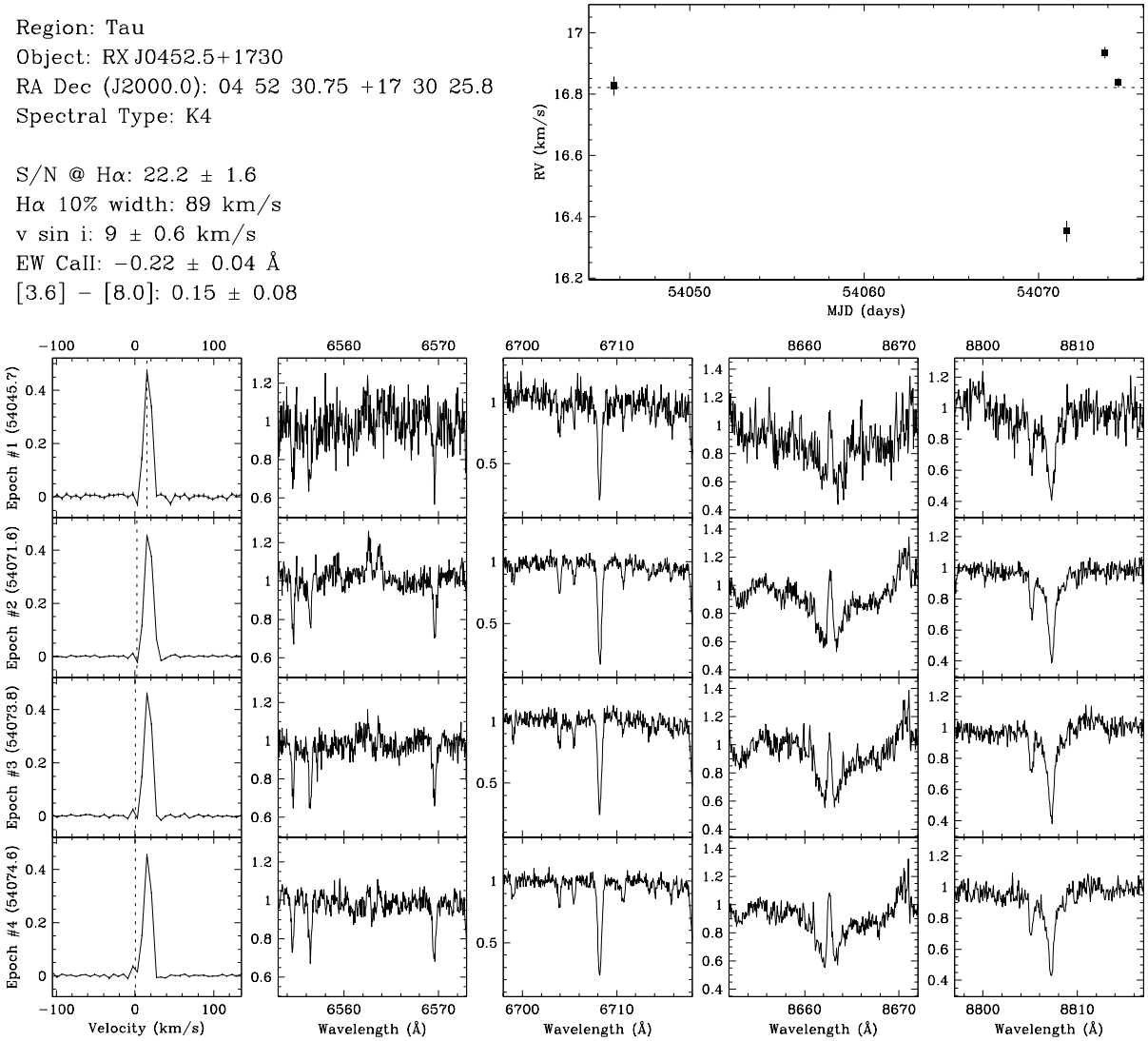

Figure 4.206 RX J0452.5+1730 shows no clear evidence of a close companion. The star has a single-line profile, and a radial velocity scatter not significant relative to variations observed within each observing run. The radial velocity scatter within the second observing run (epochs #2, #3 and #4) is consistent with that expected from systematic line profile variations, e.g. from star spots rotating with the star. For epoch #4, the small peak in the line profile at the observer's rest frame is due to moonlight, and may have biased the radial velocity estimate toward the observer's rest frame. This target has been previously reported by Köhler & Leinert (1998) to have no resolved companions.

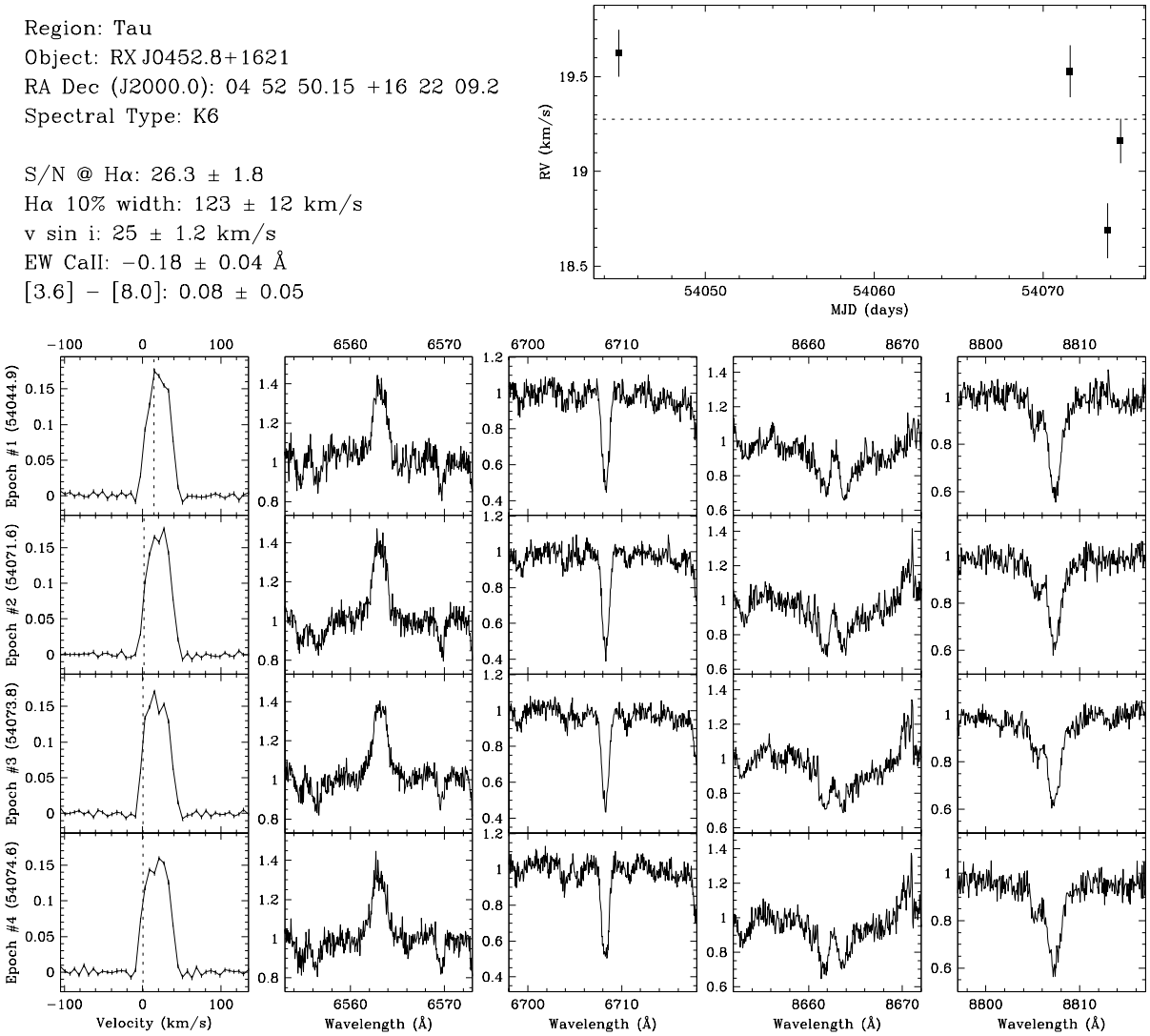

Figure 4.207 RX J0452.8+1621 shows no clear evidence of a close companion. The star has a single-line profile, and a radial velocity scatter not significant relative to variations observed within each observing run. The radial velocity scatter within the second observing run (epochs #2, #3 and #4) is consistent with that expected from systematic line profile variations, e.g. from star spots rotating with the star. This target has been previously reported by Köhler & Leinert (1998) to have a resolved companion with a separation of $\sim 0\farcs478$ (~ 67 AU) at a position angle of $\sim 294\fdg7$, and an R-band flux ratio of ~ 0.67 ($\Delta K \sim 0.19$). However, there is no clear evidence in the line profile of the resolved companion. Since the resolved companion has an expected circular orbital speed of $\sim 4\,\mathrm{km\,s^{-1}}$, a second profile could be obscured if the primary star and the resolved companion have similar projected rotational velocities.

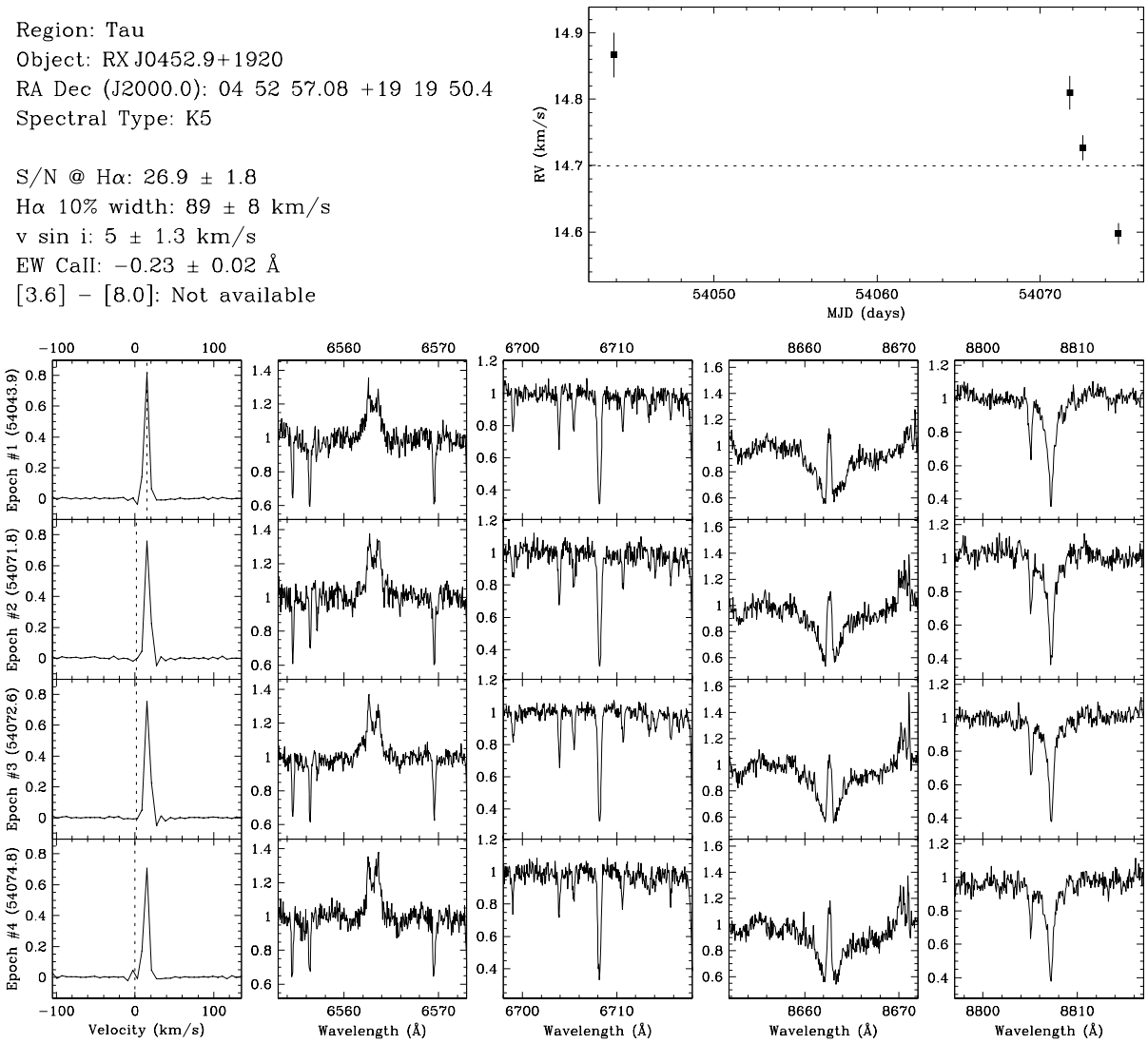

Figure 4.208 RX J0452.9+1920 shows no clear evidence of a close companion. The star has a single-line profile, and a radial velocity scatter not significant relative to variations observed within each observing run. The radial velocity scatter within the second observing run (epochs #2, #3 and #4) is consistent with that expected from systematic line profile variations, e.g. from star spots rotating with the star. For epoch #4, the small peak in the line profile at the observer's rest frame is due to moonlight, and may have biased the radial velocity estimate toward the observer's rest frame. This target has been previously reported by Köhler & Leinert (1998) to have a resolved companion with a separation of $\sim 0\farcs425$ (~ 60 AU) at a position angle of $\sim 304\fdg5$, and an R-band flux ratio of ~ 0.01 ($\Delta K \sim 1.85$). Given the flux ratio, the expected contribution to the line profile from the resolved companion is negligible.

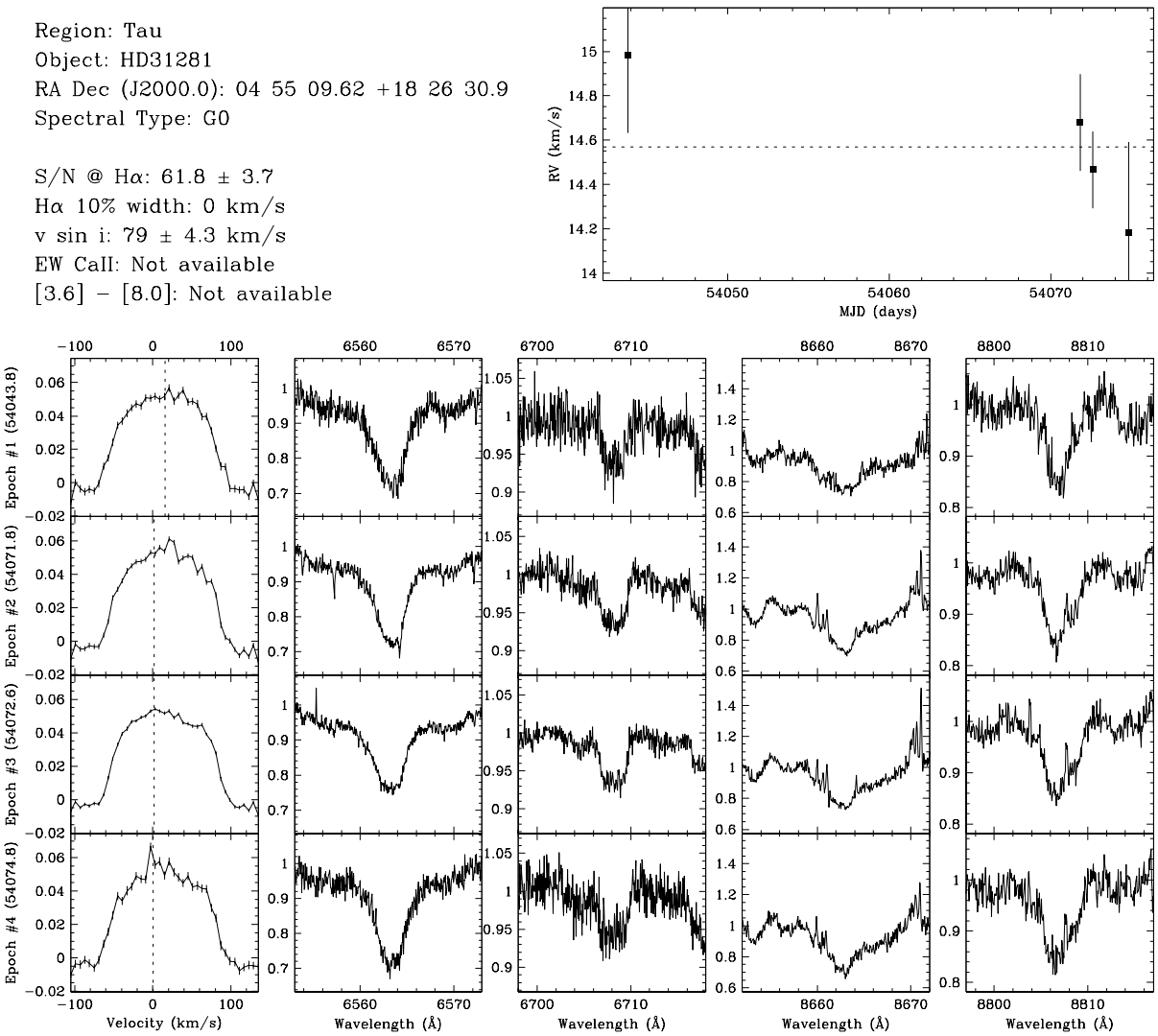

Figure 4.209 HD31281 shows no evidence of a close companion. The star has a single-line profile, and the radial velocity scatter is not significant relative to the measurement uncertainties. This target has been previously reported by Köhler & Leinert (1998) to have no resolved companions.

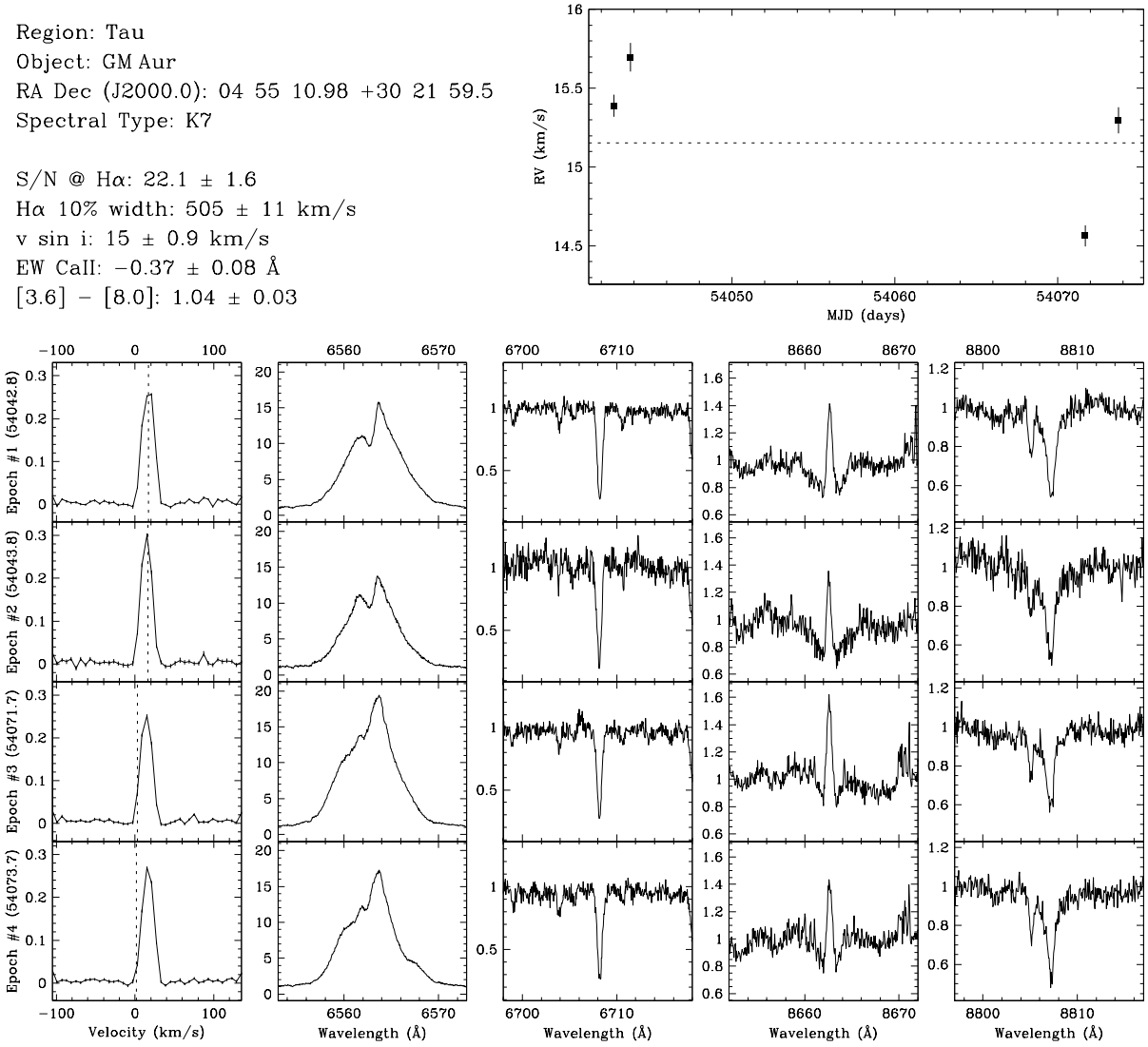

Figure 4.210 GM Aur shows no clear evidence of a close companion. The star has a single-line profile, and a radial velocity scatter not significant relative to variations observed within each observing run. The radial velocity scatter within each observing run is consistent with that expected from systematic line profile variations, e.g. from star spots rotating with the star. This target has been previously reported by Leinert et al. (1993) to have no resolved companions.

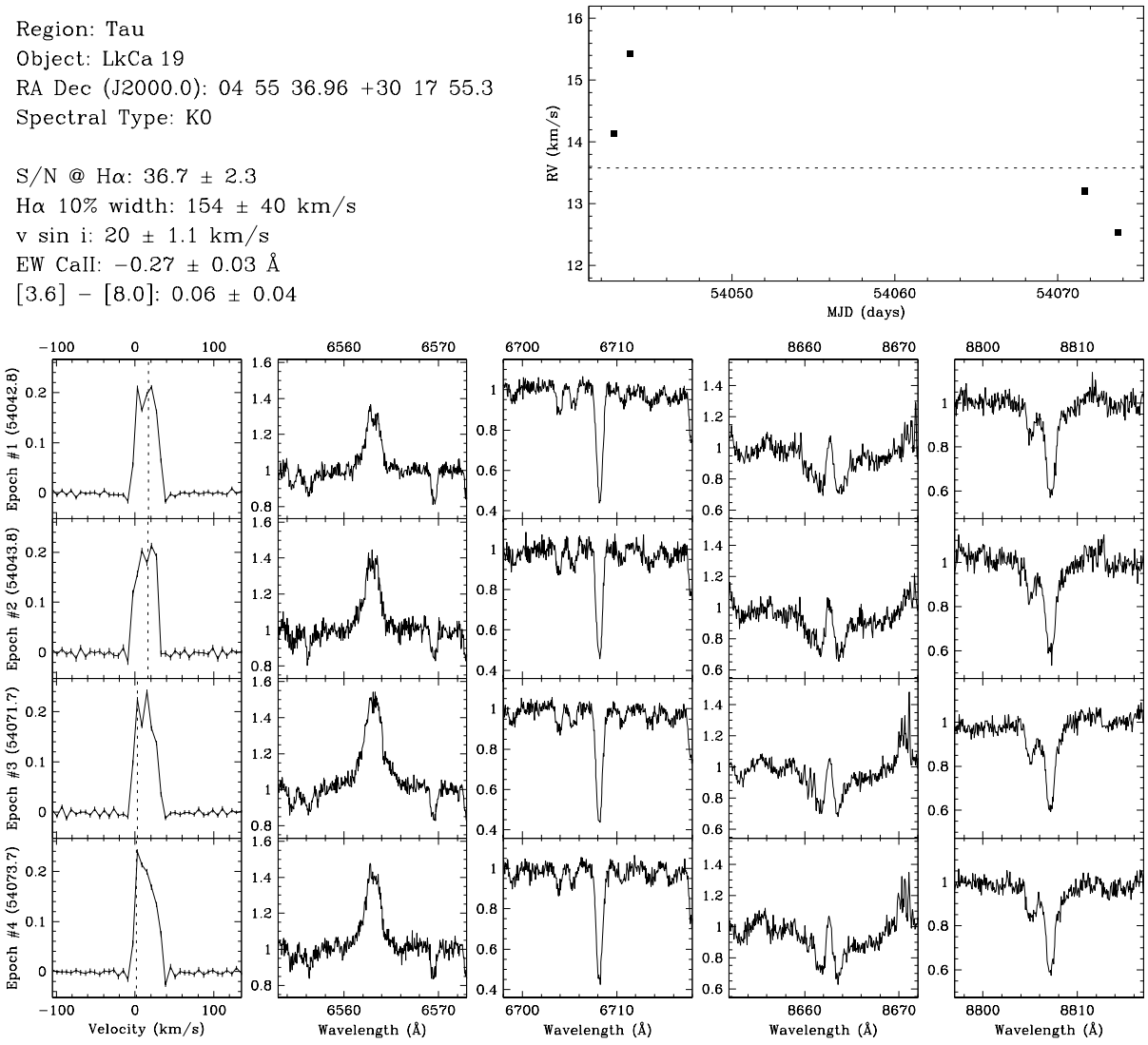

Figure 4.211 LkCa 19 shows no clear evidence of a close companion. The star has a single-line profile, and a radial velocity scatter not significant relative to variations observed within each observing run. The line profile has unusual shape changes over time. These changes are almost certainly due to star spots, since Huerta et al. (2008) found that the radial velocity variations and the evidence from line bisector analysis for this target are fully consistent with the presence of large star spots. This target has been previously reported by Leinert et al. (1993) to have no resolved companions.

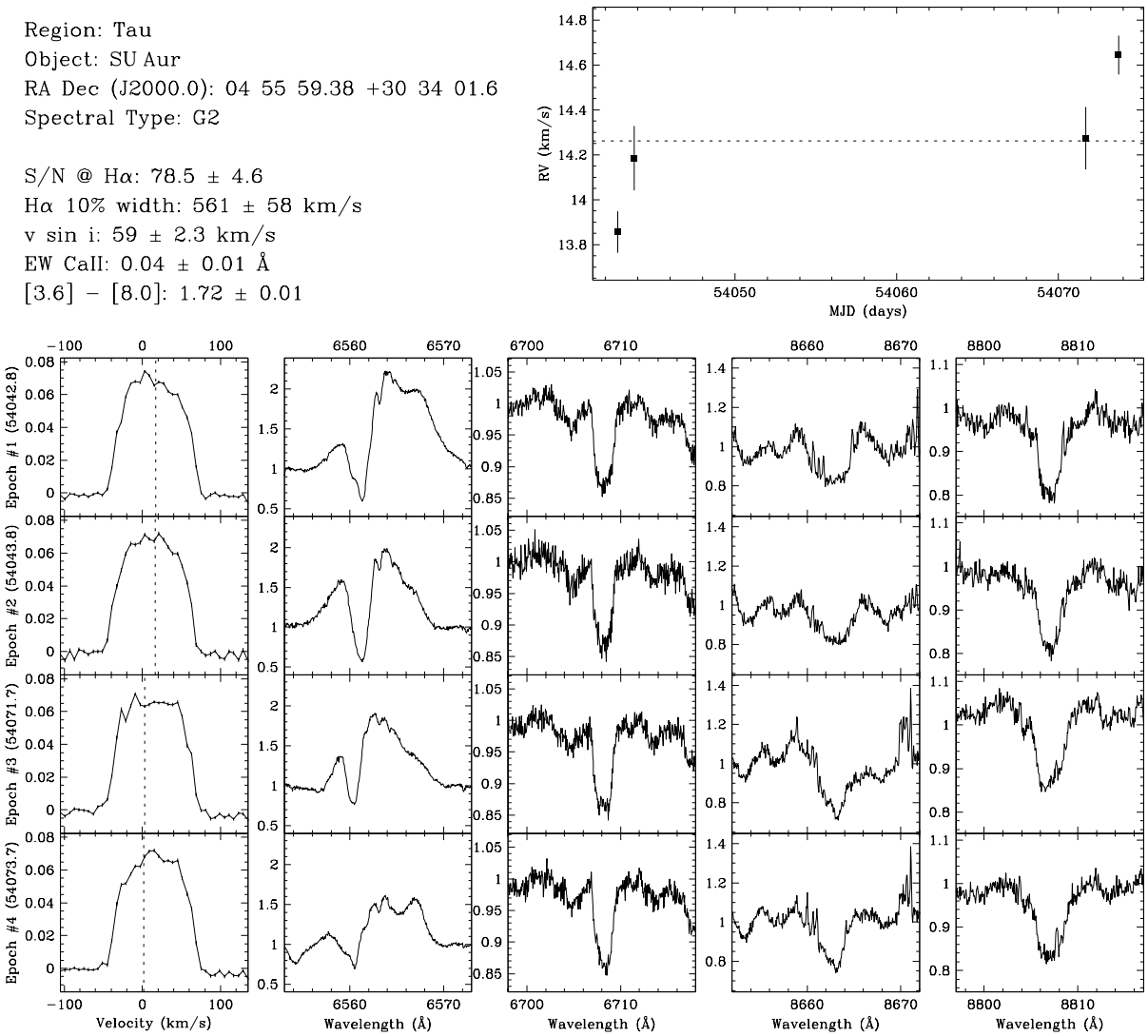

Figure 4.212 SU Aur shows no clear evidence of a close companion. The star has a single-line profile, and a radial velocity scatter not significant relative to variations observed within each observing run. The radial velocity scatter within each observing run is consistent with that expected from systematic line profile variations, e.g. from star spots rotating with the star. This target has been previously reported by Leinert et al. (1993), and Ghez et al. (1993) to have no resolved companions.

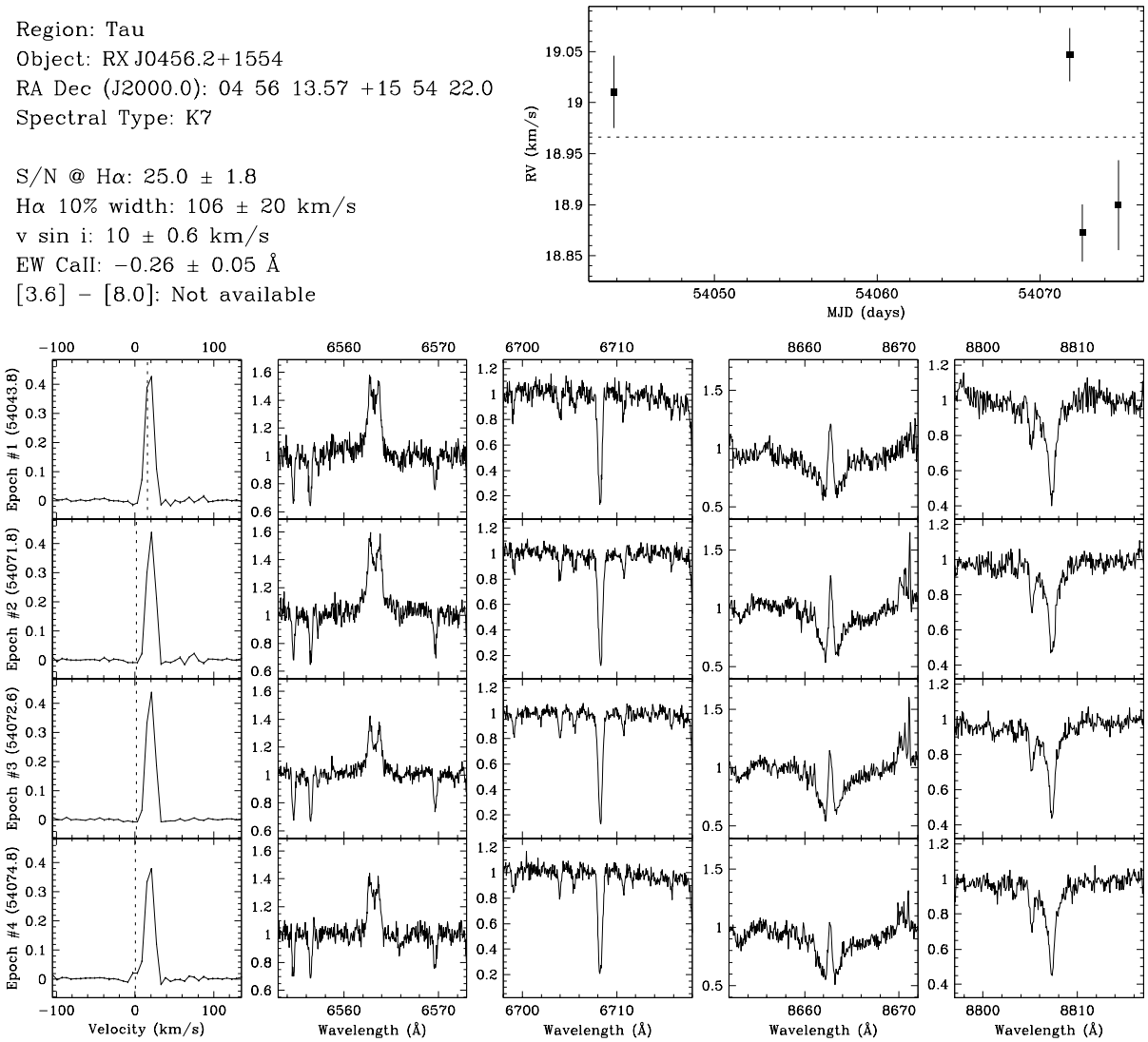

Figure 4.213 RX J0456.2+1554 shows no clear evidence of a close companion. The star has a single-line profile, and a radial velocity scatter not significant relative to variations observed within each observing run. The radial velocity scatter within the second observing run (epochs #2, #3 and #4) is consistent with that expected from systematic line profile variations, e.g. from star spots rotating with the star. For epoch #4, the small bulge in the line profile at the observer's rest frame is due to moonlight, and may have biased the radial velocity estimate toward the observer's rest frame. This target has been previously reported by Köhler & Leinert (1998) to have no resolved companions.

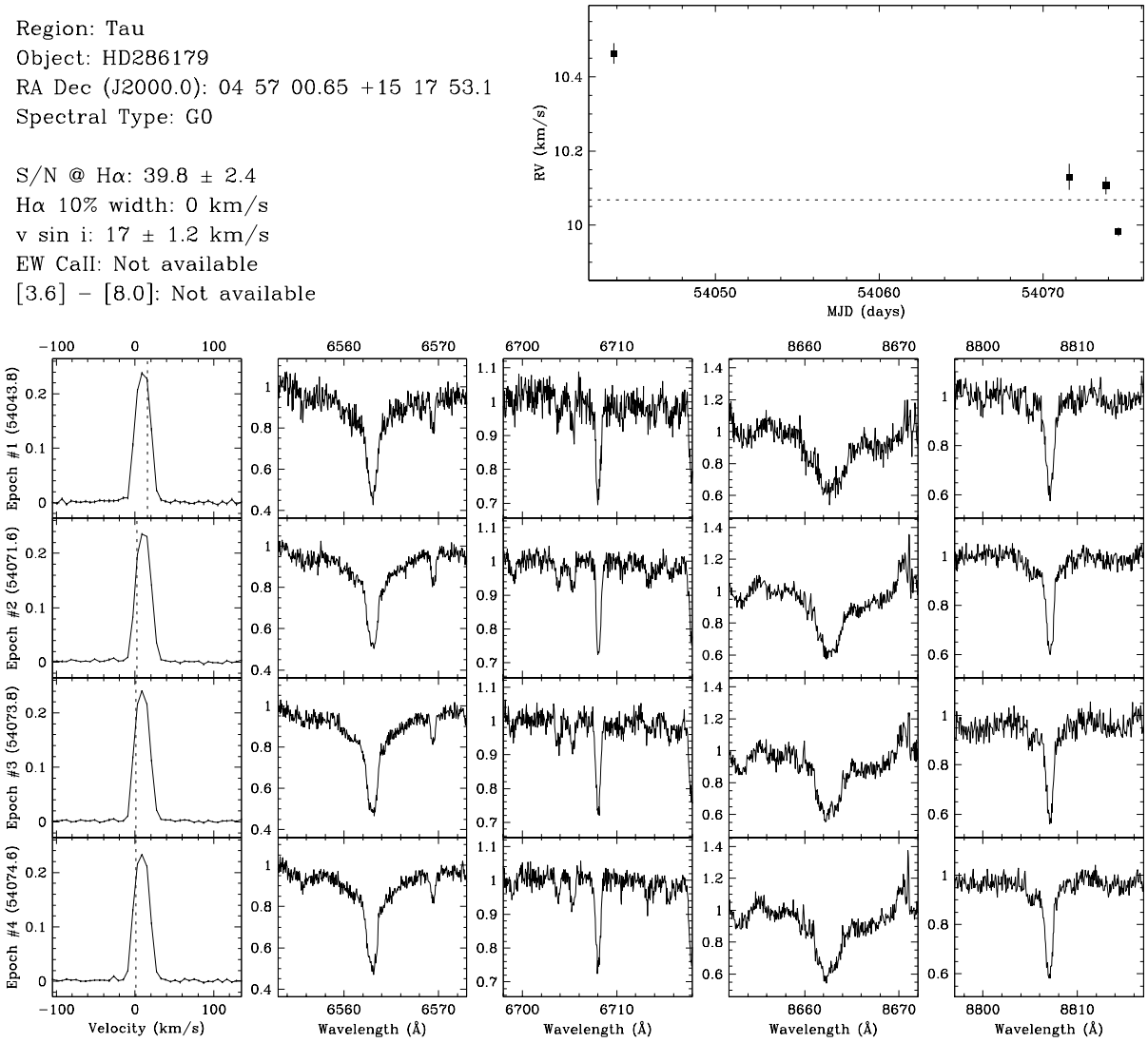

Figure 4.214 HD286179 shows no clear evidence of a close companion. The overall radial velocity scatter is consistent with that expected from systematic line profile variations, e.g. from star spots rotating with the star. The radial velocity scatter within the second observing run (epochs #2, #3 and #4) is consistent with that expected from systematic line profile variations, e.g. from star spots rotating with the star. The overall radial velocity deviates from that of the star forming region. However, cluster membership is supported by Li-λ6708 absorption. This target has been previously reported by Köhler & Leinert (1998) to have a resolved companion with a separation of $\sim$0.″112 ($\sim$16 AU) at a position angle of $\sim$208.°3, and an R-band flux ratio of $\sim$0.22 ($\Delta K \sim 1.26$). However, there is no clear evidence in the line profile of the resolved companion. Since the resolved companion has an expected circular orbital speed of $\sim$16 km s^{-1}, a second profile could be obscured if the primary star and the resolved companion have similar projected rotational velocities.

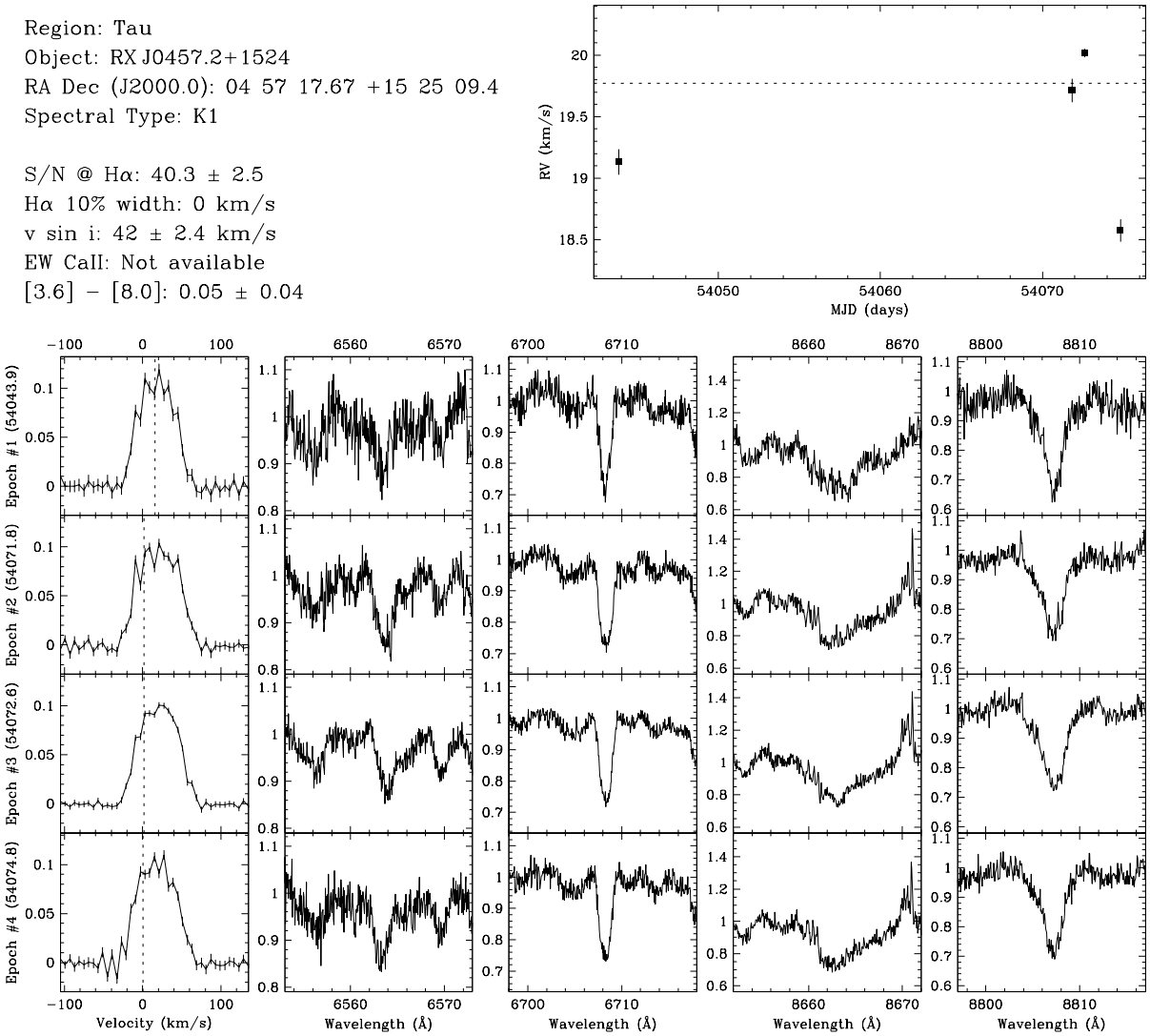

Figure 4.215 RX J0457.2+1524 shows no clear evidence of a close companion. The star has a single-line profile, and a radial velocity scatter not significant relative to variations observed within each observing run. The radial velocity scatter within the second observing run (epochs #2, #3 and #4) is consistent with that expected from systematic line profile variations, e.g. from star spots rotating with the star. This target has been previously reported by Köhler & Leinert (1998) to have a resolved companion with a separation of $\sim 0\farcs57$ (~ 80 AU) at a position angle of $\sim 43\fdg9$, and an R-band flux ratio of ~ 0.94 ($\Delta K \sim 0.05$). However, there is no clear evidence in the line profile of the resolved companion. Since the resolved companion has an expected circular orbital speed of $\sim 6\,\mathrm{km\,s^{-1}}$, a second profile could be obscured if the primary star and the resolved companion have similar projected rotational velocities.

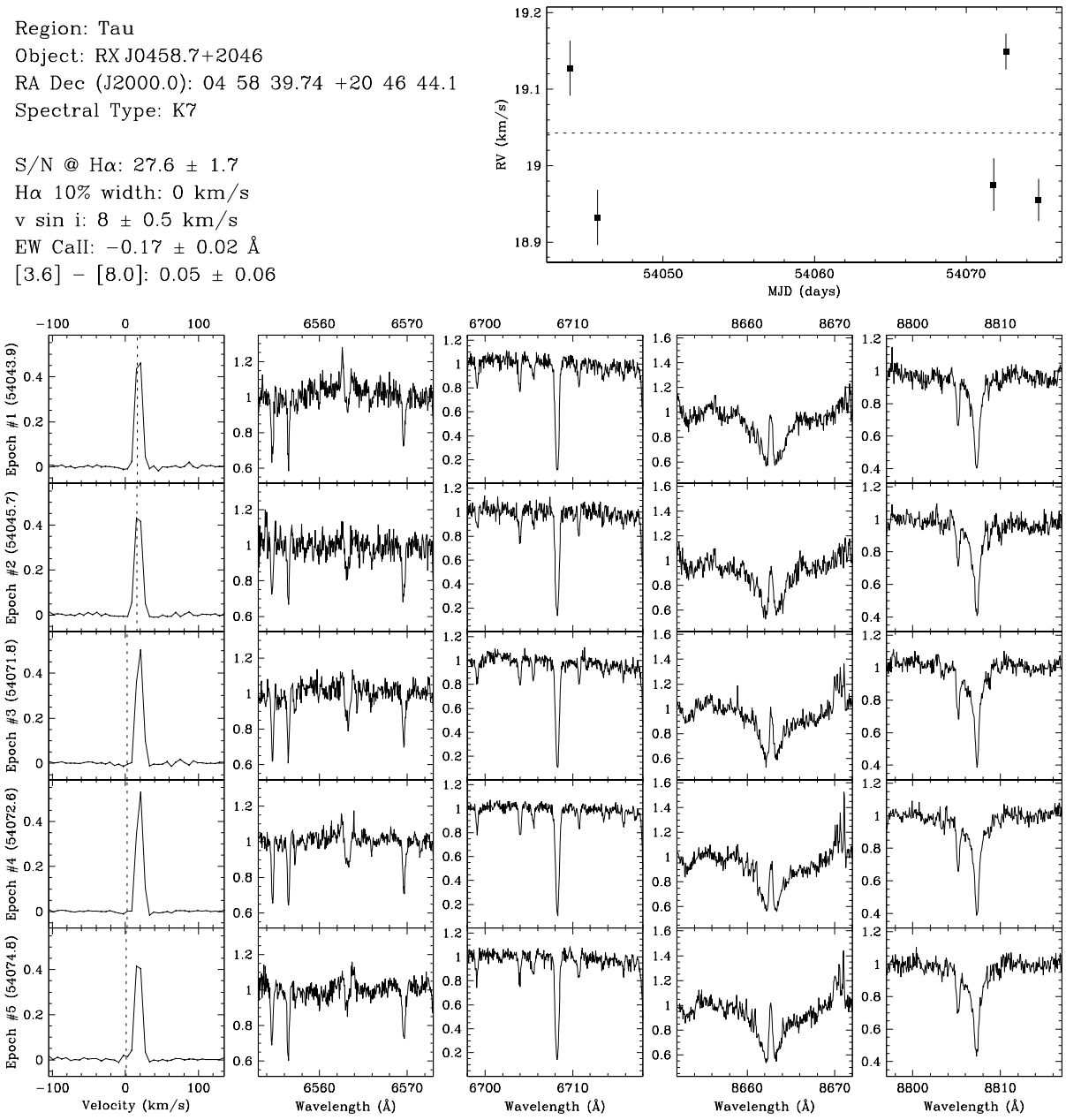

Figure 4.216 RX J0458.7+2046 shows no clear evidence of a close companion. The star has a single-line profile, and a radial velocity scatter not significant relative to variations observed within each observing run. The radial velocity scatter within each observing run is consistent with that expected from systematic line profile variations, e.g. from star spots rotating with the star. This target has been previously reported by Köhler & Leinert (1998) to have a resolved companion with a separation of $\sim 6\farcs113$ ($\sim$860 AU) at a position angle of $\sim 220\fdg4$, and an R-band flux ratio of $\lesssim 0.01$ ($\Delta K \sim 6.75$). Given the flux ratio and separation, the expected contribution to the line profile from the resolved companion is negligible.

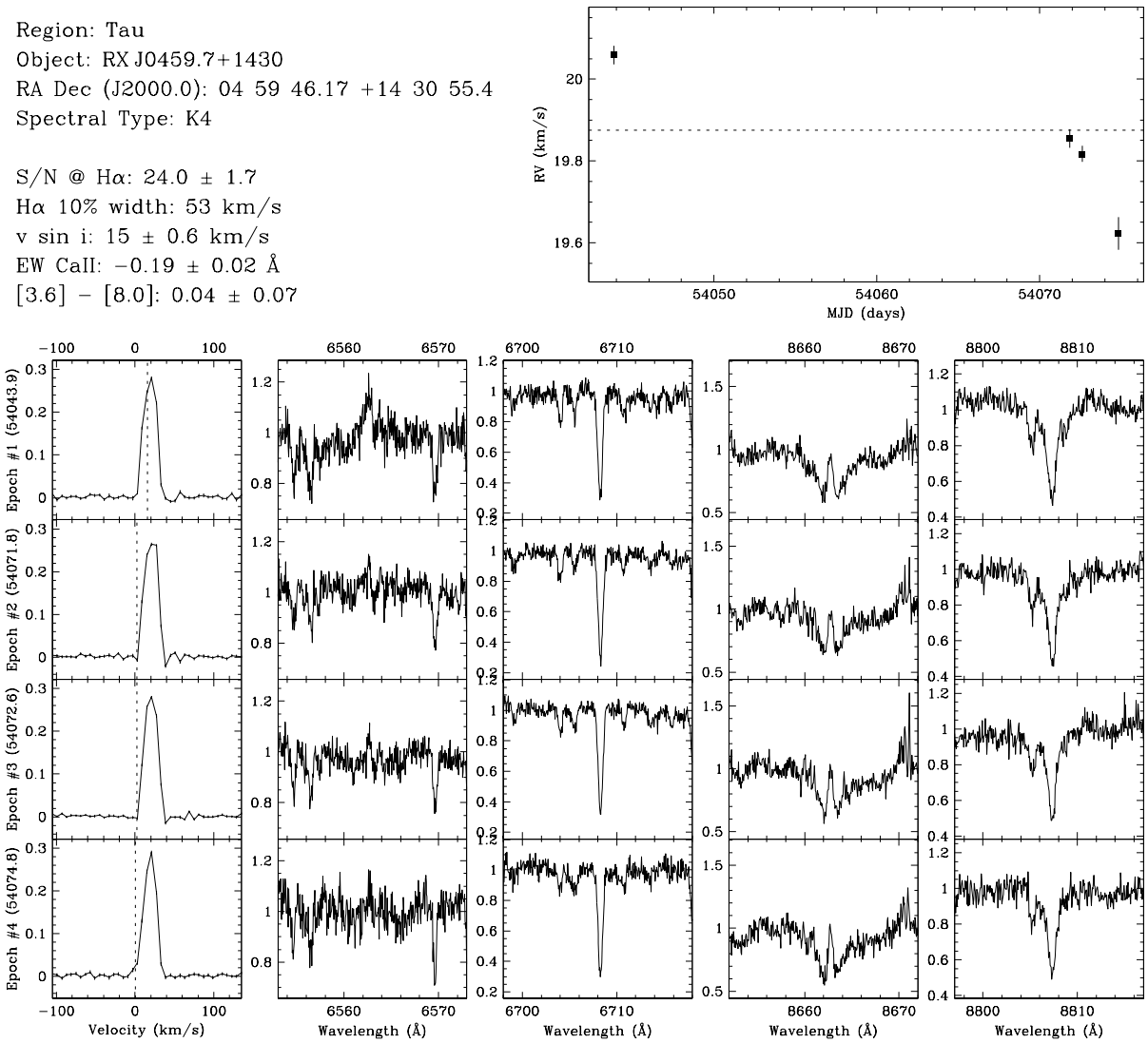

Figure 4.217 RX J0459.7+1430 shows no clear evidence of a close companion. The star has a single-line profile, and a radial velocity scatter not significant relative to variations observed within each observing run. The radial velocity scatter within the second observing run (epochs #2, #3 and #4) is consistent with that expected from systematic line profile variations, e.g. from star spots rotating with the star. This target has been previously reported by Köhler & Leinert (1998) to have no resolved companions.

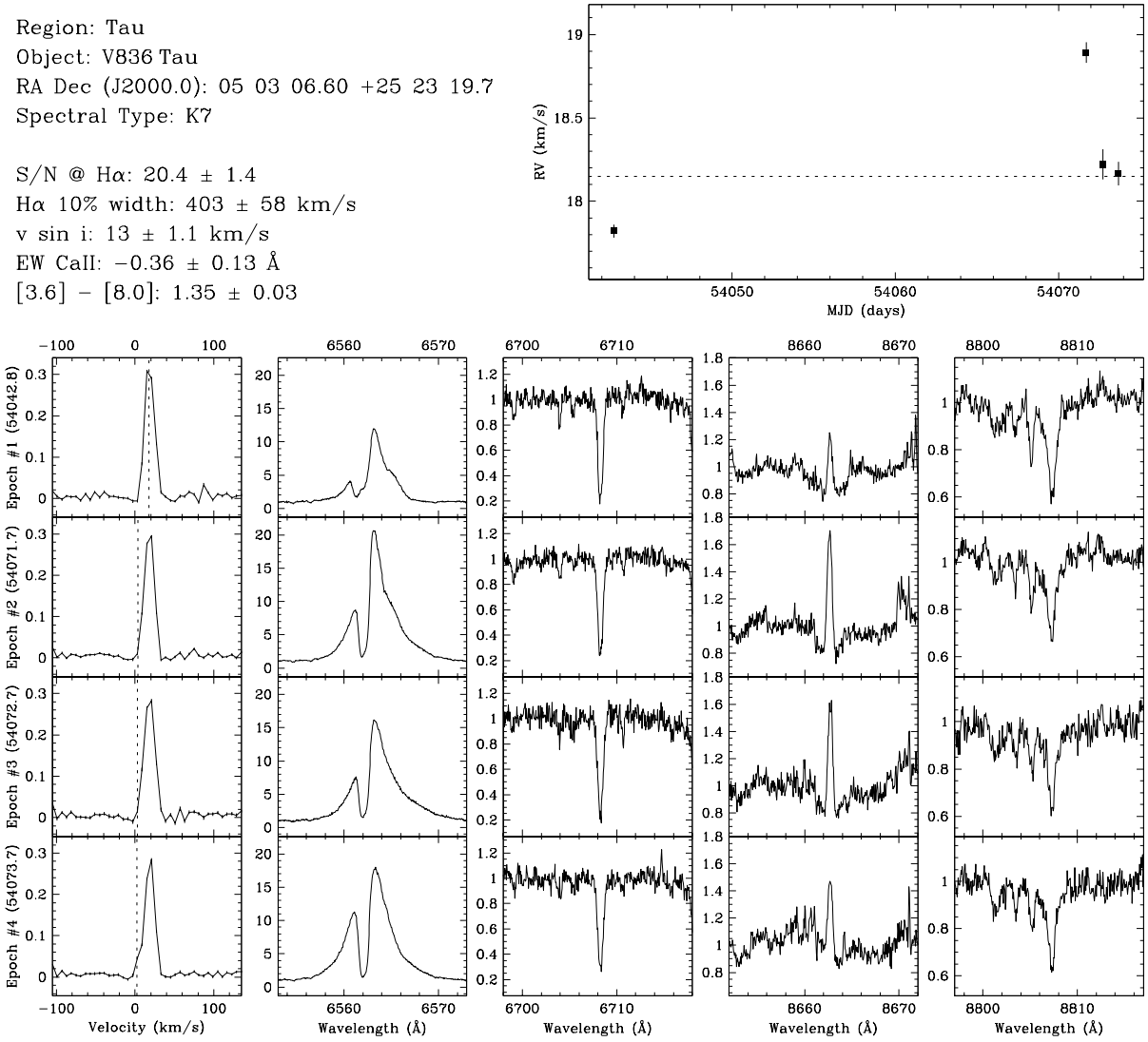

Figure 4.218 V836 Tau shows no clear evidence of a close companion. The star has a single-line profile, and a radial velocity scatter not significant relative to variations observed within each observing run. The radial velocity scatter within the second observing run (epochs #2, #3 and #4) is consistent with that expected from systematic line profile variations, e.g. from star spots rotating with the star. For epoch #4, the small bulge in the line profile at the observer's rest frame is due to moonlight, and may have biased the radial velocity estimate toward the observer's rest frame. This target has been previously reported by Leinert et al. (1993), and Simon et al. (1995) to have no resolved companions.

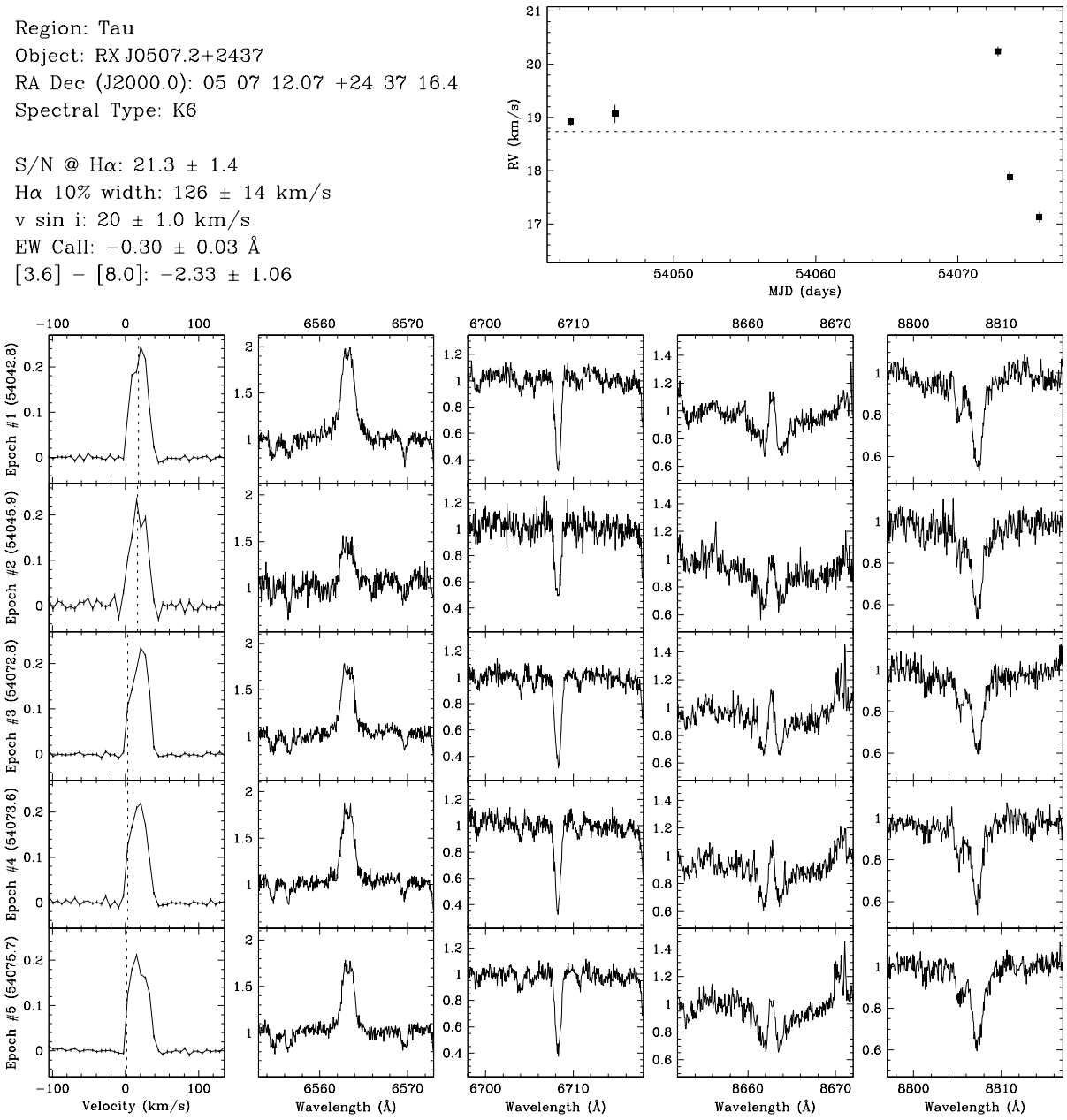

Figure 4.219 RX J0507.2+2437 shows no clear evidence of a close companion. The star has a single-line profile, and a radial velocity scatter not significant relative to variations observed within each observing run. The radial velocity scatter within each observing run is consistent with that expected from systematic line profile variations, e.g. from star spots rotating with the star.

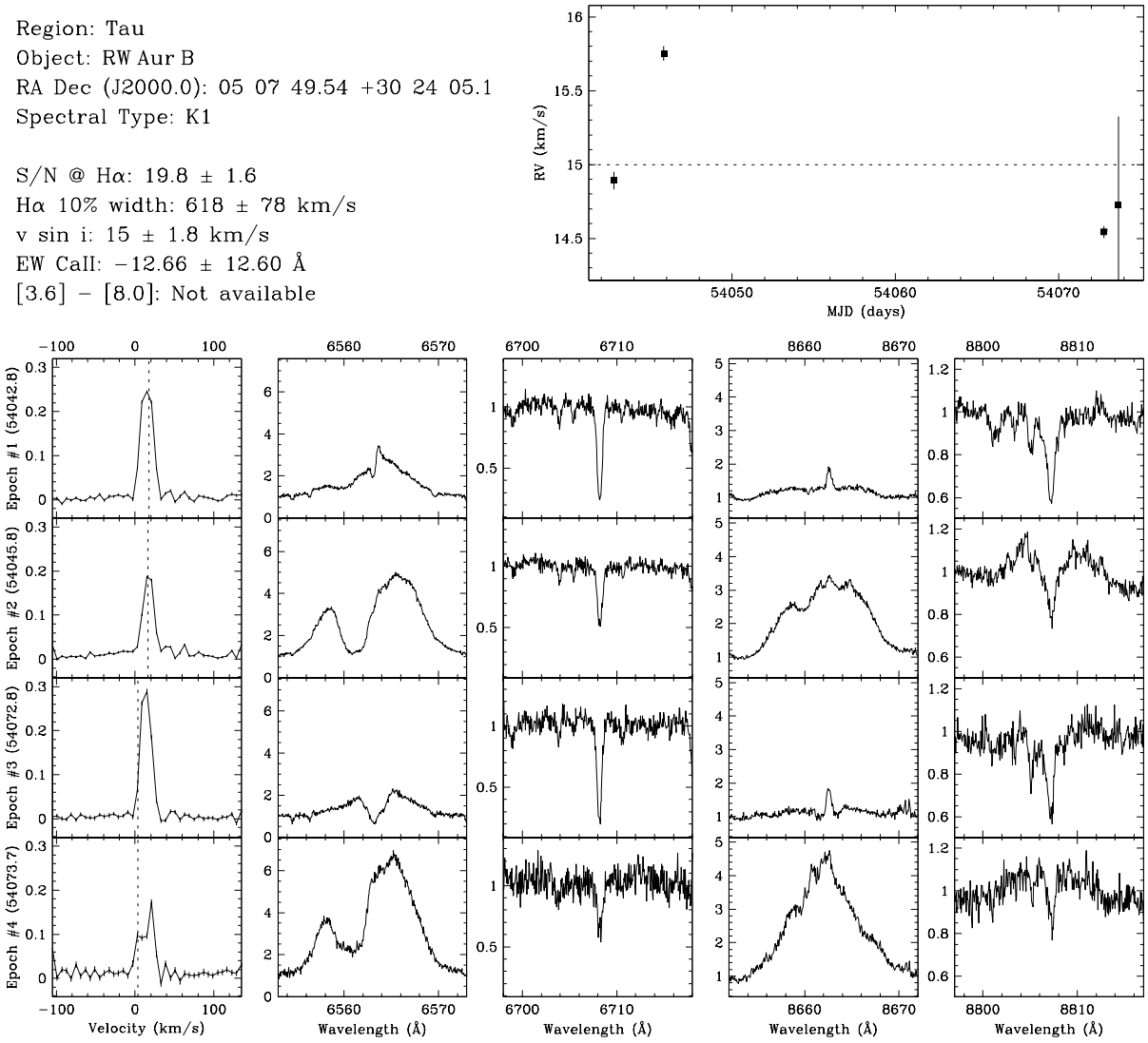

Figure 4.220 RW Aur B shows no clear evidence of a close companion. The star has a single-line profile, and a radial velocity scatter not significant relative to variations observed within each observing run. The radial velocity scatter within each observing run is consistent with that expected from systematic line profile variations, e.g. from star spots rotating with the star. For epoch #4, the peak in the line profile at $\sim 5\,\mathrm{km\ s^{-1}}$ is likely due to contamination from RW Aur A, and may have biased the radial velocity estimate. This target has been previously reported by Leinert et al. (1993) to have two resolved companions (RW Aur A and RW Aur C) with A–B and B–C separations of $\sim 1\farcs5$ ($\sim 210\,\mathrm{AU}$) and $\sim 0\farcs2$ ($\sim 17\,\mathrm{AU}$) at A–B and B–C position angles of $\sim 258°$ and $\sim 111°$, and A–B and B–C R flux ratios of ~ 0.08 ($\Delta K \sim 1.60$) and $\lesssim 0.01$ ($\Delta K \sim 4.03$). For epoch #4, the peak in the line profile at $\sim 5\,\mathrm{km\,s^{-1}}$ is likely due to contamination from RW Aur A, and may have biased the radial velocity estimate. Given the B–C flux ratio, the expected contribution to the line profile from RW Aur C is negligible.

Chapter 5

Conclusion

We have presented results on the variability of accretion in young stars, the early evolutionary influence of circumstellar disks, and the role of multiplicity on the properties of young systems. The thesis chapters stand alone as separate papers with their own conclusion sections, so it would be repetitious to include an additional summary of those chapters here. Instead, this concluding chapter is presented as a discussion connecting the results from the individual chapters into a larger world view and prospects for future work.

5.1 Disk Braking

This thesis has focused on the T Tauri phase of star formation when stars are still surrounded by a circumstellar disk. During the beginning of this stage, gas from the inner disk is accreting onto the central star. According to magnetospheric accretion theory, the infalling gas is channeled by the stellar magnetic field, and the magnetic field lines couple the star and the inner disk. This coupling would work to retard the spin-up of the star as it contracts toward the main sequence because the star would be essentially locked to a rotation period matching the orbital period at the magnetospheric radius.

5.1.1 Rotational Velocity Distributions

The presence of accretion or an inner disk is not strongly connected with the distribution of rotational velocities in the Chamaeleon I and Taurus-Auriga star forming regions. The rotational braking of young stars based on magnetic coupling between star and disk, i.e.,

disk braking has been investigated observationally by many groups. Some photometric studies (e.g. Herbst et al., 2002; Rebull et al., 2006) have found a connection between rotation and IR colour excess, suggestive of disks, while other groups fail to detect such a correlation (e.g. Stassun et al., 1999; Littlefair et al., 2005). In our survey of T Tauri stars in Cha I and Tau-Aur, we used mid-IR photometry from the *Spitzer Space Telescope* to detect disk presence, Hα 10% width to identify on-going accretion, and projected rotational velocity $v \sin i$ to estimate rotation rate. K-S tests showed that the $v \sin i$ distributions of accretors and non-accretors as well as of stars with and without inner disks differed by less than $2\,\sigma$. In other words, we did not observe evidence of significant disk braking in our sample.

One suggestion to explain the lack of strong evidence for disk braking in our sample is that insufficient time has elapsed for the effects of disk braking to be significant. In Orion, where disk braking is observed, accretion rates suggest a disk braking timescale of ~ 1 Myr which is comparable to the cluster age. In contrast, the typical disk braking timescale of our sample based on accretion rates and stellar masses is ~ 6 Myr which is significantly longer than the estimated age of ~ 2 Myr for Chamaeleon I and Taurus-Auriga. This implies that we should see more pronounced disk braking by observing similar populations at slightly older ages that still have accretors such as Upper Scorpius (~ 5 Myr). Furthermore, the disk braking timescale is proportional to stellar mass (Hartmann, 2002). Therefore, we expect the rotation rates of higher mass stars to be less affected by disk braking than their lower mass counterparts at the same ages.

5.1.2 Mass-Rotation Connection

We observed that higher mass stars in our sample have faster overall rotational velocities than their lower mass counterparts. Moreover, the overall specific angular momentum j increases with increasing stellar mass. By combining observed $v \sin i$ and physical parameters from the models of D'Antona & Mazzitelli (1997), we find in Chamaeleon I and Taurus-Auriga (~ 2 Myr) the upper envelope of $j \sin i$ varies as $M^{0.5}$. This result contrasts that of Wolff et al. (2004). They found in Orion an upper envelope trend of $M^{0.25}$ for stars on convective tracks (~ 1 Myr), and a steep downturn for stars on radiative tracks (~ 5 Myr) with masses less than $2\,M_{\odot}$. Since over 90% of the stars we measured j had masses less than $2\,M_{\odot}$, the specific angular momentum trend we observed may hint at the beginning stages of rotational braking. To further investigate this hypothesis,

we should observe other regions with different ages such as Upper Scorpius ($\sim 5\,\mathrm{Myr}$) mentioned above. For Upper Scorpius, we would expect a trend in j closer to that of the older population in Orion.

5.2 Accretion

5.2.1 Sources of Variability

Stellar rotation may contribute to observed variability in accretion. Accretion rates were measured from Hα 10% widths and Ca II-λ8662 fluxes using the formulations of Natta et al. (2004) and Mohanty et al. (2005). The change in the accretion rate measurements over time were tracked for a subgroup of accreting single stars in our sample. The amplitude of the variability reached a maximum on timescales of a few days. This timescale suggests that accretion rates at the stellar surfaces depend solely on phenomena within a few stellar radii. Based on the model stellar radii of D'Antona & Mazzitelli (1997) and observed $v \sin i$, the median rotational period of our targets assuming average $\sin i$ is 5.8 days. This is consistent with the median photometric period of 5.6 days for a subset of 30 targets within our sample reported by Bouvier et al. (1993, 1995), and Preibisch & Smith (1997). Therefore, stellar rotation is a possible source of the observed accretion variability.

Another accretion influence close to the star we should consider is that of the inner disk. The disk structure may vary on several timescales. If the star and disk are locked, then the natural timescale of the star-disk couple is the rotation period of the inner disk. The shortest characteristic timescale of the disk is the dynamical infall timescale $t_\phi \sim \Omega_K^{-1}$ where Ω_K is the Keplerian angular velocity. At the typical inner disk radius of $5\,R_\odot$ around a solar mass star, the dynamical timescale is approximately five hours. Therefore, inhomogeneities on the disk surface could be responsible for the very short-term accretion scatter we observed, but not for the overall peak variations we see on intervals of several weeks.

Next, from Frank et al. (2002), the viscous timescale t_{visc} using an α-disc model is given by the approximation,

$$t_{\mathrm{visc}} \sim 3.9 \times 10^3 \alpha^{-4/5} (\dot{M}/(M_\odot\,\mathrm{yr}^{-1}))^{-3/10} (M/M_\odot)^{1/4} (R/R_\odot)^{5/4}\,\mathrm{s} \qquad (5.1)$$

Assuming a typical accretion rate of $10^{-10}\,M_{\odot}\,\mathrm{yr}^{-1}$ and an α parameter of 0.01, the viscous timescale at the inner disk is of the order of 10^9 seconds or about 30 years. Variations on this timescale are not easily detectable in our data. One solution would be to observe our targets with much longer time baselines than was feasible for this thesis. If no increase in the amplitude of accretion variability is observed on timescales of years, then perhaps the viscous timescale is indeed very long, or the effects of viscous torques are unimportant for accretion fluctuation.

The accretion rate fluctuations over time were less than an order of magnitude for 39 out of the 40 stars in Chamaeleon I and Taurus-Auriga that we tracked. However, the scatter in accretion rates of our sample at any given stellar mass is approximately two orders of magnitude. One possible source of this scatter could come from changes in the disks at viscous timescales which we have already estimated to be much longer than the time baseline of our observations. Another significant contribution to the overall dispersion of accretion rates in the population can come from object-to-object differences. Differences between the physical properties of young stars are often suggested to be related to environment. In particular, cluster density is commonly cited as a source of disparity. For example, multiplicity surveys have observed an excess of binary systems among the T Tauri population of diffuse star forming regions (e.g., Taurus-Auriga) relative to dense star forming regions (e.g., Orion). If accretion rates are affected by companion formation, then we should see a marked difference between the spread in accretion rates of dense and of sparse cluster populations.

5.2.2 Signatures and Robustness

When we measure physical properties like accretion rates from indirect methods (e.g., via spectral features), it is important to recognize the reliability of our measurement. We have observed that Ca II-λ8662 fluxes are a more robust quantitative indicator of accretion than Hα 10% width. Changes in accretion rates estimated from Ca II-λ8662 fluxes are an order of magnitude smaller than values obtained from Hα 10% width. Both of these accretion diagnostics based on line emissions have been shown observationally by Natta et al. (2004) and Mohanty et al. (2005) to be useful surrogates for the conventional approach of determining accretion rates from measurements of veiling, i.e., hot continuum excess. In the magnetospheric model, the continuum excess luminosity L_{acc} arises from the energy released in the impact of the accretion flow, and is related to the accretion

rate $\dot{M}$ by the equation $L_{acc} \simeq (GM_\star \dot{M}/R_\star)(1 - R_\star/R_{\rm in})$ where $M_\star$ and $R_\star$ are the stellar mass and radius, and $R_{\rm in}$ is the inner radius of the accretion disk (Gullbring et al., 1998). Furthermore, the accretion rate derived from the continuum excess also correlates well with several other emission line measurements such as He I-λ5876, Pa11, Ca II-λ8542, and O I-λ7773 & λ8446 (Muzerolle et al., 1998). Model profiles suggest the formation of these lines in the infall zone.

Our next goal should be to compare fluctuations in continuum excess simultaneously to those of Ca II-λ8662 fluxes and Hα 10% width. If changes in these accretion signatures are well correlated, it would further argue for a physical connection between these line emissions and material inflow, and justify their use as measures of accretion rate. Our current spectra are too noisy to accurately measure the continuum excess, and we would require spectra with S/N $\gtrsim$ 100. In addition, the analysis must be taken with some precautions. Gahm et al. (2008) shows that for some stars, when veiling becomes high, the photospheric lines become filled-in by line emission, which produces large veiling factors unrelated to changes in any continuous emission from shocked regions.

5.3 Multiplicity

Eventually, the inner disk clears and accretion shuts off. An open question is why the time at which accretion stops is so different for different stars. One suggestion is that some stars have close companions, which truncate the stellar disk and restrict further inflow from possible circumbinary disks. Companions are prevalent among young populations. Thus, to fully understand star formation processes, it is important to determine the frequency and physical properties of these multiple systems.

The observed fraction of T Tauri stars with spectroscopic companions in our sample does not depend on stellar mass. This result contrasts those of imaging multiplicity surveys (e.g. Kraus & Hillenbrand, 2007; Lafrenière et al., 2008) where there is an observed trend of increasing wide binary fraction with increasing primary mass. One suggestion is that perhaps primary mass is important for binaries with wide separations because of dynamical interactions within the cluster. Dynamical interactions can only eject companions if there is sufficient kinetic energy. Moreover, the kinetic energy of a passing star must be greater than the gravitational binding energy of the binary for break up to occur. Binding energy is proportional to primary mass, so higher mass stars are more likely than their lower mass counterparts to hold onto their companions. However, companions in

tight orbits are so strongly bound to their primary star that disruption from dynamical interaction is unlikely regardless of the primary mass.

Primary mass becomes important at binary separations when the total energy of the binary system is comparable to the kinetic energy of a passing star. By equating the energies, we get the following relation for this transitional binary separation distance r

$$r = \frac{M_1}{M_3}\frac{GM_2}{v^2} \tag{5.2}$$

where M_1, M_2 and M_3 are the masses of the primary, secondary and passing star, and v is the relative velocity of the encounter. We can estimate the typical encounter velocity in our sample by examining the velocity dispersion of the clusters. The radial velocity dispersions $\sigma_{\rm RV}$ of Chamaeleon I and Taurus-Auriga are $1.7\,{\rm km\,s^{-1}}$ and $3.6\,{\rm km\,s^{-1}}$, respectively. If we assume three-dimensional symmetry, then the average velocity between stars is $(4/\sqrt{\pi})\,\sigma_{\rm RV}$ which amounts to $\sim$$3.8\,{\rm km\,s^{-1}}$ and $\sim$$8.1\,{\rm km\,s^{-1}}$ for Cha I and Tau-Aur, respectively. Applying these values to Eq. 5.2 and assuming $M_1/M_3 \sim 1$, we find primary mass becomes important to ejection at binary separations of $\sim 63\,(M_2/M_\odot)\,{\rm AU}$ in Chamaeleon I, and $\sim 14\,(M_2/M_\odot)\,{\rm AU}$ in Taurus-Auriga. These separations are in the regime of imaging surveys.

Although scattering events are possible for binaries with separations of tens of AU in Cha I and Tau-Aur, the likelihood of an encounter depends on the cluster densities of the star forming regions. At current densities of $<100\,{\rm pc^{-3}}$, the interaction timescale for a typical wide binary in Cha I and Tau-Aur is on the order of a few Gyr. Moreover, the interaction timescale only becomes comparable to the current cluster age for binaries with separations of $\gtrsim 10^4\,{\rm AU}$. Visual binaries with separations much less than this show a mass dependence. Therefore, if dynamical interaction is a major source of the mass dependence of wide binaries, then those stars must have emerged from subgroups with stellar densities several orders of magnitude higher than their current sparse environment.

There is observational evidence that stellar density may not strongly influence the frequency of wide binaries. The wide binary frequency in the periphery of the ONC is similar to that in the core, where stellar densities are two orders of magnitude higher (Köhler et al., 2006). Furthermore, both wide binary frequencies in the ONC are several times lower than those of Chamaeleon I and Taurus-Auriga. If the initial binary fractions in these regions were similar, we would expect a much higher number of binaries in the

ONC periphery than observed. Aside from the dense subgroup scenario mentioned above, one possible explanation is that the initial binary frequency differs significantly between star forming regions. This suggests that the binary formation rate is influenced by environmental conditions.

Bibliography

Alencar, S. H. P., & Batalha, C. 2002, ApJ, 571, 378

Alencar, S. H. P., Basri, G., Hartmann, L., & Calvet, N. 2005, A&A, 440, 595

Alexander, R. D., & Armitage, P. J. 2006, ApJ, 639, L83

Appenzeller, I., & Mundt, R. 1989, A&A Rev., 1, 291

Armitage, P. J., Clarke, C. J., & Palla, F. 2003, MNRAS, 342, 1139

Azevedo, R., Calvet, N., Hartmann, L., Folha, D. F. M., Gameiro, F., & Muzerolle, J. 2006, A&A, 456, 225

Baraffe, I., Chabrier, G., Allard, F., & Hauschildt, P. H. 1998, A&A, 337, 403

Batalha, C., Lopes, D. F., & Batalha, N. M. 2001, ApJ, 548, 377

Bayes, T., Price, R., & Canton, J. 1763, Philosophical Transactions of the Royal Society of London, 53, 370

Beichman, C. A., Myers, P. C., Emerson, J. P., Harris, S., Mathieu, R., Benson, P. J., & Jennings, R. E. 1986, ApJ, 307, 337

Bernstein, R., Shectman, S. A., Gunnels, S. M., Mochnacki, S., & Athey, A. E. 2003, Instrument Design and Performance for Optical/Infrared Ground-based Telescopes. Edited by Iye, 4841, 1694

Bertout, C. 1989, ARA&A, 27, 351

Boden, A. F., Torres, G., Sargent, A. I., Akeson, R. L., Carpenter, J. M., Boboltz, D. A., Massi, M., Ghez, A. M., Latham, D. W., Johnston, K. J., Menten, K. M., & Ros, E. 2007, ApJ, 670, 1214

Boden, A. F., Akeson, R. L., Sargent, A. I., Carpenter, J. M., Ciardi, D. R., Bary, J. S., & Skrutskie, M. F. 2009, ApJ, 696, L111

Bodenheimer, P. 1995, ARA&A, 33, 199

Bouvier, J., Cabrit, S., Fernandez, M., Martin, E. L., & Matthews, J. M. 1993, A&A, 272, 176

Bouvier, J., Covino, E., Kovo, O., Martin, E. L., Matthews, J. M., Terranegra, L., & Beck, S. C. 1995, A&A, 299, 89

Bouvier, J., Alencar, S. H. P., Harries, T. J., Johns-Krull, C. M., & Romanova, M. M. 2007, Protostars and Planets V, 479

Branch, D. 1976, ApJ, 210, 392

Brandeker, A., Liseau, R., Artymowicz, P., & Jayawardhana, R. 2001, ApJ, 561, L199

Brandeker, A., Jayawardhana, R., & Najita, J. 2003, AJ, 126, 2009

Brandeker, A., Jayawardhana, R., Khavari, P., Haisch, K. E., & Mardones, D. 2006, ApJ, 652, 1572

Brandner, W., & Zinnecker, H. 1997, A&A, 321, 220

Briceño, C., Luhman, K. L., Hartmann, L., Stauffer, J. R., & Kirkpatrick, J. D. 2002, ApJ, 580, 317

Camenzind, M. 1990, RvMA, 3, 234

Cieza, L., & Baliber, N. 2006, ApJ, 649, 862

—. 2007, ApJ, 671, 605

Clarke, C. J., & Bouvier, J. 2000, MNRAS, 319, 457

Clarke, C. J., Gendrin, A., & Sotomayor, M. 2001, MNRAS, 328, 485

Clarke, C. J., & Pringle, J. E. 2006, MNRAS, 370, L10

Correia, S., Zinnecker, H., Ratzka, T., & Sterzik, M. F. 2006, A&A, 459, 909

Damjanov, I., Jayawardhana, R., Scholz, A., Ahmic, M., Nguyen, D. C., Brandeker, A., & van Kerkwijk, M. H. 2007, ApJ, 670, 1337

D'Antona, F., & Mazzitelli, I. 1997, Memorie della Societa Astronomia Italiana, 68, 807

Delgado-Donate, E. J., Clarke, C. J., Bate, M. R., & Hodgkin, S. T. 2004, MNRAS, 351, 617

Duchêne, G., Bouvier, J., & Simon, T. 1999, A&A, 343, 831

Duchêne, G., Ghez, A. M., McCabe, C., & Weinberger, A. J. 2003, ApJ, 592, 288

Duchêne, G., Delgado-Donate, E., Haisch, K. E., Loinard, L., & Rodríguez, L. F. 2007, Protostars and Planets V, 379

Dullemond, C. P., Natta, A., & Testi, L. 2006, ApJ, 645, L69

Duquennoy, A., & Mayor, M. 1991, A&A, 248, 485

Edwards, S., Strom, S. E., Hartigan, P., Strom, K. M., Hillenbrand, L. A., Herbst, W., Attridge, J., Merrill, K. M., Probst, R., & Gatley, I. 1993, AJ, 106, 372

Eggleton, P. P. 1983, ApJ, 268, 368

Fallscheer, C., & Herbst, W. 2006, ApJ, 647, L155

Fazio, G. G., Hora, J. L., Allen, L. E., Ashby, M. L. N., Barmby, P., Deutsch, L. K., Huang, J.-S., Kleiner, S., Marengo, M., Megeath, S. T., Melnick, G. J., Pahre, M. A., Patten, B. M., Polizotti, J., Smith, H. A., Taylor, R. S., Wang, Z., Willner, S. P., Hoffmann, W. F., Pipher, J. L., Forrest, W. J., McMurty, C. W., McCreight, C. R., McKelvey, M. E., McMurray, R. E., Koch, D. G., Moseley, S. H., Arendt, R. G., Mentzell, J. E., Marx, C. T., Losch, P., Mayman, P., Eichhorn, W., Krebs, D., Jhabvala, M., Gezari, D. Y., Fixsen, D. J., Flores, J., Shakoorzadeh, K., Jungo, R., Hakun, C., Workman, L., Karpati, G., Kichak, R., Whitley, R., Mann, S., Tollestrup, E. V., Eisenhardt, P., Stern, D., Gorjian, V., Bhattacharya, B., Carey, S., Nelson, B. O., Glaccum, W. J., Lacy, M., Lowrance, P. J., Laine, S., Reach, W. T., Stauffer, J. A., Surace, J. A., Wilson, G., Wright, E. L., Hoffman, A., Domingo, G., & Cohen, M. 2004, ApJS, 154, 10

Fernandez, M., & Eiroa, C. 1996, A&A, 310, 143

Fischer, D. A., & Marcy, G. W. 1992, ApJ, 396, 178

Frank, J., King, A. R., & Raine, D. J. 2002, Accretion Power in Astrophysics

Gahm, G. F., Walter, F. M., Stempels, H. C., Petrov, P. P., & Herczeg, G. J. 2008, A&A, 482, L35

Ghez, A. M., Neugebauer, G., & Matthews, K. 1993, AJ, 106, 2005

Ghez, A. M., McCarthy, D. W., Patience, J. L., & Beck, T. L. 1997a, ApJ, 481, 378

Ghez, A. M., White, R. J., & Simon, M. 1997b, AJ, 490, 353

Goodwin, S. P., Whitworth, A. P., & Ward-Thompson, D. 2004, A&A, 414, 633

Grankin, K. N., Melnikov, S. Y., Bouvier, J., Herbst, W., & Shevchenko, V. S. 2007, A&A, 461, 183

Gray, D. F. 2005, The Observation and Analysis of Stellar Photospheres

Gregory, S. G., Jardine, M., Simpson, I., & Donati, J.-F. 2006, MNRAS, 371, 999

Guenther, E. W., Esposito, M., Mundt, R., Covino, E., Alcalá, J. M., Cusano, F., & Stecklum, B. 2007, A&A, 467, 1147

Gullbring, E., Hartmann, L., Briceno, C., & Calvet, N. 1998, ApJ, 492, 323

Hartigan, P., Hartmann, L., Kenyon, S., Hewett, R., & Stauffer, J. 1989, ApJS, 70, 899

Hartigan, P., Kenyon, S. J., Hartmann, L., Strom, S. E., Edwards, S., Welty, A. D., & Stauffer, J. 1991, ApJ, 382, 617

Hartmann, L. 2002, ApJ, 566, L29

—. 2009, Accretion Processes in Star Formation

Herbig, G. H. 1960, ApJS, 4, 337

—. 1962, Adv. Astr. Astrophys., 1, 47

Herbst, W., Herbst, D. K., Grossman, E. J., & Weinstein, D. 1994, AJ, 108, 1906

Herbst, W., Bailer-Jones, C. A. L., Mundt, R., Meisenheimer, K., & Wackermann, R. 2002, A&A, 396, 513

Herbst, W., Eislöffel, J., Mundt, R., & Scholz, A. 2007, Protostars and Planets V, 297

Herczeg, G. J., & Hillenbrand, L. A. 2008, ApJ, 681, 594

Hoaglin, D. C., Mosteller, F., & Tukey, J. W. 2000, 472

Huélamo, N., Figueira, P., Bonfils, X., Santos, N. C., Pepe, F., Gillon, M., Azevedo, R., Barman, T., Fernández, M., di Folco, E., Guenther, E. W., Lovis, C., Melo, C. H. F., Queloz, D., & Udry, S. 2008, A&A, 489, L9

Huerta, M., Johns-Krull, C. M., Prato, L., Hartigan, P., & Jaffe, D. T. 2008, ApJ, 678, 472

Ireland, M. J., & Kraus, A. L. 2008, ApJ, 678, L59

Jayawardhana, R., Mohanty, S., & Basri, G. 2003, ApJ, 592, 282

Jayawardhana, R., Coffey, J., Scholz, A., Brandeker, A., & van Kerkwijk, M. H. 2006, ApJ, 648, 1206

Jeans, J. H. 1902, Philosophical Transactions of the Royal Society of London. Series A, 199, 1

Johns, C. M., & Basri, G. 1995, AJ, 109, 2800

Joy, A. H. 1945, ApJ, 102, 168

Kant, I. 1755, Allgemeine Naturgeschichte und Theorie des Himmels

Knott, G. 1891, The Observatory, 14, 97

Koenigl, A. 1991, ApJ, 370, L39

Köhler, R., & Leinert, C. 1998, A&A, 331, 977

Köhler, R., Petr-Gotzens, M. G., McCaughrean, M. J., Bouvier, J., Duchêne, G., Quirrenbach, A., & Zinnecker, H. 2006, MNRAS, 458, 461

Kraus, A. L., & Hillenbrand, L. A. 2007, ApJ, 662, 413

Lafrenière, D., Jayawardhana, R., Brandeker, A., Ahmic, M., & van Kerkwijk, M. H. 2008, ApJ, 683, 844

Lamm, M. H., Mundt, R., Bailer-Jones, C. A. L., & Herbst, W. 2005, A&A, 430, 1005

Leinert, C., Zinnecker, H., Weitzel, N., Christou, J., Ridgway, S. T., Jameson, R., Haas, M., & Lenzen, R. 1993, A&A, 278, 129

Littlefair, S. P., Naylor, T., Burningham, B., & Jeffries, R. D. 2005, Protostars and Planets V, 8359

Luhman, K. L. 2004a, ApJ, 602, 816

—. 2004b, ApJ, 617, 1216

Lynden-Bell, D. 1977, Star Formation; Proceedings of the Symposium, 75, 291

Makidon, R. B., Rebull, L. M., Strom, S. E., Adams, M. T., & Patten, B. M. 2004, AJ, 127, 2228

Martín, E. L., Guenther, E., Osorio, M. R. Z., Bouy, H., & Wainscoat, R. 2006, ApJ, 644, L75

Mathieu, R. D. 1994, A&A Rev., 32, 465

Mathieu, R. D., Stassun, K., Basri, G., Jensen, E. L. N., Johns-Krull, C. M., Valenti, J. A., & Hartmann, L. W. 1997, AJ, 113, 1841

Mathieu, R. D., Ghez, A. M., Jensen, E. L. N., & Simon, M. 2000, Protostars and Planets IV, 703

Matt, S., & Pudritz, R. E. 2005, ApJ, 632, L135

Matt, S., & Pudritz, R. 2008, 14th Cambridge Workshop on Cool Stars, 384, 339

Melo, C. H. F. 2003, A&A, 410, 269

Mohanty, S., Jayawardhana, R., & Basri, G. 2005, ApJ, 626, 498

Mundt, R., Walter, F. M., Feigelson, E. D., Finkenzeller, U., Herbig, G. H., & Odell, A. P. 1983, ApJ, 269, 229

Muzerolle, J., Hartmann, L., & Calvet, N. 1998, AJ, 116, 455

Muzerolle, J., Calvet, N., & Hartmann, L. 2001, ApJ, 550, 944

Muzerolle, J., Hillenbrand, L., Calvet, N., Briceño, C., & Hartmann, L. 2003, ApJ, 592, 266

Natta, A., Testi, L., Muzerolle, J., Randich, S., Comerón, F., & Persi, P. 2004, A&A, 424, 603

Nguyen, D. C., Scholz, A., van Kerkwijk, M. H., Jayawardhana, R., & Brandeker, A. 2009a, ApJ, 694, L153

Nguyen, D. C., Jayawardhana, R., van Kerkwijk, M. H., Brandeker, A., Scholz, A., & Damjanov, I. 2009b, ApJ, 695, 1648

Nidever, D. L., Marcy, G. W., Butler, R. P., Fischer, D. A., & Vogt, S. S. 2002, ApJS, 141, 503

Padoan, P., Kritsuk, A., Norman, M. L., & Nordlund, Å. 2005, ApJ, 622, L61

Preibisch, T., & Smith, M. D. 1997, A&A, 322, 825

Rebull, L. M., Hillenbrand, L. A., Strom, S. E., Duncan, D. K., Patten, B. M., Pavlovsky, C. M., Makidon, R., & Adams, M. T. 2000, AJ, 119, 3026

Rebull, L. M., Wolff, S. C., Strom, S. E., & Makidon, R. B. 2002, AJ, 124, 546

Rebull, L. M., Wolff, S. C., & Strom, S. E. 2004, AJ, 127, 1029

Rebull, L. M., Stauffer, J. R., Megeath, S. T., Hora, J. L., & Hartmann, L. 2006, ApJ, 646, 297

Reipurth, B., Lindgren, H., Nordstrom, B., & Mayor, M. 1990, A&A, 235, 197

Reipurth, B., & Zinnecker, H. 1993, A&A, 278, 81

Rucinski, S. 1999, Precise Stellar Radial Velocities, 185, 82

Rydgren, A. E., Strom, S. E., & Strom, K. M. 1976, ApJS, 30, 307

Scholz, A., Jayawardhana, R., & Brandeker, A. 2005, ApJ, 629, L41

Scholz, A., & Jayawardhana, R. 2006, ApJ, 638, 1056

Scholz, A., Coffey, J., Brandeker, A., & Jayawardhana, R. 2007, ApJ, 662, 1254

Sherry, W. H., Walter, F. M., & Wolk, S. J. 2004, AJ, 128, 2316

Shu, F. H. 1977, ApJ, 214, 488

Shu, F. H., Adams, F. C., & Lizano, S. 1987, ARA&A, 25, 23

Shu, F., Najita, J., Ostriker, E., Wilkin, F., Ruden, S., & Lizano, S. 1994, ApJ, 429, 781

Simon, M., Ghez, A. M., Leinert, C., Cassar, L., Chen, W. P., Howell, R. R., Jameson, R. F., Matthews, K., Neugebauer, G., & Richichi, A. 1995, ApJ, 443, 625

Stassun, K. G., Mathieu, R. D., Mazeh, T., & Vrba, F. J. 1999, AJ, 117, 2941

Steffen, A. T., Mathieu, R. D., Lattanzi, M. G., Latham, D. W., Mazeh, T., Prato, L., Simon, M., Zinnecker, H., & Loreggia, D. 2001, AJ, 122, 997

Stelzer, B., Scholz, A., & Jayawardhana, R. 2007, ApJ, 671, 842

Terebey, S., Shu, F. H., & Cassen, P. 1984, ApJ, 286, 529

Walter, F. M., Brown, A., Mathieu, R. D., Myers, P. C., & Vrba, F. J. 1988, AJ, 96, 297

White, R. J., & Basri, G. 2003, ApJ, 582, 1109

Woitas, J. 2003, A&A, 406, 685

Wolff, S. C., Strom, S. E., & Hillenbrand, L. A. 2004, ApJ, 601, 979

Zucker, S., & Mazeh, T. 1994, ApJ, 420, 806